UC Berkeley
UC Berkeley Electronic Theses and Dissertations

Title
Kinetic Inductance Detectors for Dark Matter Searches

Permalink
https://escholarship.org/uc/item/7q85w8vj

Author
Daal, Miguel Demetrius

Publication Date
2015

Peer reviewed|Thesis/dissertation

eScholarship.org Powered by the California Digital Library
University of California

Kinetic Inductance Detectors for Dark Matter Searches

by

Miguel Demetrius Daal

A dissertation submitted in partial satisfaction of the
requirements for the degree of
Doctor of Philosophy

in

Physics

in the

Graduate Division

of the

University of California, Berkeley

Committee in charge:

Professor Bernard Sadoulet, Chair
Professor Adrian T Lee
Professor Leo Blitz

Summer 2015

Kinetic Inductance Detectors for Dark Matter Searches

Copyright 2015
by
Miguel Demetrius Daal

Abstract

Kinetic Inductance Detectors for Dark Matter Searches

by

Miguel Demetrius Daal

Doctor of Philosophy in Physics

University of California, Berkeley

Professor Bernard Sadoulet, Chair

Decades of astrophysical observations suggest that 23% of the mass energy of the universe is dark. Meanwhile, particle physics theories favor the existence of a stable and weakly interacting particle, which has yet to be detected. These realities combine to formulate a very well motivated particle dark matter candidate, which was produced in the early universe and still lingers in abundance today. The expectation of a small weak interaction cross-section enables the instrumentation of experiments designed to discover the nature of the dark matter which continues to be an overarching question of cosmology. A detector for this dark matter candidate senses energy from occasional collisions between the dark matter and atomic nuclei; the more nuclei in the detector, the greater its sensitivity to dark matter. The detectors of the Cryogenic Dark Matter Search (CDMS) measure phonons and charge emanating from recoiling germanium nuclei. Its phonon sensors, though exquisitely sensitive, are relatively complicated to fabricate and deploy. Responding to the scientific imperative to increase dark matter sensitivity, we look for a simpler phonon sensor technology. Kinetic inductance based phonon sensors (KIPS) are superconducting thin film microwave frequency resonant circuits. Phonon energy impinging on the film alters its surface impedance, which alters the characteristics of the resonance. KIPS can be made with relatively large, millimeter sized features which makes them easier to fabricate and reduces variations between detectors. This instrumentation focused thesis shows that KIPS can be used as a simple and sensitive phonon sensor for the CDMS detector. KIPS design aspects, competitiveness to the current transition edge phonon sensors, readout considerations and suggestions on how to instrument them in future dark matter experiments will be presented. The broader applicability of KIPS in nuclear non-proliferation and other physics investigations is also discussed.

To my mother

Contents

Contents **ii**

List of Figures **viii**

List of Tables **xii**

1 Cosmology **1**
1.1 Theoretical Framework . . . 1
1.2 Contents of the Universe . . . 4
1.2.1 Radiation, Ω_r . . . 4
1.2.2 Matter, Ω_m . . . 5
1.2.2.1 The Neutrino Density, Ω_ν . . . 5
1.2.2.2 The Baryonic Matter Density, Ω_b . . . 6
1.2.2.3 The Non-Baryonic Matter Density, Ω_{nb} . . . 8
1.2.3 Vacuum Energy, Ω_Λ . . . 11
1.3 Evidence for Cosmic Dark Matter . . . 13
1.3.1 Evidence at Different Scales . . . 13
1.3.2 Baryonic Dark Matter . . . 17
1.3.3 Non-Baryonic Dark Matter . . . 18
1.3.4 Modified Theories of Gravity . . . 19
1.4 Leading Dark Matter Candidates . . . 21
1.4.1 Neutrinos . . . 22
1.4.2 Axions . . . 22
1.4.3 Weakly Interacting Massive Particles . . . 23

2 Dark Matter Detection **27**
2.1 Detection of WIMP dark matter . . . 27
2.1.1 Complementarity . . . 27
2.1.2 Indirect detection experiments . . . 29
2.1.3 Direct detection experiments . . . 31
2.1.3.1 Event rate . . . 32
2.1.3.2 Detection experiments . . . 33

2.1.3.2.1 Silicon and germanium detectors . . . 34
2.1.3.2.2 Oxide semiconductor . . . 36
2.1.3.2.3 Crystal scintillators . . . 37
2.1.3.2.4 Liquified nobles gases . . . 37
2.1.3.2.5 Superheated liquids . . . 38
2.1.3.2.6 Gas target materials . . . 39
2.1.4 Search status . . . 39
2.2 The CDMS experiment . . . 40
2.2.1 Technical challenges for large arrays . . . 41
2.3 Detection of axion dark matter . . . 42
2.3.1 Axion search status . . . 43

3 Kinetic Inductance Phonon Sensors for Dark Matter Detection 46
3.1 Overview of kinetic inductance detectors . . . 46
3.1.1 Kinetic inductance . . . 46
3.1.2 Principle of operation . . . 47
3.1.3 Attractive features of kinetic inductance detectors . . . 47
3.1.4 Applicability to direct detection . . . 48
3.1.5 Detector concept . . . 50
3.2 Material electrodynamics . . . 51
3.2.1 Theoretical frameworks . . . 51
3.2.1.1 Maxwell's equation . . . 52
3.2.1.2 The two-fluid model and the london equations . . . 52
3.2.1.3 BCS theory of superconductivity . . . 53
3.2.1.4 Calculation of the Density of states, N_0 . . . 55
3.2.1.5 Mattis bardeen theory of the anomalous skin effect . . . 55
3.2.2 Conceptual essentials . . . 57
3.2.2.1 Characteristic lengths . . . 57
3.2.2.2 Current-field relations . . . 59
3.2.2.3 The complex conductivity . . . 60
3.2.2.4 The surface impedance . . . 60
3.2.2.5 Surface scattering . . . 61
3.2.3 Example application: normal and superconductors in local limit . . . 61
3.3 Causes of nonlinear behavior . . . 64

4 Analysis of Resonator 68
4.1 Linear Analysis of Shunt-Coupled Resonator . . . 68
4.1.1 Review of transmission line theory . . . 68
4.1.2 Scattering matrix for the coupler, σ_{ij} . . . 72
4.1.3 Scattering matrix for resonator, ϵ_{ij} . . . 73
4.1.4 Scattering matrix for resonator coupled to feedline, S_{ij} . . . 74
4.1.5 Voltage and current amplitudes inside a $\lambda/2$ resonator . . . 74

4.1.6 Computation of coupling quality factor, Q_c . . . 76
4.1.7 Computation of termination quality factor, Q_{trm} . . . 77
4.1.8 Computation of transmission line quality factor, Q_{tl} . . . 77
4.1.9 Approximation of the resonance curve, $S_{21}(f)$ . . . 77
4.1.10 Approximation of resonator internal power, P_{int} . . . 79
4.1.11 Approximation of maximum resonator current, I_{max} . . . 80
4.2 Nonlinear Analysis of Shunt-Coupled Resonator . . . 80
4.2.1 Approach: parameterize $\delta f/f$ in terms of resonator current $|I|^2$ . . . 81
4.2.2 Approach: resonator input amplitude, V_3^-, parameterization . . . 82
4.2.3 Approach: quantum Input Output theory . . . 83
4.2.4 Comparison of approaches . . . 92

5 Detector Design, Fabrication and Readout System 94
5.1 Mask design . . . 94
5.2 Expected losses . . . 97
5.3 Expected kinetic inductance fraction, α . . . 100
5.4 KIDs fabrication . . . 103
5.4.1 Sensor Chip . . . 103
5.4.2 Ground plane chip . . . 108
5.4.2.1 Hexagonal mesh ground plane . . . 109
5.4.2.2 Ground plane porosity . . . 111
5.5 Assembly of device in test box . . . 113
5.6 Connection of test box to readout system . . . 116
5.7 Readout system . . . 120
5.7.1 "Device End" portion of readout system . . . 120
5.7.2 "Digitizer End" ROACH board configuration . . . 124
5.7.3 "Digitizer End" NI digitizer configuration . . . 125
5.7.4 "Digitizer End" network analyzer configuration . . . 125
5.7.5 System noise . . . 126
5.8 Signal estimation . . . 127
5.8.1 Relative sensitivity of trace and ground plane . . . 130

6 Detector Performance Data 132
6.1 Linear Data and Fitting . . . 132
6.1.1 Linear fitting . . . 132
6.1.2 Stepwise fitting . . . 134
6.1.3 Concurrent fitting . . . 136
6.1.4 Data . . . 140
6.1.4.1 Probe power sweeps . . . 140
6.1.4.2 Temperature sweeps . . . 147
6.2 Nonlinear Data and Fitting . . . 151
6.2.1 Least squares fit . . . 151

6.2.2 Determining the resonator amplitude . . . 151
6.3 Nonlinear Data . . . 155
6.3.0.1 Nonlinear Fit to power sweep . . . 155
6.3.0.2 Simulated Data . . . 157

7 Cryogenic methods **161**
7.1 Materials selection . . . 164
7.1.1 Thermal conductivity . . . 164
7.1.1.1 High temperatures . . . 164
7.1.1.2 Low temperatures . . . 164
7.1.1.2.1 Graphite-like materials . . . 165
7.1.1.2.2 Kapton-like materials . . . 166
7.1.1.2.3 Vespel-like materials . . . 168
7.1.1.2.4 Titanium alloys . . . 170
7.1.2 Radio purity . . . 173
7.1.3 Mechanical properties . . . 177
7.1.4 Magnetic properties . . . 180
7.2 Thermomechanical tower design . . . 182
7.3 Cryogenic cabling . . . 190
7.3.1 Scientific requirements . . . 191
7.3.2 Materials selection . . . 191
7.3.3 Considerations for plating and joining . . . 193
7.3.4 Plating . . . 199
7.3.4.1 Bulk parts . . . 199
7.3.4.2 Thin foils . . . 200
7.3.4.2.1 Electroless nickel . . . 200
7.3.4.2.2 Electrolytic nickel . . . 200
7.3.4.2.3 Electrolytic chromium . . . 201
7.3.4.2.4 Electrolytic copper . . . 201
7.3.4.2.5 Electrolytic gold . . . 202
7.3.4.2.6 Thermal evaporated copper and aluminum . . . 202
7.3.4.2.7 Ion vapor deposited aluminum . . . 204
Direct electrolytic copper plate . . . 205
Zincate then electrolytic copper plate . . . 205
Zincate, then nickel flash, then electrolytic copper plate . . . 207
7.3.5 Joining . . . 208
7.3.5.1 Methods Considered . . . 211
7.3.5.1.1 Laser Welding . . . 211
7.3.5.1.2 Diffusion Bonding . . . 211
7.3.5.1.3 Discharge Welding . . . 211
7.3.5.1.4 Ultrasonic Welding . . . 211
7.3.5.1.5 Activate Solder . . . 212

7.3.6 Heat sinking . . . 214
7.3.6.1 Boundary resistance measurement . . . 214
7.3.6.2 Cable Temperature Profile . . . 217
7.3.6.3 Cable power profile . . . 219
7.3.6.4 Sinking heat for electrical components . . . 222
7.3.7 The 4 K to 300 K cable . . . 224
7.3.8 Cable Fabrication . . . 225

8 Technology Applications and Future Work 234
8.1 Conclusions with regard to the KIDs phonon sensors . . . 234
8.2 Alternate flex cable fabrication process . . . 235
8.3 Compression interconnects . . . 235
8.4 Phonon-mediated gamma ray spectrometer for nuclear security applications . 237
8.4.1 Background . . . 237
8.4.2 Detector design features . . . 241
8.4.3 Example Detector Implementation . . . 243
8.4.4 Development requirements . . . 245
8.4.5 Conclusions . . . 246

Bibliography 248

A Quality Factor 270

B Phasors, Time Harmonic Fields and Power 272
B.1 Useful Identities . . . 272
B.2 Phasors . . . 273
B.3 Maxwell's In Phasor Form . . . 274
B.4 Power Dissipation and Poynting's Theorem . . . 275
B.5 Time-averaged quantities . . . 277

C Thermal Conductivity Measurements 278
C.1 Setup . . . 278
C.2 Thermal Conductivity Analysis Methods . . . 280
C.2.1 Method 1 . . . 280
C.2.2 Method 2 . . . 280
C.2.3 Method 3 . . . 281
C.2.4 Errors . . . 281
C.3 Materials Measured . . . 282
C.3.1 Polyimide Base Materials . . . 282
C.3.1.1 Composite Bonding Films . . . 282
C.3.1.1.1 Pyralux LF . . . 282
C.3.1.1.2 Nikaflex CISV . . . 282

C.3.1.2 Cirlex . . . 283
C.3.1.3 Vespel . . . 283
C.3.1.3.1 SP-22 . . . 285
C.3.1.3.2 SCP-5000 . . . 285
C.3.1.3.3 SCP-5050 . . . 286
C.3.2 Titanium Alloys . . . 287
C.3.2.1 Ti-15V-3Cr-3Sn-3Al Alloy . . . 289
C.3.2.1.1 Plate . . . 290
C.3.2.1.2 Foil . . . 290
C.3.2.1.3 Rod . . . 291
C.3.2.2 Ti 21S Alloy . . . 292
C.3.2.2.1 Plate . . . 293
C.3.2.3 Nb-47Ti Alloy . . . 294
C.3.2.3.1 Foil . . . 295
C.3.2.4 Nitinol Alloy . . . 295
C.3.2.4.1 Plate . . . 296
C.3.3 Graphites . . . 296
C.3.3.1 Mersen 2020 Graphite, $\perp$ to grain . . . 296
C.3.3.2 Mersen 2020 Graphite, $\parallel$ to grain . . . 297
C.3.4 Graphlite CFRP . . . 298
C.4 Fit Parameters . . . 300

D Part Drawings **302**
D.1 Thermal resistance test device . . . 303
D.2 Transition pad . . . 304
D.3 KIDs test box . . . 305
D.4 Tower standoffs . . . 308
D.5 Coaxial vacuum passthrough . . . 312

List of Figures

1.1 Cosmological timeline . . . 2
1.2 Abundances of light element predicted by big bang nucleosynthesis . . . 7
1.3 Cosmic microwave background polarization and temperature anisotropy . . . 9
1.4 Cosmic microwave background temperature-temperature power spectrum . . . 11
1.5 Gravitation lensing diagram. . . . 16
1.6 Artist visualization of dark matter halo . . . 19
1.7 Bullet cluster in x-ray, weak lensing and visible signal channels . . . 20
1.8 Artist visualization of bullet cluster collision sequence . . . 21
1.9 Boltzmann solution for WIMP decoupling . . . 25

2.1 Complementarity in dark matter research . . . 28
2.2 Direct detection in a solid target material . . . 30
2.3 Underground direct detection experiment . . . 31
2.4 WIMPS passing through the Earth . . . 33
2.5 Ionization and phonon collection in a CDMS detector . . . 35
2.6 Nucleation of bubbles in superheated liquid . . . 38
2.7 Limit plot for current and future WIMP direction detection experiments . . . 40
2.8 Fiducial volume and event discrimination . . . 42
2.9 Limit plot for current and future Axion direction detection experiments . . . 43

3.1 Separation of function . . . 50
3.2 An electromagnetic plane wave at normal incidence with conductor. [2] . . . 62
3.3 Visualization of superconducting grains . . . 65
3.4 Illustration of bulk vortex penetration . . . 67

4.1 Network diagram of $\lambda/2$ resonator coupled to feedline. . . . 69
4.2 Lumped element model of transmission line . . . 70
4.3 An N-port microwave network . . . 71
4.4 Reflected waves inside a $\lambda/2$ resonator . . . 75
4.5 Network diagram of nonlinear $\lambda/2$ resonator shunt-coupled to feedline . . . 86

5.1 Mask pattern for a sensor chip . . . 95
5.2 Kinetic inductance fraction with trace and ground plane contributions . . . 101

5.3 Kinetic inductance fractions for smaller gap and thinner films 102
5.4 Hexagonal mesh ground plane 110
5.5 SEM views of apparently porous ground planes 112
5.6 Block diagram of device press 117
5.7 KIDs readout system configurations 121
5.7 KIDs readout system configurations 122
5.8 Insertion loss of readout system cabling 123
5.9 Measured system noise at base temperature 127
5.10 Relative response of microstrip trace and ground plane 131

6.1 Linear versus nonlinear resonator 133
6.2 Flow chart of linear resonance fitting procedure 134
6.3 Geometry of the resonance loop 137
6.4 Demonstration of Complete Fit 139
6.5 Internal quality factor versus probe power 141
6.6 Internal quality factor versus current density and internal power 143
6.7 Coupling quality factor versus probe power 144
6.8 Fractional frequency shift versus probe power 146
6.9 Fractional frequency shift versus probe power and temperature 148
6.10 Internal quality factor versus probe power and temperature 150
6.11 Full nonlinear solution for 64 µm resonator 154
6.12 Nonlinear fit to power sweep of 64 µm resonator 156
6.13 Linear fits to simulated nonlinear data 159
6.14 Linear fits to simulated nonlinear data 160

7.1 SuperCDMS SNOLAB Tower 163
7.2 Temperature material dependence of Lorenz number 165
7.3 Thermal conductivity of graphite-like materials 166
7.4 Thermal conductivity of kapton-like materials 168
7.5 Thermal conductivity of vespel-like materials 170
7.6 Thermal conductivity of selected titanium alloys 171
7.7 Thermal conductivity normalized by Young's modulus of selected materials . . . 178
7.8 Carbon fiber types grouped by mechanical properties 180
7.9 SQUID array modulation in presence of nickel 181
7.10 Structures considered for tower standoffs 183
7.11 Tower standoff test modules 187
7.12 Comparison of thermal and measured mechanical properties for all the tower standoff designs studied 188
7.13 Loading conditions for the tower standoffs 189
7.14 SNOLAB tower flex cable design flowchart. 190
7.15 Thermal conductivity of cable materials 192

7.17 Gibbs free energies of metal oxide formation in kilojoule per mole of oxygen. Plot quantifies how energetically favorable it is for various metals to form oxides at a given temperature and at room pressure. Metals may also form oxides that are not present on this plot. This plot is also known as a Ellingham diagram. 194
7.16 Adhesion between layers of different materials 196
7.18 Time temperature transformation diagram for Ti 15-3-3-3 197
7.19 Equilibrium phase diagrams for: Nb-Al, Ti-Al, Nb-Cu and Ti-Cu 198
7.20 Nb-47Ti electroplated with copper 201
7.21 Heat treatment process for electroplated copper on Ti 15-3-3-3. The furnace is initially filled with argon gas. About five minutes prior to reaching 400 °C, the argon is pumped out leaving a residual pressure of $1 \cdot 10^{-5}$ torr for the remainder of the process. After 10 min at 400 °C, heating is turned off and the furnace cools at a rate of approximately $-2\,°C/\,min$. 202
7.22 Copper plated Ti 15-3-3-3 foil under several heat treatment conditions 203
7.23 Nb-47Ti with thermal evaporated Al and Cu 205
7.24 Nb-47Ti plated with Al and then Cu 206
7.25 Nb-47Ti plated with Al and then Cu 207
7.26 Ti 15-3-3-3 plated with Al and then Cu 208
7.27 Ultrasonic spot weld of Ti 15-3-3-3 to copper foils 211
7.28 Activated Solder on Nb-47Ti 212
7.29 Diagram of cable heat sink section 214
7.30 Thermal resistance test device concept 215
7.31 Microscope view of thermal resistance test device 216
7.32 Cable heat sink thermal resistance data 217
7.33 Temperature profile of phonon cable, with heat sinks 220
7.34 Thermal power profile of phonon cable, with heat sinks 222
7.35 Diagram of 4 K to 300 K cable 224

8.1 Alternate flex cable fabrication process 236
8.2 "Fuzz Button" Connectors 237
8.3 NIST microcalorimeter resolution compared to HPGe 239
8.4 Cross section closeup of proposed KIDs radiation detector 240
8.5 Position sensitivity in KIDs radiation detector 242
8.6 Pulse from CDMS detector exhibiting reverberation 244

C.1 Thermal conductivity measurement setup 279
C.2 Pyralux LF thermal conductivity 283
C.3 Nikaflex CISV thermal conductivity 284
C.4 Cirlex thermal conductivity 285
C.5 Vespel SP-22 thermal conductivity 286
C.6 Vespel SCP-5000 thermal conductivity 287
C.7 Vespel SCP-5050 thermal conductivity 288

C.8 Vespel SCP-5050 thermal conductivity, extended temperature range 289
C.9 Beta stabilization in titanium alloys 290
C.10 Ti-15V-3Cr-3Sn-3Al plate thermal conductivity 291
C.11 Ti-15V-3Cr-3Sn-3Al foil thermal conductivity 292
C.12 Ti-15V-3Cr-3Sn-3Al rod thermal conductivity 293
C.13 Ti 21s plate thermal conductivity 294
C.14 Nb-47Ti foil thermal conductivity 295
C.15 Nitinol alloy plate thermal conductivity 297
C.16 Mersen 2020 Graphite thermal conductivity, $\perp$ to grain 298
C.17 Mersen 2020 Graphite thermal conductivity, $\parallel$ to grain 299
C.18 Graphlite CFRP thermal conductivity 300

D.1 Thermal resistance sample fabrication drawing 303
D.2 Microstrip to coplanar waveguide transition pad with dimensions 304
D.3 KIDs test box top fabrication drawing 305
D.4 KIDs test box bottom fabrication drawing 306
D.5 Fabricated KIDs test box 307
D.6 Ti 15-3-3-3 X-frame fabrication drawing 308
D.7 Ti 15-3-3-3 hexipod member fabrication drawing 309
D.8 Graphlite rod X-frame fabrication drawing and gluing fixture 310
D.9 Graphlite rod hexipod member fabrication drawing 311
D.10 Coaxial vacuum passthrough fabrication drawing 312
D.11 Coaxial vacuum passthrough in preparation for use. 313

List of Tables

2.1 Evolution of CDMS experiment 45

3.1 Approximate parameter values for the local dirty limit 64

4.1 Relationships between nonlinear resonator parameters 93

5.1 Sensor chip parameters 97
5.2 Estimated and simulated microstrip losses 99
5.3 KIDs sensor chip fabrication procedure 107
5.4 Sensor chip wafer summary 108
5.5 Ground plane wafer summary 109
5.6 Mounting KIDs device in test box 116
5.7 Installation of test box into KIDs readout system 119
5.8 "S8" signal estimate parameter assumptions 129
5.9 "S8" signal estimates 129

6.1 Example χ^2 obtained using linear fitting algorithm 138
6.2 Nonlinear fit parameters 157

7.1 A few SuperCDMS SNOLAB cryogenic and electrical specifications 161
7.2 Radioactivity of potential cryogenic materials 174
7.2 Radioactivity of potential cryogenic materials 175
7.2 Radioactivity of potential cryogenic materials 176
7.3 Mechanical properties of selected materials 179
7.4 Tower mechanical specifications 182
7.5 Comparison of thermal and measured mechanical properties for all the tower standoff designs studied. 186
7.6 Plating methods tried for primary adhesion to Ti alloy foils 200
7.7 Methods tried for joining Ti alloy foils with other foils 210
7.8 Effect of different stiffener assumptions on phonon cable heat sinking 221
7.9 Raise in temperature of phonon cable due to power dissipation of components . 223
7.10 Trace scenarios for 4 K to 300 K cable 225
7.11 Phonon cable fabrication procedure 232

8.1 Low temperature contact resistance of fuzz button 238
8.2 Radiation detector technology comparison 240
8.3 Design parameters for proposed KIDs radiation detector 245

C.1 Thermal conductivity fit parameters 301

Acknowledgments

I want to thank my advisor for teaching and supporting me. I also want to thank my family for kindling my interest in science and encouraging me to pursue it.

Preface

This document is very much a rough draft for potential future work.

Chapter 1

Cosmology

We adopt the framework of Big Bang cosmology, which relies on Standard Model physics, general relativity, and the assumption of an initial instant of rapid spatial inflation. Observations of the universe are consistent with this framework. They tell a story of a hot early universe, which cooled and expanded; as the universe cooled all the known particles precipitated out; they clumped together to form structures like stars, galaxies and clusters of galaxies, Figure 1.1. The behavior of these structures suggests the abundant existence of unknown particles and energy. Determining the nature of the unknown particles, which we call dark matter, is the focus of this chapter and the guiding impetus for the rest of work described in this thesis.

1.1 Theoretical Framework

Here we present the basic equations that describe the structure and evolution of the universe [52, 135]. Astrophysical observations show that we live in an expanding universe. This means that distances between objects such as galaxies and clusters of galaxies are increasing. Data from Edwin Hubble showed us that for the not so distant universe at a given time, t, objects with at a radius $r(t)$ are receding away from us at a speed $v(t)$ proportional to their distance, $r(t)$, according to what is now known as the *Hubble Law*,

$$v(t) = H(t) \cdot r(t). \tag{1.1}$$

$H(t)$ is the Hubble constant its present day value is $H_0 = (67.6 \pm 0.6)\,\mathrm{km\,s^{-1}\,Mpc^{-1}} = 100h\ \mathrm{km\,s^{-1}\,Mpc^{-1}}$ [144], that is kilometers per second per megaparsec[1]. Here and throughout this chapter, the subscript 0 refers to value of a quantity today.

It is convenient to remove the effect of the Hubble recession when speaking about distances. The resulting stationary distance, co-moving with the expansion of the universe, is

[1]Though it varies over the course of a year, the approximate distance between the earth and the sun is defined as one astronomical unit, which is roughly equal to 150 million kilometers. A parsec is the distance at which one astronomical unit subtends an angle of one second of arc, approximately 3.26 light-years

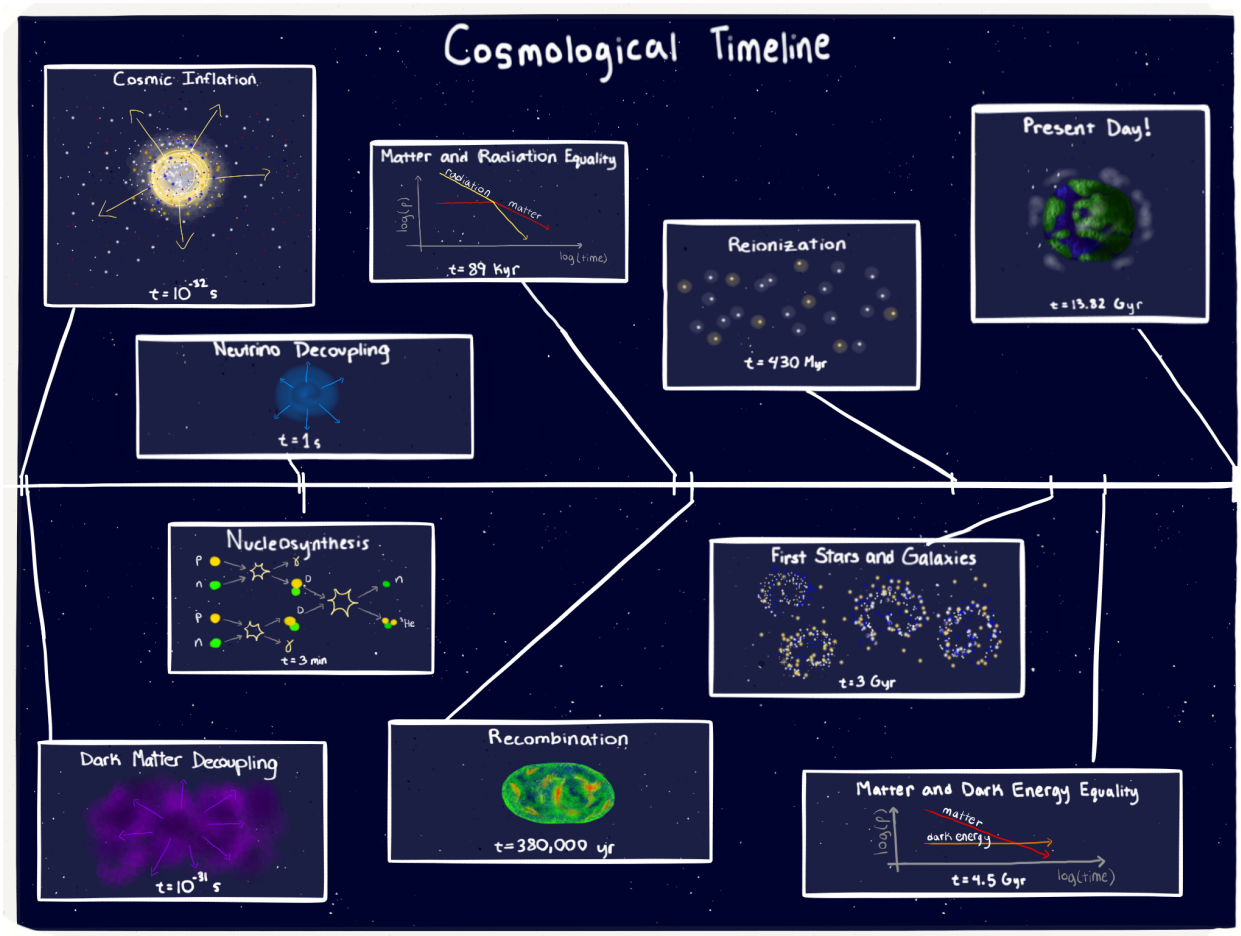


Figure 1.1: A summary of the major events that occurred between present time and the Big Bang, presented in chronological order. We see that the dark matter, which our objective is to detect and characterize, should have been around since very shortly after the big bang. [1]

known as the co-moving distance, $x(t) = x$ and it is related to $r(t)$ as,

$$r(t) = a(t) \cdot x, \tag{1.2}$$

where $a(t)$ is a dimensionless scaling called the scale factor. $a(t)$ describes the evolution of the size of the universe. By convention we define $a(t)|_{t=now} = a_0 = 1$.

Einstein's theory of general relativity connects the geometry and time-evolution of the universe with the distribution and type of its contents. The Einstein equations specify this relationship,

$$G_{\mu\nu} \equiv R_{\mu\nu} - \frac{1}{2} g_{\mu\nu} R = \frac{8\pi G}{c^4} T_{\mu\nu}. \tag{1.3}$$

The right side of the equation contains geometric terms including, the Ricci curvature tensor $R_{\mu\nu}$, the metric $g_{\mu\nu}$, the Ricci scalar curvature R, c is the phase velocity of light, and G is

Newton's constant. The right side contains the energy momentum tensor $T_{\mu\nu}$, whose elements are pressures and densities – quantities arising from the matter-energy constituents of the universe. Both μ and ν index over the three spatial dimensions plus one time dimension in which we live, so equation Equation 1.3 is actually 16 equations but only 10 of them are independent because the tensors are symmetric.

A central assumption of cosmology is that at large enough distance scales, the distribution of energy and matter throughout the universe are homogeneous and isotropic. This is known as the *cosmological principle* and can be stated in many ways such as "the universe looks the same in every direction no matter where you look or who is looking." Invocation of the cosmological principle dramatically simplifies the 10 Einstein equations to two; one of which is the Friedmann equation

$$\left(\frac{\dot{a}}{a}\right)^2 = \frac{8\pi G}{3}\rho - \frac{\kappa c^2}{a^2}. \tag{1.4}$$

Here, a is the scale factor, ρ is a mass-energy density, κ is the spatial curvature of the universe. ρ is considered the sum of the density contributions from various types of matter and energy in the universe $\rho = \sum_i \rho_i$. Usually these component densities are taken as: the matter density (assumed non-relativistic including baryons, non-relativistic neutrinos, electrons, etc.) ρ_m, the radiation density (assumed relativistic including photons, etc.) ρ_r, and the dark energy density ρ_Λ, such that $\rho = \rho_m + \rho_r + \rho_\Lambda$[2]. However these components may be split up further.

In a positively curved universe $\kappa > 0$ initially parallel lines will ultimately intersect, like on the surface of a sphere, a familiar positively curved object. Such a universe is called closed and will ultimately collapse upon itself, in the absence of dark energy. In a negatively curved universe $\kappa < 0$ initially parallel lines will diverge, like on the surface of a saddle, a familiar negatively curved object. Such a universe is called open and, in the absence of dark energy, will accelerate in its expansion isolating its constituent structures by vast distances. A flat universe has $\kappa = 0$ and parallel lines remain parallel. In the absence of dark energy, a flat universe expands at a constant rate forever. Mounting observational evidence suggests our universe is spatially flat.

Equation 1.1 and Equation 1.2 imply that $H = \dot{a}/a$. The value of $\rho = \rho(t)$ which forces $\kappa = 0$ is called the critical critical density, ρ_{cr}. Using Equation 1.4 with $\kappa = 0$ we find that,

$$\rho_{cr}(t) = \frac{3H^2(t)}{8\pi G}. \tag{1.5}$$

This allows us to define the density parameter, Ω, a convenient parameter for quantifying

[2]In the case where $\kappa \neq 0$, one may define a density corresponding to curvature, $\rho_\kappa = -\frac{3H^2(t)\kappa c^2}{8\pi G a^2(t)}$. In which case we need an Ω_κ modifying equation 1.6 to be $1 = \Omega_m(t) + \Omega_r(t) + \Omega_\Lambda(t) + \Omega_\kappa(t) = \Omega(t) + \Omega_\kappa(t)$. A closed, open or flat universe is no longed implied by Ω greater than, less then or equal to 1. It is determined by $\Omega_\kappa(t)$ greater than, less then or equal to 1

the relative abundances of different types of matter and energy in the universe,

$$\Omega(t) \equiv \frac{\rho(t)}{\rho_{cr}(t)} = \sum_i \frac{\rho_i(t)}{\rho_{cr}(t)} = \sum_i \Omega_i(t) = \Omega_m(t) + \Omega_r(t) + \Omega_\Lambda(t). \tag{1.6}$$

When $\Omega > 1$ the universe is open, if $\Omega < 1$ the universe is closed and if $\Omega = 1$ the universe is flat. Determination of the present day values, $\Omega_{i,0}$, currently receives great experimental attention.

1.2 Contents of the Universe

We can determine the $\Omega_{i,0}$ by making various astrophysics measurements. In this section we survey such measurements.

The expansion of the universe, the Cosmic Microwave Background (CMB) and the measurement of the primordial abundance of light nuclear elements suggest that the universe began with an initial singularity where the mass-energy density was unbounded. This is known as the *Big Bang*[3]. The environment of space in the early universe is described as a primordial plasma where elementary particles were coupled and in equilibrium, until the temperature and density dropped low enough for each particle species to decouple and allow the species to coalesce into aggregate particles, annihilate or free stream forever.

1.2.1 Radiation, Ω_r

At about 14 seconds after the Big Bang, protons had long since formed and the photon temperature had dropped enough so that electron-positron pairs, the lightest of the stable electromagnetically interacting particles, ceased to be produced. The positrons and electrons annihilated away leaving a relatively tiny excess of electrons due to matter-antimatter asymmetry. The photons remained in equilibrium with electrons and protons for until approximately 380,000 years after the Big Bang. At this time, two things happened. One, the photon temperature dropped far below the ionization energy of hydrogen, 13.6 eV, creating the energetically favorable condition for hydrogen atoms to form. And, two, the expansion rate of the universe, $H(t)$, begins to exceed the rate of photons Compton scattering off electrons[4]. As a result, the photons are free to stream unobstructed. The energy spectrum the photons had at that time was frozen into their population. We can see this spectrum, redshifted[5] from the photons' 14 billion year journey to our telescopes, today. Such photons

[3]It is tempting to think that the initial singularity occurred at one distinct point from which all the universe as we know it issued forth. This is not correct. The initial singularity happened everywhere, rather, in a vast yet smaller universe. If our universe is infinite, then this primordial space was also infinite.

[4]The two things are related. When hydrogen formed, the cross-section for photons to scatter off electrons, now bound to protons, decreased. This reduced the scattering rate.

[5]Because of the expansion of the universe, the frequency of a photon emitted at some distance away from us, ν_{emit}, is measure to be lower when it arrives at our detectors, ν_{obs}, by a fraction related to that distance,

comprise the *CMB*. The CMB is a red-shifted picture of the universe when it was approximately 380,000 years old or $z \approx 1100$ – an epoch in time known as *Recombination* or *Last Scattering*.

As expected from big bang cosmology, the CMB has a thermal black body energy spectrum. This is because in the hot primordial plasma, the photons remained in equilibrium with all other particles until that particle's decoupling. The temperature, $T_{CMB,0}$, of CMB photons distribution is related to the energy density by

$$\rho_r = \frac{1}{\pi^2 c^3} \int \frac{\hbar\omega^3}{e^{\frac{\hbar\omega}{k_b T}} - 1} \, d\omega = \frac{\pi^2}{15} \frac{k_b^4}{\hbar^3 c^3} T^4. \tag{1.7}$$

The present day temperature of the CMB has been measured by numerous experiments to be $T_{CMB,0} \approx 2.725K$. Using the present day value of the critical density, we find that,

$$\Omega_{r,0} = (4.8 \pm 0.4) \cdot 10^{-5}. \tag{1.8}$$

We see that, presently, radiation does not contribute significantly to the mass-energy of the universe.

1.2.2 Matter, Ω_m

The total matter density is considered to be the sum of baryonic[6] non-baryonic and neutrino contributions,

$$\Omega_m = \Omega_b + \Omega_{nb} + \Omega_\nu. \tag{1.9}$$

1.2.2.1 The Neutrino Density, Ω_ν

At approximately one second ofter the big bang, neutrinos decoupled from the primordial plasma. Since then, they have been free streaming and should be visible today, like the photons of the CMB. Unfortunately, these relic neutrinos have not yet been detected. Neutrino annihilation and creation reactions occur through W and Z scattering and it can be computed that they decouple[7] from the primordial plasma around $k_b T \approx$ a few MeV — slightly before the electron and positron decouple and annihilate.

At $k_b T \approx$ a few MeV, we can safely assume that the neutrinos are massless. The temperature of their Fermi-Dirac distribution would have been equal to the photon temperature at the time of their decoupling. Since both temperatures scale as $a^{-1}(t)$, they would be equal

or scale factor at the time of emission. Redshift is often denoted by z, $1 + z = \frac{1}{a} = \frac{\nu_{emit}}{\nu_{obs}} = \frac{\lambda_{obs}}{\lambda_{emit}}$, where λ is wavelength.

[6]Baryons are the bound state of three quark. Protons and neutrons and all atomic matter is considered baryonic. Like neutrinos, electrons are leptons and not baryons. Ignoring this fact and we lump free electrons and atoms into the baryon tally. Relativistic neutrinos are massless are sometimes included in $\Omega_{r,0}$. Due to the strong experimental evidence that neutrinos have mass and are non-relativictic, we count them in $\Omega_{m,0}$.

[7]Reactions decouple when their rate, Γ, falls below the expansion rate of the universe, $\Gamma < H(t)$. $\Gamma = n\sigma v$, where n is particle number density, σ is cross-section and v is particle speed.

today except that annihilation of electrons and positrons, shortly after neutrino decoupling, warmed the photon temperature. Entropy scaling arguments yield that $T_\nu = \left(\frac{4}{11}\right)^{1/3} T_\gamma$. $\Omega_{\nu,0}$ can then be calculated using T_γ and the Fermi-Dirac distribution.

Observations that neutrinos oscillate between flavors strongly suggest that neutrinos have mass. The above paragraph remains true for the early universe when neutrino mass was much less than the ambient temperature. Once the universe cools to less than the neutrino masses, provided those masses are in the range 5×10^{-4} eV and 1 MeV, the density parameter for neutrinos is predicted to be,

$$\Omega_{\nu,0} h^2 = \frac{\sum_j m_{\nu_j} c^2}{93\, eV}, \tag{1.10}$$

where the sum is over all neutrino mass eigenstates. This gives $0.0009 < \Omega_{\nu,0} < 0.0055$ [134], where the lower limit comes from neutrino oscillation experiments and the upper limit comes from Planck CMB. As we will see, large scale structure places a much smaller upper on $\Omega_{\nu,0}$.

1.2.2.2 The Baryonic Matter Density, Ω_b

The baryon density has been measured in several of ways.

CMB Anisotropy. The amplitudes of peaks and troughs in the CMB anisotropy spectrum are sensitively dependent on the baryon density. This occurs because the massive baryons increase the contraction and decrease the expansion of primordial plasma oscillations, leading to a change of even and odd peaks in the power spectrum.

Big bang nucleosynthesis. Big bang nucleosynthesis (BBN) uses Standard Model physics is to predict the abundances of light elements including D, ^4He, ^3He and ^7Li relative to abundance of hydrogen. Other measurement provide the values of the light element ratios. Knowledge of one of the light element ratios determines the value of the baryon to photon number density ratio, $\eta \equiv {}^{n_b}/_{n_\gamma}$ (Figure 1.2). The number density of photons can be calculated at any any epoch from black body physics of the CMB, $n_\gamma \approx 0.244 \left({}^{k_B T_{CMB}}/_{\hbar c}\right)^3$. For example in the light of certain distant quasars, the Lyman-α absorption of D and H are distinct enough to enable a very accurate measurement D/H; this gives $\Omega_b h^2 = 0.022 \pm 0.001$, which is in excellent agreement with Planck.

These methods yield consistent results for $\Omega_{b,0}$ whose best present day value is [145],

$$\Omega_{b,0} = 0.0499 \pm 0.0022. \tag{1.11}$$

At higher redshifts, before galaxy and cluster formation but after reionization[8], the baryon density can also be estimated by studying intergalactic gas clouds. At these times,

[8] After the epoch of recombination, the baryonic matter was in cold atomic gas form throughout the universe. It was not dense enough to form H_2 except in newly formed galaxies. This lasted until $z \approx 7$ when it is observed that the gas was reionized. Cold neutral gas is difficult to detect because of its small cross-section of interaction with light. It does not produce absorption lines unless excited.

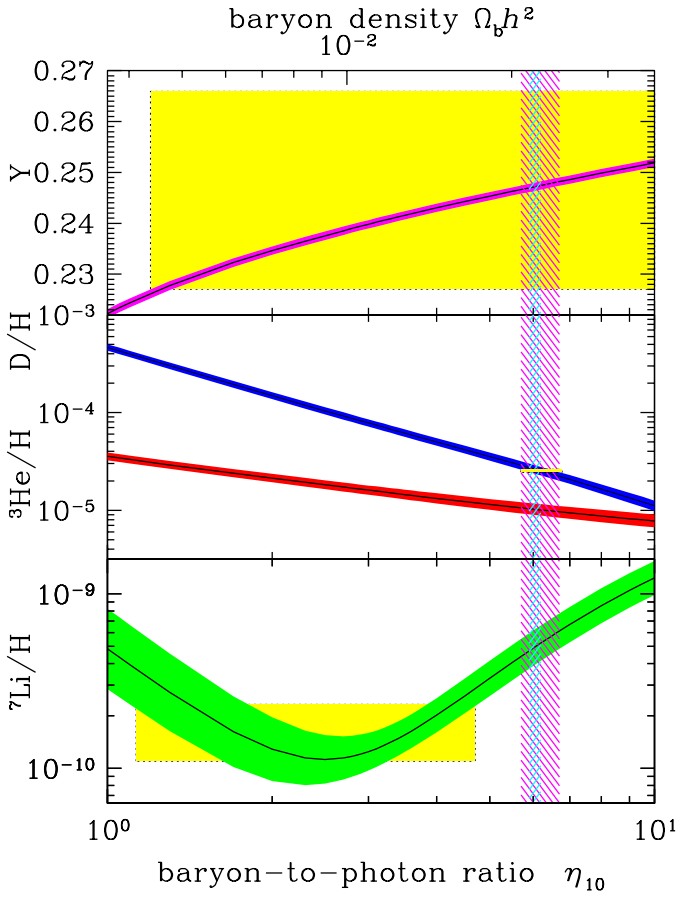


Figure 1.2: Abundances of D, ^4He, ^3He and ^7Li relative to number density of hydrogen as predicted by the BBN model. The x-axis is the baryon to photon number density fraction (bottom), η, and the corresponding value of Ω_b (top). The yellow boxes indicate the experimental detection of certain ratios at the 95% confidence level. The narrow vertical band indicates the CMB concordance range, and the wider bar is the BBN concordance range. We see the deuterium detection is consistent with the CMB concordance range and could alone be used to predict an Ω_b from BBN. However we see that the lithium detection is inconsistent with deuterium; this is the so called *lithium problem*. Image form [136]

the baryons would not yet have been incorporated into structures and would more accurately represent the actual baryon density in the universe. At more recent times however, the intergalactic gas in clusters, does not account for Ω_b. This is the *dark baryon problem*. It is suspected that at this time the baryons are in the form of warm filamentary gas located outside of galaxies an clusters. Examples of techniques to determine Ω_b in this way include

the following.

Intergalactic gas. Much of the baryonic matter is in the the form of intergalactic gas between galaxies in clusters. The gas from numerous clusters can be measured in the x-ray spectrum and turned into an estimate of Ω_b.

Lyman alpha forest. As discussed, at high redshift much of the baryonic matter has not collapsed into galaxies. Here, the hydrogen Lyman alpha forest absorption lines in quasar spectra, due to interspersed clouds of ionized hydrogen, provides a measure of hydrogen abundance. This closely approximates Ω_b because at these early times, hydrogen consumption in stars had not converted the hydrogen into appreciable quantities of heavier elements and the relative abundances of the light elements were still as predicted by big bang nucleosynthesis. Hence, knowing the hydrogen abundance reveals the abundance of the other light elements.

1.2.2.3 The Non-Baryonic Matter Density, Ω_{nb}

The non-baryonic matter density includes particles which may not interact via the electromagnetic force, e.g. light. Methods for determining this density generally rely on the gravitational influence such matter has on luminous sources. Many of these methods yield $\frac{\Omega_b}{\Omega_{nb}}$ or $\Omega_b + \Omega_{nb}$ rather than Ω_{nb}. These methods include include the following [49].

Big bang nucleosynthesis. Big bang nucleosynthesis accounts for essentially all the baryonic matter in the universe. The low value of Ω_b in comparison to Ω_m suggests the existence of a large quantity of non-baryonic matter in the universe.

Galaxy clusters. Clusters can be used to probe $\Omega_b+\Omega_{nb}+\Omega_\nu$ in two ways. In one method, the kinetic energy of the galaxies orbiting the cluster's center of mass are used to determine the gravitational potential of the cluster which effectively gives the total mass of the cluster by the virial theorem

$$\langle E_{Kinetic} \rangle = -\frac{1}{2} \langle E_{Potential.} \rangle \tag{1.12}$$

Then the mass due to baryons in the cluster, $m_{b,cluster}$, is estimated from measurements of the cluster's x-ray luminosity[9] or the effect on the CMB of hot electrons due to the Sunyaev-Zel'dovich effect. The ratio of the two measurements is $\frac{\Omega_{b,cluster}+\Omega_{nb}+\Omega_\nu}{\Omega_{b,cluster}}$. An independently measured baryon density is then multiplied by this ratio and, assuming $\Omega_{b,cluster} \approx \Omega_b$, the resulting quantity is a lower limit on Ω_m, since not all the baryons in the cluster are hot and producing x-rays. The second method is to measure the mass, M to light (bolometric luminosity in watts), L, ratio of clusters or superclusters per spatial volume, V, in which the object resides.

$$\rho_m = \langle \frac{M}{V} \rangle = \langle \frac{M}{L} \frac{dL}{dV} \rangle \tag{1.13}$$

[9] Only the baryons would be responsible for the x-rays. Also this assumes that the cold baryon mass is a negligible contribution to the cluster mass.

The ratio converges to a value of $\Omega_b + \Omega_{nb}$ consistent with other methods as the spatial volume of the object (or sum of objects) goes beyond the 1 Mpc scale.

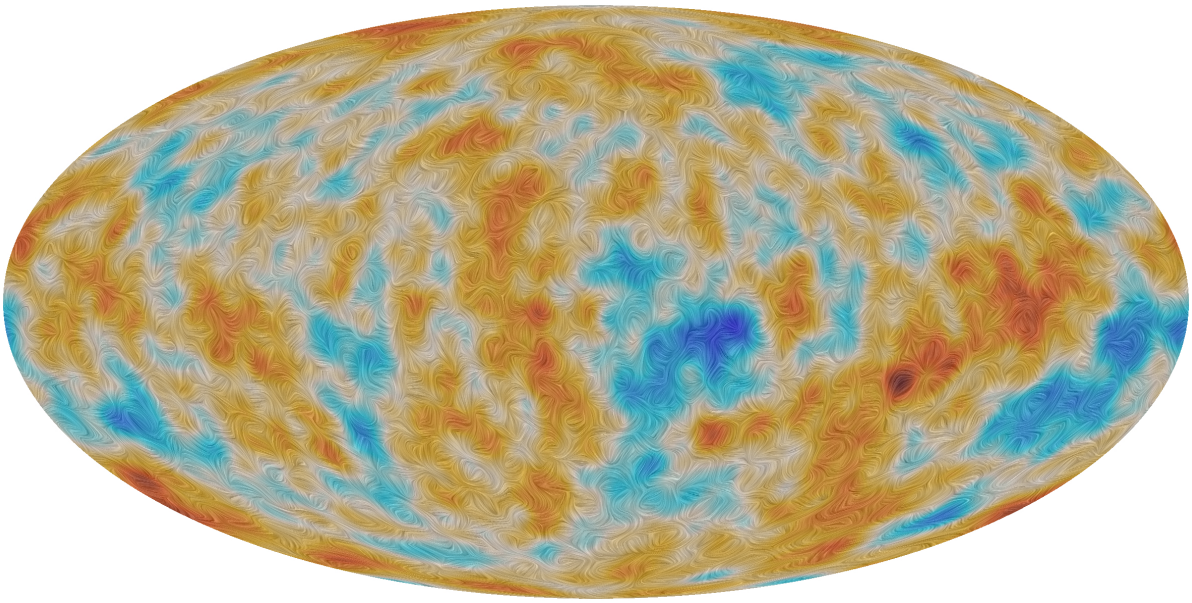


Figure 1.3: Polarization and temperature anisotropy of the CMB. The color scale represents temperature variations and the texture represents the polarization direction of the CMB photons. The polarization pattern is characteristic of *E-mode* polarization. Image from the European Space Agency's Planck website, released April 2, 2015.

Cosmic microwave background. Here one measures the polarization and temperature fluctuations ${}^{\delta T}/_{T}(\mathbf{n}) \equiv \delta_T(\mathbf{n})$ of cosmic microwave background photons at different points $\mathbf{n} \equiv (\theta, \phi)$ in the sky, Figure 1.3. The temperature fluctuations are expressed as ex-

pansions of spherical harmonics $Y_{\ell m}(\mathbf{n})$[10],

$$\delta_T(\mathbf{n}) = \sum_{\ell=1}^{\infty} \sum_{m=-\ell}^{\ell} a_{\ell m} Y_{\ell m}(\mathbf{n}), \tag{1.15}$$

whose coefficients $a_{\ell m}$ Spatial correlation functions are then computed from the fluctuation data. Of particular interest is the two point temperature correlation function,

$$\langle \delta_T(\mathbf{n}) \delta_T(\mathbf{n}') \rangle = \frac{1}{4\pi} \sum_{\ell=1}^{\infty} (2\ell+1) C_\ell P_\ell(\cos\theta), \tag{1.16}$$

where, $\cos(\theta) = \mathbf{n} \cdot \mathbf{n}'$. The *power spectrum* of the fluctuations, C_ℓ, is is then,

$$C_\ell = \frac{1}{2\ell+1} \sum_{m=-\ell}^{\ell} \left\langle |a_{\ell m}|^2 \right\rangle, \tag{1.17}$$

and the variance of the $a_{\ell m}$, $\left\langle |a_{\ell m}|^2 \right\rangle$ is a prediction of the cosmological model, which specifies the Ω_i among other things. The power spectrums (Figure 1.4)for the temperature and polarization anisotropy are fit to a cosmological model which contains specific values for numerous cosmological parameters. The parameters of the model which best fits the power spectrum are taken to be the true cosmological parameters of our universe. The bumps in the CMB power spectrum are called acoustic peaks and they represent plasma oscillations, propagating at the speed of sound in the primordial plasma of the early universe. The physics of the oscillations depend on the cosmological parameters. For example varying $\Omega_m = \Omega_b + \Omega_{nb}$ shifts the positions of acoustic peaks in the anisotropy spectrum of the cosmic microwave background. Intuitively, one can understand that the anisotropy power spectrum would depend on the matter density in the universe by realizing that changing the matter density with respect to the photon density would damp or drive plasma oscillations (e.g. change the speed of sound). Peaks in the power spectrum correspond to favored scales of matter density fluctuations. Fluctuations on these scales would have grown throughout the age of the universe and determine the large scale structure of the universe (e.g. clusters and super clusters of galaxies) we see today.

Large scale flows. One can construct a gravity field map using a catalog of measured distances and red shifts to galaxies and clusters. This map can be used to calculate the

[10]The spherical harmonics are defined as

$$Y_{\ell m}(\mathbf{n}) = \sqrt{\frac{2\ell+1}{4\pi} \frac{(\ell-m)!}{(\ell+m)!}} P_\ell^m(\cos\theta) e^{im\phi}, \tag{1.14}$$

where the P_ℓ^m are Legendre polynomials.

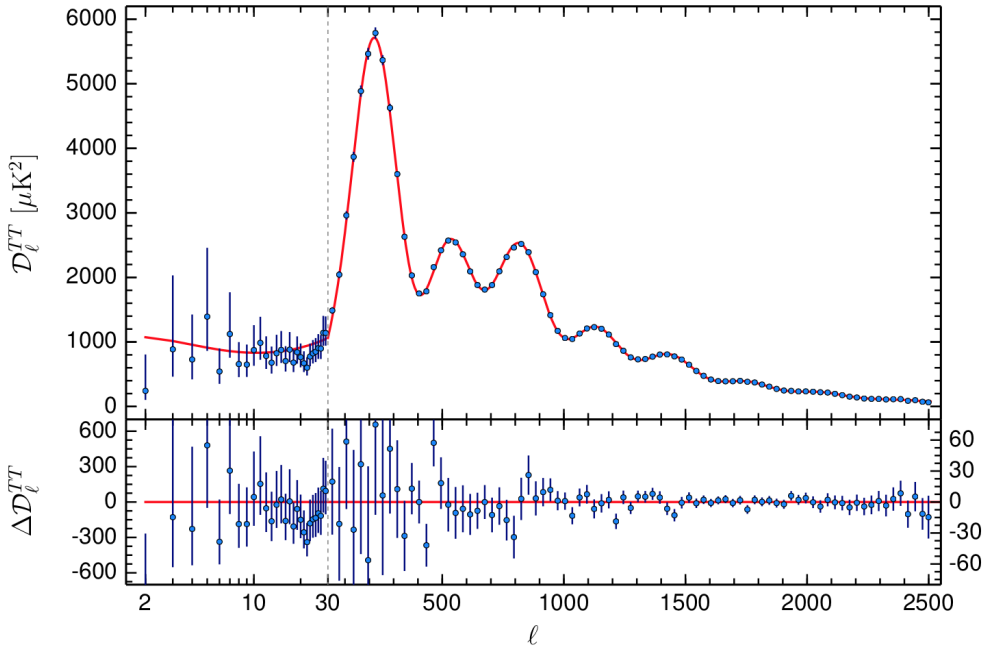


Figure 1.4: Temperature power spectrum of the CMB. Data is from the Planck Collaboration as of February 2015 and is the most accurate measurement of the CMB as of the time of this writing. Image from [144].

expected velocities of the galaxies and clusters due to their gravitation interaction by,

$$g(\vec{r}) = G\bar{\rho}\int d^3r'\delta_p(r')\frac{r'-\vec{r}}{|r'-\vec{r}|^3}, \tag{1.18}$$

$$v_g(r) = \frac{2}{3H_0\Omega_m^{0.4}}g(\vec{r}). \tag{1.19}$$

The actual velocities of the galaxies and clusters can be independently measured using the Tully-Fisher relation. Equation 1.19 provides a measure of $\Omega_b + \Omega_{nb}$.

Using the methods above, Ω_{nb} can be constrained to be [145]

$$\Omega_{nb,0} = 0.227 \pm 0.015. \tag{1.20}$$

We find that the total total mass-energy contribution to $\Omega_{tot,0}$ due to matter is [144]

$$\Omega_{m,0} = 0.3089 \pm 0.0062. \tag{1.21}$$

1.2.3 Vacuum Energy, Ω_Λ

Vacuum energy accelerates the rate of expansion of the universe. This has effects on structure formation and the apparent luminosity and size of the distant objects. Methods to measure the dark energy density include the following [66, 187].

Supernovae. Once their light curves have been corrected for rise time and width, type Ia supernovae are all identical, within about 10%. For this reason they are considered *standard candles* — once an event has been determined to be a type Ia supernova, one knows its light output, or absolute luminosity. The distance to a supernova event can then be measured by comparing its measured, or apparent, luminosity to its absolute luminosity, since brightness will have faded according to the distance over which the light has traveled to earth. This is the luminosity distance, $d_L(z)$ and its relation to comoving distance, $r(z)$ in a flat universe described in Equation 1.22 At the same time, the redshift of the supernovae is a measure of the expansion of the universe since the light left the supernova. In the presence of dark energy, the supernova appears dimmer than expected at a given redshift. A value for the dark energy density, and therefore Ω_Λ, can be employed to account for the dimmer-than-expected apparent magnitude. This method is useful over the range in which one can detect and measure supernovae light curves $z < 2$.

$$d_L(z) = (1+z)r(z) \qquad r(z) = \int_0^z \frac{dz'}{H(z')} \tag{1.22}$$

Baryon acoustic oscillations. In the primordial universe, areas which happened to be over-dense with respect to surrounding plasma were unstable. Radiation pressure in these areas forced outward the coupled plasma of baryon and photon called the phonon-baryon fluid. This fluid propagated outward from the over-dense region in an expanding shell leaving behind the dark matter, which had decoupled from the fluid approximately 10 ns after the big bang. When the photons decouple from the baryons, at the epoch of recombination, the expanding shell of baryons halts at a characteristic comoving radius called the sound horizon at decoupling, r_s. Over time the baryon shell partially falls back toward the origin of the over-density by pull of the dark matter, leaving a smaller density peak at r_s. The dark matter and the baryon densities eventually reach an equilibrium distribution featuring a larger peak at the origin of the original density perturbation and a smaller peak at r_s. Through out the subsequent evolution of the universe the two peaks amplify structure formation at that comoving separation scale. A bump in the spatial correlation function of galaxies[59] and the flux correlation function of the Lyman alpha forest [50] is now visible and corresponds to a physical distance 140 Mpc. Because r_s is independent of time since recombination and location of measurement in the universe, this absolute length scale due to baryon acoustic oscillations is considered a cosmological *standard ruler*.

Growth of fluctuations. When the expansion of the universe is too rapid, density fluctuations, including clusters, stop growing. This can be seen mathematically by considering the evolutions of a small scale matter-density perturbation, $\delta(\mathbf{x},t) = {}^{\delta\rho_m(\mathbf{x},t)}/_{\overline{\rho_m}(t)}$. In the framework of general relativity, the Fourier modes of the perturbation δ_k evolve according to

$$\ddot{\delta_k} + 2H\dot{\delta_k} - 4\pi G\rho_m\delta_k = 0. \tag{1.23}$$

The Hubble damping term, $2H\dot{\delta}_k$, is large when dark energy is dominant and can arrest structure growth. A cluster redshift survey reveals the growth history of clusters. Such information can be obtained from x-ray astronomy, for nearby clusters. For more distant clusters the distortion of the CMB by the Sunyaev-Zel'dovich effect[11] can be used to detect clusters. The epoch after which cluster growth stalls is the time at which Ω_Λ began to dominate over Ω_m. The Friedmann equation can be solved for Ω_Λ given the time at which cluster growth stalls and an independently determined Ω_m.

All methods for determining Ω_Λ produce a figure consistent with the present accepted value,

$$\Omega_{\Lambda,0} = 0.74 \pm 0.03. \tag{1.24}$$

1.3 Evidence for Cosmic Dark Matter

Dark Matter is matter that does not emit light. One can add up all the mass from the luminous sources, which includes stars, dust and warm to hot gas, and the cold gas (detected by absorption spectra) to find the portion of Ω_m that is due to non-dark, Ω_{lum}. One finds that [67],

$$\Omega_{lum,0} \approx 0.0033. \tag{1.25}$$

Considering that $\Omega_{m,0} >> \Omega_{lum,0}$ one becomes interested in nature of the cosmic dark matter. Moreover, in order to understand the structures visible in the universe today, such as galaxies clusters and superclusters of galaxies, one must know the physics of the dark matter.

1.3.1 Evidence at Different Scales

We will see that there is evidence of dark matter on a variety of scales, from the horizon[12] scale down to the galactic scale.

Galaxy rotation. The trajectories of bound objects in galaxies suggest the presence of dark matter at the galactic scale. Special considerations for different types of galaxies must be observed, to form correct conclusions [49]. All methods rely on the concept of mass to light ratio to conclude that there is more mass creating galactic gravitation potential than is represented by the light emitted for the galaxy.

Spiral Galaxies. Spiral galaxies have a flat disk of mainly younger stars rotating coherently about the galactic center; a central bulge of old stars with black hole at the

[11] CMB photons inverse-Compton scatter off of electrons from the hot cluster gas. The scattering alters the intensity of the CMB spectrum in the direction of the cluster. For example in the direction of the cluster, there are fewer low energy and more high energy photons than one would would observe in the quiescent CMB radiation when one observes around 218 GHz. This effect, called the Sunyaev-Zel'dovich effect, is independent of redshift in terms of its luminosity.

[12] The horizon is the greatest possible distance that is visible today, due to the finite speed of light and age of the universe.

galactic center; a near spherical halo of stars including globular cluster out of the galactic disk; and luminous spiral arms, density shockwaves which propagate through the disk. The velocity profiles (the rotational velocity as a radius, r, from the center of the galaxy, $v(r)$) of spiral galaxies suggest that dark matter comprises more than an order of magnitude of the galactic mass than the luminous matter. This conclusion comes from measuring the rotation rate of bound gas clouds as a function of distance from galactic center using the doppler shift of atomic hydrogen 21 cm electron spin flip line. The gas rotation rate is assumed to be an accurate tracer of the velocity profile of the galaxy. The rotation rate is found not to decrease with distance form the galactic center, implying that the mass distribution of the galaxy cannot be concentrated toward the galactic center in the way that the galaxy's light distributions is. It is found that most galaxies exhibit a rotation curve that remains relatively flat with distance from the galactic center implying that the galactic mass enclosed, $M(r)$, in that distance must increase

$$m\frac{v^2}{r} = \frac{GmM(r)}{r^2} \Longrightarrow M(r) \propto r. \tag{1.26}$$

A density profile which includes the luminous and dark matter can be reconstructed from the velocity profile by using the velocity profile to solve for $M(r)$.

Elliptical galaxies. Elliptical galaxies are characterized by their three-dimensional ellipsoidal shape; they have a nearly featureless brightness profile; old low-mass stars; a sparse interstellar medium with little or no neutral gas; and incoherent rotation of bound objects about the galactic center. The technique of using galactic rotation curves to measure mass density profile is not effective for these galaxies. Viral velocities or velocity dispersion of kinematical tracers (such as individual stars and nebulae), and gravitational lensing analyses can be used to determine elliptical galaxy mass distribution. Also at the galactic scale, one notices that the random velocities of objects in elliptical galaxies is faster than would be expected if the gravitational potential is due to the luminous matter, only.

Spheroidal galaxies. Are relatively small galaxies, with low luminosity, high velocity dispersion of bound objects, old stellar populations, and low interstellar gas. For these galaxies the high proportion of dark matter to luminous matter is deduced from the velocity dispersion. To see how velocity dispersion relates to the mass density profile, observe the Jeans equation,

$$\frac{1}{\rho}\frac{d(\rho\sigma_r^2)}{dr} + 2\frac{\beta\sigma_r^2}{r} = -\frac{d\phi}{dr}, \tag{1.27}$$

where $\rho = \rho(|\mathbf{r}|)$ is the density profile, $\phi = \phi(|\mathbf{r}|)$ is the gravitation potential, and $\beta = 1 - \sigma_\theta^2(|\mathbf{r}|)/\sigma_r^2(|\mathbf{r}|)$ is the dispersion anisotropy. One assumes a dispersion profile to extract the mass density profile.

Velocity dispersion in clusters. Similar to the above, we find that the random velocities of entire galaxies within clusters of galaxies is too large to be due to the gravitational potential created by the luminous matter within the cluster.

Hot cluster gas. The bremsstrahlung of gas within a cluster is a measure of the depth of gravitational potential of that cluster. The depth of potential provides a measure of the mass of the cluster. We find, from the bremsstrahlung spectrum, that the potential depth is greater than what would be created by the luminous matter, alone.

Gravitation lensing. Gravitational lensing is the bending of light through a gravitational field. It provides evidence for dark matter in a few different limits of mass and size scale. In a gravitation lensing system, a mass or distribution of masses is interposed between an observer, on Earth, and a distant source object. The effect of the interposed gravitational field is to bend the light of the distant source so that the source appears to the observer to be located in at a position different from its actual position. For an extended source object, this means a shifted apparent angular position in the sky, magnified light flux, or multiple or distorted images of the source (rings, arcs and caustics). The lensing equation relates the actual and apparent angular position coordinates[13] of the source object to a lensing potential ψ [92]

$$\boldsymbol{\beta} = \boldsymbol{\theta} - \nabla_\theta \psi(\boldsymbol{\theta}) = \boldsymbol{\theta} - \boldsymbol{\alpha}. \tag{1.28}$$

ψ is connected to the gravitational potential $\Phi(\boldsymbol{x}) = \Phi(D_d\boldsymbol{\theta}, z)$ as

$$\psi(\boldsymbol{\theta}) = 2\frac{D_{LS}}{D_d D_s}\int \Phi(D_L\boldsymbol{\theta}, z)dz. \tag{1.29}$$

Here we have invoked the thin lens approximation to localize the integrated effect of lensing the distance D_d. We have also assumed that most of the deflection occurs at closet approach to the cluster. and put all the Here it is apparent that the gravitational field has been collapsed into a two-dimensional sheet at . Taking the Laplacian of the lensing potential gives the convergence,

$$\kappa(\boldsymbol{\theta}) = \frac{1}{2}\nabla^2_\theta \psi(\boldsymbol{\theta}) = \frac{D_{db}D_d}{D_s}\int \nabla^2\Phi dz. \tag{1.30}$$

The Jacobian of $\boldsymbol{\beta}$ is a matrix, A, whose inverse is call the magnification tensor, $M = A^{-1}$

$$A_{ij} = \frac{\partial\boldsymbol{\beta}}{\partial\theta_i} = \begin{bmatrix} 1-\kappa-\gamma_1 & -\gamma_2 \\ -\gamma_2 & 1-\kappa-\gamma_1 \end{bmatrix}, \tag{1.31}$$

where $\gamma_1 = \gamma\cos(2\phi)$ and $\gamma_2 = \gamma\sin(2\phi)$ are the shear components of an ellipse of ellipticity γ and rotation ϕ. The magnification is related to A_{ij}, as $\mu = |A|^{-1}$. We see that β , γ_1, γ_2, μ and κ all contain information about the interposed mass distribution. Lensing preserves surface brightness (the luminosity per area of the source, which is independent of distance), so the increased size of a magnified object is accompanied by increased brightness.

[13] We define a two-dimension coordinate system on the sky. The origin can be the optical axis. The position coordinates can be angles, θ_1 and θ_2 for example. In these terms derivatives are $\frac{\partial}{\partial\theta_i}$.

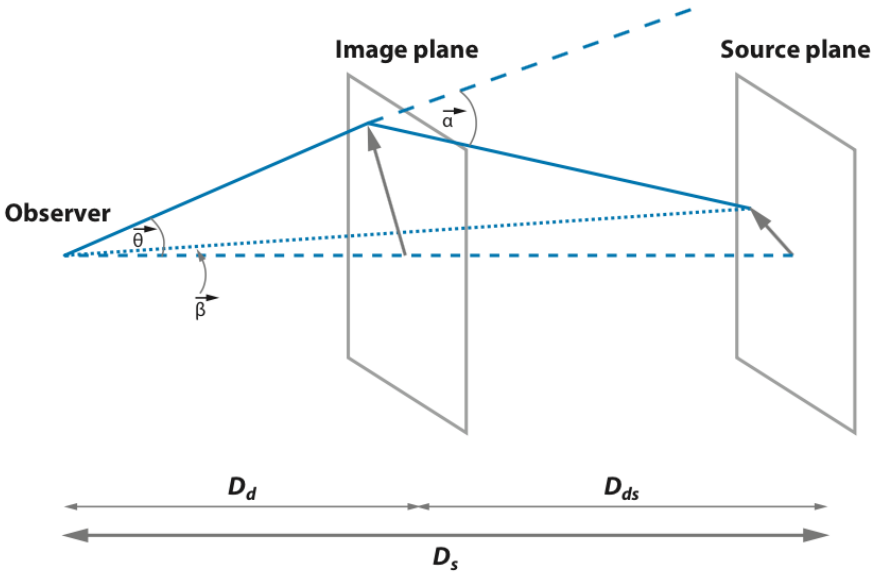


Figure 1.5: Gravitation lensing diagram. The image plane is positioned between the observer, and the source plane. The true source at β is off set for the position of its image, θ, due to the gravitational lensing effect. Image from [178]

Weak gravitation lensing. Here statistical correlations in the measured ellipticites, $\epsilon = (\epsilon_1, \epsilon_2)$, of distant background galaxies, are used to determine the gradient of a foreground gravitational potential [92], Φ. One assumes that averaged ellipticities of the background galaxies at a certain location, β are equal to the shear components, $\gamma = (\gamma_1, \gamma_2)$, $\langle\epsilon\rangle = \langle\gamma\rangle$. Using this method, one can construct a map of the true gravitational potential field in the vicinity of a cluster or super-cluster, up to a constant of integration[14]. This method can be employed can be employed on large angular field surveys. Gravity fields reconstructed from weak lensing analyses suggest the presence of dark matter. Weak lensing can also be used to measure the amplitude of the matter fluctuation spectrum at low redshifts.

Strong gravitational lensing. Strong gravitational lensing is distinguished from weak gravitation lensing by its ability to produce multiple images, arcs or Einstein rings from lensed objects. The effect can be used to measure the mass of clusters. The light from a background object such as a galaxy will be distorted due to the gravity of a foreground cluster. The amount of distortion is a measure of the cluster's mass and, in many cases, has been found to be at least 400 times greater than mass from all the luminous matter in the cluster. Because the mass densities required to produce strong gravitational lensing are large, this technique is most useful for the study of relatively

[14] This is the *mass sheet degeneracy problem*. For clusters, if information about the density profile of the matter from N-body simulations is assumed, a mass can be derived that overcomes the mass sheet. This come at the cost of assuming a specific density profile.

compact lenses, such as a small cluster or galaxy.

Microlensing. Is focused on studying the brightness magnification of point sources do to the action of an interposed compact lens. The technique is useful for detecting massive compact halo objects (MACHOs) where the source is in our galaxy, a close neighboring galaxy or globular cluster. Microlensing exploits the situation where the source and the lens are, or nearly, collinear (e.g. $\beta = 0$). The alignment will result in the source being lensed into an *Einstein ring* around the lens. The angular separation will be

$$\theta_E = \sqrt{\frac{4GMD_{LS}}{D_L D_S}}, \tag{1.32}$$

the Einstein angle. Microlensing techniques are employed in the limit where the ground-based telescope resolution (θ_{res} 1 arcsec) is much greater than the Einstein angle (θ_E 10^{-3} arcsec for a source star at 50 kpc and a lens at 10 kpc) which is much greater than the source angular diameter (for the star at 50 kpc θ_S 10^{-6}), $\theta_{res} \gg \theta_E \gg \theta_S$ [169]. Microlensing techniques have been successful in detecting baryonic dark matter in the form of massive compact objects.

Galactic cluster velocity flows. Clusters of galaxies move according to the gravitational fields they feel. As discussed before, we can measure the motion of clusters and compare it to what we would expect if the gravitation field acting on them is due to the luminous matter around them. Departures from the expected motion is due to the presence of dark matter [47]. Indeed we find such departures.

Cosmic microwave background. As stated before, estimates of Ω_b and Ω_{nb} can be derived from the CMB. The simple fact that these quantities are both much larger than Ω_{lum} is evidence of cosmic dark matter. This evidence coming from the CMB demonstrates dark matter's presence at the largest scale, the horizon scale.

Note that each distance scale implies a time scale. For example, evidence of dark matter at the galactic scale implies that it has been present throughout the recent past (hundreds of thousands of years) and is probably still present. Evidence of dark matter on the horizon scale suggests that the dark matter was present well before the epoch of recombination. Note also that the galactic rotation curves suggest the dark matter must be present in the vicinity of Earth.

1.3.2 Baryonic Dark Matter

Our physical understanding of baryonic matter makes it easy to contemplate in what forms the baryonic dark matter must be and how it must behave. Baryons do not emit light when they are relatively cold, or when they are collapsed into a black hole[15] (with low Hawking radiation). Thus the baryonic dark matter in the universe can be put into two categories:

[15]We lump black holes into baryonic dark matter because most were probably formed by collapsing baryonic structures, such as stars.

cold to warm gas and dust, and cold compact objects such as planets, brown dwarfs, faded white dwarf and black holes.

Cold to warm (e.g. a few 100 eV) galactic gas and dust is difficult to detect because of its very low spectral luminosity in comparison to other, foreground and background soft x-rays. One might quantify the amount amount of this dark matter by looking at interstellar extinction from luminous sources which are positioned on the far side of their containing galaxies.

There was much study of massive compact halo objects (MACHOs) throughout the 1990s. Experiments aimed at detecting the abundance of machos monitored the light from stars in a nearby galaxy for peaks in their luminosity. Such peaks would indicate the passage of a MACHO crossing the line of sight to the star. The frequency and durations of such dips in the data taken from numerous stars would produce an estimate of baryonic dark matter that is due to MACHOs. It was found and corroborated by a couple of experiments that the MACHOs ($10^{-6}M_{\odot} < M < 0.05M_{\odot}$) comprise less then 10% of the galactic halo mass [170]. Objects in this range of mass were at one time considered candidates to comprise a significant portion of the dark matter in the universe.

1.3.3 Non-Baryonic Dark Matter

Dark matter must be stable for a duration on the order of the life time of the universe, or else we would not be observing evidence of it today – i.e. at the galactic scale. If the dark matter decayed with shorter life times, we would also expect to see byproducts of the decay, such as photons.

Considering all the particles we know of, electrons accounted for with the baryons and neutrinos in their own category, there are no long lived candidates for the non-baryonic dark matter. The dark matter must be something new. Moreover, it must be that all the non-baryonic matter of our universe is dark. This means that 26% of the mass-energy of the universe is non-baryonic dark matter. The problem, known as *the dark matter problem*, is to determine the nature of the dark matter. Throughout the rest of this thesis, we focus entirely on the non-baryonic dark matter and the overarching scientific goal to solve the dark matter problem.

Beyond gravitational interaction, the galactic rotation curves and velocity dispersion data suggest very slight interaction between the baryonic and non-baryonic dark matter. They suggest the presence of dark matter halos which envelop the galaxies and clusters of galaxies and extend far beyond the visible matter, Figure 1.6. To be consistent with that picture, the dark matter must very rarely interact with the baryons. The dark matter in the halos would lose potential energy and collapse to less extended sizes if interactions with baryons and itself were too strong.

Non-baryonic dark matter in particle form is consistent with evidence for dark matter presented in the foregoing. Assuming a particle form for the the non-baryonic dark matter, the velocity of the particle dark matter is a very important attribute which has observable consequences. Also, once one knows the energy of a particle at its time of decoupling, the

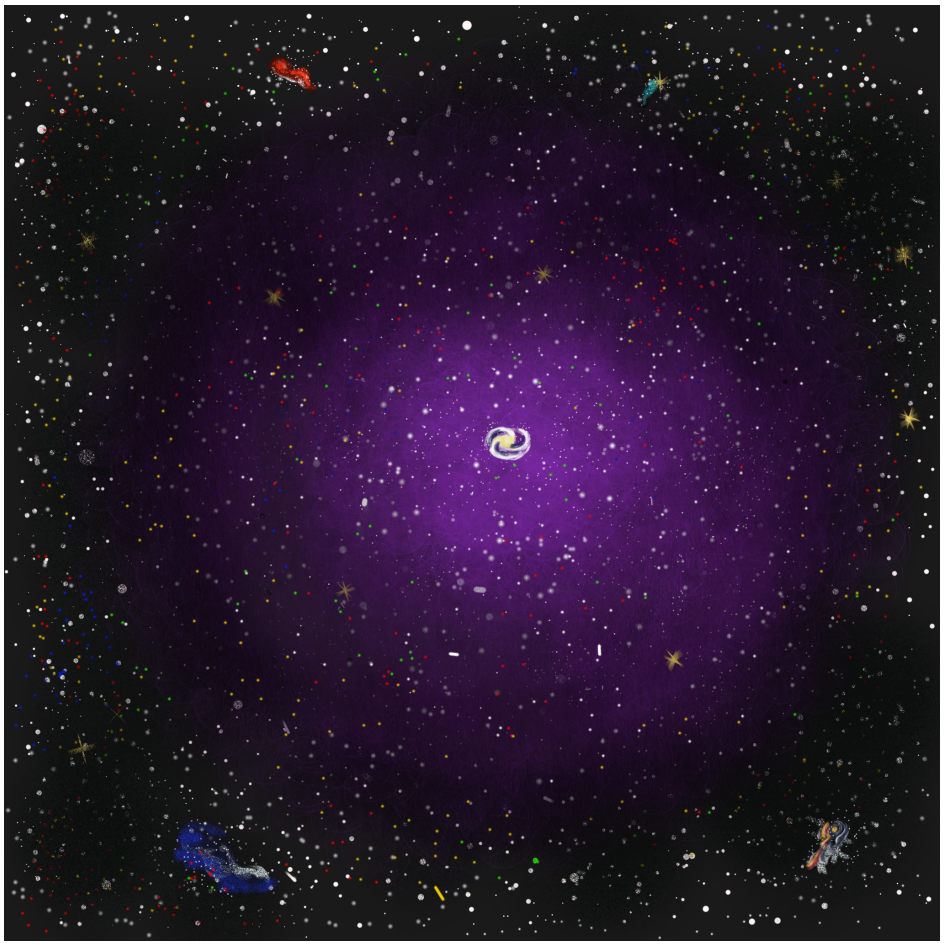


Figure 1.6: An artist's visualization of a dark matter halo. The purple dark matter halo extends far beyond the luminous matter of the spiral galaxy it surrounds. [1]

mass of the particle can be estimated given its velocity. Cold dark matter is dark matter that is non-relativistic at the time of galaxy formation. Cold dark matter clumps and thus structure formation. Warm dark matter would have been barely relativistic at the time of galaxy formation. Hot dark matter would have been relativistic at the time of galaxy formation and would have a number density roughly equal to that of the photons. Hot dark matter would delay structure formation because relativistic particles erase fluctuations at small scales. If dark matter of the universe were hot, we would observe the inverse of the hierarch of structure we see now, i.e. more structure at large scales.

1.3.4 Modified Theories of Gravity

Alternative explanations for the evidence seemingly supporting the existence of dark matter it that Einstein's theory of gravity is not entirely correct. Proponents of modified gravity

argue that, in the absence of direct detection, it is no less speculative considering that the Standard Model of particle physics does not predict candidate dark matter particles which the necessary properties [159]. There are different modified gravity theories. The modified theory of Newtonian gravity (MOND) as been constructed so that the flat rotation curves, and the relationship between luminosity and rotation rate (the Tully-Fisher relation) of spiral galaxies are natural characteristics of the theory; it violates the strong equivalence principle and is therefore not relativistic; it supposes the existence of a universal constance, the Milgrom acceleration, which defines the scale below which gravitational acceleration is enhanced as a feature of the theory. Modified gravity (MOG) theory, on the other hand has been constructed to be a fully relativistic modification of general relativity; it does not introduce new physical constants and comes in a few types including '$f(T)$' and '$f(r)$' theories. $f(r)$ theories use a spatially varying gravitational coupling with parameters that increase in size according to the mass scale and distance scale of the physical system under analysis [34, 36]. $f(T)$ theories are constructed to provide an alternative to the dark energy explanation for cosmic acceleration.

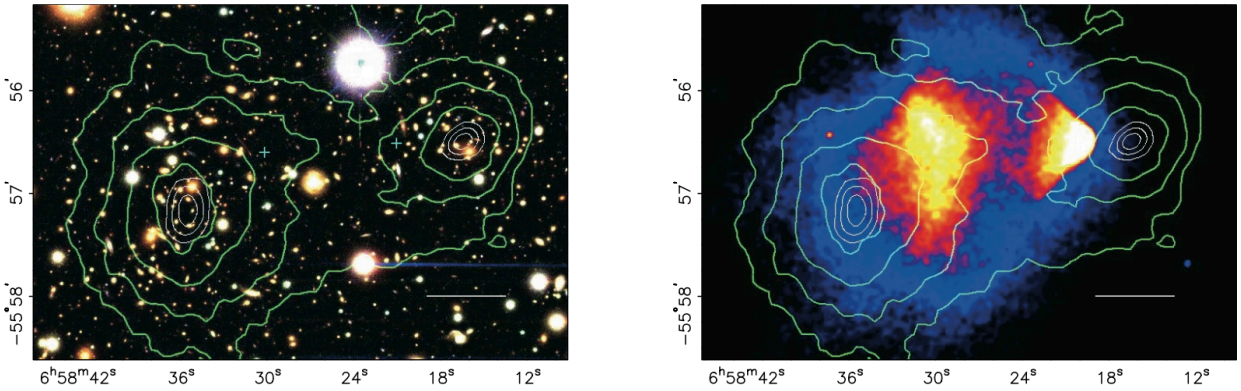


Figure 1.7: Observations of 1E 0657-558 (z=0.296) the 'bullet cluster'. On the left is cluster observed in visible light. On the right is the cluster observed in x-ray light. The contour lines overlaid on both images are map of the cluster's gravitational potential obtain from a weak gravitational lensing analysis. One can see the ram pressure shock wave of the colliding cluster gas in the x-ray image. There is clear separation between the gravitational potential well and the cluster gas. Image from [43]

There is dispute as to whether these theories are consistent with all observational evidence. Perhaps the evidence most challenging to modified theories of gravity are galaxy cluster collisions where the baryons and the inferred non-baryonic dark matter are spatially segregated. Several such collisions have been observed including, for example MS 1054-03, A520 and 1E 0657-558 – the 'bullet cluster'. The bullet cluster is a collision of smaller $7 \times 10^{13} M_{\odot}$ sub-cluster with a larger $2 \times 10^{15} M_{\odot}$ cluster. Hubble telescope observations in visible light show the dissipationless stellar component of the clusters' mass. Chandra observations of x-ray light show the fluid-like x-ray emitting gas of the clusters' mass at

the position of the shock. Ground and space-based far field observations have been used construct a map of the gravitational potential (surface mass density) using a weak lensing analysis. Overlaying the three images (Figure 1.7), we see that the gravitational potential does not trace distribution of gas, but follows the stars rather. Since the mass of the gas is by far greater than the mass of the stars, we are led to conclude that the dark matter is some third, independent, component of the cluster mass whose contribution to the total mass is dominant. This is inconsistent with MOND arguably inconsistent with MOG [43, argues consistency, 34, argues inconsistency].

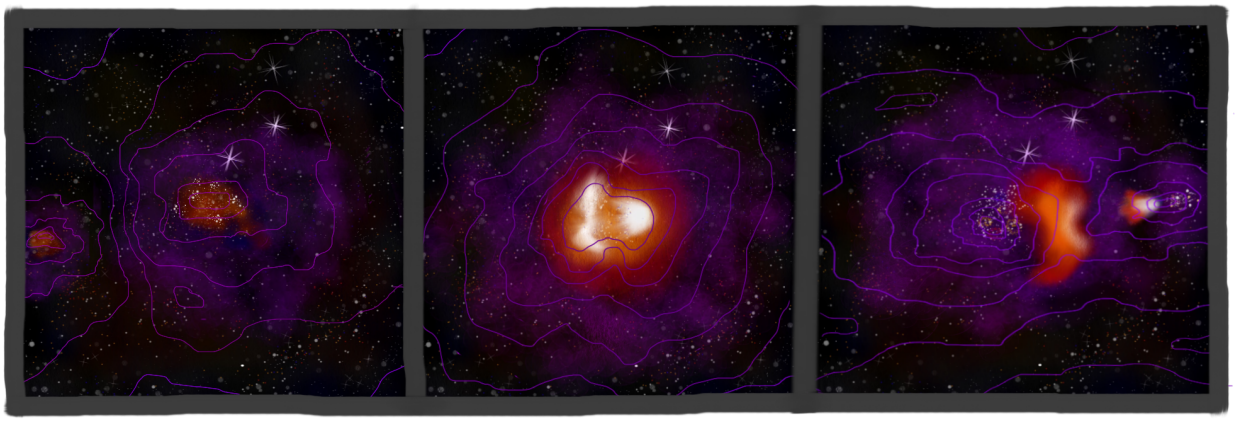


Figure 1.8: An artist's visualization of before, during an after the bullet cluster collision. Telescope images of the bullet cluster is currently observed it the stage illustrated in the right most comic strip view. In the left most view, the background light sources establish a reference frame which has the smaller cluster on the left moving toward the larger cluster in the center. The dark matter distribution is shown by weak lensing dark matter distribution contours and purple haze. In the center view, white to orange coloring emphasizes strong x-ray emission from colliding cluster gasses. In the view, we see the dark matter and compact objects moving unimpeded by the collision while the gas, indicated by the x-ray emission, lags behind due to substantial interactions in the collision. [1]

One can imagine the sequence of events that led to the images of the bullet cluster we astrophysical observations, Figure 1.8. A smaller cluster approaching a larger one, colliding with it, an exiting the other side as it components–the gas, compact light emitting objects and dark matter–interact according to their physics. Conversely, observations of the bullet cluster can be used to place limits on the self-interaction cross-section of non-baryonic (WIMP) dark matter [150].

1.4 Leading Dark Matter Candidates

The cosmic dark matter could be comprised of any one or a combination for these leading candidates [63]. It could also be something entirely different.

1.4.1 Neutrinos

Light neutrinos have masses constrained by neutrino oscillation and tritium decay experiments to be less then a few eV. Such neutrinos would be relativistic at the time of galaxy formation and therefore hot dark matter, and could not comprise the majority of the non-baryonic dark matter density because structure in the universe would have less fine scale then it is observed to have.

Sterile neutrinos, are a light right-handed neutrinos that do not interact via any of the fundamental standard model interactions apart from mixing a gravity [53]. They may have larger masses and velocities much lower than light neutrinos. If they are $\approx 10\,\mathrm{keV}$ in mass, they could be a warm dark matter candidate. These neutrinos may only interact only gravitationally, making them extremely hard to detect in the cosmos, though consistent with the expected properties of dark matter. It is also possible that the could decay into photons and neutrinos on a time scale that is comparable to the age of the universe. The phonon energies produced would be consistent with recent claims of a 3.5 keV x-ray line [33].

1.4.2 Axions

The quantum chromo dynamics Lagrangian has charge conjugation and parity (CP) symmetry violating terms which would lead, for instance, to an electric dipole moment of the neutron, contradictory to experiment.

Peccei and Quinn (1977) [138, 139] suggested that an axion field coupled with the standard model fields could dynamically bring back the CP to invariance and would appear as a light particle which couples to photons.

Non-Thermal Production. Axions are not naturally produced with correct relic density. Axions produced with small enough momenta to be cold dark matter despite $1\ \mu eV < m_a < 100\ \mu eV$ mass range.

Non-Thermal means of axion production include vacuum realignment and emission from Cosmic Strings. In the case of vacuum realignment, a potential is generated for the axion field at quark hadron transition. The axion field starts moving toward the potential minimum. Oscillations about minimum correspond to axion production. In the case of emission from cosmic strings, axions are emitted by decaying or wiggling cosmic strings.

If axions were produced thermally in the early universe, they would have relic density $\approx {}^1\!/_4\,\Omega_{DM}$ if they are to have a lifetime approximately the age of the universe. Such axions would have m_a resulting in HDM.

Direct detection exploits axion-photon coupling. It is possible to look for conversion of dark matter axions into photons scattered off a background magnetic field. The photons created are preserved in a resonant cavity long enough to be read out by a very sensitive amplifier. The coupling term in the Peccei-Quinn Lagrangian is

$$L_{a\gamma\gamma} = -g_{a\gamma\gamma}\frac{\alpha_{FS}}{\pi}\frac{a(\vec{x})}{f_a}\vec{E}\cdot\vec{B} \tag{1.33}$$

where $g_{a\gamma\gamma}$ is a model dependent coupling, α_{FS} is the fine structure constant, $a(\vec{x})$ is the position dependent axion field, and f_a is an axion decay constant.

1.4.3 Weakly Interacting Massive Particles

Attempts to calculate the physical mass of the Higgs boson within the standard model of particle physics fail due the quadratic divergence of an integral, $\int_{UV}^{\Lambda} {}^{d^4p}/_{p^2} \approx \Lambda_{UV}^2$, contributing the loop-level radiative correction contribution to its mass,

$$m_H^2 = m_{H,bare}^2 + \Delta m_H^2 \tag{1.34a}$$

$$= m_{H,bare}^2 - \frac{|\lambda_f|^2}{8\pi}\Lambda_{UV}^2 + \cdots \tag{1.34b}$$

The integral is performed up to the energy scale, Λ_{UV}, at which the standard model is no longer a valid description of nature [121]. This is known as the *gauge hierarchy problem*.

It is recognized that if the standard model breaks down at ≈ 1 TeV, the integral would yield the correct Higgs mass (and W and Z masses) and the hierarchy problem would be averted. Such a cut-off would imply new physics at the weak energy scale, $\approx 100GeV$ to $1TeV$. At this scale, physicists imagine a possible supersymmetric extension to the standard model, for instance, where all the standard model particles of one spin are paired with a particle of half that spin (e.g. a spin ½ electron is paired with a spin 1 super partner) of the same mass and internal quantum numbers. The Higgs would be accompanied by two complex scalar particles with couplings, $\lambda_s = |\lambda_f|^2$. Loop corrections to the Higgs mass from super partners would cancel those from standard model particles above the weak scale energy,

$$m_H^2 = m_{H,bare}^2 - \frac{|\lambda_f|^2}{8\pi}\Lambda_{UV}^2 + 2\left(\frac{\lambda_s}{16\pi}\Lambda_{UV}^2\right) + \cdots \tag{1.35}$$

and the physical Higgs mass could be obtained without fine tuning of other quantities.

Since these super partners are not observed at terrestrial energies, if supersymmetry exists, it must be broken, allowing the super partners to have masses higher than their standard model counterparts. Although supersymmetric scenarios vary, in most (which do not violate R-parity) the lightest supersymmetric particle is stable, since it cannot decay into something lighter. The lightest supersymmetric particle, called the neutralino, χ, particle would also have no electric charge or color. Thus, it would only interact with the weak force and gravity. The mass and annihilation cross-section of the particle would also be commensurate with weak scale values ($50\ GeV < m_\chi < 1\ TeV$).

It should be noted that a class of well motivated alternatives to supersymmetry and the idea of new physics at the weak scale are universal extra dimension models. In these models all particles propagate in compact extra dimensions of size 10^{-18} m or smaller. Every standard model particle has an infinite number of partner particles called Kaluza-Klein particles, who all have the same spin as the standard model particle. This theory

could solve the gauge hierarchy problem and it does preserve an R-parity symmetry which does result in a stable lightest Kaluza-Klein particle, which interacts weakly.

From the prospective of cosmology, a weakly interacting massive particle (WIMP) possesses properties consistent with those required of the cosmic dark matter. First, cosmology requires that dark matter must stable on time scales that are on the order of the age of the universe. Second, the annihilation cross-section, σ_A, most not be too large or the dark matter would have annihilated away before it decoupled form the primordial plasma. On the other hand, the annihilation cross-section must not be too small or its relic abundance would be in excess of the Ω_{nb} observed today (Figure 1.9).

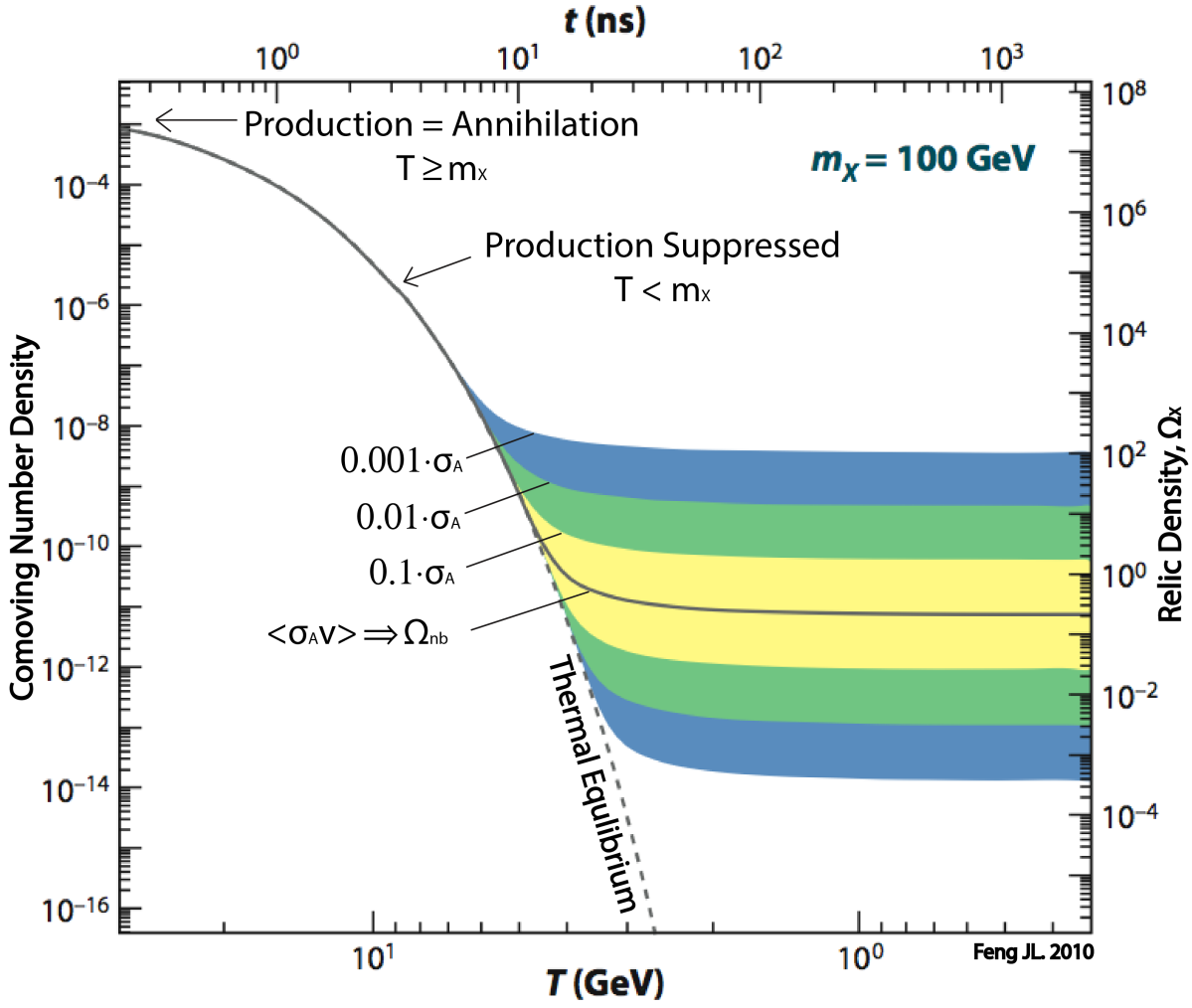


Figure 1.9: WIMP decoupling from the primordial plasma. The solution of the Boltzmann equation gives the comoving number density of the WIMP as a function of temperature or time since the big bang. As the universe cools, the WIMP number density decreases from a constant value (not visible on the plot) as annihilation is more favorable than creation, until the particle departs from thermal equilibrium with the plasma, i.e. 'freezes out'. Freezes out would have occurred when the expansion rate of the universe surpassed the WIMP annihilation rate. The final value of the number density is determined by $\langle \sigma_A v \rangle$. Assuming a WIMP mass of 100 GeV, the dark line used the value of $\langle \sigma_A v \rangle$ which yields the correct relic density. The colors separate the relic densities obtained fact of ten changes in σ_A. Modified image from [63]

WIMP decoupling is determined by the values of $\langle \sigma_A v \rangle$, where the angle brackets denote phase-space averaging and v is the relative velocity between two WIMPs. An estimation of $\langle \sigma_A v \rangle$ was given by Lee and Weinberg [108]. They obtained an approximate solution to the

Boltzmann equation for the neutralino, using the assumption $\langle \sigma_A v \rangle = a + bv^2$, that

$$\Omega_\chi h^2 = \frac{3 \cdot 10^{27} \mathrm{cm}^3\,\mathrm{s}^{-1}}{\langle \sigma_A v \rangle}. \tag{1.36}$$

This implies that σ_A must be on the order of the weak scale in order for the dark matter to yield the correct relic abundance. Thirdly, cosmology puts constraints on the velocity, v, of the dark matter to be consistent with observed large scale structure, i.e the dark matter must be relatively cold. This velocity is largely set at the time of decoupling and the larger the mass of the dark matter particle, the lower the velocity. Embedded in the Lee and Weinberg estimation is the assumption of a mass on the weak scale. For these three reasons, a weakly interacting massive particle, such as the neutralino, is a particularly strong dark matter candidate.

Point number two of the above assumes that the WIMP is its own antiparticle. If it is not, then the relic density reflects the asymmetry in the WIMP, anti-WIMP populations, i.e. the one with the larger population survives annihilation.

Attributions

Results in this chapter come from literature sources. Illustrations from [1] are original work, with her doing the drawing and both of us formulation how they should look.

Chapter 2

Dark Matter Detection

2.1 Detection of WIMP dark matter

2.1.1 Complementarity

There are two approaches to dark matter detection. One is to detect byproducts of WIMP annihilation in the cosmos and the other is to build detectors that are sensitive to WIMP interactions with detector material. The former is known as indirect detection and the latter is known as direct detection.

A third approach to detect dark matter is to produce it in collider experiments. Such detection would reveal the physical properties of the dark matter, such as cross section and mass, but would not specify the abundance in the universe of the dark matter detected. Only the former two detection methods can provide cosmic abundance information. However, the property information provided by collider detection would greatly aid in direct and in direction detection; it would enable experiments to focus their search.

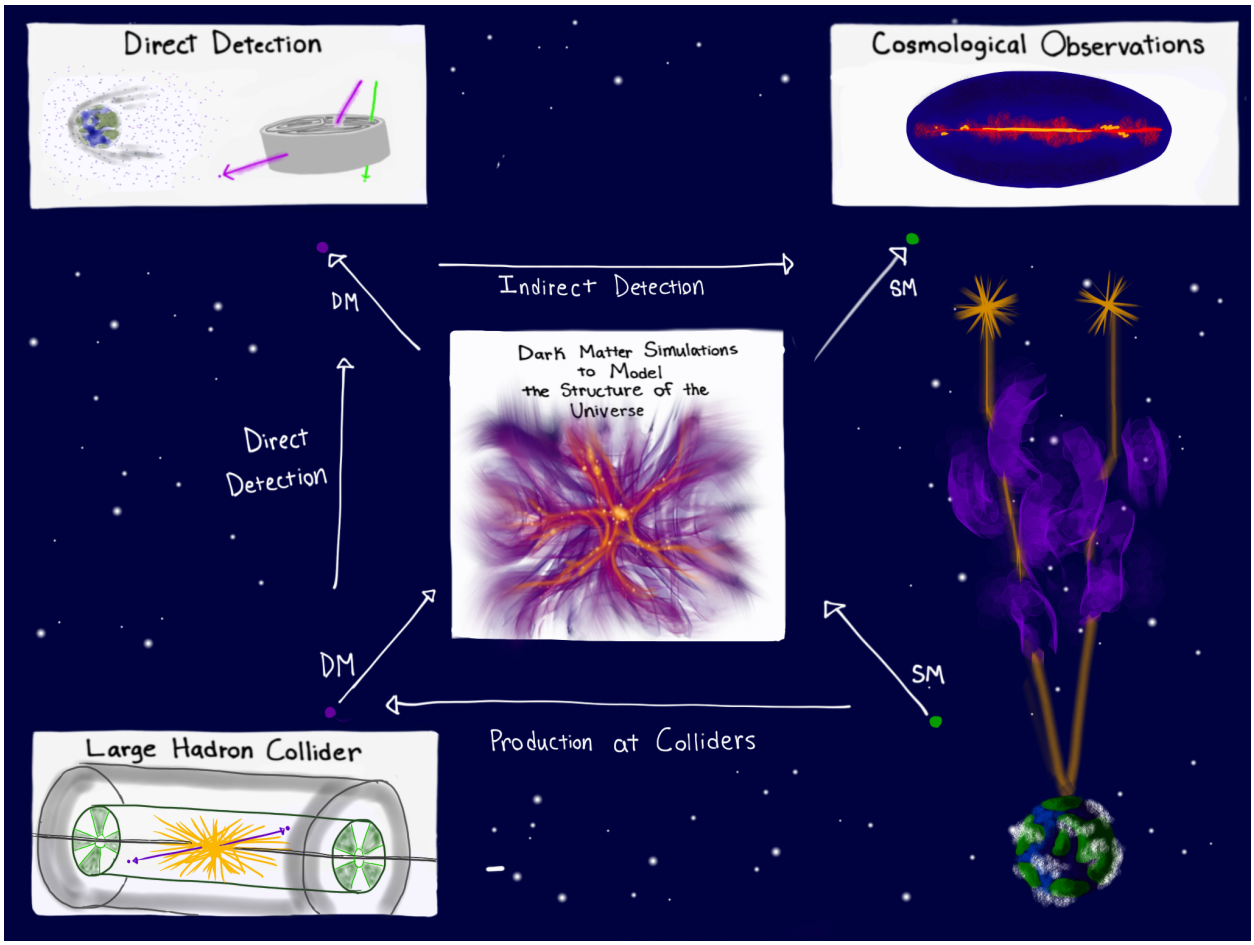


Figure 2.1: Illustration of the complementarity between dark matter detection approaches and simulations. Each of these activities benefit from the successes of the others and progress in any contributes to our understanding of the universe. At the center of the illustration we see place simulations, though this is not meant to imply they are any more important than the three detection approaches. We also indicate how the interaction of dark matter (DM) particles with standard model (SM) particles is associated with the detection approaches, for example collider detection entails production of dark matter from standard model particles, while indirect detection, such as annihilation entails dark matter particles producing standard model particles. The notable exception is lensing, which depends on fundamental physics that is not yet sorted out. Image from [1].

Once the dark matter is detected, and its physical properties known, the question remains of whether or not it is responsible for the observations that led us to believe in its existence in the first place. This can be checked, in part, by simulations. Simulations which model the evolution of the universe, and which include the correct properties of the dark matter should accord with observations at every epoch, from the epoch of last scattering to the present dawn of dark energy domination.

The complementary ways in which detection approaches and simulation work toward increasing our understanding of dark matter and the universe is acknowledged in the field as the best way forward, Figure 2.1.

2.1.2 Indirect detection experiments

The dense central regions of planets, stars and galaxies will experience a relatively high rate of WIMP scatters. Having lost their incident momentum, scattered WIMPs may become trapped in the gravitational potential well of these regions. The resulting increased WIMP density, due to the accumulation of trapped WIMPs, increases WIMP annihilation rate in these regions. Annihilating WIMPs may produce standard model particle byproducts which may be detected by detectors on earth or in orbit.

The long-lived particle byproducts of WIMP annihilations are high energy photons such as x-rays, charged particles such as electrons and positrons and neutrinos. The high energy photons and charged particles from extraterrestrial annihilation events do not penetrate earth atmosphere, so they must be detected by orbiting observatories. The photons and changed particles form annihilations occurring at the center of the earth do not make it to ground-based detectors and are lost. Neutrinos from terrestrial and extra-terrestrial annihilations would make it to ground-based neutrino observatories and may be detectable.

Several generations of orbiting observatories possibly sensitive to WIMP annihilation byproducts have been launched. For the case of high energy photons, Fermi gamma-ray space telescope (formerly GLAST), launched in June of 2008 has the widest energy sensitivity range, 10 keV to 300 GeV. Before Fermi was the Energetic Gamma-Ray Experiment Telescope (EGRET) instrument on the Compton Gamma-Ray Observatory (CGRO), launched in 1991. EGRET's energy sensitivity range was 30 MeV - 10 GeV. The high energy photon detectors for these instruments are either silicon ionization, 'drift', detectors or transition edge sensors.

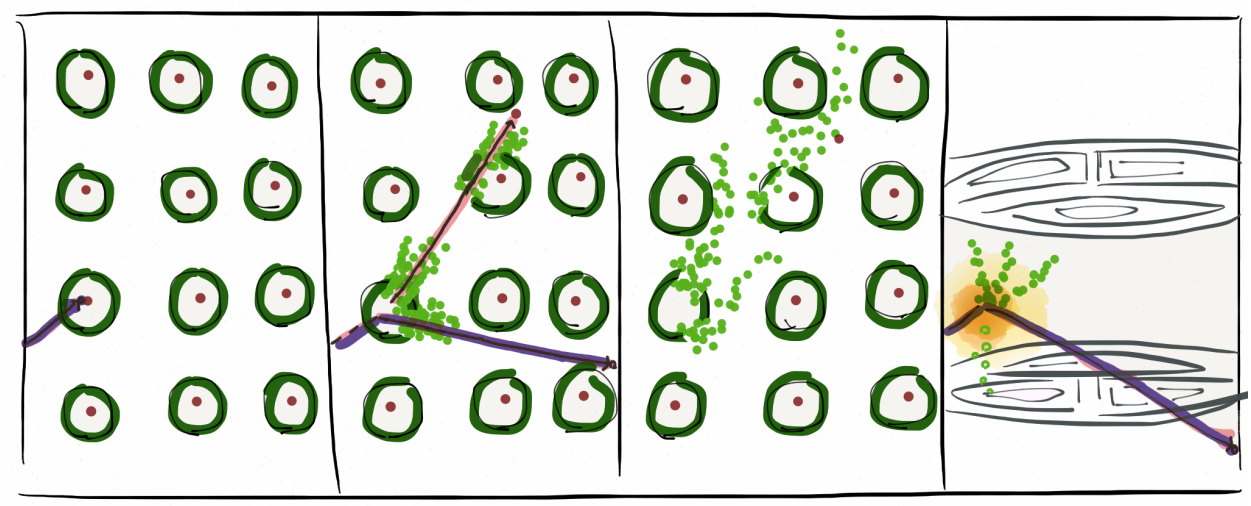


Figure 2.2: Comic strip illustration of the principle of direct detection. A WIMP of cosmic origin collides with an atomic nucleus in a target material. In this case we have a germanium crystal is in mind. The recoiling nucleus produces phonons, in orange, and ionization in the form of electrons and holes, green dots. WIMP interactions are so rare that it is exceedingly unlikely the same WIMP will interact twice in the detector. However the recoiling nucleus may be ejected several atomic spaces and interact with other atoms in the lattice as it recoils. The ionization is pulled to the surface of the detector by an electric field. Hole and electrons travel with different trajectories with respect to the field. The phonons eventually reach the surface too. Image from [1].

In the case of charged particle byproduct detection, the Alpha Magnetic Spectrometer (AMS-02), launched in May 2011, is the first magnetic spectrometer in space. It has five different instruments sensitive to changed particle radiation including positrons, anti-protons and gamma-rays. Before AMS-02, the Payload for Antimatter Matter Exploration and Light-nuclei Astrophysics (PAMELA), a space-borne magnetic calorimeter, and the Advanced Thin Ionization Calorimeter (ATIC), a balloon-borne calorimeter, have measured excesses in cosmic charged particles which could be from WIMP annihilation. There is much doubt in the scientific community this is the case, however.

Neutrino Observatories such as IceCube in Antartica, the Sudbury Neutrino Observatory in Canada, and Super-Kamiokande in Japan, may be sensitive enough to detect neutrinos from WIMP annihilations if the signal is sufficiently above background sources, solar neutrinos for example.

As discussed, indirect detection experiments search for excesses of high energy particles. The challenge for this approach is to show that a detected signal is from WIMP annihilation and not something else.

2.1.3 Direct detection experiments

The small weak interaction cross-section WIMPs are expected to have make it possible to pursue the direct detection of WIMPs. In the case of direct detection, one aims to detect energy from WIMP interactions with atomic nuclei. The picture here Figure 2.2 is of a WIMP colliding with a nucleus and causing that nucleus to recoil. Depending on the nucleus, the energy from the recoil will be released in the form of phonons, photons or ionization of nearby atoms.

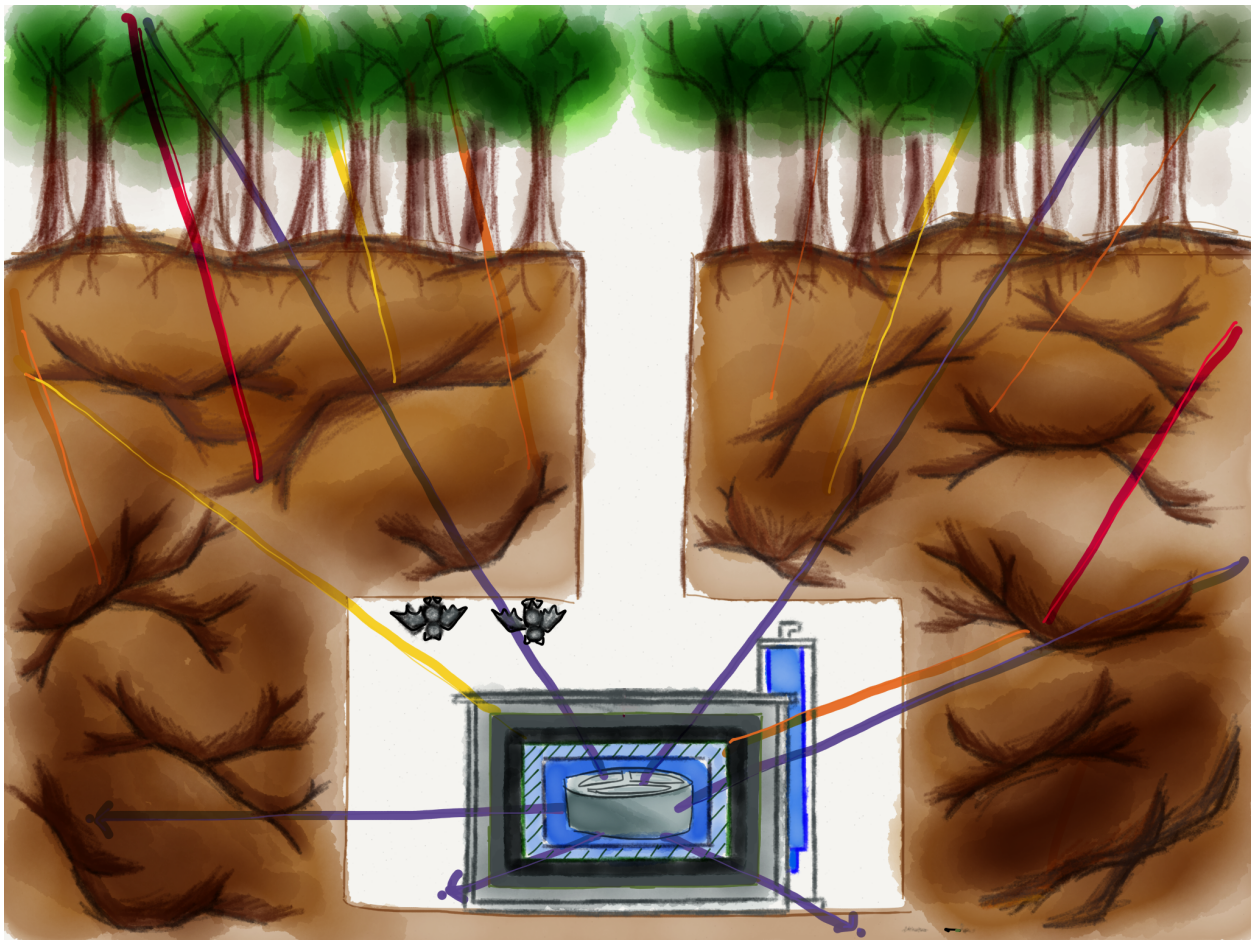


Figure 2.3: Illustration of dark matter detector deployed in an underground laboratory. The overburden of rock shields the detector from most cosmic radiation but WIMPs (in purple) would have no problem reaching the detector. The illustration depicts the CDMS detector, with its pattern of charge and phonon sensors visible, in the Soudan Underground Laboratory, which is located in Northern Minnesota. Bat are frequent visitors to the experimental chambers which are nearly a half mile underground. Image from [1].

Because WIMP detectors are very sensitive radiation detectors, much care must be taken to distinguish WIMP events from other events that trigger the detector. Discrimination is

enhanced by employing multiple detection channels, e.g. detectors sensitive to ionization and phonons or phonons and photons. Also, shielding of detectors from large radiation fluxes is crucial. Direct detection experiments are usually located in underground laboratories to protect them from cosmic radiation, Figure 2.4. They are usually surrounded by coincident vetos, as well as neutron moderating materials and contained within very low radioactivity barriers. These redoubtable barriers should have little effect on the WIMPs, who can travel through the Earth little chance of interaction

2.1.3.1 Event rate

The event rate for direct detection experiments is given by the following equation.

$$\frac{dR}{dE_r} = \frac{\sigma_0 \rho_0}{2 m_\chi \mu} F^2(E_r) \int_{v_{\min}}^{\infty} \frac{f(v)}{v} dv \tag{2.1}$$

The meaning of the terms can be organized thematically to emphasize the underlying. On the measurement side, we have the event rate, R, and the nuclear recoil energy E_r. On the particle physics side we have σ_0, the perfect coherence interaction cross section, m_χ the WIMP mass, μ, the WIMP-nucleon reduced mass in the center frame, and $F^2(E_r)$, the nuclear form factor. On the astrophysics side, we have ρ_0 the local WIMP density, and $f(v)$ the WIMP velocity distribution relative to Earth. Lastly, on the detector technology side we have $v_{\min}$ the minimum velocity required to produce a recoil that is above the detection threshold of the detector.

We see that the direct detection of WIMPs involves physics from many different areas. We also see that we can increase our event rate in two straightforward ways. One, increase the number of nucleons in the search mass. Thus, a large detector mass increases WIMP detection sensitivity. Two, decrease the threshold of the detector. This can be accomplished by decreasing noise sources and by assiduous choice of detector technology. For example, in a superconducting pair breaking detector, such as a kinetic inductance detector or a transition edge sensor, the minimum possible threshold is set by the energy required to break a pair.

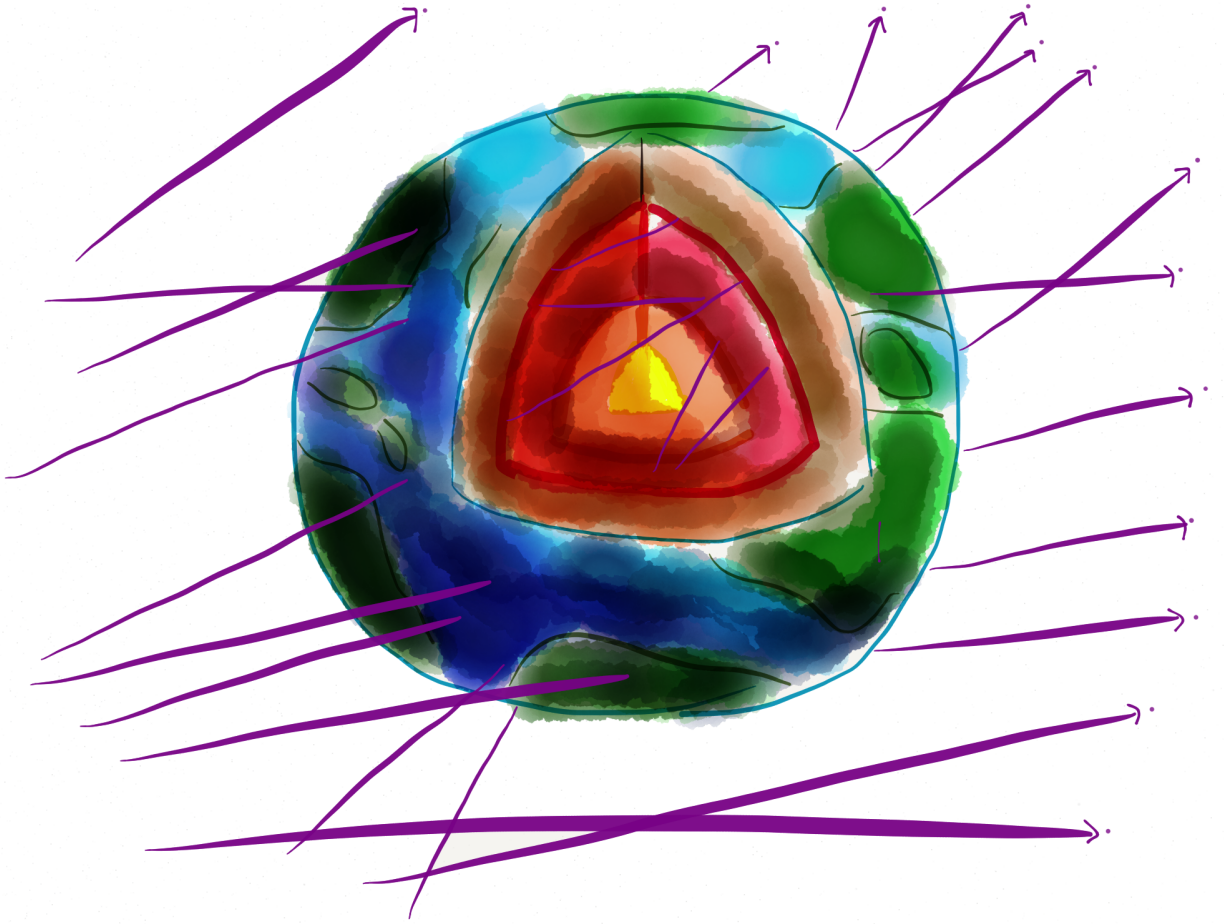


Figure 2.4: Most dark matter experiments exploit the fact that WIMPs (purple particle tracks) interact so infrequently, they can pass through the Earth unimpeded. Underground locations are chosen for the experiments so that other particles are stopped by the overburden of rock. Image from [1].

The interaction between WIMPs and standard model particles can be spin-dependent or spin-independent. The choice of detector material determines an experiment's sensitivity to the spin-dependent or spin-independent interactions. Currently, there tighter constraints on spin-independent interactions.

2.1.3.2 Detection experiments

Currently, there are a great variety of direct detection experiments in operation and in design. [161] offers a nice overview. For the most part, these experiments can be categorized in terms of their detections channels – whether it is photons, phonons ionization of a combination of two, and their target materials. We consider a few experiments.

2.1.3.2.1 Silicon and germanium detectors These detectors are comprised of monocrystalline material, usually at very high purity. When operated at low temperature, phonon produces by interaction events cant travel distances large compared to the dimension of the detector before they are scattered. These conditions also allow for charge created at interaction events to drift to collection electrodes without being trapped by impurities and escaping detection.

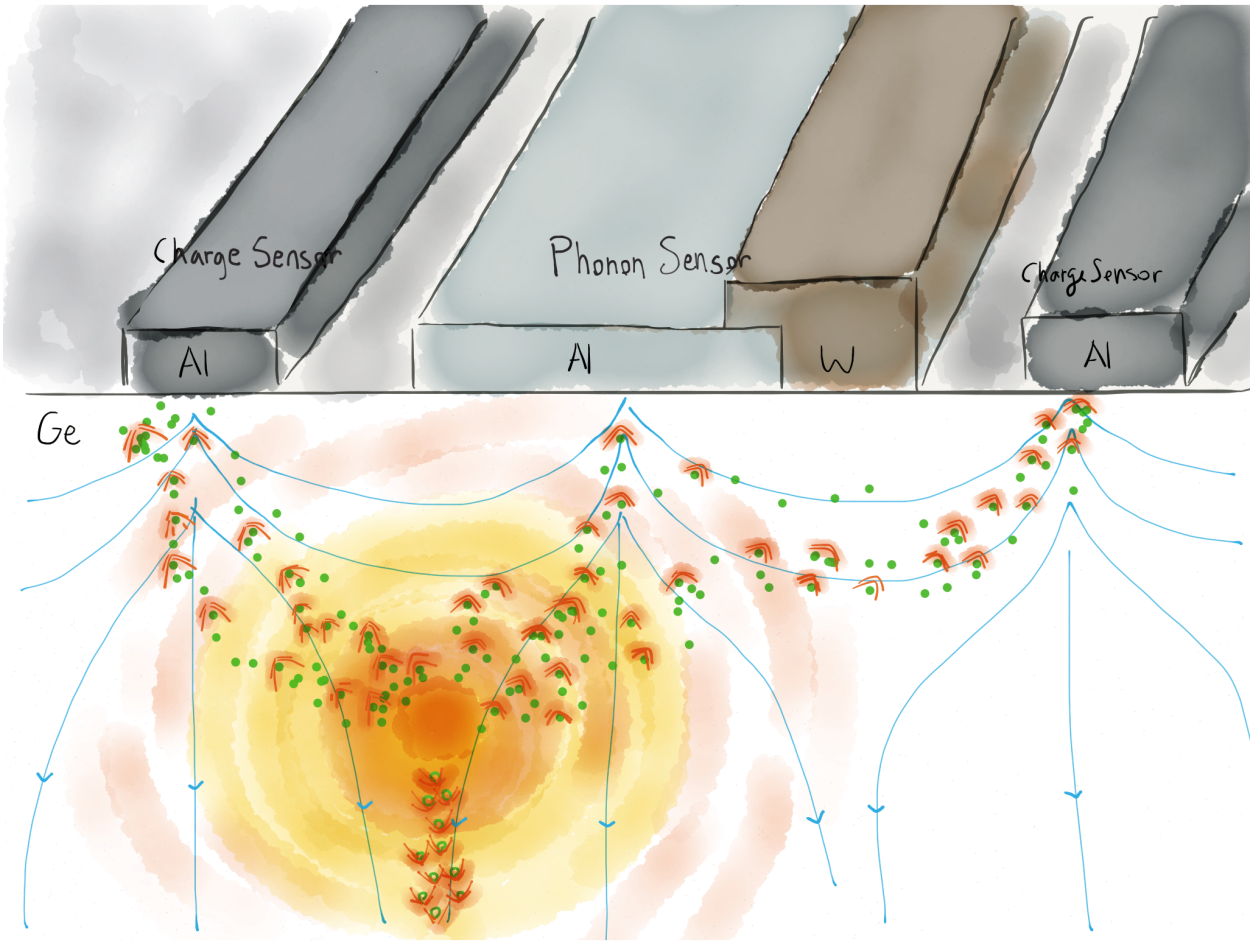


Figure 2.5: Illustration of ionization and phonon collection in a CDMS detector. Charge collection electrodes interdigitated with phonon sensors, which serve as ground, create an electric field (blue lines) that drags electrons and holes created in the particle interaction event to the surface of the detector. As the charge (green dots) is dragged, it produces secondary, "Luke phonons" (red wave fronts), at it interacts with the lattice. Primary phonons from the event (orange and yellow concentric circles) radiate from the interaction location until they are absorbed at the surface by aluminum fins, which collect the phonon energy and funnels it to the tungsten transition edge sensors. Image from [1].

The Cryogenic Dark Matter Search (CDMS) CDMS utilizes single crystal germanium detectors sensitive to ionization and athermal-phonons and cooled to an operation temperature of approximately 20 mK, Figure 2.5. The detector has arrays of superconducting transition edge sensors (TES) pattered onto the surface of a germanium absorber. These arrays are comprised of thousands of individual tungsten TESs. An electric field is set up across the absorber to drift electrons and holes created by particle interactions to the surface of the absorber where they are collected and amplified. Interaction events create pulses whose shapes are used to determine what type of particle caused it. This is called pulse shape discrimination.

The Dark Matter In CCDs (DAMIC) DAMIC uses silicon charge coupled devices (CCDS) as the target material. The devices are on 275 µm thick silicon wafers. The use of off the shelf detector technology enables a straightforward route for scaling up the experiment. These detectors have a considerable low threshold for detection. Due the pixelated natured of the change sensors, offer excellent spatial resolution. This experiment is done at room temperature.

The CoGeNT Experiment CoGeNT uses a point-contact germanium ionization detector operated at the Soudan underground mine. It is single channel experiment, but has a low energy threshold due to the production of secondary ionization as the ionization produced by the original event is dragged to the collection electrodes. This experiment published a detection result which other experiments have not been able to confirm.

The China Dark Matter Experiment (CDEX) CDEX, in its first phase, is planned to deploy one tonne of germanium target material in the Chinese Jin Ping laboratory, which has an over burden of rock affording 7000 meters of water equivalent (m.w.e) equivalent of shielding. This is another single channel point-contact detector, [93]. The experiment is to have a liquid argon active veto.

The Edelweiss Experiment The third phase of the Edelweiss experiment is to focus on low mass WIMPS (< 10 GeV). Its interdigitated electrode germanium detectors have an neutron transmutation-doped thermometer, allowing them to measure both position sensitive change and equilibrium phonons. They are expected to have a 500 eV energy resolution in ionization.

C-4 This is single channel experiment using an improved germanium p-type point-contact design, which is supposed to offer higher energy resolution than the usual N-type point contact detectors. The detectors are made by the Canberra corporation.

2.1.3.2.2 Oxide semiconductor

The CRESST Experiment CREEST stands for the Cryogenic Rare Event Search with Superconducting Thermometers. This experiment uses single crystal $CaWO_4$ as the target material. Events produce scintillation light and heat. The light is detected by a second calorimeter mounted in the detector housing and the heat is measured by a transition edge sensor thermometer connected to the target crystal. CRESST operates at around 15 mK

2.1.3.2.3 Crystal scintillators The general theme of the scintillator experiments is to check the annual modulation claim of DAMA. These single channel experiments are able to rapidly deploy large quantities of detector material.

The DAMA Experiment The DAMA experiment uses a NaI scintillator target with photomultipliers to detect the light. This experiment has a long standing discovery claim that other experiments have not been able to verify. Additionally it claims to see an annual modulation WIMP signal, due to the earth motions with respect to the WIMPs in the galactic halo. It is a single channel experiment deployed at Gran Sasso in Italy.

The KIMs Experiment KIMs is another NaI experiment which has the goal of checking the DAMA result. In addition to scintillators, KIMs deploys a phonon and light detector based on the germanium target material.

The ANAIS Experiment ANAIS stands for annual modulation with NaI Scintillators. As its name implies, the approach is to deploy a NaI scintillator (250 kg) for many years in order to accumulate dark matter data, which they hope will feature an annual modulation signal.

The DM-ICE Experiment The DM-ICE experiment positions NaI(Tl) scintillators at both the north and south poles. This separation is intended to help confirm the annual modulation signal claimed by DAMA.

2.1.3.2.4 Liquified nobles gases Liquid experiments are more easily scaled up than the solid detector experiments. They must be careful to ensure the radio-purity of the liquid because significant concentrations of long lived isotopes of the noble gas are present in natural sources. These experiments have the disadvantage of relatively high threshold.

The LZ Experiment The LZ experiment is a conglomeration of the LUX and the Zeplin liquid xenon experiments. In this experiment a large container of liquid xenon is surrounded by another liquid scintillator veto. Particle interaction events in the xenon produce ionization and primary scintillation light. The ionization is drifted to the liquid surface where it produces a secondary scintillation signal as it is extracted from the liquid. The light is measured by photomultipliers. Phonon background rejection is accomplished by looking at the ratio of the two light signals. Position resolution of a fraction of a millimeter is obtained in the horizontal direction, and of several millimeters in the vertical (perpendicular to the liquid surface) direction. Vertical spatial resolution is obtained from charge drift time information. The xenon vessel acts as at time projection chamber (TPC). LZ plans to ultimately deploy 7 tons of liquid xenon.

The Xenon Experiment The Xenon experiment, transitioning from a 100 kg phase to a one tonne phase, is a competing liquid xenon experiment at Gran Sasso. It uses ver similar detector technology to LZ.

The XMASS Experiment This is a single phase liquid xenon experiment. In a single phase liquid experiment, the electrons are not extracted from the liquid producing a secondary scintillation signal. XMASS aims to have 24 tonnes of liquid xenon deployed within

the next few years.

The DEAP/CLEAN Experiment This is a collaboration of the CLEAN single phase argon experiment and the the DEAP liquid argon experiment.The DEAP experiment deploys 3.6 tonnes of liquid argon, and it plans to rapidly scale to 50, then 150 tonnes of scintillating argon at SNOLAB. Argon admits pulse shape discrimination facilitated by a large difference in the singlet and triplet excited states yielding fast and slow light components. Additionally argon can be instrumented as a single or dual phase experiment.

The DarkSide Experiment DarkSide is a two phase liquid argon experiment deploying 50 kg of active detector mass surrounded by liquid scintillator veto, submerged in a large, shielding tank of water.

The Darwin Experiment The Darwin experiment is envisioned to be the ultimate liquid nobel experiment. It would have a 20 tonne liquid xenon target as well as a 50 tonne liquid argon target, both surrounded by a water scintillator shield.

The list of liquid experiments past, present and future goes on, including ArDM, PandaX, MAX, WARP...

2.1.3.2.5 Superheated liquids In this type of experiment, a chamber is filled with a fluid that is heated above its boiling point. A small amount of energy, such as a dark matter nuclear recoil is enough to nucleate the formation of an easily visible bubble. Fittingly, the chamber is called a bubble chamber. The presence of fluorine in the target materials used, makes these experiments particular sensitive to spin-dependent dark matter interactions [64]. A deployed detector will be monitored by cameras in a well shielded location with.

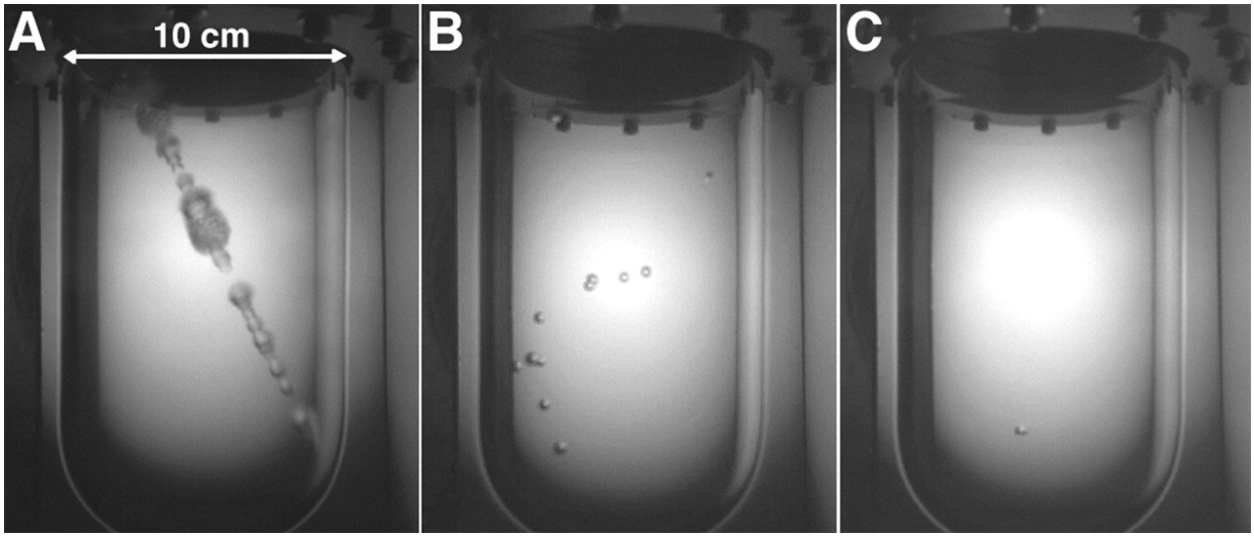


Figure 2.6: [Nucleation of bubbles in the COUP experiment. Left, a cosmic ray event. Middle, A neutron multiple scatter event. Right, A neutron single scatter. Image from [27].

The PICO Experiment The PICO experiment is a merger of two other superheated liquid detector dark matter experiments, PICASSO an COUP, deployed at SNOLAB. COUP, which stands for Chicagoland Observatory for Underground Particle Physics, experiment has recently completed a run using 37 kg of CF_3I, a fire-extinguisher agent, as its target material. PICO is running separate chamber of 2.9 kg C_3F_8.

The SIMPLE Experiment SIMPLE stands for superheated instrument for massive particle experiments [62]. It is transitioning from a C_2ClF_5 superheated droplet detector to a bubble chamber with C_2ClF_5 and C_3F_8. SIMPLE uses droplet size and location information to accomplish event discrimination.

2.1.3.2.6 Gas target materials Such experiments use low pressure gas inside a grid of wire electrodes to create a time projection chamber dark matter detector. Direction information would increase the certainty of potential dark matter detection if it is accompanied by adequate statistics. The use of a gaseous target makes it a challenge to attain large detector masses.

The DRIFT Experiment DRIFT stands for directional recoil identification from tracks and is deployed in the Boulby mine in the United Kingdom. It uses a partial pressure mixture of CS_2:CF_4 with a small addition of O_2 as the target material. The chamber is operated at about 100 torr. This choice of target material enables sensitivity to spin-dependent interactions.

MIMAC, NEWAGE and DMTCP are other gas based direct detection experiments.

2.1.4 Search status

Progress in direct dark matter detection is made by excluding, through lack of detected signal, the possibility for dark matter to exist in certain ranges of mass and cross section. On axes of WIMP mass and cross the excluded regions for each dark matter experiment can be indicated and compared. Figure 2.7 is such a plot for spin-independent detection. A similar plot can be made for spin-dependent detection.

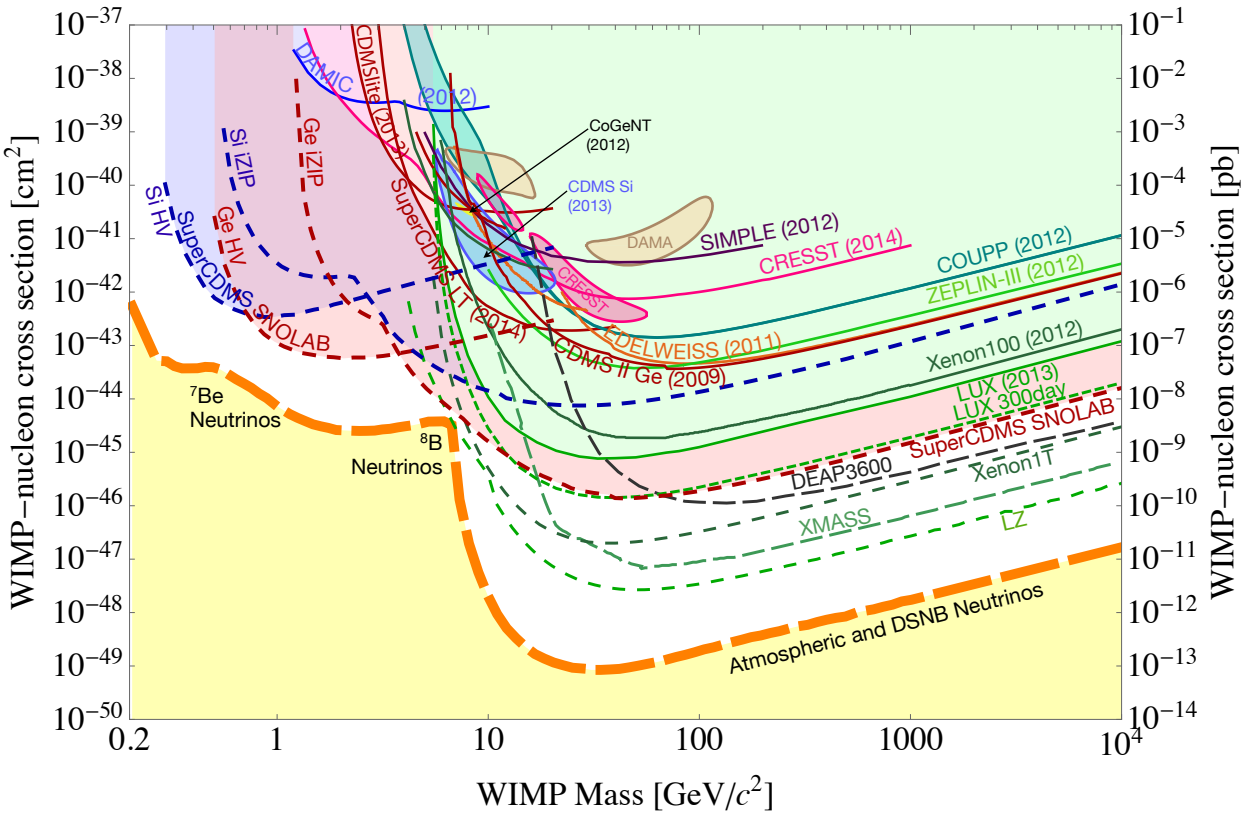


Figure 2.7: Areas of mass-cross section parameter space which lie above the curve drawn for a given experiment are excluded by that experiment's data. Closed curves indicate discover claims.

2.2 The CDMS experiment

Driven the need to increase detector mass and to suppress backgrounds, the CDMS experiment is embarking upon its fourth phase (Table 2.1) of operation, SuperCDMS at SNOLAB. The deeper SNOLAB location offers improved shielding from cosmogenic backgrounds in comparison to Soudan. The experiment is to feature larger detectors. This increases the per detector fiducial volume and decreases the per kilogram labor and cost require to produce the detector. An increased number of phonon sensors will enable improved pulse shape discrimination of background events Figure 2.8. The SNOLAB phase will entail a minor increase in dark matter sensitivity, at 60 GeV $c_0{}^{-2}$. This is because CDMS will direct its focus toward the search for WIMPs with mass <10 GeV $c_0{}^{-2}$, low mass WIMPs, moving forward. We are doing this by turning up the charge collection voltage. The higher voltage amplifies the primary charge signal of the events by increasing the phonons created as the charge is dragged by the field to the collection electrodes. These secondary phonon's are called Luke phonons and the project to enable this mode of low threshold detection is called CDMS Lite.

2.2.1 Technical challenges for large arrays

The challenge in instrumenting large dark matter detector arrays is to control background radiation, to prevent confusion of a WIMP signal with the signal from something much less interesting. Situating the detector deep underground is necessary to avoid cosmic rays which produce neutrons which can be confused as WIMPs.

Another challenge to instrumenting large arrays is the production of detectors. This is less of a challenge for the liquid detectors. But for the CDMS experiment, the challenge of rapidly fabricating numerous identical detectors is significant. The micron-scale feature size of sensors on the CDMS detector contribute to the difficulty. Also, for many of the solid state detects, the complexity of cryogenic signal wiring from is a significant problem. Hence, large arrays favor multiplexed detector readout.

Other direct detection experiments encounter different difficulties in scaling up. As an example, for the liquid noble detectors, instrumenting larger or numerous detectors carries the difficulty of maintaining the radio-purity of the liquid. Also, in scaling up safety concerns become critical when dealing with large volumes of cryogenic liquids in closed underground caverns.

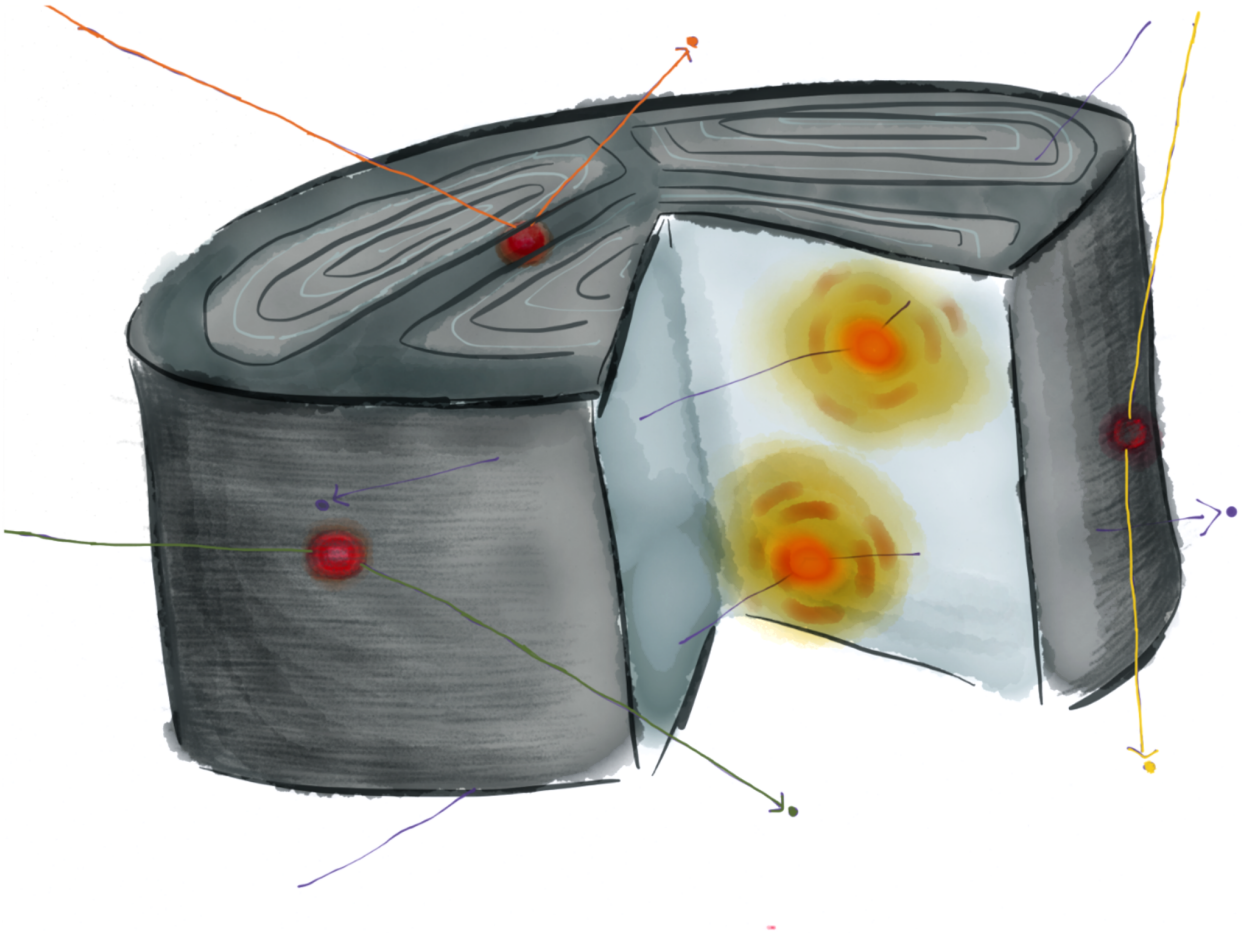


Figure 2.8: Illustration of the particle interactions in the CDMS detector. WIMPs (purple particles and tracks) are expected to interact anywhere within the detector volume. Most other particles, such as muons and phonons, have a greater chance of interacting close to the surface of the detector due their higher electromagnetic and weak interaction cross sections with standard model particles. A fiducial volume of the detector excludes the surface region where interactions will most likely be due to non-WIMP particles. Event discrimination involves fiducial volume cut to elimination event outside that volume, as well as a general comparison of the phonon to charge signal strength. The increased number of phonon sensors, as well as an improved sensor design will enhance background discrimination the SuperCDMS SNOLAB detectors. Image from [1].

2.3 Detection of axion dark matter

The leading direct detection experiment for axion dark matter is Axion Dark Matter Experiment (ADMX) [164]. This experiment sweeps the resonant frequency of a microwave cavity which is permeated by a strong magnetic field. If the axion exists, it would resonantly

convert to microwave photos at a certain frequency. The challenge is to find this expectedly narrow band frequency and stay there there long enough for sensitive microwave amplifiers to detect the photon signal. A discovery in this experiment would be a static signal.

Recently it has also been suggested that, with a low enough threshold, a germanium experiment such as CDMS or Edelweiss could sensitive to the low-energy electron recoils due dark matter axion, [20].

2.3.1 Axion search status

Axions experiments also present their search progress in the form of a limit plots. However, instead of plotting mass against cross-section, they plot the axion mass against the axion coupling coefficient $g_{a\lambda\lambda}$, which was introduced in Equation 1.33.

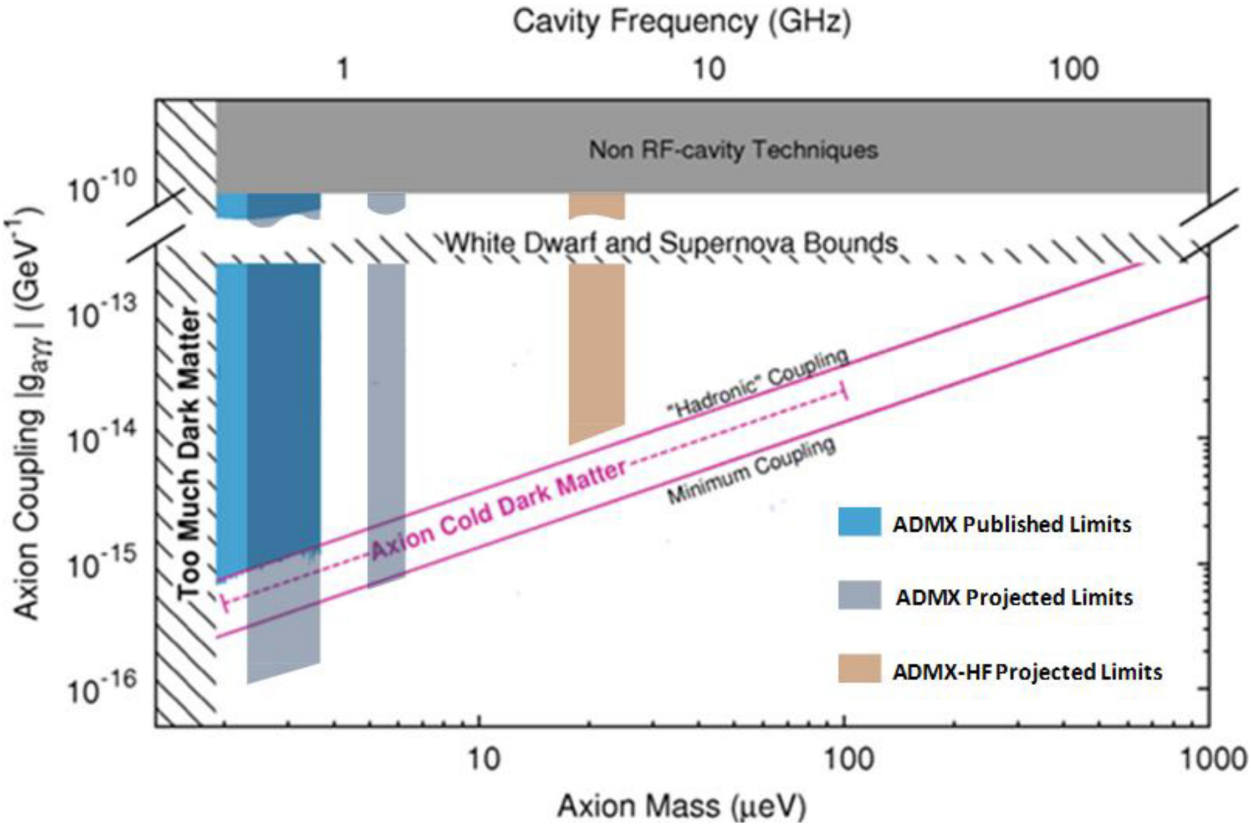


Figure 2.9: Areas of mass-coupling constant parameter space which lie within the colored regions for a given experiment are excluded by that experiment's data. Image from [167].

Attributions

Results in this chapter come from literature sources. Illustrations from [1] are original work, with her doing the drawing and both of us formulation how they should look.

	CDMS I	CDMS II	SuperCDMS	SuperCDMS
Location	SUF[a]	Soudan	Soudan	SNOLAB
Depth [m.w.e]	16	2090	2090	6010
Background[b] [n/yr/t]	182500	600	600	1
Duration	1998 - 2002	2003 - 2009	2009 - 2015	2016 -
Detector Size	∅ 3 inch × 1 cm	∅ 3 inch × 1 cm	∅ 3 inch × 2.5 cm	∅ 4 inch × 3.3 cm
Ge Detectors	4 @ 240 g	19 @ 240 g	15 @ 610 g	40 @ 14 000 g
Si Detectors	2 @ 106 g	11 @ 106 g	none	8 @ 600 g
Channel [c]	2 JFET + 4 TES	2 JFET + 4 TES	4 JFET + 8 TES	4 HEMT + 12 TES
Sensitivity[d] [cm^2]	$3.5 \cdot 10^{-42}$	$3.5 \cdot 10^{-44}$	$5 \cdot 10^{-45}$	$2 \cdot 10^{-46}$

[a] The Stanford underground research facility at Stanford University

[b] Number of cosmogenic neutron interactions per tonne of detectors per year in the nuclear recoil energy range 10–50 keV.

[c] The number of ionization channels as readout by a field effect transition or a high electron mobility transistor + the number of phonon channels as readout by transition etch sensors. All figures are per detector. Charge channels on SuperCDMS Soudan and SNOLAB detectors are interleaved.

[c] WIMP-nucleon cross section, σ, at 60 GeV ${c_0}^{-2}$

Table 2.1: The evolution of the CDMS experiment as tracked by changes in instrumentation, location and backgrounds. The SuperCDMS SNLOAB phase stands as a change in objective for the collaboration. Instead of pushing the limit for high mass WIMP detection, the SNOLAB experiment will have sensitivity leading the field in low mass detection, and it will be positioned to rapidly confirm a detection of a high mass WIMP, mostly likely made by other experiments that are more sensitive at high masses.

Chapter 3

Kinetic Inductance Phonon Sensors for Dark Matter Detection

3.1 Overview of kinetic inductance detectors

3.1.1 Kinetic inductance

Below its superconducting transition, the resistance of a superconductor drops rapidly toward zero. Its reactance, however, maintains a finite value below transition. This reactance is due to two effects. First, any change in current in the superconductor generates a change in magnetic field which the superconductor resists. Second, the collision-less motion of the Cooper-pairs admits the storage of significant kinetic energy, or momentum, and it requires work from the field to change the momentum. These effects describe a reactance that is inductive. The effects occur at the surface of a superconductor within a thickness on the order of the superconducting penetration depth where currents may flow. Thus, devices designed to exploit these effects need only be films with thickness on this order. For films with thickness much less than the penetration depth the kinetic inductance dominates providing good reason to call this reactance, kinetic inductance.

Energy quanta impinging on the superconducting film may break Cooper-Pairs into quasi-particles, out of equilibrium electrons, changing the situation described above in several ways. One, quasi-particles are a dissipative contribution to the current, introducing a resistance. Two, the penetration depth of the film increases since there are fewer Cooper pairs to sustain eddy currents that expel magnetic fields. This results in an increase of film inductance. At temperatures much lower than the superconducting transition temperature, the increase in reactance per addition of quasi-particle is greater than the increase in resistance per addition of quasi-particle. Three, the kinetic energy carried by the Cooper pairs decreases as their number decreases. As a result the kinetic inductance increases.

Here we have a system sensitive to the energies on the order of that required to break a Cooper-pair into quasi-particles, $2\Delta \approx 0.55\,\mathrm{mV}$ (for aluminum). We can make a sensitive detector out of this if we can find a way of transforming the resulting impedance changes to

voltage changes we can detect with a low noise amplifier of reasonable input impedance.

3.1.2 Principle of operation

The kinetic inductance detectors (KIDs) considered in this thesis are all superconducting thin film resonant circuits.

There are various formats in which these resonators can be implemented. One is to connect narrow inductive trace elements to an interdigitated comb-like capacitive element, to form a lumped element resonator. Another implementation is to construct transmission-line resonant circuits, such as a stub feature on micro-strip line or coplanar waveguide. In both cases, the resonant circuits are weakly coupled to a transmission-line, the "feed line", which supplies the power at the resonant frequency of the resonator. The coupling, usually capacitive, is tuned to achieve a desired quality factor for a given resonance. Up stream of the resonator the feed line is connected to a generator. Down stream of the resonator the feed line is connected to an amplifier.

At resonance, the impedance to ground across the resonator vanishes, and from the point of view of the feed line, the resonator is a short to ground at the resonant frequency. Power at the resonate frequency (over some bandwidth) is reflected back to the generator and amplifier sees a voltage minimum.

We couple the resonant circuit to the energy quanta we wish to sense. The energy impinging in the superconducting film affects a change in the film's surface impedance which changes the resonant frequency and quality factor of the resonator. In consequence, the voltage at the amplifier changes an we have detected the energy impinging on the resonator.

3.1.3 Attractive features of kinetic inductance detectors

The foregoing paragraphs describe a detector technology with several attractive features. These include the following.

- KIDs can, in principle, be very sensitive to energies greater than Cooper-pair breaking gap energy, 2Δ.
- Their operation well below the superconducting transition temperature suppresses quasi-particle generation-recombination noise.
- Their operation well below the superconducting transition also avoids the necessity to finely tuned transition temperatures.
- The weakly coupled resonant circuit implementation scheme naturally enables frequency domain multiplexed readout of multiple detectors in a single feed line.
- The single feed-line multiplexed readout also avoids signal wiring complexity in the cryostat.
- Independent of resonator format, the technology is applicable to detection of various types of signals by optimization of resonator geometry, material and energy coupling method.

3.1.4 Applicability to direct detection

The detectors we currently fabricate to probe for WIMP dark matter utilize transition edge sensors (TESs) to sense phonon energy created by interactions within the germanium absorber. Phonons from such interactions impinge on cm^2 scale regions of the absorber where they break Cooper-pairs and affect a change in resistance.

Our goal to detect the WIMPs leads to the desire to increase the number of detectors we deploy. This is because increasing the number of detectors increases the probability of WIMP nuclear recoils. Technology improvements which support the deployment of numerous detector are therefore aligned with our science objective.

A kinetic inductance phonon sensor would be applicable in our approach to direct detection if the sensors were easier to fabricate than the TES phonon sensors; the sensors had equal or better sensitivity than the TESs; the sensors offered improved uniformity in performance between detectors; and if the sensors were compatible with ionization readout.

The versatility in resonator geometry afforded by KIDs would allow us to make resonators as large as our signal area, $\approx cm^2$. The minimum feature sizes required for such large phonon sensors would simplify fabrication. It would also decrease the effect of normal process variations on detector performance, increasing performance uniformity between detectors. On paper, the sensitivity of kinetic inductance phonon sensors is competitive with TES sensitivity. Suitable choice of KID geometry could accommodate ionization readout. Due to their promise and applicability to our science objective, we pursue a kinetic inductance phonon sensor for our dark matter detectors.

These simple detectors are attractive to a number of other applications which require high energy resolution and large detector area. For example, they can be used to detect x-rays and gamma-rays as produced from astrophysical sources like active galactic nuclei and WIMP annihilations in the cosmos, or man-made sources, such as for medical imaging and nuclear non-proliferation, where they can be used to identify originating reactor of radioactive materials. Another class of fundamental physics investigations in need of large, sensitive detectors is neutrino coherent scattering experiments.

3.1.5 Detector concept

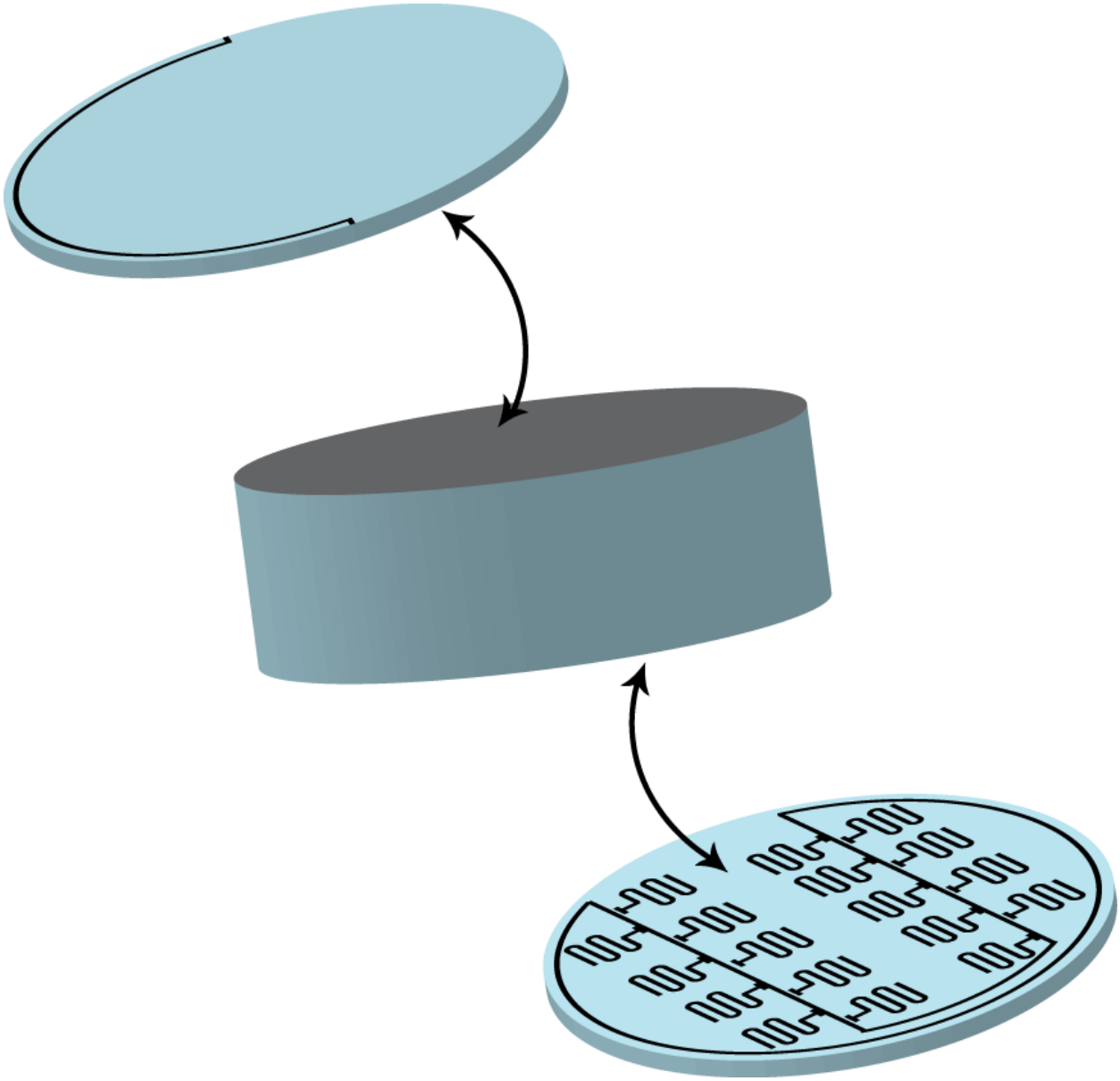


Figure 3.1: Our envisioned implementation of kinetic inductance phonon sensors for our dark matter detectors has the sensor function separated from the absorber function. Separate, standard sized, sensor wafers are attached to both faces of the germanium absorber. The sensor wafers carry the trace of a microstrip resonator, whose ground plane is directly deposited into the surface of the absorber. When an event occurs, the phonons impinge upon the ground plane and change its impedance. The change in impedance is detected as a change in the resonance by room temperature electronics. Position sensitivity is achieved by looking at the relative responses of all the sensors across the detector surface. The event will have occurred closest to the sensor (resonator) exhibiting the greatest response.

Our envisioned implementation of kinetic inductance phonon sensors would separate the sensor and absorber functions. We would use a microstrip transmission line format where the ground plane is deposited directly on the surface of the absorber and the trace is patterned on a separate standard thickness wafer, the "sensor wafer". We would attach the sensor wafer to the absorber though a bonding process or, initially for development purposes, a mechanical press. Micron-scale pillars would maintain a vacuum gap between the traces and the ground plane, and keep them from shorting together. The lack of a material dielectric avoids dielectric noise, too. We are attracted to the minimal level of fabrication needed to produce these detectors and expect that it will reduce our costs.

A priori, would intend to use niobium as the microstrip trace material and aluminum as the ground plane material. Aluminum is chosen for its low superconducting gap, and for its good quasiparticle conversion efficiency. Niobium is chosen for its relatively high critical current and gap, so that high currents can be driven through the trace and so that the trace is insensitive to events occurring in the sensor wafer.

3.2 Material electrodynamics

In order to understand the behavior of a resonator, we first look at the response of the superconductors in an electromagnetic field. Excellent comprehensive references on this topic include [56, 55, 79, 180, 201]

3.2.1 Theoretical frameworks

The relevant electrodynamic theories governing the behavior of a superconductor in a field start at Maxwell's equations, include the macroscopic models described in the London equations, and are underpinned by the microscopic theory of superconductivity from Bardeen Cooper Schriefer (BCS), which ultimately provides a formalism of how the superconductor responds to the input of energy.

3.2.1.1 Maxwell's equation

Generally, Maxwell's equations relate currents and the electric and magnetic fields in matter. Inside a material, Maxwell's equations are

$$\nabla \cdot \mathbf{D} = \rho \tag{3.1a}$$
$$\nabla \cdot \mathbf{B} = 0 \tag{3.1b}$$
$$\nabla \times \mathbf{E} = -\frac{\partial \mathbf{B}}{\partial t} \tag{3.1c}$$
$$\mathbf{D} = \epsilon_r \epsilon_0 \mathbf{E} \tag{3.1d}$$
$$\mathbf{B} = \mu_r \mu_0 \mathbf{H} \tag{3.1e}$$
$$\nabla \times \mathbf{H} = \mathbf{J} + \frac{\partial \mathbf{D}}{\partial t} \tag{3.1f}$$

Additionally, we have $\epsilon_0 \mu_0 = c^{-2}$, $\epsilon = \epsilon_r \epsilon_0$ and we assume $\mu_r = 1$ and $\rho = 0$ in the conductor. We can define a vector potential, $\mathbf{A}$ such that,

$$\mathbf{E} = -\frac{\partial \mathbf{A}}{\partial t} - \boldsymbol{\nabla} \varphi \tag{3.2a}$$
$$\mathbf{B} = \nabla \times \mathbf{A} \tag{3.2b}$$
$$0 = \nabla \cdot \mathbf{A}. \tag{3.2c}$$

In the case of a superconductor, Maxwell's equations alone do not provide a complete electrodynamic description. They will need to be supplemented to accurately describe behavior of a superconductor.

3.2.1.2 The two-fluid model and the london equations

We can obtain a more accurate electrodynamic description with the addition of the Gorter-Casimir two-fluid model [73] and the London equations [114] to Maxwell's equations. These models do not provide a microscopic quantum description of superconductivity but they do provide a good enough description of the electrodynamics of the superconductor, again assuming a local current field relationship. The two-fluid model assumes that the conduction electrons in a superconductor are either in a superfluid, state which has no resistance, or a normal state. The two states do not interact and the number density of electron in the superfluid state, n_s, varies from 0 at $T = 0\,\mathrm{K}$ to 1 at $T = T_c$, the superconducting transition temperature, according to

$$\frac{n_s}{n} = 1 - \left(\frac{T}{T_c}\right)^4 \tag{3.3}$$

The superfluid electrons have current, charge and mass, $\mathbf{J}_s$, q_s and m_s, and these quantities for the normal electrons are denoted $\mathbf{J}_n$, q_n, m_n and n_n. At all temperatures,

$$n = n_n + n_s \tag{3.4a}$$
$$\sigma = \sigma_n + \sigma_s, \tag{3.4b}$$
$$\mathbf{J} = \mathbf{J}_n + \mathbf{J}_s. \tag{3.4c}$$

As we will see in Equation 3.36 and Equation 3.38, normal conductors exclude oscillating fields from penetrating to their interior. Fields within the conductor are attenuated on a length scale, λ , that decreases with increasing conductivity and frequency''. Meissner and Ochsenfeld [127] observe the same exclusion of fields in superconductors consistent with the fact of their very large conductivity. They also observed that when a magnetic field was present inside a superconductor in its normal state, $T > T_c$, the magnetic field was expelled from the superconductor when it was cooled below T_c. This phenomenon is not described by Maxwell's equations. The London equations,

$$\mathbf{E} = \Lambda \frac{\partial \mathbf{J}_s}{\partial t}, \tag{3.5a}$$
$$0 = \Lambda \left(\nabla \times \mathbf{J}_s\right) + \mathbf{B}, \tag{3.5b}$$
$$\Lambda \equiv \frac{m_s}{n_s q_s^2} \tag{3.5c}$$

describe both phenomena. Λ is the London constant. Here again, a local field current relationship is assumed,

$$\Lambda \mathbf{J} = -\mathbf{A}. \tag{3.6}$$

Note that arbitrary large currents (and therefore magnetic fields) have no effect on the superconducting state according to Equation 3.5. This is a problem of the London equations.

3.2.1.3 BCS theory of superconductivity

BCS [23] theory provides a microscopic and quantum description of superconductivity. The theory describes an electron pairing process leading to a Bose Einstein condensate. The *Cooper pairs*[1], are of equal and opposite momentum and spin, and exchange of phonons between them provides an attraction that overcomes the Coulomb repulsion. The system of Cooper pairs comprises the coherent ground state of the quantum many body system of electrons. Excitations from this ground state are called quasiparticles. But some low temperature and all high temperature superconductors are not completely explained by the

[1]In the parlance of the two-fluid model, $n_s = 2n_{CP}$, where n_{CP} is the number density of Cooper pairs. However, $n = n_n + n_s$ fails for dirty superconductors, when $T \leq T_c$, due to quasiparticle phase coherence effects, and in strong-coupling superconductors where the effective mass of quasiparticle is enhanced to $2m(1 + \gamma_{coupling})$ in excess of the the electron mass [79, pp. 7, 26, 32]

BCS theory. The theory is in excellent agreement with measurements of specific heat, penetration depth and the Meissner effect in most low temperature and alloy superconductors. We present a brief overview of the BCS theory, following [176, Chap 2, 79, §1.3.1].

Quasiparticle states are labeled by their wave vector, $\mathbf{k}$, and spin, $\sigma = \{\uparrow, \downarrow\}$. Thus a Cooper pair is $(\mathbf{k}\uparrow, -\mathbf{k}\downarrow)$. The state has a plane-wave energy ${}^{(\hbar\mathbf{k})^2}/_{2m} = \xi_{\mathbf{k}}$. The ground state forms Fermi surface that is a perfect sphere in $\mathbf{k}$-space, with a Fermi energy is E_F. At $T = 0\,\mathrm{K}$, the density of states at the Fermi energy for electrons of one spin orientation is N_0. Each Cooper Pair has a pairing potential V, which is assumed to be so small that $\gamma_{\text{coupling}} \equiv N_0 V \ll 1$. This is the assumption of weak electron-phonon coupling upon which BCS theory is considered to be valid.

The pairing hamiltonian is

$$H = H_0 + H_{\text{interaction}} = \sum_{\mathbf{k},\sigma} \xi_{\mathbf{k}} c^*_{\mathbf{k},\sigma} c_{\mathbf{k},\sigma} + \sum_{\mathbf{k},\mathbf{l}} V_{\mathbf{k},\mathbf{l}} c^*_{\mathbf{k},\uparrow} c^*_{-\mathbf{k},\downarrow} c_{-\mathbf{l},\downarrow} c_{\mathbf{l},\uparrow} \tag{3.7}$$

where the $c^*_{\mathbf{k},\uparrow}$ are creation operators, $V_{\mathbf{k},\mathbf{l}}$ is the pairing potential due to Cooper,

$$V_{\mathbf{k},\mathbf{l}} = \begin{cases} -V & \text{if } |\epsilon_{\mathbf{k}}| \text{ and } |\epsilon_{\mathbf{l}}| \leq \hbar\omega_{\text{cutoff}} \\ 0 & \text{otherwise} \end{cases} \tag{3.8}$$

where $\epsilon_{\mathbf{k}} = \xi_{\mathbf{k}} - E_F$, is the state energy relative to the Fermi level and $\hbar\omega_{\text{cutoff}}$ is some cutoff energy. An order parameter $\Delta_{\mathbf{k}}$, interpreted as the superconducting energy gap, is defined such that,

$$\Delta_{\mathbf{k}} \equiv -\sum_{\mathbf{l}} V_{\mathbf{k},\mathbf{l}} u_{\mathbf{l}} v_{\mathbf{l}} \tag{3.9}$$

where $v_{\mathbf{l}}$ and $u_{\mathbf{l}}$ are the wave functions for occupation and non-occupation of a pair state. A quasiparticle excitation has the energy, $E_{\mathbf{k}}$

$$E_{\mathbf{k}} \equiv \left(\Delta^2_{\mathbf{k}} + \epsilon^2_{\mathbf{k}}\right)^{1/2}. \tag{3.10}$$

The step function nature of the assumed Cooper pairing potential, in addition to the assumption of a spherically symmetric $\mathbf{k}$-space, in fact implies that $\Delta_{\mathbf{k}}$ is independent of $\mathbf{k}$. It can be shown that,

$$\Delta_{\mathbf{k}} = \begin{cases} \Delta & \text{for } |\epsilon_{\mathbf{k}}| < \hbar\omega_{\text{cutoff}} \\ 0 & \text{for } |\epsilon_{\mathbf{k}}| > \hbar\omega_{\text{cutoff}}. \end{cases} \tag{3.11}$$

Equation 3.10 is the energy of a quasiparticle excitation. It shows that the energy needed to break a cooper pair into two quasi-particles is $\geq 2\Delta$.

At temperatures,T, above zero, where thermal fluctuations allow for the electrons to be excited above the ground state, we would expect a Fermi-Dirac distribution in probably of excitation,

$$f(E_{\mathbf{k}}) = \frac{1}{1 + e^{\frac{E_{\mathbf{k}}}{k_B T}}}. \tag{3.12}$$

Integrating this into the interaction Hamiltonian, one can find a temperature dependance to the gap parameter $\Delta_{\mathbf{k}}$. It ranges from

$$\frac{\Delta_0}{k_B T_c} = \frac{\pi}{\gamma} \approx 1.764, \tag{3.13}$$

, at $T \approx 0\,\mathrm{K}$, where $\gamma = 1.7811$ is Euler's constant, to

$$\frac{\Delta(T)}{\Delta_0} \approx 1.74 \left(1 - \frac{T}{T_c}\right)^{1/2}, \tag{3.14}$$

around $T \approx T_c$. $\Delta(T)$ can be used to give Equation 3.10 temperature dependence, $E_{\mathbf{k}}(T) = E_{\mathbf{k}}(\Delta_{\mathbf{k}}(T))$.

The density of states, N, at excitation energy, E, of the BCS superconductor can be related to the density of states at the Fermi level N_0 of the superconductor in it normal state as,

$$\frac{N(E)}{N_0} = \frac{E}{(E^2 - \Delta_0^2)^{1/2}}. \tag{3.15}$$

3.2.1.4 Calculation of the Density of states, N_0

For BCS superconductors the single-spin density of electron states at the Fermi surface is N_0 is related to the band structure density of states, N by

$$N_0 = N \frac{1 + \lambda_{ep}}{a^3}, \tag{3.16}$$

where a is the lattice parameter, and λ_{ep} is the electron phonon coupling constant. Depending on the lattice, a^3 can be approximated as,

$$a^3 = \frac{m_a}{g_{av}\rho}, \tag{3.17}$$

where m_a is the atomic mass, g_{av} is Avogadro's number, and ρ is the density (at the relevant temperature). [126] provides a useful, but old, tabulation of various N and λ_{ep}. More recent values can be found in the literature. One can alternatively bypass the calculation all together buy using a experimental measurement of specific heat to obtain N_0.

3.2.1.5 Mattis bardeen theory of the anomalous skin effect

Mattis and Bardeen [122] and independently Abrikosov, Gorkov and Khalatnikov [16] used first order perturbation theory to extend the BCS theory of superconductivity [23] to formulate an integral expression for the complex conductivity of isotropic normal and superconductors valid in the weak-coupling limit [146, p. 1306, 147, p. 5950].

The kernel $I(\omega, R, T)$ in Equation 3.32 may be adjusted for different assumptions about the conductor

$$I(\omega, R, T) = \int_{-\infty}^{\infty}\int_{-\infty}^{\infty}\left[L(\omega,\varepsilon,\varepsilon') - \frac{f(\varepsilon)-f(\varepsilon')}{\varepsilon'-\varepsilon}\right] \times \cos\left[\alpha(\varepsilon-\varepsilon')\right] d\varepsilon d\varepsilon', \tag{3.18}$$

where

$$L(\omega,\varepsilon,\varepsilon') = -\frac{1}{2}(1-2f(E))\left[\frac{E+\hbar(\omega-is)+\frac{\Delta_0^2+\varepsilon\varepsilon'}{E}}{E'-[E+\hbar(\omega-is)]^2} \times \frac{E-\hbar(\omega-is)+\frac{\Delta_0^2+\varepsilon\varepsilon'}{E}}{E'-[E-\hbar(\omega-is)]^2}\right]. \tag{3.19}$$

Here we have $\alpha = {}^{R}/_{\hbar v_0}$; $E^{(\prime)} = \sqrt{(\varepsilon^{(\prime)})^2+\Delta^2}$ is the excitation energy; f is the Fermi-Dirac; and s is a small perturbation parameter to be set to zero in final expressions.

In superconductors, the extreme anomalous limit occurs when, simultaneously, the mean free path is much greater than the penetration depth $l \gg \lambda$ and the Pippard coherence length (Equation 3.24) is much larger than the penetration depth $\xi_P \gg \lambda$. This occurs in clean superconductors where Equation 3.27 implies $l \gg \xi_0$. These limits imply that we set $\alpha = \frac{R}{\hbar v_0} = \frac{R}{\pi\Delta_0\xi_0} \approx 0$ in Equation 3.18. This means $I = I(\omega, R=0, T)$ can taken out of the integral Equation 3.32 and is equal to

$$\Re[I(\omega,0,T)] = -\pi\int_{-\Delta,\quad\Delta-\hbar\omega}^{\Delta} \frac{E^2+\Delta^2+\hbar\omega E}{\sqrt{\Delta^2-E^2}\sqrt{(E+\hbar\omega)^2-\Delta^2}}[1-2f(E+\hbar\omega)]dE \tag{3.20a}$$

$$\begin{aligned}\Im[I(\omega,0,T)] = \pi&\int_{\Delta-\hbar\omega}^{\infty} \frac{[1-2f(E+\hbar\omega)][E^2+\Delta^2+\hbar\omega E]}{\sqrt{E^2-\Delta^2}\sqrt{(E+\hbar\omega)^2-\Delta^2}}dE \\ &- 2\pi\int_{\Delta-\hbar\omega}^{\infty} \frac{[f(E)-f(E+\hbar\omega)][E^2+\Delta^2+\hbar\omega E]}{\sqrt{E^2-\Delta^2}\sqrt{(E+\hbar\omega)^2-\Delta^2}}dE,\end{aligned} \tag{3.20b}$$

for the superconducting state and,

$$I(\omega, 0, T_c) = -i\pi\hbar\omega, \tag{3.21}$$

for the normal state [147]. Recalling Equation 3.2a, the current is completely in phase with the electric field.

Assuming normal incidence of the field on the conductor, the ratio of the current density magnitude, J_∞, an be computed for extreme anomalous limit as,

$$\frac{J_\infty(\omega)}{J_{\infty n}(\omega)} = \frac{I(\omega,0,T)}{I(\omega,0,T_c)} = \frac{\sigma_1 - i\sigma_2}{\sigma_n}, \tag{3.22}$$

and the complex conductivities can be written as,

$$\frac{\sigma_1(\omega)}{\sigma_n} = \frac{1}{\hbar\omega}\int_{\Delta-\hbar\omega}^{-\Delta} \frac{[1-2f(E+\hbar\omega)][E^2+\Delta^2+\hbar\omega E]}{\sqrt{E^2-\Delta^2}\sqrt{(E+\hbar\omega)^2-\Delta^2}}dE + \frac{2}{\hbar\omega}\int_{\Delta}^{\infty} \frac{[f(E)-f(E+\hbar\omega)][E^2+\Delta^2+\hbar\omega E]}{\sqrt{E^2-\Delta^2}\sqrt{(E+\hbar\omega)^2-\Delta^2}}dE \tag{3.23a}$$

$$\frac{\sigma_2(\omega)}{\sigma_n} = \frac{1}{\hbar\omega}\int_{\Delta}^{\Delta-\hbar\omega,\quad \Delta} \frac{E^2+\Delta^2-\hbar\omega E}{\sqrt{E^2-\Delta^2}\sqrt{\Delta^2-(E-\hbar\omega)^2}}[1-2f(E+\hbar\omega)]dE, \tag{3.23b}$$

[122]. The first term of Equation 3.23a does not appear unless $\hbar\omega > 2\Delta$, in which case the lower limit of Equation 3.23b is Δ in stead of $\Delta - \hbar\omega$. While Equation 3.23 is only strictly valid for $l \ll \xi_0$ or $l \ll \xi_0$, the expressions seem to contain qualitatively the main features characteristic of all BCS superconductors.

3.2.2 Conceptual essentials

We begin by introducing key concepts involved in the material electrodynamics.

3.2.2.1 Characteristic lengths

The charge carriers of a normal conductor are within k_BT of the Fermi level and have a mean free path l that is related to the time between scattering (also called momentum relaxation time), τ, and their velocity of motion, v_0, the Fermi velocity by $l = v_0\tau$[2]. When the conductor is a superconductor, charge carriers (Cooper Pairs) have an effective size, ξ, the coherence length. The coherence length can be expressed in terms of various material and environmental properties (such as T and T_c). different theoretical frameworks lead to different expressions for ξ. In general, the coherence length, ξ, is empirically modeled as an intrinsic material parameter, ξ_0, which is reduced by defect scattering

$$\frac{1}{\xi_P} = \frac{1}{\xi_0} + \frac{1}{l}. \tag{3.24}$$

[2] [141, p. 261] cites 'standard monovalent metal' values to keep in mind.

$$\text{Atomic volume} = 10\,\text{cm}^{-3}$$
$$\text{Conduction electron density} = 6\cdot10^{22}\,\text{cm}^{-3}$$
$$\text{Fermi Velocity, } v_0 = 1.4\cdot10^{8}\,\text{cm}\,\text{s}^{-1}$$
$$\text{Electrical conductivity with } l \text{ free path, } \sigma = {}^{l}/_{\text{cm}} \times 1.21\cdot10^{11}\,\Omega^{-1}\,\text{cm}^{-1}$$
$$\text{Fermi energy, } E_F = 5.57\,\text{eV}$$
$$\text{Momentum relaxation time, } \tau = 10^{-14}\,\text{s}\frac{\rho_{290\,\text{K}}}{\rho_T}$$

where ρ is the resistivity.

When the conductor is in an oscillating field, the depth of penetration of the field into the conductor is limited. The penetration of an oscillating magnetic field into a normal conductor is attenuated by a factor of $1/e$ at a length of the skin depth, δ. The penetration of a weak DC magnetic field into a superconductor is attenuated by a factor of $1/e$ at a length of the penetration depth, λ.

In a normal metal, δ, which describes the spatial variation of $\mathbf{E}$, may be much greater than l. In this case the current-field relationship is local and the normal skin effect is observed in measurements of surface impedance. At low temperatures and/or high frequencies of oscillation however, it is possible to have $\delta \ll l$. In this limit, charge carriers at one point will have retained the momentum they acquired from the field at previous points, which will have had different values. A nonlocal current field relationship (Equation 3.28) is necessary to describe the current[3]. Measurements of surface impedance will indicate the anomalous skin effect[4,5,6]. Similar to the case of a normal conductor, the local current-field relationship fails when ξ is larger than the length over which the field varies appreciably, or when ξ exceeds the penetration depth, λ. In this limit the current is determined by a nonlocal field relationship, Equation 3.29, Equation 3.30. In §3.2.2.2, the local and nonlocal field relationships are made explicit.

At $T = 0\,\mathrm{K}$[7], Londons' equations can be used to derive a DC penetration depth, λ_L, called the London penetration depth and equal to

$$\lambda_L = \sqrt{\frac{\Lambda}{\mu_0}} = \sqrt{\frac{m_s}{\mu_0 n_s {q_s}^2}}, \tag{3.26}$$

In the framework of the BCS theory, the penetration depth can be approximated as

$$\lambda(l,T) \approx \lambda_L(T)\sqrt{1+\frac{\xi_0}{l}}, \tag{3.27}$$

[3]in the case of a nonlocal current field relationship, the attenuation of the field occurs on the order of some other length scale depending on material parameters (e.g. the 5 parameter Mattis-Bardeen equation, § 3.2.1.5).

[4]Transmission of light through thin films is typically used to measure the surface impedance of both normal and superconductors [71, 175]. Evidently, is it possible for electromagnetic waves to travel through superconductors so long as they are thin enough.

[5]In the extreme anomalous limit the conductivity becomes a tensorial quantity that depends on wavenumber and frequency. The effect can be used to map out the Fermi surfaces in metals [88, p. 332] [141, p. 222] [88, p. 332, 141, p. 222].

[6]In the extreme anomalous limit, the surface reactance and resistance should be in a ratio of $\sqrt{3}$ rather than unity as in the normal skin effect [143, p. 110].

[7]Note that the temperature dependence of n_s results in a temperature dependence on λ_L,

$$\lambda_L(T) = \lambda_L|_{T=0\,\mathrm{K}}\left[1-\left(\frac{T}{T_c}\right)^4\right]^{-1/2}. \tag{3.25}$$

$\lambda_L(T)$ diverges at $T \geq T_c$.

[176, p. 67] which yields the correct scaling of λ in the limits when l is very small or very large in the impure limit. Generally, λ is larger in dirty superconductors than it is in clean superconductors.

3.2.2.2 Current-field relations

Currents flow in conductors due to the influence of applied field. The relationship between the current and the field depends on material properties and the frequency of oscillation of the applied field, and may be either local or nonlocal. Superconductors and normal metals may have local or nonlocal current-field relationships.

Ohms law,

$$\mathbf{J} = \sigma \mathbf{E}, \tag{3.28}$$

describes a local field-current relationship and it is always valid unless conditions for a nonlocal relationship emerge. In attempt to explain the Anomalous Skin effect in normal metals [142] Chambers proposed an expression in which the current density at a point is given by an integral of the electric field over a region surrounding the point,

$$\mathbf{J}(\mathbf{r}) = \frac{-3\sigma}{4\pi l} \int_{V'} \frac{\mathbf{R}\left[\mathbf{R}\cdot\mathbf{E}(\mathbf{r}')\right]}{R^4} e^{-|\mathbf{R}|/l} d^3\mathbf{r}'. \tag{3.29}$$

where $R = |\mathbf{r}-\mathbf{r}'|$, and in Gaussian units. Pippard realized that currents in a superconductor could be described in an analogous way

$$\mathbf{J}(\mathbf{r}) = \frac{-3}{4\pi\xi_0\Lambda} \int_{V'} \frac{\mathbf{R}\left[\mathbf{R}\cdot\mathbf{A}(\mathbf{r}')\right]}{R^4} e^{-|\mathbf{R}|/\xi_P} d^3\mathbf{r}' \tag{3.30}$$

where $\mathbf{R} = \mathbf{r} - \mathbf{r}'$. Bardeen et al [23, p. 1195, p. 1196 fig. 5] proposed

$$\mathbf{J}(\mathbf{r}) = \frac{-3}{4\pi\xi_0\Lambda} \int_{V'} \frac{\mathbf{R}\left[\mathbf{R}\cdot\mathbf{A}(\mathbf{r}')\right] J(R,T)}{R^4} d^3\mathbf{r}' \tag{3.31}$$

to accord with their microscopic theory superconductivity in the weak electron-phonon coupling limit, where low frequency is assumed ($\omega \approx 0$). $J(R,T)$ is a non-specific, relatively slowly varying function of temperature. The substitution of the exponential with the $J(R,T)$ term gives the correct temperature dependence to the current density. Finally, Mattis and Bardeen, modify the $J(R,T)$ term in the superconducting current density to allow for frequency dependence accurate at microwave to infrared frequencies [122, p. 416, eq. 3.3]

$$\mathbf{J}(\mathbf{r}) = \sum_{\omega} \frac{\cdots}{\cdots} \times \frac{\mathbf{R}\left[\mathbf{R}\cdot\mathbf{A}_\omega(\mathbf{r}')\right] I(\omega,R,T)}{R^4} e^{-|\mathbf{R}|/l} d^3\mathbf{r}', \tag{3.32}$$

where the sum is over the frequency components of the vector potential. When the field does not vary appreciably over the distance ξ_P or l, Equation 3.30 and Equation 3.31 reduce to

Ohms Law (Equation 3.28). In both Equation 3.29 and Equation 3.30, the $e^{-|\mathbf{R}|/l}$ accounts for the effect of scattering.

Although it is not always possible to know a priori which current-field relationship is appropriate for a given conductor and test condition (e.g. temperature and drive frequency), we can list a few rules of thumb.

- Type I superconductors are usually nonlocal.
- Mean free path, l, typically dominates ξ per Equation 3.24 and local current-field relationships hold in impure or alloyed superconductors [79, p. 5].
- All known high temperature superconductors are local [163, p. 32].
- In the case of superconducting films, the ratio of the coherence length to the film thickness determines the relationship between the current and the fields, and also the surface impedance ([***Discussed in section ...***]).
- Except at low temperatures and high frequencies, normal conductors are local.

3.2.2.3 The complex conductivity

To be consistent with the expectation of a principally imaginary super current conductivity from the London equations [114] (Equation 3.5a), Tinkham [71, 175] introduced the complex conductivity,

$$\sigma = \rho^{-1} = \sigma_1 - i\sigma_2. \tag{3.33}$$

He measured the microwave and infrared transmission through superconducting thin films. In such a measurement the transmission is directly proportional to the admittance per square, and the conductive is directly proportional to the admittance because the film is thin enough for the field to be treated at uniform with depth. The complex conductivity allows currents to be both in phase and out of phase with the field. Assuming that for $T \ll T_c$, the imaginary part of the conductivity is dominant and for $T \gg T_c$, the real part of the conductivity is dominant, Tinkham used the Kramers-Kronig relations to map out σ_1 and σ_2 as a function of frequency for frequencies above and below the gap frequency.

3.2.2.4 The surface impedance

Since the currents induced by an oscillating field are expected to be confined to the surface region of a conductor, and since determination of the current may be complicated by the necessity to perform a potentially complicated integral (in the case of a non-local current-field relationship, § 3.2.2.2), it is helpful to define define a surface impedance, Z_s, to provide a local relationship between currents, voltages and field values

$$Z_s = R_s + iX_s = \left.\frac{E_t}{H_t}\right|_{\text{surface}} = \frac{E_t}{\int_0^\infty J(z)dz}. \tag{3.34}$$

The surface impedance is the ratio of the tangential fields at the surface of the conductor and can also be calculated from the current density. The surface reactance, X_s, is connected to the

field penetration depth, λ, and the kinetic inductance in both normal and superconductors. It would appear that Z_s has the units of resistance, Ω[8]. But consideration of the current density in the definition of Z_s suggests a dependence on aspect ratio. So in fact Z_s has the units of sheet resistance, ohms per square $\Omega/\square$.

In order to calculate Z_s, five material parameters are needed [146]: the zero-temperature energy gap 2Δ, the critical temperature T_c, the London penetration depth, λ_L at $T = 0\,\mathrm{K}$, the Fermi velocity v_0 or the BCS coherence length ξ_0 and the mean free path l.

3.2.2.5 Surface scattering

The superconducting penetration depth and the surface impedance for a given material depend on the boundary conditions for scattering of electrons at the surface [23, pp. 1196–1197]. There are two relevant scattering limits. *Specular scattering*, in which an electron incident with the surface will come off at the same angle as its incident path. Or *Diffuse scattering* (random scattering), in which the reflected electron path is scattered in a random direction [180, p. 122].

Diffuse surface scattering reduces surface impedance, Z_s, in comparison to specular scattering [141, p. 221]. Diffuse surface scattering increases penetration depth, λ, in comparison to specular scattering [23, p. 1196, and fig. 7 on p. 1197].

Pippard [141, p. 220] remarks *'The assumption of specular reflection of electrons which hit the surface appears from experiment to be unsound, and is indeed theoretically improbable, for irregularities on an atomic scale are sufficient to cause large-angle diffraction of the de Broglie waves.'* Chambers [37], in fact found that diffuse scattering is present in bulk copper, silver and tin ($T = 2 - -90\,\mathrm{K}$). In general experimental evidence indicates that specular surface scattering seldom plays an important role in films, either in the normal or the superconducting states [176, p. 86].

3.2.3 Example application: normal and superconductors in local limit

We shall employ Maxwell's equations (Equation 3.1a), Ohms laws (Equation 3.28), London's Equations (Equation 3.5) and the two-fluid model to derive a macroscopic, local description of the currents and the surface impedance of the conductor, which may be in its superconducting or normal states.

Let us assume there is electromagnetic plane wave at normal incidence with a bulk conductor, as depicted in Figure 3.2. The magnetic field of our wave is,

$$\mathbf{H}(z,t) = \hat{y} H_0 e^{i(\omega t - kz)} e^{-z/\lambda}. \tag{3.36}$$

[8]
$$Z_s\ [\Omega] = \frac{\mathbf{E}\ [\mathrm{V/m}]}{\mathbf{H}\ [\mathrm{A/m}]} \tag{3.35}$$

The field is written is a form suggestive of the expectation that the its amplitude will be attenuated as it penetrates into the conductor, in the length scale λ. Notice that the propagation constant is,

$$\Gamma = ik + 1/\lambda. \tag{3.37}$$

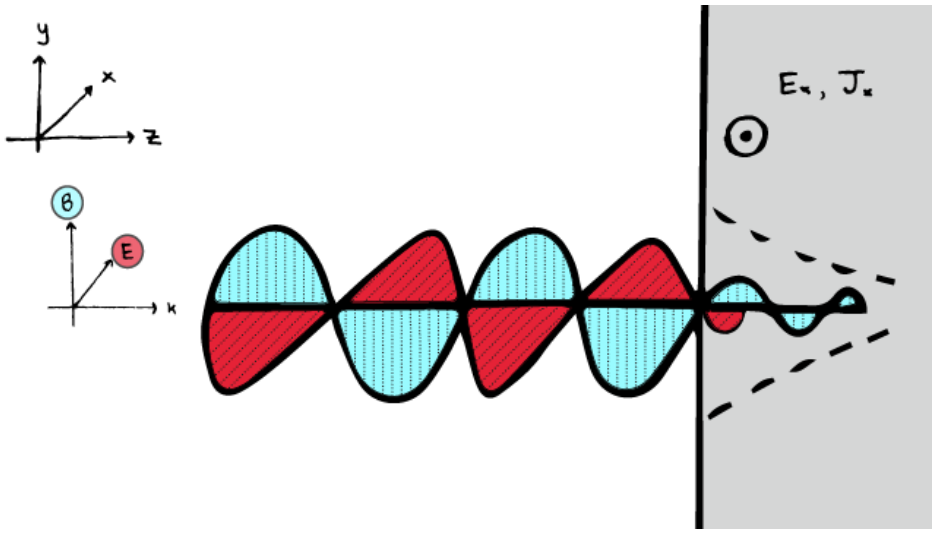


Figure 3.2: An electromagnetic plane wave at normal incidence with conductor. [2]

Immediately, we can use Equation 3.1c to write down the tangential electric field

$$\mathbf{E}(z,t) = \hat{x} H_0 \frac{\omega\mu_0}{k - i/\lambda} e^{i(\omega t - kz)} e^{-z/\lambda}. \tag{3.38}$$

We now proceed to find equations for k and λ. Ampere's Law, Equation 3.1f, relates the magnetic field to the transport and displacement currents. The transport current is taken as the sum of its superconducting and normal fluid constituents (Equation 3.4c). We then related the transport currents to the electric field, utilizing the first Londons equation, Equation 3.5a, for the case of $\mathbf{J}_s$, and Ohms law for the case of $\mathbf{J}_n$,

$$\begin{aligned} \nabla \times \mathbf{B} &= \mu_0 \mathbf{J} + \mu_0 \frac{\partial \mathbf{D}}{\partial t} \\ &= \mu_0 \mathbf{J_s} + \mu_0 \mathbf{J_n} + \mu_0 \epsilon \frac{\partial \mathbf{E}}{\partial t} \\ &= \mu_0 \left(\frac{1}{i\Lambda\omega} + \sigma_n \right) \mathbf{E} + i\omega\mu_0\epsilon\mathbf{E}. \end{aligned} \tag{3.39}$$

Note we have used the time harmonic nature of the fields and currents to substitute $\partial/\partial t = i\omega$. We can now take the curl of both sides of the equation and use Faraday's Law, Equation 3.1c,

to find a relation for the magnetic field only,

$$\begin{aligned}\nabla \times (\nabla \times \mathbf{B}) &= \mu_0 \left(\frac{1}{i\Lambda\omega} + \sigma_n\right) \nabla \times \mathbf{E} + i\omega\mu_0\epsilon \nabla \times \mathbf{E}, \\ \nabla(\nabla \cdot \mathbf{B}) - \nabla^2\mathbf{B} &= -\mu_0 \left(\frac{1}{\Lambda} + i\omega\sigma_n\right) \mathbf{B} + \omega^2\mu_0\epsilon\mathbf{B}, \\ \nabla^2\mathbf{B} &= \left(\frac{1}{\lambda_L^2} + i\omega\mu_0\sigma_n\right) \mathbf{B} - \omega^2\mu_0\epsilon\mathbf{B}.\end{aligned} \tag{3.40}$$

At this point, it is convenient to observe out that the displacement current term is negligibly small. The ratio of the supercurrent term to the displacement current term is $1/\lambda_L^2\omega^2\mu_0\epsilon \approx c^2/\lambda_L^2\omega^2\epsilon_r \gg 1$ for typical λ_L and ω. The ratio of the normal current term to the displacement current term is $\sigma_n/\epsilon\omega \gg 1$ for a good conductor. After removing the displacement current term and evaluation of the Laplacian, we have a relationship for λ and k,

$$\begin{aligned}\left(ik + \frac{1}{\lambda}\right)^2 &= \frac{1}{\lambda_L^2} + i\omega\mu_0\sigma_n \\ &= \left(\frac{1}{\lambda_L^2} + \omega\mu_0\sigma_{n2}\right) + i\omega\mu_0\sigma_{n1} \\ &= \omega\mu_0\left(\sigma_{s2} + \sigma_{n2}\right) + i\omega\mu_0\sigma_{n1} \\ &= i\omega\mu_0\sigma\end{aligned} \tag{3.41}$$

where we have invoked the complex conductivity $\sigma = \sigma_n + \sigma_s = (\sigma_{n1} + \sigma_{s1}) - i(\sigma_{n2} + \sigma_{s2})$ and find σ_{s2} and σ_{s1} by association,

$$\sigma_{s2} = \frac{1}{\lambda_L^2\omega\mu_0} = \frac{1}{\Lambda\omega} = \frac{n_s q_s^2}{m_s\omega} \tag{3.42a}$$

$$\sigma_{s1} = 0. \tag{3.42b}$$

Expressions for σ_{n1} and σ_{n2} can be found by considering the field acceleration and collision dampening force on the normal electrons. The normal current density is,

$$\mathbf{J}_n = n_n q_n \langle \mathbf{v} \rangle , \tag{3.43}$$

where $\mathbf{v}$ is the average normal electron velocity. The normal electrons have a dampening term, $\langle \mathbf{v} \rangle/\tau$, in their equation of motion which accounts for scattering,

$$q_n\mathbf{E} = m_n \left[\frac{d\langle \mathbf{v} \rangle}{dt} + \frac{\langle \mathbf{v} \rangle}{\tau}\right]. \tag{3.44}$$

τ is the momentum relaxation for electron scattering. Assuming a time harmonic field incident on the conductor, its relationship with $\mathbf{E}$,

$$\mathbf{J}_n = \left(\frac{n_n q_n^2}{m_n}\right) \frac{\tau}{1 + i\omega\tau}\mathbf{E} = \left(\frac{n_n q_n^2 \tau}{m_n}\right) \frac{1 - i\omega\tau}{1 + (\omega\tau)^2}\mathbf{E} = \sigma_n\mathbf{E}. \tag{3.45}$$

Thus the normal fluid components of complex conductivity are,

$$\sigma_{n2} = \frac{n_n q_n^2 \omega \tau^2}{m_n(1+(\omega\tau)^2)} \tag{3.46a}$$

$$\sigma_{n1} = \frac{n_n q_n^2 \tau}{m_n(1+(\omega\tau)^2)}. \tag{3.46b}$$

For convenience, let us now collect terms and only speak about σ_1 and σ_2. After expanding and equating real and imaginary parts, Equation 3.41 yields

$$\lambda^2 = \frac{2}{\mu_0\omega}\left[\frac{\sqrt{\sigma_1^2+\sigma_2^2}-\sigma_2}{\sigma_1^2}\right] \tag{3.47a}$$

$$k = \frac{\mu_0\omega}{2}\sigma_1\lambda. \tag{3.47b}$$

Lastly, we write down the expression for Z_s in the local limit, using its definition Equation 3.34, $\mathbf{H}$ (Equation 3.36), $\mathbf{E}$ (Equation 3.38), and Equation 3.41,

$$Z_s = \left.\frac{E_t}{H_t}\right|_{\text{surface}} = \frac{\omega\mu_0}{k - {}^{i}/_{\lambda}} = \sqrt{\frac{i\omega\mu_0}{\sigma}}. \tag{3.48}$$

In Table 3.1, λ, k,Γ and Z_s are approximated for the limits $\sigma_1 \ll \sigma_2$ and $\sigma_1 \gg \sigma_2$. Reference to the normal metal skin depth, δ, is made.

	$\sigma_1 \gg \sigma_2$	$\sigma_1 \ll \sigma_2$
λ	$\delta = \sqrt{\frac{2}{\omega\mu_0\sigma_1}}$	$\lambda_L = \sqrt{\frac{1}{\omega\mu_0\sigma_2}}$
k	$\frac{1}{\delta}$	$\frac{\lambda_L}{\delta^2}$
Γ	$\frac{1+i}{\delta}$	$\frac{1}{\lambda_L}\left[1+\frac{\sigma_1}{2\sigma_2}i\right]$
Z_s	$\frac{1+i}{\delta\sigma_1}[1-\frac{i\sigma_2}{2\sigma_1}]$	$\omega\mu_0\lambda_L\left[\frac{\sigma_1}{2\sigma_2}+i\right]$

Table 3.1: Approximate values of λ, k, Γ, and Z_s in the local limit obtained from assuming $\sigma_1 \gg \sigma_2$ or $\sigma_1 \ll \sigma_2$. λ_L is the London penetration depth and δ is the normal metal skin depth.

The exponential suppression of the fields is due to dissipation in the case of normal conductor and its due to screening currents in the case of a superconductor.

3.3 Causes of nonlinear behavior

Later we will look at the response of resonant circuits with then are driven at high power. Here they exhibit a nonlinear response which motivates the question as to the origin of

the nonlinearity. There are several possible origins cited in the literature, particularly for nonlinearity in thin film superconductors [173, 72].

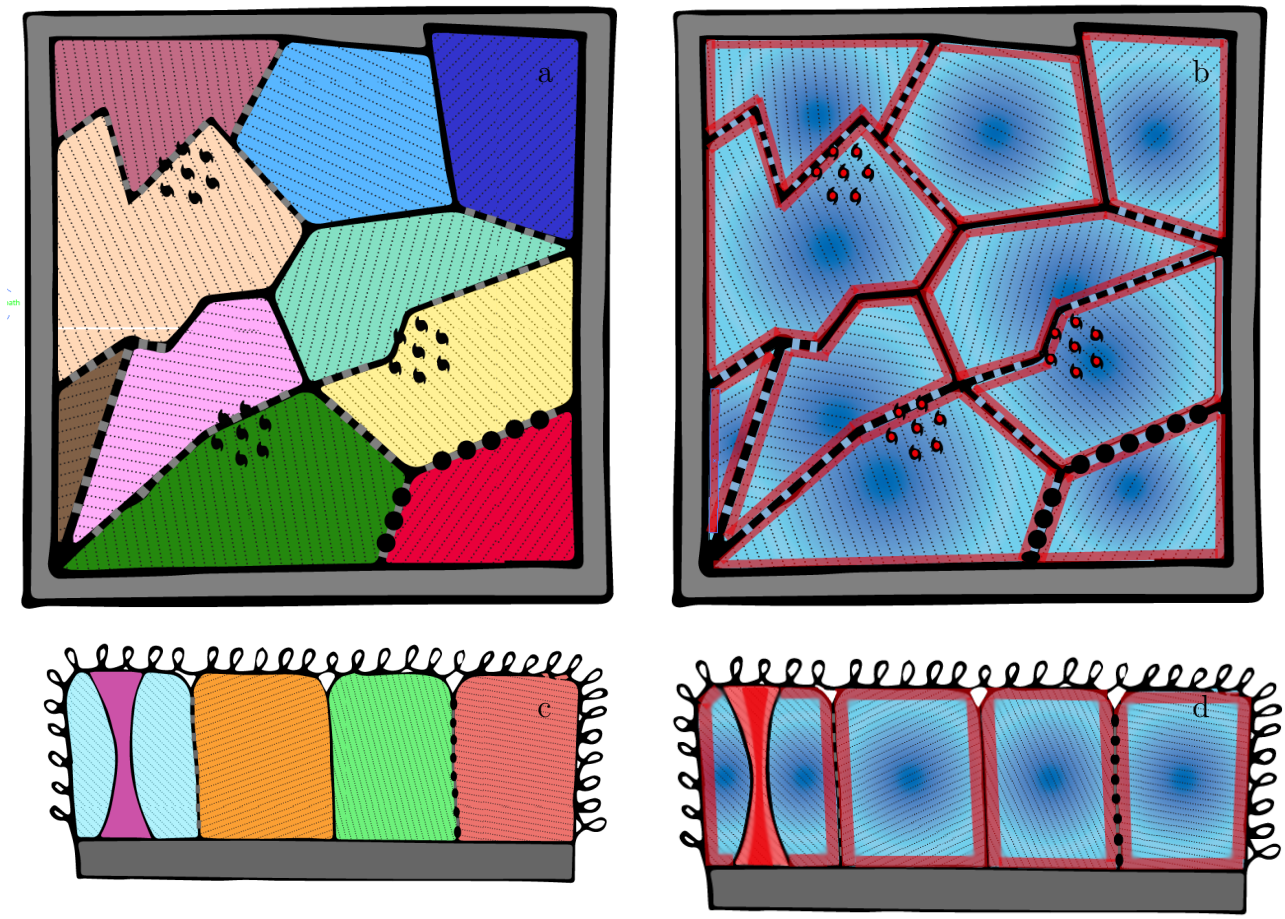


Figure 3.3: Visualization of superconducting grains, their linkages, two-level systems, and how current and vortices interact with them. A superconductor with grains much larger than the penetration depth (i.e. vortex diameter much smaller than grain size) is illustrated. Top views *a* and *b*, emphasize the interconnections between grains. Dashed grain boundaries denote the weak lines; dotted grain boundaries denote impurity contamination, e.g. hydrocarbon contamination. *b* – larger penetration depths near the grain boundaries result in higher current densities there; vortices may exist in the grains or tunnel through the grain boundaries. Cross section views *c* and *d*, show two-level systems distributed across the surface of the film and the funnel-shaped profile of a vortex. Illustration inspiration from [80], which discusses the coupled grain model. [2]

Current dependent σ_1 *and* λ This is suggested by Dahm and Scalapino [46] to explain intermodulation in thin film high T_c superconductors. The found a simple relationship

between the current and the inductance and resistance,

$$L(I) = L_0 + \Delta L \left(\frac{I}{I_c}\right)^2 \tag{3.49a}$$

$$R(I) = R_0 + \Delta R \left(\frac{I}{I_c}\right)^2. \tag{3.49b}$$

Quasi-particle heating Readout power absorbed in the films causes heating of the quasi-particle system and its temperature switches between well defined states. This leads the resonance curve to exhibit hysteresis [48, 174].

Intrinsic nonlinearity There is intrinsic nonlinearity associated with the super current. This can be described within the formalism of Ginzburg-Landau theory. The current corresponding to the Ginzburg-Landau equations in the case of a thin film is

$$I = -Aen_s \left(1 - \frac{v_s^2}{3v_m^2}\right) v_s \tag{3.50a}$$

where A is cross sectional area, n_s and v_s are the pair density in the absence of current and carrier velocity. v_m is a critical velocity. This equation can be used to obtain [41, 42],

$$L(T, I) = L_0 \left(1 - \frac{T}{T_c}^{\alpha}\right)^{-1} \left(1 + \frac{4}{9I_c^2} I^2\right) \tag{3.51a}$$

Vortex penetration The current may become so large that the field accompanying it is enough to create vortices Figure 3.4. The vortices may occur in the grain boundaries or in the bulk grain. Nonlinearity arrises from the dependence of vortex concentration on magnetic field and their motion due to viscous forces [72], .

Weakly coupled grins This model assumes a network of weak links with uniform current flowing presumably at grain boundaries. The nonlinearity arrises from the nonlinear inductance of weak links [72]. Another thing that can happen is that a weak link becomes normal, diverts current, and causes surrounding links to become normal. The result is an overall nonlinear current behavior.

Some of these nonlinearity mechanisms have consequences on the scaling laws of parameters (e.g. magnetic field and resistance) that are measurable allowing them to be ruled out.

Considering the various possible origins of the nonlinearity brings to minds a complicated picture of what is happening at the microscopic level of the superconductor. We have illustrated this picture, Figure 3.3.

Attributions

Results in this chapter come primarily from literature sources. Illustrations from [2] are original work, with him doing the drawing and both of us formulation how they should look.

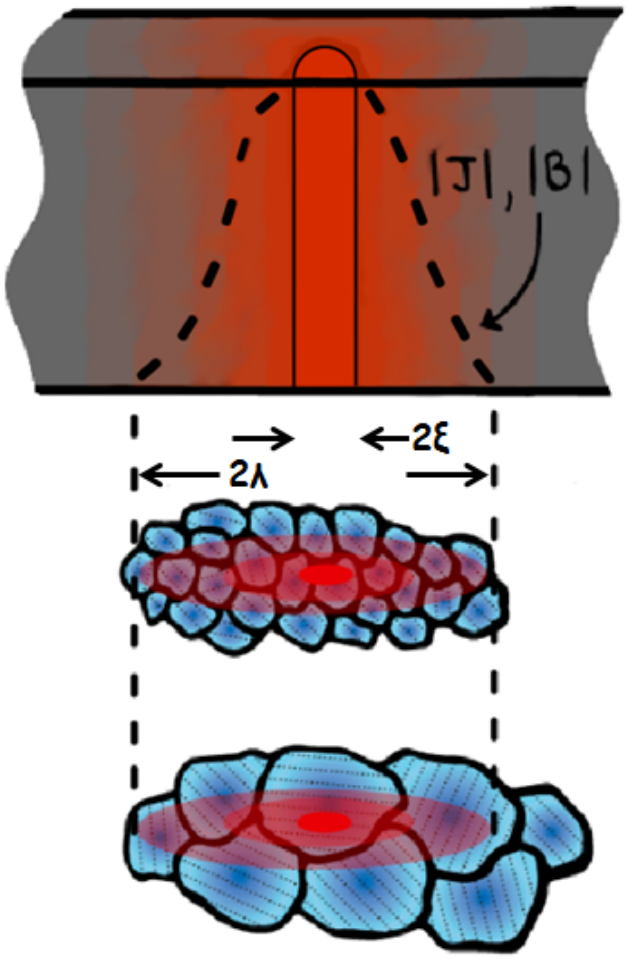


Figure 3.4: We illustrate three scenarios for bulk vortex penetration. On top, a vortex is inside of a thick conductor.The normal metal core of an Abrikosov vortex is about two times the coherence length in diameter. The decay from its critical value at the core of the current density is set by the penetration depth. The situation where the vortex core is much larger than, or about the same size as the grains is illustrated in the center and bottom views, respectively. Illustration from [2]

Chapter 4

Analysis of Resonator

4.1 Linear Analysis of Shunt-Coupled Resonator

We will model the case of a half-wave resonator coupled at one end to the feedline using the parameters labeled in Figure 4.1. We begin with a review of transmission line theory, to remind ourselves of the basic relations, definitions and quantities to be used in subsequent analyses. When the wavelength of a voltage wave is about the size of its containing circuit or smaller, then it is necessary to use transmission line theory and microwave network theory to analyze the circuit. These formalism reduce to basic circuit theory in the opposite limit.

4.1.1 Review of transmission line theory

We imagine a transmission line as the series cascade of infinitesimal circuit elements containing

$$\overline{L} = \text{Series inductance per unit length, for both conductors in } \mathrm{H\,m^{-1}}$$
$$\overline{R} = \text{Series resistance per unit length, for both conductors in } \Omega\,\mathrm{m^{-1}}$$
$$\overline{G} = \text{Shunt conductace per unit length, in } \mathrm{S\,m^{-1}}$$
$$\overline{C} = \text{Shunt capacitance per unit length, in } \mathrm{F\,m^{-1}}$$

configured as in Figure 4.2.

After applying Kirchhoff's laws and taking the limit $\Delta z \to 0$, the following coupled first-order differential equations are obtained:

$$\frac{\partial v(z,t)}{\partial z} = -\overline{R} i(z,t) - \overline{L}\frac{\partial i(z,t)}{\partial t} \tag{4.1a}$$
$$\frac{\partial i(z,t)}{\partial z} = -\overline{G} v(z,t) - \overline{C}\frac{\partial v(z,t)}{\partial t} \tag{4.1b}$$

Equation 4.1 are called the transmission line, or telegraphist's, equations. In general, the solutions are of the form $v(z,t) = v(z)\cos(\omega t + \phi)$, and similarly for $i(z,t)$. We can alternatively use cosine-based phasors for convenience $v(z,t) = v(z)\Re[\cos(\omega t + \phi) + i\sin(\omega t + \phi)] =$

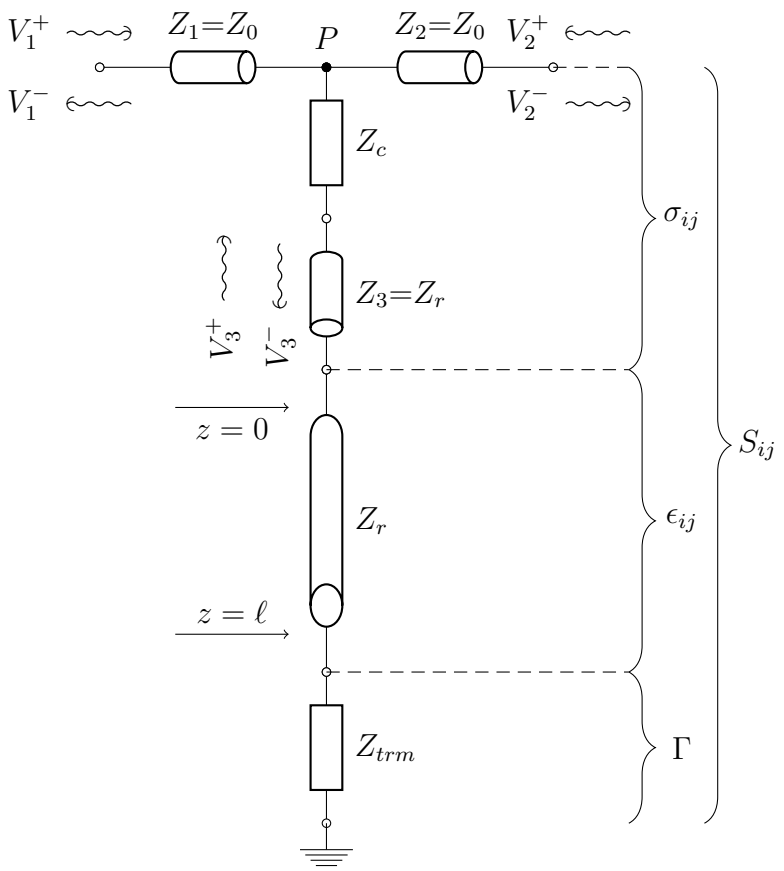


Figure 4.1: Network diagram of $\lambda/2$ resonator coupled to feedline. σ_{ij}, ϵ_{ij} are the scattering matrices for the 3-port coupler and the 2-port $\ell = \lambda/2$ resonator section, respectively. The resonator termination, Z_{trm}, is represented as a reflection coefficient, Γ, and ideally it is a perfect open, $\Gamma = 1$. S ports one and two are the same as σ ports one and two. σ port three is ϵ port 1 and ϵ port 2 is the port of Γ.

$\Re[V(z)e^{i\omega t}]$, where $V(z) = v(z)e^{i\phi}$ is complex, and the transmission line equations simplify to

$$\frac{dV(z)}{dz} = -(\overline{R} + i\omega\overline{L})I(z) = -\gamma Z I(z) \tag{4.2a}$$

$$\frac{dI(z)}{dz} = -(\overline{G} + i\omega\overline{C})V(z) = -\frac{\gamma}{Z}V(z). \tag{4.2b}$$

Equation 4.2 can be combined to form second-order, uncoupled differential equations:

$$\frac{d^2V(z)}{dz^2} = \gamma^2 V(z) \tag{4.3a}$$

$$\frac{d^2I(z)}{dz^2} = \gamma^2 I(z), \tag{4.3b}$$

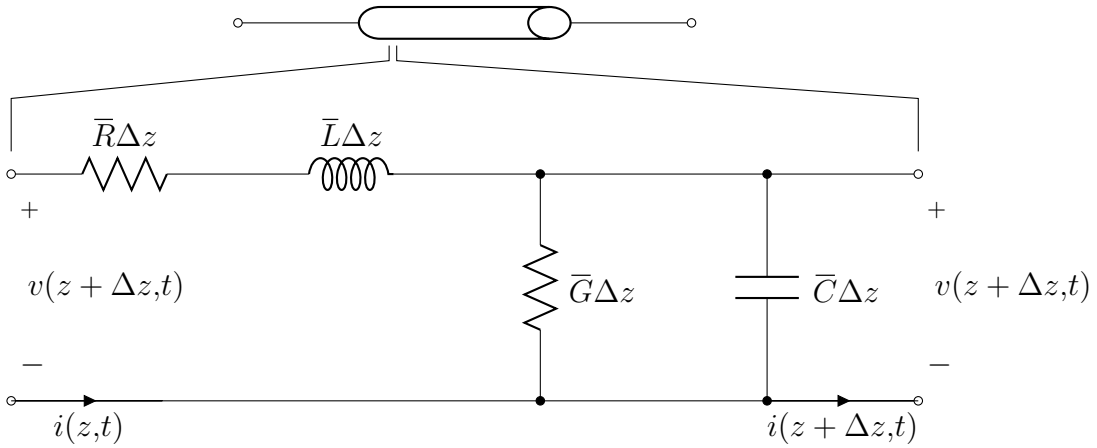


Figure 4.2: A transmission line is the series cascade of infinitesimal circuits whose elements describe the line characteristics, i.e. wave impedance and phase velocity of propagation.

where,

$$\gamma = \alpha + i\beta = \sqrt{(\overline{R} + i\omega\overline{L})(\overline{G} + i\omega\overline{C})}, \tag{4.4}$$

is the complex propagation constant[1]. The solutions to Equation 4.2 and Equation 4.3 describe current and voltage waves traveling into, V_n^+ and I_n^+, and out of, V_n^- and I_n^-, each port, n, of an N-port network.

$$V_n(z) = V_n^+ e^{-\gamma_n z} + V_n^- e^{\gamma_n z} \tag{4.5a}$$

$$I_n(z) = I_n^+ e^{-\gamma_n z} + I_n^- e^{\gamma_n z} = \frac{V_n^+}{Z_n} e^{-\gamma_n z} - \frac{V_n^-}{Z_n} e^{\gamma_n z}, \tag{4.5b}$$

where,

$$Z_n = \sqrt{\frac{\overline{R} + i\omega\overline{L}}{\overline{G} + i\omega\overline{C}}}, \tag{4.6}$$

is the wave impedance [2]. The wave impedance is complex when the transmission line is lossy, $\overline{R}, \overline{G} > 0$, and there may be dispersion, $v_p = f(\omega)$. When $\overline{R} = \overline{G} = 0$, the line is lossless and

[1] In the case of non-uniform lines, γ and Z are not constant.

[2] For a discussion of the impedance concept, and how it evolved, see [160].

$$\left.\begin{aligned} \beta &= -i\gamma = \omega\sqrt{\overline{L}\overline{C}}, \\ Z &= \sqrt{\frac{\overline{L}}{\overline{C}}}, \\ \alpha &= 0, \\ v_p &= \frac{\omega}{\beta} = \frac{1}{\sqrt{\overline{L}\overline{C}}}. \end{aligned}\right\} \quad \text{Lossless Line} \tag{4.7}$$

Junctions of one or more transmission lines are called microwave networks, Figure 4.3. A network may have N ports, which are imagined as zero to finite length transmission lines. Therefore, each port has its own wave impedance, Z_n and propagation constants, $\gamma_n = \alpha_n + i\beta_n$.

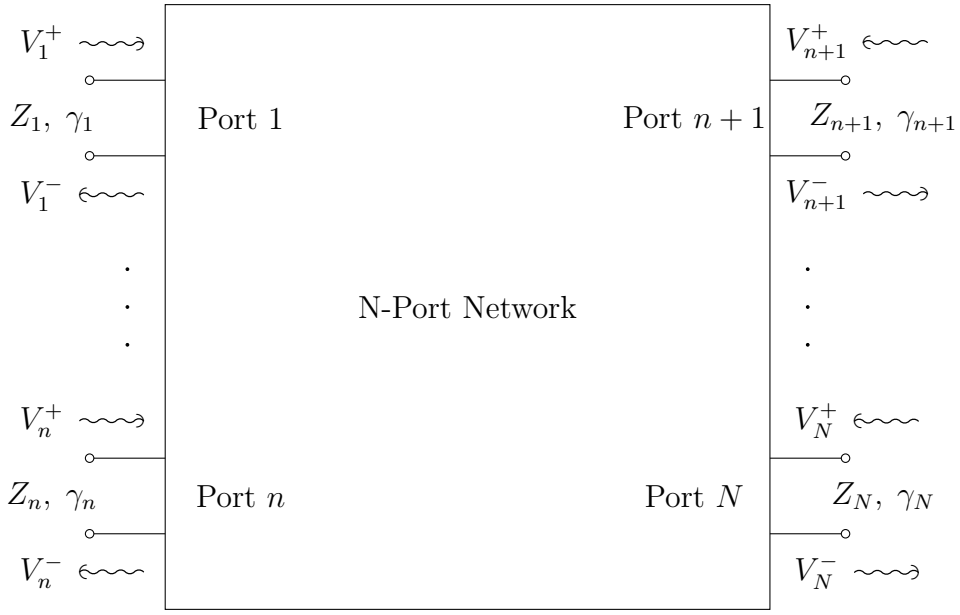


Figure 4.3: An N-port microwave network has a Z_n and γ_n at each port, which are imagined as zero to finite length transmission lines.

The scattering matrix, S_{ij}, relates voltage and current waves going into and out of each of the network ports. It is defined as

$$S_{ij} = \left.\frac{\sqrt{Z_j}}{\sqrt{Z_i}}\frac{V_i^-}{V_j^+}\right|_{V_n^+=0 \text{ for } k\neq j} \tag{4.8}$$

for $i, j = 1, 2, 3$. Observe that S_{ij} is the voltage wave exiting port i, due to a voltage wave entering port j. In general, S_{ij} are complex numbers, $S_{ij} = |S_{ij}| \cdot e^{i\phi_{ij}}$. The condition, $V_n^+ = 0$ for $n \neq j$, is achieved when all ports except j are terminated with resistances equal

to their wave impedance. Thus the scattering matrix for an N-port network is an $N \times N$ matrix. The scattering matrix for a 1-port network, a single complex number, is the refection coefficient, Γ, due to termination of the port transmission line with a impedance, Z_{trm},

$$\Gamma = \frac{Z_{trm} - Z_1}{Z_{trm} + Z_1}, \tag{4.9}$$

where Z_1 is the wave impedance of port 1.

4.1.2 Scattering matrix for the coupler, σ_{ij}

The coupler is the three-port network σ_{ij}.To determine the nine σ_{ij}, we first observe some network characteristics.

symmetric. The network is symmetric in ports 1 and 2. This implies

$$\sigma_{11} = \sigma_{22}, \quad \sigma_{12} = \sigma_{21}, \quad \sigma_{13} = \sigma_{23} = \sigma_{31} = \sigma_{32}.$$

reciprocal. The network is reciprocal since all its components are isotropic, i.e. wave propagation is the same no matter the propagation direction.

$$\sigma_{ij} = \sigma_{ji} \text{ i.e. } \sigma^T = \sigma.$$

lossless. The network is lossless and source free provided that $\Re[Z_c] = 0$ and $\Im[Z_i] = 0$.

$$\sigma^\dagger \cdot \sigma = I, \tag{4.10}$$

where † is conjugate transpose, and I is the identity matrix. This enforces conservation of power, $P = \frac{1}{2} \cdot VI^* = \frac{1}{2Z} \cdot VV^*$, e.g.

$$\begin{gathered} P_1^+ = P_1^- + P_2^- + P_3^- \\ \frac{|V_1^+|^2}{2Z_1} = \frac{|V_1^-|^2}{2Z_1} + \frac{|V_2^-|^2}{2Z_2} + \frac{|V_3^-|^2}{2Z_3} \\ 1 = |\sigma_{13}|^2 + |\sigma_{23}|^2 + |\sigma_{33}|^2 \end{gathered}$$

These condition on σ_{ij} reduce the number of independent indices in from nine to four.

$$\sigma = \begin{bmatrix} \sigma_{11} & \sigma_{12} & \sigma_{13} \\ \sigma_{21} & \sigma_{22} & \sigma_{23} \\ \sigma_{31} & \sigma_{32} & \sigma_{33} \end{bmatrix} \Rightarrow \begin{bmatrix} \sigma_{11} & \sigma_{12} & \sigma_{13} \\ \sigma_{12} & \sigma_{11} & \sigma_{13} \\ \sigma_{13} & \sigma_{13} & \sigma_{33} \end{bmatrix} \tag{4.11}$$

The lossless condition, $\sigma^\dagger \cdot \sigma = I$, implies that

$$1 = |\sigma_{11}|^2 + |\sigma_{12}|^2 + |\sigma_{13}|^2 \tag{4.12a}$$

$$0 = (\sigma_{11}^* \cdot \sigma_{12} + \sigma_{12}^* \cdot \sigma_{11}) + |\sigma_{13}|^2 \tag{4.12b}$$

$$0 = \sigma_{11}^* \cdot \sigma_{13} + \sigma_{12}^* \cdot \sigma_{13} + \sigma_{13}^* \cdot \sigma_{33} \tag{4.12c}$$

$$1 = |\sigma_{33}|^2 + 2 \cdot |\sigma_{13}|^2. \tag{4.12d}$$

We can apply Kirchhoff's current and voltage laws at point P in Figure 4.1 to obtain the conditions,

$$V_1^+ + V_1^- = V_2^+ + V_2^- = V_3^+ + V_3^- - Z_c(I_3^+ - I_3^-) \tag{4.13a}$$

$$(I_1^+ - I_1^-) + (I_2^+ - I_2^-) + (I_3^+ - I_3^-) = \frac{V_1^+ - V_1^-}{Z_1} + \frac{V_2^+ - V_2^-}{Z_2} + \frac{V_3^+ - V_3^-}{Z_3} = 0 \tag{4.13b}$$

Equation 4.13 and Equation 4.8 allow us to solve for each of the four independent σ_{ij}

$$\begin{aligned} \sigma_{11} &= \frac{-\frac{1}{2}Z_0}{\frac{1}{2}Z_0 + Z_c + Z_r} \quad & \sigma_{13} &= \frac{\sqrt{Z_0 Z_r}}{\frac{1}{2}Z_0 + Z_c + Z_r} \\ \sigma_{21} &= \frac{Z_c + Z_r}{\frac{1}{2}Z_0 + Z_c + Z_r} \quad & \sigma_{33} &= \frac{\frac{1}{2}Z_0 + Z_c - Z_r}{\frac{1}{2}Z_0 + Z_c + Z_r}. \end{aligned} \tag{4.14}$$

The coupling impedance, Z_c will be designed to be large in the frequency range of interest, $Z_c \gg Z_0$ and $Z_c \gg Z_r$. Using this to expand Equation 4.14 to second order in Z_c^{-1}, we get

$$\begin{aligned} \sigma_{11} &\approx -\frac{\frac{1}{2}Z_0}{Z_c} + \frac{\frac{1}{4}Z_0^2}{Z_c^2} \quad & \sigma_{13} &\approx \frac{\sqrt{Z_0 Z_r}}{Z_c} - \frac{\sqrt{Z_0 Z_r}(\frac{1}{2}Z_0 + Z_r)}{Z_c^2} \\ \sigma_{21} &\approx 1 - \frac{\frac{1}{2}Z_0}{Z_c} + \frac{\frac{1}{4}Z_0^2}{Z_c^2} \quad & \sigma_{33} &\approx 1 - \frac{2Z_r}{Z_c} + \frac{2Z_r^2 + Z_0 Z_r}{Z_c^2}. \end{aligned} \tag{4.15}$$

There are two notable coupler choices consistent with Figure 4.1 and the assumption of losslessness, Equation 4.10. These are inductive coupling, $Z_c = i\omega L$ and capacitive coupling $Z_c = (i\omega C)^{-1}$. One can check that Equation 4.15 obeys Equation 4.12d with correct attention to expansion order and requiring $\Re[Z_c] = 0$.

There are a few notable identities that can be extracted from Equation 4.14. These include

$$\sigma_{21} = \sigma_{11} + 1 \tag{4.16a}$$

$$\sigma_{33} = 1 - 2\sqrt{\frac{Z_r}{Z_0}}\sigma_{13} \tag{4.16b}$$

$$\sigma_{21} = 1 - \frac{1}{2}\sqrt{\frac{Z_0}{Z_r}}\sigma_{13} \tag{4.16c}$$

4.1.3 Scattering matrix for resonator, ϵ_{ij}

Because the resonator is a section of transmission line, its scattering matrix simply describes propagation of a voltage wave over its length, ℓ,

$$\epsilon = \begin{bmatrix} \epsilon_{11} & \epsilon_{12} \\ \epsilon_{21} & \epsilon_{22} \end{bmatrix} = \begin{bmatrix} 0 & e^{-\gamma\ell} \\ e^{-\gamma\ell} & 0 \end{bmatrix}, \tag{4.17}$$

consistent with Equation 4.5.

4.1.4 Scattering matrix for resonator coupled to feedline, S_{ij}

The symmetries of the network, Figure 4.1, provide that $S_{11} = S_{22}$ and $S_{12} = S_{21}$. If we direct a voltage wave into S port one and terminate S port two with a resistor equal to its wave impedance, the voltage wave leaving S port two, is composed of the signal coming directly from σ port one and the signal exiting the resonator via σ port three,

$$V_2^- = V_1^+ \sqrt{\frac{Z_2}{Z_1}} \sigma_{21} + V_3^+ \sqrt{\frac{Z_2}{Z_3}} \sigma_{23}. \tag{4.18}$$

By the same logic, the voltage wave reflected off σ port one is,

$$V_1^- = V_1^+ \sigma_{11} + V_3^+ \sqrt{\frac{Z_1}{Z_3}} \sigma_{13}. \tag{4.19}$$

The voltage wave entering the resonator is composed of the wave entering from σ port one and the portion of the wave exiting the resonator which is reflected off σ port three,

$$V_3^- = V_1^+ \sqrt{\frac{Z_3}{Z_1}} \sigma_{31} + V_3^+ \sigma_{33}. \tag{4.20}$$

The voltage wave entering σ port three is the wave that started at ϵ port one, reflected off Z_t,

$$V_3^+ = V_3^- \epsilon_{21} \Gamma \epsilon_{12}. \tag{4.21}$$

These equations allow us to solve for elements of S,

$$S_{21} = \frac{V_2^-}{V_1^+} = \sigma_{21} + \frac{\epsilon_{21}^2 \Gamma \sigma_{13}^2}{1 - \epsilon_{21}^2 \Gamma \sigma_{33}}, \tag{4.22a}$$

$$S_{11} = \frac{V_1^-}{V_1^+} = \sigma_{11} + \frac{\epsilon_{21}^2 \Gamma \sigma_{13}^2}{1 - \epsilon_{21}^2 \Gamma \sigma_{33}}, \tag{4.22b}$$

where we have used only the unique elements of σ and ϵ. Assuming $|\Gamma| = 1$ and $\gamma = i\beta$, one can check for power conservation, $S^\dagger S = 1$ and $\sum_n V_n^{-2} = \sum_n V_n^{+2}$. Note that we have σ_{13}^2 and not $|\sigma_{13}|^2$ in the numerator. Recalling Equation 4.16a, we see that $S_{11} = S_{21} - 1$ as should be the case for a shunt-coupled resonator.

4.1.5 Voltage and current amplitudes inside a $\lambda/2$ resonator

The approach of § 4.1.4 allows us to calculate the voltage and current wave amplitudes evaluated at the various ports of interest. Here, we determine the voltage and current wave amplitudes at any point, z, within the $\lambda/2$ resonator. We do this by summing all the reflected wave contributions present at z. Figure 4.4 shows the infinite number of wave amplitude contributions at z, assuming reflection coefficients Γ_1 at the open end of the $\lambda/2$ resonator, Γ_2

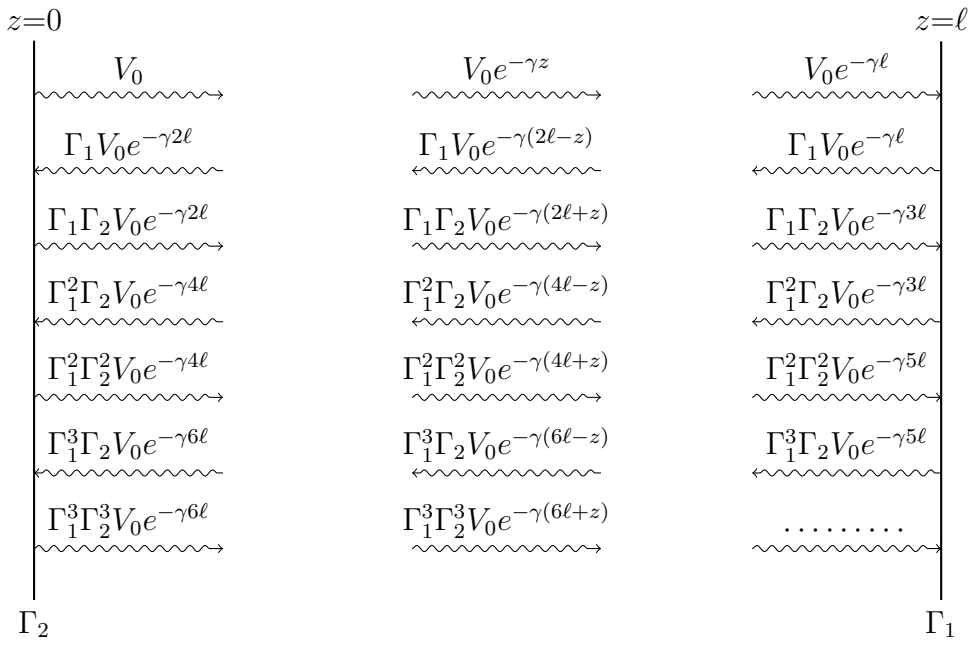


Figure 4.4: Inside the $\lambda/2$ resonator, the total voltage amplitude at any point z along the length is the sum of contributions from reflected waves.

at the coupling end of the resonator and a propagation constant γ. The reference amplitude V_0, is related to the in probe amplitude V_1^+ as $V_0 = V_3^- = V_1^+\sqrt{\frac{Z_3}{Z_1}}\sigma_{31}$.

The voltage amplitude $V(z)$ can be determine from Figure 4.4. The current amplitude can be determined from $V(z)$ using the transmission line equations, Equation 4.2.

$$\begin{aligned} V(z) &= V_0e^{-\gamma z}\sum_{n=0}^{\infty}\left(\Gamma_1\Gamma_2\right)^n e^{-\gamma n2\ell} + V_0\Gamma_1e^{-\gamma 2\ell}e^{\gamma z}\sum_{n=0}^{\infty}\left(\Gamma_1\Gamma_2\right)^n e^{-\gamma n2\ell} \\ &= V_0\frac{e^{-\gamma z}+\Gamma_1e^{-\gamma 2\ell}e^{\gamma z}}{1-\Gamma_1\Gamma_2e^{-\gamma 2\ell}} \qquad (4.23a) \\ I(z) &= \frac{V_0}{Z_3}\frac{e^{-\gamma z}-\Gamma_1e^{-\gamma 2\ell}e^{\gamma z}}{1-\Gamma_1\Gamma_2e^{-\gamma 2\ell}} \qquad (4.23b) \end{aligned}$$

Presently, we shall assume that $\gamma = i\beta$, $\Gamma_2 = \sigma_{33}$ and $\Gamma_1 = 1$. So,

$$\begin{aligned} V(z) &= V_0\frac{e^{-i\beta z}+e^{-i\beta 2\ell}e^{i\beta z}}{1-\sigma_{33}e^{-i\beta 2\ell}} \\ &= 2V_0\frac{e^{-i\beta\ell}}{1-\sigma_{33}e^{-i\beta 2\ell}}\cos\left(\beta\ell-\beta z\right) \qquad (4.24a) \\ I(z) &= \frac{2iV_0}{Z_3}\frac{e^{-i\beta\ell}}{1-\sigma_{33}e^{-i\beta 2\ell}}\sin\left(\beta\ell-\beta z\right) \qquad (4.24b) \end{aligned}$$

4.1.6 Computation of coupling quality factor, Q_c

Starting from the general definition of the resonate cavity quality factor[3], we define the coupling quality factor, Q_c, of the resonator coupled to the feedline in terms of the power lost through the coupler per oscillation, P_{out}.

$$Q_c = \omega \cdot \frac{\text{Total Energy Stored in Cavity}}{\text{Power Lost per Oscillation}} = \omega \cdot \frac{E_{total}}{P_{out}}. \tag{4.25}$$

Using Equation 4.24a and Equation 4.50, we can compute the total time averaged energy in the resonator, which is the sum of the electric and magnetic energies, $E_{total} = E_{mag} + E_{ele}$, where

$$E_{ele} = \frac{\overline{C}}{4}\int_0^\ell |V(z)|^2 dz = \overline{C}|V_0|^2 \left|\frac{e^{-i\beta\ell}}{1-\sigma_{33}e^{-i\beta 2\ell}}\right|^2 \int_0^\ell \cos^2(\beta z - \beta\ell) dz \tag{4.26a}$$

$$E_{mag} = \frac{\overline{L}}{4}\int_0^\ell |I(z)|^2 dz = \frac{\overline{L}|V_0|^2}{Z_3^2} \left|\frac{e^{-i\beta\ell}}{1-\sigma_{33}e^{-i\beta 2\ell}}\right|^2 \int_0^\ell \sin^2(\beta z - \beta\ell) dz. \tag{4.26b}$$

From Equation 4.7 we have $Z_3^2 = \frac{\overline{L}}{\overline{C}}$ and as always $1 = \cos^2 x + \sin^2 x$. We get,

$$E_{total} = E_{mag} + E_{ele} = \overline{C}|V_0|^2 \left|\frac{e^{-i\beta\ell}}{1-\sigma_{33}e^{-i\beta 2\ell}}\right|^2 \int_0^\ell 1\, dz = \overline{C}|V_0|^2 \left|\frac{e^{-i\beta\ell}}{1-\sigma_{33}e^{-i\beta 2\ell}}\right|^2 \ell. \tag{4.27}$$

The power leaving the resonator at σ port three is the difference between the power entering σ port three and power reflected from σ port three,

$$P_{out} = \frac{1}{2}\frac{|V_3^+|^2}{Z_3} - \frac{1}{2}\frac{|V_3^-|^2}{Z_3} = \frac{1}{2}\frac{|V_3^+|^2}{Z_3}\left[1 - |\sigma_{33}|^2\right] = \frac{|V_3^+|^2}{Z_3}|\sigma_{13}|^2 = \frac{|V_0|^2}{Z_3}\left|\frac{e^{-i\beta 2\ell}}{1-\sigma_{33}e^{-i\beta 2\ell}}\right|^2 |\sigma_{13}|^2, \tag{4.28}$$

where we have used Equation 4.12d, $|\sigma_{33}|^2 = \frac{|V_3^-|^2}{|V_3^+|^2}$ and picked out $V_3^+ = V_0\frac{e^{-i\beta 2\ell}}{1-\sigma_{33}e^{-i\beta 2\ell}}$ from Equation 4.24a. Using $\beta = {}^{2\pi}/_{\lambda} = \omega\sqrt{\overline{L}\overline{C}}$ from Equation 4.7 we arrive at,

$$Q_c = \left|e^{i\beta\ell}\right| \frac{\beta\ell}{|\sigma_{13}|^2} = \frac{\beta\ell}{|\sigma_{13}|^2}. \tag{4.29}$$

This expression for P_{out} assumes that the voltage traveling wave is incident on σ port three once per oscillation, as is the case for a ${}^{\lambda}/_{2}$ resonator ($\theta = 0$). For a ${}^{\lambda}/_{4}$ resonator ($\theta = \pi$), P_{out} would be doubled because the voltage traveling wave is incident on σ port three twice per oscillation. Thus for the case of $\ell = {}^{\lambda}/_{2}$,

$$Q_c = \frac{\pi}{|\sigma_{13}|^2}. \tag{4.30}$$

[3] E_{total} and P_{out} must both be time-averaged when performing this computation.

4.1.7 Computation of termination quality factor, Q_{trm}

The method used to calculate Q_c in § 4.1.3 can also be used to calculate Q_{trm}. For Q_{trm}, we allow $|\Gamma| < 1$, and we set $|\sigma_{33}| = 1$. Analogous to Equation 4.28, the power lost to the termination is

$$P_{trm} = \frac{1}{2}\frac{|V_3^+|^2}{Z_3}\left[1 - |\Gamma|^2\right]. \tag{4.31}$$

Thus, for a $\lambda/2$ resonator, Q_{trm} is

$$Q_{trm} = \frac{2\pi}{1 - |\Gamma|^2}. \tag{4.32}$$

The lost power described by Q_{trm} can be attributed, to radiation at the open end of the $\lambda/2$ resonator, which includes radiations and surface wave production, or to a loading element.

This result may not be entirely correct. We have not considered the situation of the other open end of the resonator. A $\lambda/2$ open-ended microstrip resonator would radiate at both ends, for example. If the microstrip is loaded equally on both end, such as the case of radiation for an open ended resonator, the associated quality factor is [58, 90],

$$Q_{trm} = \frac{\pi(n+1)|\Gamma|}{1 - |\Gamma|^2}, \tag{4.33}$$

where n is the order of the resonance, $n = 0$ for the fundamental.

4.1.8 Computation of transmission line quality factor, Q_{tl}

When $\alpha > 0$, the amplitude of a voltage or current wave will decrease as it travels down a transmission line. The quality factor of that line can be defined as $Q = \pi \cdot N_{1/e}$, where $N_{1/e}$ is the number of cycles the wave can propagate before its amplitude is attenuated by a factor of $1/e$. $V(z) = e^{-\alpha z}e^{-i\beta z}$, so the attenuation length is $\ell_{1/e} = \frac{1}{\alpha}$. The number of wavelengths per attenuation length is $\frac{\ell_{1/e}}{\lambda} = \frac{\beta \ell_{1/e}}{2\pi}$. Thus, the quality factor of the transmission line is

$$Q_{tl} = \frac{\beta}{2\alpha}. \tag{4.34}$$

We see that a lossless line has infinite quality factor. This quality factor general for any transmission line, not necessarily a resonator.

4.1.9 Approximation of the resonance curve, $S_{21}(f)$

We would like to rewrite Equation 4.22a in a form more useful for measurement, analysis of data and design of resonator. In this form, S_{21} will have explicit frequency and quality factor dependence. $S_{21}(f)$ will be valid for the linear regime, only.

Recalling that $\epsilon_{21} = e^{-\gamma\ell}$ (Equation 4.17), Equation 4.22a can be written slightly differently as

$$S_{21} = \sigma_{21} + \frac{\sigma_{13}^2}{\frac{e^{2\gamma\ell}}{\Gamma} - \sigma_{33}}. \tag{4.35}$$

Combining Equation 4.16a with Equation 4.12c gives a useful identity,

$$\sigma_{21} = \frac{1}{2}\left[1 - \frac{\sigma_{13}}{\sigma_{13}^*}\sigma_{33}\right] = \frac{1}{2}\left[1 - e^{2i\phi_{13}}\sigma_{33}\right]. \tag{4.36}$$

Substituting Equation 4.36 into Equation 4.35 gives,

$$S_{21} = \frac{1}{2} + \frac{\sigma_{13}}{2\sigma_{13}^*}\left[\frac{1 - \frac{e^{2\gamma\ell}}{\Gamma}\sigma_{33}^*}{\frac{e^{2\gamma\ell}}{\Gamma} - \sigma_{33}}\right] = \frac{1}{2} + \frac{e^{2i\phi_{13}}}{2}\left[\frac{1 - \frac{e^{2\gamma\ell}}{\Gamma}\sigma_{33}^*}{\frac{e^{2\gamma\ell}}{\Gamma} - \sigma_{33}}\right] \tag{4.37}$$

The exponent, $2\gamma\ell$, can be expanded about the unloaded resonant frequency of the $\lambda/2$ transmission line, $f_{\lambda/2} = v_p/\lambda = v_p/2\ell$

$$\begin{aligned}
\pm 2\ell\gamma &= \pm 2\ell\left(\alpha + i\beta\right) \\
&= \pm i\lambda\beta\left(\frac{-i}{2Q_{tl}} + 1\right) \\
&= \pm i\frac{v_p}{f_{\lambda/2}}\left(2\pi\frac{f_{\lambda/2} + \delta f}{v_p}\right)\left(\frac{-i}{2Q_{tl}} + 1\right) \\
&= \pm i2\pi\left(1 + \frac{f - f_{\lambda/2}}{f_{\lambda/2}}\right)\left(\frac{-i}{2Q_{tl}} + 1\right) \\
&= \pm 2\pi\left(\frac{f - f_{\lambda/2}}{f_{\lambda/2}}\frac{1}{2Q_{tl}} + i\frac{f - f_{\lambda/2}}{f_{\lambda/2}} + \frac{1}{2Q_{tl}} + i\right),
\end{aligned} \tag{4.38}$$

where we have used Equation 4.34, and $v_p = \omega/\beta$. Approximate expressions for each of the variables in Equation 4.35 can be obtain by expanding each of them to comparable order,

$$e^{\pm 2\gamma\ell} \approx 1 \pm i2\pi\frac{f - f_{\lambda/2}}{f_{\lambda/2}} \pm \frac{\pi}{Q_{tl}} \tag{4.39a}$$

$$\frac{1}{\Gamma} = \frac{1}{|\Gamma|}e^{-i\theta} = \frac{1}{\sqrt{1 - \frac{2\pi}{Q_{trm}}}}e^{-i\theta} \approx 1 + \frac{\pi}{Q_{trm}} - i\theta \tag{4.39b}$$

$$\sigma_{33} = |\sigma_{33}|e^{i\phi_{33}} = \sqrt{1 - 2|\sigma_{13}|^2}e^{i\phi_{33}} \approx 1 - \frac{\pi}{Q_c} + i\phi_{33}. \tag{4.39c}$$

Substituting these approximations (Equation 4.39) in to Equation 4.37, we get

$$\begin{aligned}
S_{21} &\approx \frac{1 - e^{i2\phi_{13}}}{2} + \frac{\frac{1}{Q_c}}{\left(\frac{1}{Q_c} + \frac{1}{Q_{trm}} + \frac{1}{Q_{tl}}\right) + 2i\left(\frac{f - f_{\lambda/2}}{f_{\lambda/2}} - \frac{\theta}{2\pi} - \frac{\phi_{33}}{2\pi}\right)} \cdot e^{i2\phi_{13}} \\
&\approx \frac{1 - e^{i2\phi_{13}}}{2} + \frac{\frac{Q}{Q_c}}{1 + 2iQ\left(\frac{f - f_0}{f_0}\right)} \cdot e^{i2\phi_{13}}
\end{aligned} \tag{4.40}$$

Here we have defined the total or external quality factor of the resonator coupled to the feedline as,

$$\frac{1}{Q} = \frac{1}{Q_c} + \frac{1}{Q_{trm}} + \frac{1}{Q_{tl}} + \cdots ; \tag{4.41}$$

quality factors for other additional loss mechanisms can be added in this way. Also we have defined the loaded resonant frequency, f_0, as that which makes the complex term in the denominator of Equation 4.40 vanish,

$$\begin{aligned} 0 &= \frac{f_0 - f_{\lambda/2}}{f_{\lambda/2}} - \frac{\theta}{2\pi} - \frac{\phi_{33}}{2\pi} \\ f_0 &= f_{\lambda/2}\left(1 + \frac{\theta}{2\pi} + \frac{\phi_{33}}{2\pi}\right) \end{aligned} \tag{4.42}$$

Lastly, since $\Re[Z_c] = 0$, we see most clearly from the approximate form of σ_{13} (Equation 4.15) that $2\phi_{13} \approx \pi$,

$$S_{21} \approx 1 - \frac{\frac{Q}{Q_c}}{1 + 2iQ\left(\frac{f-f_0}{f_0}\right)} \tag{4.43}$$

4.1.10 Approximation of resonator internal power, P_{int}

We can calculate the time averaged power entering the resonator, $P_{int} = |V_3^-|^2/2Z_3$. Equation 4.20 and Equation 4.21 are used to solve for V_3^-,

$$V_3^- = \frac{V_1^+\sqrt{\frac{Z_3}{Z_1}}\sigma_{31}}{1 - \sigma_{33}\Gamma e^{-2\ell\gamma}}. \tag{4.44}$$

Expressions for σ_{33}, σ_{13}, and $e^{2\gamma\ell}$ have been presented previously. Γ can be approximated as

$$\Gamma = |\Gamma|e^{i\theta} = \sqrt{1 - \frac{2\pi}{Q_{trm}}}e^{i\theta} \approx 1 - \frac{\pi}{Q_{trm}} + i\theta. \tag{4.45}$$

An approximate equation for P_{int} is obtained by substitution of the above expressions into V_3^-,

$$P_{int}(f) = \frac{|V_3^-|^2}{2Z_3} \approx \frac{|V_1^+|^2}{2\pi Z_1}\frac{\frac{Q^2}{Q_c}}{|1 + 2iQ\left(\frac{f-f_0}{f_0}\right)|^2} = \frac{P_{probe}}{\pi}\frac{\frac{Q^2}{Q_c}}{|1 + 2iQ\left(\frac{f-f_0}{f_0}\right)|^2}. \tag{4.46}$$

P_{probe} is the power on the feedline at the position of the resonator.

4.1.11 Approximation of maximum resonator current, I_{max}

In § 4.1.5 we found that the current amplitude in the resonator is given by Equation 4.23b, which we now rewrite with $\Gamma_1 = \sigma_{33}$, $\Gamma_2 = \Gamma$ and $V_0 = V_1^+\sqrt{Z_3/Z_1}\sigma_{31}$,

$$I(z) = V_1^+ \frac{\sigma_{13}}{\sqrt{Z_1 Z_3}} \frac{\frac{e^{2\gamma\ell}}{\Gamma} e^{-\gamma z} - e^{\gamma z}}{\frac{e^{2\gamma\ell}}{\Gamma} - \sigma_{33}}. \tag{4.47}$$

The maximum current occurs at the coordinate z_{max} for which $\left.\frac{dI(z)}{dz}\right|_{z_{max}} = 0$, i.e. $I_{max} = I(z_{max})$. We find that,

$$z_{max} = \ell - \frac{i\pi}{2\gamma} - \frac{\ln(\Gamma)}{2\gamma}, \tag{4.48a}$$

$$I_{max} = 2iV_1^+ \frac{\sigma_{13}}{\sqrt{Z_1 Z_3}} \frac{1}{\frac{e^{\gamma\ell}}{\sqrt{\Gamma}} - \sigma_{33}\frac{\sqrt{\Gamma}}{e^{\gamma\ell}}}. \tag{4.48b}$$

Equation 4.39c gives an approximate form for σ_{33}. Approximate forms for $\sqrt{\Gamma}^{\pm 1}$ and $e^{\pm\gamma\ell}$ are,

$$e^{\pm\gamma\ell} \approx -1 \mp \frac{\pi}{2Q_{tl}} \mp i\pi\frac{f - f_{\lambda/2}}{f_{\lambda/2}}, \tag{4.49a}$$

$$\sqrt{\Gamma}^{\pm 1} \approx 1 \pm \frac{i\theta}{2} \mp \frac{\pi}{2Q_{trm}}. \tag{4.49b}$$

Substituting these approximate expressions into Equation 4.50, and using the definitions for Q and f_0 given in § 4.1.9, we get

$$I_{max} \approx -2iV_1^+ \frac{e^{i\phi_{13}}}{\sqrt{Z_1 Z_3}} \frac{\frac{Q}{\sqrt{\pi Q_c}}}{1 + 2iQ\left(\frac{f - f_0}{f_0}\right)}. \tag{4.50}$$

4.2 Nonlinear Analysis of Shunt-Coupled Resonator

For a variety of reasons Figure 3.3, superconducting films can exhibit nonlinear behavior when high currents are driven through them. The nonlinear dependence of current on film parameters can take a variety of different forms. We consider one such form in which the inductance and the resistance obey,

$$L = L_0 + \Delta L \left(\frac{I}{I_c}\right)^2 \tag{4.51a}$$

$$R = R_0 + \Delta R \left(\frac{I}{I_c}\right)^2. \tag{4.51b}$$

Our aim is to model the effect on the resonance transmission, S_{21} that this nonlinearity has. We expect that the resistive and inductive nonlinearity bring about nonlinearity in the transmission line quality factor Q_{tl} and in the fractional frequency shift $\delta f/f$, respectively.

4.2.1 Approach: parameterize $^{\delta f}/_{f}$ in terms of resonator current $|I|^2$

This is the approach of Swenson et al. in [173] who focused on the inductive nonlinearity, which they observe to be present before 'the abrupt onset of additional dissipation in the resonator'. The resonators in their case are made of TiN and are lumped element in format. They observe a downward shift in resonant frequency with increasing probe power. as this occurs, the transmission curve, $S_{21}(f)$, becomes up to triple valued and resembles a soft spring Duffing oscillator curve. It is easy to see, upon study of Equation 4.43, that one way to achieve a probe power dependent shift in resonant frequency, $^{\delta f}/_{f}$ is parameterized in terms of resonator 'current' ($|I|^2$) which ought to increase with probe power. Although resonator current is not a uniquely defined quantity since the current varies across the resonator, the choice makes sense for the lumped element format where the wave impedance of the resonator is not well defined. One could alternatively parameterize in terms of V_3^-, the voltage amplitude entering the resonator, and get the same results concerning nonlinearity.

The parameterization

$$\frac{f-f_0}{f_0} \longrightarrow \frac{f-f_r}{f_r} = \frac{f-f_0}{f_0} - \kappa\frac{|I|^2}{|I_*|^2} \tag{4.52}$$

is made to Equation 4.43, now $S_{21}(f,|I|)$. Note that This parameterization can be interpreted in several ways: as the fractional resonant frequency shift from the low power value, f_0; as the shift in the resonator inductance, L, as the current increases; as a measure of how the energy in the resonator compares to a some sort of scaling energy E_* which may be on the order of the condensation energy of the superconductor,

$$\kappa\frac{|I|^2}{|I_*|^2} = -\frac{\delta f_r}{f_0} = \frac{1}{2}\frac{\delta L}{L} = \frac{E}{E_*} \tag{4.53}$$

Note that $f_r = f_0 + \kappa(^{|I|^2}/_{|I_*|^2})f_0 = f_0 - \delta f_r$ Since power must be conserved in the resonator system we have,

$$P_{diss} = P_{probe}[1 - |S_{11}|^2 - |S_{21}|^2] \tag{4.54}$$

where the power dissipated in the resonator is P_{diss} and the power from the generator on the feedline exciting the resonator is P_{probe}. For a shunt-coupled resonator, we have $S_{11} = S_{21} - 1$. The transmission line quality factor, Q_{tl}, is related to the dissipated power, resonator energy E and resonance frequency (at least in the linear regime) by

$$Q_{tl} = \frac{2\pi f_r E}{P_{diss}}. \tag{4.55}$$

After substituting Equation 4.43 into Equation 4.54 and using Equation 4.55 to eliminate P_{diss}, we have,

$$E = \frac{2Q^2}{Q_c}\frac{1}{1+4Q^2\left(\frac{f-f_0}{f_0} - \kappa\frac{|I|^2}{|I_*|^2}\right)^2}\frac{P_{probe}}{2\pi f_r}. \tag{4.56}$$

The fractional frequency shift at high probe power is then expressed as,

$$\frac{f-f_r}{f_r}-\frac{f-f_0}{f_0}=-\kappa\frac{|I|^2}{|I_*|^2}=-\frac{E}{E_*}\approx-\frac{2Q^2}{Q_c}\frac{1}{1+4Q^2\left(\frac{f-f_0}{f_0}-\kappa\frac{|I|^2}{|I_*|^2}\right)^2}\frac{|I_1^+|^2Z_1}{2\pi f_r E_* 2}. \tag{4.57}$$

This equation is a cubic polynomial relating $|I|^2$ to the generator power, $P_{probe}={}^{|I_1^+|^2Z_1}\!/_2$,

$$\frac{f_0^2\kappa^2}{|I_*|^4}|I|^6+2(f-f_0)\frac{f_0\kappa}{|I_*|^2}|I|^4+\left(\frac{f_0^2}{4Q^2}+(f-f_0)^2\right)|I|^2-\frac{f_0}{2\pi}\frac{f_0}{2Q_c}\frac{|I_*|^2}{f_rE_*\kappa}\frac{|I_1^+|^2Z_1}{2}\approx 0. \tag{4.58}$$

Its real roots, $|I(f,I_1^+)|$, can be used to determine the transmission

$$S_{21}(f,|I(f,I_1^+)|)\approx 1-\frac{\frac{1}{Q_c}}{\frac{1}{Q}+2i\left(\frac{f-f_0}{f_0}-\kappa\frac{|I(f,I_1^+)|^2}{|I_*|^2}\right)} \tag{4.59}$$

This solution is a bit unsatisfying because the constant term of the cubit polynomial involves κ and $f_r=f_0-\delta f_r$. This might go away if we take $2Z_r=2\pi f_rE_*\kappa/|I_*|^2$, but it not clear if that this would be a true assumption.

4.2.2 Approach: resonator input amplitude, V_3^-, parameterization

In this straight forward approach, we begin with an expression for the amplitude, V_3^-, entering the resonator in terms of Q_{tl}^{-1} and ${}^{\delta f}\!/_f$. A perturbation proportional to $|V_3^-|^2$ is then added to those terms.

Equation 4.44 can be approximated as,

$$V_3^-\approx V_1^+\frac{\sqrt{\frac{1}{\pi Q_c}}\sqrt{\frac{Z_3}{Z_1}}e^{i\phi_{31}}}{\frac{1}{Q_c}+\frac{1}{Q_{tl}}+2i\frac{f-f_0}{f_0}}, \tag{4.60}$$

where we have used $\Gamma=1$, Equation 4.39a, Equation 4.39c, and Equation 4.42. Next we introduce the parameterization

$$\frac{1}{Q_{tl}}\longrightarrow\frac{1}{Q_{tl}}\left(1+\eta\left|\frac{V_3^-}{V_{3,0}^-}\right|^2\right) \tag{4.61a}$$

$$\frac{f-f_0}{f_0}\longrightarrow\frac{f}{f_0}\left(1+\delta\left|\frac{V_3^-}{V_{3,0}^-}\right|^2\right)-1. \tag{4.61b}$$

The parameterization results in a cubic equation for V_3^-,

$$\left[\eta\frac{f_0}{2Q_{tl}\left|V_{3,0}^-\right|^2}+\delta\frac{if}{\left|V_{3,0}^-\right|^2}\right]\left|V_3^-\right|^2V_3^-+\left[\frac{f_0}{2Q_c}+\frac{f_0}{2Q_{tl}}+i(f-f_0)\right]V_3^-\approx\frac{f_0}{2}\sqrt{\frac{1}{\pi Q_c}}\sqrt{\frac{Z_3}{Z_1}}e^{i\phi_{31}}V_1^+. \tag{4.62}$$

To solve for $V_3^- = V_3^-(f, V_1^+)$, each side of the equation is multiplied by its complex conjugate,

$$\left[\delta^2 \frac{f^2}{|V_{3,0}^-|^4} + \eta^2 \frac{f_0^2}{4Q_{tl}^2 |V_{3,0}^-|^4}\right] |V_3^-|^6 + 2\left[\delta \frac{(f-f_0)f}{|V_{3,0}^-|^2} + \eta \frac{f_0}{2Q_{tl}|V_{3,0}^-|^2}\left(\frac{f_0}{2Q_c} + \frac{f_0}{2Q_{tl}}\right)\right] |V_3^-|^4 + \left[(f-f_0)^2 + \left(\frac{f_0}{2Q_c} + \frac{f_0}{2Q_{tl}}\right)^2\right] |V_3^-|^2 - \frac{f_0}{2\pi}\frac{f_0}{2Q_c}\frac{Z_3}{Z_1}|V_1^+|^2 \approx 0 \tag{4.63}$$

The real roots of the resultant cubic in $\left|V_3^-\right|^2$ give the magnitude, $\left|V_3^-\right|$. The phase of V_3^- is determined by substituting the real roots back into Equation 4.62.

A nonlinear expression for $S_{21}(f)$ can be obtained from $V_3^-(f, V_1^+)$ (Equation 4.62) by using network theory to convert it to V_2^- or by direct substitution of the above parameterization into Equation 4.43,

$$S_{21}(f, V_3^-(f, V_1^+)) \approx \sigma_{21} + \sigma_{13}\Gamma e^{-2\gamma\ell}\sqrt{\frac{Z_1}{Z_3}}\frac{V_3^-(f, V_1^+)}{V_1^+} \tag{4.64a}$$

$$\approx 1 - \frac{\frac{1}{Q_c}}{\frac{1}{Q_c} + \frac{1}{Q_{tl}}\left(1 + \eta\left|\frac{V_3^-(f,V_1^+)}{V_{3,0}^-}\right|^2\right) + 2i\left(\frac{f-f_0}{f_0} + \delta\left|\frac{V_3^-(f,V_1^+)}{V_{3,0}^-}\right|^2 \frac{f}{f_0}\right)}. \tag{4.64b}$$

4.2.3 Approach: quantum Input Output theory

We follow the formalism of the quantum network theory [200] and input output theory [69, 70]. Assume we have a lossless transmission line extending from $z = -\infty$ to $z = +\infty$. If $\bar{\rho}(z,t)$ is the charge density per unit length, then it is related to the charge field $Q(z,t)$ by

$$Q(z,t) = \int_z^\infty dz' \bar{\rho}(z',t). \tag{4.65}$$

$Q(z,t)$ is the total charge between $z = z'$ and $z = +\infty$ The voltage across the transmission line is

$$V(z,t) = \frac{\bar{\rho}}{\overline{C}} = -\frac{1}{\overline{C}}\frac{\partial Q}{\partial z} \tag{4.66}$$

where $\overline{C}$ is the capacitance per unit length of the transmission line. The current on the transmission line is

$$I(z,t) = \frac{\partial Q}{\partial t}. \tag{4.67}$$

The Lagrangian density for the charge field is,

$$\overline{\mathscr{L}} = \frac{1}{2}[\overline{L}I^2 - \overline{C}V^2] = \frac{1}{2}\left[\overline{L}\left(\frac{\partial Q}{\partial t}\right)^2 - \frac{1}{\overline{C}}\left(\frac{\partial Q}{\partial z}\right)^2\right]. \tag{4.68}$$

A wave equation for the charge field is obtained by setting $\overline{\mathscr{L}} = 0$. We see that the propagation velocity is, $v_p = \sqrt{\overline{L}\overline{C}}^{-1}$, as usual. The general solution to the wave equation is,

$$Q(z,t) = Q^+(t - z/v_p) + Q^-(t + z/v_p), \tag{4.69}$$

where the + and − superscripts remind us of the propagation direction of each term, in this case positive and negative going waves, respectively. A momentum field, $\overline{\Phi}(z,t)$, canonically conjugate to the charge field is obtained by

$$\overline{\Phi}(z,t) = \frac{\partial \mathscr{L}}{\partial\left(\partial Q/\partial t\right)} = \overline{L} I(z,t), \tag{4.70}$$

where $\mathscr{L} = \int dz \overline{\mathscr{L}}$ is the Lagrangian. $\overline{\Phi}$ is the magnetic flux per unit length along the transmission line. A canonical quantization proceed is performed wherein Q and $\overline{\Phi}$ are defined to satisfy commutation relations

$$[Q(z,t), Q(z',t)] = \left[\overline{\Phi}(z,t), \overline{\Phi}(z',t)\right] = 0 \tag{4.71a}$$

$$\left[Q(z,t), \overline{\Phi}(z',t)\right] = i\hbar\delta(z - z'). \tag{4.71b}$$

The operators Q^+ and Q^- can be Fourier expanded

$$Q^+(t - z/v_p) = \sqrt{\frac{\hbar}{4\pi Z}} \int_0^\infty \frac{d\omega}{\sqrt{\omega}} \left[a^+(\omega) e^{-i\omega(t - z/v_p)} + a^{+\dagger}(\omega) e^{i\omega(t - z/v_p)}\right] \tag{4.72a}$$

$$Q^-(t + z/v_p) = \sqrt{\frac{\hbar}{4\pi Z}} \int_0^\infty \frac{d\omega}{\sqrt{\omega}} \left[a^-(\omega) e^{-i\omega(t + z/v_p)} + a^{-\dagger}(\omega) e^{i\omega(t + z/v_p)}\right]. \tag{4.72b}$$

where Z is the transmission line impedance. The a^+ and a^- are annihilation operators single quanta propagating in the positive and negative directions, respectively, satisfying

$$\left[a^\nu(\omega), a^{\nu'}(\omega')\right] = 0 \tag{4.73a}$$

$$\left[a^\nu(\omega), a^{\nu'\dagger}(\omega')\right] = \delta_{\nu\nu'}\delta(\omega - \omega'). \tag{4.73b}$$

where ν is + or −. Equation 4.66 and Equation 4.72 can be used to obtain an expression for the voltage in terms of the operators a^+ and a^-.

$$V^+(z,t) = -i\sqrt{\frac{\hbar Z}{4\pi}} \int_0^\infty \sqrt{\omega} d\omega [a^+(\omega) e^{-i\omega(t - z/v_p)} - a^{+\dagger}(\omega) e^{i\omega(t - z/v_p)}] \tag{4.74a}$$

$$= -i\sqrt{\frac{\hbar Z\omega_0}{2}} [a^+(t) e^{i\omega z/v_p} - a^{+\dagger}(t) e^{-i\omega z/v_p}] \tag{4.74b}$$

$$V^-(z,t) = i\sqrt{\frac{\hbar Z}{4\pi}} \int_0^\infty \sqrt{\omega} d\omega [a^-(\omega) e^{-i\omega(t + z/v_p)} - a^{-\dagger}(\omega) e^{i\omega(t + z/v_p)}] \tag{4.74c}$$

$$= i\sqrt{\frac{\hbar Z\omega_0}{2}} [a^-(t) e^{-i\omega z/v_p} - a^{-\dagger}(t) e^{i\omega z/v_p}]. \tag{4.74d}$$

The Fourier from $a(\omega)$ to $a(t)$ has been performed here, with the assumption the physical system of interest is narrow in band so that we can take $\int_0^\infty \to \int_\infty^\infty$. as well as $\sqrt{\omega} \to \sqrt{\omega_0}$ in the integrand. This is a *Markov approximation.*

We consider a $\lambda/2$ resonator shunt coupled to a feedline. Nonlinear and linear dissipation are modeled by photon baths connected only to the resonator.

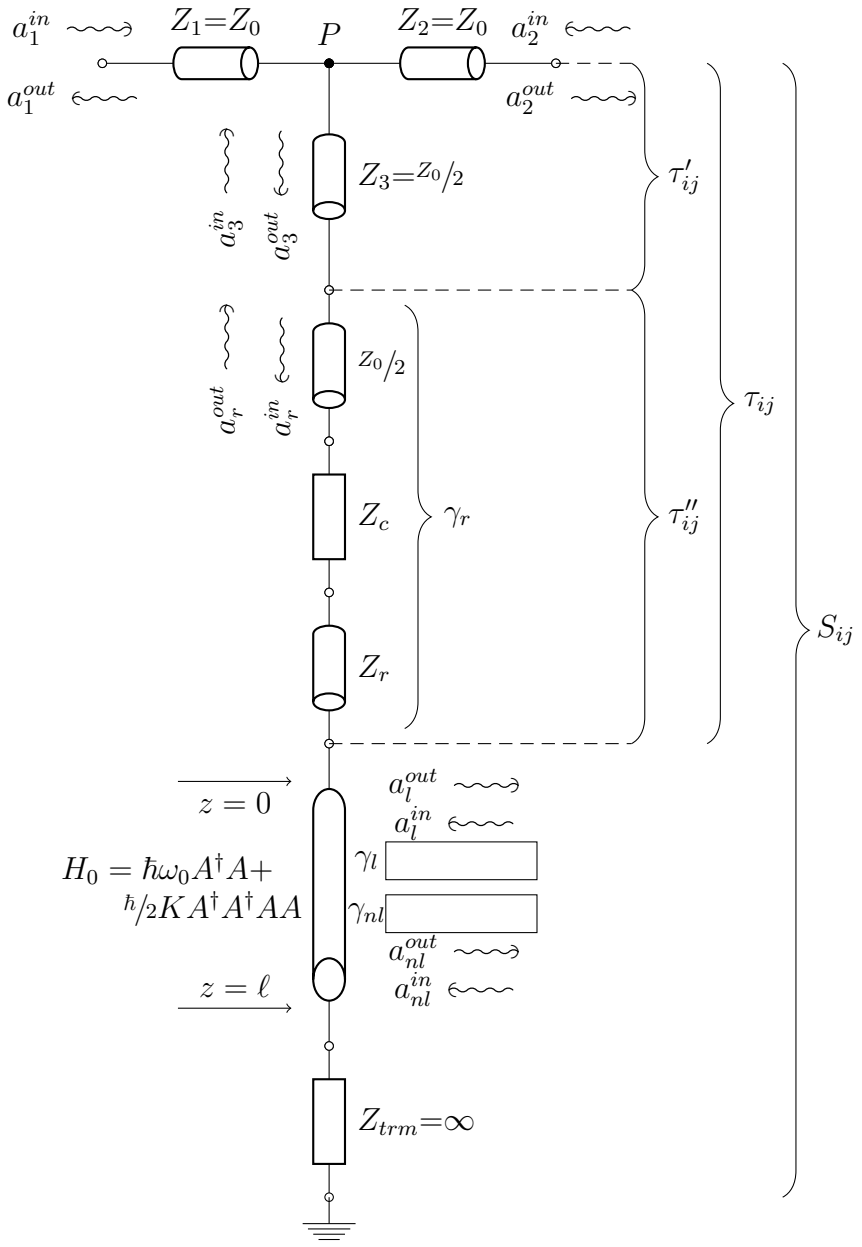


Figure 4.5: Network diagram of nonlinear $\lambda/2$ resonator shunt-coupled to feedline. The coupler τ_{ij}, is composed of a three-port junction of three transmission lines, τ'_{ij}, and a two-port coupling to the nonlinear resonator, τ''_{ij}. A is the resonator mode and the resonator Hamiltonian includes a non-dissipative Kerr nonlinearity, K. The resonator is coupled to bath modes a_r, a_l and a_{nl} via coupling constants γ_r, γ_l and γ_{nl} allowing exchange of resonator energy with the pump/detector, linear losses, and nonlinear (two-photon) losses, respectively. Z_{trm} is the resonator termination. The a_r are the same as the a_3 except that their directions are reversed. S ports one and two are the same as τ ports one and two. τ' port three is τ'' port 1 and τ'' port 2 is τ port 3.

We would like to use the results presented in a 2006 paper by Yurke [199]. To do this, we modify the coupler $\sigma_{ij}(Z_0, Z_c, Z_r)$ depicted in Figure 4.1, so that it has two parts, τ_{ij}, as depicted in Figure 4.5. One part is the three port intersection of three transmission lines, τ'_{ij}. The other part is a two port coupling to the nonlinear resonator τ''_{ij}. τ_{ij} is obtained from σ_{ij} by substituting,

$$\tau_{ij}(Z_0, Z_c, Z_r) = \sigma_{ij}(Z_0, Z_c + {}^{Z_0}\!/_2, Z_r). \tag{4.75}$$

Thus the normalized unique elements of τ are

$$\begin{aligned} \tau_{11} &= \frac{-\frac{1}{2}Z_0}{Z_0 + Z_c + Z_r} \qquad \tau_{13} = \frac{\sqrt{Z_0 Z_r}}{Z_0 + Z_c + Z_r} \\ \tau_{21} &= \frac{\frac{1}{2}Z_0 + Z_c + Z_r}{Z_0 + Z_c + Z_r} \qquad \tau_{33} = \frac{Z_0 + Z_c - Z_r}{Z_0 + Z_c + Z_r}. \end{aligned} \tag{4.76}$$

One concludes that τ' has the same symmetries of τ,

$$\tau' = \begin{bmatrix} \tau'_{11} & \tau'_{12} & \tau'_{13} \\ \tau'_{12} & \tau'_{11} & \tau'_{13} \\ \tau'_{13} & \tau'_{13} & \tau'_{33} \end{bmatrix}. \tag{4.77}$$

Additionally, the impedance of τ' port 3 is chosen so that there is no reflection off this port. The normalized elements of τ' are,

$$\tau'_{11} = -{}^1\!/_2 \qquad \tau'_{12} = {}^1\!/_2 \qquad \tau'_{13} = {}^1\!/_{\sqrt{2}} \qquad \tau'_{13} = 0. \tag{4.78}$$

Lastly, one finds that the coupling to resonator τ'' is symmetric and reciprocal from a straightforward two-port analysis

$$\tau'' = \begin{bmatrix} \tau''_{11} & \tau''_{12} \\ \tau''_{12} & \tau''_{11} \end{bmatrix}, \tag{4.79}$$

where

$$\tau''_{11} = \frac{Z_c + Z_r - \frac{1}{2}Z_0}{Z_c + Z_r + \frac{1}{2}Z_0} \qquad \tau''_{12} = \frac{\sqrt{2Z_r Z_c}}{Z_c + Z_r + \frac{1}{2}Z_0}. \tag{4.80}$$

In this nonlinear treatment, we assume that the resonator is pumped through τ''. A coupling κ_r describes the strength the of the coupling between the resonator and τ' port 3. The linear and nonlinear dissipation baths are coupled to the resonator with couplings κ_l and κ_{nl}, respectively. In the terms of Equation 4.51, the linear dissipation arising from R describes the cavity's internal quality factor, and the nonlinear coupling describes nonlinear dissipation arising from $\Delta R(I/I_c)^2$. The couplings are assumed to be independent of frequency, an assumption called the first Markov approximation. They are related to dampening constants γ as $\kappa \propto \sqrt{\gamma}e^{i\theta}$ and the dampening constants have units of s and quantify the associated cavity ring-down time for the dissipation mechanism it they each refer. On the other hand, the inductive nonlinearity arising from $\Delta L(I/I_c)^2$ is modeled as a Kerr coupling, K, between two photons.

The Hamiltonian of the system is

$$H = H_r + H_{a_r} + H_{a_l} + H_{a_{nl}} + H_{T_r} + H_{T_l} + H_{T_{nl}}. \tag{4.81}$$

The Hamiltonian of the nonlinear resonator is

$$H_r = \hbar\omega_0 A^\dagger A + \frac{\hbar}{2} K A^\dagger A^\dagger A A. \tag{4.82}$$

The bath Hamiltonians are

$$H_{a_r} = \int d\omega\, \hbar\omega a_r^\dagger(\omega) a_r(\omega) \tag{4.83a}$$

$$H_{a_l} = \int d\omega\, \hbar\omega a_l^\dagger(\omega) a_l(\omega) \tag{4.83b}$$

$$H_{a_{nl}} = \int d\omega\, \hbar\omega a_{nl}^\dagger(\omega) a_{nl}(\omega). \tag{4.83c}$$

Notice, from inspection of Equation 4.82, that A and $A^\dagger$ are unitless. However, inspection of Equation 4.83, that the a and $a^\dagger$ have units of $\sqrt{\text{Hz}}^{-1}$. The hopping Hamiltonians are

$$H_{T_r} = \hbar \int d\omega \left[\kappa_r A^\dagger a_r(\omega) + \kappa_r^* a_r^\dagger(\omega) A\right] \tag{4.84a}$$

$$H_{T_l} = \hbar \int d\omega \left[\kappa_l A^\dagger a_l(\omega) + \kappa_l^* a_l^\dagger(\omega) A\right] \tag{4.84b}$$

$$H_{T_{nl}} = \hbar \int d\omega \left[\kappa_{nl} A^\dagger a_{nl}(\omega) + \kappa_{nl}^* a_{nl}^\dagger(\omega) A\right]. \tag{4.84c}$$

The time dependence of A can be obtained using the Heisenberg equation of motion

$$i\hbar \frac{dO}{dt} = [O, H]. \tag{4.85}$$

Using the boson commutation relation

$$[A, A^\dagger] = AA^\dagger - A^\dagger A = 1, \tag{4.86}$$

one obtains

$$\begin{aligned} \frac{dA}{dt} = &-i\omega_0 A - iKA^\dagger AA - i\kappa_r \int d\omega\, a_r(\omega) \\ &-i\kappa_l \int d\omega\, a_l(\omega) - i2\kappa_{nl} \int d\omega\, A^\dagger a_{nl}(\omega). \end{aligned} \tag{4.87}$$

Using the boson commutation relation for the bath modes

$$\left[a_i^{in}(\omega), a_j^{in\dagger}(\omega')\right] = \left[a_i^{out}(\omega), a_j^{out\dagger}(\omega')\right] = \delta_{i,j}\delta(\omega - \omega') \tag{4.88a}$$

$$\left[a_i^{in}(\omega), a_j^{in\dagger}(\omega')\right] = \left[a_i^{out}(\omega), a_j^{out\dagger}(\omega')\right] = 0. \tag{4.88b}$$

for i, $j \in \{r, l, nl\}$, one obtains the following equations for the bath modes,$a_r(\omega)$, $a_l(\omega)$, $a_{nl}(\omega)$

$$\frac{da_r(\omega)}{dt} = -i\omega a_r(\omega) - i\kappa_r^* A \tag{4.89a}$$
$$\frac{da_l(\omega)}{dt} = -i\omega a_l(\omega) - i\kappa_l^* A \tag{4.89b}$$
$$\frac{da_{nl}(\omega)}{dt} = -i\omega a_{nl}(\omega) - i\kappa_{nl}^* AA. \tag{4.89c}$$

An equation of motion for the cavity mode, A, driven by the incoming bath mode, a_i^{in}, can be obtained from these relations using the methods of Gardiner and Collett,

$$\begin{aligned}\frac{dA}{dt} = -i\omega_0 A - iKA^\dagger AA - (\gamma_r + \gamma_l)A - \gamma_{nl}A^\dagger AA \\ -i\sqrt{2\gamma_r}e^{i\phi_r}a_r^{in}(t) - i\sqrt{2\gamma_l}e^{i\phi_l}a_l^{in}(t) - i2\sqrt{\gamma_{nl}}e^{i\phi_{nl}}a_{nl}^{in}(t).\end{aligned} \tag{4.90}$$

Here we have reexpressed the κ_i in polar coordinates.

$$\kappa_r = \sqrt{\frac{\gamma_r}{\pi}}e^{i\phi_r} \tag{4.91a}$$
$$\kappa_l = \sqrt{\frac{\gamma_l}{\pi}}e^{i\phi_l} \tag{4.91b}$$
$$\kappa_{nl} = \sqrt{\frac{\gamma_{nl}}{2\pi}}e^{i\phi_{nl}} \tag{4.91c}$$

The γ_i and ϕ_i are real and constant.

Gardiner and Collett can again be used to find the relationships between outgoing $a_i^{out}(t)$ and incoming $a_i^{in}(t)$ bath modes,

$$a_r^{out}(t) - a_r^{in}(t) = -i\sqrt{2\gamma_r}e^{-i\phi_r}A(t) \tag{4.92a}$$
$$a_l^{out}(t) - a_l^{in}(t) = -i\sqrt{2\gamma_l}e^{-i\phi_l}A(t) \tag{4.92b}$$
$$a_{nl}^{out}(t) - a_{nl}^{in}(t) = -i\sqrt{\gamma_{nl}}e^{-i\phi_{nl}}A(t)A(t). \tag{4.92c}$$

A Markov approximation (that the coupling constants are independent of frequency) on the annihilation operators $a_i^{in}(t)$ has been used to obtain the above. With this approximation, the operators satisfy

$$\left[a_i^{in}(t), a_j^{in\dagger}(t')\right] = \left[a_i^{out}(t), a_j^{out\dagger}(t')\right] = \delta_{i,j}\delta(t-t') \tag{4.93a}$$
$$\left[a_i^{in}(t), a_j^{in\dagger}(t')\right] = \left[a_i^{out}(t), a_j^{out\dagger}(t')\right] = 0, \tag{4.93b}$$

for $i, j \in \{1, 2, 3, r, l, nl\}$.

Meanwhile, the incoming and outgoing radiation fields of the three port network τ' are related as,

$$\begin{bmatrix} a_1^{out}(\omega) \\ a_2^{out}(\omega) \\ a_3^{out}(\omega) \end{bmatrix} = \begin{bmatrix} \tau'_{11} & \tau'_{12} & \tau'_{13} \\ \tau'_{12} & \tau'_{11} & \tau'_{13} \\ \tau'_{13} & \tau'_{13} & \tau'_{33} \end{bmatrix} \begin{bmatrix} a_1^{in}(\omega) \\ a_2^{in}(\omega) \\ a_3^{in}(\omega) \end{bmatrix} \tag{4.94}$$

Relevant to the current analysis, we have

$$a_3^{out}(\omega) = \tau'_{13} a_1^{in}(\omega) + \tau'_{13} a_2^{in}(\omega) + \cancelto{0}{\tau'_{33} a_1^{in}(\omega)} \tag{4.95a}$$

$$a_2^{out}(\omega) = \tau'_{12} a_1^{in}(\omega) + \tau'_{11} a_2^{in}(\omega) + \tau'_{13} a_3^{in}(\omega) \tag{4.95b}$$

The three port network is connected to the capacitively coupled resonator by defining,

$$a_3^{out}(\omega) = a_r^{in}(\omega) \tag{4.96a}$$

$$a_3^{in}(\omega) = a_r^{out}(\omega), \tag{4.96b}$$

or after Fourier transforming,

$$a_3^{out}(t) = a_r^{in}(t) \tag{4.97a}$$

$$a_3^{in}(t) = a_r^{out}(t). \tag{4.97b}$$

Substituting this into Equation 4.90, we get

$$\begin{aligned} \frac{dA}{dt} &= -i\omega_0 A - iKA^\dagger AA - (\gamma_r + \gamma_l)A - \gamma_{nl} A^\dagger AA \\ &-i\sqrt{2\gamma_r} e^{i\phi_r} \left[\tau'_{13} a_1^{in}(t) + \tau'_{13} a_2^{in}(t)\right] - i\sqrt{2\gamma_l} e^{i\phi_l} a_l^{in}(t) - i2\sqrt{\gamma_{nl}} e^{i\phi_{nl}} a_{nl}^{in}(t), \end{aligned} \tag{4.98}$$

and Equation 4.92a becomes

$$a_r^{out}(t) = \left[\tau'_{13} a_1^{in}(t) + \tau'_{13} a_2^{in}(t)\right] - i\sqrt{2\gamma_r} e^{-i\phi_r} A(t) \tag{4.99}$$

Now we move from the quantum view of the system to a classical view. We assume that the system is pumped with an intense sinusoidal field at port 1. Additionally we assume that any other signals or noise from port 2, the linear dissipation bath and the nonlinear dissipation bath are small compared to the pump,

$$a_2^{in}(t) = 0 \tag{4.100a}$$

$$a_l^{in}(t) = 0 \tag{4.100b}$$

$$a_{nl}^{in}(t) = 0. \tag{4.100c}$$

The incoming pump field, outgoing transmitted field, and cavity amplitudes are written in polar coordinates as

$$a_1^{in} = a_1^{in}(t) = b_1^{in} e^{-i(\omega_p t + \psi_1)} \tag{4.101a}$$

$$a_2^{out} = a_2^{out}(t) = b_2^{out} e^{-i(\omega_p t + \psi_2)} \tag{4.101b}$$

$$A = A(t) = B e^{-i(\omega_p t + \phi_B)}, \tag{4.101c}$$

where all the polar angles and magnitudes are real constants.

The driven cavity mode reduces to

$$\frac{dA}{dt} = -i\omega_0 A - iKA^\dagger AA - (\gamma_r + \gamma_l)A - \gamma_{nl} A^\dagger AA - i\sqrt{2\gamma_r} e^{i\phi_r} \tau'_{13} a_1^{in}(t), \tag{4.102}$$

or

$$-i\sqrt{2\gamma_r}\tau'_{13} b_1^{in} = \left[\{i(\omega_0 - \omega_p) + (\gamma_r + \gamma_l)\} B + \{iK + \gamma_{nl}\} B^3\right] e^{-i(\phi_r + \phi_B - \psi_1)} \tag{4.103}$$

The mode leaving τ' port 2 is determined by substituting Equation 4.97b and Equation 4.100a into Equation 4.95b,

$$a_2^{out}(t) = \tau'_{12} a_1^{in}(t) + \tau'_{13} a_r^{out}(t). \tag{4.104}$$

Equation 4.104 can be related to the cavity mode, A, using Equation 4.92a. This relation, expressed in polar coordinates (Equation 4.101), is

$$b_2^{out} e^{-i\psi_2} = \left(\tau'_{12} + \tau'^2_{13}\right) b_1^{in} e^{-i\psi_1} - i\tau'_{13}\sqrt{2\gamma_r} B e^{-i(\phi_r + \phi_B)}. \tag{4.105}$$

The ratio of the incoming complex pump amplitude to the complex amplitude leaving τ' port 2 is the transmission term of the scattering matrix for the circuit,

$$S_{21} = \frac{a_2^{out}(t)}{a_1^{in}(t)} = \frac{b_2^{out} e^{-i\psi_2}}{b_1^{in} e^{-i\psi_1}}. \tag{4.106a}$$

To determine B, we multiply each side of Equation 4.103 by its complex conjugate. The resulting equation,

$$\begin{aligned} &\left[K^2 + \gamma_{nl}^2\right] B^6 + 2\left[(\omega_0 - \omega_p)K + (\gamma_r + \gamma_l)\gamma_{nl}\right] B^4 \\ &+ \left[(\omega_0 - \omega_p)^2 + (\gamma_r + \gamma_l)^2\right] B^2 - 2\gamma_r (\tau'_{13} b_1^{in})^2 = 0, \end{aligned} \tag{4.107}$$

is a cubic in B^2, so its root will be positive and real or complex. The equation will either have three real roots, or one real and two complex roots. Only the real roots are physical. The case of three real roots indicates bistability and only two will be stable. The ϕ_B are determined by substituting each solution for B into Equation 4.103. b_2^{out} and ψ_2 are then determined by substituting B and ϕ_B into Equation 4.105. The Kerr constant, K, is computed assuming the general case of position dependent L and R in the cavity.

4.2.4 Comparison of approaches

We will express I_1^+, I_* and I, the current in the inductor, of § 4.2.1 in terms of a_1^{in}, A, b_1^{in} and B of § 4.2.3. Then, we will substitute these expressions for the current into Equation 4.58. Comparison with Equation 4.107 will reveal relationships between the other quantities in these equations.

$$I_1^+(x,t) \propto i\sqrt{\frac{\hbar\omega_0}{2Z_1}}[a_1^{in}(t)e^{i\omega x/v_p} + a_1^{in\dagger}(t)e^{-i\omega z/v_p}]$$
$$\longrightarrow |I_1^+(x,t)|^2 \propto \frac{\hbar\omega_0}{Z_1 2}(b_1^{in})^2 \tag{4.108a}$$
$$I(z,t) \propto \frac{\omega_0}{\pi}\sqrt{\frac{\hbar}{Z_r\pi}}\sin\left(\frac{\pi z}{\ell}\right)[A(t)e^{-i\omega t} + A^\dagger(t)e^{-i\omega t}]$$
$$\longrightarrow |I|^2 \propto \frac{\omega_0^2\hbar}{Z_r\pi^3}B^2 \tag{4.108b}$$
$$I_*(z_0,t_0)I_* =\propto -\frac{\omega_0}{\pi}\sqrt{\frac{\hbar}{Z_r\pi}}\sin\left(\frac{\pi z_0}{\ell}\right)[A(t_0)e^{-i\omega t_0} + A^\dagger(t_0)e^{-i\omega t_0}]$$
$$\longrightarrow |I_*(z_0,t_0)|^2 \propto |I_*|^2 = \frac{\omega_0^2\hbar}{Z_r\pi^3}B_0^2. \tag{4.108c}$$

We do the same for V_1^+, $V_{3,0}^-$ and V_3^-, the voltage at the input of the resonator, of § 4.2.2. Expressions for the voltages in terms of a_1^{in}, A, b_1^{in} and B are substituted into Equation 4.63 and compared to Equation 4.107.

$$V_1^+(x,t) \propto -i\sqrt{\frac{\hbar Z_1\omega_0}{2}}[a_1^{in}(t)e^{i\omega x/v_p} - a_1^{in\dagger}(t)e^{-i\omega z/v_p}]$$
$$\longrightarrow |V_1^+(x,t)|^2 \propto \frac{\hbar Z_1\omega_0}{2}(b_1^{in})^2 \tag{4.109a}$$
$$V_3^-(z,t) \propto -\frac{\omega_0}{\pi}\sqrt{\frac{\hbar Z_r}{\pi}}\cos\left(\frac{\pi z}{\ell}\right)[A(t)e^{-i\omega t} - A^\dagger(t)e^{-i\omega t}]$$
$$\longrightarrow |V_3^-(z,t)|^2 \propto \frac{\omega_0^2\hbar Z_r}{\pi^3}B^2 \tag{4.109b}$$
$$V_{3,0}^-(z_0,t_0) = V_{3,0}^- \propto -\frac{\omega_0}{\pi}\sqrt{\frac{\hbar Z_r}{\pi}}\cos\left(\frac{\pi z_0}{\ell}\right)[A(t_0)e^{-i\omega t_0} - A^\dagger(t_0)e^{-i\omega t_0}]$$
$$\longrightarrow |V_{3,0}^-(z_0,t_0)|^2 \propto |V_{3,0}^-|^2 = \frac{\omega_0^2\hbar Z_r}{\pi^3}B_0^2 \tag{4.109c}$$

Attributions

Except where reference are given, all results in this chapter are my work. In some cases this work was done collaboratively with my advisor and with Professor Yurke.

Input/Output Theory	V_3^- Parameterization	${}^{\delta f}/_{f}$ Parameterization
K		$\delta \frac{\omega}{B_0^2} \left(\overset{e.g.}{=} \delta \frac{\omega \omega_0^2 \hbar Z_r}{\pi^3 \lvert V_{3,0}^- \rvert^2} \right)$
γ_{nl}	0	$\eta \frac{\omega_0}{2Q_{tl} B_0^2}$
γ_r	$\frac{\omega_0}{2Q_c}$	$\frac{\omega_0}{2Q_c}$
γ_l	$\frac{\omega_0}{2Q_{tl}}$	$\frac{\omega_0}{2Q_{tl}}$

Table 4.1: Relationships between nonlinear resonator parameters in § 4.2.1, § 4.2.2§ 4.2.3

Chapter 5

Detector Design, Fabrication and Readout System

In the chapter we describe the detector readout system in the 75μW fridge at UCB. We present system performance information (including noise, signal return loss, calibrations), testing cold hardware and its compatibility with CDMS cold hardware, and discuss readout electronics and software.

In order to develop the separated function kinetic inductance phonon sensor, as described in § 3.1.5, we design and construct simple test devices on standard sized wafers. A test device will consist of a probe chip mated to a ground plane chip. The details are explained in the chapter.

5.1 Mask design

Most of the KIDs data presented in this thesis comes from sensor chips defined in a single lithography mask set. The goal of this mask is to parametrically study the current carrying capability of the half-wave vacuum microstrip resonators, as a function of trace width. The "current test mask" set contains resonators of different trace widths that are designed to have the same resonant frequency and coupling quality factor. To avoid confusion between resonators, each probe chip has only one resonator. Figure 5.1 is a probe chip on the mask.

A computer program was written, in python, to draw the mask. The program takes an input file specifying, among other things, desired resonator widths, coupling quality factors and resonant frequencies. The specifications are then used to define a series of Sonnet simulations that are primarily intended to determine scattering parameters, S_{ij}, between the feedline and resonator as a function of resonator's coupler length. Other important electrical information, including the impedance and the effective dielectric constant of the resonator, can also be extracted from the simulations.

These coupling simulations only include a small section of the resonator, the section that comes close enough to the feedline to have a significant capacitance with it. This section if

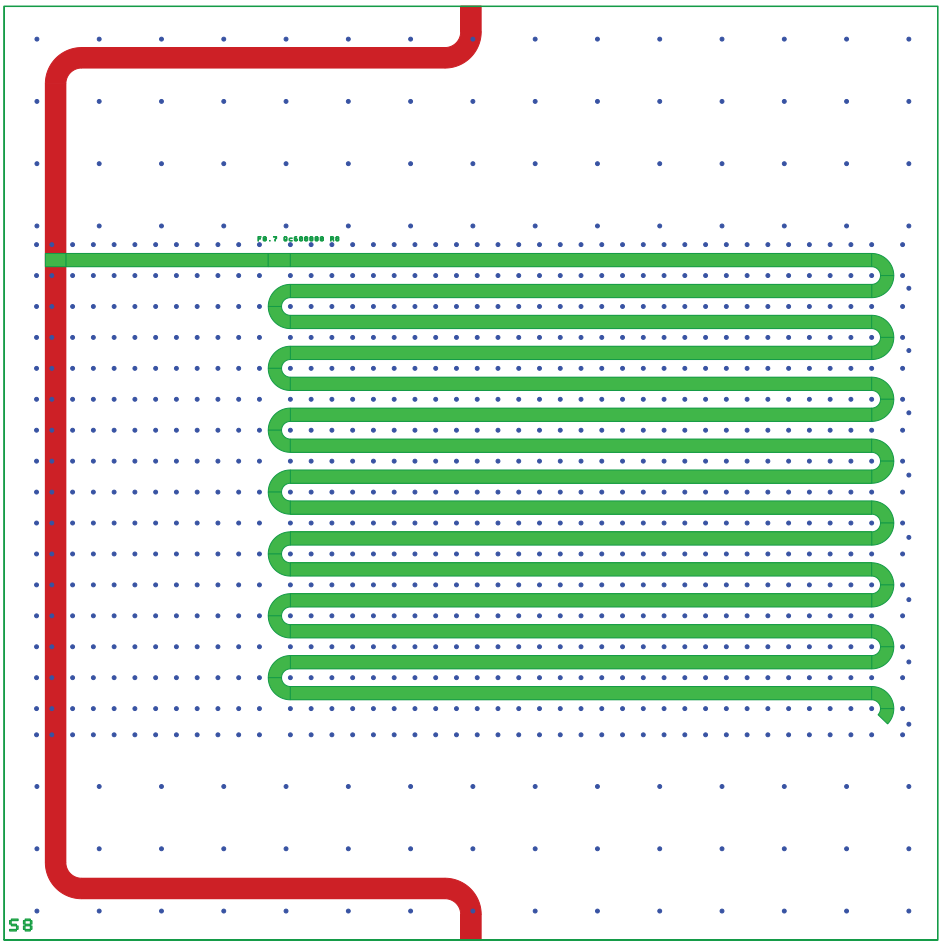


Figure 5.1: Lithography mask pattern for sensor chip "S8". Each of the three colors represents a different mask layer. The pillars are in blue. The resonator is in green and the feedline is in red. The pillars and the resonator are on one side of the wafer and the feeline is aligned to them on the other side of the wafer. In interspersion of pillars within the meandered area of the resonator is an important design feature which prevents the resonator trace from shorting to the ground plane. When fabricated, the resonator and feedline traces are made of niobium.

the resonator is called the coupler. The coupler and the feedline form a T-shaped three-port network. The ports are all assumed to be 50 Ω, which is close to the truth for the feedline since its width is already chosen to give 50 Ω given its position in the surrounding environment. The resonators however are usually not 50 Ω in impedance which leads to a mismatch at the simulation port and the mismatch affects the computed scattering parameters. The mask program takes the simulation results, extracts the impedance and the effective dielectric constant of each port, renormalizes the coupling scattering parameters using a transformation described in [102] to the extracted port impedance for the resonator port, then performs an

optimization to determine the length of the resonator coupler that achieves the desired coupling quality factor. Equation 4.30 is used to relate the scattering parameter to the coupling quality factor which we rewrite here,

$$Q_c = \frac{\pi}{|\sigma_{13}(f_0)|^2}. \tag{5.1}$$

. f_0 is the desired resonant frequency and $\sigma_{13}(f_0) = |\sigma_{13}(f_0)|e^{i\theta_{13}(f_0)}$.

Now that the coupler dimensions have been determined, the program uses the extracted effective dielectric constant, ϵ_{eff}, to determine determine the phase change per unit length, β, of the resonator trace by,

$$\beta = \frac{2\pi f_0 \sqrt{\epsilon_{\text{eff}}}}{c}. \tag{5.2}$$

The rest of the length of the resonator, l is determined so that the $\lambda/2$ resonance condition is met,

$$\pi = \theta_{13}(f_0) + \beta l. \tag{5.3}$$

Thus, the phase change contribution of the coupler is added to the length calculation. Although the coupler may be no different in geometry than the rest of the resonator, it proximity to the feedline gives it a slightly different phase change per unit length from the rest of the line. A subroutine is then used to the meander the resonator and place the pillars all around it, but no closer than a distance specified in the input file. The parameters of the sensor chips on the mask are listed in Table 5.1.

This method of automatically drawing the mask, as currently implemented, has two important shortcomings. It does not account for impedance variations due to bends in the meander pattern of the resonator. The tighter the curve, the greater the impedance disruption. There are analytical methods available for dealing with this [190], but a simple attempt to avoid the issue was made on this mask by choosing the radius of the bends to be much larger than the resonator width whenever possible. The other shortcoming is that the method does not account for the accumulation of broadside couple between the feedline and the resonator portions that come close to it. The resonator in Figure 5.1, S8, is coupled to the feedline primarily by capacitance with the coupler, at the top if the die. Smaller capacitive coupling exists between the meandered region of the resonator and the feedline. The additional coupling will decrease the coupling quality factor and alter the resonant frequency. Additionally, there is a small inductive coupling between the resonator and the feedline which is also unaccounted for. Ideally what one should do it perform a full simulation of the resonator from the method described above, and then tune coupler length and resonator length to get as close as possible to quality factor and resonant frequency objectives. However, a full simulation of these[1] resonators can take days to weeks depending on the computational power at hand. Also, there were uncertainties in vacuum gap height

[1]Computational difficulty increases when different size scales are represented in the resonator. The resonator in Figure 5.1 has a relatively uniform size scale. But if that 256 µm wide resonator were replaces with a 2 µm wide that is meandered using the same large bend radius. This would be difficult to simulate.

Sensor ID		S1	S2	S3	S4	S5	S6	S7	S8
Resonator									
Width	[μm]	2	4	8	16	32	64	128	256
F_0	[MHz]	700	700	700	700	700	700	700	700
Q_c	[10^3]	600	600	600	600	600	600	600	600
Impedance	[Ω]	85.78	67.83	50.18	33.82	21.25	12.73	7.19	3.58
ϵ_{eff}		4.20	3.81	3.25	2.62	2.09	1.70	1.45	1.28
Length	[10^3 μm]	99.24	105.13	113.85	125.79	140.35	155.91	170.35	182.23
Trace Area	[10^6 μm^2]	0.20	0.42	0.91	2.01	4.49	9.98	21.81	46.65
Patch Area	[10^6 μm^2]	37.34	29.01	33.13	37.90	44.08	55.77	89.16	109.73
Feedline									
Impedance	[Ω]	52.16	52.16	52.16	52.16	52.15	52.14	52.14	52.06
ϵ_{eff}		7.03	7.03	7.03	7.03	7.04	7.04	7.04	7.05
α_{ms}	[10^{-3}]		23.9	17.8	13.8	12.1	11.4	11.2	10.7
α_g	[10^{-3}]		2.4	3.1	3.6	4.2	4.6	4.9	4.9

Table 5.1: Parameters for each sensor chip on the current test mask. Impedances and effective dielectric constants are obtained from Sonnet simulations assuming that the temperature is less than 1 K, conductors are aluminum and niobium, that a vacuum gap is approximately 3 μm between the trace and the ground plane, that the sensor wafer substrate is Sapphire (birefringence is accounted for), and a layer of teflon (see Figure 5.6) is between the feedline and a superconducting plate. Low temperature dielectric properties of sapphire and teflon are obtained from [101, 39]. α_{ms} and α_g are the kinetic inductance fractions for the microstrip and ground plane respectively. They were calculated using Induct and the same assumptions as Figure 5.2

and lithographic alignment of the feedline to the resonator that made perfecting the resonator design a background issue. Nevertheless, full simulations of the resonators were performed as a way of studying losses experienced by the resonator.

5.2 Expected losses

We would like to estimate the losses experienced by the microstrip resonator in terms of quality factors. (See Appendix A for a background on quality factor.) Generally, these include conductor losses, dielectric losses and radiation losses. Q_{tl} of Equation 4.34 can be considered a component of the total conductor loss. If the conductor losses are taken only as those arising from the residual quasiparticle population in the superconductor, one gets a very high conductor loss quality factor, $Q_{\text{cond}} \approx 10^{39}$, and this is what we had in mind in describing Q_{tl}. To get this number, we simply compute the complex conductivity of the

aluminum and niobium metals, convert it to a resistance and then to an attenuation constant and then to a quality factor. Alternatively, if one, additionally, includes dissipation in non-superconducting metals electromagnetically coupled the resonator (e.g. the box walls), one gets a much lower value for $Q_{\rm cond}$ and this is beyond what we had in mind for Q_{tl}. We will not consider these losses because all the metals around the resonator are superconductors[2] for most of the data we acquired. Another potentially large conductor loss mechanism is that which is due to vortices in the superconductor and we denote its associated quality factor as Q_v.

The dielectric quality factor, $Q_{\rm d}$ is given by [28],

$$Q_{\rm d} = \frac{1}{\tan\delta}\left(1 + \frac{1-q}{q\epsilon_r}\right), \tag{5.4}$$

where $\tan\delta$ is the dielectric loss tangent, ϵ_r is the dielectric constant, and filling factor is given by

$$q = \frac{\epsilon_{\rm eff} - 1}{\epsilon_r - 1}. \tag{5.5}$$

is the isotropic filling due to Wheeler [191]. The formulation for the filling factor probably overestimates the loss from the dielectric since it is meant for normal microstip with the dielectric between the ground plane and the trace.

The radiation quality factor has been worked out by several researches and they get different answers in different limits. We have the most confidence in the James, Henderson solution [90], which takes in to account surface evanescent waves and is based on the variational technique. They find that the radiation escaping from an open ended microstrip in terms of a radiation conductance. The conductance can be transformed into quality factor,

$$Q_{\rm rad} = \frac{Z\epsilon_{\rm eff}}{640\pi}\left(\frac{\lambda_0}{h}\right)^2, \tag{5.6}$$

where λ_0 is the free space wavelength and h is the microstrip height. This equation is not quite right for right or our inverted microstrip resonators, because James, Henderson assumed the dielectric to be between the strip and the group plane, however we think that at low frequency, such as our own, the approximation should not be too bad. We have introduced a factor of two in the formula to account for both ends of the microstrip. We imagine the radiated power to be less than this figure because the microstrip is in a shielding box. Radiated power can only be lost in dissipative materials inside the box or coupled out either of the two box ports.

Lastly, we perform a full resonator simulation using the shielded domain method of moments solver, Sonnet. The simulation treats the aluminum and niobium films as perfect

[2]As presented in chapter 6, resonator data from use of a non-superconducting box has markedly low internal quality factor. This could be due to conductor losses or magnetic flux penetration in the films of the resonator.

conductors; it uses the the low temperature dielectric constants and loss tangents of teflon ($\epsilon_r = 2.08$, $\tan\delta = 10^{-5}$) and sapphire ($\epsilon_r = 9.265$, $\tan\delta = 10^{-8}$) from [101, 39]; Lossless top and bottom covers for the shield domain are used, with the bottom cover being the microstrip ground plane; the ground plane to microstrip trace gap is set to 3 µm; the aluminum pillars were not included in the simulation; care was taken to ensure that the trace had at least three simulation cells across its width. The simulation computes the S_{21} and we use our resonator fitting code to extract the resonant frequency, coupling quality and internal quality factors. The coupling quality factor should take into account all coupling between the resonator and the feedline, capacitive and inductive, intended and parasitic. The internal quality factor should reflect losses in the dielectrics including those from radiated power. Table 5.2 presents estimations of the quality factor associated with the loss mechanism consider and the fitted quality factors from full resonator simulations.

Table 5.2 presents the values obtained for the losses considered.

Sensor ID		S1	S2	S3	S4	S5	S6	S7	S8
Formulae									
$Q_{\rm d}$	$[10^7]$	5.25	5.42	5.78	6.47	7.67	9.70	12.9	18.4
$Q_{\rm rad}$	$[10^7]$	365	262	165	89.7	45.9	22.7	10.9	5.85
Sonnet									
Q_c	$[10^3]$			419	447	504	532	506	552
Q_i	$[10^7]$			5.5	5.1	7.2	2.3	3.5	1.3
f_0	[MHz]			742	743	741	738	729	731
ϕ	[deg]			0.13	−0.31	0.02	0.21	0.72	−0.02

Table 5.2: Dielectric, $Q_{\rm d}$, and radiative, $Q_{\rm rad}$, quality factors are estimated for each sensor chip. Notice the anti-proportional relationship between $Q_{\rm d}$ and $Q_{\rm rad}$, which limits the total Q. The results of fitting full resonator Sonnet simulations provide figures for the coupling quality factor, Q_c, internal quality factor, Q_i, resonant frequency, f_0, and loop rotation ϕ. See § 6.1.1 for more on fitting. No simulations were performed for S1 and S2. Losses due to quasiparticles are not listed here because they are negligibly low.

Note that the internal quality factor measured in real dat will encompass all the dissipation mechanisms considered here, and any other possibilities that exist. Mathematically,

$$\frac{1}{Q_i} = \frac{1}{Q_{\rm cond}} + \frac{1}{Q_v} + \frac{1}{Q_{\rm d}} + \frac{1}{Q_{\rm rad}} + \cdots . \tag{5.7}$$

Thus, we underscore the distinction that Q_c is not a associated with a dissipation.

5.3 Expected kinetic inductance fraction, α

We have calculated the kinetic inductance fraction for the sensors on the current test mask using a numerical approach. As discussed before, and elsewhere [68], the total inductance, L_{tot}, of a superconducting transmission line, such as our microstrip resonators, is comprised of a part due to the magnetic field in a vacuum, L_{mag}, and a part due to the magnetic field and the kinetic energy stored in the Cooper pairs, L_{kin} (measured in henry per meter),

$$L_{tot} = L_{kin} + L_{mag}. \tag{5.8}$$

L_{kin} is called the kinetic inductance. The kinetic inductance fraction, α, is the fraction of the total inductance that is kinetic inductance,

$$\alpha = \frac{L_{kin}}{L_{kin} + L_{mag}}. \tag{5.9}$$

The conductors in the transmission line have a surface inductance, L_{surf} (measured in henry per square), which is specified by the electrodynamics governing that material and depends on the material properties. L_{sur} is related to the L_{kin} via a geometric conversion factor, g (has no physical units but mathematically has the units of "squares"),

$$L_{kin} = g \cdot L_{surf}. \tag{5.10}$$

g is obtained by doing a contour integral that essentially finds the ratio between the field qualities, i.e. the magnetic field parallel to the conductor $H_{\parallel}$, and circuit quantities, e.g. the current I,

$$g = \frac{\int_C H_{\parallel}^2 dl}{I^2}. \tag{5.11}$$

For the case of the microstrip, there are two different conductors, so we can break the kinetic inductance into two parts, one for each conductor

$$L_{kin} = L_{kin,1} + L_{kin,2} = g_1 L_{surf,1} + g_2 L_{surf,2}. \tag{5.12}$$

The contour integrals for g_1 and g_2 are performed around the boundary of the conductor for which is stands. The surface impedances $L_{surf,1}$ and $L_{surf,2}$ are determined from material properties according to the electrodynamics of the materials for which it stands. This multi-component kinetic inductance opens up the possibility of defining partial kinetic inductance fractions, which correspond to each metal in the transmission line, e.g.

$$\alpha = \alpha_1 + \alpha_2 = \frac{L_{kin,1}}{L_{kin} + L_{mag}} + \frac{L_{kin,2}}{L_{kin} + L_{mag}}. \tag{5.13}$$

The concept of partial kinetic inductance fractions is useful for devices like the vacuum microstrip, where energy can be deposited into one of the conductors, the other, or both.

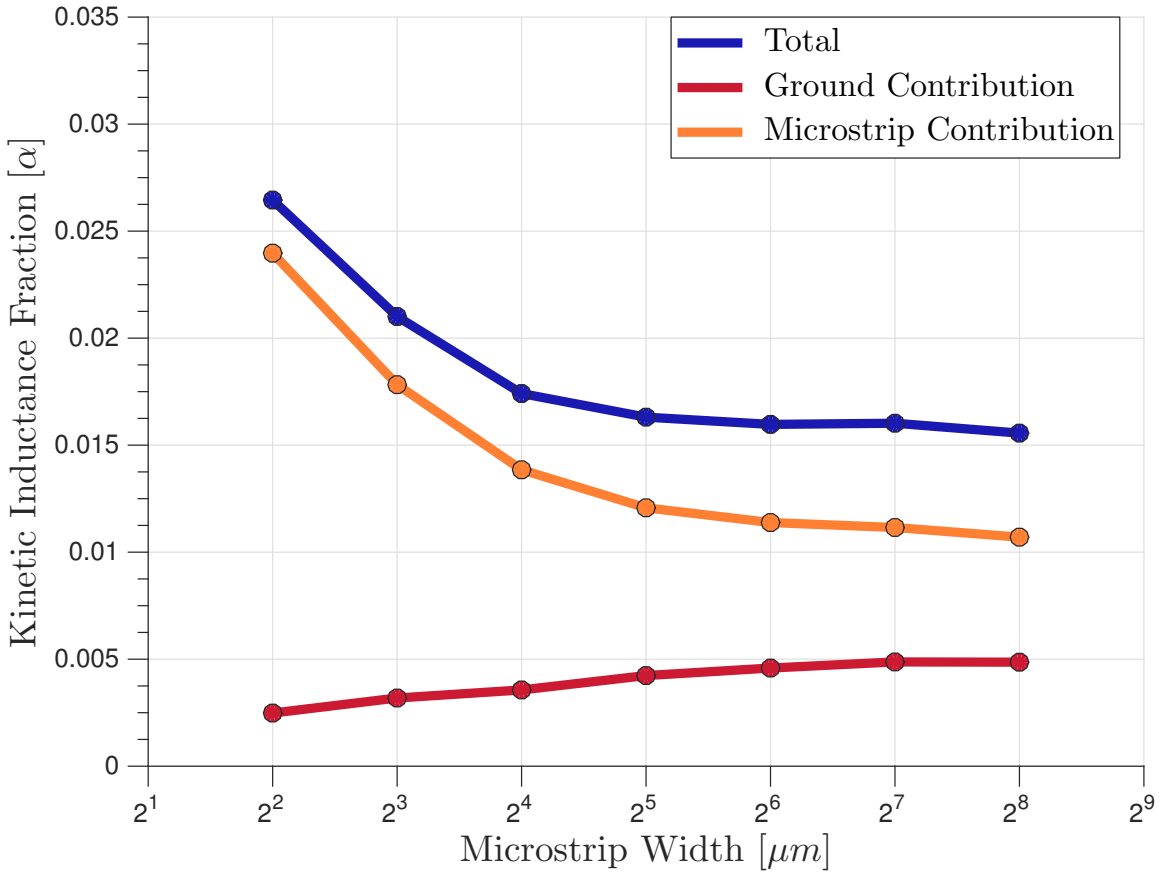


Figure 5.2: We use the procedure described in § 5.3 to calculate the kinetic inductance fractions for the sensor chips on the current test mask, calling out the contributions from the trace and the ground plane. We assume local and dirty electrodynamics; ground plane thickness 300 nm; ground plane penetration depth 39 nm; trace thickness 200 nm; trace penetration depth 16 nm; gap height 3000 nm. These values are also included in Table 5.1.

If we assume the superconductors of the vacuum microstrip are in the local and dirty limit, then this choice of electrodynamics gives a formulation for the surface impedance [98],

$$L_s = \mu_0 \lambda \coth\left(\frac{t}{\lambda}\right), \tag{5.14}$$

where λ is the penetration depth and t is the film thickness. Since, $\coth z = {}^1\!/_z + {}^z\!/_3 - {}^{z^3}\!/_{45} + {}^{2z^5}\!/_{945} - \cdots$, we have $L_s \approx \mu_0\lambda$ when ${}^t\!/_\lambda \gg 1$ and $L_s \approx \mu_0\lambda^2/t$ when ${}^t\!/_\lambda \ll 1$. Thus, the electrodynamics gives us a relationship between λ and L_s, $L_s(\lambda)$.

We can now used the program "Induct" to calculate the geometric factors g_1 and g_2. Induct is the implementation of an algorithm proposed by Chang [38] to calculate the in-

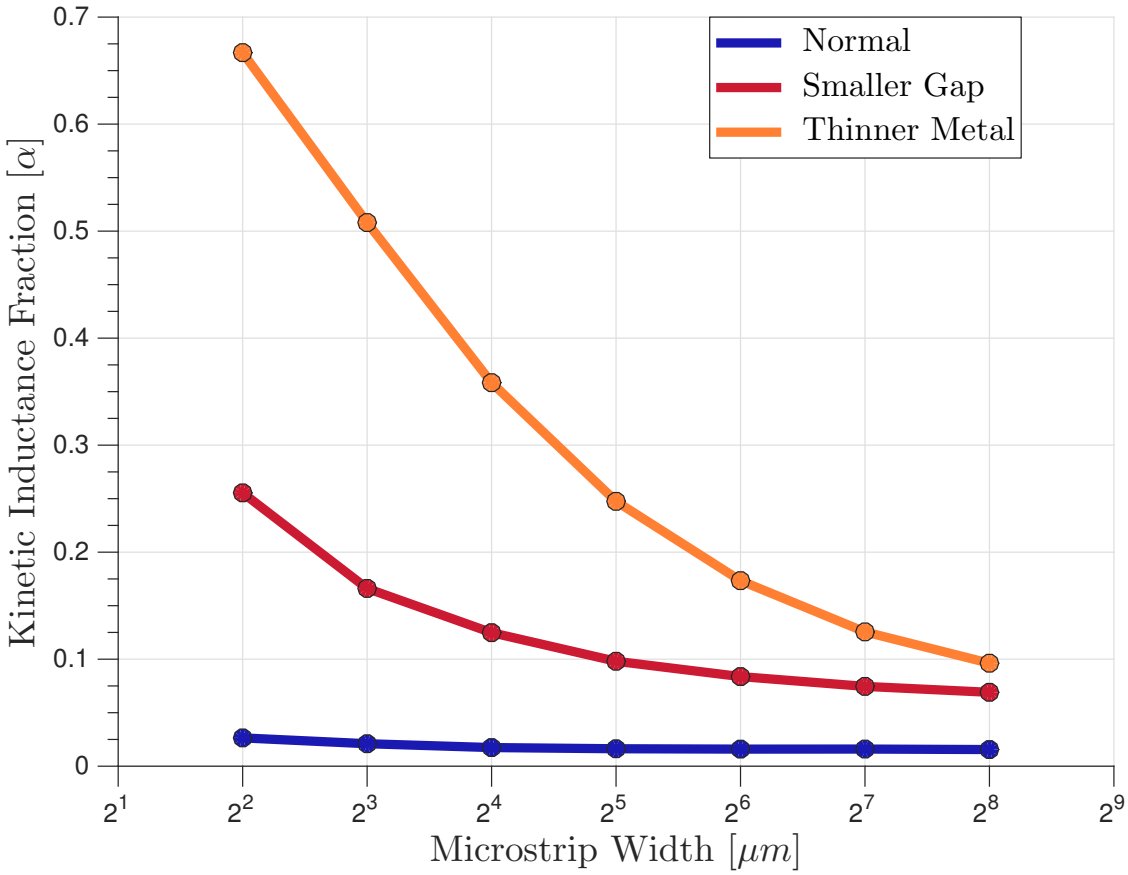


Figure 5.3: We use the procedure described in § 5.3 to calculate the kinetic inductance fractions for the sensor chips on the current test mask under two hypothetical conditions. One – the microstrip gap is held at its true value and the thicknesses of the conductors are reduced by a factor of ten. Two – the microstrip gap is reduced by a factor of ten and the thicknesses of the conductors are held at their true values.

ductance (in henry per meter) of multi-conductor transmission line system. The program takes as input the configuration of conductors in cross section and each of their penetration depths. It subdivides the conductors into cells and assumes a trail current in each and then computes the total kinetic and magnetostatic energy using a Green's function. The energy is varied using Lagrange multipliers to find the minimum, and the inductance is derived from the current distribution that minimizes the energy.

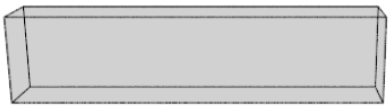
Thus, the program outputs the total inductance, L_{tot}, and takes as an input the conductor geometry and the penetration depths, λ, so the program is equivalent to a numerical function $L_{tot}(\lambda)$. Since we have $L_s(\lambda)$, we can use the program to construct $L_{tot}(L_s)$ and then to extract the geometric factors so we can compute the kinetic inductance fractions. Figure 5.2

plots the kinetic inductance fractions we obtain using this procedure. We also looked at what happens to the total kinetic inductance fraction when the thicknesses of each conductor are decreased by a factor of ten, and when the microstrip gap is decreased by a factor of ten, Figure 5.3.

5.4 KIDs fabrication

5.4.1 Sensor Chip

Sensor chip fabrication procedure



Step 1: The wafer is cleaned. If the material is sapphire, then the wafer is first heated to 85 °C, to prevent shattering, and then piranha cleaned (10 min soak in 120 °C H_2O + H_2SO_4), to remove organics. If the material is silicon, the wafer is piranha cleaned and then HF dipped (30 s soak in 10:1 49%HF) to remove oxide. All wafers are 4 inch diameter.



Step 2: Deposit niobium for resonators. Target thickness is 210 nm. Parameters for DC magnetron sputter process are: $1 \cdot 10^{-8}$–$3 \cdot 10^{-8}$ torr base pressure, deposition rate $2\,\mathrm{nm\,s^{-1}}$, 7 mtorr argon process pressure, $25\,\mathrm{V\,cm^{-1}}$ DC field strength, approximately 25 °C substrate temperature.

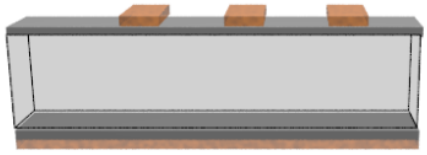


Step 3: Deposit niobium for feedlines. Target thickness is 210 nm. Flip wafer and use the same process parameters and deposition tool as above.

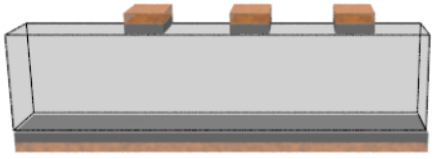
Sensor chip fabrication procedure



Step 4: Apply photoresist to both sides of wafer in preparation for resonator patterning. Spray aerosol MicroChem MicroSpray positive resist on feedline side; to remove bubbles, let sit for 5 min; hard bake for 20 min at 120 °C. This is to protect it wile the wafer is handled in the course of resonator patterning. Vapor deposit HMDS adhesion promoter on the wafer, then spin on 1.2 µm OiR 906-12 i-line resist, no bake. Pre-develop resist to make it less sticky, using half the time of the standard full develop recipe, 20 s.

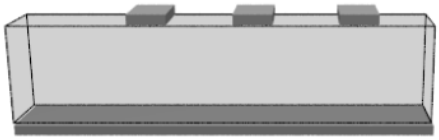


Step 5: Pattern photoresist on resonator side. Use contact aligner to expose resist selecting hard contact mode hard contact during exposure. Promote cross-linking in resist with post exposure bake, 2 min at 120 °C. Execute a 60 s standard i-line develop. Hard bake wafer for 40 min at 120 °C.

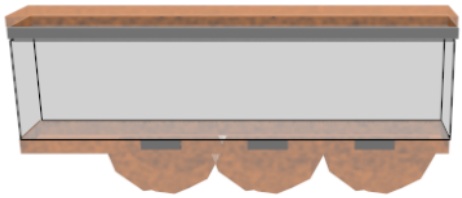


Step 6: Etch resonator pattern into niobium and strip resist. Pump down wafer in reactive ion etching chamber. Perform O_2 plasma descum to remove excess photo resist; process parameters set to 100 sccm O_2, 1 min duration, moderate power. After the descum, introduce O_2 and CF_4 gasses into chamber setting flows rates to 7.1 sccm and 100 sccm (chamber pressure is approximately 150 mtorr), respectively, and etch at moderately high power until spectrometer detects endpoint. Silicon substrates are susceptible to over-etch and pitting due to confusion of niobium and silicon etch signals.

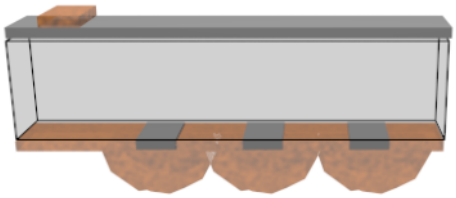
Sensor chip fabrication procedure



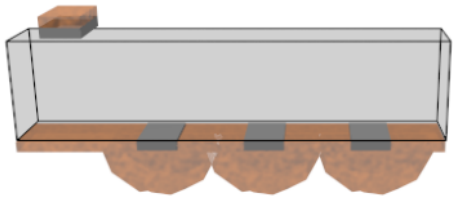
Step 7: Strip hard baked resist from etched wafer with 2–4 h soak in 80 °C PRS-3000.



Step 8: Apply photo resist to both sides of wafer in preparation for feedline patterning. Prime wafer with vapor deposited HMDS. Spin 1.2 µm thick protective layer of i-line resist onto resonator side of wafer; no bake; half time pre-develop. Flip wafer and follow the same procedure to apply resist on the feedline side.

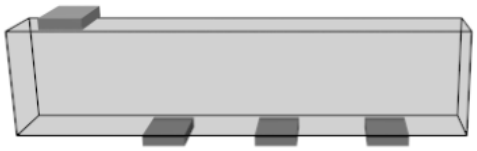


Step 9: Pattern photoresist on feedline side. Use contact aligner and settings as were used for resonator side. Perform a 2 min post exposure bake followed by a standard i-line develop followed by a hard bake. It is best practice to check the mask for resist residue and clean it if needed prior to every use.

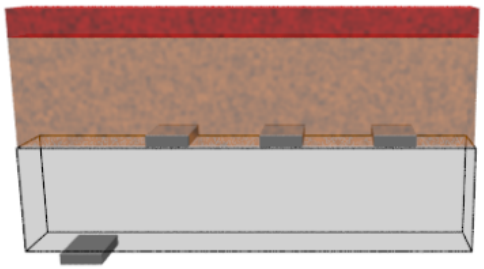


Step 10: Etch feedline pattern into niobium and strip resist. Execute the same etch procedure as was used for the resonators, including the descum.

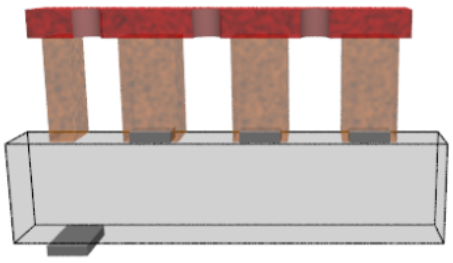
Sensor chip fabrication procedure



Step 11: Strip hard baked resist from etched wafer with 2–4 h soak in 80 °C PRS-3000.

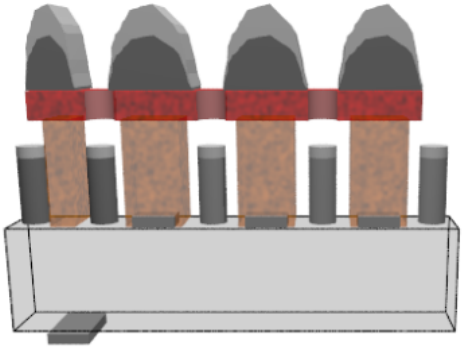


Step 12: Apply photo resist to resonator side of wafer in preparation for pillar patterning. The pillars, which are intended to be 3 µm tall, will be fabricated by a lift off process, so total of 6.5 µm of resist will be deposited into the wafer. The wafer is first primed with vapor deposited HMDS. Spin on 5.3 µm of OCG 825 g-line resist using three separate applications; no baking between them. On top of that, spin on an additional 1.2 µm i-line resist; no bake. Pre-develop with using i-line developer.

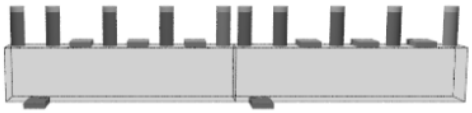


Step 13: Pattern photoresist for pillars. Use contact aligner, but increase exposure time (roughly 2x) to accommodate the thicker resist. Develop the wafers twice using i-line developer, 60 s each. Since the i-line developer attacks even unexposed g-line resist, the pattered i-line resist is significantly undercut. Do not hard bake resist. The i-line over hand will prevent coverage of the resist sidewall with aluminum when the pillars are deposited. Descum wafer O_2 plasma; low power, 7.1 sccm.

Sensor chip fabrication procedure



Step 14: Deposit material for pillars. Use electron beam evaporator to deposit approximately 2.9 µm of aluminum, and then approximately 0.1 µm of Al_2O_3, starting from a base pressure of less than $2 \cdot 10^{-6}$ torr. To prevent the photo resist from burning, deposit the aluminum at a rate of 30–38 Å s^{-1} and deposit the Al_2O_3 at a rate of 5–8 Å s^{-1} using a beam sweep to prevent burning through the crucible. The Al_2O_3 is intended as a barrier to prevent quasi-particles and phonons from absorber from entering the sensor chip. Note that aluminum forms a nasty intermetallic with carbon, so graphite crucibles should be avoided or used for no more than 2 melts.



Step 15: Strip resist and dice wafer. Soak wafers for 2–3 d in 80 °C SVC-14, a gentle stripper that does not attack aluminum. If photoresist residue remains, soak wafers in PRS-3000 for several hours. This will attack the aluminum pillars, but the damage done by a several hour soak will not degrade their functionality. The resonators are then inspected under the microscope to confirm their quality. The height of the pillars is sampled in six places across the wafers with a profilometer. A final coat of HMDS plus 1–3 µm of i-line or g-line resist is applied to protect the die from abrasive silicon particles created during dicing. Position the wafer on dicing tape. Dice the wafer using a rotary dicing saw. While the silicon wafers are easily diced using a diamond blade, dicing the sapphire wafers requires a resin blade, high blade speed (40 000 rpm) and slow feed (0.3 mm s^{-1}). Cut the die 18 mm × 18 mm square

Table 5.3: Illustrated [2] step-by-step description of KIDs sensor chip fabrication process.

Sensor chips are fabricated on C and R plane sapphire and <100> silicon wafers.

ID	Material	Orientation	Wafer Thickness [µm]	Production Method	Trace Thickness [nm]
FHN1	Sapphire	R plane	435–485	Kyropoulos	202
FHN2	Sapphire	C plane	492–513	EFG	196
FSN3[a]	Silicon	<100>	520–530	Float Zone	281

[a] This wafer is ≥10 000 Ω cm, P-type, boron doped.

Table 5.4: Summary of probe wafer characteristics. The niobium trace metallization thickness is as measured by profilometer at one point in the center of the wafer. Metallization thickness for this deposition to typically falls off from the center to 5% to 8% of the center thickness at the edge.

5.4.2 Ground plane chip

Fabrication of the ground planes proceeds as follows.

Step 1: Clean wafer substrate. 4 inch silicon ground plane wafers are cleaned in piranha and then dipped in HF to remove surface oxides. 4 inch germanium ground plane wafers are only cleaned in HF because piranha etches germanium.

Step 2: Deposit ground plane metal. This is done in a DC sputtering system with a base pressure of less than $7 \cdot 10^{-8}$ torr, 275–315 V cm^{-1} DC field strength, 5–8 mtorr process pressure. "Aluminum" ground planes are actually 98% aluminum and 2% silicon by weight, because the aluminum target used in the sputterer has been presaturated with silicon to prevent interdiffusion of the two in junction fabrication processes.

Step 3: *(optional)* Etch pattern into ground plane metal.

Step i: Apply photoresist vapor deposit HMDS adhesion promoter. Spin on 1.2 µm thick layer of i-line resist resist; no bake and pre-develop.

Step ii: Pattern resist. Use contact aligner set to make hard contact. Perform a 2 min post exposure bake followed by a standard i-line develop; no hard bake. Note that TMAH in the developer attacks aluminum, but this is not an issue since the aluminum exposed by the developer will be etched away in the next step.

Step iii: Etch ground plane metallization. The wafers are etched for 35–45 s in liquid etch containing H_3PO_4 as the active ingredient heated to 40–50 °C. The wafers are dunked in several deionized water baths to thoroughly halt the etch.

Step iv: Strip photoresist. The wafers are soaked for 45–60 min in 80 °C bath of SVC-14 and then in room temperature acetone for 2 min.

Step 4: Apply protective layer of photoresist for dicing. Vapor deposit HMDS adhesion promoter and then spin on 1–3 µm of i-line or g-line resist.

Step 5: Dice wafers. Use the dicing saw and a diamond blade for silicon and germanium ground plane substrates. Cut them 21 mm × 21 mm square.

The actual thickness of the metallization is measured by a scanning electron microscope. One chip from each wafer is mounted with its edge perpendicular to the focal plane of the microscope and several thickness measurements are taken from points along the edge, and averaged. The metal thickness across the wafer is expected to be uniform because the sputter system target (about 12 inch square) is much larger than the wafer and during deposition the wafer is moved on a conveyor across the target, about 0.5 inch below it.

ID	Thickness [nm]	Substrate	Run
DSAT3	348	Si Test Wafer[b]	44b, 48b
DSAT4	309	Si Test Wafer	45a, 49a
DSAT5	309	Si Test Wafer	46a, 47a, 48a
DSAT7	85	Si Test Wafer	44a, 45b
GSAT1	306	Si Test Wafer	51a, 51b, 52b
HSA2[a]	265	Si Prime Wafer[c]	52a

[a] The ground planes on this wafer are patterned with a hexagonal mesh.
[b] Silicon test wafers have low resistivity (1–50 Ω cm) and loose geometrical tolerances.
[c] This prime wafer is float zone silicon, ≥10 000 Ω cm, P-type, boron doped.

Table 5.5: Summary of ground plane wafer characteristics. The metallization thickness is as measured by scanning electron microscope. The runs in which a ground plane from each wafer was used are indicated. Ground plane chips are fabricated on <100> silicon.

Although the target ground plane metallization thickness was 200 nm, we see in Table 5.5, that thicknesses are closer to 300 nm in most cases. This is due to process drift. Use of the 85 nm tick ground plane was a mistake, but taking the thickness into account, the data is still meaningful.

5.4.2.1 Hexagonal mesh ground plane

Ground planes made of a hexagonal mesh of aluminum, Figure 5.4, were also studied and fabricated. These ground planes are interesting for several reasons. One, in the vacuum microstrip phonon sensor we envision, the reduced metal surface area that is obtained by slotting in the ground plane would increase the quasiparticle density due to an event occurring in the absorber wafer. Second, slotting the ground plane could be used to suppress any vortex formation that may occur there. The result would be higher internal quality factors. Third, slotting the ground plane can be used to change the metal surface area to volume ratio of the ground plane, and this can be used to increase the kinetic inductance fraction, α. Fourth, the geometry of the mesh can be used to tune the impedance and resonant frequency of the microstrip resonator.

Determination of the electrodynamic properties of metal mesh surfaces is an active area of research and formulae exist for the impedance and effective dielectric constants of some mesh patterns [177, 115, 116][3]. Metal mesh surfaces are type of high impedance surface and applications for their use range from, absorbers to phase shifters to frequency selective surfaces.

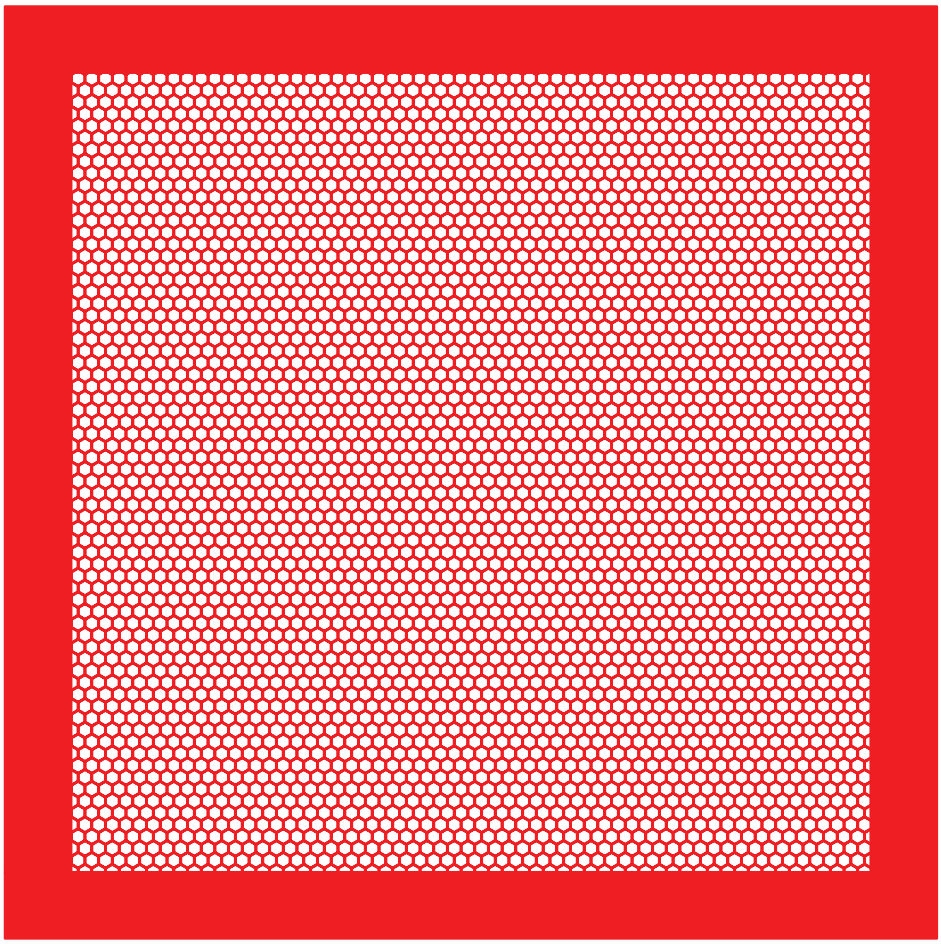


Figure 5.4: Lithography mask pattern for a hexagonal mesh ground plane fabricated in a vacuum microstrip KID. The red part is metal. The hexagon voids in this particular ground plane are 292 µm inscribed diameter; the metal mesh is 16 µm wide; and the metal area fraction is 5%.

Several different hexagonal mesh ground plan designs were fabricated, employing different

[3]This paper, and the book, present formulae for square grids. When asked about hexagonal grids, Tretyakov remarks *I recall there was a solution for rhomboidal grids, but do not remember seeing hexagonal. However, since the hexagonal mesh with small cells is pretty isotropic, I do not expect much difference with the square cells. Inductance per unit cell will be a bit larger, simply due to longer strips, and the effect will be very minor, I think.*

hexagon sizes and different metal to void are fractions, which covered the range 5–28 %. These ground planes are used with resonators whose width is at least the size of the diameter of the circle inscribed in the hexagonal void. A KIDs device using one of these ground planes is found to have resonant frequency substantially lower than it would have with a solid ground plane suggesting these ground planes are highly inductive. A potential remedy for this is to make a mesh of the microstrip trace too, in order to decrease capacitance and increase resonant frequency. Do so would suppress any vortex formation in the trace, as well. Perhaps slotting the trace and the ground plane could be done to the point where the microstrip is a frequency selective structure for phonon detection applications.

5.4.2.2 Ground plane porosity

The metal thickness of the ground planes was measured by dicing them into shape and then inspecting the cut face with a scanning electron microscope. In the course of this measurement, it was noticed that the most of the ground planes appear to be porous, Figure 5.5. The degree of porosity, as measured by pore size and density, varies across the ground planes. The cause of the porosity is unknown. One possible explanation is that it is due to corrosion. The oldest cut faces are about five years old, and the youngest are about one year old. Maybe during this time, exposure to air moister have caused a chemical reaction. To test this idea, a fresh cut was made in one of the ground planes its face was inspected in the scanning electron microscope two days later. Pores were observed in the fresh cut sample. Maybe the pores are due to particles embedding in the soft aluminum during sawing. A cleaved sample was prepared at the same time as the fresh cut sample and pores are somewhat visible in it[4]. Another possible explanation for the pores is Kirkendal voiding, due to greatly different diffusion rates of the two materials in to each other. The problem with this explanation is that the films were not exposed to the high temperatures that would be expected for this significant level of uniform voiding. Impurities, like chlorine, however can accelerate the process. It is also possible that the pores are not really there and what we are seeing is intensity variations due to an nonuniform surface.

It must be noted that although the ground planes were dices sometimes years in advance of their use, they were stored during this time with a thick layer of photoresist protecting their surface. It is not expected that the photoresist reacts with aluminum, and it should be a non-permeable interface to air and moisture. The photoresist is dissolved minutes before the device is mounted in the test box.

[4]Cleaves of aluminum layers are tricky because the aluminum bend around the cleave face and would compress the pores. Despite performing the cleave in liquid nitrogen there was still a bend. Pores were not clearly seen.

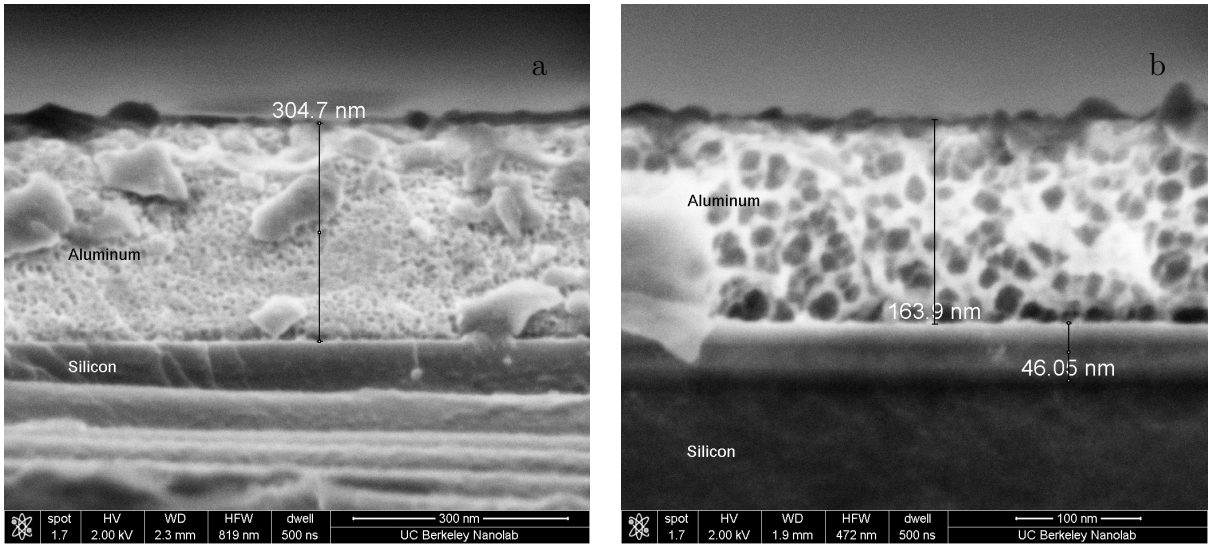
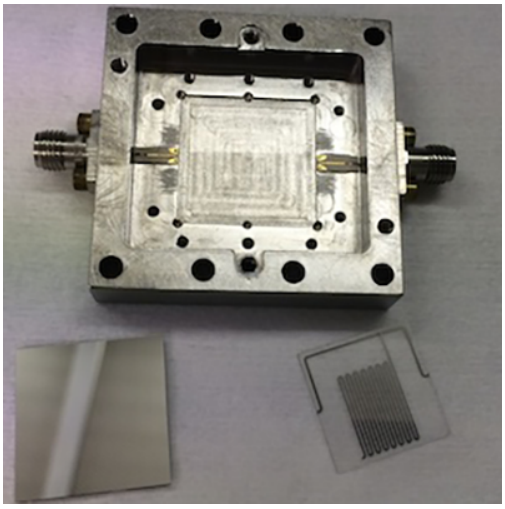


Figure 5.5: Scanning electron microscope views the saw cut surface of aluminum on silicon wafer ground planes. (a) – ground plane DSAT5. (b) – ground plane DSAT6, not used in the KIDs data presented. One notices a 46 nm interface layer perhaps suggesting diffusion processes contribute to the pores.

5.5 Assembly of device in test box

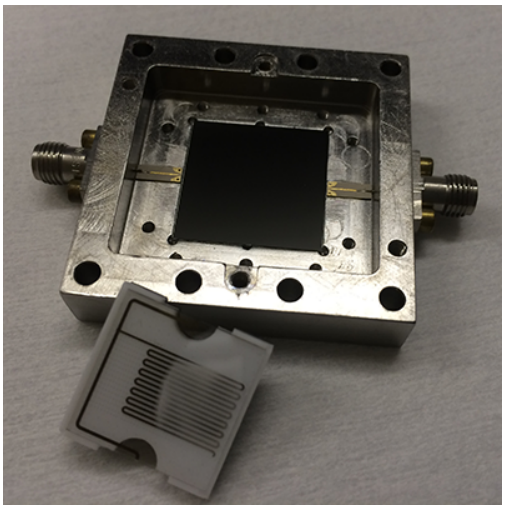
The test boxes used in the course of this research are made of copper, niobium, or Nb-55Ti. Drawings of these boxes are included in § D.3. The different materials are chosen to obtain different test conditions, e.g. excellent device heat sinking (copper) or excellent magnetic shielding (Nb-55Ti). Niobium is usually used to provide a compromise between the two extremes. The boxes have SMA connectors on their exterior for connection coaxial readout cables, although recently a switch from SMA to SMP was made. The SMP connectors have the advantage of blind-mate engagement (no screwing), more compact size (though ultra-miniature versions of the SMPs exist), and availability is brass or beryllium copper conductor materials because the steel used in the SMAs can become magnetic at low temperatures. The coaxial transmission line format of the exterior exterior connectors is then transitioned to a microstrip transmission line format on the interior of the box using a small circuit board. This board, designed by John Ward [185], is made of 6010 Rogers Duriod Microwave Laminate and is glued to interior of the test box using silver epoxy. The center pin of the SMA exterior connector is soldered to the microstrip trace on one end of the board; on the other end the transmission line format is again transitioned, this time to a coplanar waveguide (CPW) format, which makes the ground and the trace easily accessible from the top, for wire bonding.

KIDs device mounting procedure

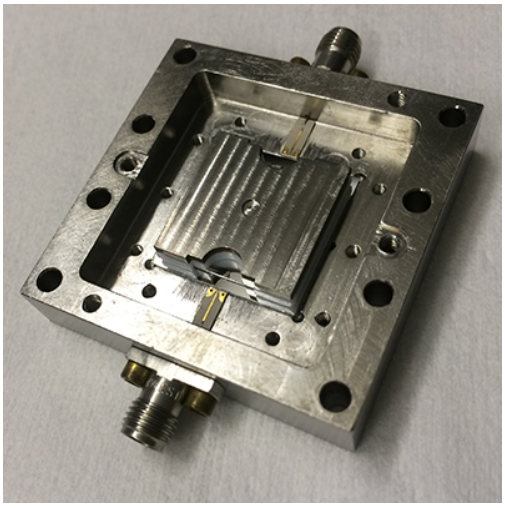


Step 1: Clean probe and ground plane chips. The first time the chips are used they must be extracted from their position on the diced wafer and the protective layer of photo resist, applied before dicing, must be removed. The chips should also be cleaned before subsequent uses to ensure removal of any dust or debris. Sonicate chips, one at a time, first in acetone, then in isopropyl, then methanol, then in deionized water. Make sure the liquid does not dry on the chip between each dip, this will deposit contaminants which cannot be removed. Do not allow chips to sonicate for more than 45 s in any liquid, particles which collect in the liquids will scratch aluminum films. Upon removal form the deionized water, immediately blow dry chips.

KIDs device mounting procedure

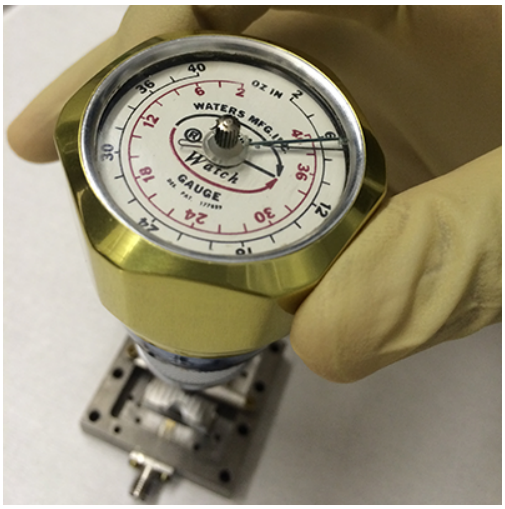


Step 2: Position ground plane in test box and probe chip in teflon backing. Handle chips with plastic tweezers to avoid scratching and plastic gloves. It is best to handle this chips in a cleanroom environment to prevent particles from landing on the films before they are mated. Notice the Duriod transiton pads in clear view; the microstrip ground of the pads is brought to the top in a transition from microstrip to CPW transmission line format, which occurs very close to the KIDs ground plane.

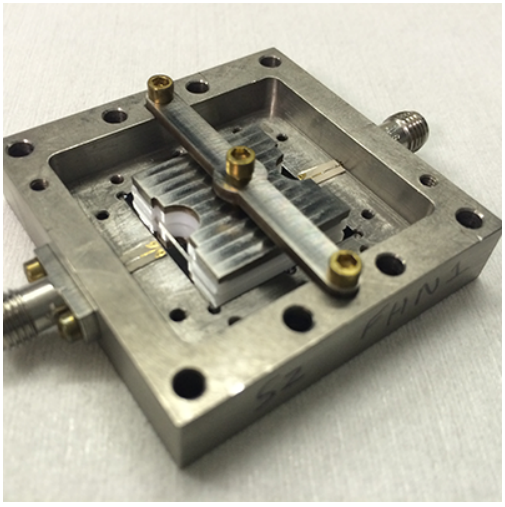


Step 3: Mate probe chip to ground plane chip. First mate rigid backing plate to dielectric backing plate, which is made of teflon. Then mate the probe chip with backing stack to the ground plane chip, centering the former on the ground plane. The rigid backing plate, made of either Ti-6Al-4V or alumina, will distribute mating force applied in the next step by a screw uniformly over the probe chip.

KIDs device mounting procedure



Step 4: Apply mating force to ground plane, probe chip, backing plate stack – now called the device. Attach cross bar to test box with screws. It will locate so that a central screw is aligned over a pocket in the rigid backing plate. Apply 8 inch oz of torque to this screw using a torque guage. Do not allow the stack rotate as it is torqued.



Step 5: Make wirebond connections between transition pad and device. On each of the two exposed sides of the device, make several wirebonds between the feeding and the transition pad trace. Next make numerous wirebonds (at least 10) between the text box metal, which is electrical ground, and the ground plane chip.

KIDs device mounting procedure	
	**Step 6:** Close the test box and perform electrical continuity measurements. The test box has coaxial connectors on both sides, which are either SMP or SMA connectors. At this point, either side can be regarded as the input or output; signal propagation direction will be chosen when the box is in install in the readout circuit. Measure DC resistance from the center pic of one connector to the center pin of the other connector. Measure feedline conductance to ground (e.g. center pin to ground). Then measure RF transmission across the box.

Table 5.6: A pictorial step-by-step description of the procedure used for mounting a KIDs device into a text box.

Figure 5.6 diagrams the layers of material that constitute the device in the press. Note that the dielectric backing prevents the microstrip on the top side of the probe wafer (the feed line) from being shorted by the rigid backing plate, which may be metallic. It also prevents the plate from disrupting the impedance of this microstrip by putting some distance between the microstrip and the plate. The effect on impedances that the presence of the dielectric and rigid backing plates have are taken in to account in the design of the probe chips.

5.6 Connection of test box to readout system

It was necessary to design the KIDs readout system so that KIDs and CDMS detectors could be measured in the same fridge cycle, though not necessarily at the same time. The 75 µW helium dilution fridge we use is customized to accept a SuperCDMS Soudan tower, which is the apparatus that supports the CDMS detectors and their associated cold electronics and provides heat sinking for the signal wires that run between them. Adaptor hardware was designed and fabricated to allow attachment of the KIDs test boxes to the tower, and to exploit the heating sinking facilities of the tower for coaxes and the primary low noise amplifier (LNA) used to read out the KIDs. Using the adaptor hardware, up to two KID devices can be installed on the tower at a time.

Coaxial cabling was installed in the fridge to provide two channels of connectivity between an external connector flange at 290 K and a 4.2 K liquid helium (LH) flange accessible within the experimental space. These ∅ 0.085 inch coaxes are have a stainless steel 304 outer jacket

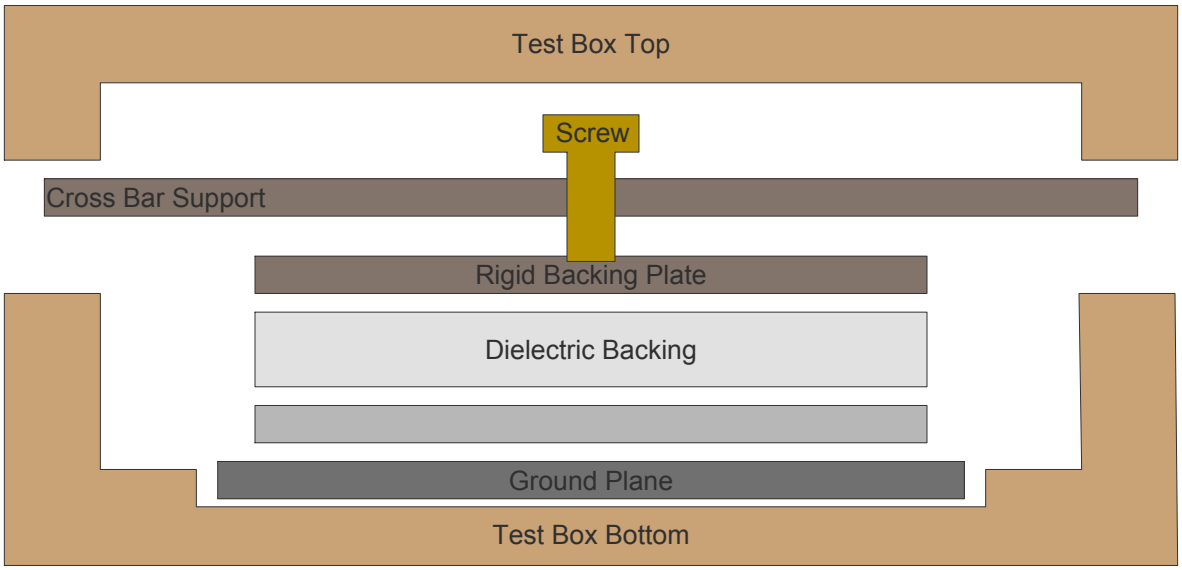
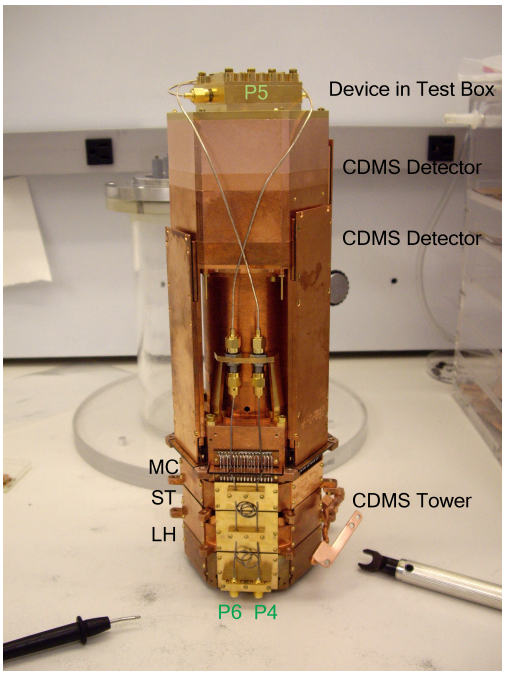


Figure 5.6: Exploded block diagram of device in screw press. The view is in cross section. The box top and bottom are either made of niobium, niobium titanium, or copper. The dielectric backing is made of teflon and is 1524 µm thick. The screw is usually brass, but could also be aluminum or Ti 6Al-4V. The rigid backing plate and cross bar support are made of Ti 6Al-4V. A rigid backing plate made of machined alumina is sometimes used as well. Although not shown, the cross bar support is screwed to the box bottom. Ti 6Al-4V becomes superconducting at 4.38 K [154]. The sensor chip is 500 µm thick

and a beryllium copper central conductor. These materials are chosen to make it relatively low thermal conductivity, as the cabling is one straight shot and heat sunk only at 290 K connectors and the 4.2 K connectors.

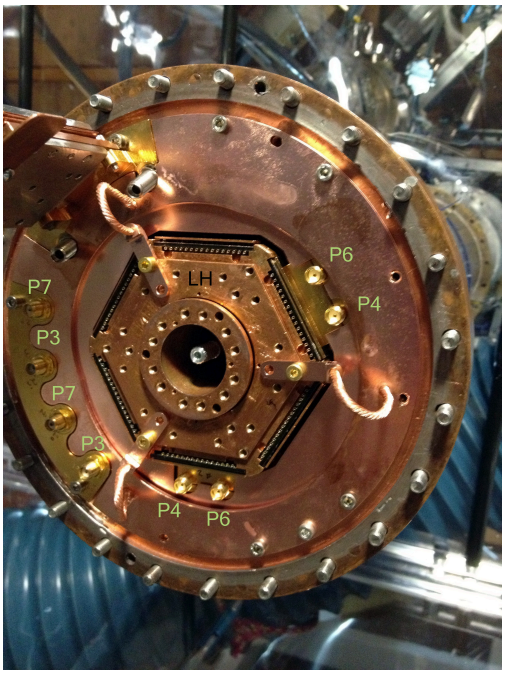
Connection of the test box to the part of the readout system that is within the cryostat is summarized in Table 5.7.

Installation of test box into KIDs readout system

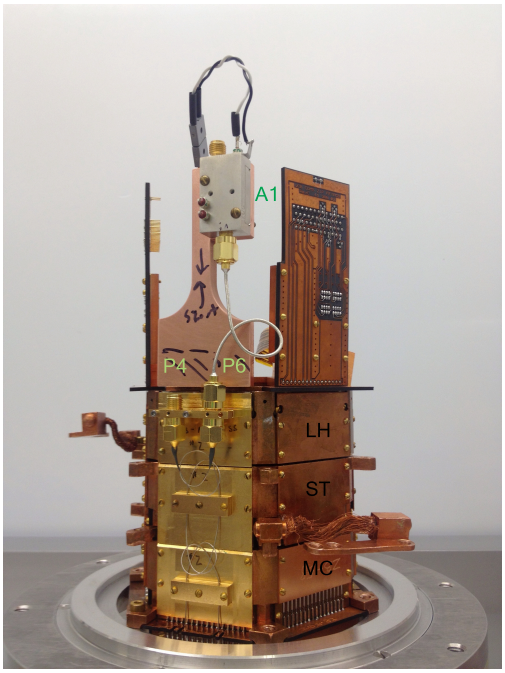


- Each hexagonal face of the CDMS tower provides signaling wires for a single CDMS detector. These faces normally have a copper face cover. The KIDs readout coaxes are clamped into modified face covers and clamping effectively heat sinks the coaxes to the temperature stage of the face. The coaxes that run down the tower are ∅ 330 µm, Nb-Ti outer and Stainless 304 inner conductor, from a Japanese company named Coax Co., LTD. They have exceptionally low thermal conductivity [103]. With the coaxes clamped to the tower faces, the CDMS detectors are stacked into place. The KID test box is bolted to the end of the CDMS detector stack with a modified detector end cap. Connection between the test box and the tower is typycally provided by ∅ 0.05 inch conformable (silver plater copper clad steel inner conductor, braided copper tin composite outer conductor), or beryllium copper (inner and outer) coaxes.

Installation of test box into KIDs readout system



• Transmission through the coaxes and device is then measured with the network analyzer as a final test of continuity before fridge installation. The tower is then installed into the fridge where numerous torqued bolted connections how it in place and ensure thorough heat sinking. The liquid helium (LH) level of the tower is exposed providing SMA interconnects for the KIDs signal path. Both the SMA connectors on the fridge flange (P3 & P7) and those on the tower (P4 & P6) are heat sunk to liquid helium.



• Connections are then made between the tower and the fridge flange. The photo shows how the primary LNA is installed, but the tower is not in place inside the fridge. The primary LNA, which dissipates 23 mW, a 40 dB attenuator, which heat sinks the center pin of the coax, and a DC block (inner & outer conductors blocked) which also helps to block heat flowing down the fridge coaxes are installed. See Figure 5.7 (*a*) for a schematic. The heat sinking on both sides of these devices facilitates removal of all this heat.

Table 5.7: The installation of the KIDS device test box into the KIDs readout system is described in words and in pictures.

Once the tower is installing in the fridge and all the KIDs readout connections have been made, the primary and secondary amplifiers are turned on and transmission is measured with a network analyzer. This is continuity check before sealing the fridge and cooling down.

A major disadvantage of integrating the KIDs readout hardware with the CDMS tower infrastructure is that it forces the KIDs readout to be modular. This means many different interchangeable components must be connected together for the test and disconnected afterwards. This situation exposes devices in the readout circuit to the possibility of damage from handling which may go unnoticed and negatively affect data. The large number of connections also increases the likelihood that at least one in the chain is weak, and has degraded transmission. This introduces an uncertainty in the power levels along the readout circuit (particularly at the resonator) which also negatively affects data. These vulnerabilities had to be tolerated since there is no alternative to tower infrastructure integration. Of course, the room temperature continuity checks are good means of detecting failures while components can still be accessed.

5.7 Readout system

The KIDs readout circuit is diagramed in Figure 5.7. It is a simple homodyne system where a copy of the local oscillator (LO) is provided to the receiver for the purpose of down conversion to a frequency within the base band which can be digitized. Three different readout configurations are used to take data. The portion of the circuit that remains unchanged in reach of these configurations, the "device end", is diagramed in Figure 5.7 (*a*). The three possibilities for the variable portion of the circuit, the "digitizer end", are diagrammed in Figure 5.7 (*b*), (*c*) and (*d*).

For each configuration, fridge temperature control and readout is done by separate system. The software the controls readout configurations (*c*) and (*d*) can also control the temperature.

5.7.1 "Device End" portion of readout system

We point out a few characteristics of this portion of the readout system.

Cabling The low temperature and fridge cabling was discussed in § 5.6. At room temperature low loss ⌀ 0.310 inch flexible coaxial cabling provides connectivity between the fridge and points P1 and P9. Care is taken to use matching cabling on the input (P1 to P5) and output (P5 to P9) sides of the device. This facilitates determination of the power at the device because one can then assume that the total insertion loss due to cabling on each side of the device is the same. Thus, one performs a calibration run where the device is replaced by a through and no amplifiers, attenuators or DC blocks are included in the circuit. One measures the insertion loss from P1 to P9, and divides this number (in dB) by two to get the loss from P1 to P5. The insertion loss over other segments of the cabling (e.g. P2 to P3 and P3 to P5) can be determined in a similar

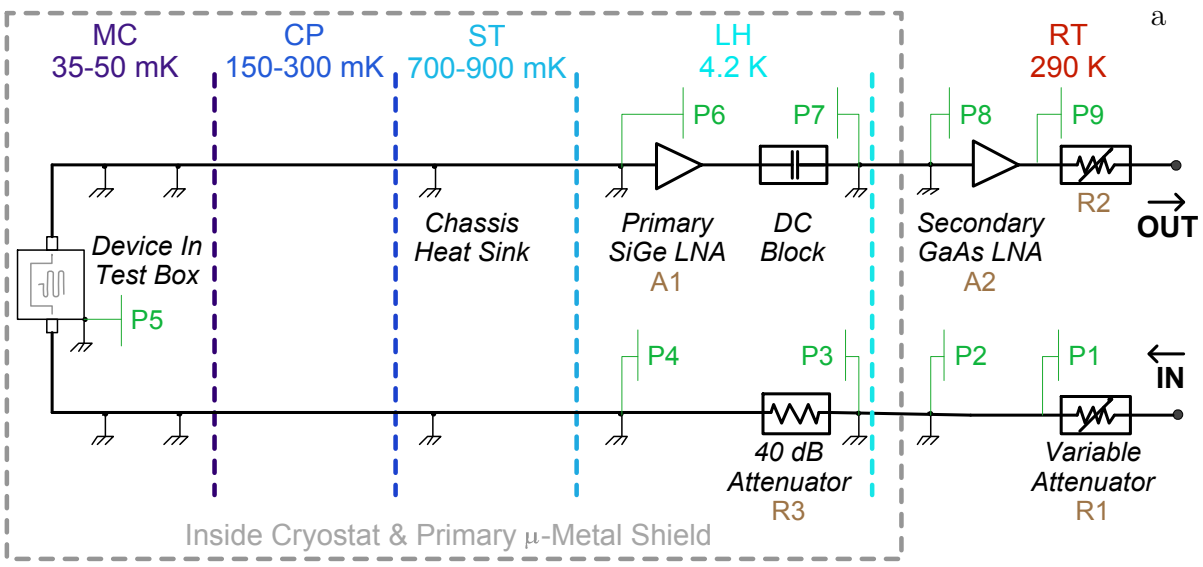


Figure 5.7: KIDs readout system configurations used to measure data. *a* – The "device end" portion of the readout system that does not change. The cryostat is a customized Oxford 75 µW helium dilution fridge. The μ-metal shield is a cylinder with one end open and one end caped and it is on the exterior of the cryostat. Chassis ground symbol denote heat sinking of the coax (ad test box) shell to the fridge chassis. Points of interest, P1 through P9 are discussed elsewhere.

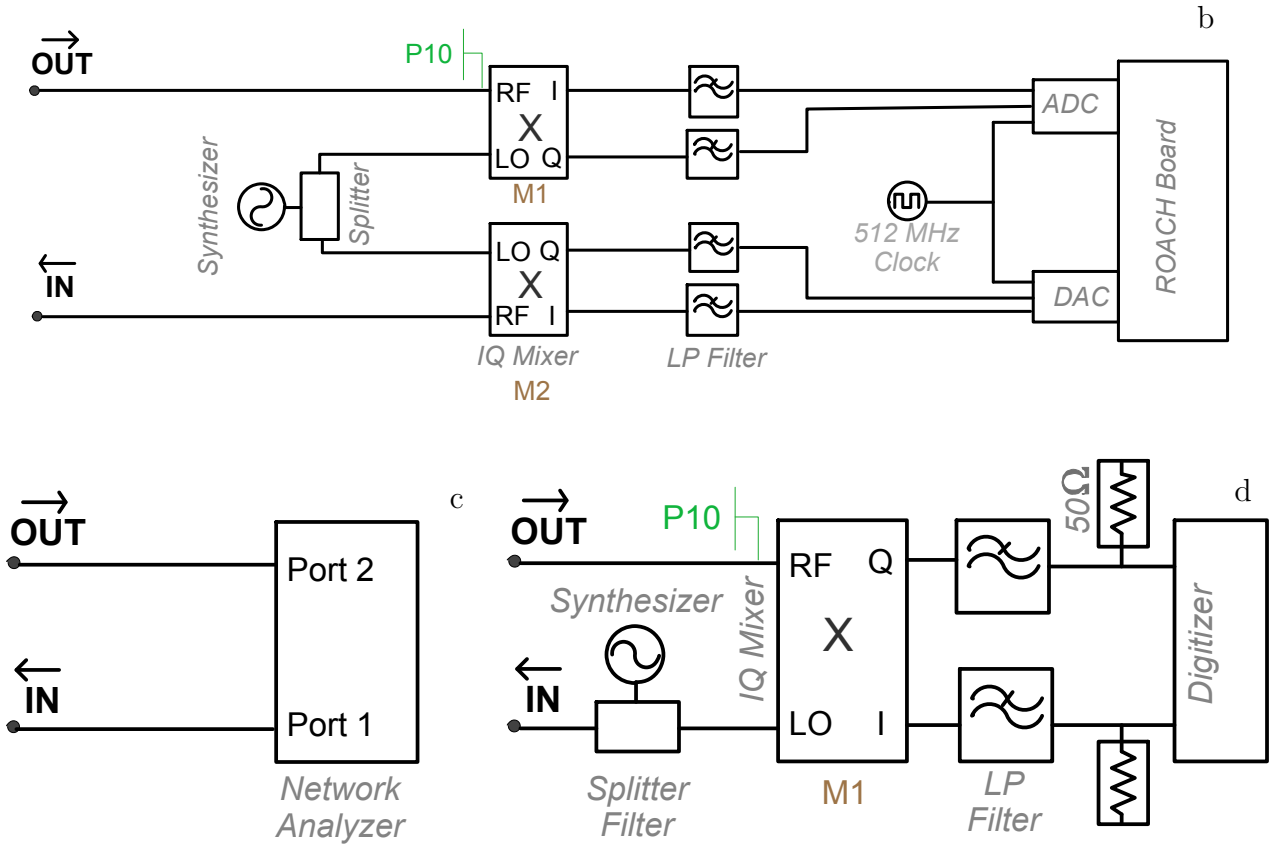


Figure 5.7: KIDs readout system configurations used to measure data. The three "digitizer end" configurations of the system are diagrammed. *b* – Readout system based around the ROACH reconfigurable computing platform [155]. This is a work in progress and used infrequently. *c* – Readout system based based around an Agilent vector network analyzer. This configuration is used to perform temperature and power sweeps. *d* – Readout system based around a National Instruments 6120 digitizer. This configuration is mainly used to measure noise. Also splitters, filters and mixers are passive components. The $\overleftarrow{\mathbf{IN}}$ and $\overrightarrow{\mathbf{OUT}}$ ports of *a* and connected to the $\overleftarrow{\mathbf{IN}}$ and $\overrightarrow{\mathbf{OUT}}$ ports of *b*, *c*, and *d* to utilize any of those configurations. (continued from page 121)

fashion, but joining other symmetric sections of the circuit by throughs, as suggested in Figure 5.8. The losses of the such cabling segments is needed to rigorous calculation of noise, where knowledge of the temperature is the cabling is needed. Of course it would be most accurate to determine these losses by direction measurements, but this would require additional setup signal detection instruments which operate at cryogenic temperatures. As a final note, the physical cable lengths are as follows: P1 - P2 is 324 inch, P2 - P3 is 90 inch, P3 - P4 is 10 inch, and P5 - P5 is 14–22 inch.

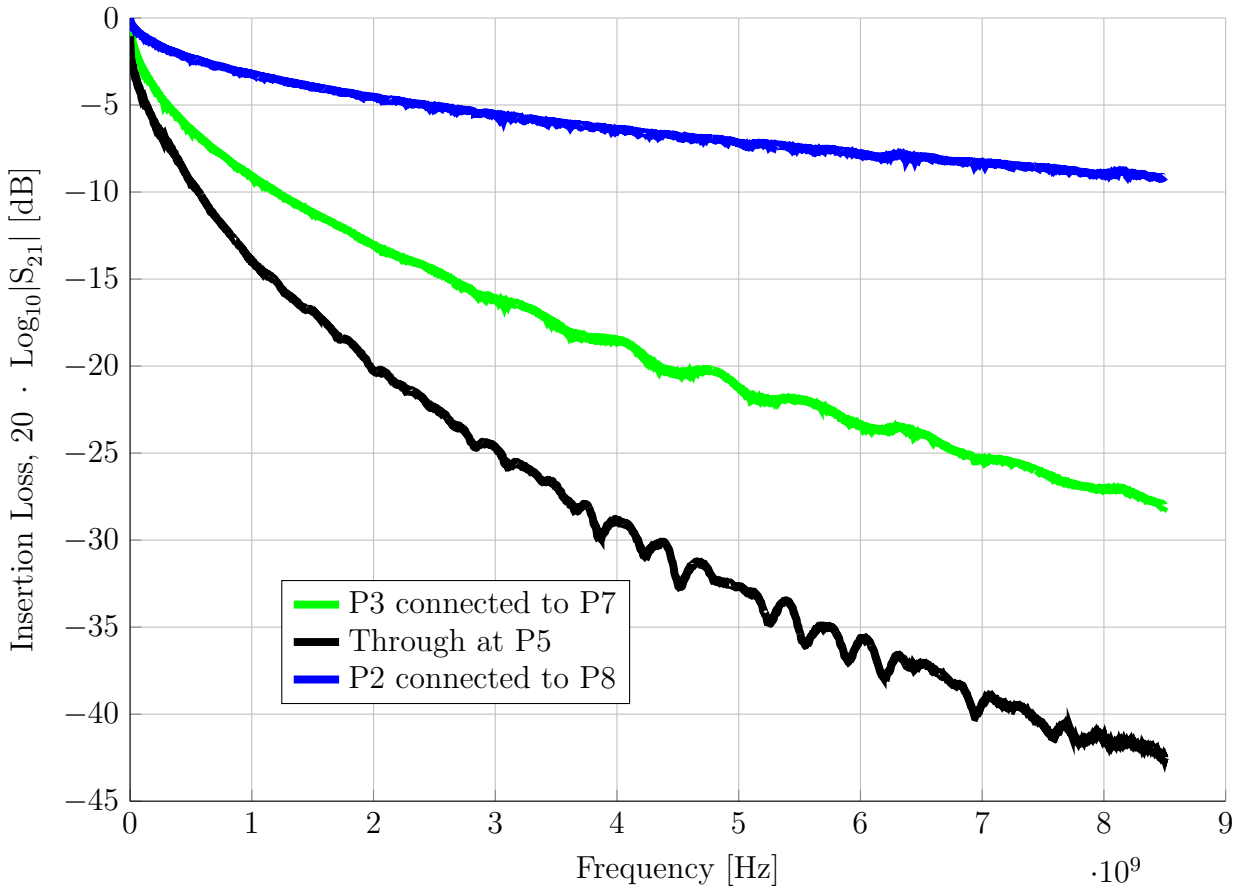


Figure 5.8: Measured round trip insertion loss of three portions of the readout system cabling. P2, P3, P5, P7, P8 are indicated on Figure 5.7 (*a*). Assuming that the cabling is symmetric in its loss characteristic on the inbound and outbound routes to the fridge, one way losses can be determined by halving the measured quantities. The losses of cabling segments can be determined by subtraction of the measured quantities. The fridge was at base temperature for the measurement of curves "P3 connected to P7" and "Through at P5".

Amplifiers The primary LNA (A1) was obtained from Sander Weinreb [188, available at 3] and the secondary (A2) was obtained from a company named Microsemi.

The primary LNA is operated at 4.2 K to obtain lowest noise an highest gain. In the frequency range 0.7–1.0 GHz, it provides 45 dB gain, has a nose temperature of 6 K and has an input -1 dB compression power of −48 dBm. Typical values for the small multiplicative noise (gain fluctuation) component of these amplifiers is presented in [189]. It is a two stage SiGe transistor design.

In the same frequency range, the secondary amplifier from Microsemi provides about 38 dB gain, has a nominal phase noise of −140 dBc/Hz at 1 kHz offset, an amplitude noise temperature of 420–390 K, and has an input -1 dB compression power of −11 dBm. It is a three stage GaAs amplifier.

Cold Attenuator The cold 40 dB attenuator (R3) thoroughly heat sinks the inner conductor of the coax, and significantly attenuates noise, in addition to the signal, from the frequency source and other warm components. The heat sinking aspect comes from the resistive connection between the coaxial outer conductor and the inner conductors, which is thermally conductive. Care must be taken in the selection of a cold attenuator. Many attenuators use resistive material that goes superconducting around 1 K.

DC Block The DC block passes frequencies above 10 MHz. Thus it rejects noise and power at low frequency, such as 60 Hz. It is a challenge to heat sink the coax on the output side of the primary amplifier without losing gain, i.e. using an attenuator. The DC block provides a compromised solution. Instead of heat sinking, the block acts as a thermal impedance since it interrupts the metal path on both the inner and outer conductors of the coaxial cable.

Magnetic Shield Our 75 µW fridge has an external magnetic shield that resides a room temperature. With this shield in place, the residual DC magnetic field due to the earth at the position of the test device is estimated to be approximately $1.6 \cdot 10^{-3}$ G. This number was obtained from room measurements using a 3-axis fluxgate magnetometer.

Vacuum Passthrough The adaptor that connects coaxial cabling from the laboratory environment to the vacuum environment of the fridge uses a pin suspended in a cylindrical glass bead to pass the center pin signal from one side to the other. The cylindrical outer surface of the bead is gold plated and soldered to a flange. SMA connectors mate on both sides to the pin and are used for cable connections. The flange carrying the passthrough is attached to the fridge using an o-ring seal. This passthrough is reliable and easy to make. Fabrication instructions as well as dimensions can be found in § D.5.

5.7.2 "Digitizer End" ROACH board configuration

We have implemented a two channel KIDs readout system using an field programmable gate array (FPGA) based reconfigurable computing platform called the ROACH [155]. Greater that two channels was not necessary because our KIDs sensor chips only have one resonator on them. The system, diagramed in Figure 5.7 (*d*), has a 16 bit 500 MHz DAC for generating the probe tones. The DAC produces IQ signals that modulate an LO signal provided by a synthesizer. It has a 12 bit ADC with a fixed input range of ±1.1 V. Its control software is capable of measuring noise and performing IQ frequency sweeps. The software is still buggy

and under development. Unfortunately, the fixed input range of the digitizer and its modest 12 bit depth limits the system's usefulness, since we don't have an input buffer amplifier in front of the digitizer. Thus our standard readout power sweep measurements quickly lose resolution at low power. We have also implemented an ionization channel readout with a second ROACH board. The digitizer was modified to operate between DC and a few hundred kilohertz.

5.7.3 "Digitizer End" NI digitizer configuration

In this configuration the readout probe tone comes directly from a synthesizer. The signal returning from the device is mixed with a copy of the the synthesizer output to produce low frequency IQ. A National Instruments (model 6120) 16 ADC digitizes the I and Q signals. This digitizer has an input range of $\pm 0.2\,\mathrm{V}$, which is much better matched to our signal level than the ROACH ADC, a sampling rate of $800\,\mathrm{kS/s}$ and a noise of 1.3 $\mathrm{LSB_{rms}}$. This leads to an expected noise floor of

$$S^{single}_{V,\mathrm{ADC}}(f) = 2 \cdot \sigma_V^2 \cdot \Gamma = 2 \cdot \left(1.3\,\mathrm{LSB_{rms}} \frac{400\,\mathrm{mV}}{2^{16}}\right)^2 \cdot \frac{1}{800\,\mathrm{kS/s}} \approx 1.6 \cdot 10^{-16}\,\mathrm{V^2/Hz}, \quad (5.15)$$

where $S^{single}_{V,\mathrm{ADC}}(f)$ is the single sided power spectrum and Γ is the sampling period. This figure is well below anything else in the system. This configuration is primarily used to measure noise.

The phase noise of the synthesizer is something to be concerned about. It is true that noise from the synthesizer should be removed from the IF (IQ signals) by the mixer. However the phase noise, which can can dominate the amplitude noise, can be transferred into the IF from the LO due to the mixer's finite noise suppression capability. Double balanced mixers have good noise suppression characteristics, but at the expense of conversion loss and the need for greater LO power.

The conversion loss of the mixer in the frequency range 0.7–1.0 GHz is 8–10 dB. The same model, Miteq IR0502LClQ, is also used in the ROACH board configuration.

5.7.4 "Digitizer End" network analyzer configuration

In this configuration, a network analyzer (Agilent model E5071B) is used to generate the probe signal and digitize the return signal. The network analyzer specifies an input trace noise of 10^{-3} dB rms in amplitude and 0.007° rms in phase at an IF bandwidth of 3 kHz and a source power of +10 dBm, which is 1 V for a 50 Ohm system, such as the present one. We would like these is physics units, rather than engineering units. Recalling that

$$V = V_0 \cdot 10^{\mathrm{dB}/20}, \quad (5.16)$$

we get

$$\frac{dV}{V} = \frac{\ln 10}{20}\, d\mathrm{dB} = 0.115\, d\mathrm{dB}. \quad (5.17)$$

So,

$$\frac{\sigma_V}{\sqrt{\text{BW}}} = \frac{dV}{d\sqrt{f}} = 0.115 \cdot V \cdot d\text{dB} \cdot \frac{1}{\sqrt{\text{BW}}} = 0.115 \cdot 1\,\text{V} \cdot \frac{10^{-3}\,\text{dB}}{\sqrt{3\,\text{kHz}}} \approx 2 \cdot 10^{-6}\,\frac{\text{V}}{\sqrt{\text{Hz}}} \tag{5.18}$$

As for the phase noise,

$$\frac{\sigma_\theta}{\sqrt{\text{BW}}} = d\text{deg} \cdot \frac{d\text{rad}}{d\text{deg}} \cdot \frac{1}{\sqrt{\text{BW}}} = 0.007\,\text{deg} \cdot \frac{\pi\,\text{rad}}{180\,\text{deg}} \cdot \frac{1}{\sqrt{3\,\text{kHz}}} \approx 2.2 \cdot 10^{-6}\,\frac{\text{deg}}{\sqrt{\text{Hz}}}. \tag{5.19}$$

The dynamic range of the network analyzer is 120 dBm at an IF bandwidth of 10 Hz.

5.7.5 System noise

We can check that the system is functioning as expected by measuring its noise. We will do this for the NI Digitizer configuration. The noise contribution of the cabling will be included for completeness.

The the noise temperature of the cabling can be computed by treating it as a fixed attenuator. When the cable has a temperature gradient, an integral over infinitesimal sections of it at different temperatures is necessary to determine effective temperature of the cable. We assume that the cable has a constant thermal conductivity $k(T) = k_0$ for this result. The assumption in not realistic, but impact on the system noise is not significant, and we know the proper way to compute it if it did have a significant influence [100, §7-2b, 83]. The cable noise temperature is

$$T_{N,\text{cable}} = \left(\frac{1}{G} - 1\right) \cdot \left(\frac{T_1 + T_2}{2}\right), \tag{5.20}$$

where T_1, T_2 are the potentially different temperatures at the ends of the cable and G is the gain of the cable, i.e. a magnitude less than 1.

The situation is remarkably similar for the IQ mixer. The relationship between the RF-to-IF gain, $G_{\text{RF-IF}}$, and the noise temperature of the mixer is [117]

$$T_{N,\text{mixer}} = \left(\frac{1}{G_{\text{RF-IF}}} - 1\right) T_d, \tag{5.21}$$

where T_d is effective diode noise temperature which typically ranges between room temperature and 500 K. It is approximately room temperature for the mixer used here.

Then the system noise referred to the input of A1 is

$$T_{N,\text{Sys}} = T_{N,\text{A1}} + \frac{T_{N,\text{P7-P8}}}{G_{\text{A1}}} + \frac{T_{N,A2}}{G_{\text{A1}} G_{\text{P7-P8}}} + \frac{T_{N,\text{P9-P10}}}{G_{A1} G_{\text{P7-P8}} G_{\text{A2}}} + \frac{T_{N,\text{M1}}}{G_{\text{A1}} G_{\text{P7-P8}} G_{\text{A2}} G_{\text{P9-P10}}} \approx 6.3\,\text{K}. \tag{5.22}$$

Values called out in the previous section were used in this calculation. Cable gains are determined from the data in Figure 5.8. To convert this to a voltage spectral density, we take

$$S_V^{single}(f) = \frac{\sigma_V^2}{BW} = G_{\text{Sys}} 4 k_b T_{N,\text{Sys}} R + S_{V,\text{ADC}}^{single}(f) \approx 2.4 \cdot 10^{-13}\,\text{V}^2/\text{Hz}, \tag{5.23}$$

where we have used $G_{\mathrm{Sys}} = 71\,\mathrm{dB}$, which is appropriate for 700 MHz. This number is found to be in reasonably good agreement with the measured system noise, Figure 5.9. The noise increases slightly with probe power, but not significantly enough to warrant concern. This is most likely due to the multiplicative gain fluctuation.

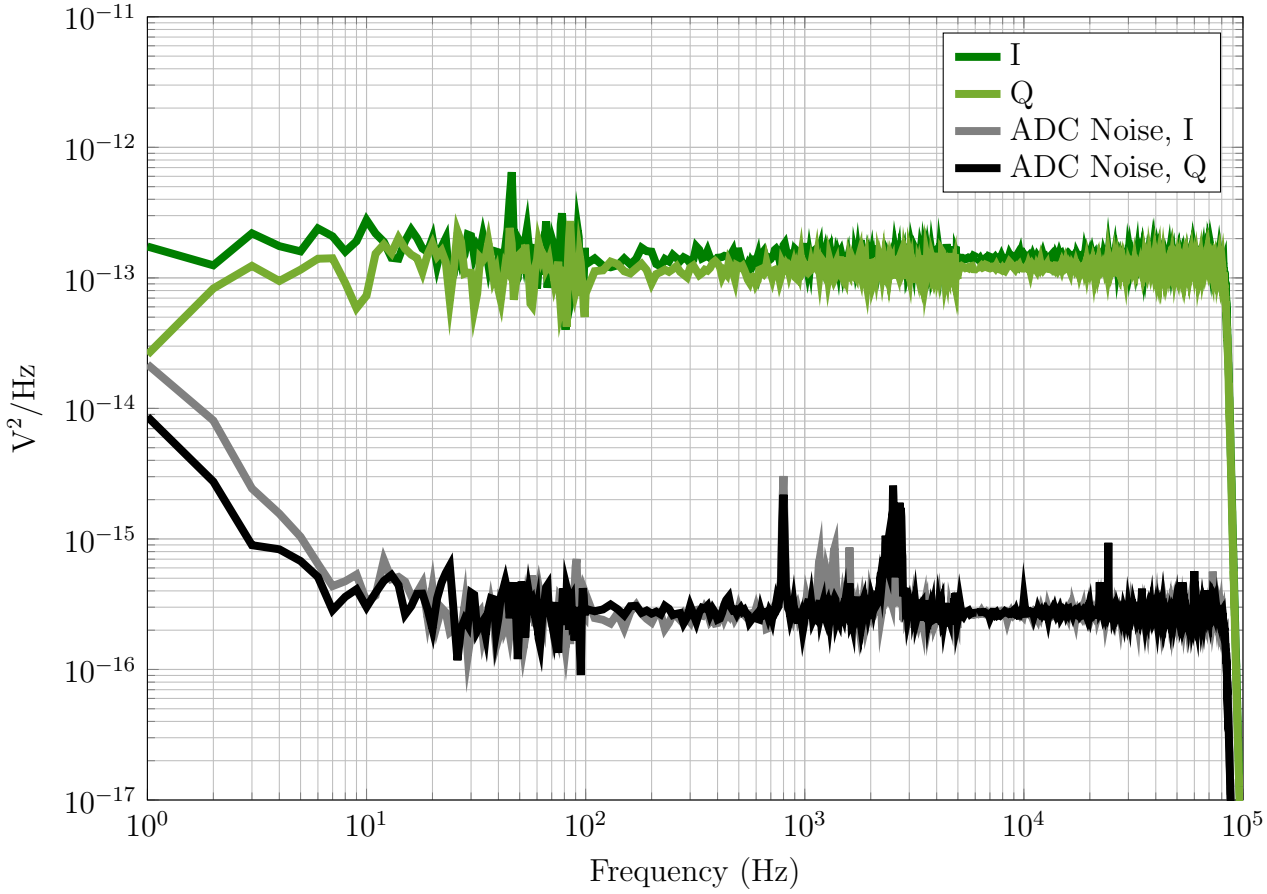


Figure 5.9: The noise of the readout system diagrammed in Figure 5.7 where (a) is connected to (d), the NI Digitizer configuration, at the output of the digitizer. I and Q noise is measured when the probe signal entering primary LNA is approximately $-90\,\mathrm{dBm}$ at a frequency of 690 MHz. The digitizer noise is measured with $50\,\Omega$ terminators in parallel to the digitizer input (which has an impedance of $1\,\mathrm{M}\Omega$). The noise is measured while the fridge is at base temperature.

5.8 Signal estimation

It is informative to consider the signal expected if a test device is used as a detector. All the formulae needed for this calculation can be found in the thesis of Jiansong Gao [68]. We

assume that the sensor chip is mated to an aluminum ground plane that is deposited on a sample of germanium thick enough to completely absorb radiation to which it is exposed.

Gao calculated the change in transmission to be,

$$\delta S_{21} = \alpha|\gamma|\kappa\frac{Q^2}{Q_c}\delta n_{qp} \tag{5.24}$$

where α is the kinetic inductance fraction; γ depends on the electrodynamics of the film

$$|\gamma| = \begin{cases} -1/2 & \text{for Thick film, local limit} \\ -1/3 & \text{for Thick film, extreme anomalous limit} \\ -1 & \text{for Thin film, local limit} \end{cases} \tag{5.25}$$

we shall assume $\gamma = -1/2$; κ is determined by the change in film conductivity due to the creation of quasiparticles,

$$\kappa \approx \frac{1}{\pi N_0}\sqrt{\frac{2}{\pi k_B T \Delta_0}}\sinh(\xi)K_0(\xi) + i\frac{1}{2N_0\Delta_0}[1 + \sqrt{\frac{2\Delta_0}{\pi k_B T}}e^{-\xi}I_0(\xi)], \tag{5.26}$$

where $\xi = \hbar\omega/2k_BT$, and I_n, K_n are the nth order modified Bessel function of the first and second kind, respectively; and δn_{qp} is the excess quasiparticle density created by the absorption of radiation,

$$\delta n_{qp} = \frac{E}{2\Delta_0 V} \tag{5.27}$$

where V is the volume of metal through which the quasiparticles diffuse and E is the energy of the radiation. Assuming the resonator is biased with a probe power corresponding to a peak RF voltage of V_{probe}, the change in transmitted amplitude is $V_{probe} \cdot \delta S_{21}$. Assuming no excess noise (e.g. from two-level systems and fluctuations in quasiparticle population) the relevant noise on in the circuit is due to the LNA and it is integrated over the bandwidth of the resonator, $\mathrm{BW} = f_0/Q$. The magnitude of the RMS signal to noise ratio, SNR, is then

$$\mathrm{SNR} = \frac{|\delta S_{21}|V_{probe}}{\sqrt{4 \cdot k_B \cdot T_{eff} \cdot R \cdot \mathrm{BW}}}, \tag{5.28}$$

where $R = 50\,\Omega$ is the system impedance. Lastly, the RMS energy resolution at the radiation energy, E, is given by

$$\delta E = \frac{E}{\mathrm{SNR}}. \tag{5.29}$$

This can be considered the baseline resolution of the KIDs phonon sensor.

Quantity	Value	Unit	Description
T_{eff}	6.3	K	Readout system effective noise temperature
T	40	mK	Temperature of device
E	100	keV	Radiation energy
α	0.005		Kinetic inductance fraction
η	50	%	Phonon-to-QP conversion efficiency
Δ_0	182	µeV	Superconducting energy gap
V	$33 \cdot 10^6$	μm^3	QP diffusion volume
Q	$33.3 \cdot 10^3$		Resonator total quality factor
Q_c	$40 \cdot 10^3$		Resonator coupling quality factor
f_0	700	MHz	Fundamental resonant frequency
N_0	$1.72 \cdot 10^{10}$	$\mu m^{-3}\,eV^{-1}$	Single spin DOS at Fermi surface

Table 5.8: Sensor "S8" is considered (see Table 5.1). 300 nm thick ground plane assumed. T_{eff} is the noise of the readout system referred to the input of the primary low noise amplifier (LNA). DOS – density of states. N_0, Δ_0 are for aluminum. α is taken from Figure 5.2.

Table 5.8 summarizes parameter assumptions and gives signal estimations for the case of using "S8" as a radiation detector. "S8" is chosen because it is approximately the resonator size we envision for use in a dark matter detector with a KIDs phonon sensor. In the calculations we assume that the quasiparticles are only allowed to diffuse through the rectangular area of aluminum directly under the resonator, the patch area for "S8" (see Table 5.1). This will lead to an overestimate of the signal because an actual detector would have more metal area for the quasiparticles to diffuse through. We also assume that the quasiparticle density is uniform within this metal volume, hence we do not consider differences in sensitivity to quasipartices due to the current distribution along the resonator.

P_{probe} [dBm]	SNR	δE [keV]
−20	360	0.28
−30	114	0.88
−40	36	2.8
−50	11	8.8
−60	4	27.7

Table 5.9: Estimated signal obtained from using "S8" as a radiation detector, including RMS signal to noise ratio, SNR, and RMS baseline energy resolution δE at the radiation energy given in Table 5.8, 100 keV. Parameters assumed are listed in Table 5.8. Figures for several different resonator probe powers are presented.

As a basis for comparison, the CDMS II detector has a phonon resolution of approximately 200 eV RMS for a radiation energy of 100 keV. Thus, Table 5.9 suggests that if we

can deliver enough power to the KIDs phonon sensors, then we can obtain energy resolutions that are comparable to the TES phonon sensors. Additional optimizations, such as use of lower noise amplifiers, ground plane meshing (see § 5.4.2.1), microstrip gap and film thickness reductions (see Figure 5.3) and quasiparticle trapping, might also be of help in arriving at energy resolutions equal to or better than the TES sensors.

5.8.1 Relative sensitivity of trace and ground plane

In view of the difference in kinetic inductance fraction for the microstrip trace and ground plane, it is interesting to consider the relative response to the creation of quasiparticles in the trace versus in the ground plane. Figure 5.10 shows this relative response assuming the trace and patch areas given in Table 5.1, parameter values given in Table 5.8 (though many cancel away), with the addition of $N_0 = 4.61 \cdot 10^{10}\,\mu\mathrm{m}^{-3}\,\mathrm{eV}^{-1}$ and $\Delta_0 = 1395\,\mu\mathrm{eV}$ for the niobium trace. Figure 5.10 is equivalent to dividing the SNR for the ground plane (e.g. as calculated above for "S8" above) to the SNR for the trace. The figure shows us that, especially for the narrower widths, the trace can be considerably more sensitive than the ground plane.

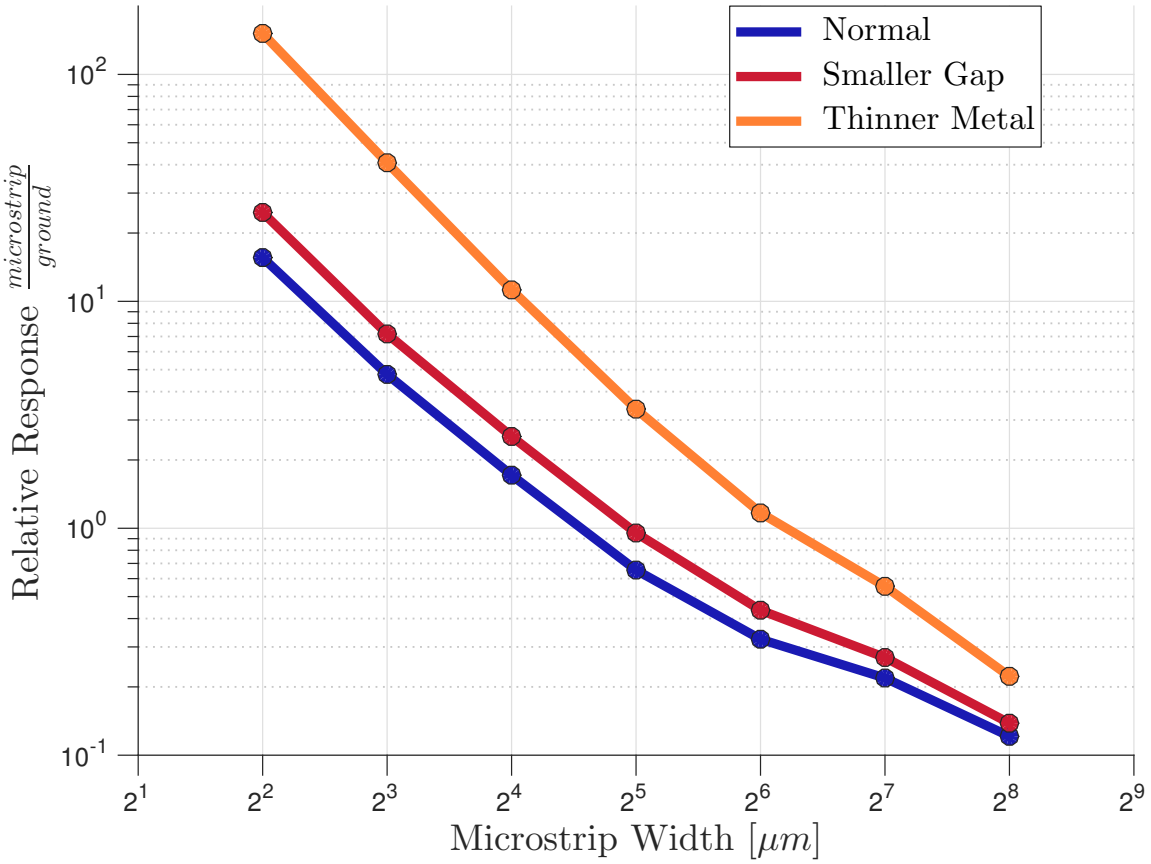


Figure 5.10: The response, $|\delta S_{21}|$, to quasiparticles in the microstrip trace relative to quasiparticles in the ground plane using probe chips "S2" through "S8" as radiation detectors. We also show the effect on the relative response which the use of a smaller gap and thinner metal would have. Taking the dimensions called out for Figure 5.2 as a baseline, the smaller gap is ten times smaller than baseline, and the thinner metal is ten times thinner than baseline.

Attributions

Most of the work presented in this chapter was done by myself alone. I asked my student Nick Zobrist to perform the simulations needed for the α calculations and the Sonnet simulations.

Chapter 6

Detector Performance Data

We present results obtained from tests of the vacuum microstrip kinetic inductance phonon sensors. The techniques used to improve and control performance will be emphasized.

We look at resonators in the linear and non-linear regimes separately.

6.1 Linear Data and Fitting

In order to determine the seven parameters of the resonance, a parameter fit is performed on the raw complex transmission data S_{21}. A primary "stepwise" fit is first executed. In this procedure, parameters related to the resonance are determined in a series of steps.

A secondary "concurrent" fit can then be performed on the raw data, where the seven parameters are determined in one fit step simultaneously. To facilitate convergence of fit, which is a minimization of χ^2, the seven parameter values determined in the stepwise fit are used as the initial guess for the concurrent fit. The value of the minimized objective function is the reduced χ^2, and to determine it, additional information from noise in the data or from all the components in the readout system is used in the fit.

Overall, we notice that for both the stepwise and concurrent fitting of data, the goodness of the fit degrades at the probe power to the loop is increased.

6.1.1 Linear fitting

The fitting model used for the linear fit is a more general form of Equation 4.43, where we additionally allow an arbitrary scaling, $a = Re^{i\beta}$, an electrical delay term, $e^{-2\pi i f \tau}$, and a loop rotation term $e^{i\phi}$,

$$S_{21}(f) = z_i = ae^{-2\pi i f \tau}\left[1 - \frac{\frac{Q}{Q_c}e^{i\phi}}{1 + 2iQ\left(\frac{f-f_0}{f_0}\right)}\right]. \tag{6.1}$$

The arbitrary scaling factor comes from system component gains and phase shifts. The electric delay comes from the signal propagation in the cables. It is not clear where the

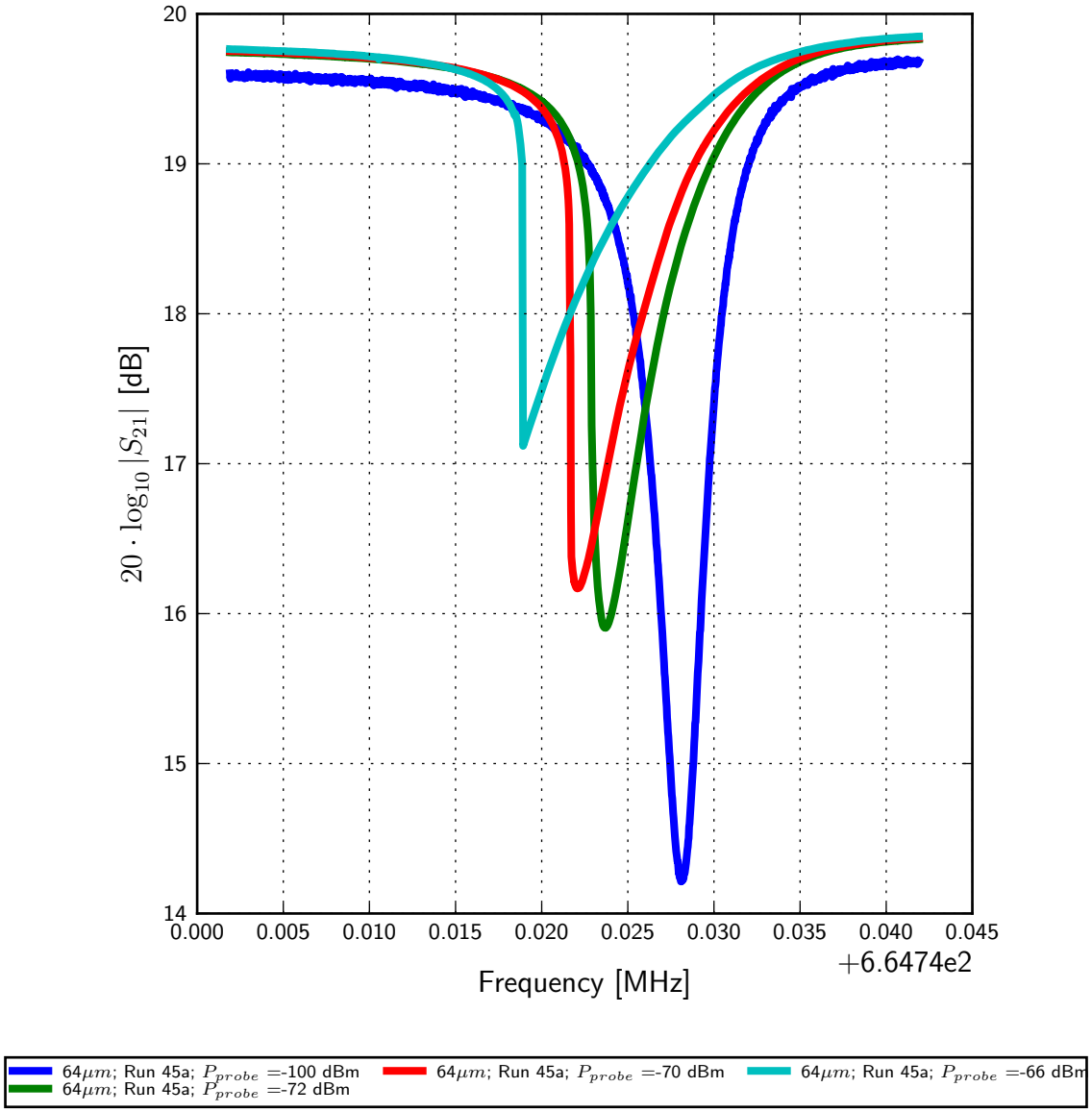


Figure 6.1: Transmission magnitude for a resonator that starts out linear and becomes nonlinear. One first notices asymmetry in the dip, and then clipping on the low frequency side. This trace is unnormalized, so the transmission level reflects the system amplification. Data run, microstrip trace width (µm) and probe power at the resonator are specified in legend.

loop rotation comes from. It could be due to multiple sources. If, in equation Equation 4.40, $\phi_{13} - \pi/2 = \Delta\phi_{13}$ this would contribution the loop rotation. As explained in [97], coupling the resonator to mismatched input and output transmission lines and non-negligible transmission line series inductance can contribute to the rotation. And as described in [130, 76, they use as

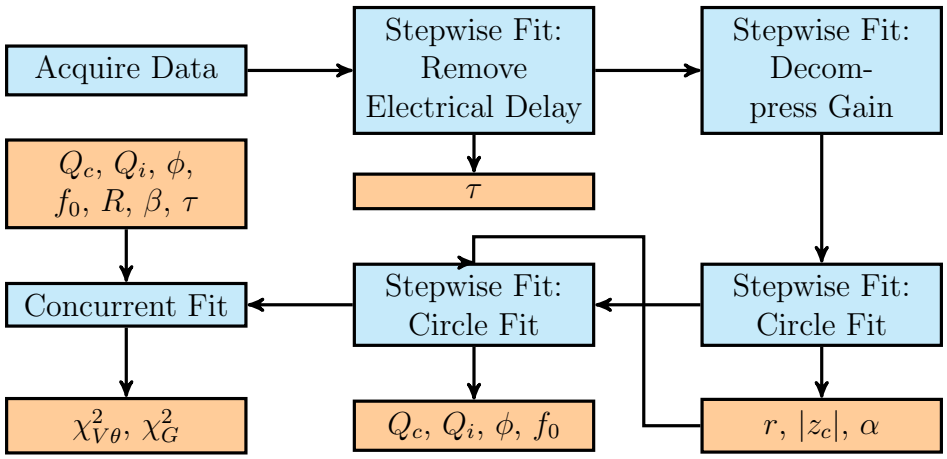


Figure 6.2: A flow chart of the procedure used to fit resonances that are in the in the linear regime. The fit parameter outputs and inputs are indicated for each step. One sees that the output of the circle fit is the circle center and radius, $r = Q/Q_c$. The concurrent fit uses parameter values determined by the stepwise fit to as its initial guess. It also, optionally, uses the reduced data set, post-cuts, rendered in the phase fit. It is performed in two different ways. One which looks at readout system component induced errors in the magnitude and phase of the measured signal and another which derives an error from the noise in the measured scattering parameter data. $z_c = |z_c|e^{i\alpha}$ is the vector to the loop center.

similar microstrip in press technique], direct transmission of the probe signal from the input port to the output port of the test box (i.e. bypassing the resonator), can also contribute to the rotation. The magnitude of Equation 6.1 traces out a Lorentzian profile. We shall refer to the $S_{21}(f)$ data points as the z_i and the frequency points as the f_i

6.1.2 Stepwise fitting

The stepwise fitting procedure, roughly outlined in Figure 6.2, we use here is essentially the same as the one outlined by Gao, [68, Appendix E]. We outline it briefly here pointing out differences with Gao.

Step 1: Remove Electrical delay. The delay is extracted from the raw data using the minimum distance method. In this method, one minimizes the distance between adjacent points $\min\left\{\sum_i |z_i - z_{i+1}|^2\right\}$ over an electrically large bandwidth.

Step 2: Remove Amplifier Gain Compression. We experience gain compression because we are interested in the high power behavior of the resonators and as a result, the amplifiers may driven into compression, but not quite to saturation. This requires a output power versus input power calibration; output powers that are less than what is expected assuming a linear gain are scaled to expectation.

Step 3: Remove out of band data points. Here we find the resonance by looking for dips in the magnitude versus frequency data, $\min\{|z_i|\} \approx z_0$, where z_0 is the amplitude

at the resonant frequency f_0. A bandwidth estimate is then derived from the width of the dip. Then a cut on the data performed to remove al point that are outside of a few bandwidths of the dip. This step is only performed when there is excessive off resonance data. For example, z_i is 5000 points but only 50 of them are in the resonance, performed the subsequence steps without removing the excess data will throw off subsequent resonance parameter estimates.

Step 4: Fit resonance loop to circle, the "circle fit". Gao uses a circle fit algorithm called Pratt's approximation to the gradient weighted algebraic fit method, described by Chernov in [40]. Algebraic methods use functions that are derived from the geometric parameters (circle center and radius). They may have the disadvantage of precision loss when the algebraic functions are converted back into the geometric parameters and slow execution due to processing of complicated formulae arising from the algebraic functions. In a more recent publication [15], Chernov proposes a faster, more numerically stable fit algorithm, which converges from virtually any starting guess for the center point. We use this method and highly recommend it. This algorithm use Newton's method with a Levenberg-Marquardt correction; an improved two phase "acceptance rule" for objective function iterations that increases the accuracy of parameter estimates; and it treats large circles (e.g. very short or low curvature arcs) different from small ones to increase stability. The circle fit determines the center of the circle and $2 \cdot r = {}^{Q}/_{Q_c}$, its radius.

Step 5: Fit speed at which points trace out loop, the "phase fit". The phase fit step is implemented as a least squares fit and uses the Powell minimization method. If $z_c = |z_c|e^{i\alpha}$ if the loop center, as determined in the previous step, we rotate the coordinate system so that z_c is aligned with the real axis then translate the loop to the origin,

$$z_i' = (z_i - z_c)\, e^{-i\alpha}. \tag{6.2}$$

Now in the prime coordinate system, we fit the phase angle of $z_i' = |z_i'|e^{-i\theta_i}$ to the phase angle of a curve parameterized in the form of the fraction term of Equation 6.1, which parameterization is called a linear fractional transformation in complex analysis. We minimize,

$$\min \left\{ \sum_i \left[\theta_i + \theta - \arctan\left(-2Q \frac{f_i - f_0}{f_0} \right) \right]^2 \right\}. \tag{6.3}$$

Note, that Q determines the speed at which the loop is traced out and f_r corresponds to the zero-crossing of the arctan. (See Appendix A for a background on quality factor.) The angle offset, θ, can be used to determine the loop rotation angle θ and the overall phase rotation α as depicted in Figure 6.3.

Additional $S_{21}(f)$ data points may be removed during the phase fit for several reasons. One, another, narrower, bandwidth cut is rendered on the measured frequency band. For loops that are significantly distorted, $S_{21}(f)$ points that is closer to or farther from the circle fit center point, than some other arbitrary band (e.g. $> 1.5r$ or $< 0.5r$) are removed. Rendering the radius cut makes the fit favor the portions of the loop that

are farthest from the resonant frequency, which are also those that correspond to lower energy inside the resonator, so the radius cut is biased to a linear resonator model.

6.1.3 Concurrent fitting

The concurrent fit uses the seven parameter values found by the stepwise fit as the initial guess in Equation 6.1. The fit uses the Powell method to minimize the reduced χ^2 and it does this in two different ways. The first way uses accuracy specifications of the components in the readout system to determine variances in the phase, σ_θ^2, and voltage magnitude, σ_V^2, directions of the measured signal. As can be seen in the diagram of the readout system, Figure 5.7 (a) connected to (c), components include cables, amplifiers and attenuators. $\chi^2_{V\theta}$ is computed as,

$$\chi^2_{V\theta} = \frac{1}{N-7}\sum_i^N \left[\frac{\left(|S_{21,i}| - |\hat{S}_{21,i}|\right)^2 |V_1^+|^2}{\sigma_V^2} + \frac{\left(|\theta_{21,i}| - |\hat{\theta}_{21,i}|\right)^2}{\sigma_\theta^2} \right], \tag{6.4a}$$

$$\sigma_V^2 = \sum_m^M \sigma_m^2 \prod_n^m g_n = \sigma_1^2 \cdot g_1 \cdot g_2 \cdot \ldots \cdot g_M + \sigma_2^2 \cdot g_2 \cdot g_3 \cdot \ldots \cdot g_M + \cdots + \sigma_M^2 \cdot g_M, \tag{6.4b}$$

$$\sigma_\theta^2 = \sum_m^M \frac{\sigma_m^2}{4|V_2^-|^2} \prod_n^m g_n^2 = \frac{\sigma_1^2}{4|V_2^-|^2} \cdot g_1^2 \cdot g_2^2 \cdot \ldots \cdot g_M^2 + \frac{\sigma_2^2}{4|V_2^-|^2} \cdot g_2^2 \cdot g_3^2 \cdot \ldots \cdot g_M^2 + \cdots + \frac{\sigma_M^2}{4|V_2^-|^2} \cdot g_M^2, \tag{6.4c}$$

where the $\sigma_m^2 = 4 \cdot k_b \cdot T_{\text{noise}} \cdot \text{BW} = \sigma_V^2$ are the voltage noise variances of the components of the readout chain, the g_n are their gains or attenuations and $S_{21} = {}^{V_2^+}\!/_{V_1^+}$ as measured at the network analyzer. Here we have only considered the additive white noise of each component. The bandwidth is taken to be the IF bandwidth of the network analyzer. noise for the passive components is as defined in Equation 5.20. We have also assumed linearity in all the components including the amplifiers so that $\sigma_V^2 = |2V^+\sigma_\theta|^2$, where V^+ is the amplitude entering the components. σ_θ is measured in radians. The $\hat{S}_{21,i}$ are the point on the curve fit.

In the second way we calculate χ^2, we assume that that the noise in $S_{21}(f)$ is Gaussian and extracts a variance from the distances between adjacent points, e.g. $|S_{21,m} - S_{21,m+1}|$,

$$\chi^2_G = \frac{1}{N-7}\sum_i^N \frac{\left|S_{21,i} - \hat{S}_{21,i}\right|^2}{\sigma_G^2} \tag{6.5a}$$

$$\sigma_G^2 = \frac{1}{2M}\sum_m^M |S_{21,m} - S_{21,m+1}|^2, \tag{6.5b}$$

were the sum in σ_G^2 is carried out over the first M data points. This method was proposed by Gao [68, Appendix E], who pointed out the convenience of using the first M data points as they are usually far away from the resonance.

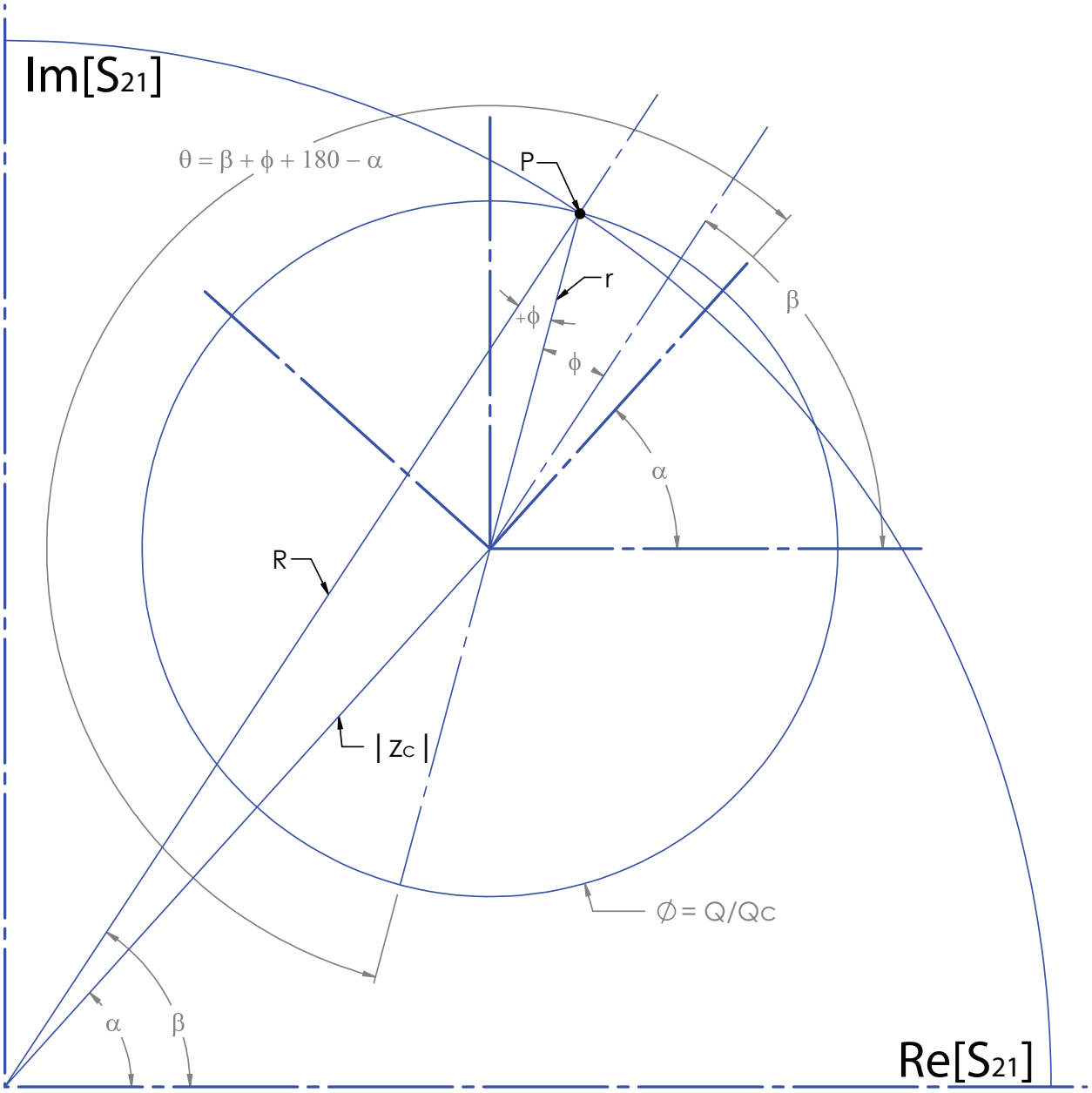


Figure 6.3: Angle and distance relationships for a resonance loop that has a rotation of $+\phi$ is diagrammed. Not that the ϕ rotation amounts to pivoting the loop at the point, P, where an unrotated resonance loop would tangentially intersect the outer loop. As depicted, the rotation can make a port of the resonance loop cross outside of the outer loop. This is the reason why some resonances, when plotted in magnitude frequency space, can have an upturn on one side of the dip.

As an example, Table 6.1 lists the χ^2 obtained for the curves in Figure 6.1. Figure 6.4 compares the resonance loops traced out using the resonance parameters obtained by the various fits to the original data. Notice the squashing of the loop and the increasingly large jump in the data points as the power is increased.

P_{probe} [dBm]	$\chi^2_{V\theta}$	χ^2_G			
		$M = 50$	$M = 100$	$M = 150$	$M = 200$
-100	0.23	1.0515	0.964 278	0.935 469	1.002 80
-72	46 822	248 196	233 317	209 739	203 426
-70	103 826	403 093	369 175	354 493	351 804
-66	204 853	640 971	635 989	592 700	610 462

Table 6.1: χ^2 obtained using the to concurrent fit methods described. Fitted curves are from Run 45a. We notice that the goodness of the fit decreases as the probe power is increased. These are the same curves which are plotted in magnitude in Figure 6.1 and as complex vectors in Figure 6.4.

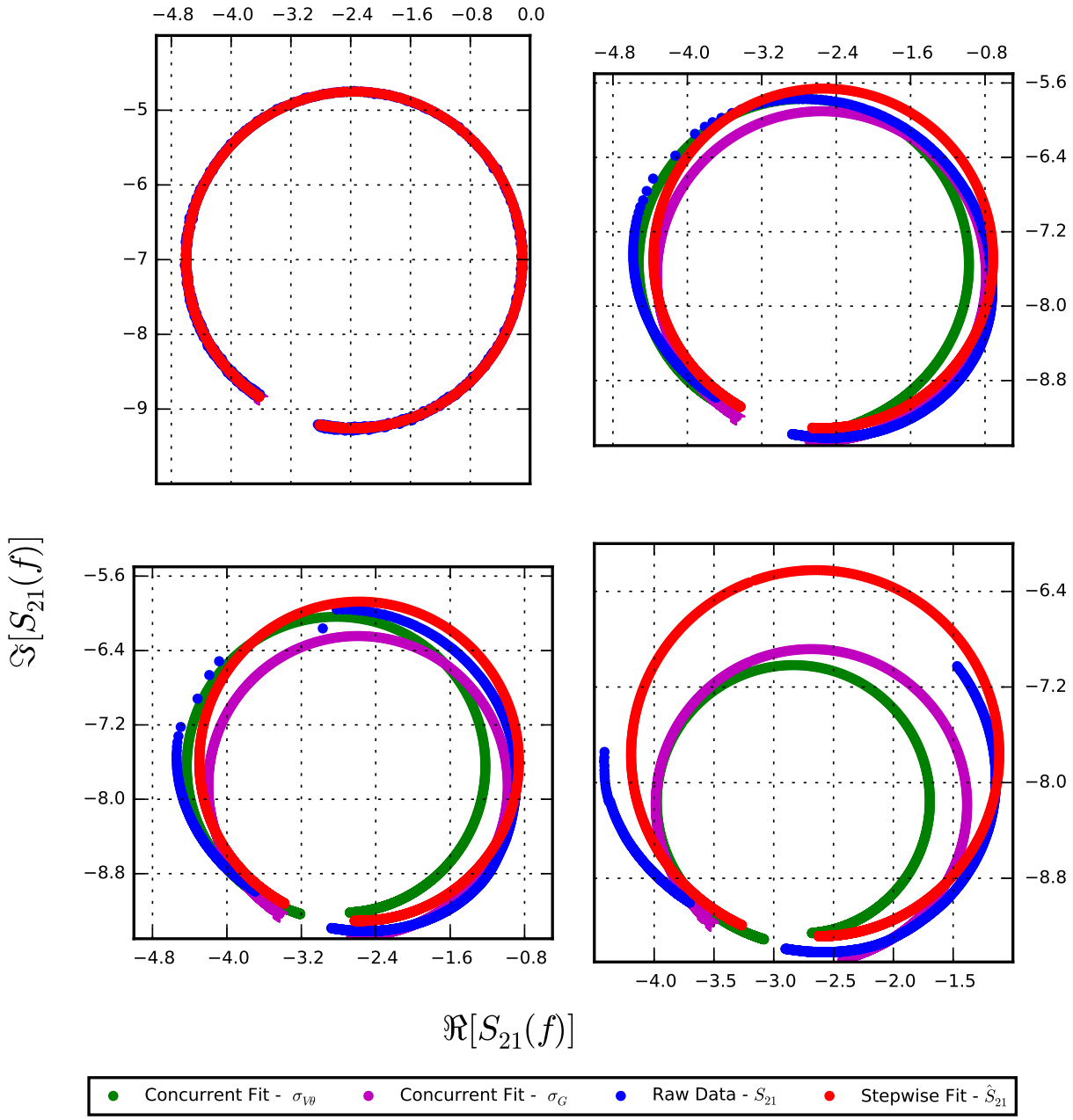


Figure 6.4: The S_{21} loops for the magnitude curves shown in Figure 6.1 are plotted along with the results from the primary fit and the secondary fit. Upper left plot is $P_{probe} = -100\,\text{dBm}$, upper right is $P_{probe} = -72\,\text{dBm}$, lower left is $P_{probe} = -70\,\text{dBm}$, and lower right is $P_{probe} = -66\,\text{dBm}$.

6.1.4 Data

In this section we present data obtained from various sensor chip ground plane combinations. The readout system is in configuration (*a*-*c*) as depicted in Figure 5.7, i.e. using the network analyzer. Two types of data are presented. Power sweep data, where we look at the change in resonance fit parameters as the probe power entering the device is swept over a wide power range. Temperature sweep data, where we look at the change in resonance fit parameters as both temperature and power are swept. All data is for the resonance at the fundamental frequency unless explicitly noted otherwise.

The principle question being explored in the data is as to the effect of resonator width on the behavior the fit parameters.

6.1.4.1 Probe power sweeps

The range of power used is limited on the low side by signal to the noise of the readout system, and on high side by the saturation of the amplifiers. The data typically goes down to a readout power of about $-100\,\mathrm{dBm}$, which is very much above the noise floor, but is chosen as a compromise between integration time and fridge access time. Also, there is little change in the parameter values at these low powers. Interestingly, no discernible change in base temperature was observed at high readout powers, but there is a small impedance between the thermometer and the device box due to several interposing interfaces. This suggests that dissipation due to heating is not a significant issue.

First we look at the effect of probe power on the internal quality factor of the resonators, Figure 6.5. We notice that the measured values of Q_i are at least two orders of magnitude lower than the values obtained from simulation, Table 5.2, suggesting the existence of an additional, significant loss mechanism. One is well positioned to speculate that this loss mechanism is related to dissipation in the superconducting films, as in the case of weak links and vortices. In support of the case for vortices, one notices that the Q_i measured when a copper box is used to house the device, are lower than when the device is housed in a niobium box, which provides a degree of superconducting shielding[1]. One additionally notices that the highest internal quality factors are measured when the hexagonal mesh ground plane is used. The narrow superconducting linkages in the mesh would discourage vortex formation, [166].

As a note, the press in Run 45b was under-torqued. This occurred because the test box from Run 44a was retested in 45b and the press was not re-torqued in between the runs. We learned that re-torquing is necessary and that the decreased torque value can cause microphonic noise and distortion of the resonance.

[1]The niobium box would however admit flux lines.

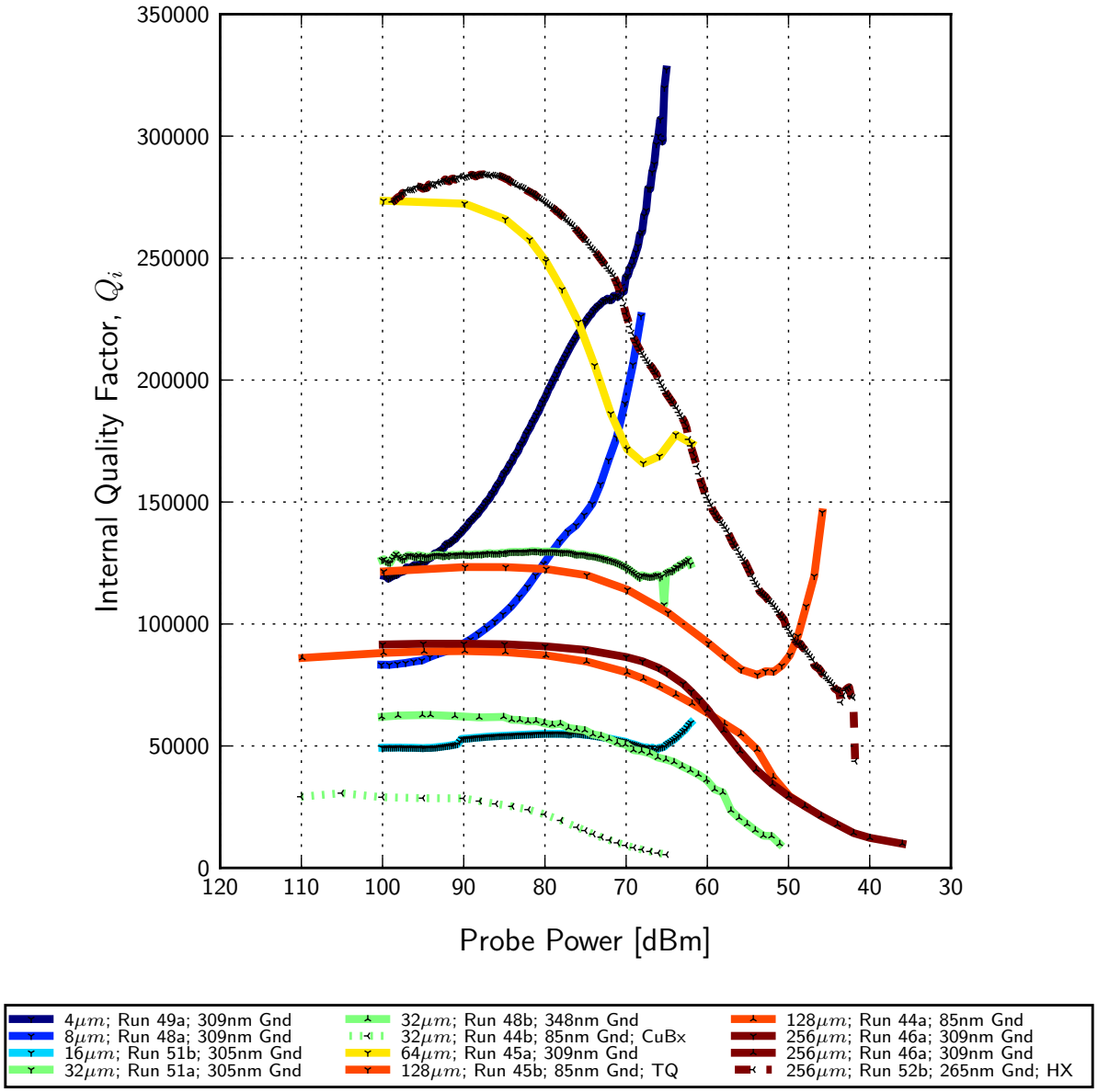


Figure 6.5: Internal quality factor versus probe power is plotted. Data run, microstrip trace (µm) and ground plane thickness (nm) are specified in legend. Abbreviations are: CB – copper box (otherwise niobium box), TQ – under-torqued press, HX – hexagonal mesh ground plane.

Puzzlingly, the internal quality factors of some devices increase with power and some decrease with power. The simplest explanation for this phenomenon is that the linear fit model is failing as the power is increased and sometimes the internal Q appears to increase in the course of this failure while other times it appears to decrease. This idea will be explored

further in § 6.3.0.2.

We also do not notice width dependence to the behavior of the quality factor in Figure 6.5. One wonders if there is a hidden width dependence, which can be made apparent if the probe power is transformed to some other measure of resonator excitation. In chapter 4, we derived equations that map readout power to the internal power circulating through the resonator, and the maximum current and current density in the resonator. The current density takes into account the thickness of the superconducting films. We can use these equations to transform the independent variable, P_{probe}, into these quantities and look for width dependence, as shown in Figure 6.6. Still no width dependence is observed.

A puzzling feature in the data is the departure of the coupling quality factor from a constant value with increasing power, Figure 6.7. Again we find that the coupling quality factors of some devices turn down with increasing power while others turn up, although most turn up. According to equations Equation 4.14 and Equation 4.30, the coupling quality factor depends only on capacitances and impedances, including the impedance of the resonator Z_r. Maybe the resonator impedance is changing, or maybe, again, the linear fit model is failing and this time the failure manifests itself in an abrupt departure from a constant coupling quality factor value.

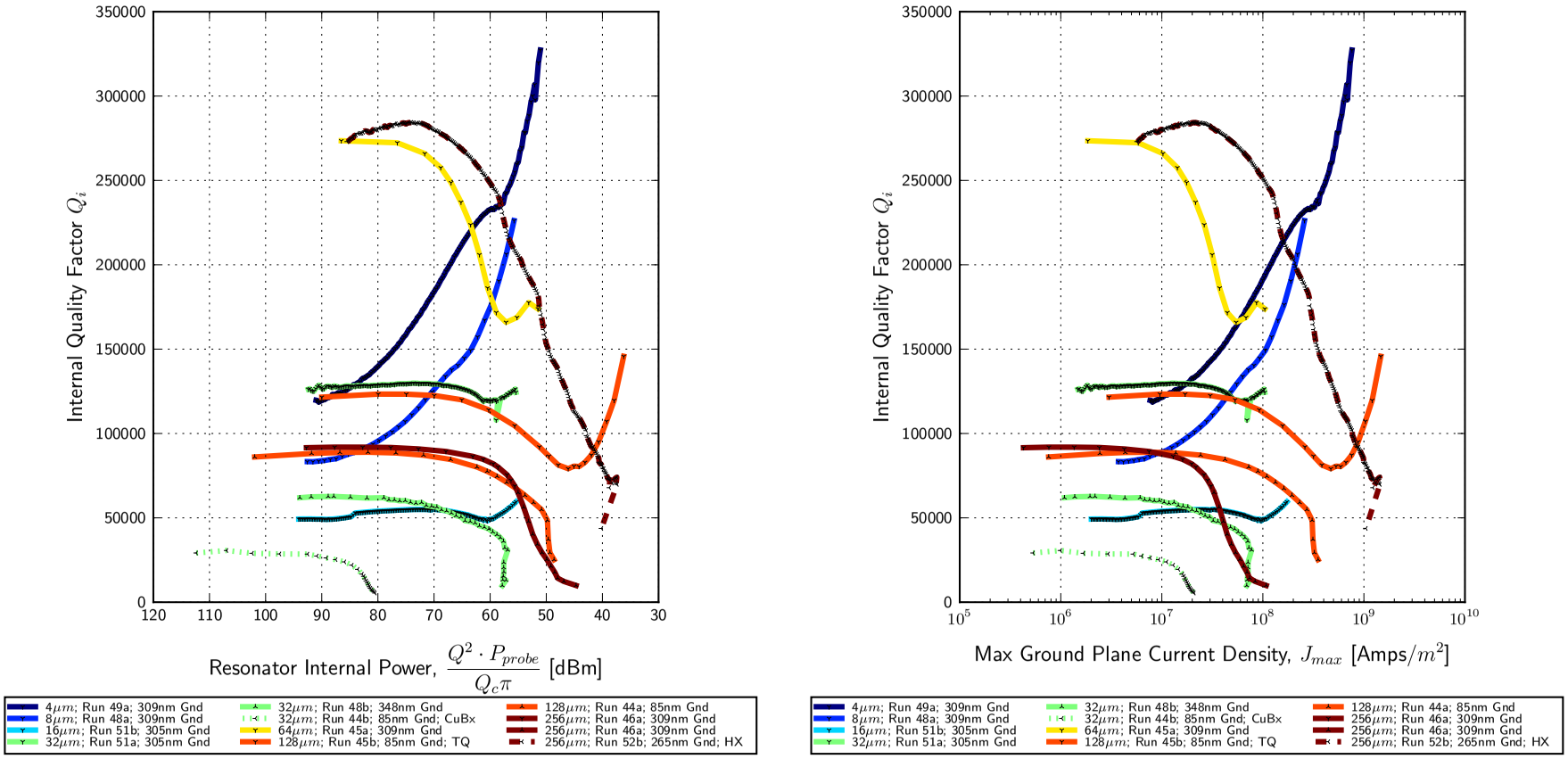


Figure 6.6: Internal quality factor versus internal power of the resonator (left) and approximate maximum current in the ground plane. No significant dependent on width is apparent. For the hexagonal mesh ground plane, the current density has been scaled by the metal fraction of mesh. Data run, microstrip trace (µm) and ground plane thickness (nm) are specified in legend. Abbreviations are: CB – copper box (otherwise niobium box), TQ – under-torqued press, HX – hexagonal mesh ground plane.

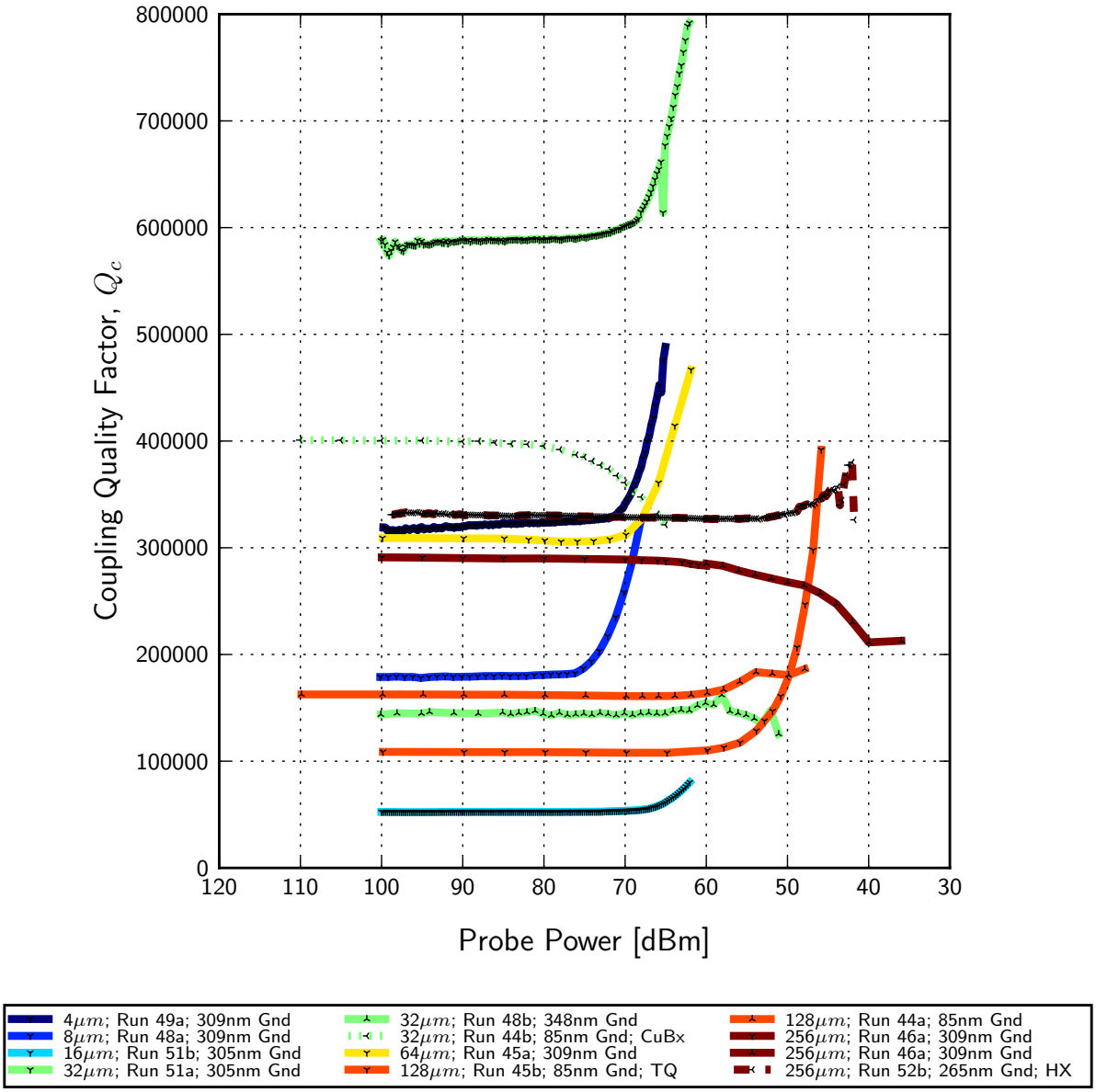


Figure 6.7: Internal quality factor probe power. The upturn in some curves at higher power is not expected from linear resonator modeling. It is most likely due to fit failure. Data run, microstrip trace (µm) and ground plane thickness (nm) are specified in legend. Abbreviations are: CB – copper box (otherwise niobium box), TQ – under-torqued press, HX – hexagonal mesh ground plane.

Another interesting feature of the power sweep data is that the fractional frequency shift of some devices exhibits and initial increase at low probe power and then decreases, Figure 6.8. This only occurs in a minority of the devices. Since it only occurs at low power,

well within the linear regime of the devices (as judged by the behavior of other parameters such as the coupling quality factor), it may be an indication that two-level systems are present. Study of the power dependence of the on resonance noise would confirm if two-level systems are the cause. If one ignores Runs 44d and 41a, one can discern a slight width dependent as the narrower resonators begin to turn downward first.

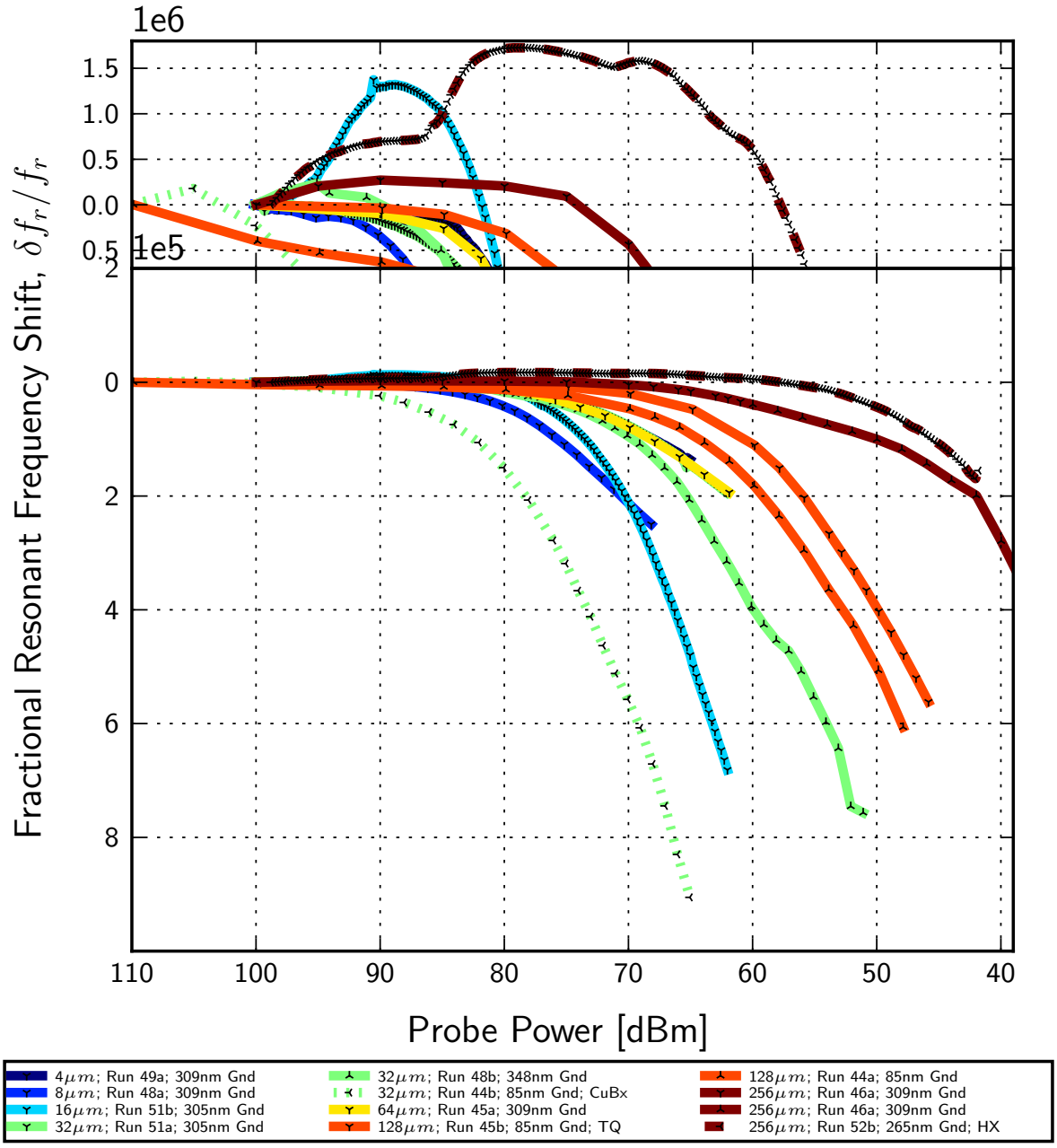


Figure 6.8: Fractional frequency shift versus maximum ground plane current density. Top plot is a zoomed on to the area around $^{\delta f}/_{f} = 0$ in the bottom plot. A slight width dependence is apparent, with narrower widths turning down first. Data run, microstrip trace (µm) and ground plane thickness (nm) are specified in legend. Abbreviations are: CB – copper box (otherwise niobium box), TQ – under-torqued press, HX – hexagonal mesh ground plane.

6.1.4.2 Temperature sweeps

Temperature sweep data is collected by applying heat to the mixing chamber, waiting for temperature equilibrium, then performing power sweeps. This sequence is repeated for every temperature increment. Some data are collected by increasing the temperature at every increment while others are collected by decreasing the temperature. The dilution fridge used does not have a temperature control and regulation system, so is in no danger of temperature oscillation during the measurement due to the controller. However, it is best practice to take multiple temperature readings throughout each scan (e.g. at a given heat applied to the mixing temperature, and probe power to the resonator) to ensure that temperature drifts are not occurring. Unfortunately, the capability to do this was only available for Runs 51a, 51b and 52b. All the other data is taken by writing down temperature readings manually at the beginning of the power sweep scans for heat applied to the mixing temperature. There is certainly an issue with temperature drifts during these measurements. Also, the uncertainty in the manual temperature readings is increased by the limited averaging one can practically do with a pencil and paper. As such, the data for Runs 51a, 51b and 52b is noticeably cleaner. Depending on the IF bandwidth setting of the network analyzer, and the number of temperature and power points, it takes between 24 and 36 hours to complete a temperature sweep data set.

The following plots present parameter change data at both different probe powers and different temperatures. The probe powers plotted are chosen to be powers used in all the run data plotted.

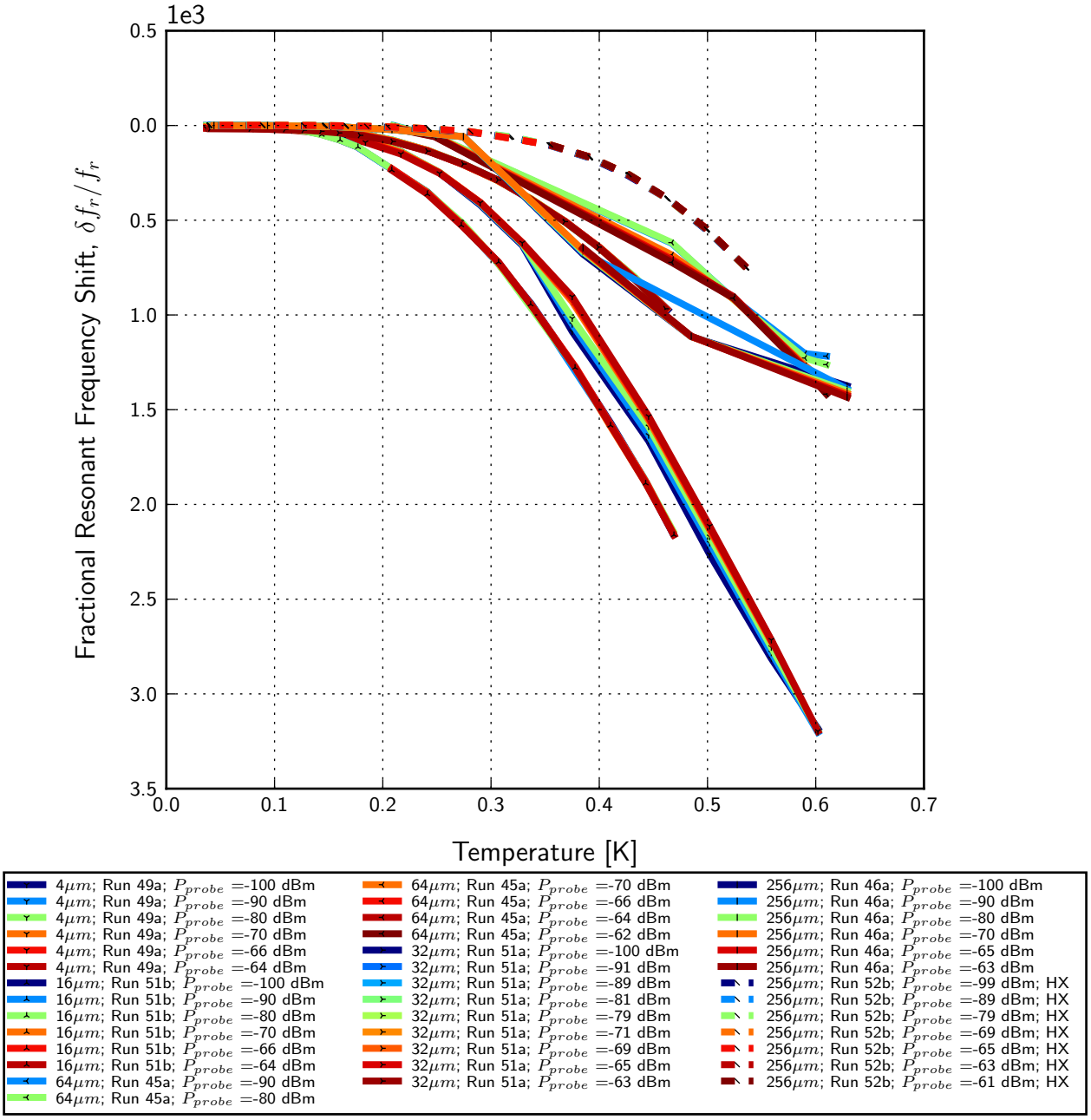


Figure 6.9: Fractional frequency shift versus probe power and temperature. Data run, microstrip trace (µm) and ground plane thickness (nm) are specified in legend. Abbreviations are: CB – copper box (otherwise niobium box), TQ – under-torqued press, HX – hexagonal mesh ground plane.

The fractional frequency shift data has a slight width dependence if one ignores the Run 49a (or 51b), one can discern a width dependence, where the narrower widths turn durn first,

Figure 6.9. A width dependence is expected because the kinetic inductance fraction varies monotonically according to width (and superconductor thickness), as we saw in chapter 5. The abrupt change in slope in Run 46a at about 300 mK is most likely due to temperature reading inaccuracy.

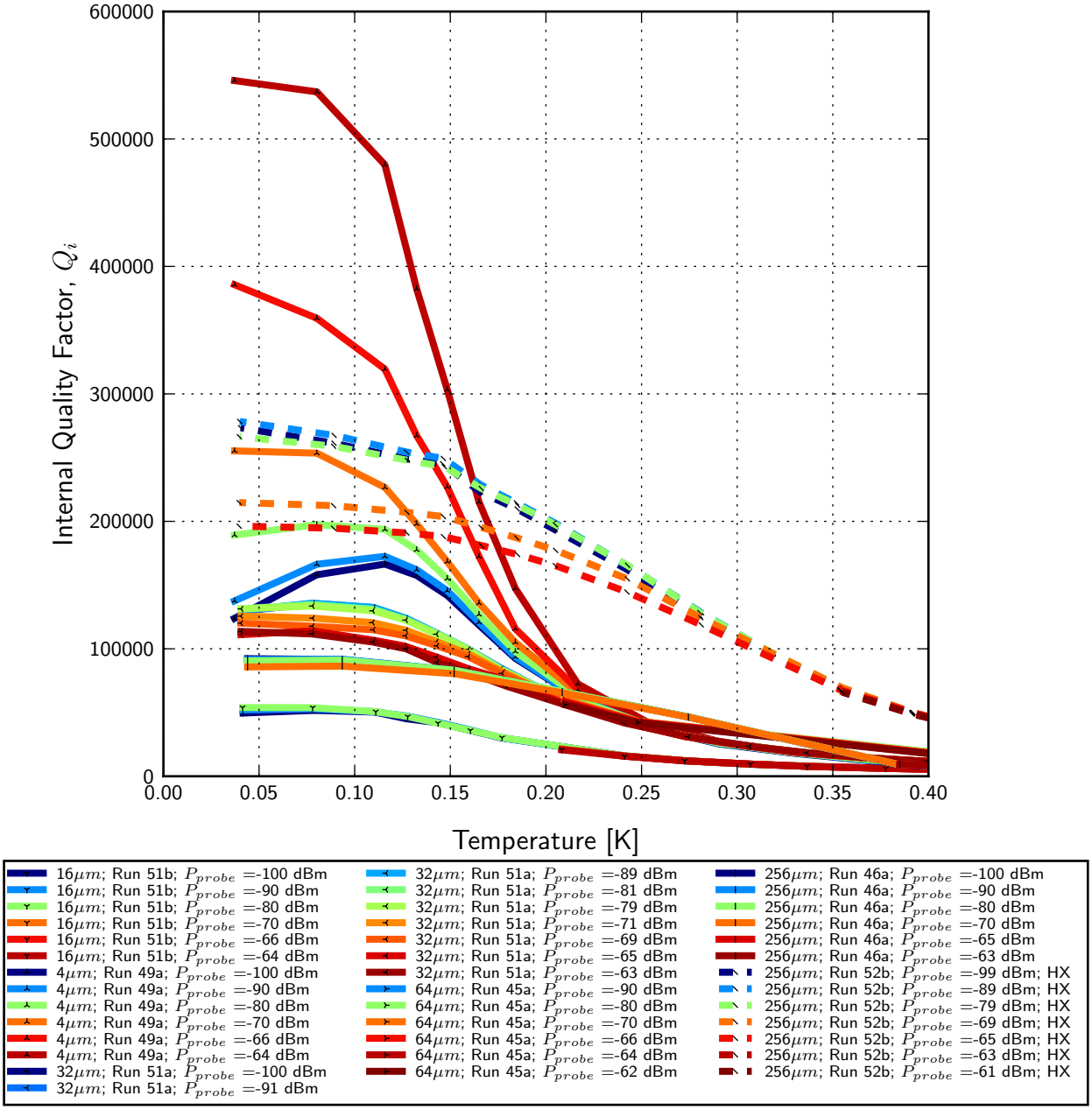


Figure 6.10: Internal quality factor versus probe power and temperature. The parameter generally decreases with temperature, as expected. Data run, microstrip trace (µm) and ground plane thickness (nm) are specified in legend. Abbreviations are: CB – copper box (otherwise niobium box), TQ – under-torqued press, HX – hexagonal mesh ground plane.

The internal quality factor behaves as expected with increasing temperature, Figure 6.10. It decreases as the conductor loss increases due to the increasing quasiparticle population.

The large power dependence in 49a, and to a lesser extent 52b, correspond to the failure of the linear fit at high powers, which we observed previously.

6.2 Nonlinear Data and Fitting

In order to extract the parameters that describe the nonlinear behavior of a resonator, we acquire transmission data, $S_{21}(f, P_{Probe})$ for each resonator over a wide range of probe powers, including low probe powers. As we saw in § 4.2, S_{21} depends on resonant frequency, f_0, and quality factors, e.g. Q_c and Q_{tl}, measured in the linear regime, at low power. At high power, the distortions to S_{21} arise from previously negligible terms which become appreciable. Accordingly we take the approach to simultaneously fit transmission data from low and high powers. The f_0, Q_c, Q_{tl} extracted from the linear regime are used as an initial guess for the values in the nonlinear fit, with the assumption that they will not turn out to be very different.

6.2.1 Least squares fit

The measured data, $S_{21}(f, P_{Probe})$, is fit to any of the nonlinear models in § 4.2 using a least squares fit. Just as in the linear resonator case, the data is conditioned in several ways prior to fitting. One, gain compression from the primary low noise amplifier and the room temperature amplifier is removed. Two, the frequency dependent electrical delay is removed. Three, the loop is normalized so that points far from the resonance lie on the unit circle. Four, points that are several bandwidths away from the resonance dip or that are outliers with respect to their nearest neighbors are removed. Five, the loops are rotated so that they are symmetric about the positive real axis. Lastly, variables are introduced that allow all the loops to be rotated and translated so that the fit loop is related to the measured loop as,

$$\hat{S}_{21}(f, P_{Probe})e^{i\varphi} - (a + ib) = S_{21}(f, P_{Probe}), \tag{6.6}$$

where a, b and φ are now fit variables and $\hat{S}_{21}$ is the fit.

A model transmission curve, $S_{21}(f, P_{Probe})$, is constructed using a model of nonlinearity. The fit is performed as a minimization of difference between the model loop and the measured and processed loop,

$$\min\left\{\sum_n \sum_m |S_{21}(f_m, P_n) - \hat{S}_{21}(f_m, P_n)|^2\right\}. \tag{6.7}$$

6.2.2 Determining the resonator amplitude

In order to construct $S_{21,Mod}(f, P_{Probe})$, one needs to know the amplitude inside the resonator. Each model of nonlinearity presented in § 4.2 has an equation relating the amplitude in the

resonator, x, to the probe amplitude $P_{Probe} = {}^{|ye^{i\theta_y}|^2}\!/_{2Z_1}$ of the form,

$$z_1|x|^2x + z_2x = z_3y \tag{6.8}$$

where x, y and z_n are complex numbers. To solve for the amplitude, multiply each side of the equation by its complex conjugate to obtain a cubic polynomial in $|x|^2 = v$ with real coefficients,

$$\begin{aligned} g(v) &= |z_1|^2v^3 + 2\Re[z_1z_2^*]v^2 + |z_2|^2v - |z_3|^2|y|^2 && \text{(6.9a)}\\ &= (v - v_1)(v - v_2)(v - v_3) && \text{(6.9b)}\\ &= 0. && \text{(6.9c)} \end{aligned}$$

The v_n are the roots of $g(v)$. Either one root will be real and the other two complex or all three will be real. Only the real roots correspond to physical resonator amplitudes, x_n. One can solve for the roots of $g(v)$ in several ways. One method is to use matrix analysis techniques (e.g. constructing the companion matrix of the polynomial and diagonalizing, [82, pp. 145-147]). Here, one may run into excessive computation times. A second method is to use a cubic formula (e.g. compute the reduced polynomial of $g(v)$ and the roots this polynomial are functions of its coefficients and are connected to the roots of $g(v)$ by a simple transformation [156, pp. 44-47]). The formula involves high roots and power of multi-term combinations of the coefficients of $g(v)$, so lose of precision during the calculation is an issue.

Another method is to notice that S_{21} is linearly related to one of the x_n by an equation that looks like

$$x_1 = \sqrt{v_1} = [S_{21} + z_a]\,\frac{yz_3}{z_b} \tag{6.10}$$

where z_a and z_b are readily obtained from the nonlinearity model[2]. Exactly which x_n is determined by the direction of frequency sweep used to acquire S_{21}. If one takes this approach to finding the amplitude, then one can find the other two amplitude by using the quadratic formula on the polynomial $f(v)$,

$$\begin{aligned} f(v) &= \frac{g(v)}{(v - v_1)} && \text{(6.12a)}\\ &= |z_1|^2v^2 + (|z_1|^2v_1 + 2\Re[z_1z_2^*])v + (|z_1|^2v_1^2 + 2\Re[z_1z_2^*]v_1 + |z_2|^2) && \text{(6.12b)}\\ &= 0, && \text{(6.12c)} \end{aligned}$$

[2]For example, in the model of § 4.2.2, comparison of Equation 4.62 and Equation 4.64a gives,

$$V_3^- = \left[S_{21} + \frac{e^{2i\phi_{13}} - 1}{2}\right] e^{-i\phi_{13}}\sqrt{\frac{Z_3}{Z_1}}\sqrt{\frac{Q_c}{\pi}}V_1^+ \tag{6.11}$$

and we get,

$$v_2 = T_1 + T_2 \tag{6.13a}$$

$$v_3 = T_1 - T_2 \tag{6.13b}$$

$$T_1 = -\frac{\Re[z_1 z_2^*]}{|z_1|^2} - \frac{v_1}{2} \tag{6.13c}$$

$$T_2 = i\frac{\sqrt{4\Im[z_1 z_2^*]^2 + 3|z_1|^4 v_1^2 + 4|z_1|^2 \Re[z_1 z_2^*] v_1}}{2|z_1|^2} \tag{6.13d}$$

Both these roots are only physical when they are real.

On the other hand, if one take the matrix approach, approach of cubic formula, then one gets all three solutions at once which is helpful but not necessary for the minimization, Equation 6.7.

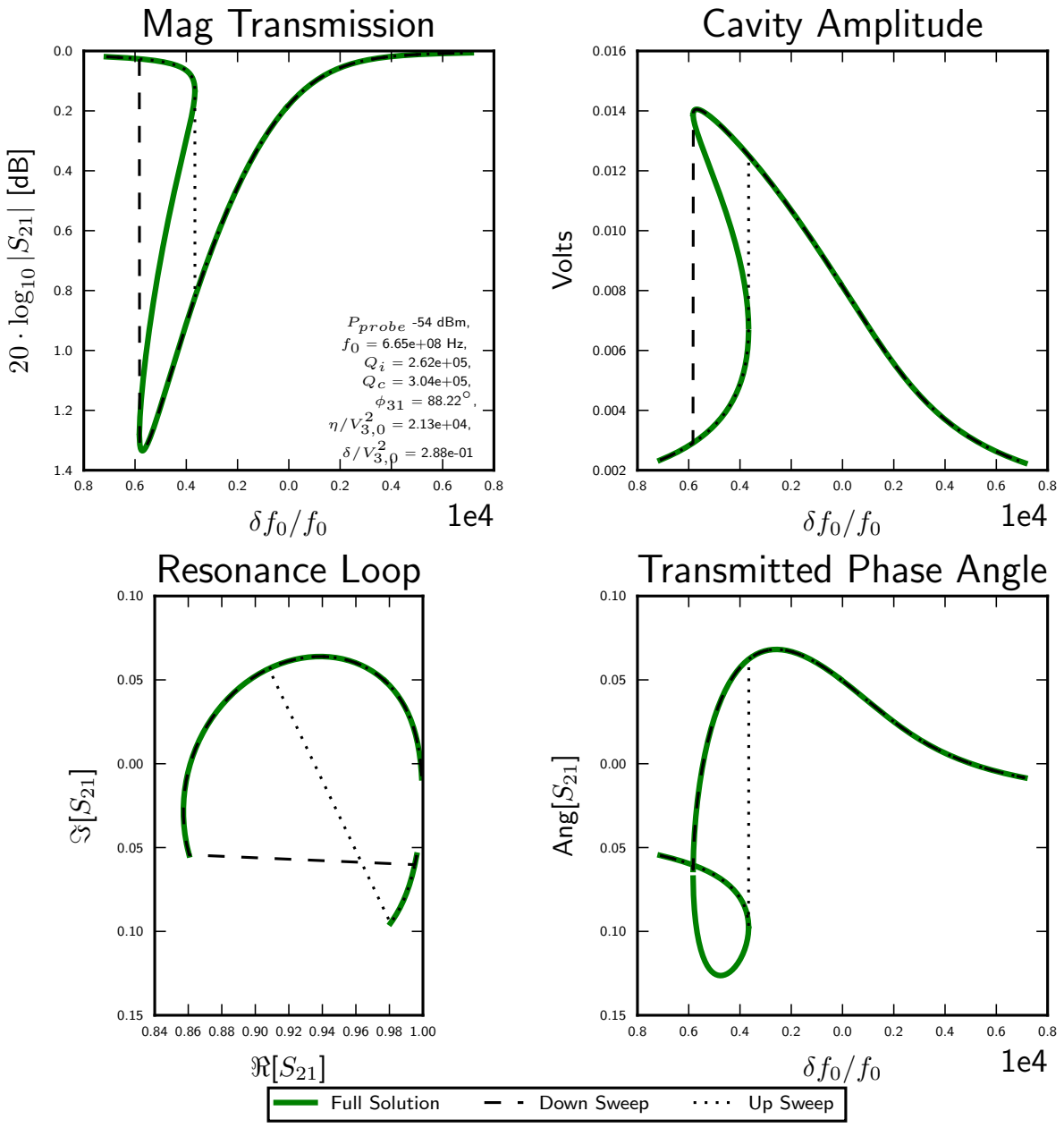


Figure 6.11: The power sweep for Run 45a, a 64 µm resonator, is fit to extract the nonlinear parameters, which are called out in the upper left plot. Additional electrical parameters are obtained from Table 5.1. The nonlinear model equations, described in § 4.2.2, are solved for $P_{probe} = -54$ dBm using the method described in the current section. Dotted and dashed lines indicate the direction of the frequency sweep. The data presented throughout this chapter uses an upward frequency sweep, unless explicitly stated otherwise.

There have been other publications of nonlinear resonance fitting, which should be acknowledged: [173, 32, 132, 182].

6.3 Nonlinear Data

Now we analyze the power sweep data presented in § 6.1.4.1 using the nonlinear fitting procedure. In total there are six independent fit variables for the nonlinear fit: $\eta/V_{3,0}^2$, $\delta/V_{3,0}^2$, ϕ_{31}, f_0, Q_i, Q_c and the geometrical transformation variables of Equation 6.6, a, b, φ. This excludes the cable delay τ, and the outer loop radius R and the resonance loop center vector z_c which were obtained from steps in the linear fit procedure and used to condition the raw data for the nonlinear fitting.

Most of the power sweep data sets can be successfully fit using the nonlinear fitting algorithm. The fit fails or performs poorly, however, on those sweeps in which the fractional frequency shift (Figure 6.8) or the quality factor do not decrease monotonically. Runs 51b and 52b are examples of this. The nonlinear model only allows monotonicity in these parameters, so it is no surprise that they do not fit well. Unfortunately, at the time of this writing, attempts to implement a χ^2 fit remain unsuccessful. The minimization will not converge using the χ^2 objective function.

6.3.0.1 Nonlinear Fit to power sweep

Run 45a serves as an example of a qualitatively good nonlinear fit, Figure 6.12. One notices that the fit becomes less accurate as the resonator becomes increasingly nonlinear, especially where there are flat sections of the loop. We claim this is less an indication of incorrect model, and more an indication of the instability of the resonance in these areas. Repeated scans of a nonlinear resonator at the same power would show considerable jitter in these areas. The fits have a similar jitter in these areas.

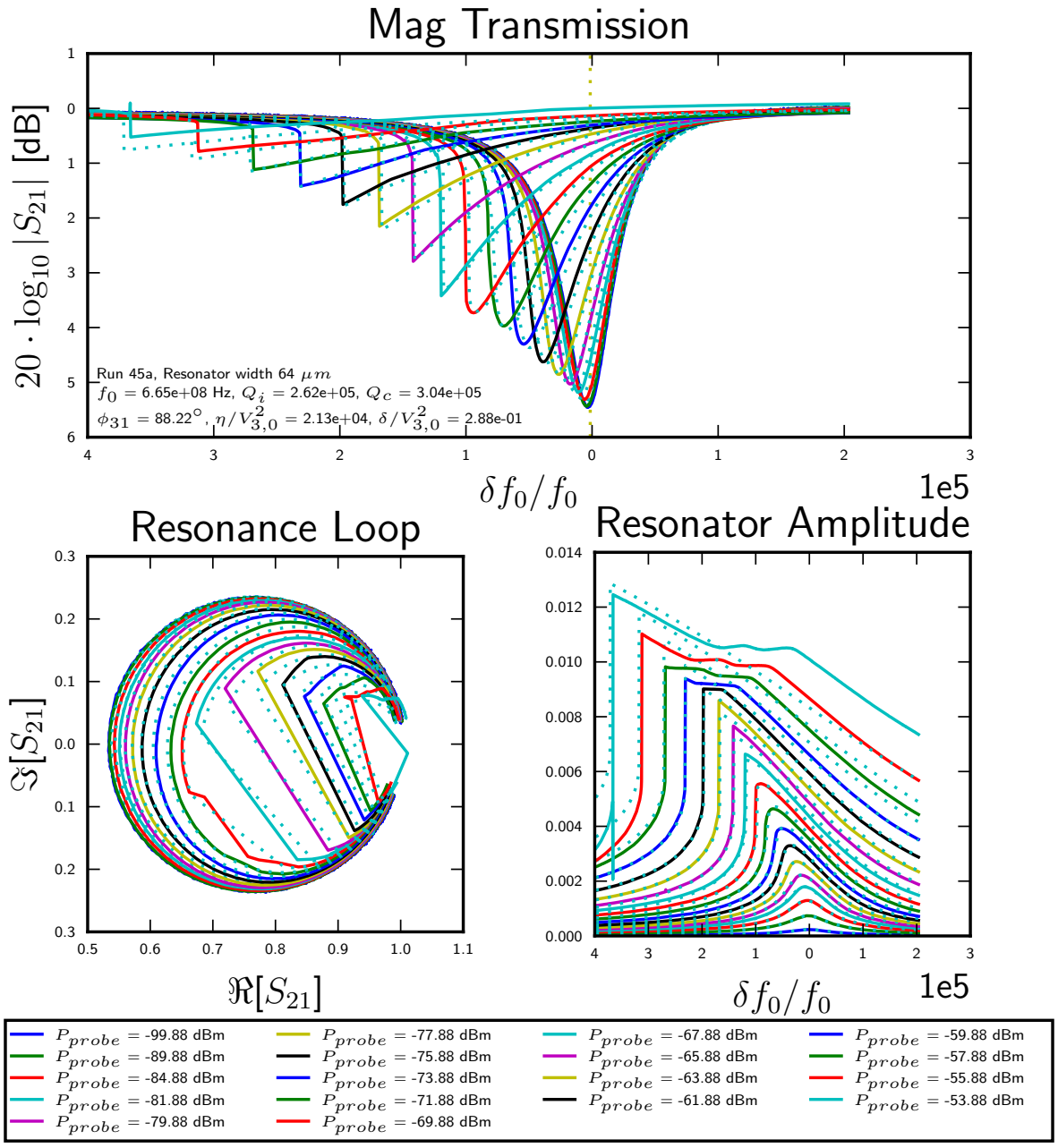


Figure 6.12: Fit to power sweep of Run 45a, a 64 µm resonator, as it becomes nonlinear. Dotted lines indicate the fit and the legend calls out the probe powers. Transmission magnitude (top), resonance loop (lower left) and the amplitude at the input of the resonator (right) are plotted. This is the same run from which the data in Figure 6.1 came. $^{\delta f_0}/_{f_0}$ uses f_0 for the lowest power resonator as fit with the stepwise procedure for linear resonators. The vertical yellow dotted line is drawn at the resonant frequency determined by the nonlinear fit.

The nonlinear fit parameters for other runs are presented in Table 6.2. No dependence on width is obvious. Perhaps this suggests that the nonlinearity in these devices comes about from something that is not controlled for in the experiment. Maybe it is the microstructure of the superconducting films, or vortex formation. Since the nonlinear model accords a single value for the resonant frequency, quality factors, and nonlinear parameters η and δ, it is convenient to compare them to simulated and estimated values. For example, we notice that the coupling quality factor values obtained from the nonlinear fits are consistent with those obtained at low power in the linear fit data, Figure 6.7, but are very different from those obtained from simulation data, Table 5.2. Since the coupling quality factor is strongly dependent on geometry, this suggests that geometries of the actual devices are different from the intended and simulated geometries. There are probably misalignments in the lithography and height variations in the pillars. This is also true for the resonant frequency and internal quality factor, whose differences with the estimated and simulated values are well beyond those expected due to superconductivity.

Lastly, we point out that runs for which the η parameter is negative are also those for which the internal quality factor, as fit by the linear model, increases monotonically. We have no explanation as to why η is negative, for these narrowest resonators.

Run	Width	f_0	Q_i	Q_c	ϕ_{31}	$\eta/V_{3,0}^2$	$\delta/V_{3,0}^2$
	[μm]	[MHz]	[10^3]	[10^3]	[deg]	[10^3]	[10^{-3}]
49a	4	642	156	316	89.25	−0.998	44.4
48a	8	737	93.9	171	92.08	−7.54	503
51b	16	703	52.4	51.6	90.33	6.38	1090
51a	32	713	130	588	90.45	7.60	394
45a	64	665	262	304	88.22	21.3	288
44a	128	663	86.6	162	90.89	10.6	370
46a[a]	256	689	92.2	292	89.71	20.4	234
46a[b]	256	689	115	304	90.13	50.4	186

[a] Low power data for Run 46a.
[b] High power data for Run 46a.

Table 6.2: Parameters extracted from nonlinear fitting. For most fits, the data used has down sampled to between 15 and 30 powers. In some cases, highly nonlinear loops have been excluded from the fit.

6.3.0.2 Simulated Data

As evidence for previous claims that certain linear parameter fit behavior with increasing probe power might be due to the failure of the linear fit model, we have done the following.

We have taken the nonlinear fit parameters for Runs 45a and 48a and plugged them into the nonlinear model to generate false S_{21} data for same probe powers used to measure these devices. We then fit the false data using the linear fitting models. Doing this, we recover similar quality features in the linear fit parameter behavior with increasing power. Figure 6.13 and Figure 6.14 plot internal and coupling quality factors against probe power. Simulated data for Run 48a, chosen for its negative η, reproduces the increasing quality factor with probe power in the stepwise linear fit. Simulated data for Run 45a, chosen for its positive η and its reoccurring use as an example in this chapter, reproduces the monotonic decrease in internal quality factor with probe power. Simulated data for both runs reproduce the upturn in coupling quality factor at high power preceded by a relatively constant value.

Attributions

The work presenting in this chapter was done by myself alone.

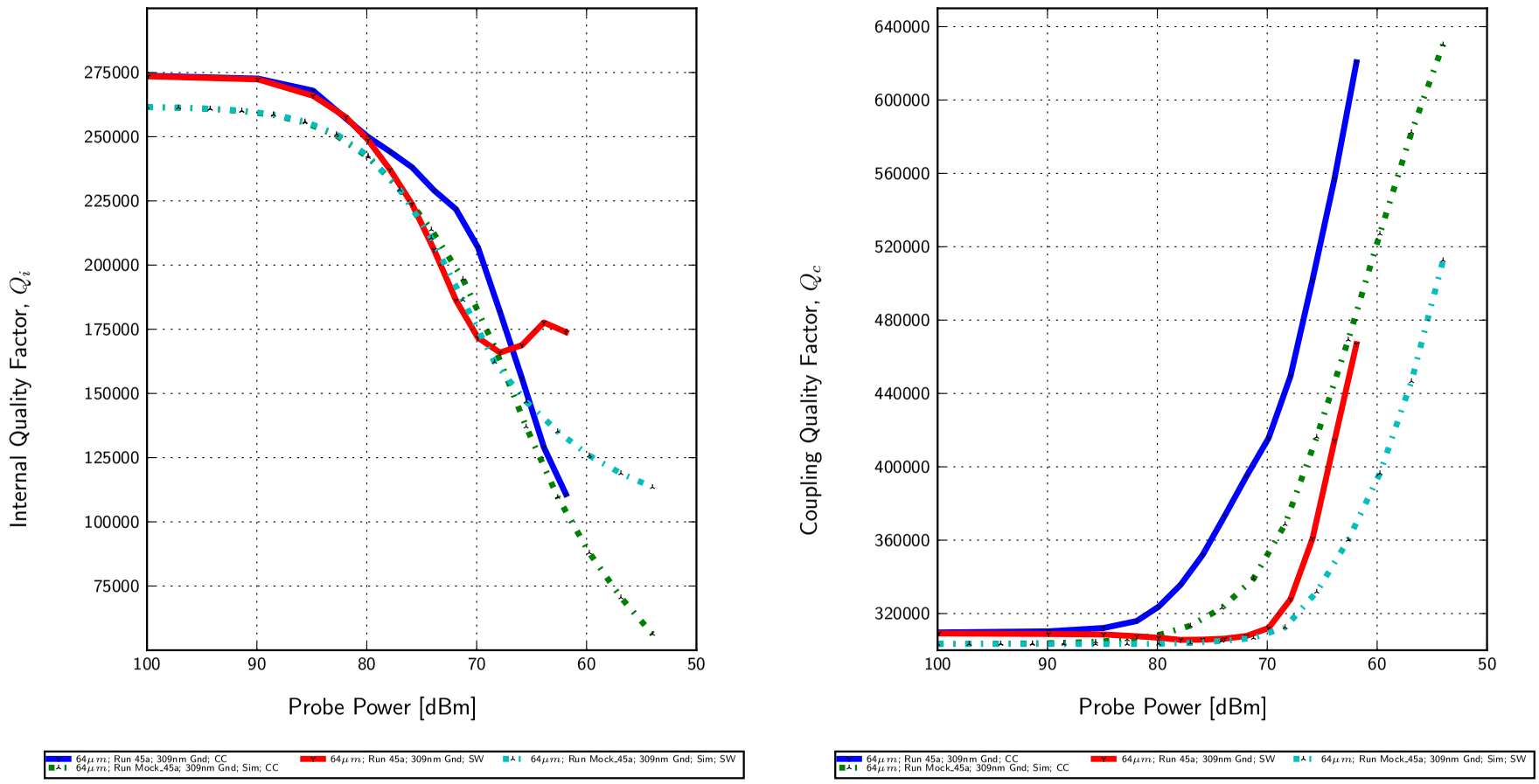


Figure 6.13: Data simulated using nonlinear resonator model of § 4.2.2 using the nonlinear parameters fitted from Run 45a (see Table 6.2 and Figure 6.12). Internal quality factor (left) and coupling quality factor versus probe power. The simulated data reproduces behavior observed in linear fits. Data run, microstrip trace (µm) and ground plane thickness (nm) are specified in legend. CC indicates concurrent fit and SW indicated stepwise fit.

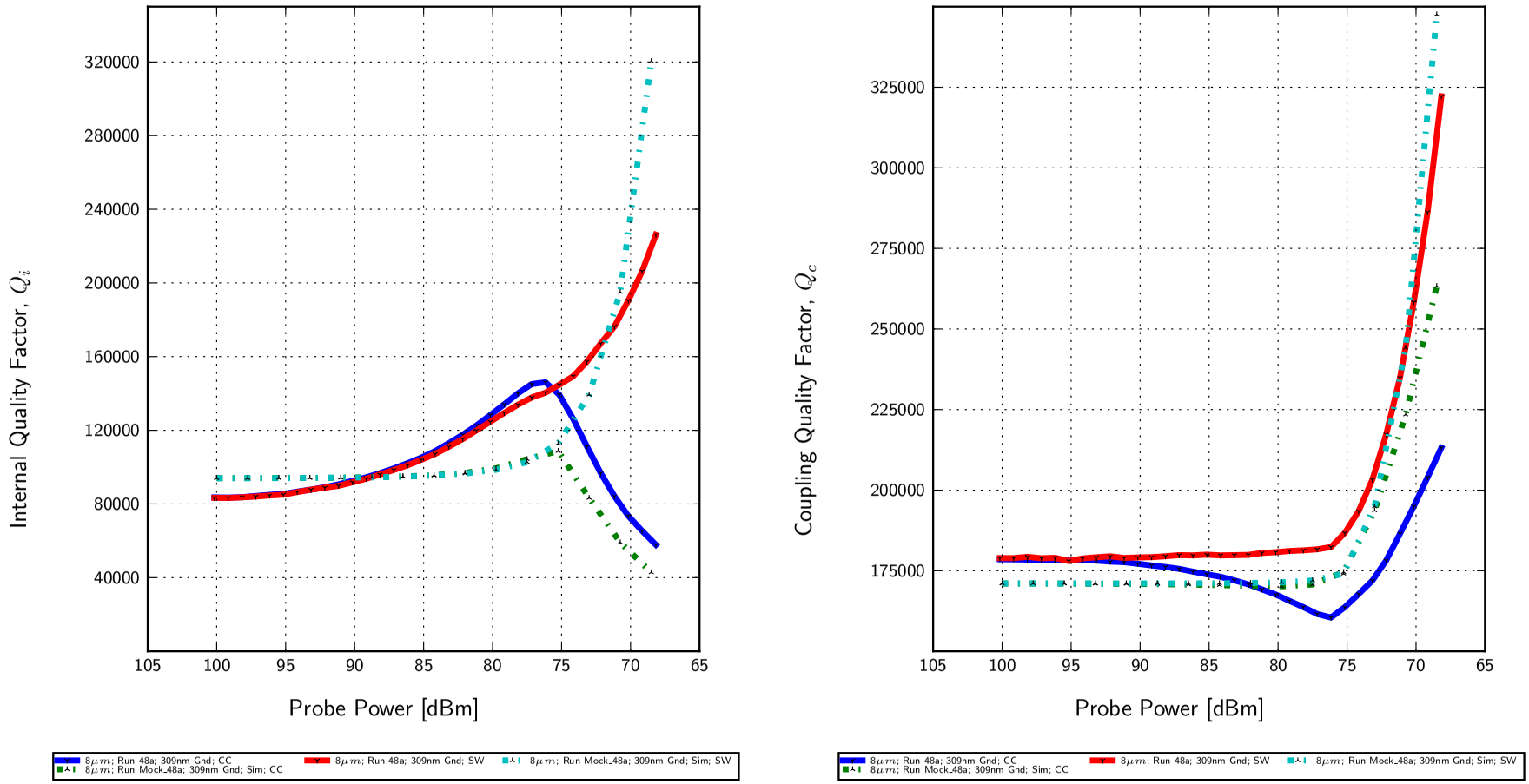


Figure 6.14: Data simulated using nonlinear resonator model of § 4.2.2 using the nonlinear parameters fitted from Run 48a (see Table 6.2. Internal quality factor (left) and coupling quality factor versus probe power. The simulated data reproduces behavior observed in linear fits. Data run, microstrip trace (µm) and ground plane thickness (nm) are specified in legend. CC indicates concurrent fit and SW indicated stepwise fit.

Chapter 7

Cryogenic methods

In service to CDMS SNOLAB research and design efforts, I have contributed work toward development of cold hardware including, tower, cabling, and interconnect design. In this chapter we explain design constraints, methods and present data collected to aid in cold hardware design. In order to improve their sensitivity to dark matter, the CDMS collaboration is modifying its detectors and the infrastructure associated with their operation, as well as changing the location of the experiment. The SNOLAB experiment also implements improvements to the data acquisition, calibration, and radioactive background controls, but this will not be our focus here. Detector modifications include better charge and phonon sensor design, an increase in detector size, and an increase in the number of phonon chan-

	System		Per Phonon Cable/Detector	
Stage	T [K]	Heat Load [W]	Components	Dissipation [W]
SH	50	137		
LH	4–5	1	4 HEMT	$400 \cdot 10^{-6}$ [b]
			500 MΩ feedback resistors	
ST	1–0.7	$6.7 \cdot 10^{-3}$	12 SQUID Arrays	$1.2 \cdot 10^{-6}$
			5 kΩ SQUID feedback resistors	
CP	0.150–0.225	$175 \cdot 10^{-6}$	12 5 mΩ TES Shunt resistors	$85 \cdot 10^{-9}$
MC	0.015–0.040[a]	$1.85 \cdot 10^{-6}$	1 detector	
			12 TES[c]	$15.6 \cdot 10^{-9}$

[a] 40 mK is max and 15–20 mK is optimal.
[b] $100 \cdot 10^{-6}$ W per HEMT, down from $5 \cdot 10^{-3}$ W per JFET.
[c] Transition Edge Sensor

Table 7.1: A few cryogenic and electrical specifications for the SuperCDMS SNOLAB experiment. System wide figures assume a 48 tower payload, though the first iteration will only have 8 towers. Per phonon cable/detector figures are of particular importance to this presentation of phonon cable design and fabrication.

nels. Noise on the phonon and charge readout circuits is reduced by use of an improved Superconducting Quantum Interference Device (SQUID) array and 4 K High Electron Mobility Transistor (HEMT) charge amplifier. A reduction in the base operation temperature of the cryostat, enables larger phonon signals. The HEMTs also have lower power dissipation in comparison to the Field Effect Transistor (FET)s they are replacing, facilitating cryogenic operations. To reduce background caused by cosmic ray strikes in the vicinity of the detectors, the location is changed from the Soudan mine in Minnesota (2090 m.w.e) to the considerably deeper SNOLAB facility in Sudbury, Canada (6010 m.w.e). Though the SNOLAB experiment is initially outfitted with 8 towers, the cryostat and the tower stationing compartment, the SNOBOX, is built to accommodate up to 48 towers in both physical space and cooling capacity. All these changes come together to necessitate a redesign of the CDMS tower and its associated detector readout cabling. All materials used in the construction of these components are required to have low radioactivity in order to achieve the background target of the experiment. CDMS utilizes the Soudan Low Background Counting Facility ([4]) to measure radioactivity. Depending on the component, additional requirements are placed on the materials such as, flexibility or rigidity, electrical and thermal conductivity. The tower and the cabling each provide connectivity between different temperature stages of the cryostat so the thermal conductivity of the materials used in their construction is great importance. For this reason, we developed the capability to measure sub-Kelvin thermal conductivities of various materials of interest in our UC Berkeley 75 µW dilution refrigerator. What follows is a presentation of the relevant properties for materials that are potentially useful in our CDMS experiment and other low background low temperature experiments. Original measurements are presented as well as other data intended to aid in material selection for this and other experiments.

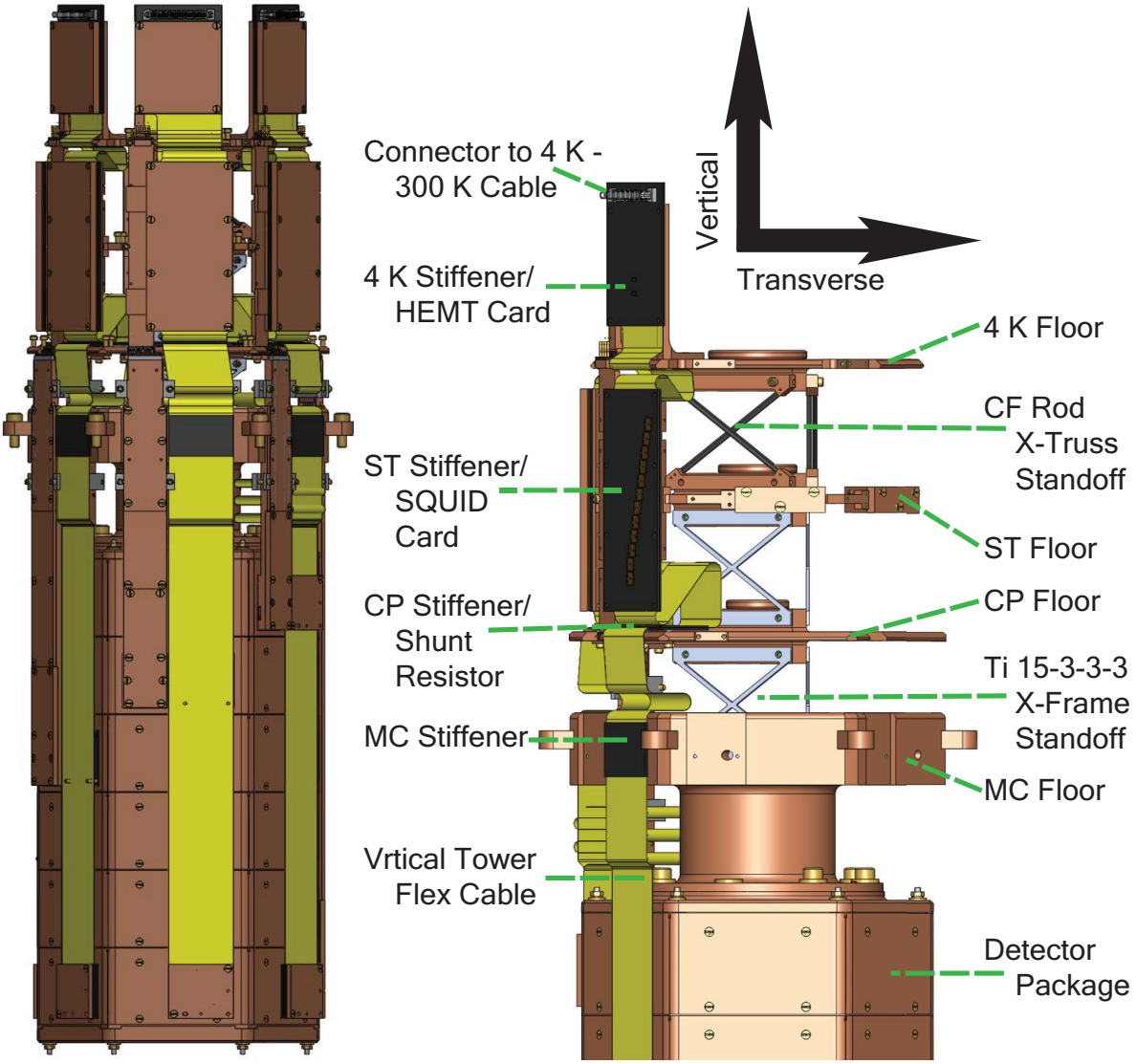


Figure 7.1: The conceptual design of the SuperCDMS SNOLAB tower. On the left, we have the full tower and detector stack assembly. Each tower holds six detectors, which are enclosed on housing packages. One notices the vertical tower flex cables which carry the signaling wires for the phonon channel, LEDs for detector neutralization, thermometry, and several charge channel bias wires. The gate wires which carry the charge signals are routed from the detectors to the HEMT Card through two (upper and lower) vacuum coaxes which can be seen running parallel to the flex cable. On the right, we zoom on on the tower, after removing four of the six phonon and charge cabling. The stiffened sections of the phonon cable are reveled by removing their copper coverings. One see that cold plate (CP) stiffener lies flat on the cold plat floor, making it difficult to see. Carbon fiber (CF) and Ti 15-3-3-3 X-frame standoffs separate the tower floors, which are abbreviated as ST – still, and MC – mixing chamber. The tower's axial and transverse directions are indicated.

7.1 Materials selection

We choose a few major material property areas in which to present data for materials of interest in low temperature, low background experiments.

7.1.1 Thermal conductivity

7.1.1.1 High temperatures

For temperatures above 4 K there is wealth of thermal conductivity data available in the literature. It was not necessary for us to make original thermal conductivity measurements in this range.

One lesson learned in dealing with thermal conductivities of metals in this temperature range is that the Wiedemann-Franz-Lorenz law (1872, [65]) is not accurate. It is approximately correct for some metals in some temperature intervals, but accurate calculations of thermal power flow should not be based on this law. Let us recall that the Wiedemann-Franz-Lorenz law assumes that the conduction electrons of a metal are a free electron gas obeying Maxwell-Boltzmann statistics. Whereas, in reality, the electrons have complicated interactions with the (non-ideal) lattice and should obey Fermi-Dirac statistics. The law is a relationship between the metals the temperature, T, the thermal conductivity $\kappa(T)$ and the electrical resistivity, $\rho(T)$,

$$\frac{\kappa(T)\rho(T)}{T} = L_0 = \frac{\pi^2}{3}\left(\frac{k_B}{e}\right)^2 = 2.44 \cdot 10^{-8}\,\mathrm{W\,\Omega\,K^{-2}}. \tag{7.1}$$

L_0 is the Lorenz number and it is suppose to be the same for different metals and temperatures. In Figure 7.2, we plot the Lorenz number for a few common metals. For copper in particular, the Lorenz number–just like the thermal conductivity–varies widely with temperature between specimens of different purity and microstructure (e.g. grain size and work condition). The type of impurity also impacts L_0 and $\kappa(T)$.

Unfortunately many times, the resistivity $\rho(T)$ is usually least sensitive to purity and microstructure variations between specimens. Perhaps consequently, $\rho(T)$ can be easier to find in the literature than $\kappa(T)$. Our lesson learned is to make the effort to find the thermal conductivity instead of using $\rho(T)$ and Wiedemann-Franz-Lorenz when making heat transfer calculations.

7.1.1.2 Low temperatures

Low temperature (<5 K) thermal conductivity data for materials of potential use in the SNOLAB experiment were obtained from extensive literature research and, when necessary, original laboratory measurement. Appendix C presents the measurement techniques and error analysis and thermal conductivity data for all materials we measured ourselves. Additional material specific information is also provided and parameter fit coefficients. In this

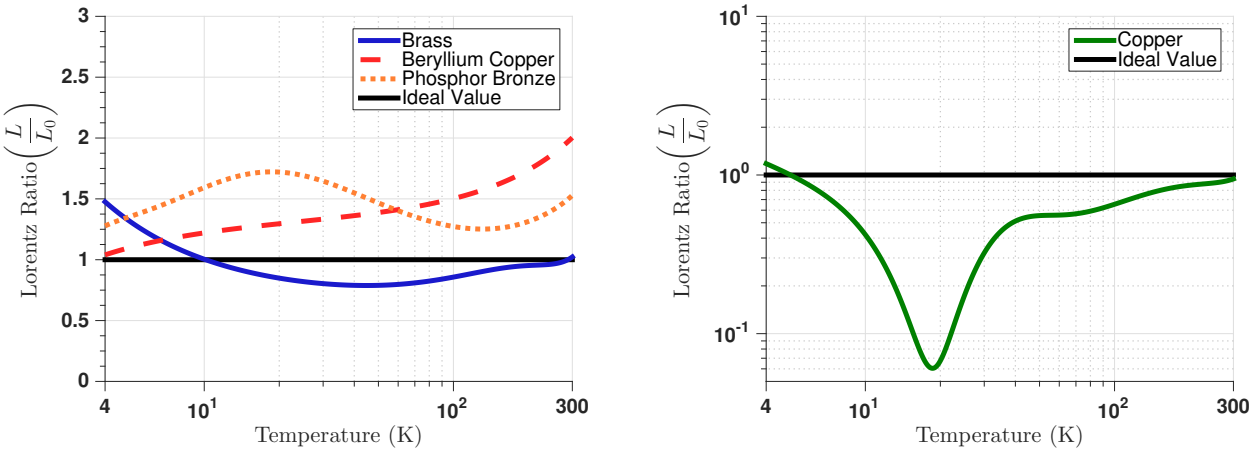


Figure 7.2: Temperature and material dependence of Lorenz number used in the Wiedemann-Franz-Lorenz law. Ideally the number should be temperature and material independent. However we observe significant temperature variation. This underscored the necessity to use measured values of thermal conductivity when making heat conduction calculations. Copper is presented by itself due to larger temperature variation in its Lorenz number. Data from [91]

section thermal conductivity data of similar materials is plotted to provide an understanding of how the materials we measured compare to other, sometimes more familiar, materials.

7.1.1.2.1 Graphite-like materials The SuperCDMS Soudan tower utilized graphite, Grade UF-4S from Mersen, tubes to provide low thermal conductivity rigid connections between temperature stages. Graphite's exceptionally low thermal expansion make it an attractive choice for standoffs that maintain critical dimensions, another reason for its use in the tower. We measured another Mersen graphite (grade 2020), as well as a carbon fiber product ("graphlite") and present thermal conductivity data in Figure 7.3.

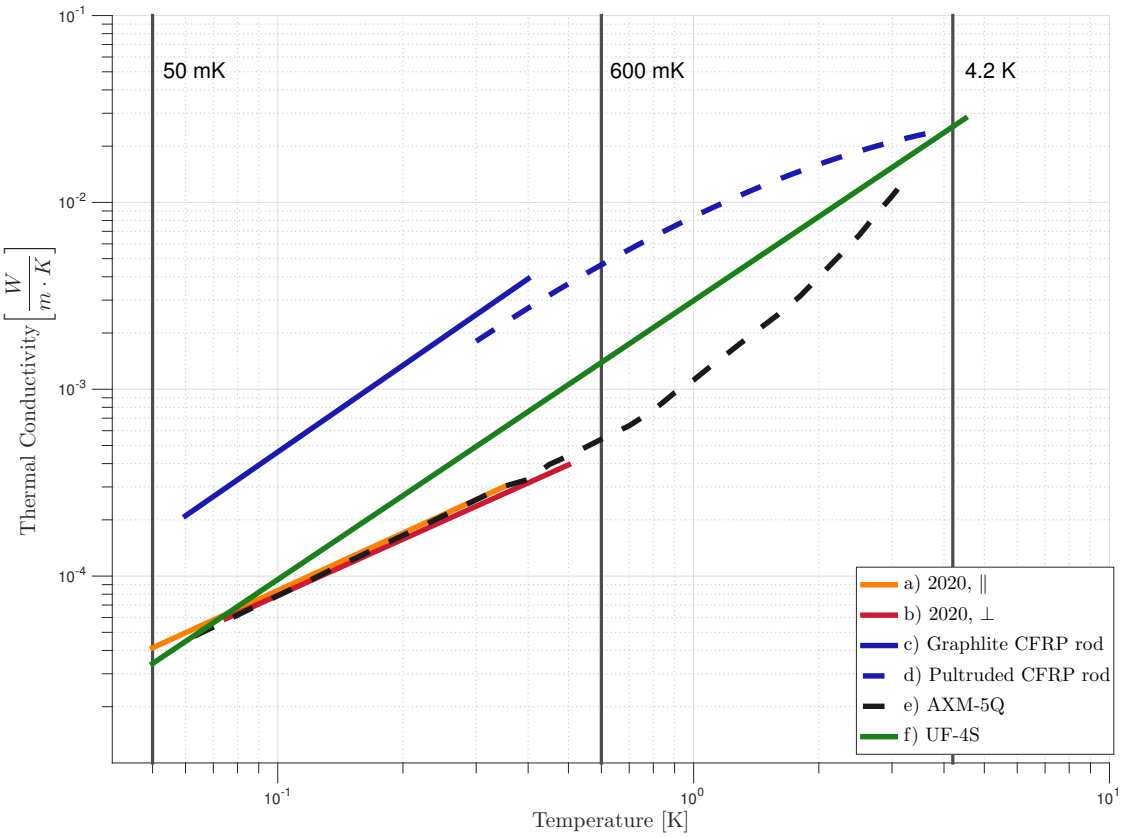


Figure 7.3: Thermal conductivity of graphite-like materials. Data source, additional sample information and the direction of heat flow (when known) are as follows : *a)* original data [5], ∥ to grain structure in bulk rod sample material manufactured by the Mersen Corporation; *b)* original data [5, 95], ⊥ to grain structure in bulk rod sample material manufactured by the Mersen Corporation; *c)* original data [5, 95], ∥ parallel to the axis of rod sample, carbon fibers aligned to this axis on average and made by Avia Sport Composites; *d)* from Runyan et al. [158], ∥ parallel to the axis of rod sample, carbon fibers aligned to this axis in average; *e)* from Woodcraft at al [195], industrial grade petroleum coke based fine-grained isotropic moulded graphite, graphitized at 2500 °C by the Poco Corporation, and *f)* from Leman at al. [110] an unpublished CDMS internal report, ∥ to axis of tubular sample from material manufactured by the Mersen Corporation

7.1.1.2.2 Kapton-like materials Kapton is a polyimide based film developed and manufactured by DuPont. It and cirlex, kapton in thick sheet format, were also used in the SuperCDMS Soudan experiment for in flexible cable, tower wiring heatsinks, detector crystal clamps, cold hardware circuit boards. Polyimides are generally attractive for their thermal

stability (including low coefficient of thermal expansion (CTE)), wear and chemical resistance, and dielectric and mechanical strength. Our measurements are in good agreement with others available in the literature. As a polymer, kapton contains long molecules. The film manufacturing process imparts an orientation to these molecules both in the plane of the film–DuPont distinguishes between the machine direction in the transverse direction–and perpendicular to the plane of the film. We expect that, when the film products are the same, differences in the conductivities measured here and elsewhere in the literature are due, in part, to the molecular orientation of the samples measured with respect to the direction of the heat flowing through them. In Figure 7.4, we present thermal conductivity data for kapton-like materials indicating the direction of hear flow when that information is available.

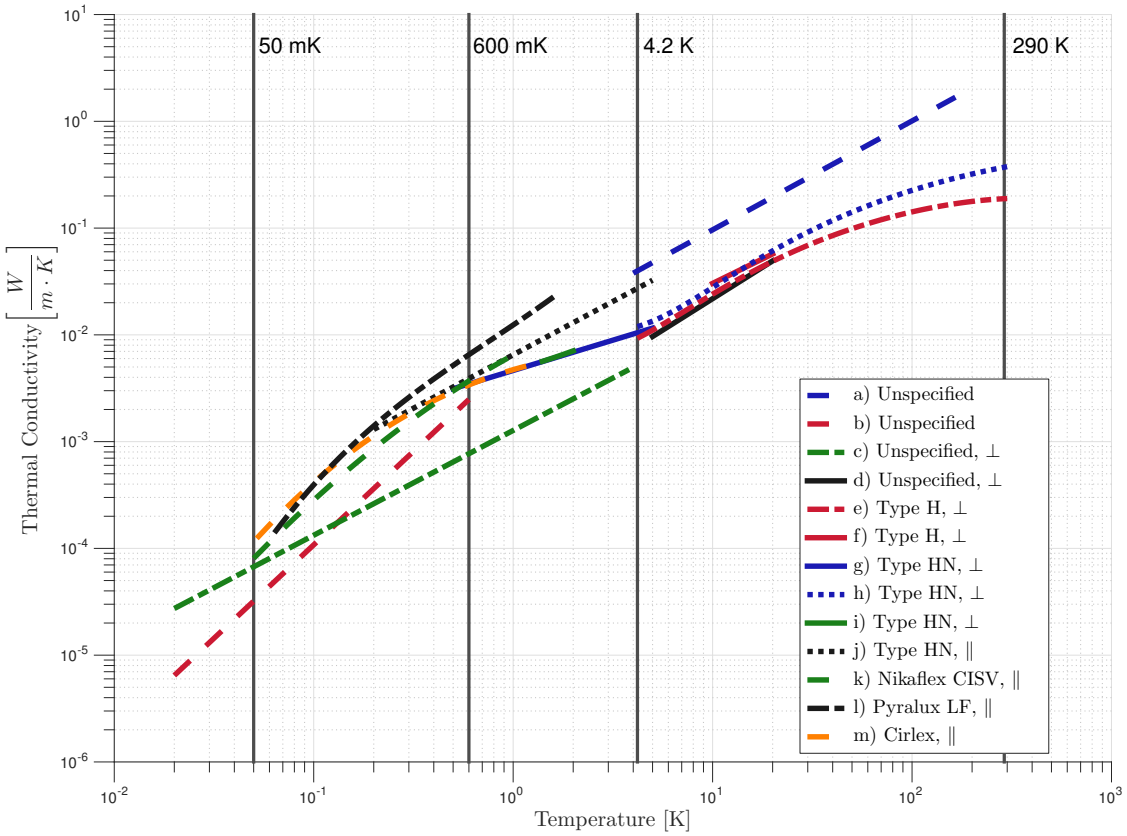


Figure 7.4: Thermal conductivity of polyimide "Kapton" laminates. Kapton is a sheet form of polyimide polymer made by Dupont. These samples are thin sheets. When indicated, ⊥ means that heat was made to flow perpendicular to the face of sheet (usually a stack of sheets) and ‖ means that the heat was made to flow parallel to the face of the sheet. Data sources and additional sample information (when known) are as follows : *a)* from Akerib [18] an unpublished CDMS internal report, unspecified kapton type; *b)* from Akerib [18] an unpublished CDMS internal report, unspecified kapton type; *c)* from Radebaugh et al. [148], unspecified kapton type; *d)* from Wipf et al. [193], unspecified kapton type; *e)* from Rule et al. [157]; *f)* from Yokoyama et al. [198]; *g)* from Lawrence et al. [107]; *h)* from Rule et al [157]; *i)* from Baudouy et al. [26]; *j)* from Barucci et al. [24]; *k)* original data [5, 95]; *l)* original data [6], and *m)* original data [6]

7.1.1.2.3 Vespel-like materials Vespel is also polyimide-based bulk material formed by molding (e.g. isostatic or compression) for basic stock shapes (e.g. plates, rods, tubes) or directly molded to custom shapes. Its shares the attractive properties named for Kapton, and is in wide use in aerospace industry and for cryogenic applications. Grades are available with

additives, such as graphite and lubricants for certain commercial applications, and we find that the additives profoundly affect the thermal conductivity of those grades. Dupont has developed a family of enhanced vespel products, the vespel SCP family, which improve upon the thermal stability, chemical and wear resistance, and strength of its vespel descendants, at lower specific gravity and higher stiffness. We find that the SCP products have lower thermal conductivity and radioactivity than their SP counterparts. Unfortunately, all vespel products are relatively expensive. Thermal conductivity data for vespel-like materials are presented in Figure 7.5

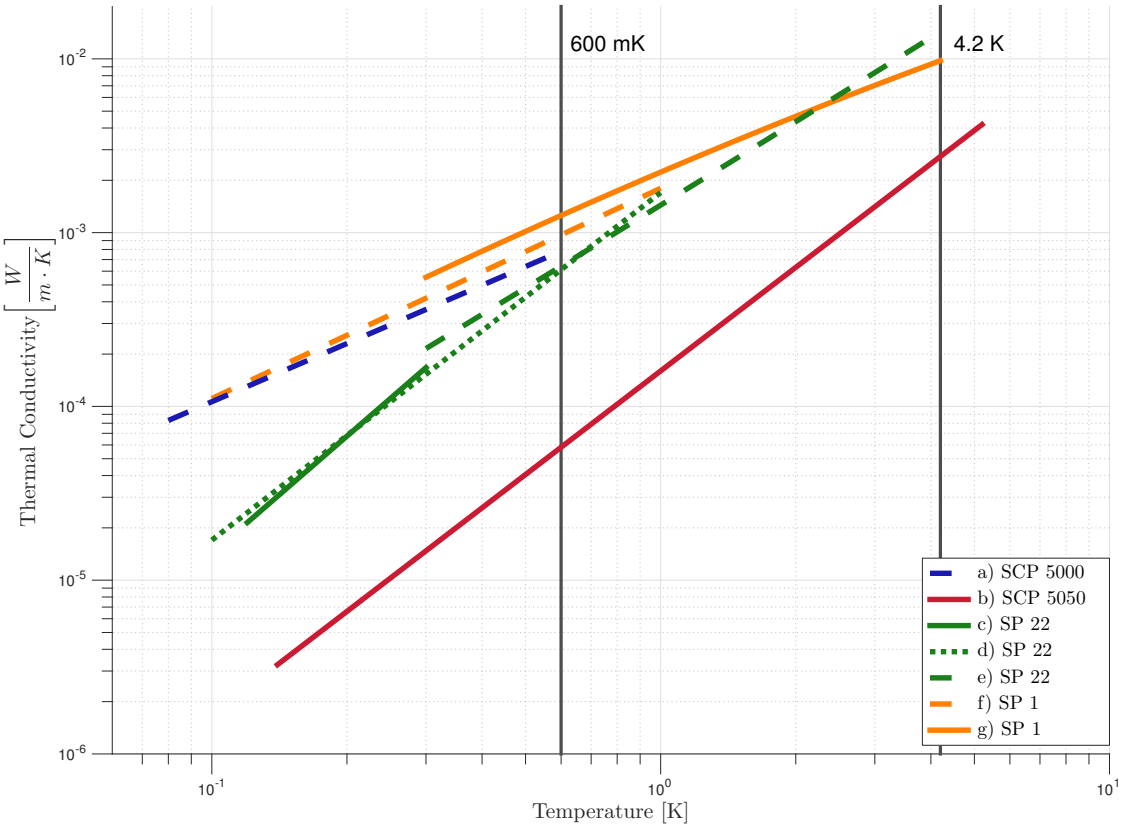


Figure 7.5: Thermal conductivity of vespel-like materials. Vespel is a bulk solid form of polyimide polymer made by DuPont. Data source, additional sample information and the direction of heat flow (when known) are as follows : *a)* original data [5, 95], ∥ parallel to the axis of rod sample, unfilled polymer; *b)* original data [5, 95], ∥ parallel to the axis of rod sample, proprietary filler composition; *c)* original data [5, 95], ∥ parallel to the axis of rod sample, 40 wt% graphite filler; *d)* data from Locatelli et al. [113], 40 wt% graphite filler; *e)* from Runyan et al. [158], ∥ parallel to the axis of rod sample, 40 wt% graphite filler; *f)* data from Locatelli et al. [113], base polyimide resin, and *g)* from Runyan et al. [158], ∥ parallel to the axis of rod sample, base polyimide resin

7.1.1.2.4 Titanium alloys Depending on the alloying ingredients, titanium alloys offer the lowest thermal conductivities of metallic materials, superconductivity, the highest tensile strength to mass density ratios available in commercial materials, superelasticity or shape memory and relatively low radioactivity. The availability of these alloys is increasing due to their usefulness in the defense and areospace industries–for the case of pate and strip alloys such as Ti 6-4 and Ti 15-3-3-3; the medical imaging (e.g. MRIs) and big science (e.g.

the LHC) industries–for the case of Nb-Ti; the medical device and eyewear industries–for the case of Ni-Ti. When used as cryogenic support materials, attention must be given to the crack tolerance of these alloys [153]. We present thermal conductivity data for titanium alloys in Figure 7.6.

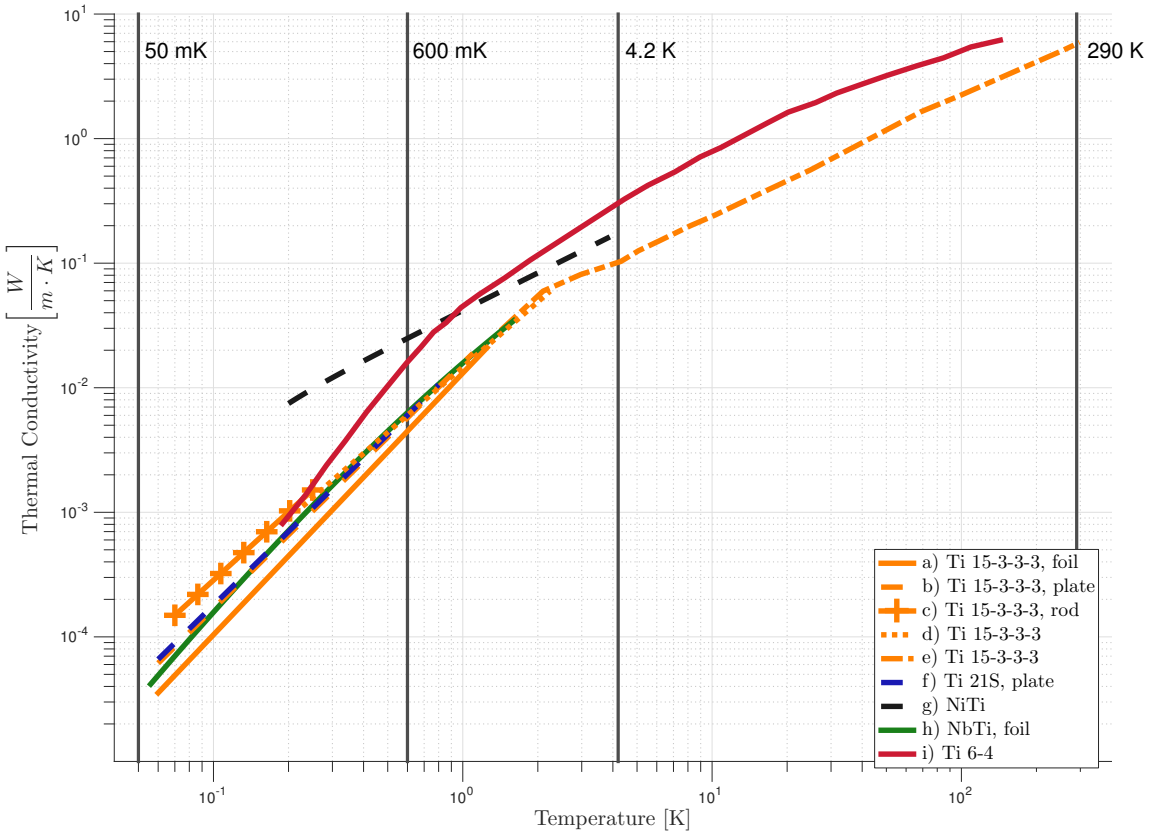


Figure 7.6: Thermal conductivity of selected titanium alloys. Data source, additional sample information and the direction of heat flow (when known) are as follows : *a)* original data [5, 95], ‖ to face of foil sample,; *b)* original data [5], ‖ to face of plate sample; *c)* original data [5], ‖ parallel to the axis of rod sample, annealed condition, sourced from China; *d)* unpublished data from Runyan and collaborators, annealed ingot manufactured in and sourced from China; *e)* from Tuttle et al. [179], sample was wire EDM cut from a 1.6 mm thick plate of TIMET manufactured material; *f)* original data [5], ‖ to plate; *g)* original data [6], ‖ to foil, and *h)* from Woofcraft et al. [196]

One notices that the titanium alloys can have exceptionally low thermal conductivities. The alloys with the low thermal conductivity are usually superconducting and have

a secondary phase precipitate in their solid solution. In searching for other low thermal conductivity alloys, it is advisable to look for these characteristics.

Functional fits for all of our thermal conductivity measurements are given in Table C.1

7.1.2 Radio purity

As a low background experiment, we must be certain that the materials we use in the experiment have very low levels of radio activity themselves. We therefore measure the radio activity of all the materials we consider using, and intend to use in the experiment. It turned out that our work with the tower standoff design and tower flex cable design required that numerous materials be counted, i.e. to determine their suitability for use in these components. Table 7.2 lists the materials we had counted as well as a few others of interest. Notice the activities of the tower standoff materials. Also notice the activities of the polymer thermoplastic materials. We had these counted because we needed to select a connector for connecting the phonon cable to the outside world. The vast majority of off the shelf connector body materials are made of liquid crystal polymer with some sort of filler material to provide strength and fracture toughness. It turns out these materials, in particular the filler materials, are usually very radio active[1]. These results encouraged us to pursue FuzzButton connectors (§ 8.3), which can be made of virtually any material of our choosing.

Another generally radio active class of material is stainless steel. However, the XENON100 dark matter experiment has found that alloy 316Ti has relatively low radioactivity [19]. Pre-nuclear steel, manufactured prior to the 1950s, is also of generally low activity.

[1]Reasons include: one, the industrial requirements for the chemical purity of polymers are not nearly as stringent as the radio purity requirements of a low background experiment; two, polymer synthesis may include inorganic (potassium) salts or metal catalysts which are radio active; three, borosilicate glass, known to be radio active, is a standard filler material. To get around the contamination of fillers, it is possible to use custom made fillers, for example low activity alumina. There are specialty companies, called compounders, that process custom materials for use as fillers.

Material	Contamination [mBq/kg]			
	^{238}U	^{232}Th	^{40}K	^{137}Cs
2020 Gr. (p)	3.89 ± 0.60	79.63 ± 4.97	4.10 ± 1.65	<0.20
AXM-5Q Gr. (u-p)	117.71 ± 47.41	217.13 ± 138.62	3.59 ± 3.28	<1.25
AXM-5Q Gr. (p)	0.93 ± 0.26	4.93 ± 0.70	0.96 ± 1.16	<0.28
ZXF-5Q Gr. (u-p)	159.731 ± 4.374	218.112 ± 5.256		
ZXF-5Q Gr. (p)	<1.880	3.05 ± 0.75	<1.761	<0.159
ACF-10Q Gr. (u-p)	406.771 ± 6.508	286.649 ± 5.731	35.900 ± 8.021	
UF-4S Gr. (old)	1.328 ± 2.176			
UF-4S Gr. (new, p)		52.03 ± 3.11		
Vespel SP-1	<16.77	5.39 ± 4.80	<13.09	<2.04
Vespel SP-22	48.38 ± 4.83	211.10 ± 8.99	7.82 ± 6.09	<2.47
Vespel SCP-5050	7.72 ± 0.88	9.95 ± 2.01	7.26 ± 2.18	0.48 ± 0.26
Kapton HN[a]	14.0 ± 1.0	1.4 ± 0.7	<5.4	
Cuflon[a]	<0.84	<0.19	48.0 ± 15.0	

[a] From [35]. Cuflon is a microwave circuit board material that is made of PTFE dielectric with copper cladding electroplated directly to it. A sodium etch process is used to condition bare PTFE film so the copper adhesion can occur; plated through holes are also possible. Unfortunately, Cuflon is limited to a maximum panel size of 16 inch × 22 inch. The use of the PTFE dielectric results in a very low loss tangent. Cuflon can withstand temperatures up to 225 °C for short durations. Kapton HN is as discussed previously.

Table 7.2: Activity of listed isotope for each sample. Missing figures are indication of low contamination levels which were either undetermined in the analysis or below detector sensitivity. Unless otherwise noted, counting occurred at the Soudan low background counting facility [4] and contamination levels were determined by GEANT4 Monte Carlo simulations. For graphite, (u-p) refers to unpurified samples, while (p) refers to samples which underwent the purification described in this section. Numbers preceded by < are upper limits, and are calculated at 90% CL. ^{60}Co contamination is noted when high. Notice the drastic effect purification has on radioactive contaminants in graphite as shown by AXM-5Q Gr. (p) and (u-p). Judging from on their porosity, Poco ZXF-5Q and ACF-10Q graphites are potentially lower thermal conductivity alternatives to AXM-5Q, and are stronger than UF-4S, but UF-4S has lower CTE. The old UF-4S was purchased in 2000 and the new UF-4S was purchased 2011.

Material	Contamination [mBq/kg]			
	^{238}U	^{232}Th	^{40}K	^{137}Cs
Ti 15-3-3-3 foil	20.40 ± 3.33	7.97 ± 1.79	3.26 ± 2.14	<0.30
Phosphor-Bronze[b]	0.97 ± 0.67	1.47 ± 0.43	5.22 ± 1.51	<0.18
BeCu[c]	$11\,936 \pm 2383$	980 ± 196		
Graphlite CFRP[d]	2.79 ± 0.89	<2.76	23.95 ± 4.96	<0.62
Multi-ply CFRP[e]	0.815 ± 0.621	2.93 ± 1.60	8.21 ± 2.36	

[b] Phosphor-Bronze wire coil from MWS Industries. Alloy UNS C51000, is 94.8 wt% Cu, 5.0 wt% Sn 0.2 mt% P.

[c] Internal data from the Edelweiss Collaboration obtain from ICPMS technique. Specimen is the press fit contact of a Mill-Max connector. Mill-Max uses alloy UNS C17200 per ASTM B 194, 98.1 wt% Cu and 1.9 wt% Be.

[d] We assume 67% carbon fiber and 33% bisphenol f epoxy.

[e] The Multi-ply CFRP is from a vendor named Dragonplate. It is in quasi-isotropic plate, 1 mm thick and has four layers of carbon fiber. We assume a 50-50 carbon fiber and epoxy fill. Dragonplate is the manufactures of this product.

Table 7.2: Contamination of metals and CFPR. (continued from page 174)

Material	Contamination [mBq/kg]			
	^{238}U	^{232}Th	^{40}K	^{137}Cs
LCP + Glass[f]	8.234 ± 0.097	10.990 ± 1.574	1.647 ± 0.098	0.079 ± 0.011
LCP + Mica[g]	0.380 ± 0.015	0.073 ± 0.008	99.150 ± 2.950	
LCP + Talc[h]	2788.00 ± 20.53	29.380 ± 7.323	13.170 ± 3.680	
Nylon[i]	<1.34	1.644 ± 0.473	1.513 ± 1.377	<0.2528
PEEK[j]	20.530 ± 0.763	11.85 ± 0.78	10.90 ± 1.49	<0.13
PES[k]	1.208 ± 0.360	1.141 ± 0.447	1000.00 ± 30.43	<0.45
PCTFE[l]	5.6 ± 1.2	<2.3	<30	

[f] Sumika E6007LHF-MRZ liquid crystal polymer filled with 35 wt% Owens Corning E-glass fiber for strength, and fracture toughness in particular. Specimen is in pellet form for use in injection molded parts. Tensile strength 157 MPa.

[g] Sumika SZ6505HF liquid crystal polymer filled with 25 wt% mica for strength, and fracture toughness in particular. Specimen is in pellet form for use in injection molded parts. Tensile strength 130 MPa.

[h] Sumika E6807 T/SCZ liquid crystal polymer filled with 35 wt% talc for strength, and fracture toughness in particular. Specimen is in pellet form for use in injection molded parts. ^{60}Co contamination is (0.532 ± 0.289) mBq/kg. Tensile strength 106 MPa.

[i] DuPont Zytel 101 NC010 is a general purpose polyamide 66 resin for injection molding and extrusion. Specimen is in plate form. No filler material. Tensile strength 82 MPa.

[j] High performance Victrex 450G903B thermoplastic material is unreinforced semi-crystalline Polyetheretherketone (PEEK). Specimen is in pellet form for use in extrusion/injection molded parts. Lubricants cleaned from pellets prior to counting. Tensile strength 100 MPa.

[k] SUMIKAEXCEL Polyethersulfone (PES) 3600G is a transparent thermoplastic with a slightly amber color. It is considered a performance plastic because of its such as heat resistance (high softening temperature), creep resistance, dimensional stability, flame resistance and hot water resistance. Specimen is in pellet form. Tensile strength 84 MPa.

[l] From [111]. Diakin specializes manufacturing chemically resistant polymers for applications that require high purity. Diakin Neoflon PCTFE (Kel-F) M-400H, raw material. Can be injection molded so long as spaces are not too narrow, such as those encountered in miniature connector bodies. Diakin PFA, specifically AP-201SH or AP-211SH, are potential high purity alternatives for molds with narrow spaces. Equipment used to process fluoropolymers must be corrosion resistant at all points of contact with the polymer. ^{60}Co contamination is <0.58 mBq/kg.

Table 7.2: Contamination of polymers. These materials are of particular interest for injection molded parts, such as connector bodies. (continued from page 175)

7.1.3 Mechanical properties

Materials with low thermal expansion and either higher rigidity or flexibility are desired for low temperature instrumentation as cryogenic supports and for use in flexible circuitry.

In the course of our studies, we have determined that the combination of stiffness (rather than strength) and thermal conductivity are the most important material parameters for cryogenic standoff design, at least for our application, provided that the radio activity constraints are satisfied. We find it most helpful in the selection of structural material to plot the quotient of thermal conductivity and Young's modulus versus temperature, Figure 7.7. The materials with the lowest value of the quotient over the temperature range of their use are the most well suited for the job. These ideas are explained in greater detail in our paper [99].

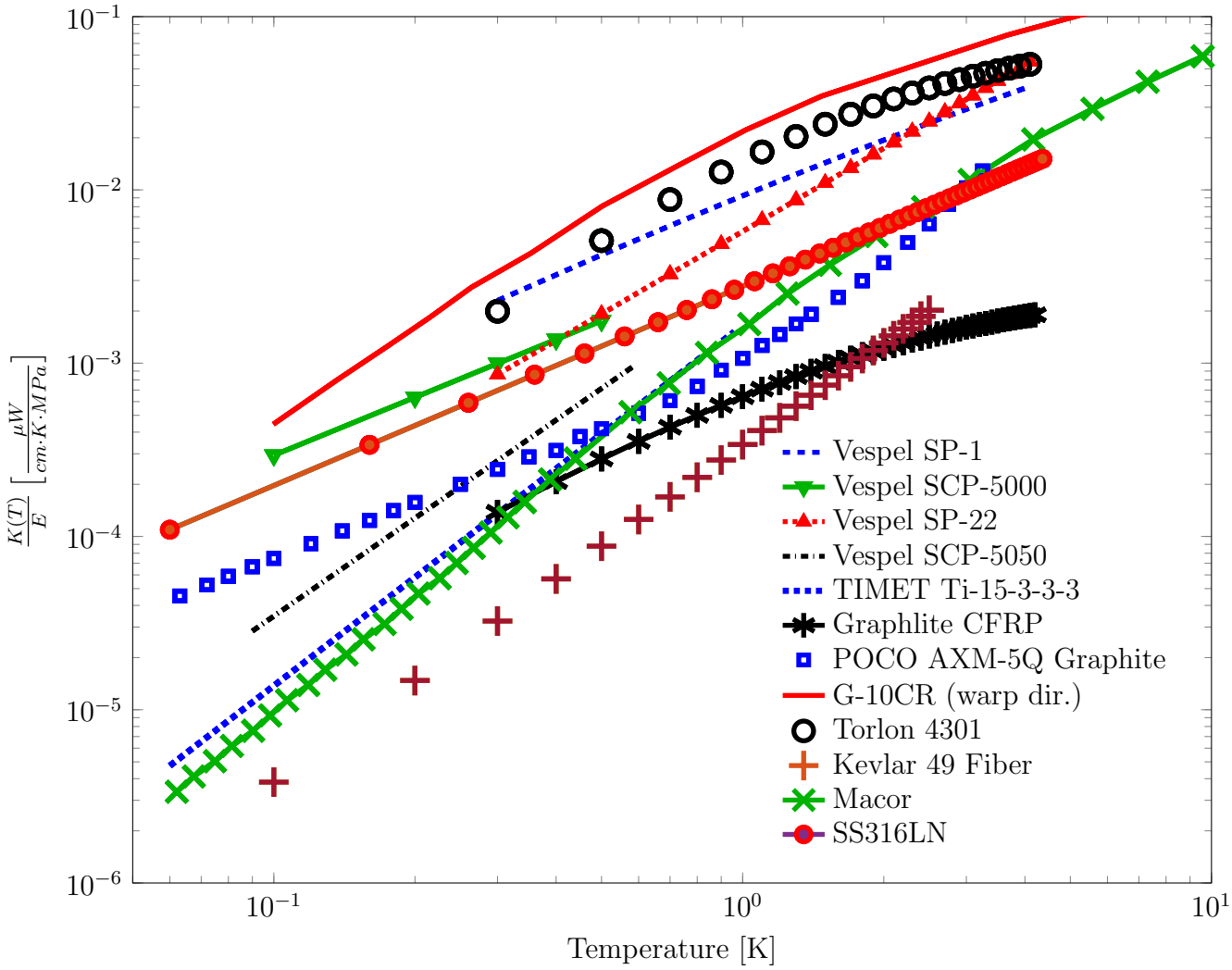


Figure 7.7: A selection of useful materials with their thermal conductivity normalized by their room temperature Young's modulus. Lower values are desirable as support materials. Thermal conductivity references: Vespel SP-1, Vespel SP-22, Graphlite CFRP, and Torlon 4301 from Runyan [158]; Vespel SCP-5000, Vespel SCP-5050, and Ti 15-3-3-3 from our original data [95]; AXM-5Q, G-10CR, and Macor from Woodcraft[195, 196]; Kevlar 49 from Ventura [183]; Stainless Steel 316LN from Barucci[25]. Young's moduli from Table 7.3

When it comes to carbon fiber containing materials we would like to point out that there are different grades, which have vasty different mechanical properties, Figure 7.8.

Material	ρ [g cm^{-3}]	ν	σ_t [MPa]	σ_c [MPa]	TM [GPa]	CM [GPa]
AXM-5Q Gr.	1.73	0.27	48^U	124^U	10.5	
Ti 15-3-3-3	4.78	0.36	766^Y	810^Y	82.0	90.0
Stainless 316LN	7.99	0.29	690^Y		200.0	
Vespel SP-1	1.43	0.41	86	133^*	$2.5^\dagger$	2.4
Vespel SCP-5000	1.46		163	230^*	4.0	9.1
Vespel SP-22	1.65		52	112^*	2.5	3.3
Vespel SCP-5050	1.76	0.22	72	172^*	8.9	3.0
Torlon 4301	1.46		113^U	166^U	6.8	5.3
G-10CR	1.90	0.18	429^U	374^U	27.9	15.0
Graphlite CFRP	1.55		2340	1900	134.0	131.0
Kevlar 49 Fibers	1.44	0.36	3000^U		112.4	
Macor	2.52	0.29	90^U	345^U	66.9	64.0

^{U} Ultimate strength
^{Y} Yield strength
* Compressive load at %10 strain
† Tensile modulus estimated from manufacturer's stress-strain plot

Table 7.3: Some room temperature physical and mechanical properties of candidate materials. ν is the Poisson's ratio for the material, while σ_t and σ_c are the tensile and compressive strengths for the material, respectively. Unmarked numbers have unknown failure conditions. TM and CM are the tensile and compressive elastic moduli respectively. A blank indicates that the specified property could not be found in the literature for a given material. Data comes largely from manufacturer's literature; where values were missing from manufacturer literature, outside references were used; references as well as relevant notes about the material properties are as follows: POCO AXM-5Q – ν from [171]; Ti 15-3-3-3 – ν, σ_t, σ_c, CM from [105, 168, 131]. All properties were for solution-treated material; SS316LN – ν from [162]. Other data are from SS316LN data sheet for cold worked material (www.finetubes.com); Vespel – TM for SP-1 from [54]. All data were for isostatically formed parts. G-10CR – all data from [94, 120]. Properties taken in the warp direction; Graphlite CFRP – properties along the fiber axis; Kevlar 49 – all data are for unfilled fibers; Macor – σ_t and CM from [120, 7].

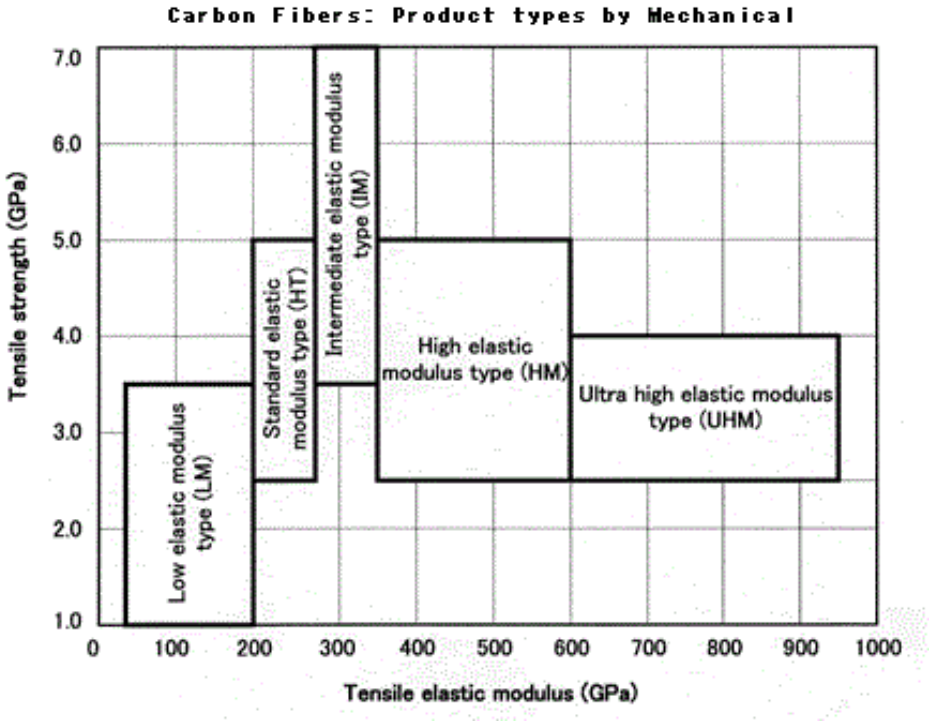


Figure 7.8: Carbon fiber can have a wide range of mechanical properties, which can be can be selected for the usage application. Image from [8].

7.1.4 Magnetic properties

Whenever a superconducting quantum device, such as a Transition Edge Sensor (TES), SQUID, for Kinetic Inductance Detector (KID) are in use, it is important to control the surrounding magnetic field environment. Magnetic fields can produce vortices in superconductors which introduce reactance and dissipation in the films and which may lead to substantially degraded device performance. This is relatively common knowledge, but what is forgotten are the sources of magnetic fields.

In the SuperCDMS SNOLAB experiment, SQUID arrays used to amplify the phonon signal are mounted on stiffened portions of the phonon cable. The metal traces in the immediate vicinity of the phonon cable require copper plating in order to form interconnections between circuit layers. Standard copper plating processes often use a thin, e.g. 0.000 05 inch, layer of nickel plating to facilitate copper adhesion. Figure 7.9 shows what happens to the modulation of a SQUID array when it is mounted on top of copper which has a thin plating of nickel. The use of nickel is therefore avoided in the vicinity of the SQUIDs. Chromium is a potential substitute for nickel. It remains paramagnetic at cryogenic temperatures and we have verified that our SQUIDs performance is not degraded when they are mounted on copper with a 0.000 05 inch plating of chromium.

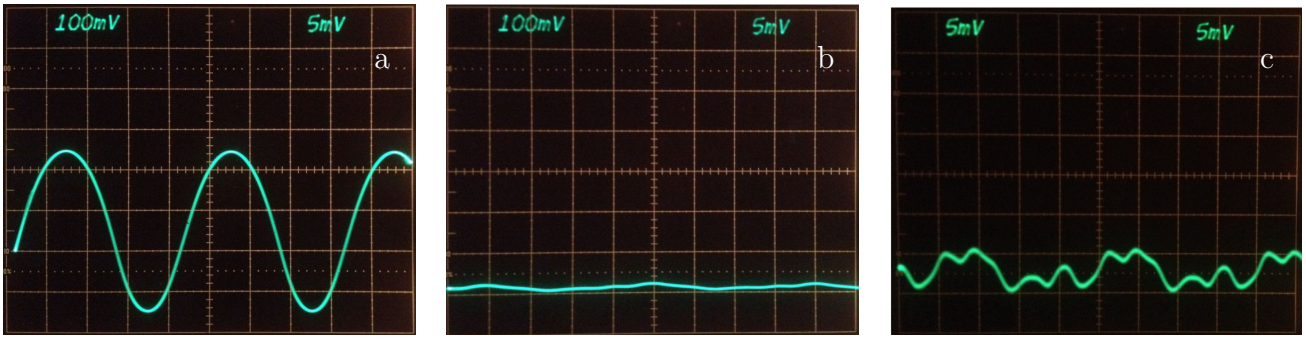


Figure 7.9: The modulation of a SuperCDMS SNOLAB SQUID array in the presence of nickel. View *a* shows the $V - \Phi$ curve of a SQUID array without nickel; the modulation depth is 4 mV. View *b* shows the $V - \Phi$ curve of a SQUID array but this time it is mounted on time of a 0.0014 inch thick copper foil that is plated with 0.000 05 inch of nickel. View *c* is a fine scale view of *b*. All measurements are done inside a magnetic shield – two-nested cryoperm cans around SQUID. Data from [9]

Stainless steels can be another ferromagnetic magnetic source. They are attractive for use at low temperature because of their high strength and low thermal conductivity. Their corrosion resistance and inexpensive availability underpins their widespread use in connector contacts. Their high stiffness makes them a standard option for spring material. The desirable mechanical characteristics of steel are qualities of its Austenitic crystal phase which is obtained by thermal processing. Unfortunately the Austenite phase of steel can transform into the Martensite phase when it sustains mechanical stress including machining, forming, temperature cycling. The Martensite phase can be ferromagnetic. Thus as a consequence of working steel or cooling it to cryogenic temperatures it may become ferromagnetic. As a rule of thumb, steels most likely to become ferromagnetic include 316, 304, 321, 310. Those unlikely to become ferromagnetic include 316L, 316N, 336LN, and 304N, [186, 74, 106]. It is pointed out in the literature that inhomogeneities in the composition Austenitic steel may be a source of magnetism, even in those unlikely to become ferromagnetic.

7.2 Thermomechanical tower design

The tower, Figure 7.1, is the apparatus that provides mechanical support for sets of six CDMS detectors and their associated cold electronics including readout wiring. It is composed of four copper "floors" which are heat sunk to different temperature stages of the cryostat. Each floor provides heat sinking attachment surfaces for all signal wiring that travels between 4 K to the coldest stage at 15–30 mK where the detectors. The floors are separated by standoffs which are designed have very low thermal conductivity, but sufficiently high rigidity and strength to meet certain mechanical specifications.

	Stiffness [N mm^{-1}]		Strength [N]	
	Axial	Vertical	Axial	Vertical
LH-ST	36.8	35.8	84	87
ST-CP	622.6	564.8	198	183
CP-MC	1048.2	35.8	261	264

Table 7.4: Summary of Tower mechanical specifications. Accelerations, loading conditions, and displacement limits have been translated into strength and stiffness specifications for the tower stages. Abbreviations are: LH – liquid helium, ST – still, CP – cold plate, and MC – Mixing chamber. Figures include a safety factor of 3. We apply the vertical specifications to the mechanical performance of standoff test modules in the condition of compression and transverse specifications in the condition of bending.

The mechanical specifications arise from various considerations. The tower body must support its own weight and the weight of the copper "lids" that provide thermal connection between its floors and the temperature stages of the cryostat, and serve as heat shields from the blackbody radiation and other stray light from higher temperatures.

The tower must withstand the accelerations encountered during handling, shipment, insertion and extractions of connectors, and seismic events without structural failure. We estimate the maximum acceleration to be 3 g and tack on a safety factor of three in our design specification. Additionally, the tower must be rigid enough to limit flexure under these loading conditions, to avoid damage to interconnections (e.g. wirebonds, and the vacuum dielectric coaxial cable the connects the HEMTS gate wires to the detector housing.) Table 7.4 summarizes the mechanical specifications on the strength and stiffness of the tower.

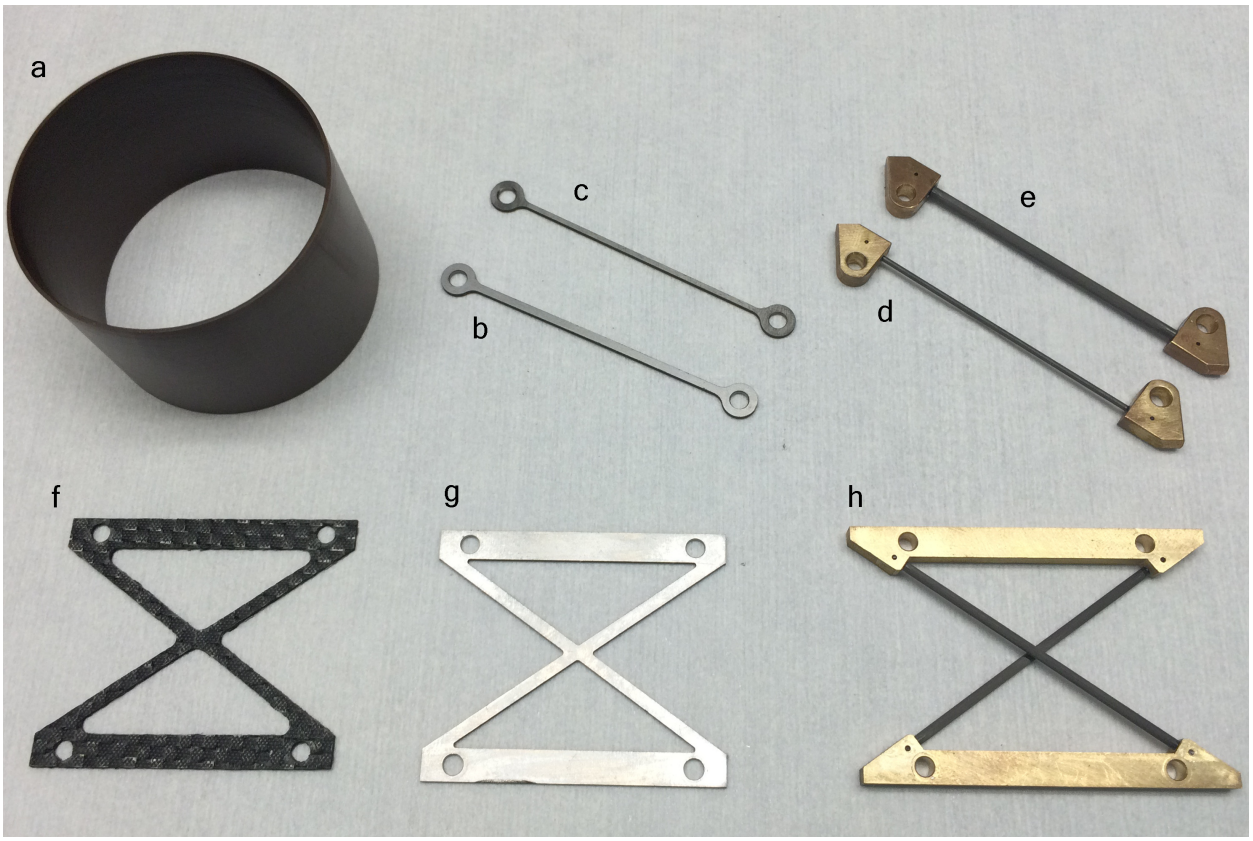


Figure 7.10: Structures considered for tower standoffs. All structures would be fastened by screws to the tower floors, except the tubes which would be glued. The standoffs are: *a* – tubes, made of either vespel, graphite or Ti 15-3-3-3; *b* (and *c*) – Ti 15-3-3-3 hexipod truss member 0.04 inch thick by 0.04 inch (0.06 inch) wide; *d* (and *e*) – graphlite rod hexipod truss member ∅0.08 inch (∅0.04 inch); *f* (and *g*) – carbon fiber reinforced epoxy (Ti 15-3-3-3) X-frame member 0.04 inch thick by 0.083 inch; and *h* – graphlite X-frame using using ∅0.062 inch rods

The towers of SuperCDMS Soudan and before used graphite tubes as the standoffs. These tubes were very rigid, dimensionally stable under cooling, strong. They were however made out of a non-optimal graphite, Mersen UF-4S, which is higher thermal conductivity and lower strength than others we have studies, e.g. Poco AXM-5Q. These tubes were epoxied into the tower floors and as a result, those towers could not be disassembled. The stiffness and strength specification for SNOLAB tower have been substantially relaxed, in favor of disassemblability and minimizing heat conduction[2]. As a result, alternate structures were considered, including hexipod truss structures and X-shaped frame type structures, Figure 7.10. A few variations of each type, using different dimensions and different mate-

[2]The tube design can be made disassemblable and heat conduction can be substantially lowered, but the aesthetic of the designers did not favor tubes, so alternate standoff structures were pursued.

rials, were investigated in effort to optimize mechanical mechanical performance. Selected fabrication drawings in § D.4.

An Instron 5965 tension and compression tester with a 500 N load cell was used to measure the strength and stiffness of tower standoff prototypes. The machine applies force vertically in either the up or down direction, and it provide connection points for custom fixturing hardware on the force axis. In order to measure bending strength and stiffness, a symmetric arrangement of two tower standoff modules would need to be held in place so that the compression ram could push down on both simultaneously. If only one tower module were used in the measurement, then the cantilever deflection would introduce a force that is perpendicular to the motion of the ram and would result in an error in the load cell reading or damage to the load cell. A steel frame, thick enough to contribute no additional deflection to the measurement, was designed and built to hold tower standoff modules in this arrangement. The same issue is present for compression testing, where perpendicular force shows up as the standoff fails and buckles to one side. An additional steel frame, with a compression plate constrained to vertical motion by dowel pins, was built for compression testing. Aluminum adaptor flanges were made to connect the standoff structures and the testing frame. The assembly made by fastening the standoff structures to the aluminum flanges is what we call the tower standoff module Figure 7.11. Tubes standoffs were glued to the their flanges in a 0.02 inch groove; metal hexipods were fastened to their flanges using shoulder screws; the graphlite carbon fiber hexipods with brass end caps and all the X-shaped frames were fastened to their flanges using machine screws.

The measurements are destructive. The data obtained is a stream of force applied and displacement imparted tuples, which we interpret as stress and strain figures, respectively. Typical ram speeds used are 1–2 $\mathrm{mm\,min^{-1}}$. There is a settling period at the beginning of each measurement when data suggests slippage in the test assembly. This is to be expected when screw fasteners are used to attach the standoffs to the flanges, and the flanges to the test frames. Ideally, one would want to do numerous measurements, each time pushing pristine standoff to failure. This ways, one accumulates statistics which can be used to remove the effect of manufacturing, material, and testing variations. Limited time and money prevented us from doing this. So in most cases we only have data from one or two modules per standoff variety. We did however, measure the elasticity of a graphlite rod X-frame, where ram force was cycled from zero to a maximum below the predetermined failure load. After settling, the rod X-frame performed repeatedly elastically.

Initially our approach was to calculate, analytically, what the strength and stiffness of various standoff structures would be. This works moderately well for very simple and symmetric structures [77]. We developed solid predictions for the stiffness and strength of tubes, where the diameter is approximately equal to the length as is our case [96, Chap 4]. The buckling and material failure where found to be the principle failure modes of concern or our vespel and graphite tubes. We were advised, however, by structural engineering faculty member, Sanjay Govindjee, that in reality, especially with asymmetrical standoffs like our X-frame, it is best to perform repeated tests to determine mechanical properties. The tests identify faults which limit the theoretical performance of structures as well as intrinsic

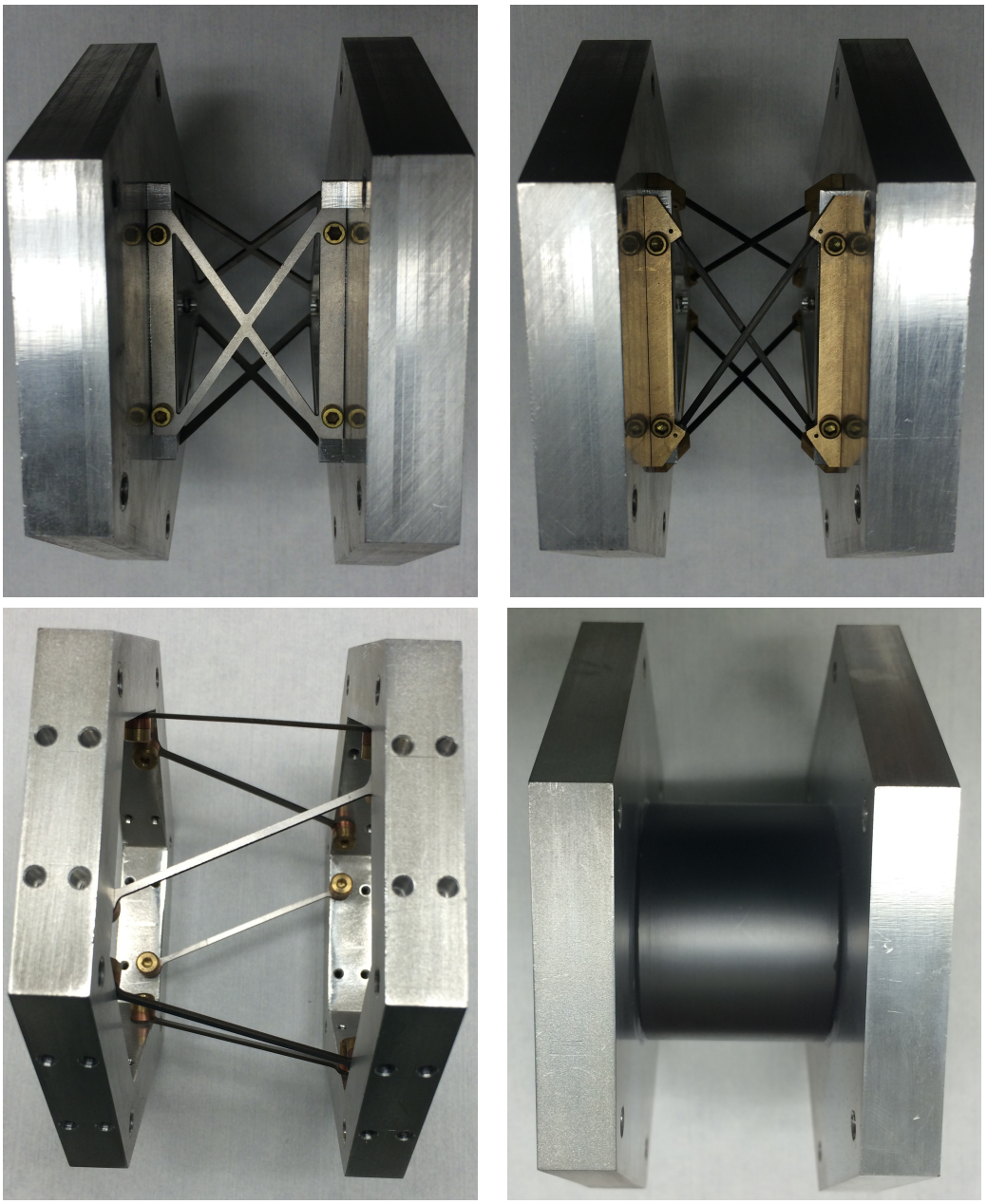
mechanical performance. For example, we found that our graphlite rod hexipod truss has strength limited by twisting of the brass end caps about the shoulder screw fasteners. The failure due to twisting is a mix of material and mechanical failure. In general, end conditions, such as pinned versus clamped, can have on the order of a factor 4 influence on strength. We also found that materials non-uniformities in the carbon fiber reinforced epoxy limited the performance of X-frames made from this material. Material failure occurred at places with visually obvious defects. Both on axis and off axis compression was measures. Point up and point down bending measurements were made for the X-frame structures since the asymmetry could have an effect on the mechanical properties Figure 7.13. The data we collected from our mechanical testing is presented in Table 7.5. Figure 7.12 presents this data in graphically. Vertical lines indicate strength and stiffness specifications in relation to values measured from test modules. Also presented is the predicted amount of heat the structure would transfer between various temperature stages. Note that we measured the performance of both mill cut and water jet cut X-frames. This was to allay concerns that process of mill cutting may inflict internal damage to the carbon fibers.

Based on our thermomechanical performance data of the tower standoffs, in addition to ease of fabrication considerations, the Ti 15-3-3-3 X-frames were chosen to be the standoff for the mixing chamber to cold plate stage and the cold plate to still stage. The graphlite carbon fiber rod X-frame was chosen as the standoff for the still to liquid helium stage.

	Hexipod				Tube			X-Frame			
	Ti-40P	Ti-60P	CF-40R	CF-80R	SP-22	AXM-5Q	UF-4S	Ti-83P	mCF-83P	wCF-83P	CF-62R
Stiffness [N/mm]											
Bending	489.52	789.86	647.69	1061.1	2762.1	4817.5	4441.5	$1495.0^{\triangle}$	$582.72^{\triangle}$	$549.4^{\triangle}$	$1567.3^{\triangle}$
								$1256.3^{\triangledown}$	$534.4^{\triangledown}$	$514.6^{\triangledown}$	$1491.2^{\triangledown}$
Compressive								$2801.8^{\parallel}$		$979.0^{\parallel}$	$2973.6^{\parallel}$
								$673.2^{\nparallel}$		$742.2^{\nparallel}$	$1267.7^{\nparallel}$
Strength [N]											
Bending	110	180	90	275	1688.6	>2361.8[a]	947.16	$400^{\triangle}$	$50^{\triangle}$	$40^{\triangle}$	$500^{\triangle}$
								$400^{\triangledown}$	$50^{\triangledown}$	$55^{\triangledown}$	$500^{\triangledown}$
Compressive								$800^{\parallel}$		$62^{\parallel}$	$1500^{\parallel}$
								$230^{\nparallel}$		$37^{\nparallel}$	$475^{\nparallel}$
Heat Load [µW]											
LH-ST	38.5	57.8	7.0	27.9	98.5	156.4	183.5	82.6	19.1	19.1	16.9
ST-CP	0.33	0.50	0.17	0.69	0.74	0.68	1.65	0.71	0.47	0.47	0.42
CP-MC [$\times 10^{-3}$]	3.29	4.93	4.31	1.73	7.01	23.9	27.7	7.04	11.8	11.8	10.4

$^{\triangle}$ ($^{\triangledown}$) Vertex of X-Frame pointing up (down), opposite (in the) the direction of the ram force.
$^{\parallel}$ ($^{\nparallel}$) Force applied on (off) central axis of the X-Frame (roughly over one of the points).
[a] Load cell sensitivity exceeded before tube failure.

Table 7.5: A comparison of thermal and measured mechanical and properties for tower standoff designs. Strength is the failure load which we defined as lowest value of force necessary to observe buckling or fracture depending on the structure. Some structures can perform beyond their failure load. Heat loads are calculated assuming the following tower stage temperatures: the liquid helium (LH) stage at 5 K at, the still (ST) stage at 760 mK, the cold plate (CP) stage at 150 mK, and the mixing chamber (MC) stage at 20 mK. Note that tubes used in the SuperCDMS Soudan and prior were UF-4S graphite with 0.028 inch wall thickness, exactly like the specimen tested here. The following additional abbreviations are used: Ti-##P – Ti 15-3-3-3 members that are 0.04 inch thick and 0.0## inch wide, CF-##R – is a graphlite rod of diameter 0.0## inches, CF-##P – quasi-isotropic carbon fiber reinforced epoxy laminate members that are 1 mm thick and 0.0## inch wide, from a company named DragonPlate, m – indicates that the part was milled, w – indicates that the part was water jet cut. All tube wall thicknesses are 0.028 inch. The difference in values between point up/down and on/off axis loading conditions reminds us of the asymmetry of the structures.



b

d

Figure 7.11: Tower standoff test modules. Strength and stiffness measurements of the standoff structures considered were done when the standoff structures installed in aluminum adaptor flanges. The assembly of the structures installed in the flanges are what we call test modules. the orientation positioning of the standoff structures are exactly as it would be if the structures were installed on towers. View *a* is a Ti 15-3-3-3 X-frame; *b* is a graphlite X-frame; *c* is a Ti 15-3-3-3 hexipod; and *d* is graphite tube. The rods in *b* have about 0.018 inch of clearance at the crossing point.

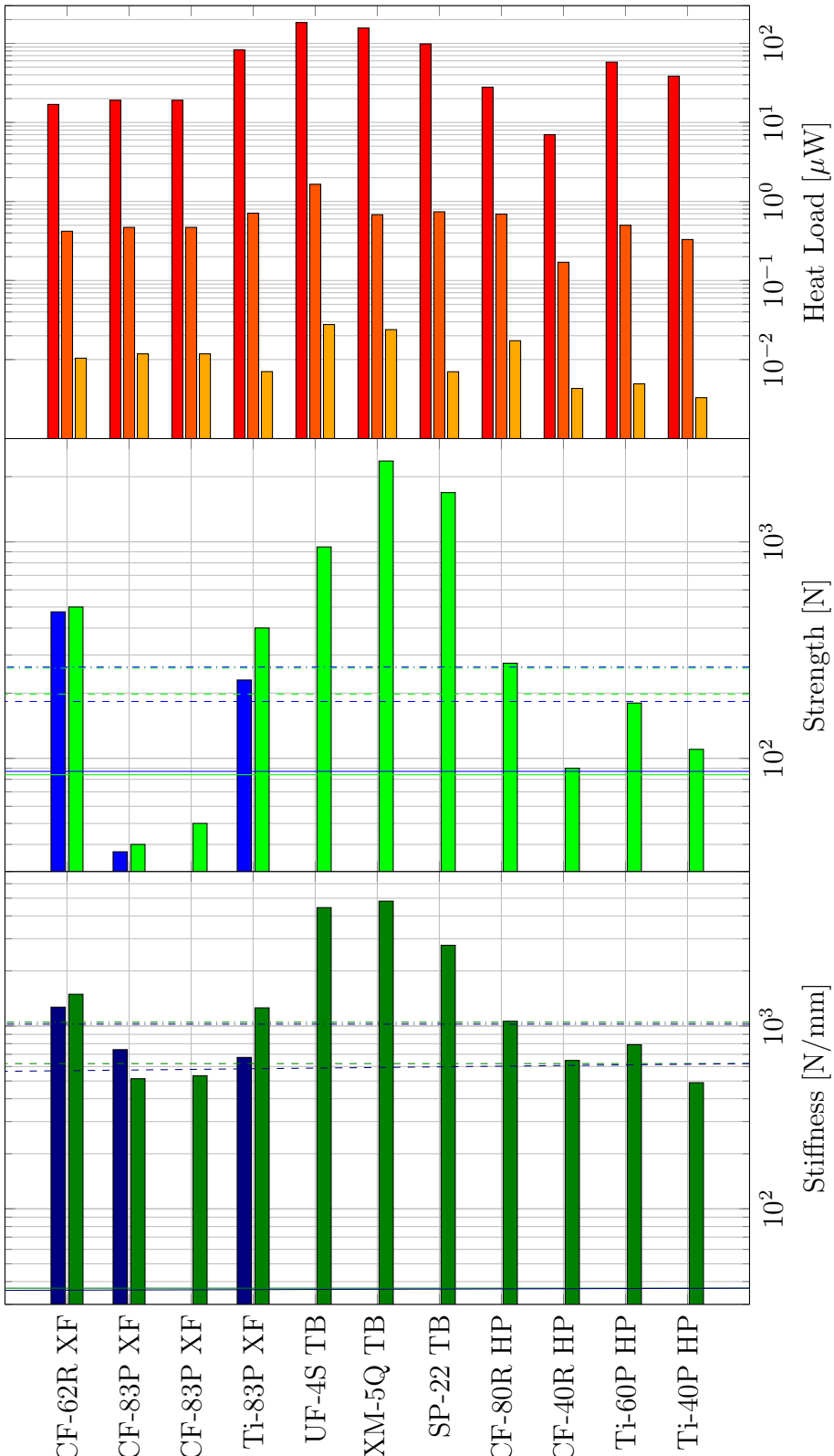


Figure 7.12: Comparison of thermal and measured mechanical properties for all the tower standoff designs studied. Standoff structure abbreviations same as Table 7.5. Figures shown include: ■ – bending stiffness, ■ – compression stiffness, ■ – bending strength, ■ – compression strength, ■ – MC-CP load, ■ – CP-ST load, ■ – ST-LH load. Vertical lines represent minimum strength/stiffness specifications for: "-." – MC-CP, "- -" – CP-ST, "_" – ST-LH. Minimum values chosen for on/off axes and point up/down loading conditions. Ti-83P XF was select for MC-CP and CP-ST. CF-62R XF was chosen for ST-LH.

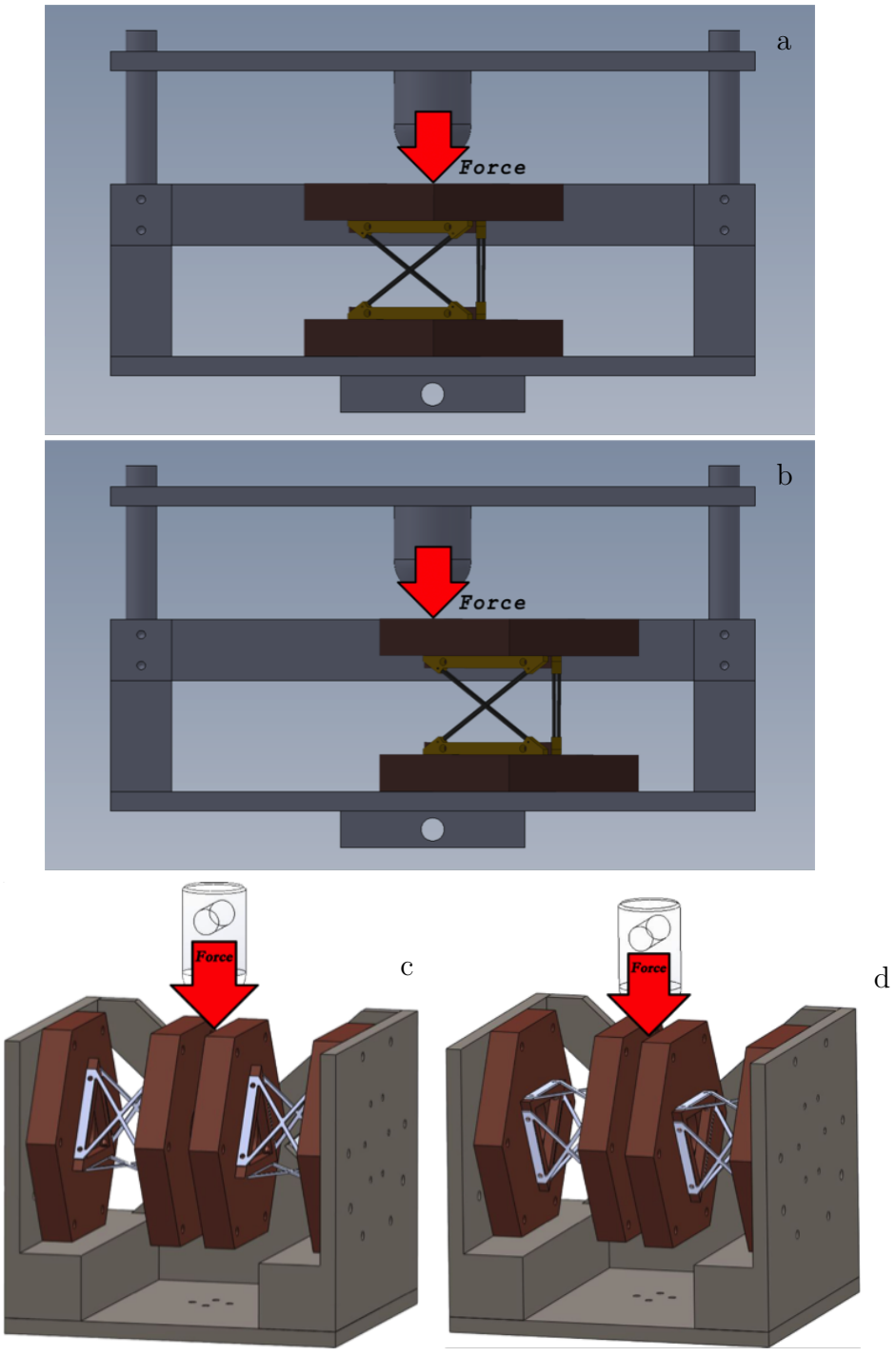


Figure 7.13: Loading conditions for the tower standoff mechanical testing. *a* – on axis compression, *b* – off axis compression, *c* – bending point up, *d* – bending point down. Adjustments are made to the data to correct for the weight of the press, in the case of the compression test frame, and the factor two multiplier from the symmetric module arrangement, in the case of the bending test frame.

7.3 Cryogenic cabling

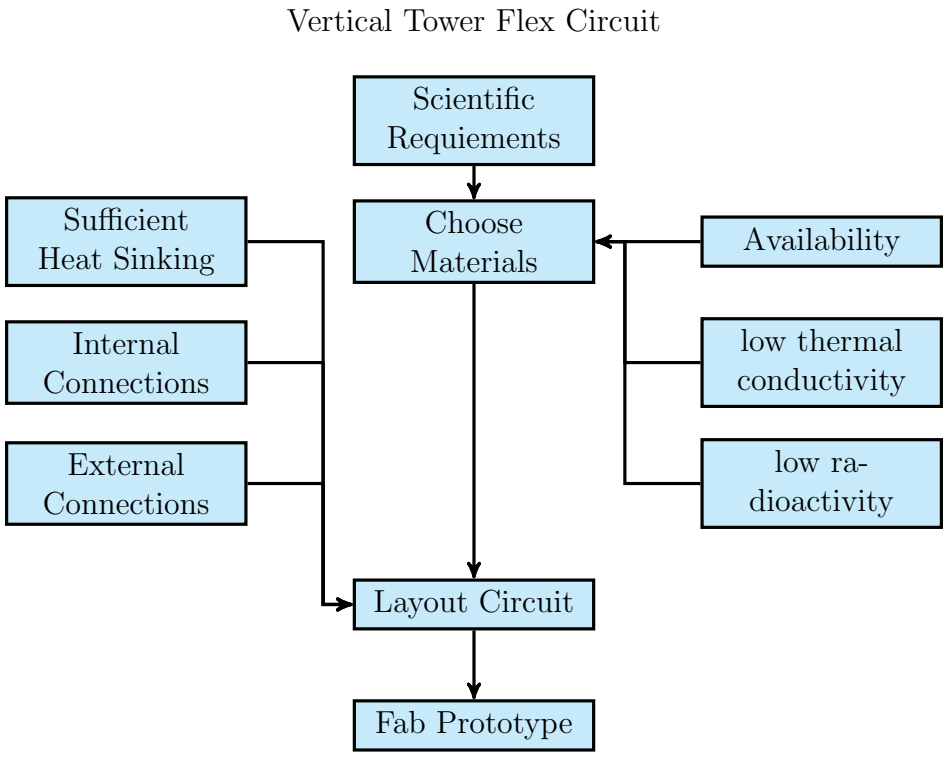


Figure 7.14: A flow chart representing the considerations and steps involved in designing the tower flex cable for the SuperCDMS SNOLAB experiment.

As mentioned above, we need to make a cable that runs down the tower to provide electrical connectivity between the detectors at base temperature, and components that are located at other temperatures, including the readout electronics at room temperature. Figure 7.14 diagrams the design process and considerations for this cable.

7.3.1 Scientific requirements

There are various design constrains placed in the cable that come from other aspects of the experiments. These constraints include limitations on its thermal conductivity, limitations on its radio activity, specifications on its size and shape, and specifications on its electrical properties. The total cooling powers for the SNOLAB cryostat are listed in Table 7.1. Those figures determine a total allowance for the heat dissipation of each stage of the cryostat so the heat dissipation of the cable is traded off with other heat contributes at each stage. Radio activity constrains are satisfied by using materials with known low radioactivity. As for the electrical properties, the phonon traces will need to be superconducting and also have a low inductance to match the impedance of the SQUIDS and TESs. We can use the data collected from our thermal conductivity studies to select appropriate conductor and insulator materials for the cable given the design constraints.

7.3.2 Materials selection

In item 7.15 we present thermal conductivity data for materials of potential use in the our cable, including both dielectric and conductor materials. The superconducting titanium alloys offer the lowest thermal conductivities. Fabrication capabilities limit our choice of dielectric materials. Though teflon would be a better choice (even for its lower radio activity), we choose kapton because it is a standard flex cable material. Upilex is another polyimide base material; it is not available in the United States.

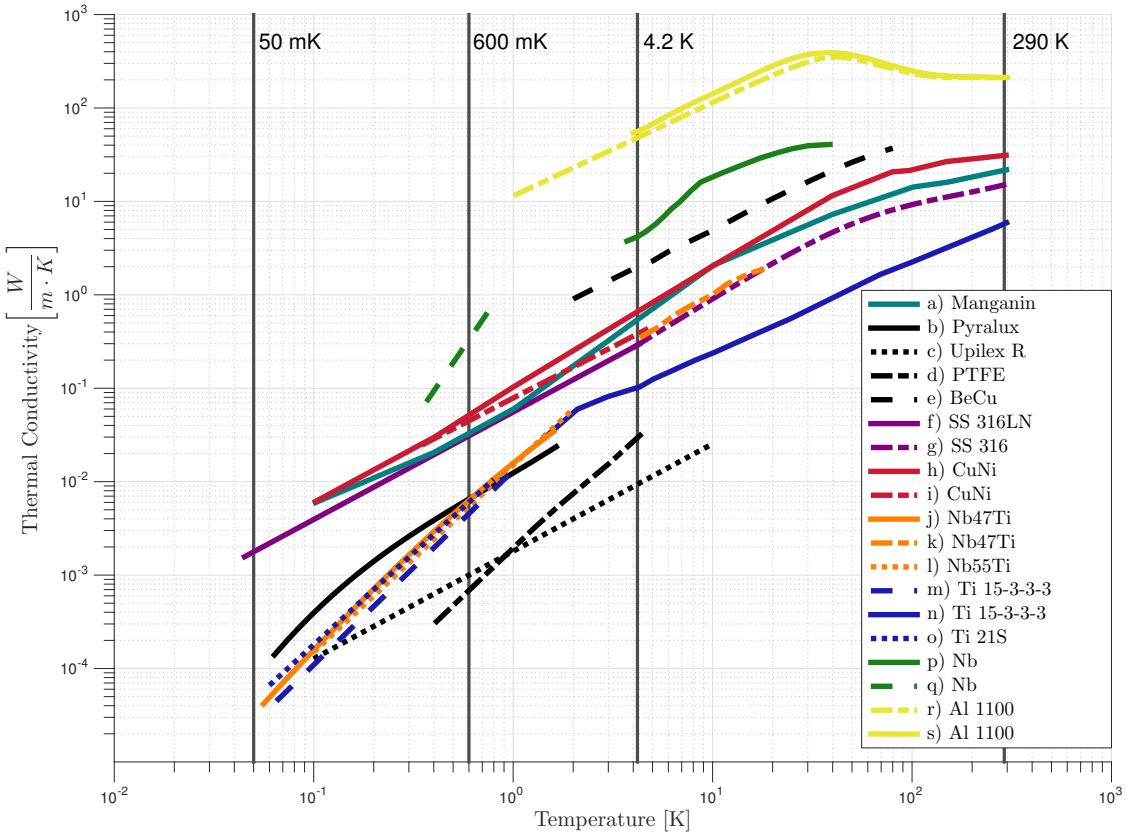


Figure 7.15: Thermal conductivities of materials useful for low temperature flexible circuits and cables. Data sources are : *a)* from Blake [31]; *b)* original data [6], ‖ to sheet; *c)* from Barucci et al. [24], ‖ to sheet; *d)* from Kushino et al. [104], ‖ axis of tubular sample; *e)* from Berman [30], alloy containing 2 wt% beryllium was held at 300 °C for 2 h and the resulting hardness was 41 Rockwell units and the electrical resistivity was $8.25 \cdot 10^{-6}\,\Omega\,\text{cm}$ at room temp, $6.2 \cdot 10^{-6}\,\Omega\,\text{cm}$ at 77 K, and $5.5 \cdot 10^{-6}\,\Omega\,\text{cm}$ at 4.2 K; *f)* from Barucci et at. [25], Stainless steel 316LN is an austenitic SS with 18 wt% Cr and 8 wt% Ni and the addition of 2-3 wt% of molybdenum assures good corrosion resistance; *g)* from NIST, [10]; *h)* from Blake [31]; *i)* from Kushino et al. [104], ‖ axis of tubular sample; *j)* original data [6], ‖ to foil; *k)* from Dyachkov et al. [57], wire sample; *l)* from Olson et al. [137], wire sample; *m)* original data [5, 95], ‖ to foil face; *n)* from Tuttle et al. [179], sample was wire EDM cut from a 1.6 mm thick plate of TIMET manufactured material; *o)* original data [5], ‖ to plate; *p)* from Reiche et al. [152]; *q)* from Mendelssohn et al. [128], polycrystalline rod of Johnson Matthey material (JM 4526) of 99.99% purity; *r)* from Woodcraft at al. [194], commercially pure wrought aluminum 99 wt% minimum, and *s)* from NIST, [10]

7.3.3 Considerations for plating and joining

In view of the goal of plating the titanium alloy foil, we posit a few overarching considerations.

Firstly, it is helpful to have a mental picture of what could be happening at the interface between the base material and the plated material. Figure 7.16 illustrates some possibilities. Perhaps the best adhesion is obtained in scenarios (c) and (b), compound interface and diffusion interface. Heat treatment can enhance inter-diffusion and compound formation. When the two materials are sharing atoms, it can become[3] difficult to separate the to layers, which is what it means to have good adhesion. In most real situations mechanical anchoring is an aid to adhesion. Roughening the surface can enhance the role of mechanical anchoring in adhesion. Also, in most real situations there is an interfacial layer between the base material and the plating material. If the base material was cleaned properly, the interface will be free of organic contaminants and debris, which would certainly inhibit adhesion. A layer of oxygen (or even nitrogen) chemically bonded to the base material will remain, and may have a thickness of several nanometers. It is usually the central plating challenge to remove this oxide layer and keep it at bay for long enough to plate the base material. Sometimes interfacial materials are intentionally added to assist with adhesion. Such materials are reactive themselves and will bond with both the plating material and the base material. Examples include aluminum, titanium, chromium and nickel.

We suspect that the presence of surface oxidation on the titanium alloy degrades the adhesion of plated layers. If this is the case, then one would like to somehow remove the surface oxidation. Oxidation removal, or disruption[4], can be accomplished mechanically, for example by bead blasting or scraping the surface, but these processes my damage a thin foil. It can be accomplished chemically, for example using reducing acids like HCl or HF, but the foil may be laminated to something which cannot withstand acid treatment, or the fabrication facility may not have access to these acid treatments. Additionally, the surface oxidation will begin to reform immediately upon exposure of the foil to atmosphere and even to the plating solution, which usually has oxidizing chemicals in it. Another oxidation removal method is plasma etch. Here the oxidation layer is sputtered away or disrupted, but will begin to reform when vacuum is broken. Finally another approach at oxidation removal which we suggest as an unusual technique is first to do whatever is practically possible to remove the oxide, working with whatever constraints are at hand, then deposit a seed layer of a material with which it is more energetically favorable to form an oxide than to oxidize the titanium alloy. In this approach, the surface oxide will either serve as an interfacial material promoting adhesion or the deposited material will pull oxygen away from the interface making room for metallic bonds between the deposited material and the titanium base material. We suggest that the the Gibbs free energy of metal oxide formation can be used as a guide to choose the deposition material, Figure 7.17 – it should have an oxidation free energy lower than any of the constituents of the titanium alloy; it should be chemically compatible with

[3] An important exception occurs when the compound created at the interface is mechanically weak and splits apart. We discuss this later.

[4] In a disrupted oxidation layer, the base material is exposed through cracks and gaps in the oxide.

the titanium alloy base material and not form undesired compounds; and it should be, itself, readily plated.

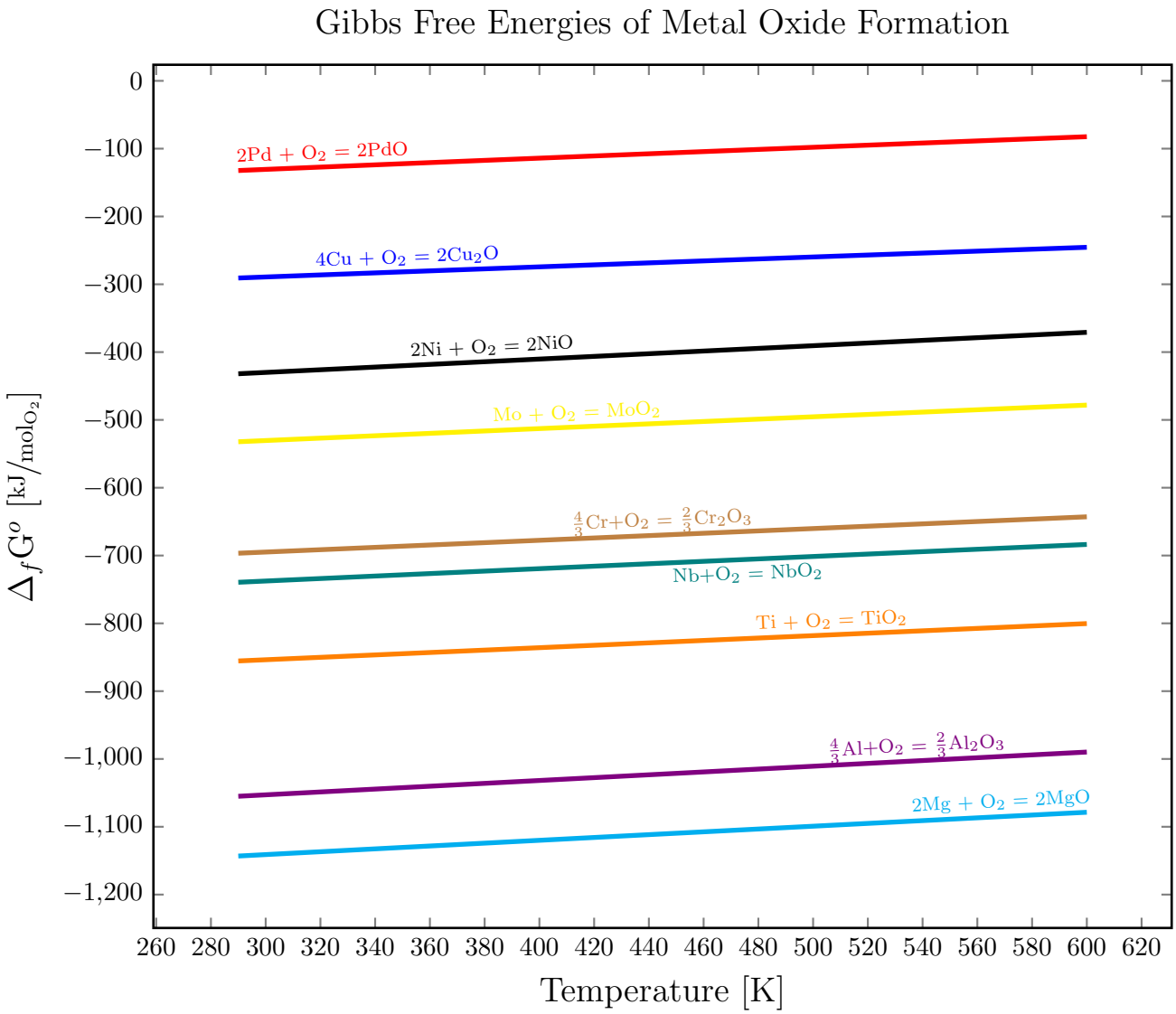


Figure 7.17: Gibbs free energies of metal oxide formation in kilojoule per mole of oxygen. Plot quantifies how energetically favorable it is for various metals to form oxides at a given temperature and at room pressure. Metals may also form oxides that are not present on this plot. This plot is also known as a Ellingham diagram.

Precipitation of the alpha phase increases the strength and stiffness of the base titanium alloy material (see § C.3.2). The transformation may have an impact on the transition temperature of the titanium alloy (if it is a superconductor) and, it may have an impact on the thermal conductivity of the alloy since, for instance the titanium rich alpha precipitate

would probably have a thermal conductivity closer to that of pure titanium, and higher than the desired β-phase conductivity. For applications requiring minimal thermal conductivity the transformation is worrisome.

If Ti 21S foil were chosen instead of Ti 15-3-3-3, the heat treatment process would also be designed to avoid the alpha boundary on the Ti 21S time temperature transformation diagram (which can be found in [87]) and equilibrium threshold temperatures for the formation of intermetallics.

It is important to choose plating materials and design plating processes so as to avoid the formation of undesired intermetallic compounds between the base material and the material that is being plated onto it. One way to go about this is to consult the equilibrium phase diagrams Figure 7.19 for the metals involved. Narrow vertical lines are an indication of intermetallic compound formation. If the lines form within the operating temperature range of the plated part, formation of those intermetallics will certainly be an issue.

It should be noted, that although copper connections (e.g. wire bonds) and plating layers on aluminum are metallurgically stable, gold connections or plating layers to aluminum are unstable, and form interface voids and an intermetallic compound whose purple color has earned it the title “purple plague”. The voids undermine adhesion and cause high electrical conductivity.

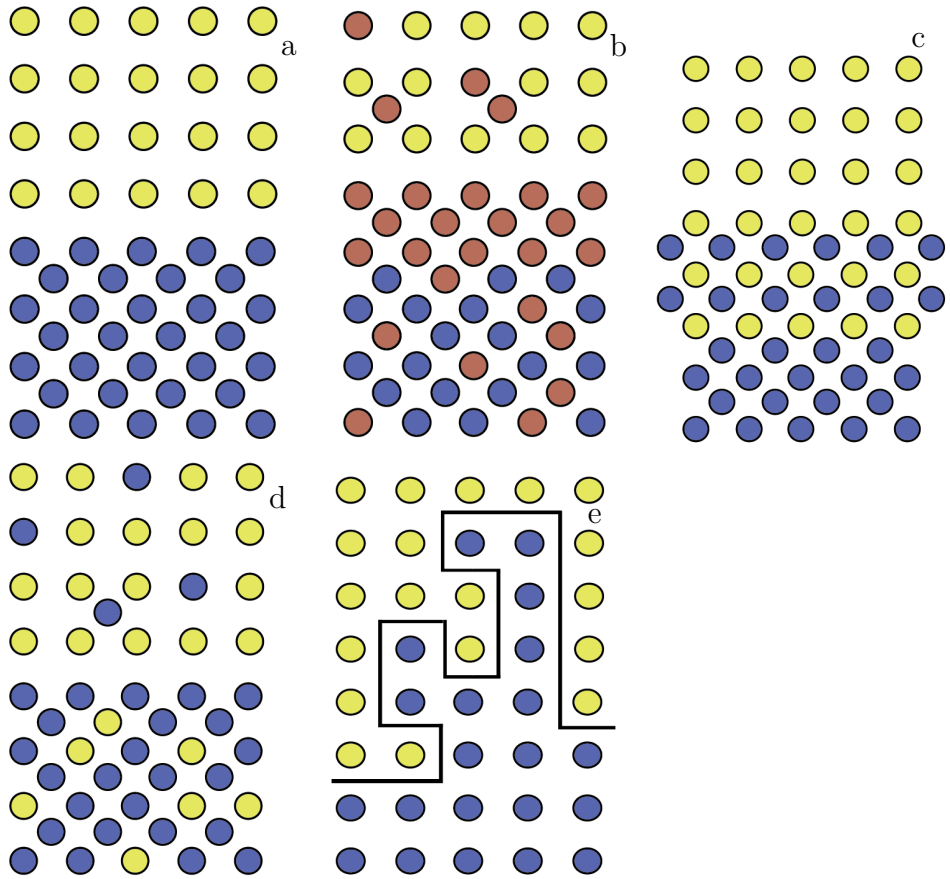


Figure 7.16: The five images depict different types of interfaces involved in the adhesion between different materials. (a) – an abrupt interface where the first material transitions to the second in the length if a few atomic separations. Adhesion would be weak in this case. (b) – The two materials attach to a common third material interfacial layer, such as oxygen or a reactive metal. Adhesion has the potential to be excellent here because the third material can be chosen to be very reactive with the other two. (c) – the two materials form a chemical compound (e.g. an intermetallic) at the interface. The adhesion can be good if the compound has good mechanical properties. (d) – the two materials diffuse in to each other. Adhesion can be great if the two materials are mutually soluble and if the materials have similar mobilities into the other. Kirkendall voiding can occur if the mobilities are not similar. (d) – mechanical interlocking of the two materials at the interface enhances adhesion generate adhesion. Roughening of the surfaces can thus be used to enhance adhesion through this mechanism. Mechanical interlocking is important for the adhesion of vacuum metallized and electroplated layers. Interfaces (b), (c), (d) can be influenced by heat treatment. Illustration by [2] and inspired by [133, Figure 12-22].

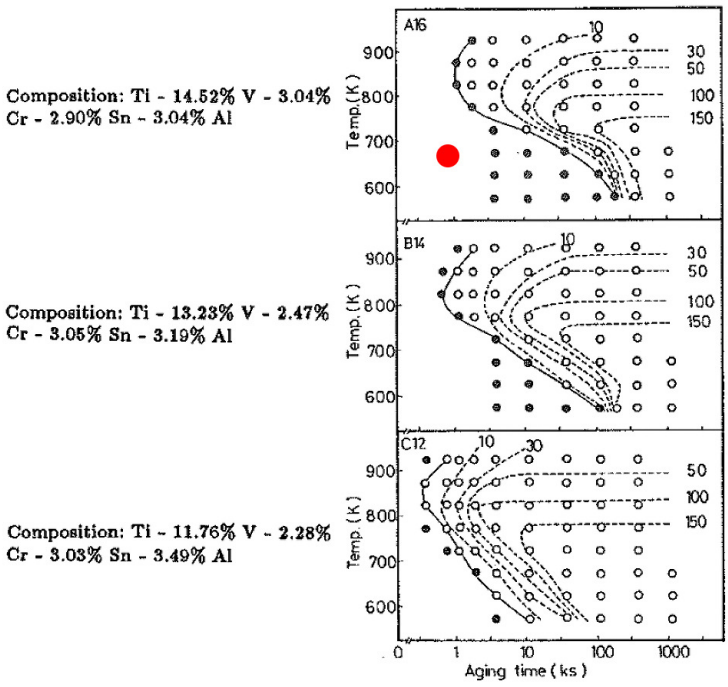


Figure 7.18: Time temperature transformation diagram for Ti 15-3-3-3 (top). Material began in solution treated condition. Lines show increase in Vickers hardness with aging. ○, ● – alpha precipitation observed and not observed through optical microscope, respectively; solid line – alpha phase detected through x-ray diffraction; dashed line – equal hardness increase with aging from solution treated condition. Numbers beside lines indicate the amount of hardness increase. The red dot indicates our plating heat treatment. The middle and bottom panels underscore the sensitivity of the transition behavior to variations in the alloy composition; consider this vis-à-vis the allowed tolerance of 14–16 wt% V and 2.5–3.5 wt% Cr, Sn, and Al for the Ti 15-3-3-3 alloy. From [181]

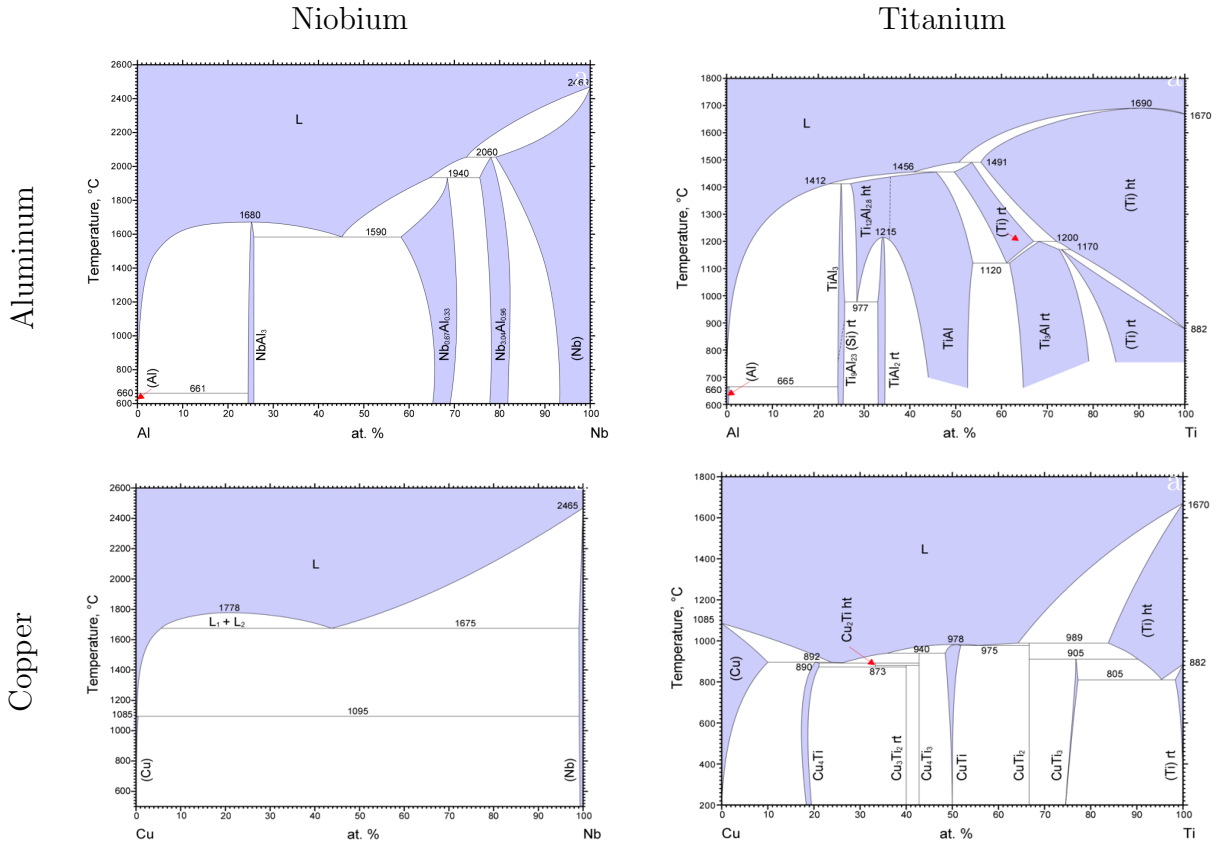


Figure 7.19: Equilibrium binary phase diagrams for: Nb-Al (1990 Kattner U.R.; exp.), Ti-Al (2006 Schuster J.C.; exp.), Nb-Cu (1984 Terekhov G.I.; exp.) and Ti-Cu (1996 Kumar K.C.H.; calc) from [14]. Diagrams are either calculated (calc.) or experimentally determined (exp.). We immediately notice the at Nb-Cu are immiscible. Ti-Cu forms several intermetallic compounds, while Ti-Al and Nb-Al form solid solutions.

7.3.4 Plating

In this section we describe method of making electrical connections to the titanium foils. We have to be able to make electrical connections to foil if we are to use it as the conductor material in our flex circuits.

In summary, we find that we can obtain good adhesion to the titanium alloy foils using an electrolytic copper plate process followed by a heat treatment; or by first plasma cleaning the foils then vapor depositing aluminum onto them. Copper can be readily electroplated to the aluminum, and the aluminum helps with the electroplating process by increasing the conductivity of the base material. Scanning electron microscope inspection of the interface supports the conclusion that good adhesion is obtained, as do results from tape tests[5]. We speculate that the electrolytic copper plus heat treatment process works by fist by attaining low quality adhesion to the titanium surface oxide and also via mechanical anchoring. The heat treatment then facilitates inter-diffusion and the adhesion is improved. The obvious plating methods we have not tried are electroless copper and sputtering. Sputtering is especially interesting because it can be used as a roll to roll titanium alloy foil plating process, which would be needed for the practical fabrication of long flex circuits. At this point of process development, all of our plating results have to be taken as preliminary because we do not yet have long term plating performance data. It is possible, for example, that adhesion could degrade over time due to thermal cycling or to the formation of intermetallics.

Joining was less successful than plating. We were able use an activated solder to make a mechanical bond, which peels off when aggressive force is used. At the limited of destroying the foil, ultrasonic welding worked too. We expect that electric discharge welding will be a successful joining method, but our attempt with it was unsuccessful.

7.3.4.1 Bulk parts

The plating of bulk titanium alloy parts, is a standardized[6] but relatively specialty process. Though processes vary, they usually involve a bead blast step, to disrupt the oxide on the titanium alloy surface, and/or they use a nickel adhesion layer. We have tried both these things. As to be discussed in the next section, nickel plating is somewhat successful, but we would like to avoid using nickel close to our SQUIDs. The bead blast process crinkles the foils, but we think this can be avoided with better fixturing. We are somewhat concerned about the use of glass beads leaving radioactive residues on our foils however.

[5]In the tape test, scotch tape is applied to the plated surface and then rapidly ripped away. If no plating has been removed, then the sample has passed the tape test. Unfortunately, there is not much in the way of control specs for electroless copper. However, using the parameters for electroless nickel and or electrodeposition of copper AMS 2418 may be a more effective test than the tape test.

[6]The standard is ASTM designation B481-68,"Standard Practice for Preparation of Titanium and Titanium Alloys for Electroplating".

7.3.4.2 Thin foils

To accommodate the plated through holes in the flex cable, a plating copper plating thickness of 0.001 inch is targeted. In this section we review various attempts, some successful and some not, for achieving this plating.

There are several ways we assess the quality of our plated layers. The tape test is the minimum challenge of plating quality and is usually tried first. Our plating thickness is large enough to allow us to attempt using a razor blade to peel it away from the foil, as a second plating quality challenge. A further challenge, is repeated dunking the plated specimen liquid helium or nitrogen. It is a test against adhesion failure due to differential thermal expansion, or CTE mismatch. The toughest challenge of plating adhesion we perform is to solder a heavy gauge wire to the plated layer and measure the force needed to rip away the plating under the solder.

	Electroless	Electrolytic				Thermal Evap	Ion Vapor Dep
	Nickel	Nickel	Chromium	Copper	Gold	Al+Cu	Aluminum
Ti 15-3-3-3	$\oplus$	$\odot$	$\ominus$	$\oplus$	$\oplus$	$\ominus$	$\oplus$
Nb-47Ti	$\otimes$	$\otimes$	$\otimes$	$\oplus$	$\ominus$	$\oplus$	$\oplus$

Table 7.6: Methods of plating attempted on thin Ti 15-3-3-3 and Nb-47Ti foils. The table emphasizes degree of success for establishing adhesion between the Ti alloy and the plated material. If successful, the primary adhesion layer is followed by secondary adhesions layers, which enable and include the application of a 300–500 µinch (7.62–12.7 µm) thick copper layer. Table symbols have the following meetings: $\oplus$ – successful, $\ominus$ – failure, $\otimes$ – not tried, $\odot$ – inconclusive or mixed results.

7.3.4.2.1 Electroless nickel We had success obtaining adhesion to Ti 15-3-3-3 with electroless nickel (per AMS 2404 with mid (6%-9%) phosphorous content). This was performed by Titanium Finishing Company (who sold their process to Alexandria Metal Finishers) and Alexandria Metal Finishers. The plate passed the tape test and also liquid helium dunk test, but had some issues with bubbles under the plated metal.

7.3.4.2.2 Electrolytic nickel Here we tried a nickel strike followed by a nickel plate with and without an abrasive blast step. Additionally, in attempt to activate the surface, a duration of reverse bias plating (i.e corrosive etch) was attempted prior to commencement of nickel plating. The plating was performed by the Stanford Linear Accelerator Laboratory (SLAC) plating shop and by Omni Metal Finishing, who immediately attempted to plate copper on top of the nickel. These attempts had mixed results. The copper plate sometimes passed the tape test, always passed the liquid helium dunk test, but could be ripped off by yanking on a wire soldered to the copper surface. The copper surface was rough and blotchy.

7.3.4.2.3 Electrolytic chromium We were unsuccessfully in obtaining adhesion of chromium on Ti 15-3-3-3 foil. The test was performed by UC Chrome whose process includes a blast step, a reverse bias etch, a Woods nickel strike, and finally the chromium plate-up. The process is performed under liquid at all times, to avoid excessive oxidation.

Copper Plated by PNNL

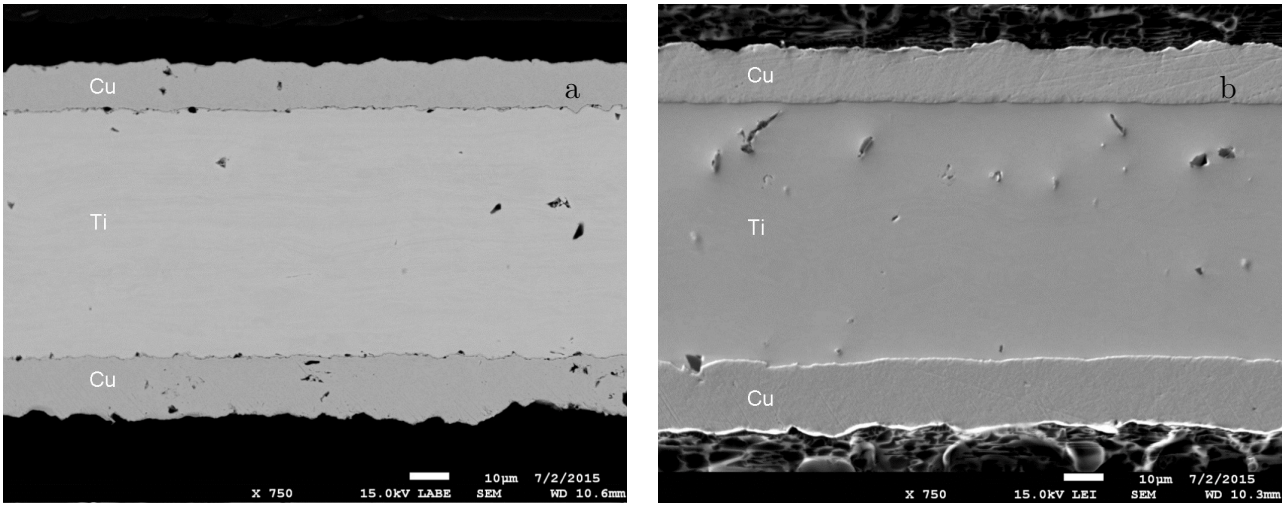


Figure 7.20: SEM micrographs of Nb-47Ti foil electroplated on both sides with copper. The bare Nb-47Ti foils is approximately 0.003 inch thick. The plated samples are epoxied between two glass slides and then the stack is sanded and etched. The effect of heat treatment can be seen in the two views. (a) – No heat treatment. Noticeable voids are present between the copper and the Nb-47Ti. d – Heat treatment using the 400 °C recipe described in Figure 7.21.

7.3.4.2.4 Electrolytic copper A successful process for electroplating copper onto Ti 15-3-3-3 foil was developed by the Pacific Northwest National Laboratory (PNNL) [11]. The process is capable of plating 10–20 µm of copper on foils that are 14.5 inch × 29 inch large, which is clipped on a rack and dangled into solution with the clipped end not submerged. The first step is to condition the surface: hand wipe with Micro-90 cleaning solution, then ethanol, then acetone, then C_6H_6 and finally etch for 30 min in 9% H_2O_2+ 1% H_2SO_4 which creates limited bubbles and strong yellow color liquid. Copper plating is then initiated at a potential of −0.68 V with some current-voltage modulation in an aqueous solution of 1.0 $^{mol}/_{L}$ $CuSO_4$ + 0.6 $^{mol}/_{L}$ H_2SO_4; this is an acid copper plating solution. The plating duration is split into three sessions, with pauses between them, in part, so that, the foil can be flipped and rotated on its racking. The copper on the plated foil, can be forcibly peeled away from the titanium surface. To prevent this, a heat treatment process was developed, where the plated exposed to a peak temperature of 400 °C for 10 min in a 10^{-5} torr vacuum atmosphere, as diagramed in Figure 7.21. We arrived at this process after trying several others, Figure 7.22.

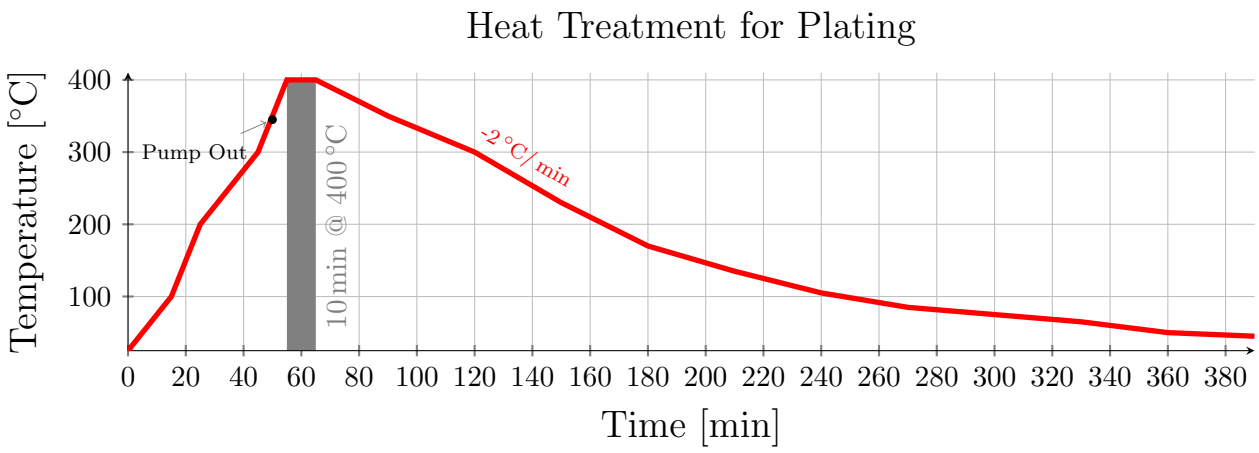


Figure 7.21: Heat treatment process for electroplated copper on Ti 15-3-3-3. The furnace is initially filled with argon gas. About five minutes prior to reaching 400 °C, the argon is pumped out leaving a residual pressure of $1 \cdot 10^{-5}$ torr for the remainder of the process. After 10 min at 400 °C, heating is turned off and the furnace cools at a rate of approximately −2 °C/ min.

Initial results for using the same plating and heat treatment process on Nb-47Ti foils are also positive, but only small foils (several inches square) have been plated so far, Figure 7.20.

It should be mentioned that at temperatures above 400 °C, brittle intermetallic compounds of titanium and copper form and will most likely degrade electrical conductivity through the copper titanium interface as well as degrade adhesion. One potential remedy is to use electroplated silver as a interface layer, [109, 149, 112].

7.3.4.2.5 Electrolytic gold An attempt to use gold as an adhesion layer was successful on Ti 15-3-3-3, but not on Nb-47Ti. In this process approximately 0.25 µm gold was electrodeposited on the foil an then heat treated, 400 °C for 10 min with 45 min ramp up and down in argon atmosphere. Copper was electroplate to finished thickness following the heat treatment. Other than some cosmetic discoloration due to a final weak acid clean, the plated foil was of high quality; it survived the tape test and pulling a wire soldered to the plated foil does not peel up the plating . Prodigy Surface Tech did this plating work.

7.3.4.2.6 Thermal evaporated copper and aluminum Two independent attempts were made to obtain primary adhesion via thermal evaporation. One attempt was performed at the UC Berkeley Nanolab by a collaborator [12] and the following process was used to deposit aluminum and then copper onto Nb-47Ti. First the Nb-47Ti surface is wiped with isopropyl alcohol. Next the foil was plasma conditioned. It was placed in an moderately high power argon plasma for 20 min. It is then taken out of the plasma and transferred to an

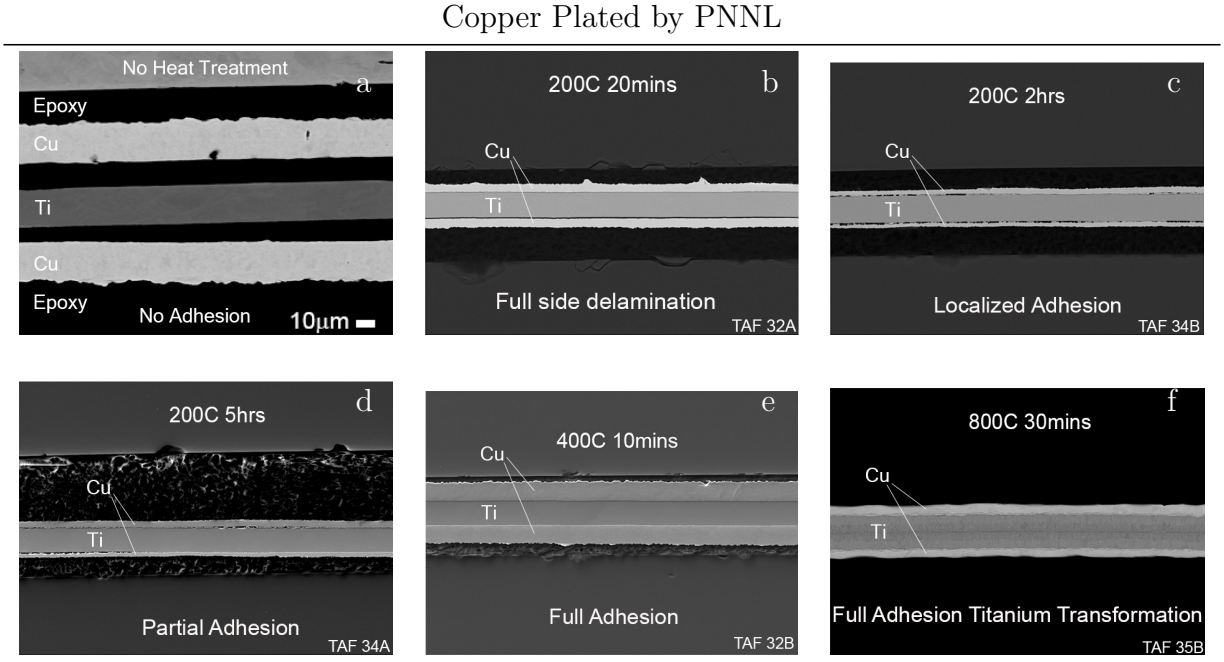


Figure 7.22: SEM micrographs of Ti 15-3-3-3 foil electroplated on both sides with copper viewed in cross section. In all images, the Ti 15-3-3-3 foil is approximately 0.0008 inch thick. The plated samples are epoxied between two glass slides and then then stack is polished to expose the metal layers. The heat treatment occurs in a vacuum atmosphere, 10^{-5} torr, which is initially back filled with argon to remove the air. The peak temperature and time at this temperature for each heat treatment process is indicated on the images. Dark voids between the Ti 15-3-3-3 and the copper can be seen in images *a*, *b*, *c* and *d* indicated lack of adhesion. Image *f* has full adhesion, but the duration and temperature of the heat treatment resulted in a transformation of the Ti 15-3-3-3 microstructure; α-titanium precipitate is visible. Image *e* has full adhesion and no discernible transformation; this heat treatment process is successful.

electron beam evaporation system. Care is taken to limit the foil's exposure to atmosphere to less than two minutes. A 0.5 µm layer of aluminum is deposited onto the film, immediately followed (without breaking vacuum) by a 2 µm layer of copper. Both depositions were done at a rate of $10\,\text{Å}\,\text{s}^{-1}$. Good adhesion is obtained using this process. We find it possible to solder to the copper.

The other attempt was made by PF Technologies Inc. in a large evaporation system with a base pressure of $7.5 \cdot 10^{-5}$ torr. Ti 15-3-3-3 and Nb-47Ti samples were first cleaned with alcohols. At base pressure, a 2 min N_2 and O_2 plasma clean was performed to remove organic contaminants, and then a 3 min CF_4 and O_2 plasma clean was performed to lightly etch the foil surface. Four combinations of materials were deposited: aluminum and then copper on Ti 15-3-3-3, copper only on Ti 15-3-3-3, aluminum and then copper on Nb-47Ti,

and copper only on Nb-47Ti. The aluminum and copper bi-layer was deposited without breaking vacuum. Plating thickness was sacrificed in order to try all four combinations at low cost; as a result the plated material thickness for the Nb-47Ti was 1.6 µm and about 4.8 µm for the Ti 15-3-3-3. Both plating combinations on the Ti 15-3-3-3 initially failed the tape test, although the aluminum and copper treatment had much better adhesion than the copper only treatment. However, when the test test was performed one year later on the same samples, after storage in room air for that long, they both passed. Both plating combinations on the Nb-47Ti passed the tape test, though two things should be pointed out. One, the Nb-47Ti foil surface is much rougher than the Ti 15-3-3-3 foil surface which would help establish mechanical anchoring of the deposited layers. Two, CF_4 and O_2 only etches niobium efficiently, so the Ti 15-3-3-3 foil probably did not benefit from this surface activation measure.

Unfortunately, subsequent attempts by Prodigy Surface Tech to plate up copper on the two PF Technologies deposition combinations involving Nb-47Ti failed. According to Prodigy, the failure mechanism was insufficient copper (or aluminum and copper) thickness, which was rapidly etched in the course of their plating procedures. SEM micrographs of the Nb-47Ti samples confirm there is very little seed material to work with, but also suggest that the seed material is well adhered to the Nb-47Ti, Figure 7.23. A future attempt depositing a thicker seed a layer is well justifies by existing results.

7.3.4.2.7 Ion vapor deposited aluminum Ion vapor deposition (IVD) of aluminum was originally developed by McDonnell Douglas Corp. as a replacement for the corrosion resistant cadmium plating on steel. It is effective at depositing aluminum on nearly any metal and has the added advantage of producing no hazardous waste products and being generally safe for the environment.

The Titanium Finishing Company applied a 0.0007–0.001 inch thick coating of IVD aluminum on our Nb-47Ti and Ti 15-3-3-3 foils. We choose this (excessive) thickness to avoid any subsequent copper adhesion issue due to inadvertent loss of the aluminum layer,e.g. from a scratch or surface preparation treatments for the the copper plate. The aluminum deposition process begins by wiping the parts with isopropyl alcohol; the parts are then positioned in a large (120 inch × 60 inch) vacuum chamber; after the chamber is pumped to base pressure, $8 \cdot 10^{-5}$ torr, a 15 min argon plasma clean is performed at $6 \cdot 10^{-3}$ torr, then the deposition of aluminum begins. 99.99% aluminum is vaporized by an ion beam from and extendable wire source. The parts receiving the aluminum coating do not exceed 120 °C. The quality of the aluminum coating, including adhesion, conforms to MIL-DTL-83488D Class 1 Type I.

Use of the IVD aluminum process transforms that delicate, non-standard job of plating titanium alloy foils with copper to the industry standard job of plating aluminum with copper. Several independent processes were used to plate copper onto the aluminum plated foils provided by The Titanium Finishing company.

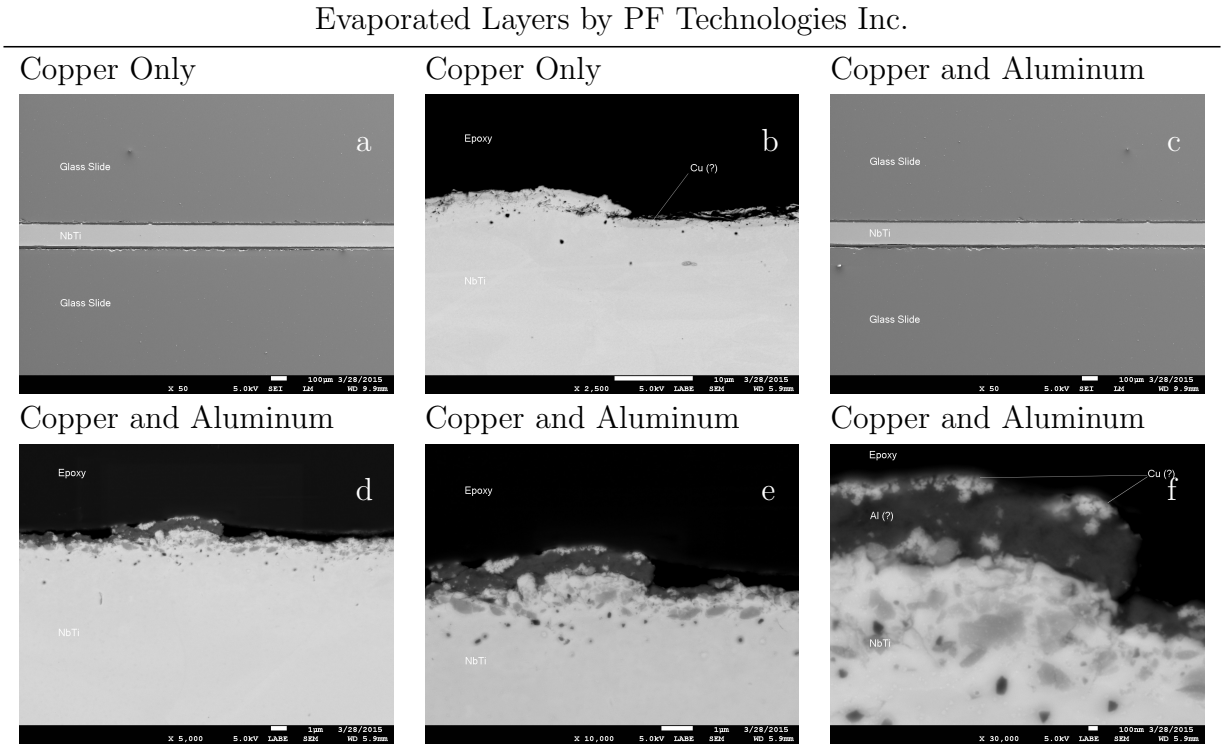


Figure 7.23: SEM micrographs of Nb-47Ti foil with aluminum and copper evaporated onto plated on both sides. Two samples are shown. The first, views *a* and *b*, is copper plated only with a target thickness of about 1.6 µm. The second, views *c* through *f*, is plated with 0.8 µm aluminum, then 0.8 µm copper. For both samples the platings are not clearly evident. Perhaps this is because the layers are so thin, or because adhesion may not be good. The is likely a combination of both. The plated samples are epoxied between two glass slides and then the stack is polished to expose the metal layers. No heat treatment on the plated sample was used. Views increase in magnification from *a* to *d*, and from *c* to *f*, which *a* and *c* the lowest magnification.

Direct electrolytic copper plate Uyemura International Corp. manufactures and sells plating solutions as opposed to providing the plating surface itself. Their "CL-NC-alkaline copper" process is a cyanide free, semi-bright alkaline copper plating process which does not require a zincate step, allowing copper to be plated directly onto most aluminum alloys. The part is pretreated with a degreasing agent, then soaked in a mix of H_2SO_4 and HNO_3. The cleaned part is then placed in the Uyemura copper electroplate solution with less than 30 s exposure to air. Uyemura performed a successful test plate for us on an aluminum plated Nb-47Ti foil, Figure 7.24.

Zincate then electrolytic copper plate Zincation is a standard processing step for adhesion promotion in plating processes, aluminum and magnesium plating processes in

Copper Plated by Uyemura International Corp.

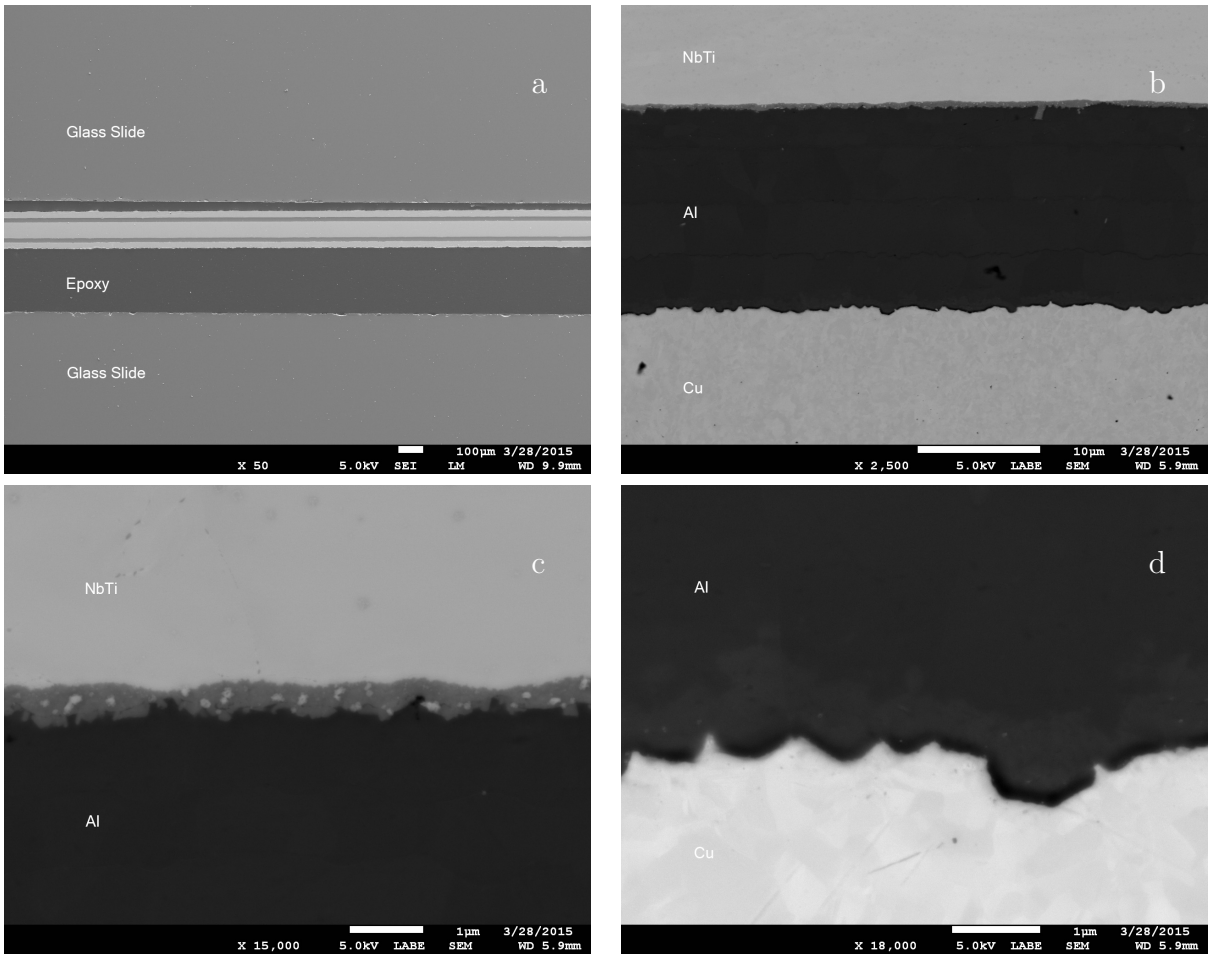


Figure 7.24: SEM micrographs of Nb-47Ti foil plated on both sides with aluminum via ion vapor deposition, and then electroplated copper. The bare Nb-47Ti foils is approximately 0.003 inch thick. The plated samples are epoxied between two glass slides and then the stack is polished to expose the metal layers. No heat treatment on the plated sample was used. Views increase in magnification from *a*, to *d*.

particular. It is an electroless process that deposits a layer of zinc, a few atoms thick, that prevents oxidation of the base metal surface before and during the plating process. The zinc layer is supposed to be etched away by the plating solution, but this may depend on the particular plating solution.

Prodigy Surface Tech had no problem plating copper onto an aluminum plated Nb-47Ti foil, Figure 7.25. They told us they conditioned the foil with a neutral base clean, then a weak acid etch, then a zincate and then, they used a cyanide copper plating solution to build up the desired copper thickness. Another company, Klein Plating Works, also had no

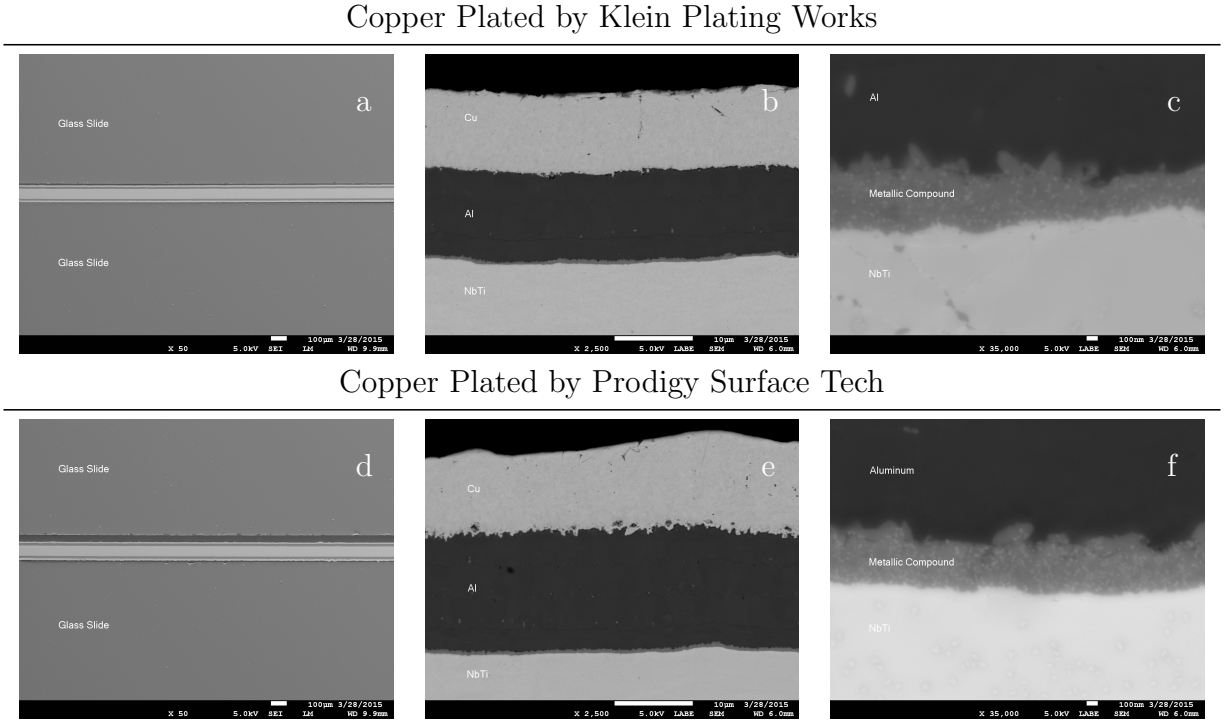


Figure 7.25: SEM micrographs of Nb-47Ti foil plated on both sides with aluminum via ion vapor deposition, and then electroplated copper. The aluminum surface was lightly etched and then zincated to promote the subsequent adhesion of copper. There should only be a few atomic layer of zinc. The bare Nb-47Ti foil is approximately 0.003 inch thick. The plated samples are epoxied between two glass slides and then the stack is polished to expose the metal layers. No heat treatment on the plated sample was used. View magnification increase from left to right with view *a* and *d* being the lowest magnification and *c* and *f* being the highest. The aluminum surface activation, zincate and copper electroplate have been performed by two different companies. The similarity in the plating microstructure between of the two companies speaks to the reproducibility of this process approach.

problem plating copper onto an aluminum plated Nb-47Ti foil. Their process was essentially the same as Prodigy's.

Zincate, then nickel flash, then electrolytic copper plate Omni Metal Finishing Inc. had no problem plating copper onto an aluminum plated Ti 15-3-3-3 foil. Their process involved a zincate step, then a Nickel flash, and finally copper copper electroplate to finished thickness. The microstructure of the plated foil cross section suggests excellent adhesion, Figure 7.26.

Copper Plated by Omni Metal Finishing Inc.

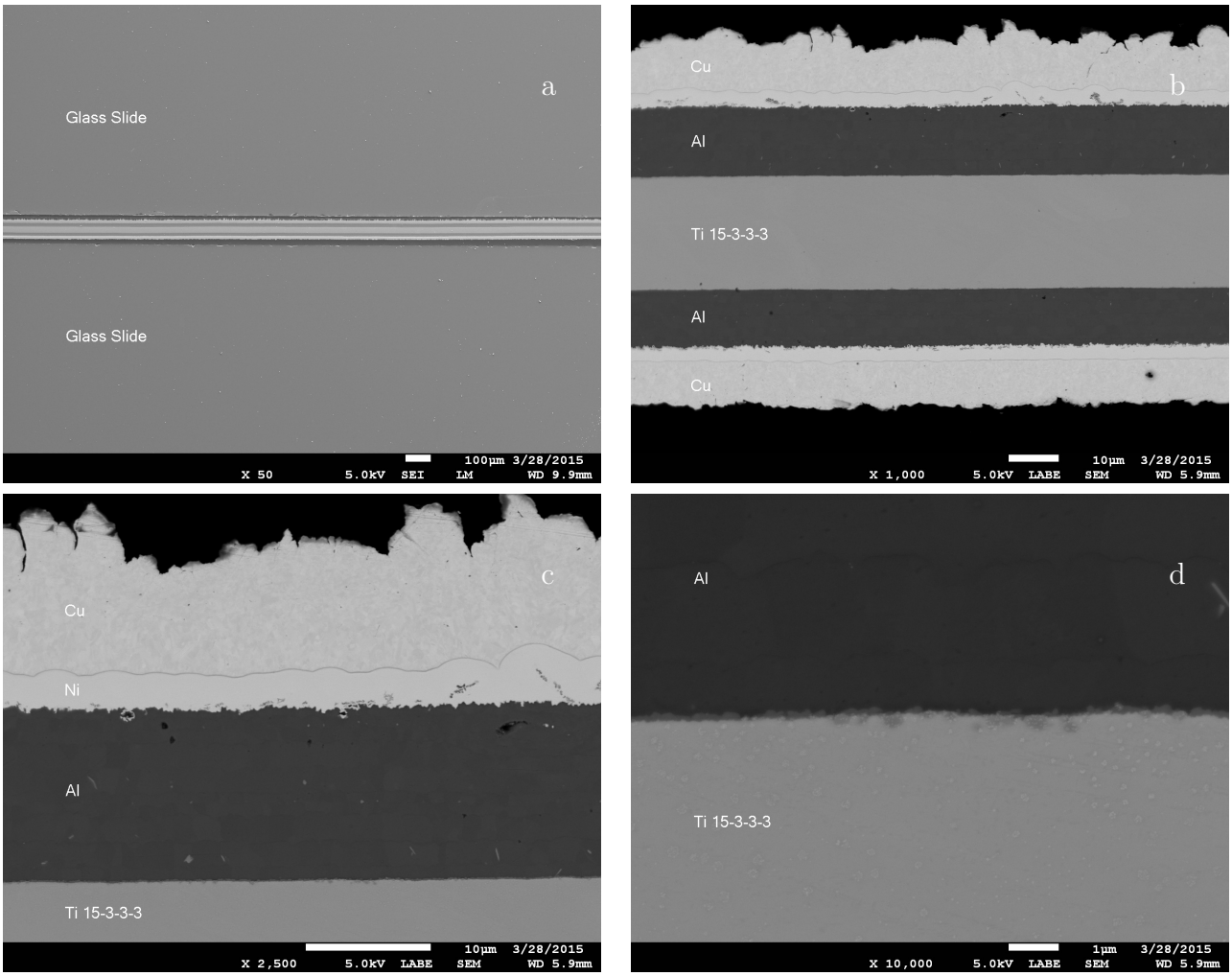


Figure 7.26: SEM micrographs of Ti 15-3-3-3 foil plated on both sides with aluminum via ion vapor deposition, and then electroplated Cu. In order to promote copper adhesion, the aluminum surface was lightly etched, then zincated, then thin layer of electroless nickel was applied. There should only be a few atomic layer of zinc, so it should not be visible in the micrographs. The bare Ti 15-3-3-3 foil is approximately 0.000 84 inch thick. The plated samples are epoxied between two glass slides and then the stack is polished to expose the metal layers. No heat treatment on the plated sample was used. View magnification increase from view *a* to *d*.

7.3.5 Joining

Whereas plating is the atomic deposition of material onto a bulk material, joining is connecting two bulk materials together. We explored joining as an alternative to plating.

The desire here is to join foils that are easy to plate, to the difficult to plate titanium

alloy foils. Then plated through holes will can be made in the easy to plate material. The through hole locations correspond to the ends of the foil, in the long dimension, so we would like to attach a foil with a joint all along the width of the titanium alloy at each end[7]. Such a joint is called a seam weld in the terminology of that industry. Several methods of making the joint were considered, Table 7.7.

[7]Another approach is to make individual spot welds to titanium alloy traces, joining them to a material where the inter-layer connections are made.

	Laser Welding	Diffusion Bonding	Discharge Welding	Ultrasonic Welding	Soldering
Ti 15-3-3-3	$\otimes$	$\otimes$	$\ominus$	$\ominus$	$\odot$
Nb-47Ti	$\otimes$	$\otimes$	$\otimes$	$\otimes$	$\odot$

Table 7.7: Method, attempted or contemplated, of joining easily plated foils to Ti 15-3-3-3 and Nb-47Ti foils. The table summarizes the degree of success for each method. In many cases, the method was not attempted because a clear reason for which it would fail was known. Table symbols have the following meetings: $\oplus$ – successful, $\ominus$ – failure, $\otimes$ – not tried, $\odot$ – inconclusive or mixed results.

7.3.5.1 Methods Considered

7.3.5.1.1 Laser Welding We consulted with a company named Laser Services, who told us that our seam weld application was very non-standard application for laser welding technique, especially with respect to the foil thickness involved. They thought it could be done, but it would require potentially extensive modification of their equipment. We did not pursue this option further.

7.3.5.1.2 Diffusion Bonding In this technique, two parts are joined by pressing them together at high pressure and temperature in an inert atmosphere. Under these conditions, the atoms of one part diffuse into the other resulting in a chemical bond. We consulted with a company named Vacco Industries about bonding a nickel or copper foil to a Ti 15-3-3-3 foil. We were told that the two materials being bonded had to have very similar anneal temperatures, and ours were mismatched by 100–200 °C. The temperature at which diffusion bonding is performed is close to the anneal temperature.

7.3.5.1.3 Discharge Welding In this technique a DC, AC or Pulsed current is passed through the parts to be joined. A combination high temperature from the resistive contact and the migration of atomic species accomplish a bond. The use of this technique to make a seam weld between two foils has been done before, mainly in stainless steel. A rolling spot weld tool head, which looks a lot like a pizza cutter, is used to make the joint. A company named Sunstone Engineering attempted to seam weld Ti 15-3-3-3 and Nb-47Ti foils to aluminum and copper and was unsuccessful. They told us that for best results, the conductivities of the materials to be joined need to very similar. Using nickel, manganin or stainless steel instead of aluminum and copper, might yield better results.

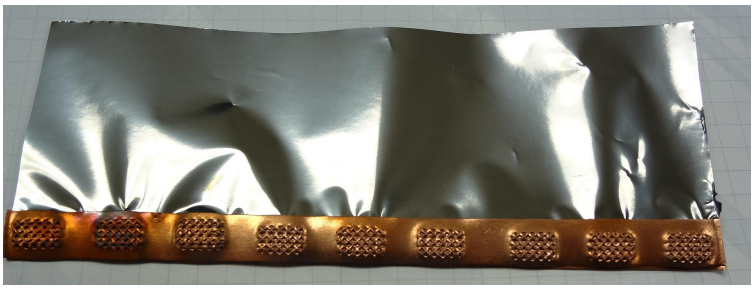


Figure 7.27: An attempt to join a copper foil to a Ti 13-3-3-3 foil by ultrasonic welding. The tool head is waffle patterned for focused ultrasonic contact. Weld attempts using fine patterned ultrasonic tool heads were unsuccessful. Process parameters, including the coarseness of the tool head, were dialed up until a successful weld was made. The welded foil, however, is unusable due to the deep waffle pattern imparted by the weld.

7.3.5.1.4 Ultrasonic Welding In an ultrasonic weld, two foils are pinched together between an ultrasonic “horn” and “anvil”, which have a knurled pattern on them. The

weld is created when ultrasonic energy is focused down the horn making the foils under it vigorously rub together. In this action, surface oxides and contaminates are presumably rubbed away alloy the two materials to form a metallurgical bond. Ultrasonic seam welding of foils is relatively standard and used commonly in the fabrication of batteries and solar panels. We had a company named Stapla Ultrasonics Corp. attempt a ultrasonic seam weld between Ti 15-3-3-3 foil and aluminum, copper, nickel and stainless steel foils. They were not successful at making a smooth continuous seam we wanted. But failing that, they increased process parameters (time, force and knurl coarseness) until they were successful at ultrasonic spot welding the Ti 15-3-3-3 foil to a copper foil, Figure 7.27. With these results, they advised us that ultrasonic seam welding works best when joining materials of similar hardness, ideally the two material would be the same.

S-Bond 220 Activated Solder.

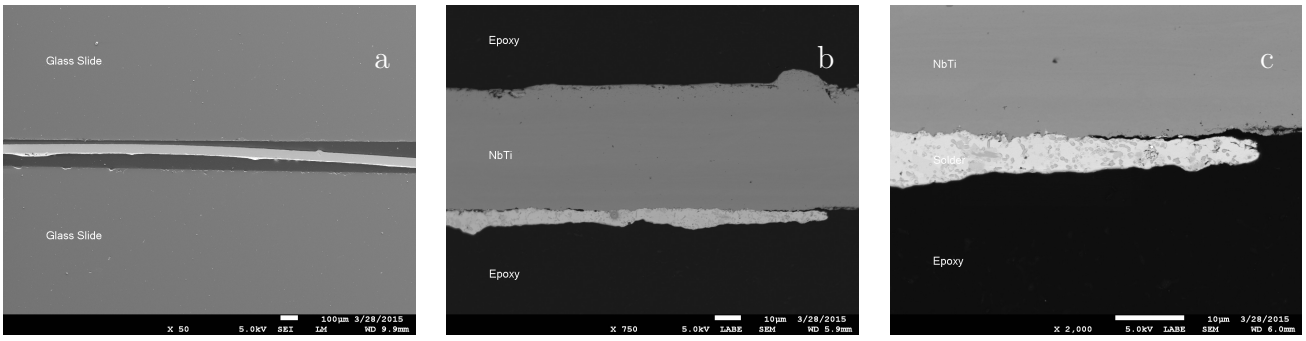


Figure 7.28: SEM micrographs of activated solder on Nb-47Ti foil. The solder was applied using and ultrasonic soldering iron only to the bottom side of the foil, which is approximately 0.003 inch thick.

7.3.5.1.5 Activate Solder Activated solder incorporate small quantities of elements that are highly reactive, such as titanium. The goal is for the active ingredient, dissolved in the liquid solder, to react with the base material and form metallic compounds at its surface that stay there enabling wetting and serving as the foundation of a sound joint. The base material does not even have to be a metal; for example, active solders can join to ceramics, glasses, silicon, diamond and graphites. In the absence of other adjustments, the addition of the reactive ingredients increase the melting point of the solder, even up to brazing temperatures[8]. Fortunately, it has been found that process temperatures around

[8]As a slight digression, let us observe the differences between soldering a brazing [85, §1.1.6]. Most simply and although exceptions apply, solders have lower working temperatures than brazes; 450 °C is a convenient line of demarcation, with brazes seldom having working temperatures higher than 1200 °C. Whereas solders dissolve up to a few microns of the base material, brazes often dissolve 10s of microns. Whereas, solder usually react with the surface of the base material to form intermetallic phases, brazes from solid solutions, i.e. alloys, with the atoms within their depth of penetration. Solders are generally eutectics and soft in

250 °C can be obtained in silver-tin solder activated with approximately 4 wt% titanium, with the addition of trace amounts, less than 1 wt%, of gallium and lanthanide elements (e.g. cerium). Such a solder is sold by a company named S-Bond Technologies, S-Bond 220. Beside lowering the melting point, the trace additions are thought to protect the titanium dissolved in the liquid solder from oxidation and other reactions useless to joining before it reacts with the base metal by doing two things: one, by encapsulating the titanium; and two, by enhancing the formation of surface oxide on the liquid solder. The titanium and other additions also increase the strength of the bulk solder and enhance resistance to corrosion caused by aqueous chlorides. This solder requires mechanical activation order to break the oxide skin and free the titanium from encapsulation, so that wetting of the base material can occur and spread. Although this solder requires no flux and no special atmospheres, best results are obtained using an ultrasonic soldering iron, or some other source of agitation, and pressure, when applying it. [85, 89, 165].

S-Bond technologies successfully wetted samples of Ti 15-3-3-3 and Nb-47Ti foil we provided them. The microstructure, Figure 7.28 of the bond suggests intimate contact with the base material but intermittent contact. This could probably be improved by using a more specialized application technique. They applied the 220 (lead free) solder, with an ultrasonic soldering iron. For future work with the solder, they advised us not to exceed an application temperature of 280 °C (the quoted joining temperature is 240–260 °C); not to exceed 30–60 min liquid working time and to be aggressive when rubbing the solder onto the base metal, especially if it has texture. They advised us to clean off excess oxidation as dross if necessary.

comparison to brazes. Solders are used at temperatures that are 50–90 % of their melting point and up to 10% strain; as a result they are metallurgically unstable. Typically brazes are used at temperatures lower than half their melting point.

7.3.6 Heat sinking

The cable must be adequately heat sunk in order to control the heat load reaching the layers of the tower and ultimately the detectors. Stiffened sections of the cable are design to support electronic components and serve as heat sinking areas. It behooves us to check that these sections are effective at heat sinking every layer of the cable (including the metallic traces and dielectric layers) as well as the power dissipated from the components. What we need to check is that the temperature of the cable emerging from the cold side of the heat sink, Figure 7.29, is the same temperature as the heat sink, $T_{\text{Cold}} = T_{\text{Heat Sink}}$. This calculation requires knowledge the thermal conductivities of each material in the cable and heat sink, their dimensions, and the power dissipation from the components. Additionally, it requires knowledge of the thermal boundary resistance [75, Chap 1, 172] of the interfaces between the materials. This boundary resistance increases as temperature decreases and is best measured experimentally.

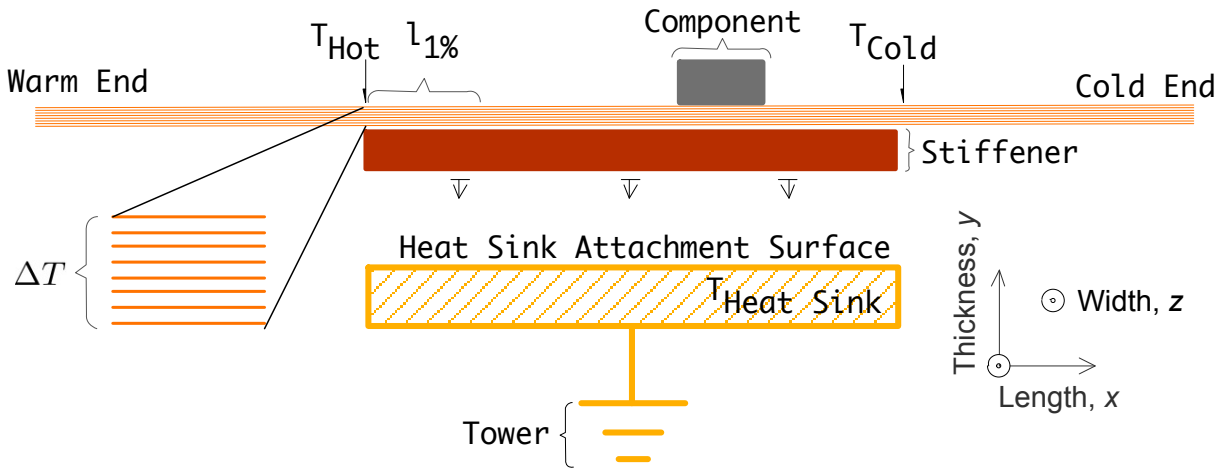


Figure 7.29: A diagram of a heat sink section of the vertical phonon cable. The base of the heatsink, the stiffener, attaches to the heat sink attachment surface of the tower. In addition to the heat coming from the warm end, power dissipation from electrical components (e.g. HEMTs, SQUIDs, shunt resistors) also add to the heat load.

7.3.6.1 Boundary resistance measurement

We use the same methods described in Appendix C to measure the thermal boundary resistance. We simply make the substitution,

$$\kappa(T) \longrightarrow \frac{l}{R(T)} \tag{7.2}$$

in Equation C.1 through Equation C.7, and solve for $R(T)$ or $R(\bar{T})$. For the present situation of the heat sink, the l variable in Equation C.1 through Equation C.7 and Equation 7.2 is

the layer thickness, t, of any cable material layer. If we assume that the thermal resistance, $R(T)$, is roughly constant over the range $[T_{\text{Hot}}, T_{\text{Cold}}]$, then it is given by the formula

$$R = \sum_j \frac{t_j}{\kappa_j} + \sum_j R_j, \tag{7.3}$$

where t_j and κ_j are the respective thicknesses and thermal conductivities of each layer of the cable. The R_js are the boundary resistances between adjacent layers. We expect R be a small quantity, so we design a measurement sample that maximizes our signal to noise. This is accomplished by stacking up multiple copies of the cable layering and forcing heat through the stack. Additionally, we can tack on a multiplicative enhancement to the R we measure by constructing a serpentine path for the heat to travel, as depicted in Figure 7.30 and dimensioned in § D.1.

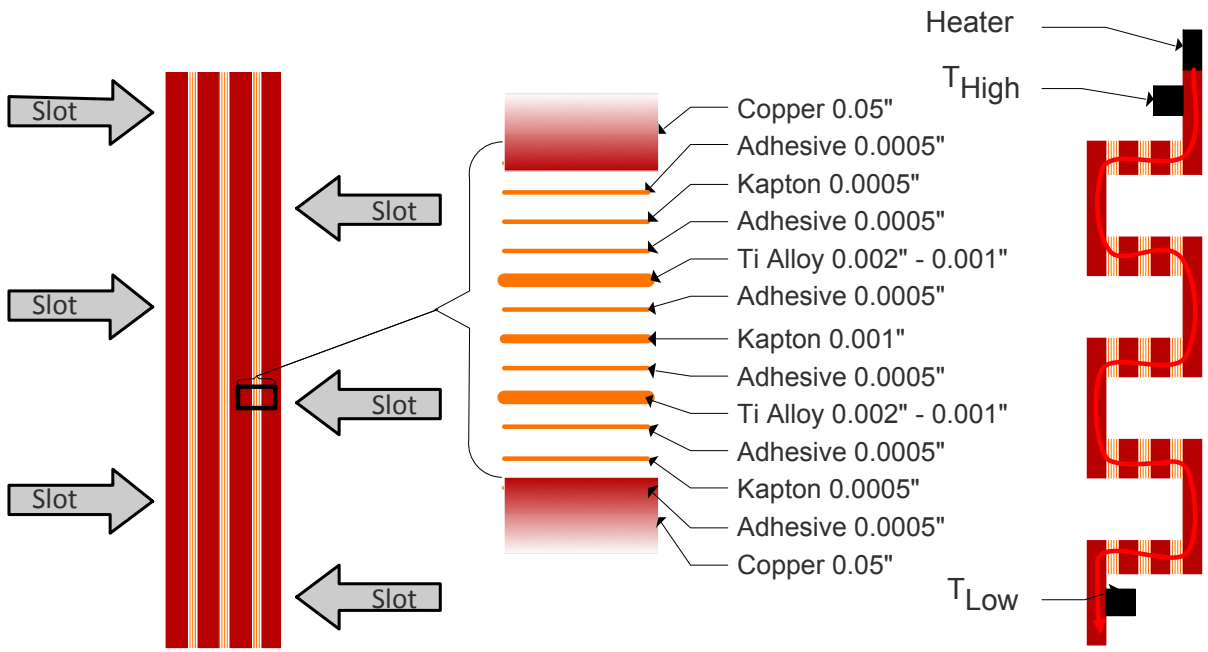


Figure 7.30: Design concept for the test device used to measured the thermal boundary resistance of the vertical phonon cable. The vertical orange line represent copies of the cable layering, which is annotated with thicknesses. The titanium alloy layers were not etched into the trace patterns planned for the cable. The thick vertical dark red bars represent thick layers of copper, whose thermal resistance is so small that these layers can be ignored in the measurement. Slots are milled into the stack to create a serpentine path for heat to travel, as illustrated by the meandered red arrow.

The device was fabricated by laminating together three copper plates with the copies of the phonon cable layering in between them. The serpentine pattern was then milled out of the composite laminated structure, making sure to completely mill through the last cable layer. On total, our device passes heat through the equivalent to 36 copies of the vertical phonon cable. The heat also passes through thick layers of copper, which provides structural support for the device. Since the thermal resistance of copper is so low (i.e. high thermal conductivity), it has a negligible effect on our measurement. Figure 7.31 is a close up of a rung in the serpentine structure, and one observes that each rung has three copies of the cable layering.

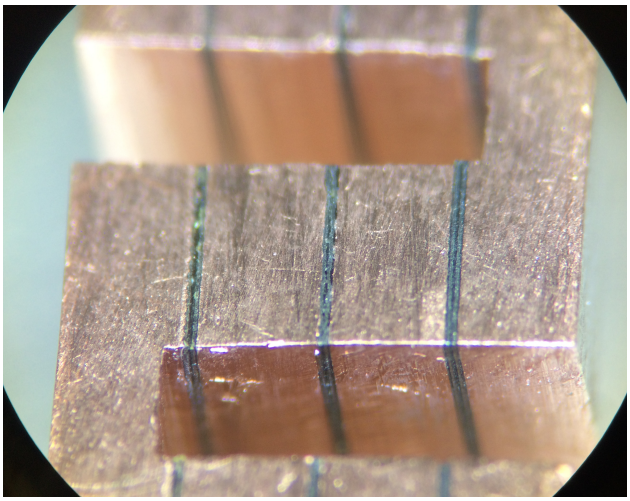


Figure 7.31: A view of a rung on the thermal resistance test device under 20x magnification. Layers appear to be reasonably well separated even after the trauma of milling the slots.

Our results, corrected for the factor 36 enhancement, are shown in Figure 7.32. Also plotted is the expected value of the resistance considering only the resistances of the material layers and ignoring the boundary resistances. At lower temperatures, the boundary resistance dominates. At 50 mK the difference is about a factor of 10. At 500 mK the difference is about a factor of 3. These results underscore the importance of accounting for boundary resistance in cable heat sinking at low temperatures.

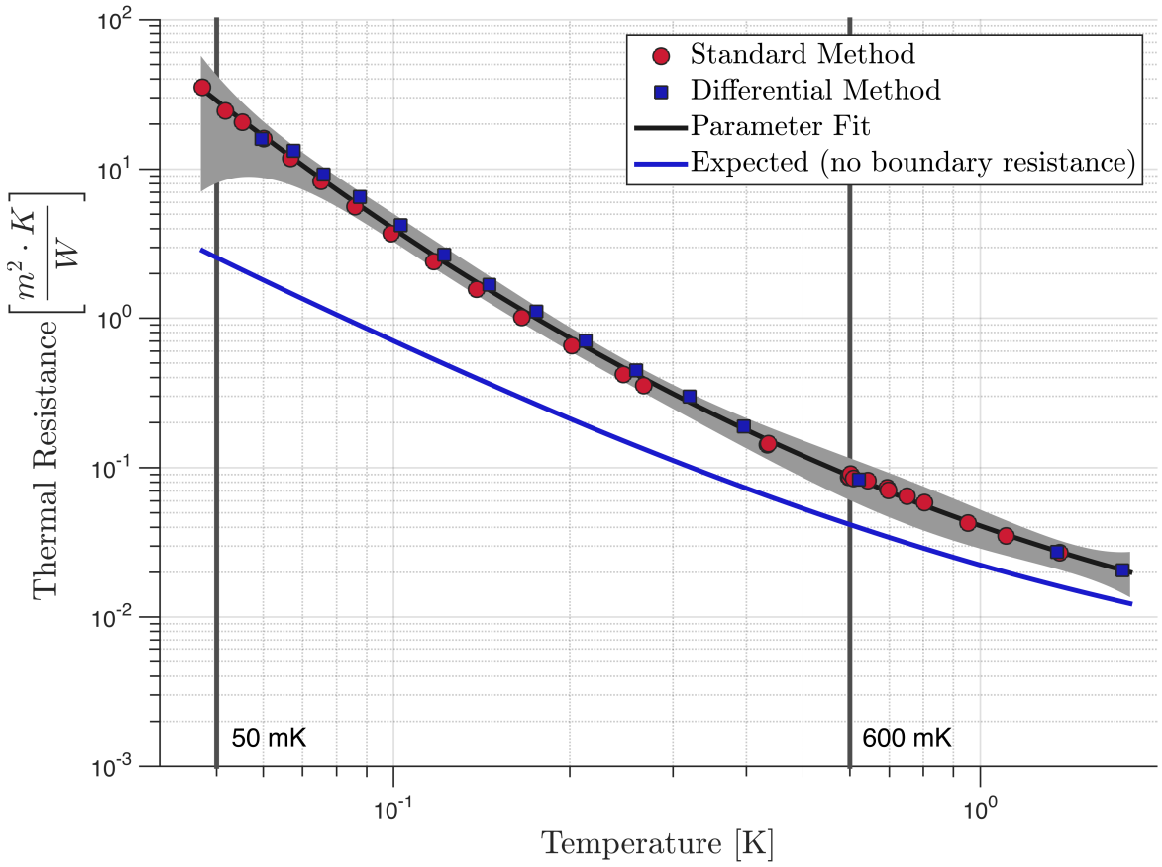


Figure 7.32: The measured total thermal resistance of the vertical cable heat sink compared to the expected total thermal resistance if no boundary resistances are present. The shaded region represents the measurement uncertainty at the 60% confidence level. We use the three different analyses described Appendix C to obtain the data point, except that we solve for $R(T) = \frac{t}{\kappa(T)}$, where the thickness t takes the place of length l.

The fitting parameters derived form method 3 in Appendix C are found to be $a_i = [-1.3878, -1.366, 0.5969, -0.0259]$ for the function,

$$\log_{10}(R(T)) = \sum_{i=0}^{3} a_i \cdot [\log_{10}(T)]^i \; T \in [0.0473\,\mathrm{K}, 1.8\,\mathrm{K}]\,. \tag{7.4}$$

7.3.6.2 Cable Temperature Profile

In the course of studying the problem of adequate cable heat sinking, we have developed a formalism and computer code for computing the temperature profile of the cable that has heat sources, sinks at specified locations along its length. Our formalism [203, 204] accounts

for the effect of boundary resistances at the heat sink. It reduces the heat flow problem to one dimension – the length dimension, and calculates the temperature at each point. This is much faster (and cheaper) than modeling the cable and solving for the three dimensional temperature field, which can be done when the application requires that level of detail. In the present application, we want to determine if the heat sink is large enough, given the materials in and geometry of our cable, to completely remove the heat from the higher temperature stages and our formalism is well suited for that calculation.

We approximate the heat traveling down the non-heat sunk parts of the cable as the sum of the heat traveling though each of its constituent materials as if they were thermally isolated from one another but sharing the same thermal boundary conditions at the beginning of the cable, throughout the heat sink, and at the end of the cable. Thus the total power flowing through the insulated portion of the cable is given by,

$$P = \sum_i P_i = \sum_i \frac{A_i}{l} \int dT \kappa_i(T), \tag{7.5}$$

where the index runs over the material constituents of the cable. We call the thermal conductivity extracted form this type of parallel power flow the aggregate conductivity. The heat sink is assumed to have uniform thermal resistance to the entire portion of the cable that is heat sunk (e.g. a flat, constant width cable on a flat heat sink, or a round cable penetrating an annular heat sink of constant length). The thermal material and boundary resistances of the cable layers are also assumed to be constant[9], which is a good approximation when the temperature gradient in the thickness direction is a small fraction of the heat sink temperature. Also, the heat flowing in the thickness direction (perpendicular to the heat sink attachment surface) is assumed to be much larger than the heat flowing in the length direction. Equivalently, the aggregate thermal resistance across the cable in its thickness direction is much smaller than the aggregate thermal resistance of the cable along its length.

Using the above assumptions, one arrives at the following non-linear second order differential equation,

$$\frac{d}{dx}P(x) = \frac{d}{dx}\left(A \cdot \kappa(T)\right) = \begin{cases} \dfrac{w_{\text{width}}}{\sum_j \frac{t_j}{\kappa_j} + \sum_j R_j}\left[T(x) - T_{\text{Heat Sink}}\right], & \text{if heat sunk} \\ 0, & \text{otherwise} \end{cases} \tag{7.6}$$

where P is the power flowing through the position x, and the sums are carried out over the interface layers between the cable surface and the heat sink attachment surface. For example, in Figure 7.29, a stiffener is glued to the bottom side of the cable and to the heat sink attachment surface. The sum would include three thicknesses (the first glue layer, the stiffener and the second glue layer) and four boundary resistances (cable-glue, glue-stiffener, stiffener-glue, glue-heat sink). Notice that the order in which the heat encounters the boundary resistances as it flows into the heat sink does not matter.

[9]This assumption can be discarded at the expense of complexity in Equation 7.6, which would then involve integrals.

Equation 7.6 can be solved perturbatively and analytically [119], by matching boundary conditions. However, we find it more straightforward to solve it using a finite difference method. In this method a mesh of N points with optionally nonuniform spacing is laid along the length of the cable, the x-axis; the differential equation is discretized using the center different approximation for the derivative; $N-2$ nonlinear equations emerge, one for each non-boundary mesh point, relating the temperatures at that point and its adjacent points; the temperatures at the boundary points are given; and the system of equations is minimizes using Newton-Raphson. Figure 7.33 shows the temperature profile calculated using our formalism, assuming a 0.06 inch thick cirlex stiffener, but assuming a perfect interface between the cirlex and the heat sink attachment surface[10].

One may be concerned that the assumption of an aggregate thermal conductivity would lead to a large temperature gradient across the thickness of the cable, at the heat sink. If so, then the gradient would be largest at the T_{Hot} location because the largest amount of power is flowing through that location. Having measured the boundary resistance, we are able to estimate the temperature gradient. From Equation 7.5, we calculate the P_i corresponding to the top material layer of the cable. Then we use our computer program to calculate the temperature at T_{Hot}, assuming that the cable is, one, made of only that top material, two, has P_i flowing through it (i.e. a boundary condition in power rather than temperature), and three that the thermal resistance from the top material to the stiffener is the quantity we measured minus the resistance of the top material. Performing this calculation will give $T_{\text{Hot, Top}}$. We can find the temperature of the bottom of the cable, $T_{\text{Hot, Btm}}$, just about the stiffener, using our program to run a similar calculation. In this calculation, we assume the complete composition of the cable so that the total power, $P = \sum_i P_i$ is flowing in the x-direction into the heatsink, but then we set the thermal resistance between the cable and the heat sink equal to just one factor of the boundary resistance, i.e. just R_j of Equation 7.3. Thus we have scaled the boundary resistance we measured to extract the relevant portion involved in the heat flow form the top and bottom layers of the cable. We have done the calculation assuming three different stiffener thicknesses and find the temperature gradient, $\Delta T_{\text{Hot}} = T_{\text{Hot, Top}} - T_{\text{Hot, Btm}}$, to be comfortably small, Table 7.8. This calculation of ΔT_{Hot} neglects the raise in temperature of $T_{\text{Hot, Btm}}$ due to heat flowing from the top layer which would decrease the temperature difference; it also neglects the stiffener-related boundary resistances.

7.3.6.3 Cable power profile

As mentioned, the formalism can be used the compute the power flow at any given point along the one-dimensional cable. It is interesting to look at the power flow as a function of position for our cable Figure 7.34. One observes that the thermal power from the warm end of the cable is rapidly shunted into the heat sink, which is precisely the desire. As a measure of the adequacy of the heat sink, we can calculate the distance from warm end edge of the

[10]The thickness of the cirlex and whether or not it would be used had not been decided at the time of the design of the thermal resistance test device

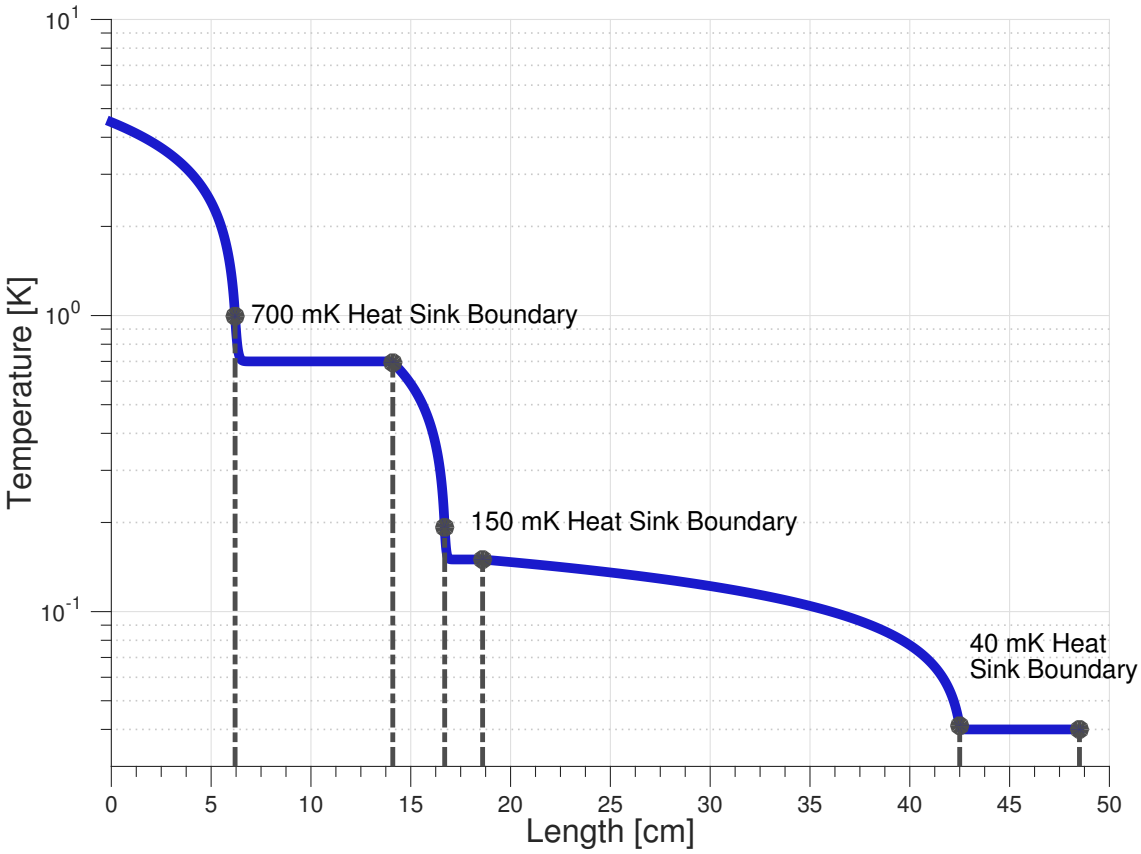


Figure 7.33: The temperature profile of the vertical phonon cable including the effect heat sinking but not the effect of added electronic component heat dissipation. The heatsinks include the total thermal resistance plotted in Figure 7.32. Length = 0 cm is the cryocooler stage of the tower whose temperature is estimated to be around 4.5 K due to the low altitude of the SNOLAB facility. The cable extends considerably beyond the 40 mK heat sink to reach the detector, but we truncate to plot at this heat sink. This plot assumes a 0.06 inch thick cirlex stiffener is located between the cable and heat sink attachment surface, which represents the worst case heat sinking efficiency. Even in this scenario, the cable is rapidly brought to the heat sink temperature.

heatsink that the un-shunted power in the cable is 1% of the value at the warm edge of the heat sink, Table 7.8; call this distance $l_{1\%}$. One also observes that power is drawn out of the heat sink and into the cable at the cold end of each heat sink. Thus, the total heat load on the heat sink is properly calculated as the difference between the power flowing into the heat sink at its warm end, and the power flowing out of the heat sink at its cold end. This

	ΔT_{Hot} [mK]	Δp [W]	$l_{1\%}$ [mm]
700 mK			
0 mil	19	$22.0 \cdot 10^{-6}$	
30 mil	10	$21.9 \cdot 10^{-6}$	
60 mil	7.3	$21.8 \cdot 10^{-6}$	3.9
150 mK			
0 mil	14	$467 \cdot 10^{-9}$	
30 mil	7.8	$453 \cdot 10^{-9}$	
60 mil	5.5	$447 \cdot 10^{-9}$	2.4
40 mK			
0 mil	0.88	$716 \cdot 10^{-12}$	
30 mil	0.73	$713 \cdot 10^{-12}$	
60 mil	0.60	$712 \cdot 10^{-12}$	1.6

Table 7.8: Effect of different stiffener assumptions on phonon cable heat sinking. ΔT_{Hot} is the temperature difference between the top and bottom (above the stiffener) layers of the cable at the warm end of the heat sink. Δp is the net thermal power absorber by the heat sink; at its warm end power flows into the heat sink; and at its cold end power flows out of the heat sink. The total load on the heat sinks for the 48 tower maximum payload would be $48 \cdot 6 \cdot \Delta p$. $l_{1\%}$ is the distance from the edge of the heat there only 1% of the incoming thermal power remains in the cable. Stiffener thickness given in milli-inches, mil.

Δp is given per heat sink[11] in Table 7.8 for three stiffener scenarios.

[11] There are six phonon cables per tower, so $6 \cdot \Delta p$ would be the per tower heat at the respective temperature stage.

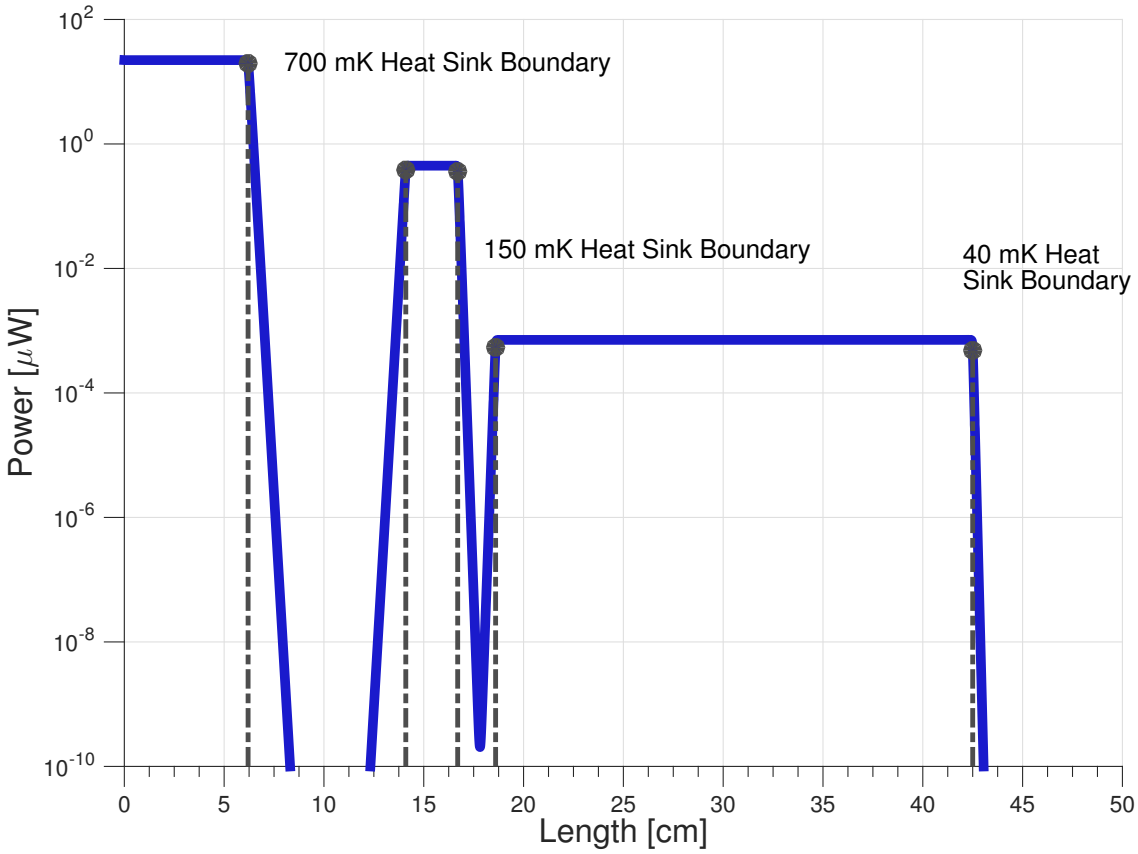


Figure 7.34: The thermal power profile of phonon cable. The power flow is constant in the insulated portions of the cable, but drops rapidly to toward zero in the heat sunk portions of the cable. Power flows out of the heat sinks and into the cable at the cold end of each heat sink.

With such short $l_{1\%}$ lengths, it may seem like we are needlessly worrying about adequate heat sinking. For this case, it is not such an issue. However for other cases, usually involving large thermal resistances to the heat sink in comparison to the thermal resistance of the cable, it can be an issue.

7.3.6.4 Sinking heat for electrical components

Now that it is clear that our heat sinks are adequate and in fact quickly remove heat from the cable, we can ask ourselves if there will be any issue removing the heat dissipated by the electrical components on the stiffened portion of the cable.

The length of the heat sink attachment surface is designed to be as large as the stiffener, and the stiffener supplies rigid support for the circuity and electrical components located on

	$\Delta T_{\text{Components}}$ [mK]
700 mK	
0 mil	0.8516
30 mil	1.865
60 mil	2.878
150 mK	
0 mil	1.167
30 mil	1.917
60 mil	2.666

Table 7.9: The raise in temperature of phonon cable due to power dissipation of components. Figures represent the situation where the componnts on each heat sink are grouped together on the heat sink and their total heat is heat radiated over its contact area with the heat sink only. Component power dissipation, per phonon cable, are as given in Table 7.1 and contact areas are $2.38 \cdot 10^{-4}\,\text{m}^2$ for the SQUIDs and $1.12 \cdot 10^{-4}\,\text{m}^2$ for the shunt resistors. In this table, $\Delta T_{\text{Components}} = T_{\text{Top}} - T_{\text{Heat Sink}}$ is the temperature difference from the top of the cable in comparison to the heat sink temperature. Stiffener thickness given in milli-inches, mil.

the cable directly above. The components constrain the size of the stiffened cable portions to be rather large. So it is no surprise that the heat sinks are much larger than necessary to accomplish the task of removing the heat coming from the warm end of the cable. We can safely assume that each component is mounted on cable that would be the same temperature as the heat sink and we can ask how hot the component should get, based on its power dissipation and the thermal resistances between it and the reservoir sustaining the temperature of the heat sink. The temperature difference is given by

$$\Delta T_{\text{Components}} = P_{\text{Component}} \frac{R_{\text{Total}}}{A_{\text{Component}}}, \tag{7.7}$$

where $P_{\text{Component}}$ is the power dissipation of the components, R_{Total} is thermal resistance of the cable plus the stiffener and $A_{\text{Component}}$ is the area of the component. Equation 7.7 represents a, "hot spot", scenario because we spread the contact area of the component, and not over a larger portion of the heat sink area.

We see that the temperature rinse due to power dissipation from the components is not going to be a problem. We also see that the component power dissipation Table 7.1 is smaller than the heat transfer load from the warm end of the cable Figure 7.34, implying that the heat from the component will be removed by the heat sink in a similarly short distance around the components.

7.3.7 The 4 K to 300 K cable

Electrical connectivity between room temperature and the warm end of the towers is accomplished by a twisted pair ribbon cable[12]. The signaling needs of each detector require that it be read out by roughly 50 pairs (100 traces). The minimum length of the cable is set by the layout of the SNOLAB experiment and, given the trace material and size, the minimum length sets the minimum cable resistance heat load on the towers. The detector readout system will impose constraints on the round trip resistance, inductance and capacitance of the cable. The cooling power the cryogenic system at its heat sink locations impose constraints on the heat load due to the cable. The minimum aperture diameter in the route the cables must travel from the tower to their connection point at 300 K limits the width of the cables to be no larger than 2 inch, implying a 0.02 inch maximum wire diameter.

For a variety of reasons, including heat load control, durability, and electrical grounding, the cable will have four sections, Figure 7.35. Section two is 50 K heat sink and circuit board with copper traces and section four is a copper twisted pair ribbon cable that reaches between a 4 K heat sink and a tower. For the maximum tower payload of 48 towers, a heat load of approximately 150 W is allotted for the 50 K heat sink and 2.7 W is allotted for the 4 K heat sink, for the task of heat sinking the cables.

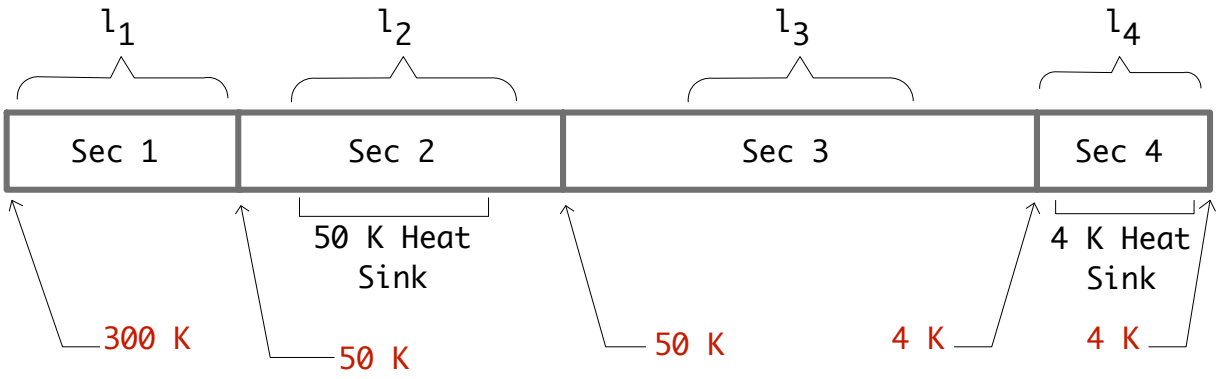


Figure 7.35: Block diagram of 4 K to 300 K cable. Section one and three are a low thermal conductivity trace material; sections two and four are copper. Section two is a circuit board that is heat sunk on its top and bottom faces. There is a heat sink in section four, but its dimensions are not determined. Approximate lengths are as follows: l_1 = 20–25 inch, l_2 = 3.5–10 inch, l_3 = 255–283 inch, and l_4 = 12–36 inch.

To choose the trace material and size, we consider the resistances and thermal conductivities of standard low temperature wire materials, including copper brass beryllium copper,

[12]such cables are typically woven together with an inert polymer like nomex and can be obtained from vendors such as Tekdata and CMR-Direct.

phosphor bronze and manganin. Constantan, evanohm, bronze and cupro-nickel are also an options, but not considered. The electrical and thermal conductivities for these materials were pulled from the literature and an exact relation between these quantities and the resistance and area per trace was derived,

$$R \cdot A = l_1 \frac{\int_{50\,\mathrm{K}}^{300\,\mathrm{K}} \kappa(T)\rho(T)dT}{\int_{50\,\mathrm{K}}^{300\,\mathrm{K}} \kappa(T)dT} + l_2 \cdot \rho_{Cu}(50\,\mathrm{K}) + l_3 \frac{\int_{4\,\mathrm{K}}^{50\,\mathrm{K}} \kappa(T)\rho(T)dT}{\int_{4\,\mathrm{K}}^{50\,\mathrm{K}} \kappa(T)dT} + l_4 \cdot \rho_{Cu}(4\,\mathrm{K}), \quad (7.8)$$

where R and A are the one-way resistance and cross-sectional area of the trace. Notice that Equation 7.8 accounts for the copper sections of the cable. Using this formula we can calculate the cross sectional areas necessary to achieve different target resistances with different trace materials. Then we can use those areas to calculate the heat loads Δp, on to the 50 K and 4 K heat sinks. These figures are presented in Table 7.10.

	Area [mil^2]	Diameter[mil]	$\Delta p_{50\,\mathrm{K}}$ [mW]	$\Delta p_{4\,\mathrm{K}}$ [mW]
10 Ω				
Brass	38.5	7.0	85.8	0.283
BeCu	63.6	9.0	196	0.448
Phr. Brz.	97.9	11.2	167	0.527
33 Ω				
Brass	11.7	3.85	26.1	0.0859
BeCu	19.3	4.96	59.6	0.136
Phr. Brz.	29.7	6.15	50.8	0.160
100 Ω				
Brass	3.85	2.21	8.58	0.0283
BeCu	6.63	2.85	19.6	0.0448
Phr. Brz.	9.79	3.53	16.7	0.0527

Table 7.10: Table of dimension and heat load figures for different 4 K to 300 K cable trace resistance and material scenarios. Trace alternatives for 4 K to 300 K cable. The total load on the heat sinks for the 48 tower maximum payload would be $48 \cdot 6 \cdot \Delta p$. Dimensions given in milli-inches, mil.

Additional discussion and a derivation of Equation 7.8 can be found in [204].

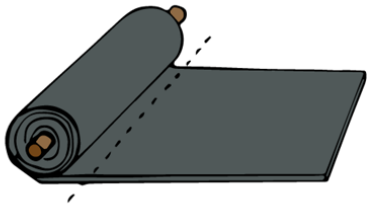
7.3.8 Cable Fabrication

We describe the fabrication process for the phonon flex cable. This process is a considerable departures from the standard copper kapton flex fabrication process used in industry because

it involves etch of and plated through hole connections to titanium alloy foils. We emphasize innovations on the standard process, which we have had to develop. We believe this process is generally useful for making titanium flex circuits for other applications apart from our own.

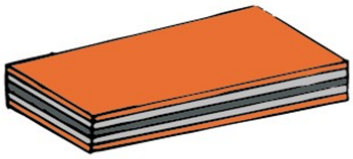
In § 8.2 we propose an alternative fabrication process to the one proposed here.

Phonon cable fabrication process

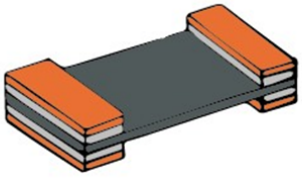


Step 1: Acquire titanium alloy foil. Choose for their low thermal conductivities and superconducting transition temperatures, the SuperCDMS SNOLAB vertical cable will use either Ti 15-3-3-3 or Nb-47Ti foil as the conductor trace material. Foil thickness in the range 0.5–1 minch offers a good combination of low cross section and durability for handling. One wants a low cross section to limit heat conduction an to attain good etching resolution. Poor etching resolution limits the minimum trace width and separate. One also prefers the foil to be roll form, so that whomever is fabricating the cable can cut it into sheets at their preferred length. 12 inch width is good choice for compatibility with standard processing equipment. Narrower than 8 inch may result in increased fabrication labor costs.

Phonon cable fabrication process

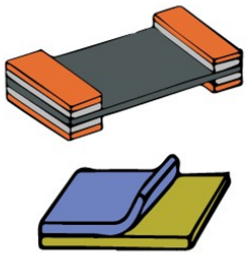


Step 2: Plate the foil. Standard plated through hole (PTH) interconnect processing relies on the ability to plate a tiny annular exposed portion of the foil with copper. Since Ti alloys are difficult to plate, the standard PTH process is doomed to failure if done without innovation. As such, we pre-plate the foil (either on a roll-to-roll or sheet-by-sheet basis) on both sides with copper. Methods getting the copper to stick on the foil have been discussed before; sometimes an intermediate adhesion layer (e.g. aluminum) is used, as depicted. Target copper thickness is 300–500 µinch, which is on the thicker side to ensure the layer is not inadvertently etched away during cable fabrication.

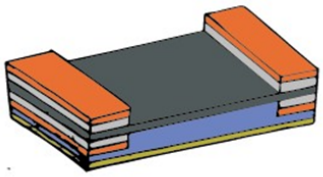


Step 3: Remove copper from low thermal conductivity regions. The copper, and any adhesion layer used, should be removed from places where it is not needed for the PTHs or else it will be the source of significant heat conduction. The copper mush be removed prior to laminating lamination to dielectric layers, because after lamination access is lost to the copper surface. Bands of copper are depicted at the ends of the foil because in the vertical cable design, these correspond to sections of the cable that are heat sinks, so the copper is helpful in these locations.

Phonon cable fabrication process

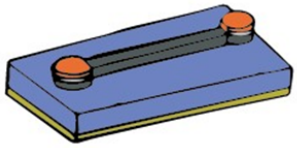


Step 4: Choose the dielectric layers. There are several choices of standard dielectric-adhesive composite laminates. Then the adhesive is on only one side of the dielectric, the composite is called a coverlay and when its on both sides the composite is called a bondply. There are adhesive-less options as well (e.g. adhesive less kapton), which are typically thermal plastics and become sticky when heated. We have looks at kapton dielectric coverlay options having either epoxy or acrylic adhesives. Dielectric thickness between 0.5–3 µinch and adhesive thickness between 12.5–1 µinch are standard. Low loss tangent fluorinated polymer composite options also exist. Controlled impedance circuitry is also achievable with appropriate choice of composite. In general, one might base their choice on thermal conductivity, dielectric constant, loss tangent, and processing temperature of the composite. The vertical cable will most likely use Pyralux.

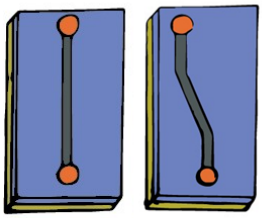


Step 5: Laminate foil to dielectric composite. Lamination is performed under vacuum (approximately 1 atm), at temperatures between 190–315 °C depending on the composite, at elevated mechanical pressure (250 psi), for a certain duration of time (e.g. 30 min). The laminated foil obtained will become one layer of the flex circuit.

Phonon cable fabrication process

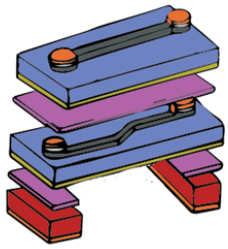


Step 6: Etch trace pattern into laminated foil. This step is made difficult by the titanium alloy. Chemicals that are nonstandard to the copper flex cable industry are require etching titanium. Moreover, these chemicals attack standard processing equipment, so specialized inert (fluoropolymer) infrastructure is necessary. Fortunately, etchants for the metals, including titanium etchants, do not aggressively attack the dielectric composite.

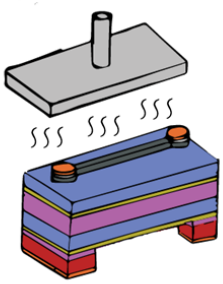


Step 7: Etch trace patterns into remaining laminated foil panels. Sufficient material must be available to provide for not just the the layers of the flex circuit, but also for failed etch attempts and other process step failures. This is what we have learned from other titanium flex circuit prototypes. The nonstandard aspect of the precess results in an imperfect process step success rate.

Phonon cable fabrication process

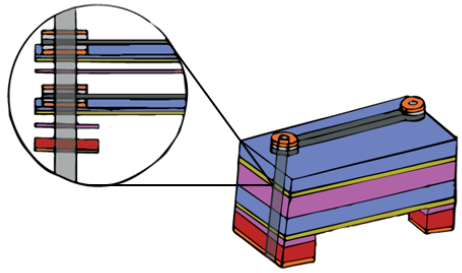


Step 8: Align laminated foil layers and stiffeners. The party fabricating the circuit will have included alignment features on each layer to help help with this step. Layer-to-layer registration is typically on the order of ± 0.001 inch and greater. Layers of bondply are used to adhere adjacent laminated foil layers. Also, stiffeners are included in the stack, according to the circuit design plan. In order to avoid curling due to stresses in the circuit, it is a good idea to design symmetry in the stack. For example a simple flex circuit with just one layer of patterned metal on a dielectric composite will curl. Curling will be reduced if an additional cover layer of dielectric composite is use on top of the metal.

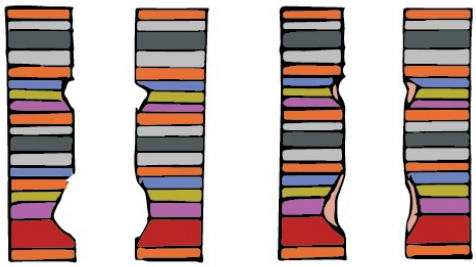


Step 9: Laminate all layers together. This, again, requires vacuum, heat and mechanical pressure for a duration of time. The adhesive layers conform to the patterns in the metal layers. That is, if the metal foil is thick compared to the adhesive thickness used to bond together layers, the patterns in the covered layer will make noticeable imprints in the covering layers.

Phonon cable fabrication process



Step 10: Drill through stack for PTHs. The disk shaped metal areas through which the drill penetrates are enough larger than the drill diameter that an annulus of metal is left around the hole.



Step 11: Etch and apply copper seed layer to PTH surface. It standard in flex circuit manufacturing to etch organic materials (including oils, debris, and the dielectric-adhesive composite) back from the inner edge of the metal annuluses formed by the drill step. The 'etch back' is accomplished using an oxygen plasma and typically about 0.001–0.003 inch of metal rim is exposed. The result is a cleaned through hole with the top, bottom and the cylindrical edges of the metal layers exposed. After some additional cleaning, the wall of the through hole is sensitized to accept the adherence of a thin electroless copper seed layer, as depicted in the right illustration.

Phonon cable fabrication process

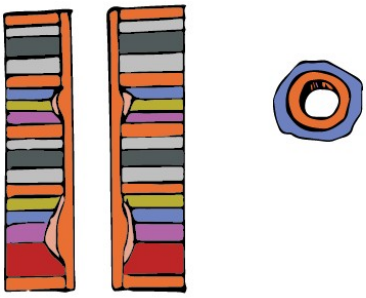
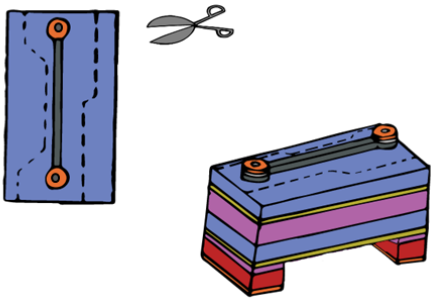
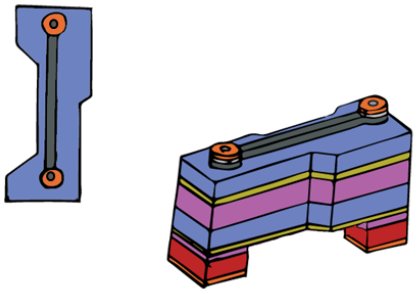
	**Step 12:** Electroplate through holes with copper. The electroless copper seed layer enables subsequent electrolytic copper plating. The plated copper thickness is typically at least 0.0014 inch. The copper connects all layers, including the pad visible on top of the stack. However, the copper is not expected to adhere to the cylindrical edges of titanium by the drill cut. Fortunately, it will adhere to the pre-plated copper on the titanium foils to ensure sound electric connection to the titanium alloy.
	**Step 13:** Cut out individual circuits from panel. A routing tool is used to release the individual circuits form the panel, which may have carried several side-by-side.
	**Step 14:** Inspect and test each circuit. The fabricating party can be expect to perform quality assurance testing at room temperature and maybe some testing slightly below 0 °C. It is necessary for the end user to perform testing at base operating temperature. The concern is that cooling induced stresses could result in open circuits.

Table 7.11: Illustrated [2] step-by-step description of phonon cable fabrication process.

Attributions

Results presented in this chapter were obtained working with my students. Nick Kellaris and I developed the thermal conductivity readout. He and Kick Zobrist performed many of the thermal conductivity measurements. Nick Zobrist worked on flat cable heat sinking calculations. Erik Kramer worked on the tower standoff and collected data on them.

Chapter 8

Technology Applications and Future Work

8.1 Conclusions with regard to the KIDs phonon sensors

The goal of the work on KIDs phonon sensors was to explore to feasibility of using this technology as a future replacement to the TES phonon sensors on the CDMS detector. To be a viable replacement, KIDs phonon sensors would need to have comparable sensitivity to the TESs. Potential advantages of the KIDs phonon sensor scheme considered here include simplified fabrication, due to separation of sensor and absorber functions (§ 3.1.4); simplified readout, due to frequency domain multiplexing of each sensor; increased uniformity in the performance of the phonon sensors, due to the simplification of their design; and increased scalability of the dark matter experiment due to the relative ease of KIDs phonon sensor fabrication. Over the course of research, we determined that in order to use an unpatterned ground plane, which is desired for its simplicity, with sensitivity anywhere near the TES sensitivity, separated function microstrip resonators would have to be driven at high probe power, due to relatively low ground plane kinetic inductance fraction. It was quickly found that nonlinear resonances resulted from level of probe power required. Consequently, research was directed toward understanding the nonlinearity, in particular finding a way to design the resonators so that they could tolerate high probe power without becoming nonlinear. At the time of this writing, such a design has not been found, and data from experiments does not satisfactorily confirm the hypothesis that wider resonators can tolerate higher probe powers. Data from experiments also shows that the resonant frequencies and internal and coupling quality factors for test devices varied from run to run, for a given device, and for all devices, with respect to simulated values. Possible contributing factor to this variation include the presence of vortices, as suggested by data from use of a hexagonal mesh ground plane; imperfect control of the microstrip gap; and lithographic misalignment between the resonator coupler and the feedline. The nonlinearity and the variations in res-

onator parameters represent challenges to the goals of obtaining comparable sensitivity to the TES phonon sensors and the goal of improving upon the uniformity of the TES sensors. It may be possible to overcome these challenges with further work.

8.2 Alternate flex cable fabrication process

The good adhesion of aluminum to to titanium alloys makes it possible to proposed an alternate fabrication route for the flex cable described in . This is probably simpler than the one described previously. Its disadvantage is that it nonstandard and may make the party doing the fabricating uncomfortable for this reason.

Instead of plating copper onto the titanium allow foil, we deposit IVD aluminum and only one side (a). Then the titanium alloy side is laminated to the overlay (b and c). Next we pattern and etch the aluminum away from all places except the plated through hole contact areas (d). Then we pattern and etch the traces into the titanium foil (e). This is done for all layers of the cable (f). The layers are then aligned, and laminated together (g). Finally the holes for the plated through holes are drilled in the appropriate locations. Cleaning, "etch back", and lastly copper plating are done.

This process relies on two details presented earlier. Once, that it is easy to achieve good adhesion of aluminum to titanium foils; and two, that aluminum can be readily plated with copper. The Uyemura copper plating solution, which requires not zincation or other pre-plated layer, is particularly attractive. One would use their usual electroless see layer to plate the organics then plate up the through hole with the Uyemura solution, for example. Adhesion and electrical connection would be attained between the copper and the aluminum, and then the aluminum will provide electrical connection to the titanium alloy.

8.3 Compression interconnects

As we saw in chapter 7 typical connector body dielectric materials, such as liquid crystal polymer, are usually very radioactive, Table 7.2. Moreover, contact materials, like beryllium copper, can also be radioactive. Even the contact plating, which usually involves a surface hardening nickel under plate that also acts as a diffusion barrier between gold and copper, can be problematic when components sensitive to magnetic fields are close by. Lastly, the high density and compact connectors usually needed in a space constrained cryogenic experiment typically expensive as well.

As an remedy to all these issue, we suggest the use of compression "Fuzz Button" connectors. These connector are sections of wire that have been randomly compressed into a cylindrical shape Figure 8.2. They are positioned into an "interposer" which holds them in place by a pinch point. Mating boards, with contact patterned onto them, are are aligned and pressed against the interposer so that the fuzz buttons bridge a electrical connection between corresponding contacts.

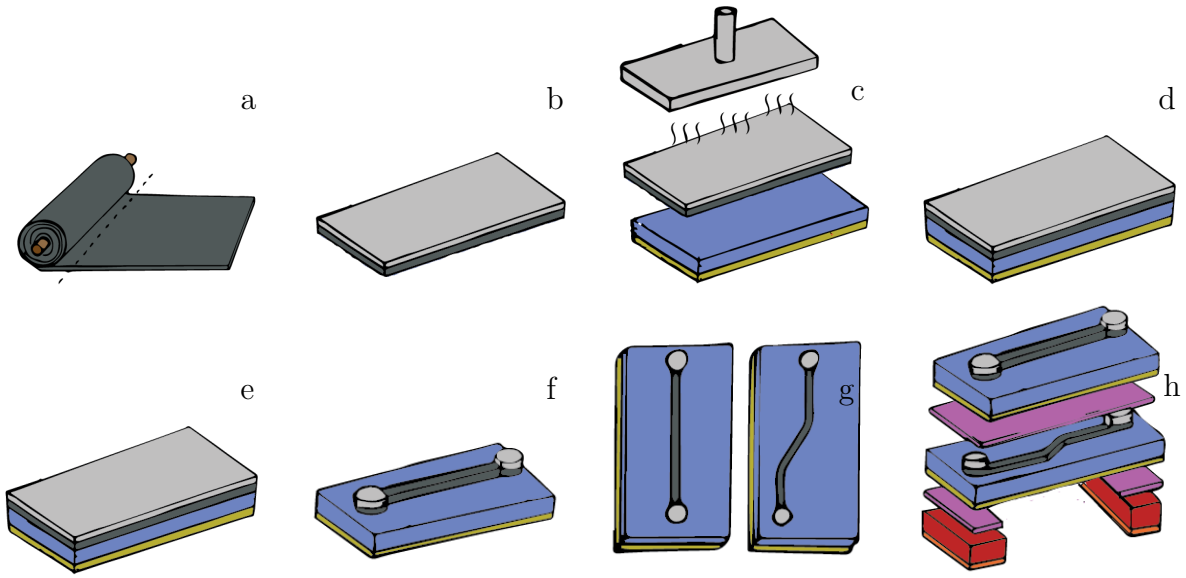


Figure 8.1: An alternate flex cable fabrication route is depicted. This route does not involve copper plating of the titanium foil and plates it with aluminum on only one side.

The advantages of these connectors are many. The can be made out of custom materials, which may have been counted prior to use in the fuzz buttons, and which may also be superconducting or superelastic to prevent plastic deformation. The interposer can be fabricated by molding or machining processes, out of a variety of materials. They have, in fact, been made of cirlex, single crystal sapphire as well as the usual circuit board materials before. The buttons have been made in a variety of sizes (e.g. $\varnothing 0.01\,\text{inch}$ by $0.04\,\text{inch}$) to accommodate contact resistance and contact density requirements. Positioning of the contacts has been used to approximate transmission line structures, such as a coaxial cable low loss transmission at up to $50\,\text{GHz}$ has been obtained. A possible disadvantage of these connectors is that one must take care that the contact is not in plastic deformation stress.

These connections, available at the time of this writing from companies named Cinch and Custom Interconnects, currently fly on fighter jets, orbit in satellites and are used at milli-Kelvin by groups working on quantum computers [44, 118].

Collaborators at SLAC [13] recently measured the low temperature contact resistance of the 12 fuzz buttons in series Table 8.1. The data was analyzed and a resistance value per fuzz button extracted.

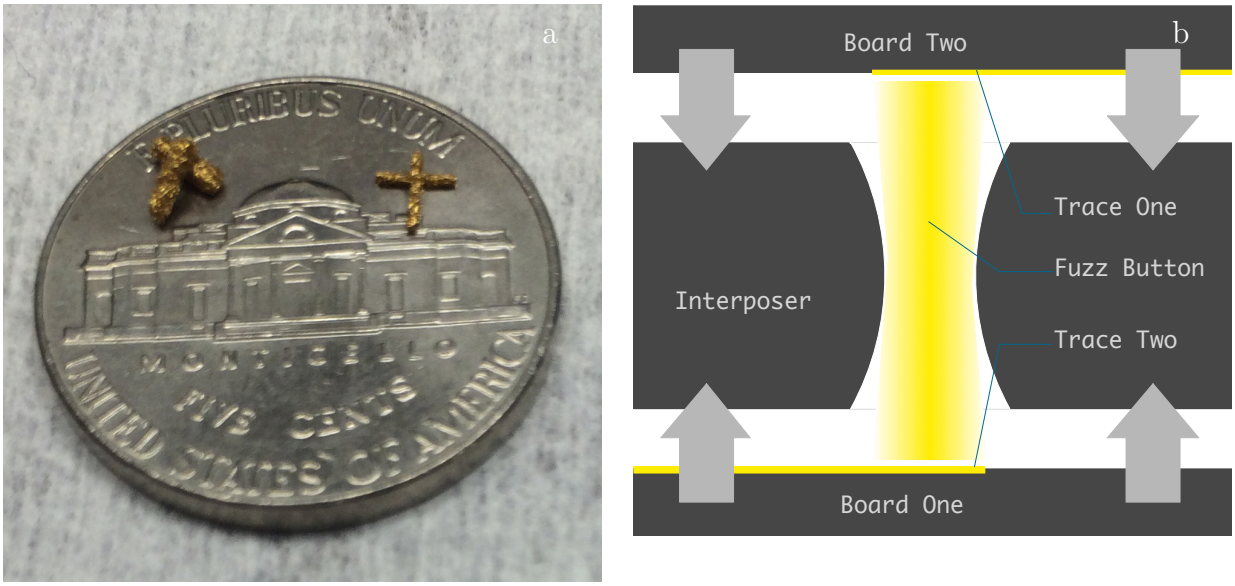


Figure 8.2: Fuzz button connectors are highly customizable. Custom materials can be used to make the. Those depicted in figure (a) are made of a molybdenum alloy. As seen in (b) they are instrumented in an interposer, which can be machined or molded a out of any dielectric material. Traces on the mating boards are aligned and mated together, usually with a screwable fastener simultaneously accomplishing both functions, such that the fuzz button is compressed and forms an electrical connection.

8.4 Phonon-mediated gamma ray spectrometer for nuclear security applications

The kinetic inductance athermal phonon sensor technology can be useful for other radiation detection applications besides that of dark matter detection. Additionally, each aspect of the sensors, e.g. phonon collection fin, resonator, amplifier, film materials, can be optimized for the application at hand as well as generally improved upon to obtain maximum overall sensor performance.

8.4.1 Background

The world is increasingly relying on nuclear materials for peaceful purposes including medicine, food and agriculture, basic science and energy. Meticulous accounting and access control are essential in preventing their use for non-peaceful purposes. Precision gamma ray spectroscopy is a powerful tool for the control of nuclear materials. With a suitable detector, one can determine the composition, intended purpose, origin and processing history of a nuclear specimen, without destroying it. Possessing such analysis capability both assists in the advancement of the peaceful nuclear material applications, and is a critical component

	$R_{290\,\mathrm{K}}$	$R_{90\,\mathrm{K}}$	$R_{50\,\mathrm{K}}$	$R_{5\,\mathrm{K}}$
Gold Plated Nickel [mΩ]	15.66	11.51	8.27	6.65
Gold Plated Moly Alloy [mΩ]	7.33	3.31	1.56	1.02

Table 8.1: The measurement was made with 12 fuzz buttons places in series, connected by a copper trace. The resistance of the copper trace alone was measured as well. These results were used to obtain a contact resistance per fuzz button for its connection to copper pads on both ends. Both fuzz buttons are ∅0.02 inch by 0.08 inch long and have gold plating. One is made of nickel and the other is made of a molybdenum alloy. The interposer used is 0.062 inch thick.

of our national nuclear security as a deterrent for non-peaceful nuclear activities and as a threat investigation tool.

Forensic analysis, also called 'fingerprinting', of nuclear specimens uses precision gamma ray spectroscopy to measure the presence and relative intensities of gamma ray emission lines emitted from decaying isotopes. For example, the age of a specimen since it was last processed can be determined by the ratio of parent to daughter nuclides which is ascertained by their respective gamma ray fluxes. The ratio of certain target isotopes tell us if the material was intended for weapons (e.g. high concentration of fissile ^{239}Pu, ^{235}U, etc) or energy (e.g. high ^{240}Pu/^{239}Pu). The composition of Uranium (U) and Plutonium (Pu) isotopes hint at the type of reactor where the material was utilized, due in part to the neutron energies that must have been necessary to produce them, and the presence of certain U isotopes suggest if the material is from reprocessed or virgin stocks. The ability to distinguish background gamma ray emission from the above also speaks to the necessity for high resolution detection. For example, distinguishing naturally occurring ^{226}Ra at 186.211 keV from ^{235}U at 185.715 keV, requires an gamma ray energy resolution of much better than 0.3% [140]. The ability to rapidly and accurately resolve densely spaced lines in the 100–300 keV range (Figure 8.3) is a design requirement for the spectrometer.

With the assistance of complementary characterization methods, the geolocation of the facility and mine from where the material originated can be estimated. For example, ^{18}O to ^{16}O ratios vary with temperature, latitude and distance from the sea, the ratio of anionic impurities suggest what uranium mining and milling processes were used and are different in different parts of the world [151]. The Nuclear Energy Institute reports that there were 435 nuclear power plants in operation across the world and another 70 on the way in 2012. Using high resolution gamma ray spectroscopy, for example, it is conceivable to identify nuclear materials confiscated from hostile interests as spent material diverted from any of these plants or at least their broader geographical location, and ascribe an estimated date that the material must have become unaccounted for and/or last processed.

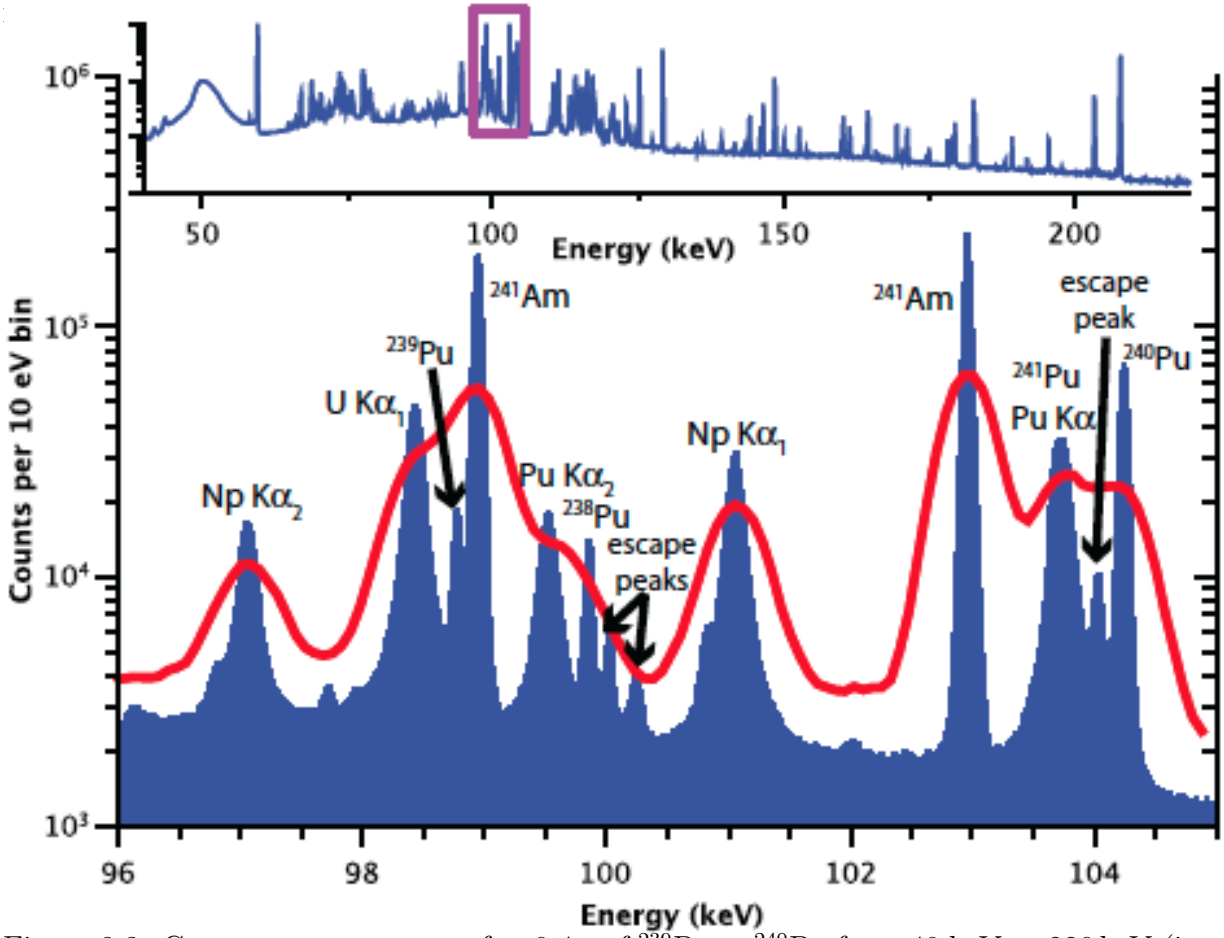


Figure 8.3: Gamma ray spectrum of $\sim 0.4\,\mathrm{g}$ of $^{239}\mathrm{Pu} + {}^{240}\mathrm{Pu}$ from 40 keV to 220 keV (inset) as measured by the microcalorimeter array developed by [29] (blue) and a leading edge HPGe detector (red). Data is magnified in the the 100 keV region. The proposed detector would produce an spectrum competitive with the microcalorimeter array. Image taken from [29].

Here we envision and describe a high resolution gamma ray spectrometer capable of performing the type of analyses described above. As of the present, there are two leading spectrometer options setting the bar for the performance of the proposed instrument. Operated at 77 K, high purity germanium (HPGe) ionization detectors are currently the most commonly used gamma ray spectrometer. They are commercially available and relatively low cost. Although they have an energy resolution of about 400 eV at 100 keV, 0.4% (Table 8.2), HPGe detector crystals can be made rather large and thick (10s of cm^3). The detector thickness improves gamma ray absorption efficiency, which enables swift analysis. Large detection area expedites the analysis of faint sources. Even better resolution is obtained by low temperature detectors. The current state of the art is National Institute of Standards and Technology (NIST) and Los Alamos National Laboratory (LANL) microcalorimeter [29] which have an energy resolution of better then 100 eV at 100 keV. These detectors have approximately $5\,\mathrm{cm}^3$ area arrays of tin absorbers, each 0.038 cm thick, epoxied to the TES

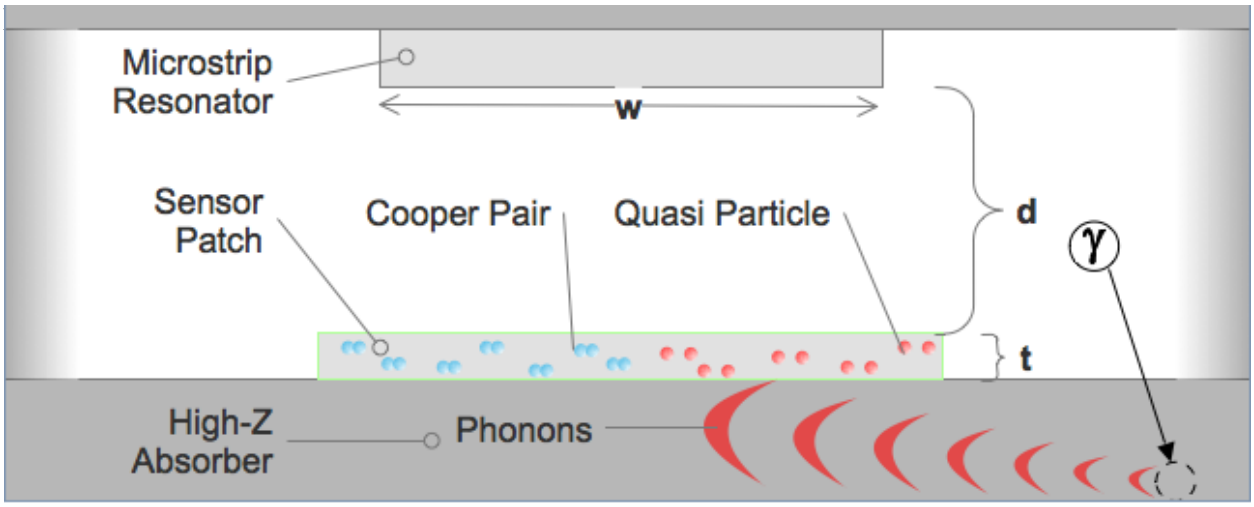


Figure 8.4: Magnified cross section of detector concept utilizing vacuum gap microstrip resonators to sense phonons. A patch of low gap superconductor (e.g. Al or TiN) is located beneath each resonator. Phonons impinging on the patch emanating from within the superconductor absorber break Cooper pairs and change its surface impedance which alters the resonance. Likely dimensions are $w = 200\,\mu m$; $t = 200\,nm$; $d = 3\,\mu m$.
and are operated at approximately 100 mK and their factor 4 resolution advantage allows them to resolve spectral lines unseen by the HPGe.

Technology	Temp	$\Delta E/E$	$\Delta E(E)$	Absorber	Transmission	Cts/Sec
Planar HPGe	77 K	$3 \cdot 10^{-3}$–$5 \cdot 10^{-3}$	$\sqrt{F_{fano} \cdot \epsilon_{gap} \cdot E}$	Sn	23%, $5\,mm$	$40 \cdot 10^3$
NIST-LANL	0.1 K	$4 \cdot 10^{-4}$	$T\sqrt{k_B \cdot C}$	Ge	63%, $0.38\,mm$	$2.5 \cdot 10^3$
Proposed	0.1 K	$\sim 10^{-4}$	$\sqrt{T_{amp}}$ Equation 8.1	Nb	10^{-6}%, $5\,mm$	$40 \cdot 10^3$

Table 8.2: Comparison of technology between the NIST-LANL microcalorimeter and HPGe ionization detector, representing the most sensitive and most used gamma-ray detectors respectively. C is the combined heat capacity of the TES and the absorber, F_{fano} is the Fano factor and other parameters are as defined in Table 8.3. The transmission column is the percentage of incident 100 keV gammas that make it through the absorber. Figures listed for the proposed detector represent performance objective achievable on paper.

The envisioned detector would have (a) greater sensitivity and gamma ray stopping power in comparison to the microcalorimeters, due to the use of a large, 50–100 cm^3, high-Z absorber. This detector would have (b) similar energy resolution to the microcalorimeters when operated near 100 mK, or be adapted to higher temperature operation, e.g. near 2 K, at the expense of energy resolution. In comparison to the NIST-LANL microcalorimeters (c) fabrication would be simpler using only 1 to 3 lithography layers. And, (d) the detector could resolve the position of the event within the detector, enabling identification of radiation type - neutron, gamma, alpha or beta. With sensitivity to neutrons, the exciting prospect of nuclear material detection at $>$ 100 m standoff distance may be achievable in later design

iterations of this detector concept. At baseline, the proposed detector would have energy resolution comparable to the NIST-LANL microcalorimeters and simplicity of design and efficiency comparable to the HPGe detectors.

8.4.2 Detector design features

In the envisioned detector, gamma rays would deposit their energy into a voluminous (75 mm diameter, 5–25 mm thick) high-Z absorber and produce out of equilibrium (athermal, $E > k_B \cdot T_{bath}$) phonons that would travel through the absorber until they impinge upon its surfaces Figure 8.4, an approach of several dark matter direct detection experiments including the CDMS experiment. Kinetic Inductance Detectors (KIDs) [202] fabricated on the surfaces of the detector would be used to sense the arriving phonons. Arrays of numerous KIDs phonon sensors could be fabricated directly on the absorber surface to achieve position resolved detection and more complete energy collection Figure 8.5. Whereas the NIST-LANL microcalorimeters are equilibrium phonon detectors, the concept proposed here detects out of equilibrium phonons, which are of greater energy and are therefore of high contrast against the background of thermal phonons suggesting the opportunity for higher temperature operation. Also, athermal phonon detection avoids count rate slowed by C/G time constants of absorber-coupled thermal phonon detection. The challenge overshadowing this research is to demonstrate that one can achieve the $\frac{\Delta E}{E} \approx 4 \cdot 10^{-4}$ and at least $40 \cdot 10^3$ count rates with position sensitivity using a simple athermal phonon detection approach.

The Phonon Sensor. NIST has strong expertise in the design and fabrication of KIDs which will benefit the project. This technology is based on measuring the change in complex surface impedance of superconducting films due to incident energy. The incident energy breaks Cooper pairs into quasiparticles (QPs, energetic electrons) which increases both its surface inductance and resistance. These changes in surface impedance are detected by patterning the superconductor into a high quality factor (Q) resonant circuit. The circuits resonant frequency f_0 and Q change due to impedance changes, which can be read out by room temperature and cold electronics. The resonant circuit sensor format lends itself to a natural frequency domain multiplexing scheme where numerous individual spatially separated sensors, all sharing a single readout transmission line, are addressed by a unique resonant frequency encoded by engineered geometrical differences between each resonator. For example, [123] demonstrated simultaneous readout of a 2024 KID array. The format of the resonator can be determined later based on capability with the absorber, ease of fabrication and responsivity to signal. A microstrip resonator format described in is the preferred for the phonon sensor, but Lumped element, disk, coplanar waveguide will also be considered. The preferred resonator materials are non-stoichiometric titanium nitride (TiN) or proximitized TiN/Ti [84, 125, 184] for its especially large kinetic inductance and ability to yield high Q resonators, and aluminum (Al) for its well-understood response to QPs and phonons [197].

The Absorber. The ideal is to use a material that converts all the energy of the particle interaction into athermal phonons which have sufficiently long lifetime before they are down

r

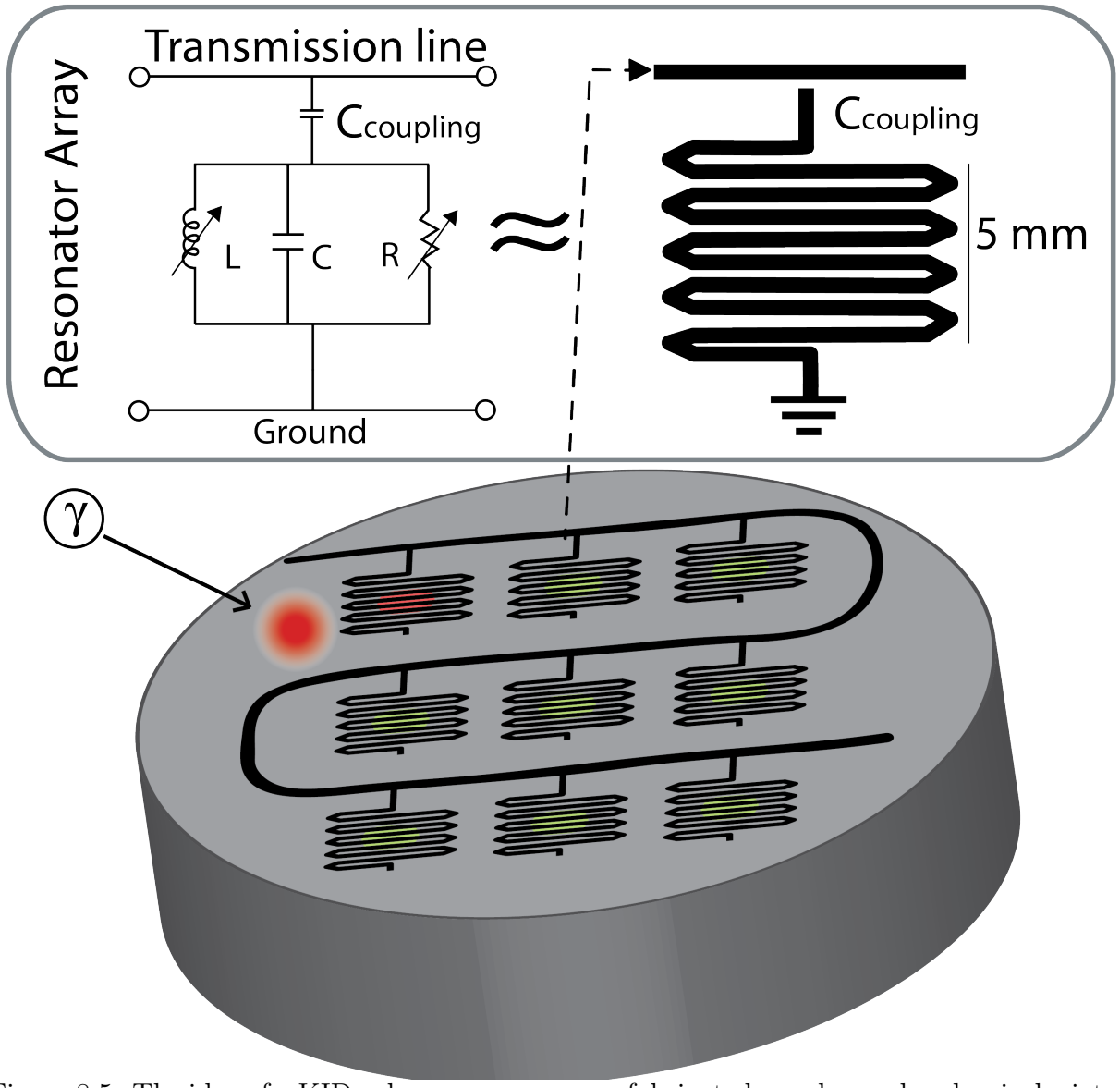


Figure 8.5: The idea of a KIDs phonon sensor array fabricated on a large absorber is depicted. Gamma rays deposit energy in the absorber. The energy is radiated away from the interaction location by phonons. The phonons arrive at the surface of the detector where they create quasi-particles in patches of low gap superconductor there are patterned onto it. The patches are part of the ground plane of a superconducting resonant circuit and the quasi-particles affect a change in quality factor and resonant frequency for of the resonant circuit, which is detected by room temperature electronics. The interaction location can be reconstructed from analysis of the responses of all the resonators. E.g the resonator that is closet to the interaction location will have the greatest response.

converted to energies not detectable by the sensor. Also, the material must be highly uniform with respect to athermal phonon transmission because non-uniformities would degrade event energy and position resolution. Finally, the material should be relatively high-Z to maximize the gamma ray absorption efficiency of the detector. The preferred absorber materials for the proposed detector are mono-crystalline superconductors. In these materials, absorbed energy from gamma ray interactions produces phonons at the interaction location. The phonons created will either be of energy less than the superconducting gap energy, $E_{ph} < 2 \cdot \Delta$, and propagate ballistically until they scatter off an obstacle, or they will be of energy greater than the superconducting gap, $E_{ph} > 2 \cdot \Delta$, and will decay into QPs in the absorber which will then decay into sub-gap phonons who travel ballistically until they scatter off an obstacle (i.e. quasi-ballistically). The quasi-ballistic phonons will arrive to the surface of the absorber where they may be detected if they impinge upon a phonon sensor, or they may scatter off the surface and continue their travel until they expire. They may also scatter within the absorber, off defects in the crystal or thermal QPs. These unwanted scattering modes can be controlled by using crystals of high perfection and purity, and by working at low temperatures.

Since we want the quasi-ballistic phonons to create QPs in the phonon sensors, we need $\Delta_{absorber} > \Delta_{sensor}$, or $T_{c,absorber} > T_{c,sensor}$, using $2 \cdot \Delta = 3.5 \cdot k_B \cdot T_c$ from BCS theory. The lower gap of the sensor traps the QPs created there, enabling their measurement. Moreover, the operation temperature T_{bath} of the proposed detector is constrained by the desire to suppress the thermal QP population and to optimize the responsivity of the KID, $T_{bath} \approx T_{c,sensor}/10$; this comes to 100–200 mK. Absorber materials satisfying all these characteristics include niobium (Nb, $T_c = 9.3\,\mathrm{K}$) and tantalum (Ta, $T_c = 4.5\,\mathrm{K}$). As an example, Hauser [78] measured ballistic phonon transport via laser induced heat pulse techniques in a mono-crystalline Nb sample 1.8 mm long and ⌀ 10 mm. The measurements were performed at 1.56 K and 2.09 K. Calculations presented in [78] suggest phonon lifetimes,τ_{ph}, greater than tens to hundreds of microseconds are achievable for our T_{bath} and ballistic transport velocities in the range of 2–5 mm μs^{-1}.

The Primary Amplifier. Provided that the phonons are designed to minimize two-level system noise, the noise of the primary amplifier for the phonon sensors limits the energy resolution of the detector. The proposed detector will use either a high HEMT amplifier or a parametric amplifier [81]. NIST and the NASA Jet Propulsion Laboratory (JPL) are developing such parametric amplifiers which currently have better than 10 dB gain in the 10 GHz region and are almost quantum noise limited. The latter is preferred for its lower noise, but the maturity of this new technology may not be sufficient for use in this application. It would be great to take advantage of NISTs expertise to fabricate these amplifiers.

8.4.3 Example Detector Implementation

A possible implementation of this detector concept is to use vacuum microstrip resonators Figure 8.4 as the phonon sensors and Nb at the absorber. The common ground plane of an array of microstrip KID phonon sensors would be the surface of the superconducting

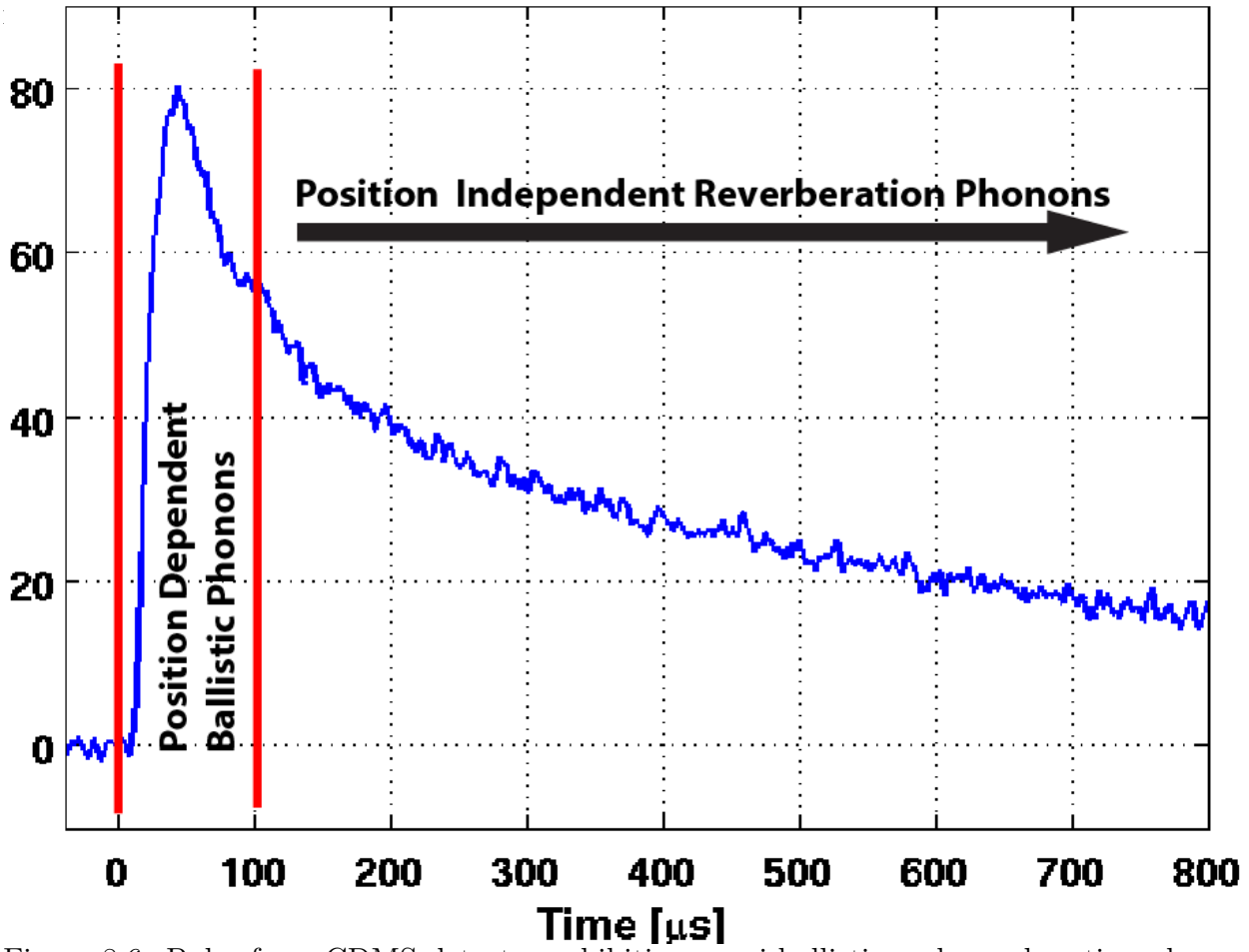


Figure 8.6: Pulse from CDMS detector exhibiting quasi-ballistic and reverberating phonon contributions.

absorber, except that a patches of low gap superconductor (e.g. TiN or Al) would be aligned with the most sensitive (highest current) portion of the resonators. The patch would collect energy from athermal phonons, which have traveled quasi-ballistically from the event, and reverberation athermal phonons which have reflected off surfaces several times before arriving at the sensor. The reverberation phonons will have lost memory of the initial event position and therefore be position independent. The pulse duration and therefore the maximum count rate of the detector would be limited by, the ring-down time of the resonator, the QP recombination time, ≈50 µs for TiN and 50–500 µs for Al, and the (reverberation) phonon lifetime, τ_{ph}, whichever is longest. Fortunately each of these things can be engineered, the first with the resonator coupling to the feedline (Q_c, the coupling quality factor), the second with film type and composition, the third with sensor patch size, absorber volume and the possibility of trenching which also controls the proportion of reverberation phonons. The pulses acquired from this detector would feature an initial ballistic phonon generated peak, which would carry event position information, and a position independent reverberation phonon tail Figure 8.6, whose duration and magnitude would

Quantity	Value	Unit	Description
T_{amp}	5	K	HEMT noise temp
$N_{sensors}$	40		Number of phonon sensors per detector
V_{probe}	1	mV	Resonator probe power in 50 Ω system
E	100	keV	Gamma ray energy
α	0.025	%	Kinetic inductance fraction
η	20	%	phonon-to-QP conversion efficiency
Δ	180	µeV	Superconducting energy gap
$l \cdot w \cdot t$	$8 \cdot 10^5$	µm^3	QP diffusion (patch) volume
τ_{res}	100	µs	Resonator $1/e$ decay time

Table 8.3: Design parameters used in the calculation of detector performance where a KID + HEMT phonon sensor scheme is utilized. Al is assumed to be the sensor patch on the absorber surface.

assist in event energy estimation. Such pulses are typical in the CDMS detector.

While the NIST-LANL spectrometer demonstrates that the TES + SQUID phonon sensor solution has the baseline resolution to produce $\sim 5 \cdot 10^{-4}$ energy resolution, on paper, the case of the KID + HEMT phonon sensor also has promising performance. The fractional energy resolution of the sensor array is limited by the HEMT voltage noise integrated over the $N_{sensors}$, δV,

$$\delta V = \sqrt{4 \cdot k_B \cdot T_{amp} \cdot BW \cdot Z_0 \cdot N_{sensors}}, \tag{8.1}$$

and signal voltage amplitude V_θ due to the creation of $N_{qp} = \frac{E \cdot \eta}{2 \cdot \Delta}$ QPs from an event of energy E,

$$V_\theta = K \cdot V_{probe} \cdot \frac{\alpha \cdot Q^2 \cdot N_{qp}}{l \cdot w \cdot t \cdot Q_c} \tag{8.2}$$

[124], where $BW = \frac{f_0}{Q} = \frac{1}{2 \cdot \pi \cdot \tau_{res}}$, $K = 2 \cdot 10^{-7}\,\mathrm{V\,\mu m^{-3}}$ is a constant, V_{probe} is the voltage amplitude of the readout power. We assume that τ_{res} sets the pulse time. Aiming for a count rate of $40 \cdot 10^3$, one gets a fractional energy resolution of $\frac{\Delta E}{E} = \frac{\delta V}{V_\theta} \approx 10^{-4}$ with the parameters shown in Table 8.3.

8.4.4 Development requirements

Development of this detector technology will require certain specialized equipment, facilities and further technology review. In the case of technology review, the availability of large single crystal high-gap superconductors needs to be established. This includes the available purity, and crystalline perfection *after* shaping a polishing. Also, taking Hauser's [78] measurements as a data point at RRR $= 1 \cdot 10^4$, it must be established, preferably from literature data as opposed to in-house measurement, the minimum acceptable purity and crystalline perfection required for the energy resolution goals of this detector.

Detector development will require the use of a cryostat capable of sustained <100 mK operation temperature, equipped with high frequency readout cabling connecting 300 K to the detector location. The cryostat will need a low-Z aperture for ambient nuclear specimen placement. Microwave test equipment including, amplifiers, mixers, attenuators, frequency synthesizers and network and spectrum analyzers will be necessary to provide system tuning and troubleshooting support. Generation of the probe signals for and digitization pulse signals from the sensor array would be most easily accomplished using the ROACH reconfigurable computing platform [155] as in the 2024 sensor ARCONs system [123]. Here, one can take advantage of existing control software.

Cold hardware to house the detector which permits transmission of radiation from nuclear specimens to the detector and mounts it to the cryostat is required. The housing should have large enough thermal impedance to the cryostat to prevent the phonon signal from being lost, but small enough so that the crystal can expeditiously cool down and cool down between events.

Micro-fabrication facilities capable of accommodating the large absorber crystal and producing the materials (e.g. TiN) used in the detector will be needed. One should expect several fabrication runs to try alternate absorber crystals, and implement design enhancement to the detector, in order to attain optimal performance. One should also expect to have numerous fridge runs to test these detectors. Access to radiation sources will be necessary for these runs. Ultimately, one should benchmark the performance of the detector against the Pu isotopic standards (PIDIE and CBNM[1]) at LANL. This establishes the usefulness of the detector for Pu nuclear material fingerprinting.

The basic questions that testing and characterization will answer are: what is the energy resolution of the detector; what is its efficiency to stop gammas and detect them; what is the event energy range over which the detector exhibits useful sensitivity; how stable and reproducible are the results. The entire development process discussed here should also emphasize manufacturability of the proposed detector so that a successful detector design has an obvious and unchallenging path to field deployment. For example the availability of the absorber crystal, and cost of the readout system (including the primary amplifier) and ease of fabrication must be optimized.

8.4.5 Conclusions

The detector concept described here engages the issue of nuclear security, offering powerful tool for nuclear material identification and accountancy. The nations lack of preparedness in this area has been underscored most recently in a January 2014 Defense Science Board report [21]. This gamma ray spectrometer is enhanced by the use of a large absorber, which should have the effect of increasing sensitivity to gamma rays and even neutrons, including gamma rays which existing spectrometers struggle to detect due to their smaller absorber size. It is

[1]These sources are mixtures of different Pu isotopes covering a range of relative concentrations. They are good at testing the detector's ability to sense trace isotopic abundances in the presence of a large background constituent.

also of a much simpler design than its high-resolution peer, the NIST-LANL spectrometer, which will ultimately have cost and availability implications. Also, with available cooling technology, this detector could be adapted, probably at the expense of performance, to be field deployable. Sensitivity to high energy gamma rays and neutrons opens up the possibility of future application to nuclear material detection at >100 m standoff distance as called for in the January 2014 report.

The key technology components of the detector include the phonon sensors, the absorber and the primary amplifier. On paper, one can get the desired energy resolution and efficiency using the performance demonstrated in the literature of the component choices suggested in this description. Fortunately, all the technology pieces needed for the detector are available at a constellation of research institutions, NIST, JPL, LANL, etc. Development of this detection approach will also be benefitted by the experience of CDMS collaboration, who have demonstrated success at the detection of athermal phonons by sensors directly fabricated onto the absorber.

Attributions

With the exception of the fuzz button contact resistant measurement the working presented in this chapter was done by myself alone.

Bibliography

[1] Illustrations produced by Talya Malahat Sindel as part of UC Berkeley Undergraduate Research Apprentice Program project. Says Talya: *I used a combination of Ipad applications "Paper" and "Procreate" to create all the illustrations. These applications have a wide variety of effects and drawing tools to enhance images. My illustration philosophy is to accurately depict scientific ideas and concepts in a simple and aesthetically pleasing way.* (cit. on pp. 2, 19, 21, 26, 28, 30, 31, 33, 35, 42, 44).

[2] Illustrations produced by Maccallum Robertson as part of UC Berkeley Undergraduate Research Apprentice Program project. Says Maccallum: *The more sophisticated designs used to document the nanofabrication procedure were made with a program called POV-Ray, which is tailored made for 3D vector art. The sketched images were hand drawn and converted into vector art and then colorized using the image trace feature of Adobe Illustrator CS6. The philosophy behind the images is to create a simplified design of a complicated system so as to clearly convey the "bigger-picture" concepts and help the reader visualize the systems in question.* (cit. on pp. 62, 65–67, 107, 196, 232).

[3] Research group website of Sander Weinreb. Contains papers, research activities and ordering information for the low noise amplifiers the group fabricates. URL: http://www.caltechmicrowave.org (cit. on p. 123).

[4] Low background counting is performed by a 2.075 kg HPGe detector, called GOPHER, located in the Soudan Underground Laboratory. A low background counting environment is provided by multiple shields: The location of the facility provides 2,200 m.w.e of shielding from cosmic rays; the detector itself is housed within an active muon veto, surrounded by (innermost to outermost): 2 inch of OFHC copper, followed by 2 inch of ultra low activity (ULA) lead, and finally, 10 inch of commercial lead. URL: http://www.hep.umn.edu/lbcf/ (cit. on pp. 162, 174).

[5] Work done with Nicholas Kellaris as part of his undergraduate research and honors thesis projects. (cit. on pp. 166, 168, 170, 171, 192, 278).

[6] Work done with Nick Zobrist as part of his UC Berkeley Undergraduate Research Apprentice Program and honors thesis projects. (cit. on pp. 168, 171, 192, 278).

[7] Materials properties table on Ferroceramic website. URL: http://www.ferroceramic.com/macor_table.htm (cit. on p. 179).

[8] from the Japan Carbon Fiber Manufacturers Association website. URL: http://www.carbonfiber.gr.jp/english/ (cit. on p. 180).

[9] Measurements and data from SuperCDMS SNOLAB collaborators Martin Huber and Bruce Hines at University of Colorado, Denver. (cit. on p. 181).

[10] From the NIST cryogenic material properties database, a product of the Cryogenic Technologies Group in the Materials Measurement Laboratory. URL: http://www.cryogenics.nist.gov/MPropsMAY/material%20properties.htm (cit. on p. 192).

[11] Work done by Martin Mathews at the Pacific Northwest National Lab. (cit. on p. 201).

[12] The process was developed and executed by Yasuto Hori, on patterned Nb-47Ti laminated to kapton with epoxy adhesive. (cit. on p. 202).

[13] Data measured at SLAC by Dave Nelson summer students Maxwell Lee, Roger Romani. (cit. on p. 236).

[14] ASM Alloy Phase Diagrams Database, P. Villars, editor-in-chief; H. Okamoto and K. Cenzual, section editors. Materials Park, OH: ASM International, 2006. URL: http://www1.asminternational.org/AsmEnterprise/APD (cit. on p. 198).

[15] H. Abdul-Rahman and N. Chernov. "Fast and Numerically Stable Circle Fit". In: *Journal of Mathematical Imaging and Vision* 49.2 (Sept. 2013), pp. 289–295. ISSN: 0924-9907. DOI: 10.1007/s10851-013-0461-4. URL: http://link.springer.com/10.1007/s10851-013-0461-4 (cit. on p. 135).

[16] A A Abrikosov, L P Gor'kov, and I M Khalatnikov. "Superconductor in a high-frequency field". In: *Zhurnal Eksperimental'noi i Teoreticheskoi Fiziki* 35.1(7) (1958), pp. 265–275 (cit. on p. 55).

[17] N V AGEEV and L A PETROVA. "THE THEORETICAL BASES OF THE DEVELOPMENT OF THE HIGH-STRENGTH METASTABLE β-ALLOYS OF TITANIUM". In: *The Science, Technology and Application of Titanium*. Ed. by R. I. Jaffee. London, England: Oxford Pergamon Press Ltd., 1970, pp. 809–814. ISBN: 978-0-08-006564-9. DOI: http://dx.doi.org/10.1016/B978-0-08-006564-9.50087-7. URL: http://www.sciencedirect.com/science/article/pii/B9780080065649500877 (cit. on pp. 287, 288).

[18] D.S. Akerib. *Thermal Conductivity Data for Materials used in CDMS*. Tech. rep. Berkeley: UC Berkeley (cit. on p. 168).

[19] E. Aprile, K. Arisaka, F. Arneodo, a. Askin, L. Baudis, a. Behrens, K. Bokeloh, E. Brown, J. Cardoso, B. Choi, D. Cline, S. Fattori, a. Ferella, K.-L. Giboni, a. Kish, C. Lam, J. Lamblin, R. Lang, K. Lim, Q. Lin, S. Lindemann, M. Lindner, J. Lopes, K. Lung, T. Marrodán Undagoitia, Y. Mei, a. Melgarejo Fernandez, K. Ni, U. Oberlack, S. Orrigo, E. Pantic, G. Plante, a. Ribeiro, R. Santorelli, J. dos Santos, M. Schumann, P. Shagin, H. Simgen, a. Teymourian, D. Thers, E. Tziaferi, H. Wang, M. Weber, and C. Weinheimer. "Study of the electromagnetic background in the XENON100

experiment". In: *Physical Review D* 83.8 (Apr. 2011), pp. 1–10. ISSN: 1550-7998. DOI: 10.1103/PhysRevD.83.082001. URL: http://link.aps.org/doi/10.1103/PhysRevD.83.082001 (cit. on p. 173).

[20] E Armengaud, Q Arnaud, C Augier, a Benoit, L Bergé, T Bergmann, J Blümer, a Broniatowski, V. Brudanin, P Camus, a Cazes, B Censier, M Chapellier, F. Charlieux, F. Couëdo, P. Coulter, G.a Cox, T. De Boissière, M. De Jesus, Y. Dolgorouky, a.a Drillien, L Dumoulin, K Eitel, D Filosofov, N Fourches, J. Gascon, G. Gerbier, M. Gros, L. Hehn, S. Henry, S. Hervé, G. Heuermann, N. Holtzer, V. Humbert, a. Juillard, C. Kéfélian, M. Kleifges, H. Kluck, V. Kozlov, H. Kraus, V.a Kudryavtsev, H. Le Sueur, M. Mancuso, C. Marrache-Kikuchi, S. Marnieros, a. Menshikov, X-F. Navick, C. Nones, E. Olivieri, P. Pari, B. Paul, M.C Piro, O. Rigaut, M. Robinson, S. Rozov, V. Sanglard, B. Schmidt, B. Siebenborn, D. Tcherniakhovski, M. Tenconi, L. Vagneron, R.J Walker, M. Weber, E. Yakushev, and X. Zhang. "Axion searches with the EDELWEISS-II experiment". In: *Journal of Cosmology and Astroparticle Physics* 2013.11 (2013), pp. 067–067. ISSN: 1475-7516. DOI: 10.1088/1475-7516/2013/11/067. arXiv: 1307.1488. URL: http://arxiv.org/abs/1307.1488$%5Cbackslash$nhttp://stacks.iop.org/1475-7516/2013/i=11/a=067?key=crossref.29026565eb683552afc40368855739d7 (cit. on p. 43).

[21] *Assessment of Nuclear Monitoring and Verification Technologies*. Tech. rep. January. Washington D.C.: Office of the Under Secretary of Defence for Acqusition, Technology and Logistics, Jan. 2014. URL: http://www.acq.osd.mil/dsb/reports/NuclearMonitoringAndVerificationTechnologies.pdf (cit. on p. 246).

[22] P J BANIA. "BETA-TITANIUM ALLOYS AND THEIR ROLE IN THE TITANIUM INDUSTRY". In: *BETA TITANIUM ALLOYS IN THE 1990S*. MINERALS MET & MAT SOC. 420 COMMONWEALTH DR, WARRENDALE, PA 15086: MINERALS, METALS & MATERIALS SOC, 1993, pp. 3–14. ISBN: 0-87339-200-0 (cit. on p. 290).

[23] J Bardeen, L N Cooper, and J R Schrieffer. "Theory of Superconductivity". In: *Physical Review* 108.5 (1957), pp. 1175–1204 (cit. on pp. 53, 55, 59, 61).

[24] M Barucci, E Gottardi, I Peroni, and G Ventura. "Low temperature thermal conductivity of Kapton and Upilex". In: *Cryogenics* 40.2 (Feb. 2000), pp. 145–147. ISSN: 00112275. DOI: 10.1016/S0011-2275(00)00013-8. URL: http://linkinghub.elsevier.com/retrieve/pii/S0011227500000138 (cit. on pp. 168, 192).

[25] M. Barucci, L. Lolli, L. Risegari, and G. Ventura. "Measurement of thermal conductivity of the supports of CUORE cryostat". In: *Cryogenics* 48.3-4 (Mar. 2008), pp. 166–168. ISSN: 00112275. DOI: 10.1016/j.cryogenics.2008.03.018. URL: http://linkinghub.elsevier.com/retrieve/pii/S0011227508000428 (cit. on pp. 178, 192).

[26] B. Baudouy. "Kapitza resistance and thermal conductivity of Kapton in superfluid helium". In: *Cryogenics* 43.12 (Dec. 2003), pp. 667–672. ISSN: 00112275. DOI: 10.1016/S0011-2275(03)00178-4. URL: http://linkinghub.elsevier.com/retrieve/pii/S0011227503001784 (cit. on p. 168).

[27] E Behnke, J I Collar, P S Cooper, K Crum, M Crisler, M Hu, I Levine, D Nakazawa, H Nguyen, B Odom, E Ramberg, J Rasmussen, N Riley, A Sonnenschein, M Szydagis, and R Tschirhart. "Spin-dependent WIMP limits from a bubble chamber." In: *Science (New York, N.Y.)* 319.5865 (2008), pp. 933–936. ISSN: 0036-8075. DOI: 10.1126/science.1149999. arXiv: 0804.2886 (cit. on p. 38).

[28] E. Belohoubek and E. Denlinger. "Loss Considerations for Microstrip Resonators (Short Papers)". In: *IEEE Transactions on Microwave Theory and Techniques* 23.6 (1975), pp. 522–526. ISSN: 0018-9480. DOI: 10.1109/TMTT.1975.1128615 (cit. on p. 98).

[29] D A Bennett, R D Horansky, D R Schmidt, A S Hoover, R Winkler, B K Alpert, J A Beall, W B Doriese, J W Fowler, C P Fitzgerald, G C Hilton, K D Irwin, V Kotsubo, J A B Mates, G C O'Neil, M W Rabin, C D Reintsema, F J Schima, D S Swetz, L R Vale, and J N Ullom. "A high resolution gamma-ray spectrometer based on superconducting microcalorimeters." In: *The Review of scientific instruments* 83.9 (Sept. 2012), p. 093113. ISSN: 1089-7623. DOI: 10.1063/1.4754630. URL: http://www.ncbi.nlm.nih.gov/pubmed/23020368 (cit. on p. 239).

[30] R Berman, E L Foster, and H M Rosenberg. *The thermal conductivity of some technical materials at low temperatures*. 1955. DOI: 10.1088/0508-3443/6/5/111 (cit. on p. 192).

[31] R Blake. "Tekdata Interconnections: Cryoconnect". In: *Cold Facts* 22 (2006), p. 5 (cit. on p. 192).

[32] James C. Booth, Kenneth Leong, Susan a. Schima, C. Collado, J. M. Offfdfffdfffd-Callaghan, and J. Mateu. "Unified Description of Nonlinear Effects in High Temperature Superconductor Microwave Devices". In: *Journal of Superconductivity and Novel Magnetism* 19.7-8 (2007), pp. 531–540. ISSN: 1557-1939. DOI: 10.1007/s10948-006-0126-2 (cit. on p. 155).

[33] Alexey Boyarsky, Oleg Ruchayskiy, Dmytro Iakubovskyi, and Jeroen Franse. "An unidentified line in X-ray spectra of the Andromeda galaxy and Perseus galaxy cluster". In: *arXiv preprint arXiv:1402.4119* (2014), pp. 1–7. ISSN: 10797114. DOI: 10.1103/PhysRevLett.113.251301. arXiv: 1402.4119. URL: http://arxiv.org/abs/1402.4119 (cit. on p. 22).

[34] J. R. Brownstein and J. W. Moffat. "The Bullet Cluster 1E0657-558 evidence shows modified gravity in the absence of dark matter". In: *Monthly Notices of the Royal Astronomical Society* 382.1 (2007), pp. 29–47. ISSN: 00358711. DOI: 10.1111/j.1365-2966.2007.12275.x. arXiv: 0702146 [astro-ph] (cit. on pp. 20, 21).

[35] D. Budjás, a. M. Gangapshev, J. Gasparro, W. Hampel, M. Heisel, G. Heusser, M. Hult, a. a. Klimenko, V. V. Kuzminov, M. Laubenstein, W. Maneschg, H. Simgen, a. a. Smolnikov, C. Tomei, and S. I. Vasiliev. "Gamma-ray spectrometry of ultra low levels of radioactivity within the material screening program for the GERDA experiment". In: *Applied Radiation and Isotopes* 67.5 (2009), pp. 755–758. ISSN: 09698043. DOI: 10.1016/j.apradiso.2009.01.019 (cit. on p. 174).

[36] S. Capozziello and M. De Laurentis. "The dark matter problem from f(R) gravity viewpoint". In: *Annalen der Physik* 524.9-10 (2012), pp. 545–578. ISSN: 00033804. DOI: 10.1002/andp.201200109. URL: http://doi.wiley.com/10.1002/andp.201200109 (cit. on p. 20).

[37] R. G. Chambers. "Anomalous Skin Effect in Metals". In: *Nature* 165.4189 (Feb. 1950), pp. 239–240. ISSN: 0028-0836. DOI: 10.1038/165239b0. URL: http://www.nature.com/doifinder/10.1038/165239b0 (cit. on p. 61).

[38] W H Chang. "Numerical Calculation of the Inductances of a Multi-Superconductor Transmission Line System". In: *IEEE Transactions on Magnetics* 17.1 (1981), pp. 764–766 (cit. on p. 101).

[39] M.J. Chant. "Dielectric properties of some insulating materials over the temperature range 4fffdfffd2fffdfffdfffd300fffdfffd K". In: *Cryogenics* 7.1-4 (1967), pp. 351–354. ISSN: 00112275. DOI: 10.1016/S0011-2275(67)80116-4 (cit. on pp. 97, 99).

[40] N. Chernov and C. Lesort. "Least squares fitting of circles". In: *Journal of Mathematical Imaging and Vision* 23.3 (2005), pp. 239–252. ISSN: 09249907. DOI: 10.1007/s10851-005-0482-8. arXiv: 0301001 [cs] (cit. on p. 135).

[41] Shinho Cho. *Inductance measurements in thin films*. 1999. DOI: 10.1088/0953-2048/10/8/012 (cit. on p. 66).

[42] P. V. Christiansen, E. B. Hansen, and C. J. Sjöström. "Negative self-inductance in superconducting thin wires and weak links". In: *Journal of Low Temperature Physics* 4.4 (1971), pp. 349–389. ISSN: 00222291. DOI: 10.1007/BF00628738 (cit. on p. 66).

[43] Douglas Clowe, Marusa Bradac, Anthony H. Gonzalez, Maxim Markevitch, Scott W. Randall, Christine Jones, and Dennis Zaritsky. "A direct empirical proof of the existence of dark matter". In: *The Astrophysical Journal* 648 (2006), pp. 109–113. ISSN: 0004-637X. DOI: 10.1086/508162. arXiv: 0608407 [astro-ph]. URL: http://arxiv.org/abs/astro-ph/0608407 (cit. on pp. 20, 21).

[44] Ji Colless and Dj Reilly. "Modular Cryogenic Interconnects for Multi-Qubit Devices". In: *arXiv preprint arXiv:1405.3371* (2014). arXiv: arXiv:1405.3371v1. URL: http://arxiv.org/abs/1405.3371 (cit. on p. 236).

[45] E W Collings. *A Sourcebook of Titanium Alloy Superconductivity*. New York: Plenum Press, 1983, pp. 213–299. ISBN: 0306413442 (cit. on p. 294).

[46] T. Dahm and D. J. Scalapino. "Theory of intermodulation in a superconducting microstrip resonator". In: *Journal of Applied Physics* 81.4 (1997), p. 2002. ISSN: 00218979. DOI: 10.1063/1.364056. URL: http://link.aip.org/link/JAPIAU/v81/i4/p2002/s1%5C&Agg=doi (cit. on p. 65).

[47] Marc Davis, Adi Nusser, and KL Masters. "Local Gravity versus Local Velocity : Solutions for β and nonlinear bias". In: *Monthly Notices of* January (2011). arXiv: arXiv:1011.3114v2. URL: http://onlinelibrary.wiley.com/doi/10.1111/j.1365-2966.2011.18362.x/full (cit. on p. 17).

[48] P. J. De Visser, S. Withington, and D. J. Goldie. "Readout-power heating and hysteretic switching between thermal quasiparticle states in kinetic inductance detectors". In: *Journal of Applied Physics* 108.11 (2010), pp. 1–9. ISSN: 00218979. DOI: 10.1063/1.3517152 (cit. on p. 66).

[49] Antonino Del Popolo. "Nonbaryonic Dark Matter in Cosmology". In: *International Journal of Modern Physics D* 23.3 (2014), p. 1430005. ISSN: 0218-2718. DOI: 10.1142/S0218271814300055. URL: http://www.worldscientific.com/doi/abs/10.1142/S0218271814300055 (cit. on pp. 8, 13).

[50] Timothée Delubac, Julian E. Bautista, Nicolás G. Busca, James Rich, David Kirkby, Stephen Bailey, Andreu Font-Ribera, Anze Slosar, Khee-Gan Lee, Matthew M. Pieri, Jean-Christophe Hamilton, Éric Aubourg, Michael Blomqvist, Jo Bovy, J. Brinkmann, William Carithers, Kyle S. Dawson, Daniel J. Eisenstein, Jean-Paul Kneib, J. -M. Le Goff, Daniel Margala, Jordi Miralda-Escudé, Adam D. Myers, Robert C. Nichol, Pasquier Noterdaeme, Ross O'Connell, Matthew D. Olmstead, Nathalie Palanque-Delabrouille, Isabelle Pâris, Patrick Petitjean, Nicholas P. Ross, Graziano Rossi, David J. Schlegel, Donald P. Schneider, David H. Weinberg, Christophe Yèche, and Donald G. York. "Baryon Acoustic Oscillations in the Ly{\alpha} forest of BOSS DR11 quasars". In: (2014), p. 17. ISSN: 14320746. DOI: 10.1051/0004-6361/201423969. arXiv: 1404.1801. URL: http://arxiv.org/abs/1404.1801 (cit. on p. 12).

[51] I. Didschuns, a. L. Woodcraft, D. Bintley, and P. C. Hargrave. "Thermal conductance measurements of bolted copper to copper joints at sub-Kelvin temperatures". In: *Cryogenics* 44.5 (2004), pp. 293–299. ISSN: 00112275. DOI: 10.1016/j.cryogenics.2003.11.010 (cit. on p. 280).

[52] S Dodelson. *Modern Cosmology*. San Diego, Calif.: Academic Press, 2003. ISBN: 0122191412 (cit. on p. 1).

[53] Scott Dodelson and Lawrence M. Widrow. "Sterile Neutrinos as Dark Matter". In: March (1993), p. 10. ISSN: 00319007. DOI: 10.1103/PhysRevLett.72.17. arXiv: 9303287 [hep-ph]. URL: http://arxiv.org/abs/hep-ph/9303287 (cit. on p. 22).

[54] F. David Doty and Paul D. Ellis. "Design of High Speed Cylindrical Nmr Sample Spinners." In: *Review of Scientific Instruments* 52.12 (1981), pp. 1868–1875. ISSN: 00346748. DOI: 10.1063/1.1136530 (cit. on p. 179).

[55] M. Dressel. "Electrodynamics of metallic superconductors". In: *Advances in Condensed Matter Physics* 2013 (2013). ISSN: 16878108. DOI: 10.1155/2013/104379 (cit. on p. 51).

[56] Martin Dressel and George. Grfffdfffdfffdner. *Electrodynamics of solids optical properties of electrons in matter*. English. Cambridge; New York, 2002. URL: http://site.ebrary.com/id/10005054 (cit. on p. 51).

[57] EI Dyachkov, R Herzog, IS Khukhareva, and A. Nichitiu. *Thermal conductivity and electrical resistivity of Nb-Ti (HT-50) as a function of temperature and magnetic field*. 1981. DOI: 10.1016/0011-2275(81)90109-0. URL: http://www.sciencedirect.com/science/article/pii/0011227581901090 (cit. on p. 192).

[58] T C Edwards. *Foundations for microstrip circuit design*. English. 2nd ed. Chichester; New York: Wiley, 1981. ISBN: 0471279447 9780471279440 (cit. on p. 77).

[59] Daniel J. Eisenstein and Charles L. Bennett. "Cosmic sound waves rule". In: *Physics Today* 61.4 (2008), pp. 44–50. ISSN: 00319228. DOI: 10.1063/1.2911177 (cit. on p. 12).

[60] J C FANNING. "TIMETAL(R)21S PROPERTY DATA". In: *BETA TITANIUM ALLOYS IN THE 1990S*. MINERALS MET & MAT SOC. 420 COMMONWEALTH DR, WARRENDALE, PA 15086: MINERALS, METALS & MATERIALS SOC, 1993, pp. 397–410. ISBN: 0-87339-200-0 (cit. on p. 290).

[61] J.C. Fanning and S.P. Fox. "Recent Developments in Metastable β Strip Alloys". In: *Journal of Materials Engineering and Performance* 14.6 (Dec. 2005), pp. 703–708. ISSN: 10599495. DOI: 10.1361/105994905X75484. URL: http://www.ingentaselect.com/rpsv/cgi-bin/cgi?ini=xref%5C&body=linker%5C&reqdoi=10.1361/105994905X75484 (cit. on p. 293).

[62] M Felizardo, Ta Girard, T Morlat, a C Fernandes, a R Ramos, J G Marques, a Kling, J Puibasset, M Auguste, D Boyer, a Cavaillou, J Poupeney, C Sudre, F P Carvalho, M. I. Prudencio, and R. Marques. "The SIMPLE Phase II Dark Matter Search". In: 072013 (2014), p. 20. ISSN: 15502368. DOI: 10.1103/PhysRevD.89.072013. arXiv: 1404.4309. URL: http://arxiv.org/abs/1404.4309 (cit. on p. 39).

[63] Jonathan L. Feng. "Dark Matter Candidates from Particle Physics and Methods of Detection". In: (2010), p. 62. ISSN: 0066-4146. DOI: 10.1146/annurev-astro-082708-101659. arXiv: 1003.0904. URL: http://arxiv.org/abs/1003.0904 (cit. on pp. 21, 25).

[64] a. Liam Fitzpatrick, Wick Haxton, Emanuel Katz, Nicholas Lubbers, and Yiming Xu. "The effective field theory of dark matter direct detection". In: *Journal of Cosmology and Astroparticle Physics* 2013.02 (2013), pp. 004–004. ISSN: 1475-7516. DOI: 10.1088/1475-7516/2013/02/004. URL: http://stacks.iop.org/1475-7516/2013/i=02/a=004?key=crossref.f8d4bb53172a7cfb7e56f50919d9383c (cit. on p. 38).

[65] R Franz and G Wiedemann. "Ueber die Wärme-Leitungsfähigkeit der Metalle". In: *Annalen der Physik* 165.8 (1853), pp. 497–531. ISSN: 00033804. DOI: 10.1002/andp.18531650802 (cit. on p. 164).

[66] Joshua Frieman, Michael Turner, and Dragan Huterer. "Dark Energy and the Accelerating Universe". In: (2008), pp. 385–432. ISSN: 0066-4146. DOI: 10.1146/annurev.astro.46.060407.145243. arXiv: 0803.0982. URL: http://arxiv.org/abs/0803.0982 (cit. on p. 11).

[67] Masataka Fukugita and P. J. E. Peebles. "The Cosmic Energy Inventory". In: *The Astrophysical Journal* 1936 (2004), pp. 643–668. ISSN: 0004-637X. DOI: 10.1086/425155. arXiv: 0406095 [astro-ph]. URL: http://arxiv.org/abs/astro-ph/0406095 (cit. on p. 13).

[68] Jiansong Gao. "The Physics of Superconducting Microwave Resonators". PhD thesis. Pasadena: California Institute of Technology, 2008 (cit. on pp. 100, 127, 134, 136).

[69] C. W. Gardiner and M. J. Collett. "Input and output in damped quantum systems: Quantum stochastic differential equations and the master equation". In: *Physical Review A* 31.6 (1985), pp. 3761–3774. ISSN: 10502947. DOI: 10.1103/PhysRevA.31.3761 (cit. on p. 83).

[70] C. W. Gardiner, a. S. Parkins, and M. J. Collett. "Input and output in damped quantum systems II Methods in non-white-noise situations andapplcation to inhibition of atomic phase decays". In: *Journal of the Optical Society of America B* 4.10 (1987), p. 1683. ISSN: 0740-3224. DOI: 10.1364/JOSAB.4.001683 (cit. on p. 83).

[71] R E Glover and M Tinkham. "Conductivity of Superconducting Films for Photon Energies between 0.3 and 40 kT_c". In: *Physical Review* 108.2 (1957), pp. 243–256 (cit. on pp. 58, 60).

[72] M. A. Golosovsky, H. J. Snortland, and M. R. Beasley. "Nonlinear microwave properties of superconducting Nb microstrip resonators". In: *Physical Review B* 51.10 (1995), pp. 6462–6469. ISSN: 01631829. DOI: 10.1103/PhysRevB.51.6462 (cit. on pp. 65, 66).

[73] C J Gorter and H Casimir. "Thermodynamics of the supraconducting state". In: *Zeitschrift fur Technische Physik* 35.12 (1934), pp. 539–542 (cit. on p. 52).

[74] J Grangle, A Fogarty, and MJ Taylor. "Weak ferromagnetism in 'non-magnetic' austenitic stainless steel". In: *Journal of Magnetism and Magnetic Materials* 111 (1992), pp. 255–259 (cit. on p. 181).

[75] Kenneth E. Gray, ed. *Nonequilibrium Superconductivity, Phonons, and Kapitza Boundaries*. Plenum, 1981. ISBN: 978-1-4684-3937-3. DOI: 10.1007/978-1-4684-3935-9. URL: http://link.springer.com/10.1007/978-1-4684-3935-9 (cit. on p. 214).

[76] Daniel Hafner, Martin Dressel, and Marc Scheffler. "Surface-resistance measurements using superconducting stripline resonators". In: *Review of Scientific Instruments* 85.1 (2014), pp. 35–39. ISSN: 00346748. DOI: 10.1063/1.4856475. arXiv: 1309.5331 (cit. on p. 133).

[77] P.R Hastings and D.M. Montgomery. "Support of cooled components in astronomical instruments". In: 33.11 (1993), pp. 1032–1036 (cit. on p. 184).

[78] Matt Russell Hauser. "Acoustic Waves in Crystals: I. Ultrasonic Flux and Internal Diffraction, II. Imaging Phonons in Superconducting Niobium". PhD thesis. University of Illinois at Urbana-Champaign, 1995, p. 131. DOI: 10.1108/eb050773 (cit. on pp. 243, 245).

[79] Matthias Hein. "Temperature and Frequency Dependent Surface Impedance". In: *High-Temperature-Superconductor Thin Films at Microwave Frequencies*. Berlin, Heidelberg: Springer, 1999. Chap. 1, pp. 1–42 (cit. on pp. 51, 53, 54, 60).

[80] J.S. Herd, J Halbritter, and K.G. Herd. "Microwave power dependence of HTS thin film transmission lines". In: *IEEE Transactions on Applied Superconductivity* 5.2 (1995), pp. 1991–1993. ISSN: 1051-8223. DOI: 10.1109/77.402976 (cit. on p. 65).

[81] Byeong Ho Eom, Peter K. Day, Henry G. LeDuc, and Jonas Zmuidzinas. "A wideband, low-noise superconducting amplifier with high dynamic range". In: *Nature Physics* 8.8 (July 2012), pp. 623–627. ISSN: 1745-2473. DOI: 10.1038/nphys2356. URL: http://www.nature.com/doifinder/10.1038/nphys2356 (cit. on p. 243).

[82] Roger A Horn and Charles R Johnson. *Matrix analysis*. English. Cambridge [Cambridgeshire]; New York: Cambridge University Press, 1999, 1985. ISBN: 0521305861 9780521305860 0521386322 9780521386326 (cit. on p. 152).

[83] Robert Hu. "Analysis of the input noise contribution in the noise temperature measurements". In: *IEEE Microwave and Wireless Components Letters* 15.3 (Mar. 2005), pp. 141–143. ISSN: 1531-1309. DOI: 10.1109/LMWC.2004.842832. URL: http://ieeexplore.ieee.org/lpdocs/epic03/wrapper.htm?arnumber=1406056 (cit. on p. 126).

[84] J Hubmayr, J Beall, D Becker, H Cho, M Devlin, B Dober, C Groppi, G C Hilton, K D Irwin, D Li, P Mauskopf, D P Pappas, J Van Lanen, M R Vissers, and J Gao. "Photon-noise limited sensitivity in titanium nitride kinetic inductance detectors J.Hubmayr, 1," in: (2014), pp. 1–10. arXiv: arXiv:1406.4010v1 (cit. on p. 241).

[85] Giles. Humpston and David M Jacobson. *Principles of soldering*. English. Materials Park, Ohio, 2004. URL: http://site.ebrary.com/id/10320352 (cit. on pp. 212, 213).

[86] JG Hust and AB Lankford. "Comments on the Measurement of Thermal Conductivity and Presentation of a Thermal Conductivity Integral Method". In: *International Journal of Thermophysics* 3.1 (1982), pp. 67–77 (cit. on pp. 280, 281).

[87] M A Imam and C R Feng. "STUDY OF TRANSFORMATION KINETICS IN TIMETAL-21S TITANIUM ALLOY". In: *Proceedings of the Eighth World Conference on Titanium*. Ed. by P Blenkinsop, W Evans, and H Flower. Birmingham, UK, 1996, pp. 2361–2368 (cit. on p. 195).

[88] John David Jackson. *Classical electrodynamics*. English. 3rd ed. New York: Wiley, 1962. ISBN: 0471431311 9780471431312 (cit. on p. 58).

[89] David M Jacobson and Giles. Humpston. *Principles of brazing*. English. Materials Park, NY: ASM International, 2005. ISBN: 0871708124 9780871708120 (cit. on p. 213).

[90] J.R. James and a. Henderson. "High-frequency behaviour of microstrip open-circuit terminations". In: *IEE Journal on Microwaves, Optics and Acoustics* 3.5 (1979), p. 205. ISSN: 03086976. DOI: 10.1049/ij-moa.1979.0046 (cit. on pp. 77, 98).

[91] J Jensen, R Stewart, W Tuttle, H Brechna, and A Prodell. *Brookhaven national laboratory selected cryogenic data notebook*. Tech. rep. Brookhaven National Laboratory, 1980 (cit. on p. 165).

[92] Nick Kaiser and Gordon Squires. "Mapping the dark matter with weak gravitational lensing". In: *The Astrophysical Journal* 404 (1993), p. 441. ISSN: 0004-637X. DOI: 10.1086/172297 (cit. on pp. 15, 16).

[93] Ke-Jun Kang, Qian Yue, Yu-Cheng Wu, Jian-Ping Cheng, Yuan-Jing Li, Yang Bai, Yong Bi, Jian-Ping Chang, Nan Chen, Ning Chen, Qing-Hao Chen, Yun-Hua Chen, You-Chun Chuang, Zhi Dend, Qiang Du, Hui Gong, Xi-Qing Hao, Qing-Ju He, Xin-Hui Hu, Han-Xiong Huang, Teng-Rui Huang, Hao Jiang, Hau-Bin Li, Jian-Min Li, Jin Li, Jun Li, Xia Li, Xin-Ying Li, Xue-Qian Li, Yu-Lan Li, Heng-Ye Liao, Fong-Kay Lin, Shin-Ted Lin, Shu-Kui Liu, Lan-Chun Lv, Hao Ma, Shao-Ji Mao, Jian-Qiang Qin, Jie Ren, Jing Ren, Xi-Chao Ruan, Man-Bin Shen, Lakhwinder Singh, Manoj Kumar Singh, Arun Kumar Soma, Jian Su, Chang-Jian Tang, Chao-Hsiung Tseng, Ji-Min Wang, Li Wang, Qing Wang, Tsz-King Henry Wong, Shi-Yong Wu, Wei Wu, Hao-Yang Xing, Yin Xu, Tao Xue, Li-Tao Yang, Song-Wei Yang, Nan Yi, Chun-Xu Yu, Hao Yu, Xun-Zhen Yu, Xiong-Hui Zeng, Zhi Zeng, Lan Zhang, Yun-Hua Zhang, Ming-Gang Zhao, Wei Zhao, Su-Ning Zhong, Zu-Ying Zhou, Jing-Jun Zhu, Wei-Bin Zhu, Xue-Zhou Zhu, and Zhong-Hua Zhu. "The CDEX-1 1 kg Point-Contact Germanium Detector for Low Mass Dark Matter Searches". In: (2013), p. 6. ISSN: 16741137. DOI: 10.1088/1674-1137/37/12/126002. arXiv: 1305.0401. URL: http://arxiv.org/abs/1305.0401 (cit. on p. 36).

[94] M B Kasen, G R MacDonald, D H Jr. Beekman, and R E Schramm. "Mechanical, electrical, and thermal characterization of G-10CR and G-11CR glass-cloth/epoxy laminates between room temperature and 4K". In: *Advances in Cryogenic Engineering. Materials. Vol.26. Proceedings of the Third International Cryogenic Materials Conference*. Ed. by A F Clark and R P Reed. New York, NY, USA: Plenum, 1980, pp. 235–244 (cit. on p. 179).

[95] N. Kellaris, M. Daal, M. Epland, M. Pepin, O. Kamaev, P. Cushman, E. Kramer, B. Sadoulet, N. Mirabolfathi, S. Golwala, and M. Runyan. "Sub-kelvin thermal conductivity and radioactivity of some useful materials in low background cryogenic experiments". In: *Journal of Low Temperature Physics* 176.3-4 (2014), pp. 201–208. ISSN: 15737357. DOI: 10.1007/s10909-013-1048-6 (cit. on pp. 166, 168, 170, 171, 178, 192, 278, 296).

[96] Nicholas Kellaris. "The Development of Thermal Stand-offs and Electronic Connections for the SuperCDMS SNOLab Tower". PhD thesis. Berkeley: UC Berkeley, 2013 (cit. on p. 184).

[97] M. S. Khalil, M. J a Stoutimore, F. C. Wellstood, and K. D. Osborn. "An analysis method for asymmetric resonator transmission applied to superconducting devices". In: *Journal of Applied Physics* 111.5 (2012), pp. 1–6. ISSN: 00218979. DOI: 10.1063/1.3692073. arXiv: 1108.3117 (cit. on p. 133).

[98] N Klein, H Chaloupka, G. Mufffdfffdller, S Orbach, H Piel, B. Roas, L Schultz, U. Klein, and M. Peiniger. "The effective microwave surface impedance of high Tc thin films". In: *Journal of Applied Physics* 67.11 (1990), p. 6940. ISSN: 00218979. DOI: 10.1063/1.345037. URL: http://scitation.aip.org/content/aip/journal/jap/67/11/10.1063/1.345037 (cit. on p. 101).

[99] Erik Kramer, Nicholas Kellaris, Miguel Daal, Bernard Sadoulet, Sunil Golwala, and Matthew Hollister. "Material selection for cryogenic support structures". In: *Journal of Low Temperature Physics* 176.5-6 (2014), pp. 1103–1108. ISSN: 15737357. DOI: 10.1007/s10909-013-1052-x (cit. on p. 177).

[100] John Daniel Kraus. *Radio astronomy*. English. 2nd. Powell, Ohio: Cygnus-Quasar Books, 1986 (cit. on p. 126).

[101] Jerzy Krupka, Krzysztof Derzakowski, Michael Tobar, John Hartnett, and Richard G Geyer. "Complex permittivity of some ultralow loss dielectric crystals at cryogenic temperatures". In: *Measurement Science and Technology* 10.5 (1999), pp. 387–392. ISSN: 0957-0233. DOI: 10.1088/0957-0233/10/5/308 (cit. on pp. 97, 99).

[102] K Kurokawa. "Power Waves and the Scattering Matrix". In: *IEEE Transactions on Microwave Theory and Techniques* 13.2 (Mar. 1965), pp. 194–202. ISSN: 0018-9480. DOI: 10.1109/TMTT.1965.1125964. URL: http://ieeexplore.ieee.org/lpdocs/epic03/wrapper.htm?arnumber=1125964 (cit. on p. 95).

[103] A. Kushino, S. Kasai, S. Kohjiro, S. Shiki, and M. Ohkubo. "Development of Superconducting Coaxial Cables for Cryogenic Detectors". In: *Journal of Low Temperature Physics* 151.3-4 (Jan. 2008), pp. 650–654. ISSN: 0022-2291. DOI: 10.1007/s10909-008-9721-x. URL: http://www.springerlink.com/index/10.1007/s10909-008-9721-x (cit. on p. 118).

[104] a. Kushino, M. Ohkubo, and K. Fujioka. "Thermal conduction measurement of miniature coaxial cables between 0.3 and 4.5K for the wiring of superconducting detectors". In: *Cryogenics* 45.9 (Sept. 2005), pp. 637–640. ISSN: 00112275. DOI: 10.1016/j.cryogenics.2005.07.002. URL: http://linkinghub.elsevier.com/retrieve/pii/S0011227505001001 (cit. on p. 192).

[105] Roland Lang and Klaus Hofmann. "Cold Forming of Beta Titanium Sheet". In: *Proc of Cost Effective Application of Titanium Alloys in Military Platforms*. Vol. 069. Loen, Norway: Platforms, RTO AVT specialistsfffdfffdfffd meeting on cost effective application of titanium alloys in military. URL: http://ftp.rta.nato.int/Public/PubFullText/RTO/MP/RTO-MP-069(II)/MP-069(II)-(SM2)-07.pdf (cit. on p. 179).

[106] D.C. Larbalestier and H.W. King. *Austenitic stainless steels at cryogenic temperatures 1: Structural stability and magnetic properties*. 1973. DOI: 10.1016/0011-2275(73)90285-3 (cit. on p. 181).

[107] Jason Lawrence, a.B Patel, and J.G Brisson. "The thermal conductivity of Kapton HN between 0.5 and 5 K". In: *Cryogenics* 40.3 (Mar. 2000), pp. 203–207. ISSN: 00112275. DOI: 10.1016/S0011-2275(00)00028-X. URL: http://linkinghub.elsevier.com/retrieve/pii/S001122750000028X (cit. on p. 168).

[108] Benjamin W. Lee and Steven Weinberg. "Cosmological lower bound on heavy-neutrino masses". In: *Physical Review Letters* 39.4 (1977), pp. 165–168. ISSN: 00319007. DOI: 10.1103/PhysRevLett.39.165 (cit. on p. 25).

[109] M.K. Lee, J.G. Lee, J.K. Lee, J.J. Park, G.J. Lee, Y.R. Uhm, and C.K. Rhee. "Strong bonding of titanium to copper through the elimination of the brittle interfacial intermetallics". In: *Journal of Materials Research* 23.08 (2008), pp. 2254–2263. ISSN: 0884-2914. DOI: 10.1557/JMR.2008.0269 (cit. on p. 202).

[110] Steve Leman and Scott Hertel. *Graphite Conductance*. Tech. rep. Boston: MIT, May 2008 (cit. on p. 166).

[111] D. S. Leonard, P. Grinberg, P. Weber, E. Baussan, Z. Djurcic, G. Keefer, a. Piepke, a. Pocar, J. L. Vuilleumier, J. M. Vuilleumier, D. Akimov, a. Bellerive, M. Bowcock, M. Breidenbach, a. Burenkov, R. Conley, W. Craddock, M. Danilov, R. DeVoe, M. Dixit, a. Dolgolenko, I. Ekchtout, W. Fairbank, J. Farine, P. Fierlinger, B. Flatt, G. Gratta, M. Green, C. Hall, K. Hall, D. Hallman, C. Hargrove, R. Herbst, J. Hodgson, S. Jeng, S. Kolkowitz, a. Kovalenko, D. Kovalenko, F. LePort, D. Mackay, M. Moe, M. Montero Díez, R. Neilson, a. Odian, K. O'Sullivan, L. Ounalli, C. Y. Prescott, P. C. Rowson,

D. Schenker, D. Sinclair, K. Skarpaas, G. Smirnov, V. Stekhanov, V. Strickland, C. Virtue, K. Wamba, and J. Wodin. "Systematic study of trace radioactive impurities in candidate construction materials for EXO-200". In: *Nuclear Instruments and Methods in Physics Research, Section A: Accelerators, Spectrometers, Detectors and Associated Equipment* 591.3 (2008), pp. 490–509. ISSN: 01689002. DOI: 10.1016/j.nima.2008.03.001. arXiv: 0709.4524 (cit. on p. 176).

[112] J Liotard. "Intermetallic compound formations in titanium-copper thin films couples". In: *Journal of Applied Physics* 57.1985 (1985), pp. 1895–1901. ISSN: 00218979. DOI: 10.1063/1.334422 (cit. on p. 202).

[113] M. Locatelli, D. Arnaud, and M. Routin. "Thermal conductivity of some insulating materials materials below 1 K". In: *Cryogenics* 16.6 (1976), pp. 374–375. ISSN: 00112275. DOI: 10.1016/0011-2275(76)90220-4 (cit. on p. 170).

[114] F London, H London, The Royal Society, Royal Society, and Physical Sciences. "Electromagnetic equations of the supraconductor". In: *Proceedings of the Royal Society of London, Series A (Mathematical and Physical Sciences)* 149 (1935), pp. 71–88 (cit. on pp. 52, 60).

[115] Olli Luukkonen, Constantin Simovski, Gérard Granet, George Goussetis, Dmitri Lioubtchenko, Antti V. Raisanen, and Sergei a Tretyakov. "Simple and Accurate Analytical Model of Planar Grids and High-Impedance Surfaces Comprising Metal Strips or Patches". In: *IEEE Transactions on Antennas and Propagation* 56.6 (June 2008), pp. 1624–1632. ISSN: 0018-926X. DOI: 10.1109/TAP.2008.923327. arXiv: arXiv:0705.3548v3. URL: http://ieeexplore.ieee.org/lpdocs/epic03/wrapper.htm?arnumber=4538157 (cit. on p. 110).

[116] Olli Luukkonen, Constantin Simovski, Grard Granet, George Goussetis, Dmitri Lioubtchenko, Antti V. Raisanen, and Sergei a Tretyakov. "Corrections to "Simple and Accurate Analytical Model of Planar Grids and High-Impedance Surfaces Comprising Metal Strips or Patches" [Jun 08 1624-1632]". In: *IEEE Transactions on Antennas and Propagation* 58.6 (June 2010), pp. 2162–2162. ISSN: 0018-926X. DOI: 10.1109/TAP.2010.2047371. arXiv: arXiv:0705.3548v3. URL: http://ieeexplore.ieee.org/lpdocs/epic03/wrapper.htm?arnumber=5443648 (cit. on p. 110).

[117] Stephen A Maas. *Microwave mixers*. English. Dedham, MA: Artech House, 1986. ISBN: 0890061718 9780890061718 (cit. on p. 126).

[118] Morten Madsen. "Bachelor fffdfffdfffd s Thesis in Experimental Physics Modular Low-Temperature Load-Locked Sample System for Quantum Devices". PhD thesis. Copenhagen: University of Copenhagen, 2014. URL: http://qdev.nbi.ku.dk/student%5C_theses/pdf%5C_files/Morten%5C_Madsen%5C_BA.pdf (cit. on p. 236).

[119] M. P. Markakis. "Exact solutions for certain nonlinear autonomous ordinary differential equations of the second order and families of two-dimensional autonomous systems". In: *International Journal of Differential Equations* 2010 (2010), pp. 1–13. ISSN: 1687-9643. DOI: 10.1155/2010/436860 (cit. on p. 219).

[120] F W Markley, J A Hoffman, and D P Muniz. "Cryogenic Compressive Properties of Basic Epoxy Resin Systems". English. In: *Advances in Cryogenic Engineering Materials SE - 14*. Ed. by R P Reed and A F Clark. Vol. 32. Advances in Cryogenic Engineering Materials. Cambridge, Massachusetts: Springer US, 1986, pp. 119–126. ISBN: 978-1-4613-9873-8. DOI: 10.1007/978-1-4613-9871-4_14. URL: http://dx.doi.org/10.1007/978-1-4613-9871-4%5C_14 (cit. on p. 179).

[121] Stephen P. Martin. "A Supersymmetry Primer". In: Version 6 (2011), p. 152. arXiv: 9709356 [hep-ph]. URL: http://arxiv.org/abs/hep-ph/9709356 (cit. on p. 23).

[122] D C Mattis and J Bardeen. "Theory of the Anomalous Skin Effect in Normal and Superconducting Metals". In: *Physical Review* 111.2 (1958), pp. 412–417 (cit. on pp. 55, 57, 59).

[123] B A Mazin, Seth R Meeker, M J Strader, P Szypryt, D Marsden, J C van Eyken, G E Duggan, A B Walter, G Ulbricht, and M Johnson. "ARCONS : A 2024 Pixel Optical through Near-IR Cryogenic Imaging Spectrophotometer". In: *Publications of the Astronomical Society of the Pacific* 125.993 (2013), pp. 1348–1361 (cit. on pp. 241, 246).

[124] Benjamin A Mazin. "Microwave Kinetic Inductance Detectors". PhD thesis. California Institute of Technology, Pasadena, 2004, p. 179 (cit. on p. 245).

[125] Christopher M. McKenney, Henry G. Leduc, Loren J. Swenson, Peter K. Day, Byeong H. Eom, and Jonas Zmuidzinas. "Design considerations for a background limited 350 micron pixel array using lumped element superconducting microresonators". In: *Proceedings of SPIE* 8452 (Sept. 2012). Ed. by Wayne S. Holland, 84520S. DOI: 10.1117/12.925759. URL: http://proceedings.spiedigitallibrary.org/proceeding.aspx?doi=10.1117/12.925759 (cit. on p. 241).

[126] W L McMillian. "Transition Temperature of Strong-Coupled Superconductors". In: *Physical Review* 167.2 (1968), pp. 331–344 (cit. on p. 55).

[127] W Meissner, F Heidenreicht, R Ochsenfeld, and F Leiri. "Alteration in current distribution and magnetic induction with onset of supraconductivity". In: *Physikalische Zeitschrift* 37 (1936), pp. 449–470 (cit. on p. 53).

[128] K. Mendelssohn and C. a. Renton. "The Heat Conductivity of Superconductors below 1 degrees K". In: *Proceedings of the Royal Society A: Mathematical, Physical and Engineering Sciences* 230.1181 (1955), pp. 157–169. ISSN: 1364-5021. DOI: 10.1098/rspa.1955.0119 (cit. on p. 192).

[129] Richard K Miller, Terri C Walker, and Inc.) (Future Technology Surveys. *Survey on shape memory alloys*. English. Lilburn, GA: Future Technology Surveys, 1989. ISBN: 1558651004 9781558651005 (cit. on p. 296).

[130] M. Mola, S. Hill, P. Goy, and M. Gross. "Instrumentation for Millimeter-wave Magnetoelectrodynamic Investigations of Low-Dimensional Conductors and Superconductors". In: 71.1 (1999), p. 20. ISSN: 00346748. DOI: 10.1063/1.1150182. arXiv: 9907310 [cond-mat]. URL: http://arxiv.org/abs/cond-mat/9907310 (cit. on p. 133).

[131] S.L. Nyakana, J.C. Fanning, and R.R. Boyer. "Quick Reference Guide for β Titanium Alloys in the 00s". In: *Journal of Materials Engineering and Performance* 14.6 (Dec. 2005), pp. 799–811. ISSN: 10599495. DOI: 10.1361/105994905X75646. URL: http://www.ingentaselect.com/rpsv/cgi-bin/cgi?ini=xref%5C&body=linker%5C&reqdoi=10.1361/105994905X75646 (cit. on pp. 179, 290, 293).

[132] John H. Oates, Robert T. Shin, Daniel E. Oates, Michael J. Tsuk, and Paul P. Nguyen. "Nonlinear transmission line model for superconducting stripline resonators". In: *IEEE Transactions on Applied Superconductivity* 3.1 pt 1 (1993), pp. 17–22. ISSN: 10518223. DOI: 10.1109/77.233413 (cit. on p. 155).

[133] Milton Ohring. *Materials science of thin films deposition and structure*. English. San Diego, CA, 2002. URL: http://www.engineeringvillage.com/controller/servlet/OpenURL?genre=book%5C&isbn=9780125249751 (cit. on p. 196).

[134] K. A. (The Particle Data Group) Olive. "2014 Review of Particle Physics: 2. astrophysical constants". In: *Chin. Phys. C* 38.090001 (2014) (cit. on p. 6).

[135] K. A. (The Particle Data Group) Olive. "2014 Review of Particle Physics: 22. big-bang cosmology". In: *Chin. Phys. C* 38.090001 (2014), pp. 1–33 (cit. on p. 1).

[136] K. A. (The Particle Data Group) Olive. "2014 Review of Particle Physics: 23. big-bang nucleosynthesis". In: *Chin. Phys. C* 38.090001 (2014), pp. 1–15 (cit. on p. 7).

[137] J.R. Olson. "Thermal conductivity of some common cryostat materials between 0.05 and 2 K". In: *Cryogenics* 33.7 (1993), pp. 729–731. ISSN: 00112275. DOI: 10.1016/0011-2275(93)90027-L (cit. on p. 192).

[138] R. D. Peccei and Helen R. Quinn. "Constraints imposed by CP conservation in the presence of pseudoparticles". In: *Physical Review D* 16.6 (Sept. 1977), pp. 1791–1797. ISSN: 0556-2821. DOI: 10.1103/PhysRevD.16.1791. URL: http://link.aps.org/doi/10.1103/PhysRevD.16.1791 (cit. on p. 22).

[139] R. D. Peccei and Helen R. Quinn. "CP conservation in the presence of pseudoparticles". In: *Physical Review Letters* 38.25 (1977), pp. 1440–1443. ISSN: 00319007. DOI: 10.1103/PhysRevLett.38.1440 (cit. on p. 22).

[140] Gary W Phillips, David J Nagel, and Timothy Coffey. *A Primer on the Detection of Nuclear and Radiological Weapons*. Tech. rep. July. Washington D.C.: National Defense Uiversity Center for Technology, July 2005, pp. 1–71 (cit. on p. 238).

[141] A. B. Pippard. "Experimental analysis of the electronic structure of metals". In: *Reports on Progress in Physics* 23.1 (Jan. 1960), pp. 176–266. ISSN: 00344885. DOI: 10.1088/0034-4885/23/1/304. URL: http://stacks.iop.org/0034-4885/23/i=1/a=304?key=crossref.96914d2d9c9b05ac0bdeee375d37f292 (cit. on pp. 57, 58, 61).

[142] A B Pippard. "The anomalous skin effect in anisotropic metals". In: *Proceedings of the Royal Society of London, Series A (Mathematical and Physical Sciences)* 224.June (1954), pp. 273–282 (cit. on p. 59).

[143] A. B. Pippard. "The Surface Impedance of Superconductors and Normal Metals at High Frequencies. IV. Impedance at 9400 Mc./sec. of Single Crystals of Normal and Superconducting Tin". In: *Proceedings of the Royal Society A: Mathematical, Physical and Engineering Sciences* 203.1072 (Sept. 1950), pp. 98–118. ISSN: 1364-5021. DOI: 10.1098/rspa.1950.0128. URL: http://rspa.royalsocietypublishing.org/cgi/doi/10.1098/rspa.1950.0128 (cit. on p. 58).

[144] Planck Collaboration. "Planck 2015 reslts. XIII. Cosmological parameters". In: *Astronomy & Astrophysics* (2015), p. 20. arXiv: 1502.0158. URL: http://arxiv.org/abs/1502.01589 (cit. on pp. 1, 11).

[145] Planck Collaboration et al. "Planck 2013 results. XVI. Cosmological parameters". In: (2013), pp. 1–69. DOI: 10.1051/0004-6361/201321591. arXiv: 1303.5076. URL: http://arxiv.org/abs/1303.5076%20http://dx.doi.org/10.1051/0004-6361/201321591 (cit. on pp. 6, 11).

[146] R. Popel. "Exact Solutions of the Matthis Bardeen Theory for Thin Superconducting Films and Bulk Materials". In: *IEEE Transactions on Magnetics* 27.2 (1991), pp. 1306–1309 (cit. on pp. 55, 61).

[147] R. Pofffdfffdpel. "Surface impedance and reflectivity of superconductors". In: *Journal of Applied Physics* 66.12 (1989), p. 5950. ISSN: 00218979. DOI: 10.1063/1.343622. URL: http://scitation.aip.org/content/aip/journal/jap/66/12/10.1063/1.343622 (cit. on pp. 55, 56).

[148] R. Radebaugh, N.V. Frederick, and J.D. Siegwarth. "Flexible laminates for thermally grounded terminal strips and shielded electrical leads at low temperatures". In: *Cryogenics* 13.1 (1973), pp. 41–43. ISSN: 00112275. DOI: 10.1016/0011-2275(73)90264-6 (cit. on p. 168).

[149] a. H M E Rahman and M. N. Cavalli. "Strength and microstructure of diffusion bonded titanium using silver and copper interlayers". In: *Materials Science and Engineering A* 527.20 (2010), pp. 5189–5193. ISSN: 09215093. DOI: 10.1016/j.msea.2010.04.065. URL: http://dx.doi.org/10.1016/j.msea.2010.04.065 (cit. on p. 202).

[150] Scott W. Randall, Maxim Markevitch, Douglas Clowe, Anthony H. Gonzalez, and Marusa Bradac. "Constraints on the Self-Interaction Cross-Section of Dark Matter from Numerical Simulations of the Merging Galaxy Cluster 1E 0657-5". In: (2007). ISSN: 0004-637X. DOI: 10.1086/587859. arXiv: 0704.0261. URL: http://arxiv.org/abs/0704.0261 (cit. on p. 21).

[151] A Redermeier. "Fingerprinting of Nuclear Material for Nuclear Forensics". In: *Esarda Bulletin* 43 (2009), pp. 71–76 (cit. on p. 238).

[152] K. Reiche and G. Pompe. "Investigation of the thermal and electrical transport properties of niobium and niobium films at temperatures between 9 and 50 K". In: *Journal of Low Temperature Physics* 36.3-4 (1979), pp. 467–481. ISSN: 00222291. DOI: 10.1007/BF00118716 (cit. on p. 192).

[153] M Reytier, F Kircher, and B Levesy. "CHARACTERIZATION OF TITANIUM ALLOYS FOR CRYOGENIC APPLICATIONS". In: *AIP Conference Proceedings* 48 (2002), pp. 76–83. URL: http://scholar.google.com/scholar?hl=en%5C&btnG=Search%5C&q=intitle:CHARACTERIZATION+OF+TITANIUM+ALLOYS+FOR+CRYOGENIC+APPLICATIONS%5C#0 (cit. on p. 171).

[154] L. Risegari, M. Barucci, L. Lolli, and G. Ventura. "Low Temperature Thermal Conductivity offffdfffdTi6Al4Vfffdfffd Alloy". In: *Journal of Low Temperature Physics* 151.3-4 (Jan. 2008), pp. 645–649. ISSN: 0022-2291. DOI: 10.1007/s10909-008-9726-5. URL: http://www.springerlink.com/index/10.1007/s10909-008-9726-5 (cit. on p. 117).

[155] *ROACH @ casper.berkeley.edu*. Berkeley. URL: https://casper.berkeley.edu/wiki/ROACH (cit. on pp. 122, 124, 246).

[156] Joseph J Rotman. *Galois theory*. English. 2nd. New York: Springer, 1998. ISBN: 0387985417 9780387985411 (cit. on p. 152).

[157] D.L. Rule, D.R. Smith, and L.L. Sparks. "Thermal conductivity of polypyromellitimide film with alumina filler particles from 4.2 to 300 K". In: *Cryogenics* 36.4 (Apr. 1996), pp. 283–290. ISSN: 00112275. DOI: 10.1016/0011-2275(96)88788-1. URL: http://linkinghub.elsevier.com/retrieve/pii/0011227596887881 (cit. on p. 168).

[158] M.C. Runyan and W.C. Jones. "Thermal conductivity of thermally-isolating polymeric and composite structural support materials between 0.3 and 4K". In: *Cryogenics* 48.9-10 (Sept. 2008), pp. 448–454. ISSN: 00112275. DOI: 10.1016/j.cryogenics.2008.06.002. URL: http://linkinghub.elsevier.com/retrieve/pii/S0011227508000933 (cit. on pp. 166, 170, 178, 299).

[159] Robert H. Sanders and Stacy S. McGaugh. "Modified Newtonian Dynamics as an Alternative to Dark Matter". In: *Annual Review of Astronomy and Astrophysics* Cdm (2002), p. 36. ISSN: 0066-4146. DOI: 10.1146/annurev.astro.40.060401.093923. arXiv: 0204521 [astro-ph]. URL: http://arxiv.org/abs/astro-ph/0204521 (cit. on p. 20).

[160] SA Schelkunoff. "The Impedance Concept and its Applications to Problems of Reflection, Refraction, Sheilding and Power Absorbtion". In: *Bell System Technical Journal* 17 (1938), pp. 17–48 (cit. on p. 70).

[161] R. W. Schnee. "Introduction to dark matter experiments". In: (2011), p. 64. DOI: 10.1142/9789814327183_0014. arXiv: 1101.5205. URL: http://arxiv.org/abs/1101.5205 (cit. on p. 33).

[162] P. Shankar, P. Palanichamy, T. Jayakumar, Baldev Raj, and S. Ranganathan. "Nitrogen redistribution, microstructure, and elastic constant evaluation using ultrasonics in aged 316LN stainless steels". In: *Metallurgical and Materials Transactions A* 32.12 (2001), pp. 2959–2968. ISSN: 1073-5623. DOI: 10.1007/s11661-001-0170-2 (cit. on p. 179).

[163] Zhi-Yuan. Shen. *High-temperature superconducting microwave circuits*. English. Boston: Artech House, 1994. ISBN: 0890066566 9780890066560 (cit. on p. 60).

[164] T M Shokair, J Root, K. A. Van Bibber, B Brubaker, Y V Gurevich, S B Cahn, S K Lamoreaux, M A Anil, K W Lehnert, B K Mitchell, A Reed, and G. Carosi. "Future directions in the microwave cavity search for dark matter axions". In: *International Journal of Modern Physics A* 29.19 (2014), p. 1443004. ISSN: 0217-751X. DOI: 10.1142/S0217751X14430040. arXiv: arXiv:1405.3685v1. URL: http://www.worldscientific.com/doi/abs/10.1142/S0217751X14430040 (cit. on p. 42).

[165] Ronald W Smith. "Low Temperature Active Joining for Electronics and Medical Deviced". In: *International Conference on Advances in Welding Technology (ICAWT)*. Columbus, Ohio, 1998 (cit. on p. 213).

[166] C Song, T W Heitmann, M P Defeo, K Yu, R Mcdermott, M Neeley, John M Martinis, and B L T Plourde. "Microwave response of vortices in superconducting thin films of Re and Al". In: *Physical Review B* 79.174512 (2009), pp. 1–9. DOI: 10.1103/PhysRevB.79.174512 (cit. on p. 140).

[167] I. Stern. "Axion Dark Matter Searches". In: 3 (2014), pp. 1–6. DOI: 10.1063/1.4883465. arXiv: 1403.5332. URL: http://arxiv.org/abs/1403.5332%20http://dx.doi.org/10.1063/1.4883465 (cit. on p. 43).

[168] W. Steven Johnson, Edward Li, and Jennifer L. Miller. "High temperature hybrid titanium composite laminates: An early analytical assessment". In: *Applied Composite Materials* 3.6 (1996), pp. 379–390. ISSN: 0929-189X. DOI: 10.1007/BF00133681 (cit. on p. 179).

[169] Will Sutherland. "Gravitational Microlensing - A Report on the MACHO Project". In: *Reviews of Modern Physics* 71.1 (1999), p. 20. ISSN: 0034-6861. DOI: 10.1103/RevModPhys.71.421. arXiv: 9811185 [astro-ph]. URL: http://arxiv.org/abs/astro-ph/9811185 (cit. on p. 17).

[170] Will Sutherland. "Microlensing". In: *Encyclopedia of Astronomy and Astrophysics* (2001), pp. 1–4 (cit. on p. 18).

[171] David Swank, William Windes, David Swank, William Windes, and David Rohrbaugh. *Carbon Characterization Laboratory Report*. Tech. rep. INL/EXT-09-15515. Idaho Falls: Idaho National Laboratory, Mar. 2009 (cit. on p. 179).

[172] E. Swartz and R. Pohl. "Thermal boundary resistance". In: *Reviews of Modern Physics* 61.3 (July 1989), pp. 605–668. ISSN: 0034-6861. DOI: 10.1103/RevModPhys.61.605. URL: http://link.aps.org/doi/10.1103/RevModPhys.61.605 (cit. on p. 214).

[173] L J Swenson, P K Day, B H Eom, H G Leduc, N Llombart, C M Mckenney, and O Noroozian. "Operation of a Titanium Nitride Superconducting Microresonator Detector in the Nonlinear Regime". In: *Journal of Applied Physics* 104501.113 (2013), pp. 104501–9. DOI: 10.1063/1.4794808 (cit. on pp. 65, 81, 155).

[174] S E Thompson, S Withington, D J Goldie, and C N Thomas. "Dynamical behaviour of superconducting microresonators with readout-power heating". In: *Superconductor Science and Technology* 26.9 (2013), p. 095009. ISSN: 0953-2048. DOI: 10.1088/0953-2048/26/9/095009. URL: http://stacks.iop.org/0953-2048/26/i=9/a=095009?key=crossref.40a237dc73d90e44dfb56ad0aa36fb2d (cit. on p. 66).

[175] M Tinkham. "Energy Gap Interpretation of Experiments on Infrared Transmission through Superconducting Films". In: *Physical Review* 104.3 (1956), pp. 845–846 (cit. on pp. 58, 60).

[176] Michael. Tinkham. *Introduction to superconductivity*. English. 1980 Repri. New York: McGraw-Hill, 1975. ISBN: 0070648778 9780070648777 (cit. on pp. 54, 59, 61).

[177] Sergei. Tretyakov. *Analytical modeling in applied electromagnetics*. English. Boston: Artech House, 2003. ISBN: 1580533671 9781580533676 (cit. on p. 110).

[178] T. Treu. "Strong Lensing by Galaxies". In: *Annual Review of Astronomy and Astrophysics* (2010). ISSN: 0066-4146. DOI: 10.1146/annurev-astro-081309-130924. arXiv: 1003.5567. URL: http://arxiv.org/abs/1003.5567 (cit. on p. 16).

[179] Jim Tuttle, Peter Shirron, Michael DiPirro, Michael Jackson, Jason Behr, Koji Kamiya, Brent Warner, Evan Kunes, and Tom Hait. "The HAWC and SAFIRE adiabatic demagnetization refrigerators". In: *Cryogenics* 41.11-12 (2001), pp. 781–787. ISSN: 00112275. DOI: 10.1016/S0011-2275(01)00169-2 (cit. on pp. 171, 192).

[180] T Van Duzer and C W Turner. *Principles of Superconductive Devices and Circuits*. 2nd ed. Medical Intelligence Unit. Prentice Hall, 1999. ISBN: 9780132627429. URL: http://books.google.com/books?id=uoViQgAACAAJ (cit. on pp. 51, 61).

[181] George F Geroge F. Vander Voort. *Atlas of time-temperature diagrams for nonferrous alloys*. English. [United States]: ASM International, 1991. ISBN: 0871704285 9780871704283 (cit. on p. 197).

[182] O. G. Vendik, a. B. Kozyrev, T. B. Samoilova, E. K. Hollmann, G. Ockenfiifffdfffd, R. Wördenweber, and a. Zaitsev. "Modeling, simulation, and measurement of nonlinearities in superconducting transmission lines and resonators". In: *Journal of Superconductivity* 10.2 (1997), pp. 63–71. ISSN: 0896-1107. DOI: 10.1007/BF02763175 (cit. on p. 155).

[183] G. Ventura and V. Martelli. "Thermal conductivity of Kevlar 49 between 7 and 290 K". In: *Cryogenics* 49.12 (2009), pp. 735–737. ISSN: 00112275. DOI: 10.1016/j.cryogenics.2009.08.001. URL: http://dx.doi.org/10.1016/j.cryogenics.2009.08.001 (cit. on p. 178).

[184] Michael R. Vissers, Jiansong Gao, Martin Sandberg, Shannon M. Duff, David S. Wisbey, Kent D. Irwin, and David P. Pappas. "Proximity-coupled Ti/TiN multilayers for use in kinetic inductance detectors". In: *Applied Physics Letters* 102.23 (2013), p. 232603. ISSN: 00036951. DOI: 10.1063/1.4804286. URL: http://link.aip.org/link/APPLAB/v102/i23/p232603/s1%5C&Agg=doi (cit. on p. 241).

[185] John Strawn Ward. "Observations of Carbon Monoxide in the Starburst Galaxy M82 with a 690 GHz Wide Spectral Thesis by". PhD thesis. 2001 (cit. on p. 113).

[186] L.a.a. Warnes and H.W. King. "The low temperature magnetic properties of austenitic Fe-Cr-Ni alloys". In: *Cryogenics* 16.11 (1976), pp. 659–667. ISSN: 00112275. DOI: 10.1016/0011-2275(76)90038-2 (cit. on p. 181).

[187] David H. Weinberg, Michael J. Mortonson, Daniel J. Eisenstein, Christopher Hirata, Adam G. Riess, and Eduardo Rozo. "Observational probes of cosmic acceleration". In: *Physics Reports* 530.2 (2013), pp. 87–255. ISSN: 03701573. DOI: 10.1016/j.physrep.2013.05.001. arXiv: 1201.2434. URL: http://dx.doi.org/10.1016/j.physrep.2013.05.001 (cit. on p. 11).

[188] S. Weinreb, J. Bardin, H. Mani, and G. Jones. "Matched wideband low-noise amplifiers for radio astronomy". In: *Review of Scientific Instruments* 80.4 (2009), pp. 1–5. ISSN: 00346748. DOI: 10.1063/1.3103939 (cit. on p. 123).

[189] Sander Weinreb and Joel Schleeh. "Multiplicative and additive low-frequency noise in microwave transistors". In: *IEEE Transactions on Microwave Theory and Techniques* 62.1 (2014), pp. 83–91. ISSN: 00189480. DOI: 10.1109/TMTT.2013.2293123 (cit. on p. 124).

[190] A WEISSHAAR and VK TRIPATHI. "Perturbation Analysis and Modeling of Curved Microstrip Bends". In: *IEEE TRANSACTIONS ON MICROWAVE THEORY AND TECHNIQUES* 38.10 (1990), pp. 1449–1454 (cit. on p. 96).

[191] H.a. Wheeler. "Transmission-Line Properties of Parallel Strips Separated by a Dielectric Sheet". In: *IEEE Transactions on Microwave Theory and Techniques* 13.2 (1965). ISSN: 0018-9480. DOI: 10.1109/TMTT.1965.1125962 (cit. on p. 98).

[192] Patrick Wikus, Scott a. Hertel, Steven W. Leman, Kevin a. McCarthy, Steven M. Ojeda, and Enectalí Figueroa-Feliciano. "The electrical resistance and thermal conductivity of Ti 15Vfffdfffdfffd3Crfffdfffdfffd3Snfffdfffdfffd3Al at cryogenic temperatures". In: *Cryogenics* 51.1 (Jan. 2011), pp. 41–44. ISSN: 00112275. DOI: 10.1016/j.cryogenics.2010.10.010. URL: http://linkinghub.elsevier.com/retrieve/pii/S001122751000202X (cit. on p. 290).

[193] Stefan L Wipf. "Low temperature heat transfer by contact in vacuo, and thermal conductivity of Kapton". In: *Proceedings of the 9th International Conference on Magnet Technology. MT-9 1985*. Ed. by C Marinucci and P Weymuth. Villigen, Switzerland: Swiss Inst. Nucl. Res., 1985, pp. 692–695 (cit. on p. 168).

[194] Adam L. Woodcraft. "Predicting the thermal conductivity of aluminium alloys in the cryogenic to room temperature range". In: *Cryogenics* 45.6 (June 2005), pp. 421–431. ISSN: 00112275. DOI: 10.1016/j.cryogenics.2005.02.003. URL: http://linkinghub.elsevier.com/retrieve/pii/S0011227505000391 (cit. on p. 192).

[195] Adam L. Woodcraft, Marco Barucci, Peter R. Hastings, Lapo Lolli, Valentina Martelli, Lara Risegari, and Guglielmo Ventura. "Thermal conductivity measurements of pitch-bonded graphites at millikelvin temperatures: Finding a replacement for AGOT graphite". In: *Cryogenics* 49.5 (2009), pp. 159–164. ISSN: 00112275. DOI: 10.1016/j.cryogenics.2008.10.024. URL: http://dx.doi.org/10.1016/j.cryogenics.2008.10.024 (cit. on pp. 166, 178, 296).

[196] Adam L. Woodcraft, Adam Gray, Betty Young, Blas Cabrera, and Aaron Miller. "A low temperature thermal conductivity database". In: *Proceedings of the 13th International Workshop on Low Temperature Detectors* 13 (2009), pp. 681–684. DOI: 10.1063/1.3292433. URL: http://scitation.aip.org/content/aip/proceeding/aipcp/10.1063/1.3292433$%5Cbackslash$nhttp://link.aip.org/link/APCPCS/v1185/i1/p681/s1%5C&Agg=doi (cit. on pp. 171, 178).

[197] S. J. C. Yates, J. J. a. Baselmans, a. Endo, R. M. J. Janssen, L. Ferrari, P. Diener, and a. M. Baryshev. "Photon noise limited radiation detection with lens-antenna coupled microwave kinetic inductance detectors". In: *Applied Physics Letters* 99.7 (2011), p. 073505. ISSN: 00036951. DOI: 10.1063/1.3624846. URL: http://scitation.aip.org/content/aip/journal/apl/99/7/10.1063/1.3624846 (cit. on p. 241).

[198] Hirokazu Yokoyama. *Thermal conductivity of polyimide film at cryogenic temperature*. 1995. DOI: 10.1016/0011-2275(95)90918-6 (cit. on p. 168).

[199] Bernard Yurke and Eyal Buks. "Performance of cavity-parametric amplifiers, employing Kerr nonlinearites, in the presence of two-photon loss". In: *Journal of Lightwave Technology* 24.12 (2006), pp. 5054–5066. ISSN: 07338724. DOI: 10.1109/JLT.2006.884490. arXiv: 0505018 [quant-ph] (cit. on p. 87).

[200] Bernard Yurke and John S. Denker. "Quantum network theory". In: *Physical Review A* 29.3 (1984), pp. 1419–1437. ISSN: 10502947. DOI: 10.1103/PhysRevA.29.1419 (cit. on p. 83).

[201] Shu-Ang. Zhou. *Electrodynamics of solids and microwave superconductivity*. English. New York: J. Wiley, 1999. ISBN: 0471354406 9780471354406 (cit. on p. 51).

[202] Jonas Zmuidzinas. "Superconducting Microresonators: Physics and Applications". In: *Annual Review of Condensed Matter Physics* 3.1 (Mar. 2012), pp. 169–214. ISSN: 1947-5454. DOI: 10.1146/annurev-conmatphys-020911-125022. URL: http://www.annualreviews.org/doi/abs/10.1146/annurev-conmatphys-020911-125022 (cit. on p. 241).

[203] N. R. Zobrist, M. Daal, B. Sadoulet, and S. Golwala. "A distributed method for modeling effective cryogenic flat cable heat sinking". In: *Journal of Low Temperature Physics* 176.5-6 (2014), pp. 1096–1102. ISSN: 15737357. DOI: 10.1007/s10909-013-0995-2 (cit. on p. 217).

[204] Nicholas R Zobrist. "Cryogenic Cabling for the SuperCDMS SNOLAB Experiment and Future Detector Designs". PhD thesis. 2015 (cit. on pp. 217, 225, 278).

Appendix A

Quality Factor

The dimensionless quality factor is useful for comparing the loss of a circuit at different frequencies. The standard definition of the quality factor is,

$$Q = \omega \cdot \frac{\text{Total Energy Stored in Cavity}}{\text{Power Lost per Oscillation}} = 2\pi \cdot \frac{\text{Total Energy Stored in Cavity}}{\text{Energy Lost per Oscillation}}. \tag{A.1}$$

In using these definitions, one gets to choose whether the numerator and denominator are both instantaneous quantities or whether they are both time-averaged. If one is time-averaged and one is instantaneous, quality factor obtained will be incorrect – probably off by a factor of two.

The power dissipated within a circuit is typically expressed separately from the power dissipated outside of the circuit. The power dissipated inside the circuit is the unloaded quality factor

$$Q_u = \omega \cdot \frac{\text{Total Energy Stored in Cavity}}{\text{Power Lost per Oscillation in the Circuit}} \tag{A.2}$$

If the circuit is connected to external loads or has addition loss or dissipation modes, n, the power dissipated in each may be expressed as an external quality factor,

$$Q_{ex,n} = \omega \cdot \frac{\text{Total Energy Stored in Cavity}}{\text{Power Lost per Oscillation in } n}. \tag{A.3}$$

Quality factors add as resistors in parallel,

$$\frac{1}{Q_{total}} = \frac{1}{Q_1} + \frac{1}{Q_2} + \cdots + \frac{1}{Q_n}. \tag{A.4}$$

Other definitions of quality factor include the following.

In terms of power, Q is associated with full width half max (FWHM) bandwidth of the resonance dip or peak in magnitude (as opposed to log magnitude or decibels),

$$Q = \frac{\omega_0}{\Delta\omega|_{\text{FWHM}}} = \frac{f_0}{\Delta f|_{\text{FWHM}}}. \tag{A.5}$$

In terms of wave amplitude (e.g. voltage, current, electric field and magnetic field), we use the full width at $1/\sqrt{2}$ times the dip or peak magnitude value instead of $1/2$.

When θ is the phase angle of the voltage wave,

$$Q = \frac{\omega_0}{2} \left| \frac{d\theta}{d\omega} \right|_{\omega=\omega_0} \tag{A.6}$$

Also, we can define Q in terms of the number of oscillations it takes for the signal amplitude to decay by a factor of $1/e$

$$Q = \pi \cdot N_{1/e}. \tag{A.7}$$

Alternatively, as decay time, τ, can be used.

$$Q = \pi \cdot (\text{Number of cycles in a decay time}) = \pi \cdot \frac{\tau_{1/e}}{T} = \pi \cdot f \cdot \tau_{1/e} = \frac{\omega \cdot \tau_{1/e}}{2} \tag{A.8}$$

There are two greatly different ways of measuring Q. One is to measure the decay of an excitation. The other is to measure the bandwidth of the response of a system to an excitation.

Appendix B

Phasors, Time Harmonic Fields and Power

B.1 Useful Identities

For a complex number, z, we have

$$\begin{aligned} z &= \Re[z] + i\Im[z] \qquad & z^* &= \Re[z] - i\Im[z] \\ \Re[z] &= \frac{1}{2}(z + z^*) \qquad & \Im[z] &= \frac{1}{2i}(z - z^*). \end{aligned} \tag{B.1}$$

Magnitudes and phases are related as,

$$\begin{aligned} |z| &= \sqrt{\Re[z]^2 + \Im[z]^2} \qquad & z^* z &= |z|^2 \\ z &= |z| e^{i\phi_z} \qquad & \phi_z &= \arctan\left(\frac{\Im[z]}{\Re[z]}\right). \end{aligned} \tag{B.2}$$

Composition rules for complex conjugation include,

$$(z_1 + z_2)^* = z_1^* + z_2^* \qquad (z_1 z_2)^* = z_1^* z_2^* \qquad \left(\frac{z_1}{z_2}\right)^* = \frac{z_1^*}{z_2^*} \tag{B.3}$$

Eulers formula is

$$e^{iz} = \cos(z) + i\sin(z). \tag{B.4}$$

For trigonometric and hyperbolic functions it follows that

$$\begin{aligned} \cos(z) &= \frac{e^{iz} + e^{-iz}}{2} \qquad & \sin(z) &= \frac{e^{iz} - e^{-iz}}{2i} \\ \cosh(z) &= \frac{e^{z} + e^{-z}}{2} \qquad & \sinh(z) &= \frac{e^{z} - e^{-z}}{2} \\ \cosh(z) &= \cos(iz) \qquad & \sinh(z) &= -i\sin(iz). \end{aligned} \tag{B.5}$$

B.2 Phasors

Time-harmonic fields vary sinusoidally in time. A time-harmonic scalar function, $\mathcal{A}(\mathbf{x},t)$, can be written

$$\begin{aligned}\mathcal{A}(\mathbf{x},t) &= |A(\mathbf{x})|\cos(\omega t+\phi_A)\\ &= \Re[|A(\mathbf{x})|e^{i\phi_A}e^{i\omega t}]\\ &= \Re[A(\mathbf{x})e^{i\omega t}]\\ &= \frac{1}{2}[A(\mathbf{x})e^{i\omega t}+A^*(\mathbf{x})e^{-i\omega t}].\end{aligned} \tag{B.6}$$

$A(\mathbf{x})$ is called the complex amplitude or cosine-based phasor of the function $\mathcal{A}(\mathbf{x},t)$. Alternatively, one could use sine-based phasors,

$$\begin{aligned}\mathcal{A}(\mathbf{x},t) &= |A(\mathbf{x})|\sin(\omega t+\phi'_A)\\ &= \Re[|A(\mathbf{x})|]\cos(\omega t)-\Im[|A(\mathbf{x})|]\sin(\omega t)\\ &= \Im[|A(\mathbf{x})|e^{i\phi'_A}e^{i\omega t}]\\ &= \Im[A(\mathbf{x})e^{i\omega t}]\\ &= \Re[|A(\mathbf{x})|]\cos(\omega t)-\Im[|A(\mathbf{x})|]\sin(\omega t)\\ &= \frac{1}{2i}[A(\mathbf{x})e^{i\omega t}-A^*(\mathbf{x})e^{-i\omega t}],\end{aligned} \tag{B.7}$$

where $\phi_A=\phi'_A+\pi/2$. Some authors use cosine-based phasors; some authors use sine-based phasors; some authors multiply by $e^{-i\omega t}$ instead of $e^{i\omega t}$ to obtain physical field. These variations result in sign changes but do not effect the physical field.

Analogously, a time-harmonic vector function, $\boldsymbol{\mathcal{A}}=\boldsymbol{\mathcal{A}}(\mathbf{x},t)$, can be written

$$\begin{aligned}\boldsymbol{\mathcal{A}}(\mathbf{x},t) &= \hat{x}\mathcal{A}_x(\mathbf{x},t)+\hat{y}\mathcal{A}_y(\mathbf{x},t)+\hat{z}\mathcal{A}_z(\mathbf{x},t)\\ &= \hat{x}|A_x(\mathbf{x})|\cos(\omega t+\phi_{A_x})+\hat{y}|A_y(\mathbf{x})|\cos(\omega t+\phi_{A_y})+\hat{z}|A_z(\mathbf{x})|\cos(\omega t+\phi_{A_z})\\ &= \Re\left\{[\hat{x}A_x(\mathbf{x})+\hat{y}A_y(\mathbf{x})+\hat{z}A_z(\mathbf{x})]e^{i\omega t}\right\}\\ &= \Re\left[\mathbf{A}(\mathbf{x})e^{i\omega t}\right].\end{aligned} \tag{B.8}$$

$\mathbf{A}(\mathbf{x})$ is called a vector phasor. The instantaneous vector $\boldsymbol{\mathcal{A}}(\mathbf{x},t)$ is,

$$\begin{aligned}\boldsymbol{\mathcal{A}}(\mathbf{x},t) &= \Re\left[\mathbf{A}(\mathbf{x})e^{i\omega t}\right]\\ &= \Re\left\{(\Re[\mathbf{A}(\mathbf{x})]+i\Im[\mathbf{A}(\mathbf{x})])\cdot(\cos(\omega t)+i\sin(\omega t))\right\}\\ &= \Re[\mathbf{A}(\mathbf{x})]\cos(\omega t)-\Im[\mathbf{A}(\mathbf{x})]\sin(\omega t).\end{aligned} \tag{B.9}$$

When the components of $\mathbf{A}(\mathbf{x})$ all have the same phase, $\mathbf{A}(\mathbf{x})=\hat{n}_A|\mathbf{A}(\mathbf{x})|e^{i\phi_{\mathbf{A}}}$, we recover the previous expression for scalar fields,

$$\begin{aligned}\boldsymbol{\mathcal{A}}(\mathbf{x},t) &= \Re[\mathbf{A}(\mathbf{x})]\cos(\omega t)-\Im[\mathbf{A}(\mathbf{x})]\sin(\omega t)\\ &= \hat{n}_A|\mathbf{A}(\mathbf{x})|[\cos(\phi_{\mathbf{A}})\cos(\omega t)-\sin(\phi_{\mathbf{A}})\sin(\omega t)]\\ &= \hat{n}_A|\mathbf{A}(\mathbf{x})|\cos(\omega t+\phi_{\mathbf{A}})\end{aligned} \tag{B.10}$$

B.3 Maxwell's In Phasor Form

For time harmonic fields, the Maxwell equations can be written in terms of vector phasors,

$$\begin{aligned} \nabla \times \boldsymbol{\mathcal{E}} &= -\frac{\partial \boldsymbol{\mathcal{B}}}{\partial t} & \rightarrow \quad \nabla \times \mathbf{E} &= -i\omega \mathbf{B} \\ \nabla \times \boldsymbol{\mathcal{H}} &= \frac{\partial \boldsymbol{\mathcal{D}}}{\partial t} + \boldsymbol{\mathcal{J}} & \rightarrow \quad \nabla \times \mathbf{H} &= i\omega \mathbf{D} + \mathbf{J} \\ \nabla \cdot \boldsymbol{\mathcal{D}} &= \varrho & \rightarrow \quad \nabla \cdot \mathbf{D} &= \rho \\ \nabla \cdot \boldsymbol{\mathcal{B}} &= 0 & \rightarrow \quad \nabla \cdot \mathbf{B} &= 0. \end{aligned} \tag{B.11}$$

Here we have used

$$\frac{\partial}{\partial t}\mathcal{A}(\mathbf{x},t) = \Re\left[A(\mathbf{x})\frac{\partial}{\partial t}e^{i\omega t}\right] = \Re\left[A(\mathbf{x})i\omega e^{i\omega t}\right] \tag{B.12}$$

to make the transformation. Additionally the following constitutive relations apply

$$\boldsymbol{\mathcal{D}} = \epsilon_0 \boldsymbol{\mathcal{E}} + \boldsymbol{\mathcal{P}} \qquad \mathbf{H} = \frac{\boldsymbol{\mathcal{H}}}{\mu_0} + \boldsymbol{\mathcal{M}}, \tag{B.13}$$

where $\boldsymbol{\mathcal{P}}$ is the polarization vector and $\boldsymbol{\mathcal{M}}$ is the magnetization vector. In vacuum, $\boldsymbol{\mathcal{P}} = 0$ and $\boldsymbol{\mathcal{M}} = 0$. Unless otherwise noted, we assume matter is nondispersive, linear, isotropic $\boldsymbol{\mathcal{P}} = \epsilon_0 \chi_e \boldsymbol{\mathcal{E}}$ and $\boldsymbol{\mathcal{M}} = \epsilon_0 \chi_m \boldsymbol{\mathcal{H}}$, also known as simple media. In special cases, we allow for matter to be dispersive, linear and isotropic; here, $\boldsymbol{\mathcal{D}}$ and $\boldsymbol{\mathcal{B}}$ depend on time derivatives if all orders of $\boldsymbol{\mathcal{E}}$ and $\boldsymbol{\mathcal{H}}$. In summary,

Vacuum	$\boldsymbol{\mathcal{D}} = \epsilon_0 \boldsymbol{\mathcal{E}}$	$\boldsymbol{\mathcal{B}} = \mu_0 \boldsymbol{\mathcal{H}}$
Simple	$\boldsymbol{\mathcal{D}} = \epsilon_0(1+\chi_e)\boldsymbol{\mathcal{E}} = \epsilon_0\epsilon_r\boldsymbol{\mathcal{E}}$	$\boldsymbol{\mathcal{B}} = \mu_0(1+\chi_m)\boldsymbol{\mathcal{H}} = \mu_0\mu_r\boldsymbol{\mathcal{H}}$
Dispersive	$\boldsymbol{\mathcal{D}} = \epsilon\boldsymbol{\mathcal{E}} + \epsilon_1\frac{\partial \boldsymbol{\mathcal{E}}}{\partial t} + \epsilon_2\frac{\partial^2 \boldsymbol{\mathcal{E}}}{\partial t^2} + \cdots$	$\boldsymbol{\mathcal{B}} = \mu\boldsymbol{\mathcal{H}} + \mu_1\frac{\partial \boldsymbol{\mathcal{H}}}{\partial t} + \mu_2\frac{\partial^2 \boldsymbol{\mathcal{H}}}{\partial t^2} + \cdots .$

(B.14)

For each medium the phasor relations

$$\mathbf{D} = \epsilon \mathbf{E} \qquad \mathbf{B} = \mu \mathbf{H}, \tag{B.15}$$

are true, except that ϵ and μ have different forms

Vacuum	$\epsilon = \epsilon_0$	$\mu = \mu_0$
Simple	$\epsilon = \epsilon_0(1+\chi_e) = \epsilon' + i\epsilon''$	$\mu = \mu_0(1+\chi_m) = \mu' + i\mu''$
Dispersive	$\epsilon = \epsilon'(\omega) + i\epsilon''(\omega)$	$\epsilon = \mu'(\omega) + i\mu''(\omega)$

(B.16)

.

In the case of complex ϵ and μ, we quantify the loss of the material by the electric and magnetic loss tangents;

$$\tan\delta_E = \frac{\omega\epsilon' + \sigma}{\omega\epsilon''} \quad \tan\delta_M = \frac{\mu'}{\mu''}, \tag{B.17}$$

where σ is the electrical conductivity of the medium. ϵ and μ are tensors for anisotropic media; they are real for lossless media.

B.4 Power Dissipation and Poynting's Theorem

Let us consider the volume density of conducting dissipation, $\boldsymbol{\mathcal{J}}(\mathbf{x},t)\cdot\boldsymbol{\mathcal{E}}(\mathbf{x},t)$. In terms of phasors, this product is

$$\begin{aligned}\boldsymbol{\mathcal{J}}(\mathbf{x},t)\cdot\boldsymbol{\mathcal{E}}(\mathbf{x},t) &= \frac{1}{4}\left[(\mathbf{J}(\mathbf{x})e^{i\omega t}+\mathbf{J}^*(\mathbf{x})e^{-i\omega t})(\mathbf{E}(\mathbf{x})e^{i\omega t}+\mathbf{E}^*(\mathbf{x})e^{-i\omega t})\right]\\ &= \frac{1}{2}\left[\frac{1}{2}\left(\mathbf{J}(\mathbf{x})\cdot\mathbf{E}(\mathbf{x})e^{2i\omega t}+\mathbf{J}^*(\mathbf{x})\cdot\mathbf{E}^*(\mathbf{x})e^{-2i\omega t}\right)+\frac{1}{2}\left(\mathbf{J}^*(\mathbf{x})\cdot\mathbf{E}(\mathbf{x})+\mathbf{J}(\mathbf{x})\cdot\mathbf{E}^*(\mathbf{x})\right)\right]\\ &= \frac{1}{2}\Re\left[\mathbf{J}(\mathbf{x})\cdot\mathbf{E}(\mathbf{x})e^{2i\omega t}+\mathbf{J}^*(\mathbf{x})\cdot\mathbf{E}(\mathbf{x})\right].\end{aligned} \tag{B.18}$$

The time-average conducting power dissipation or Joule power loss is

$$\begin{aligned}\overline{P} &= \left\langle \iiint_V \boldsymbol{\mathcal{J}}(\mathbf{x},t)\cdot\boldsymbol{\mathcal{E}}(\mathbf{x},t)d\mathbf{x}\right\rangle_t\\ &= \frac{1}{T}\int_T\left[\iiint_V \boldsymbol{\mathcal{J}}(\mathbf{x},t)\cdot\boldsymbol{\mathcal{E}}(\mathbf{x},t)d\mathbf{x}\right]dt\\ &= \frac{1}{2}\Re\left[\iiint_V \mathbf{J}^*(\mathbf{x})\cdot\mathbf{E}(\mathbf{x})d\mathbf{x}\right]\end{aligned} \tag{B.19}$$

where, the period $T = {}^{2\pi}/_{\omega}$. The term $\mathbf{J}(\mathbf{x})\cdot\mathbf{E}(\mathbf{x})e^{2i\omega t}$ conveniently vanishes in the time average. The complex time-average power dissipation, ${}^1/_2\int_V \mathbf{J}^*\cdot\mathbf{E}d\mathbf{x}$, additionally includes power stored in the fields and is also of interest for certain applications. If, we are concerned with a two terminal, linear, passive electromagnetic system, then $\mathbf{J}^*(\mathbf{x})d\mathbf{x} = I^*\hat{\ell}d\ell$ and the time-average power is

$$\overline{P} = \frac{1}{2}\Re\left[I^*\int\hat{\ell}\cdot\mathbf{E}(\ell)d\ell\right] = \frac{1}{2}\Re\left[I^*V\right]. \tag{B.20}$$

Note that $\overline{P} = {}^{I^*V}/_2$ (that is, without the $\Re$) is the complex time-average power. It includes reactive power terms.

The quantity, $\boldsymbol{\mathcal{S}}(\mathbf{x},t) = \boldsymbol{\mathcal{E}}(\mathbf{x},t)\times\boldsymbol{\mathcal{H}}(\mathbf{x},t)$ is defined at the Poynting vector. It is an instantaneous power density with units of $\mathrm{W\,m^{-2}}$ and it describes the magnitude and direction of the power flow per unit area at any point in space. Its relationship with the power dissipation, Equation B.19, and energy stored in the field can be illustrated by considering the vector identity,

$$\begin{aligned}\nabla\cdot(\boldsymbol{\mathcal{E}}(\mathbf{x},t)\times\boldsymbol{\mathcal{H}}(\mathbf{x},t)) &= \boldsymbol{\mathcal{H}}(\mathbf{x},t)\cdot(\nabla\times\boldsymbol{\mathcal{E}}(\mathbf{x},t))-\boldsymbol{\mathcal{E}}(\mathbf{x},t)\cdot(\nabla\times\boldsymbol{\mathcal{H}}(\mathbf{x},t))\\ &= -\boldsymbol{\mathcal{H}}(\mathbf{x},t)\cdot\left(\frac{\partial\boldsymbol{\mathcal{B}}(\mathbf{x},t)}{\partial t}\right)-\boldsymbol{\mathcal{E}}(\mathbf{x},t)\cdot\left(\frac{\partial\boldsymbol{\mathcal{D}}(\mathbf{x},t)}{\partial t}+\boldsymbol{\mathcal{J}}(\mathbf{x},t)\right)\\ &= -\frac{\partial}{\partial t}\frac{\boldsymbol{\mathcal{H}}(\mathbf{x},t)\cdot\boldsymbol{\mathcal{B}}(\mathbf{x},t)}{2}-\frac{\partial}{\partial t}\frac{\boldsymbol{\mathcal{E}}(\mathbf{x},t)\cdot\boldsymbol{\mathcal{D}}(\mathbf{x},t)}{2}-\boldsymbol{\mathcal{E}}(\mathbf{x},t)\cdot\boldsymbol{\mathcal{J}}(\mathbf{x},t).\end{aligned} \tag{B.21}$$

Here we have used Faraday's law and Ampere's law to eliminate the curls. We have assumed that the medium is linear, non-dissipative (e.g. constant ϵ, $\mu \in \mathbb{C}^{3\times3}$) and either isotropic or anisotropic so that,

$$\begin{aligned}\frac{\partial}{\partial t}\frac{\boldsymbol{\mathcal{E}}\cdot\boldsymbol{\mathcal{D}}}{2} &= \frac{1}{2}\frac{\partial}{\partial t}\boldsymbol{\mathcal{E}}\cdot\boldsymbol{\mu}\cdot\boldsymbol{\mathcal{E}} \\ &= \frac{1}{2}\boldsymbol{\mathcal{E}}\cdot\frac{\partial\left(\boldsymbol{\mu}\cdot\boldsymbol{\mathcal{E}}\right)}{\partial t} + \frac{1}{2}\frac{\partial\boldsymbol{\mathcal{E}}}{\partial t}\cdot\left(\boldsymbol{\mu}\cdot\boldsymbol{\mathcal{E}}\right) \\ &= \boldsymbol{\mathcal{E}}\cdot\frac{\partial\boldsymbol{\mathcal{D}}}{\partial t} = \boldsymbol{\mathcal{D}}\cdot\frac{\partial\boldsymbol{\mathcal{E}}}{\partial t},\end{aligned} \tag{B.22}$$

and similarly for $\boldsymbol{\mathcal{H}}$ and $\boldsymbol{\mathcal{B}}$ This allows us the pull out the volume energy densities,

$$\mathcal{W}_m = \frac{1}{2}\boldsymbol{\mathcal{H}}\cdot\boldsymbol{\mathcal{B}} \qquad \mathcal{W}_m = \frac{1}{2}\boldsymbol{\mathcal{E}}\cdot\boldsymbol{\mathcal{D}}. \tag{B.23}$$

Finally we can use Stoke's theorem to present Equation B.21 in terms of the Poynting theorem,

$$\begin{aligned}-\oiint_{\partial V}\boldsymbol{\mathcal{E}}(\mathbf{x},t)\times\boldsymbol{\mathcal{H}}(\mathbf{x},t)d^2x &= \iiint_V \boldsymbol{\mathcal{E}}(\mathbf{x},t)\cdot\boldsymbol{\mathcal{J}}(\mathbf{x},t) + \left[\frac{\partial}{\partial t}\frac{\boldsymbol{\mathcal{H}}(\mathbf{x},t)\cdot\boldsymbol{\mathcal{B}}(\mathbf{x},t)}{2} + \frac{\partial}{\partial t}\frac{\boldsymbol{\mathcal{E}}(\mathbf{x},t)\cdot\boldsymbol{\mathcal{D}}(\mathbf{x},t)}{2}\right]d^3x \\ &= \iiint_V \boldsymbol{\mathcal{E}}(\mathbf{x},t)\cdot\boldsymbol{\mathcal{J}}(\mathbf{x},t) + \left[\mathcal{W}_m(\mathbf{x},t) + \mathcal{W}_e(\mathbf{x},t)\right]d^3x\end{aligned} \tag{B.24}$$

The first line of Equation B.24 is generally true because it makes no assumptions about the medium. The second line assumes a linear and non-dissipative medium. On the left hand side, the Poynting vector describes the instantaneous power radiated through ∂V, the bounding surface of the volume V. On the right hand side, we have the instantaneous time rate of change of the energy stored in the electric and magnetic fields and the power dissipation related to the current, which may have conduction, bound and convection components. The quantities in Equation B.24 have not yet been time-averaged.

In terms of phasors, the complex Poynting vector is defined as $\frac{1}{2}\mathbf{S}(\mathbf{x}) = \mathbf{E}(\mathbf{x})\times\mathbf{H}^*(\mathbf{x})$. Just as before, this is already a time-average quantity. In analog to Equation B.21, the vector identity for phasors is

$$\begin{aligned}\nabla\cdot\left(\mathbf{E}(\mathbf{x})\times\mathbf{H}^*(\mathbf{x})\right) &= \mathbf{H}^*(\mathbf{x})\cdot\left(\nabla\times\mathbf{E}(\mathbf{x})\right) - \mathbf{E}(\mathbf{x})\cdot\left(\nabla\times\mathbf{H}^*(\mathbf{x})\right) \\ &= -i\omega\mathbf{H}^*(\mathbf{x})\cdot\mathbf{B}(\mathbf{x}) - \mathbf{E}(\mathbf{x})\cdot\left(-i\omega\mathbf{D}^*(\mathbf{x}) + \mathbf{J}^*(\mathbf{x})\right) \\ &= -i2\omega\left[\frac{1}{4}\mathbf{E}(\mathbf{x})\cdot\mathbf{D}^*(\mathbf{x}) - \frac{1}{4}\mathbf{H}^*(\mathbf{x})\cdot\mathbf{B}(\mathbf{x})\right] - \mathbf{E}(\mathbf{x})\cdot\mathbf{J}^*(\mathbf{x}) \\ &= -i2\omega\left[W_e(\mathbf{x}) - W_e(\mathbf{x})\right] - \mathbf{E}(\mathbf{x})\cdot\mathbf{J}^*(\mathbf{x}).\end{aligned} \tag{B.25}$$

Here we assumed a linear and non-dissipative medium which allows us to substitute in the time-average electric and magnetic energy densities,

$$W_m = \frac{1}{4}\mathbf{H}^*\cdot\mathbf{B} \qquad W_m = \frac{1}{4}\mathbf{E}\cdot\mathbf{D}^*. \tag{B.26}$$

Thus, in terms of phasors, Poynting's theorem is,

$$-\oiint_{\partial V} \mathbf{E}(\mathbf{x}) \times \mathbf{H}^*(\mathbf{x}) d^2x = \iiint_V \mathbf{E}(\mathbf{x}) \cdot \mathbf{J}^*(\mathbf{x}) + [W_m(\mathbf{x}) - W_e(\mathbf{x})]\, d^3x. \tag{B.27}$$

Depending on the properties of media the surface ∂V, each of the terms in Equation B.27 may have real and complex components. The real part of Equation B.27 is the time-average rate of doing work on the sources in V. If we allowed two terminals to protrude from ∂V, then

B.5 Time-averaged quantities

For energies and powers where voltages and currents are squared, we can talk about time-averaged or instantaneous quantities. Instantaneous power is

$$P = i(z,t) \cdot v(z,t) = \Re[V(z)I^*(z)e^{2i\omega t - \phi_I + \phi_V}] = \Re[V(z)I^*(z)] \cos(2\omega t - \phi_I + \phi_V), \tag{B.28}$$

and it is real. The complex conjugate of the current comes from the using the Poynting vector, $S = E \times H^*$, to define the power flow. For time-average power we have $P = \Re[V(z)I^*(z)] \left\langle \cos(2\omega t - \phi_I + \phi_V) \right\rangle = \frac{1}{2}\Re[V(z)I^*(z)]$. We can also speak about time-average complex power, $P = \frac{1}{2}V(z)I^*(z)$. Energies may also be time-averaged. For example the instantaneous energy stored in a distributed capacitor is $E = \frac{1}{2}\mathcal{C}\int v^2(z,t)dz = \frac{1}{2}\mathcal{C}\int |V(z)|^2 \cos^2(\omega t)dz$. And the time average energy has an extra factor $\frac{1}{2}$,

$$E = \frac{1}{2}\mathcal{C}\int |V(z)|^2 \left\langle \cos^2(\omega t) \right\rangle dz = \frac{1}{4}\mathcal{C}\int |V(z)|^2 dz. \tag{B.29}$$

Appendix C

Thermal Conductivity Measurements

In this appendix, the experimental setup, analysis methods and post-analysis thermal conductivity results are presented for various materials. The setup, analysis methods and thermal conductivity data measured are presented in this appendix. These measurements are presented in in greater detail by Kellaris and Zobrist [95, 204] who worked with me on this research activity [5, 6]. Selected details about the materials measured are also given and parameter fit coefficients are given in the last section.

C.1 Setup

We carried out our experiments in a 75 µW helium dilution refrigerator. Figure C.1 shows an example set up for our thermal conductivity measurements. T_{base} is thermally connected to the mixing chamber of the fridge via copper interfaces and is assumed to be roughly constant throughout the experiment. The other end of the sample is thermally isolated in the fridge. Thus, any heat produced by the sample heater will flow directly through the sample toward the mixing chamber.

Heater We used a metal-film 20 kΩ resistor for the heater. While one end of the sample is assumed to be thermally insulated, the wiring to the heater provides a small parasitic heat load on the sample.[1] This heat load can be approximated after the experiment by computing the heat flowing through the sample with no heater voltage applied. To correct the thermal conductivity, we use the uncorrected thermal conductivity and the thermometer temperature difference to compute $P_{parasitic}$. We then can compute a corrected thermal conductivity. In the case of this setup, we typically measured the parasitic heat load to be less than 1 nW.

Thermometers The two sample temperatures were read out by Germanium thermistors and the base temperature was read out by a Ruthenium Oxide thermistor. All thermometer resistances were recorded using four wire measurements to minimize readout errors.

[1] In addition to the heater wiring, the thermometer wiring and, potentially, infrared radiation from warmer parts of the fridge also contribute to $P_{parasitic}$.

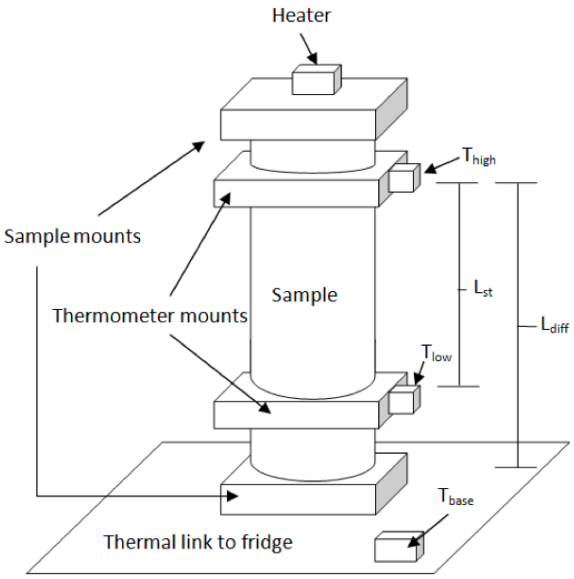


Figure C.1: This is a typical set up for our thermal conductivity measurement. This apparatus is placed inside of a 75 µW helium dilution refrigerator.

The resistances were then transformed into temperatures via a calibration curve provided by Lakeshore.

Thermometer Mounts The thermometer mounts are made of OFHC copper and attache to the sample by means of screw fasteners. They are designed to contact the sample over a narrow interval of temperature to avoid shorting out the heat flow. The are separated from the sample mounts, which add and remove heat from the sample, to avoid boundary resistance errors.

Sample Mounts The sample mounts are made of OFHC copper and are designed to spread the heat from the sample and the heater evenly over the surface of the thermal link to fridge and the warm end of the sample, respectively. The warm and cold end of the sample are glued into the sample mounts using Hardman Double-Bubble Orange (high viscosity, MFG P/N# 04007) or Stycast 1266 (low viscosity) epoxy, depending on the level of viscosity desired. The sample mounts ensures a uniform temperature boundary condition, and provide attachment points to the cryostat and the heater.

Sample Cleaning After machining the materials into the desired sample shapes, they are clean to remove grease and free particles (especially for the case of graphite). The materials are first sonicated in a dilute mix of water and Branson ultrasonic cleaning solution. Then they are sonicated in acetone, then isopropanol, then methanol and finally in deionized water. The epoxies used in the samples can be softened or attacked by the alcohols and should not come into contact with them.

C.2 Thermal Conductivity Analysis Methods

Three distinct analysis techniques were used to ensure the errors caused by the approximations were small. Each technique has different benefits in different temperature ranges. We will be using both the differential and integral definition of thermal conductivity for linear heat flow given below.

$$\begin{aligned} P = P_{heater} + P_{parasitic} &= -A \cdot \kappa(T)\frac{dT}{dx} \\ &= \frac{A}{l}\int_{T_{low}}^{T_{high}} \kappa(T)dT. \end{aligned} \tag{C.1}$$

$P_{parasitic}$ is the heat flowing through the sample not due to the heater. It is usually small but at low heater powers it can be important.

C.2.1 Method 1

This method approximates Equation C.1 by replacing $\frac{dT}{dx}$ with $\frac{\Delta T}{\Delta x}$ and T with $\bar{T} = \frac{T_{high}+T_{low}}{2}$. Equation C.1 then gives the approximate expression

$$\kappa(\bar{T}) = \frac{P \cdot L_{st}}{A(T_{high} - T_{low})}. \tag{C.2}$$

Hust shows that this method insensitive to the size of ΔT when the thermal conductivity is linear [86]. For higher order thermal conductivities, however, care must be taken to achieve a small temperature gradient. This method works well as long as $\kappa(T)$ does not vary sharply with temperature. Additionally, at low temperatures and powers, $P_{parasitic}$ can not be ignored and can lead to large errors.

C.2.2 Method 2

This method is adapted from Didschuns [51] and is intended to eliminate $P_{parasitic}$ from the equation defining $\kappa(T)$. We use two different heater powers with two corresponding equilibrium temperatures to find the thermal conductivity. We also must assume that the base temperature of the fridge is constant between two measurements. Considering the cooling power of our fridge, we did not have this problem.

Subtracting the two powers and using the integral definition of steady state heat flow,

$$P_2 - P_1 = \left(\frac{A}{L_{diff}}\int_{T_{base}}^{T_2} \kappa(T)dT - P_{parasitic}\right) - \left(\frac{A}{L_{diff}}\int_{T_{base}}^{T_1} \kappa(T)dT - P_{parasitic}\right) \tag{C.3}$$

$$\Delta P = \frac{A}{L_{diff}}\int_{T_1}^{T_2} \kappa(T)dT \tag{C.4}$$

Again, assuming $\kappa(T)$ is roughly constant around $\bar{T}$, we can integrate and solve for $\kappa(\bar{T})$.

$$\kappa(\bar{T}) = \frac{\Delta P \cdot L_{diff}}{A(T_2 - T_1)} \tag{C.5}$$

This method has the advantage of eliminating the need to know $P_{parasitic}$. Additionally, it is much easier to create small temperature gradients over different powers than it is across the sample itself. However, boundary resistances between the sample and the base temperature can cause errors, so it is important to secure a good thermal link to the fridge.

C.2.3 Method 3

The parameter fit method is essentially a χ^2 fit to the data. We choose a parameterized functional form of $\kappa(T)$ and vary those parameters until the following expression is minimized.

$$\Delta = \sum_{i=1}^{N} \left(\frac{P_{total_i} - P_{fit_i}}{\sigma_{P_i}} \right)^2 \tag{C.6}$$

This computation is done with N data points where $P_{total_i} = P_{heater_i} + P_{parasitic_i}$ is the heat flowing through the sample on each data point. σ_{P_i} is the measurement uncertainty and

$$P_{fit_i} = \frac{A}{L_{st}} \int_{T_{low_i}}^{T_{high_i}} \kappa(T) dT. \tag{C.7}$$

σ_{P_i} is determined from measurement of noise in our voltage readout and current sourcing electronics, as well as thermometer calibration uncertainties and estimates of the uncertainties our measurement of L_{diff} and L_{st}.

Because we parameterized $\kappa(T)$, P_{fit_i} can be calculated for each choice of parameters. After minimization, the result is a best fit functional form for the thermal conductivity. This method has the advantage of not being sensitive to the temperature gradient of each measurement. However, for small applied powers, $P_{parasitic}$ must still be taken into account. A full discussion of the errors in this method is discussed by Hust [86]. See Table C.1 for parameter fit coefficients.

C.2.4 Errors

All errors in the thermal conductivities obtained are between 6 and 15%, for all but the lowest temp data points, which have errors up to 20%. The conductivity plots have the 60% confidence level shaded.

C.3 Materials Measured

C.3.1 Polyimide Base Materials

Polyimides are generally inert to a broad range of chemical and environmental conditions. They are susceptible to alkaline attack, however. They exhibit relatively low moister uptake and relatively low outgassing. Polyimides, are not considered thermoplastics, have high softening temperatures, but do not melt or burn, which makes them attractive for applications at high temperature. They are formed in a condensation reaction an are available in uncured resin and solution forms.

C.3.1.1 Composite Bonding Films

Developed by Dupont, kapton is the trade name for polypyromellitimide film, which is a polyimide polymer. The film can be coated with temperature activated adhesives. The primary use for these kapton adhesive composite films is in the fabrication of flexible circuits where the kapton is used as the flexible dielectric substrate. In the terminology of the industry, a coverlay is the dielectric coated on one side with adhesive and a bondply is coated on both sides with adhesive. Sheet adhesives, with no dielectric are also available. The materials we present data on are kapton coverlay composites with acrylic adhesive (Pyralux LF) and epoxy adhesive (Nikaflex CISV). It should be noted that DuPont also makes a bondply with fluoropolymer adhesive called Pyralux TK, which has lower dielectric loss for high frequency and controlled impedance applications.

C.3.1.1.1 Pyralux LF DuPont Pyralux LF coverlay composites consist of a Dupont kapton polyimide film coated with coated on one side with proprietary B-stage acrylic adhesive. It is use to encapsulate etched layers of flexible and rigid flexible multilayer constructions for environmental and electrical insulation. The Pyralux measured is 0.001 inch thick adhesive on 0.001 inch thick kapton, product code LF0110. Two sheets of LF0110 were laminated together such that the acrylic adhesive of each sheet was adhered to the acrylic adhesive of the other (i.e. the stack-up is 0.001" kapton, then 0.001" adhesive, then 0.001" adhesive, then 0.001" kapton.) As recommended by Dupont, the lamination requires heating the part to 182–199 °C, applying pressure 200–400 psi for 1–2 h. The laminated construction was folded upon itself. The ends of the resulting fan was potted with epoxy in copper end caps, as shown in the inset of Figure C.2.

C.3.1.1.2 Nikaflex CISV Nikkan Industries' Nikaflex CISV-2525 is a 0.002 inch thick Kaptonepoxy coverlay used in making flexible circuits. The epoxy component of the coverlay is a 0.001 inch thick epoxy bonding sheetfrom Hanwhaflex (product code HFB-E250YG) in cured condition for this measurement. The Kapton component of the coverlay is a 0.001 inch thick sheet of Dupont Kapton 100V. The data presented in Figure C.3 is measured parallel to the face the coverlay.

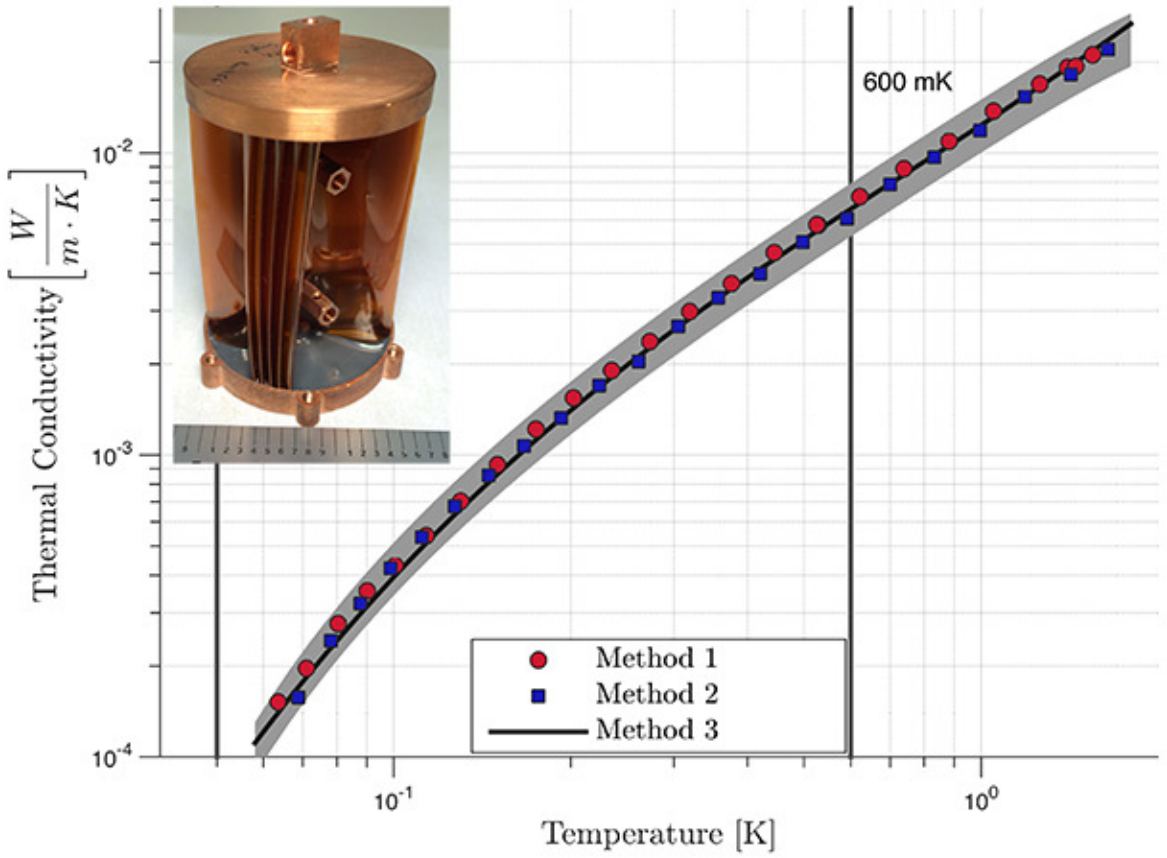


Figure C.2: Pyralux LF thermal conductivity.

C.3.1.2 Cirlex

Cirlex, is a thick composite material made entirely of polyimide kapton. It is used in a variety of applications dues to its temperature stability, chemical inertness, wear resistance, and good dielectric properties. It is of interest to our research as a relatively low radioactivity circuit board, flexible circuit stiffer, and thermal standoff material (e.g. its use as a detector crystal clamp material for the CDMS). Cirlex is a trademark of DuPont and used under license by Fralock who is the sole manufacturer of the material. The thermal conductivity data presented in Figure C.4 was acquired from 0.030 inch thick material purchased a decade ago from a company named TK Composites (product code 3000CL-HN). Fralock acquired the license from TK composites and says they have improved the material, so the thermal conductivity of Fralock cirlex may be different.

C.3.1.3 Vespel

Vespel is a bulk polyimide based polymer useful its of thermal stability (e.g. low thermal expansion), chemical and environmental inertness, creep resistance, strength and stiffness, ra-

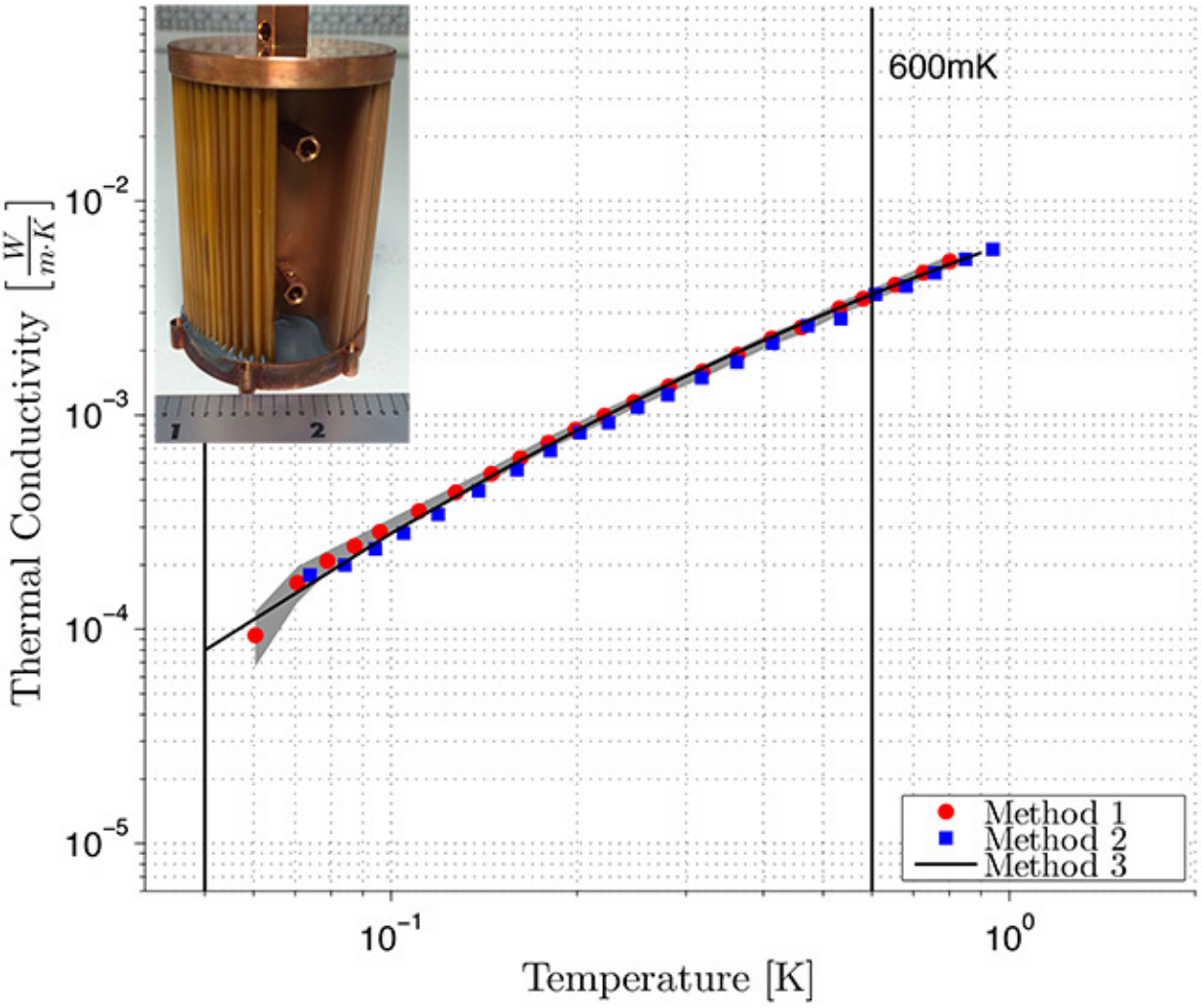


Figure C.3: Nikaflex CISV thermal conductivity.

diation resistance and low outgasing. Although other plastics surpass vespel in some of these areas, the combination of good performance in each area is the main advantage of vespel. Vespel is made in a sintering process (direct forming, hot compression molding, isostatic pressing) from polyimide powder. Filling agents, such as graphite, teflon and molybdenum disulfide may be added to the powder to obtain increased performance in certain application areas. Unfortunately, Vespel remains a relatively expensive performance plastic and its cost many times limits its use.

Four types of DuPont vespel polyimide were tested: SP-1, SP-22, SCP-5000, and SCP-5050. Data is presented for three of them. All were purchased from Curbell Plastics, certified as authentic DuPont vespel, and ∅0.5 inch rods.

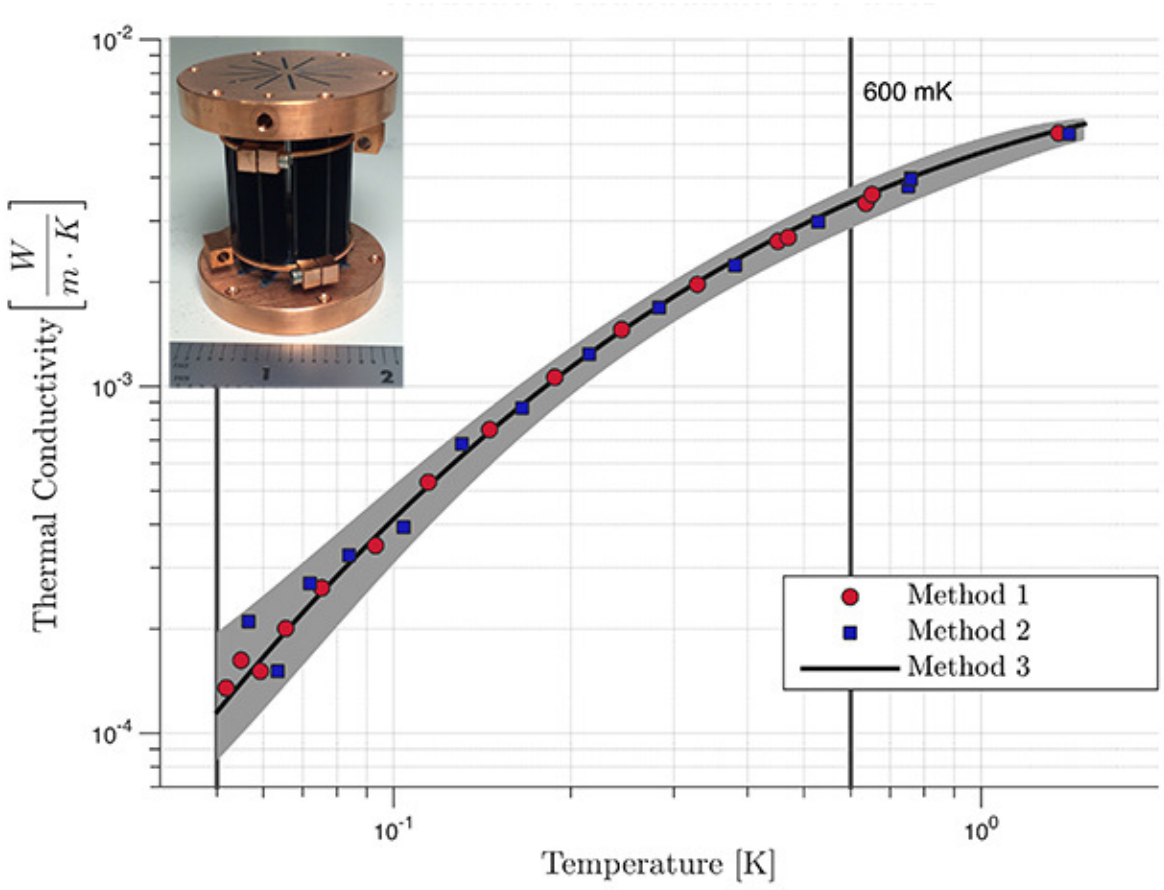


Figure C.4: Cirlex thermal conductivity

C.3.1.3.1 SP-22 The vespel SP product family was developed prior to the SCP family. SP-1 is the base, unfilled polyimide, product. SP-22, is the polyimide base (SP-1) filled with 40% graphite by weight. The SP-family has found wide use in low temperature instrumentation and the literature contains numerous measurements of its properties including its thermal conductivity. Our measurement of SP-22, Figure C.5, is meant to be a calibration benchmark for our thermal conductivity measurement and data analysis techniques. We obtain excellent agreement with literature values as can be seen in Figure 7.5.

C.3.1.3.2 SCP-5000 According to data from DuPont, the SCP family have superior mechanical properties over the SP series, especially in extreme temperature environments. SCP-5000 is unfilled material and marketed as better performing replacement for SP-1. Methods 1 and 3 thermal conductivity result are presented in Figure C.6. Method 2 data was discrepant, probably due to bad thermal connection to the fridge.

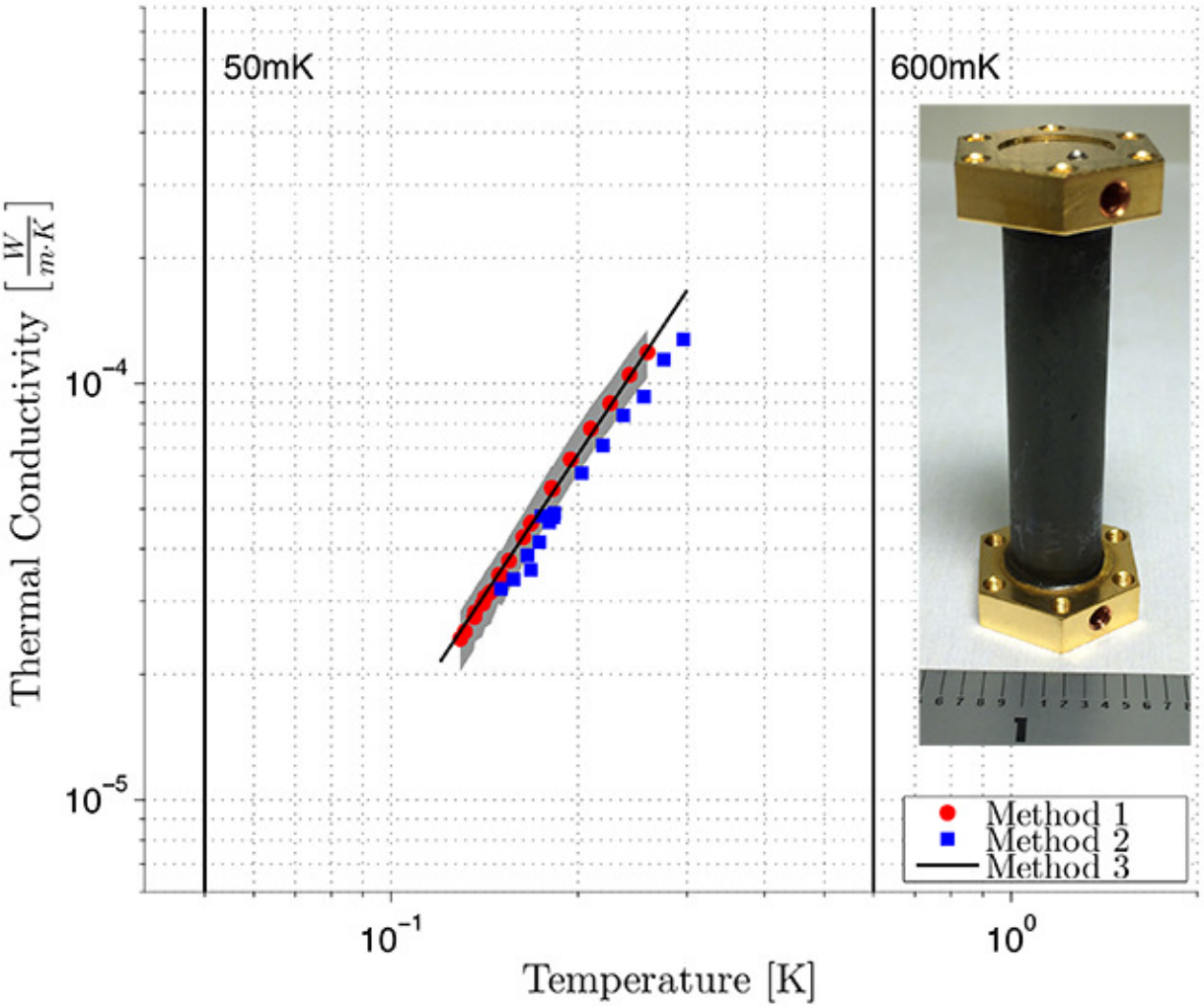


Figure C.5: Vespel SP-22 thermal conductivity.

C.3.1.3.3 SCP-5050 SCP-5050 has a proprietary filling. It is marketed as a higher performing alternative to SP-22, to which it is visually identical. It can be reasonably assumes that SCP-5050 contains a similar amount of graphite to SP-22. Results presented in Figure C.7

Two different samples, different thermometers, and different thermometer mounts were used in the two different SCP-5050 datasets. The data set for Figure C.8 used a shorter sample and thermometer mounts with narrower contact area to the sample than was used in the the data set of Figure C.7. The excellent agreement between the two sets is encouragement that our techniques are robust.

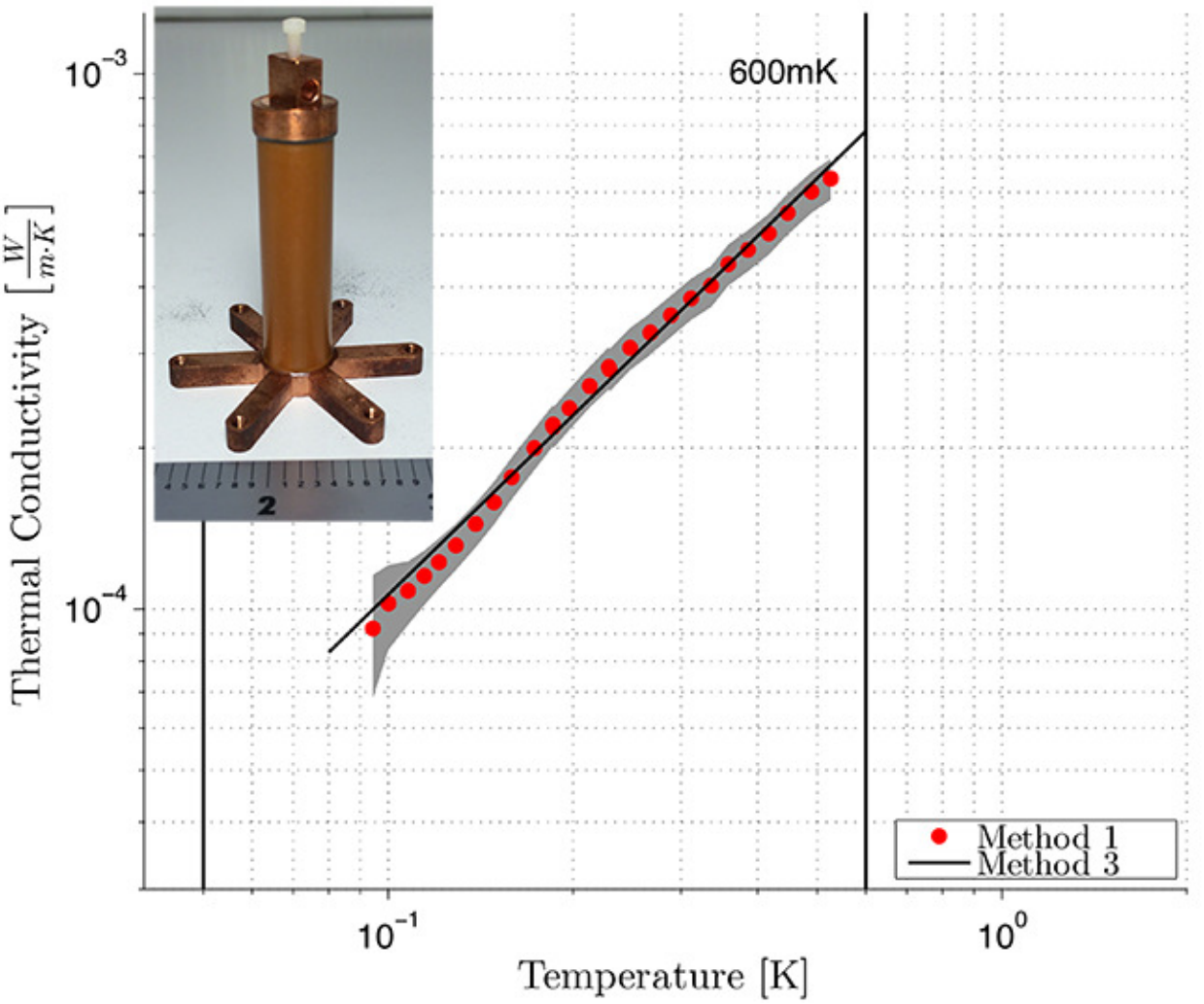


Figure C.6: Vespel SCP-5000 thermal conductivity.

C.3.2 Titanium Alloys

At standard temperature and pressure, titanium crystallizes into hexagonal-close-packed structure, but above a certain temperature it transforms to a body-centered-cubic structure. Titanium alloys in the body-centered-cubic structure, called β-phase alloys, offer the highest strength-to-weight ratio of all commercial titanium alloys, and high engineering ductility necessary for the fabrication of complex parts [17]. Unfortunately the titanium β-phase is naturally in equilibrium at temperatures much higher than room temperature. The temperature above which the β-phase is in equilibrium is called the beta transus. Below this temperature or upon cooling the β-phase decomposes to other phases. Titanium alloys in the hexagonal-close-packed, α-phase, structure are mechanically harder and stiffer than β alloys, which is usually an attractive quality for finished parts, but poses challenges for machining

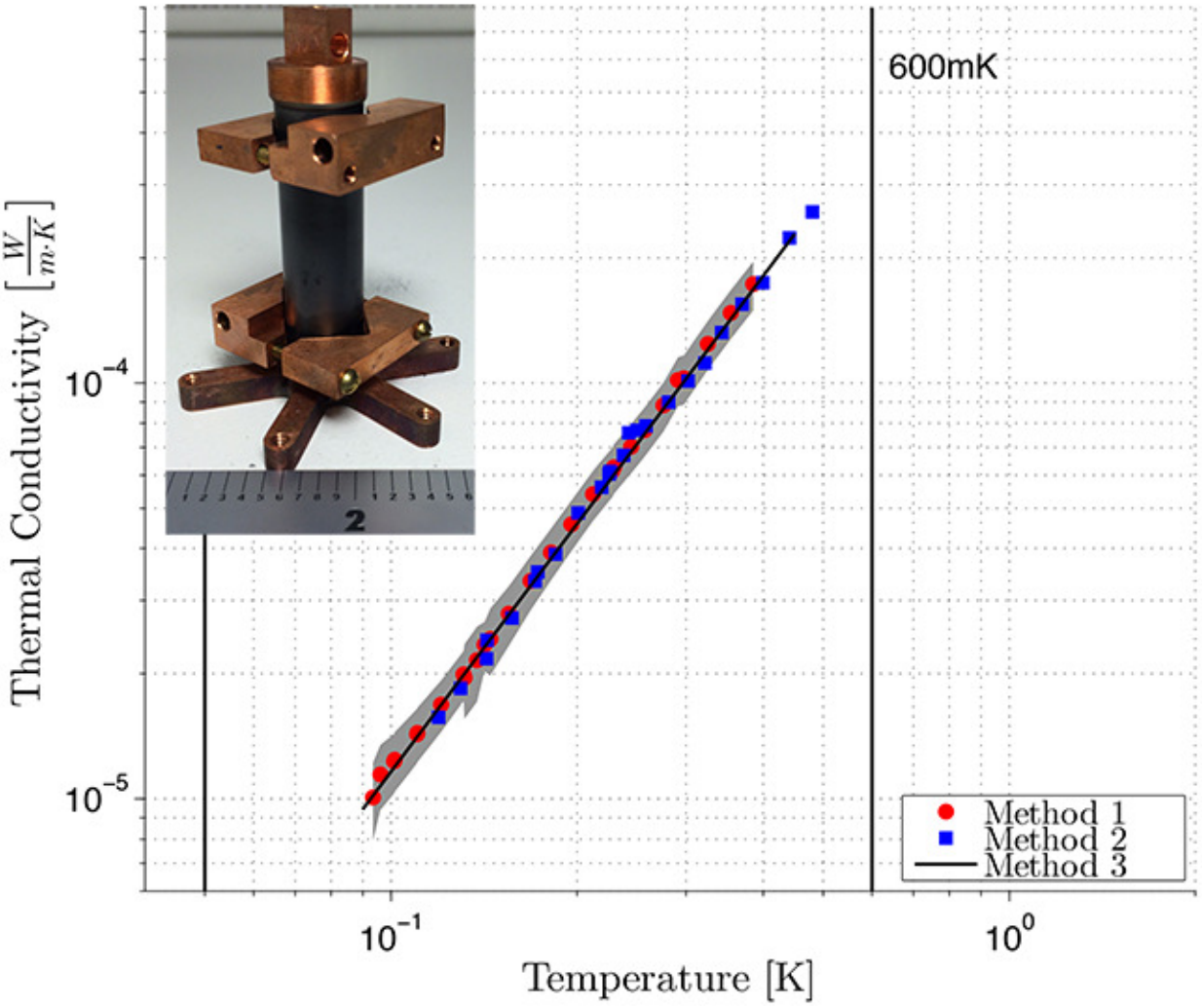


Figure C.7: Vespel SCP-5050 thermal conductivity.

those parts or producing wrought stock material (e.g. ducting, and paneling for aircrafts). The addition of certain elemental alloying constituents called beta-stabilizers can reduce the beta transus, Figure C.9. Molybdenum, niobium, vanadium, nickel and silicon are a few examples of beta stabilizers. With a sufficient concentration of the correct beta stabilizer, β_s, a titanium alloy can be made so that the β-phase is in equilibrium at room temperature. While this may be desirable for some applications, others would benefit from the presence of some α-phase to increase strength, and from larger strength-to-mass-density ratio afforded by a smaller beta stabilizer concentration [17]. Between zero and β_s, there is a critical beta stabilizer concentration β_c where the alloy can be cooled (either by water quench or air cool) from above to below the beta transus and retain 100% β-phase structure, in a region where β-phase and other phases are in equilibrium. Such alloys are called metastable β alloys.

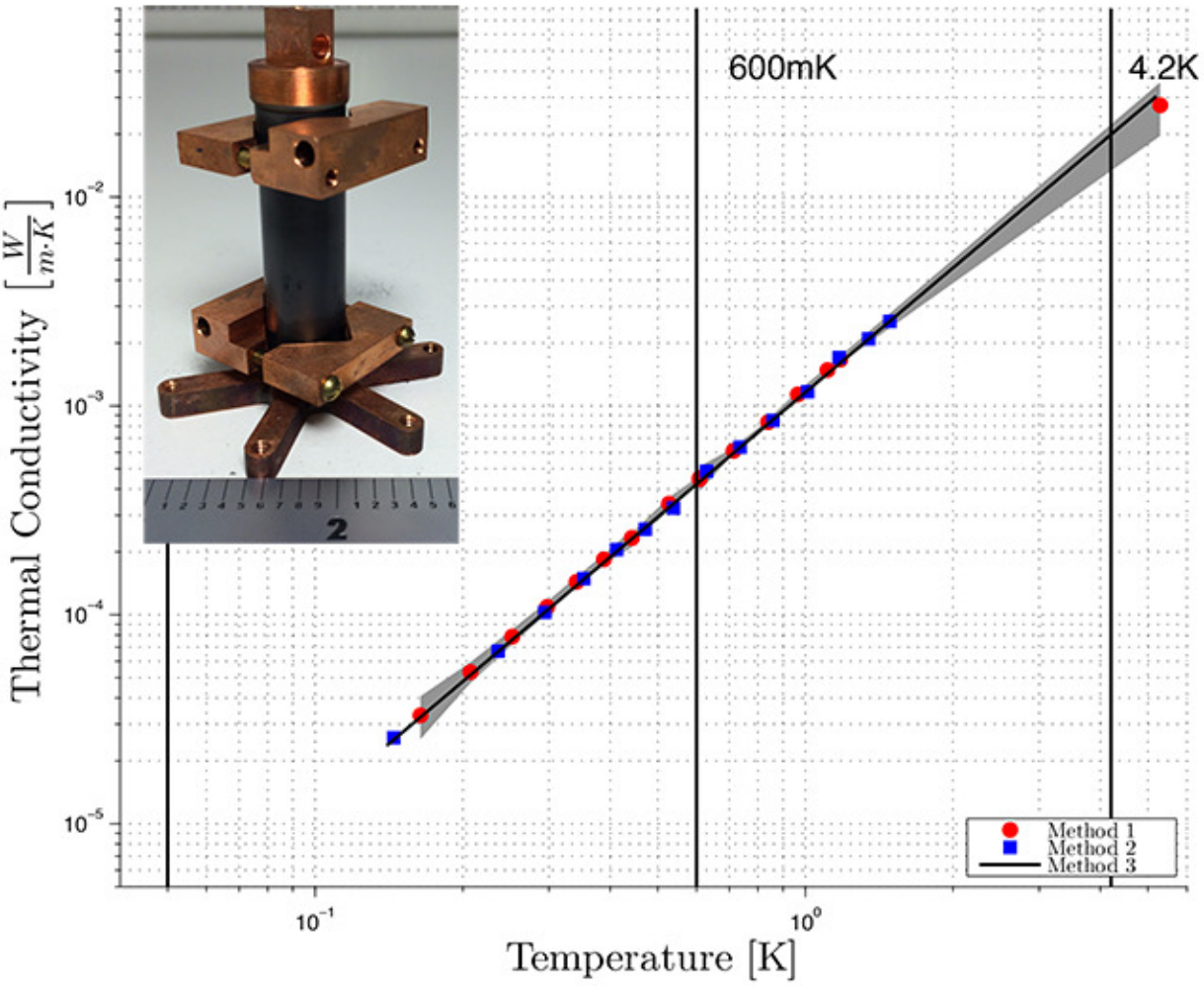


Figure C.8: Vespel SCP-5050 thermal conductivity. A second data set with extended temperature range.

These alloys will precipitate a second phase, α-phase, when they are subjects to elevated temperatures (below the beta transus) for various durations of time, which is called aging. α-phase can also precipitate due to mechanical stress. The α-phase precipitates around the grain boundaries, and it strengthens and hardens the material. Thus the process of aging is used to obtain certain mechanical properties and one can speak about age hardening parts.

C.3.2.1 Ti-15V-3Cr-3Sn-3Al Alloy

Titanium 15-3-3-3 is a strip-producible, cold formable, age hardenable and weldable metastable-β alloy. The vanadium is the chief beta stabilizing constituent for this alloy, and the aluminum suppresses the formation of an unwanted brittle ω-phase. The alloy was developed in the 1970s by Lockheed and the Titanium Metals Corporation (TIMET) on a Air Force

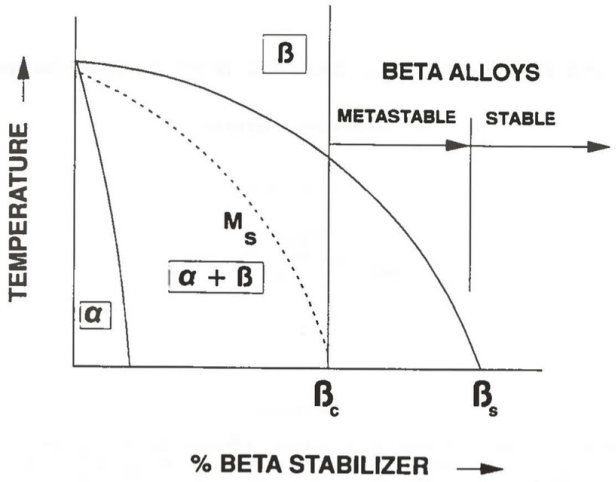


Figure C.9: The addition of beta stabilizing constituents suppress the beta transus of titanium alloys. For concentrations of beta stabilizing constituents, within a certain range, the alloys is metastable. Image from [22].

contract to lower the processing and fabrication costs associated with titanium sheet metal parts. TIMET continues to manufacture and sell this material primarily in strip form 0.016–0.094 inch thick; substantially thicker gauges are not available. Its high strength to weight ratio, due to its β-titanium structure and its relatively light alloying constituents, make it an attractive material for aerospace applications. Titanium 15-3-3-3 is heat treatable to ultimate tensile strengths of 130–190 kpsi (896–1310 MPa) and suitable for use at temperatures up to 288 °C [131, 60]. The β transus of Titanium 15-3-3-3 is 750–770 °C. The material is typically supplied in solution treated condition where it has been heated to 788–843 °C for 3–30 min and allowed to air cool. Age hardening is typically performed 480–620 °C for 4–16 h. Another attractive property of this material is that it becomes superconducting below (3.89 ± 0.01) K [192]. The data presented here shows that Titanium 15-3-3-3 has very low thermal conductivity in the sub-kelvin temperature range. These facts, in addition to the alloy's high modulus suggest low temperature mechanical support and electrical signal trace applications.

C.3.2.1.1 Plate The sample was manufactured by TIMET and it was in solution treated condition (i.e. 3–20 min in 790 °C solution, air cool) at the time of the thermal conductivity measurement. Thermal conductivity results presented in Figure C.10.

C.3.2.1.2 Foil The material was manufactured by TIMET and sold to Arnold Magnetic Technologies solution treated conduction (i.e., 3–20 min in 790 °C solution, air cool) in the form of 0.025 inch thick strip. Arnold Magnetic Technologies cold rolled the strip to a final thickness of 0.0008 inch, applying intermediate anneals as needed. The sample measured

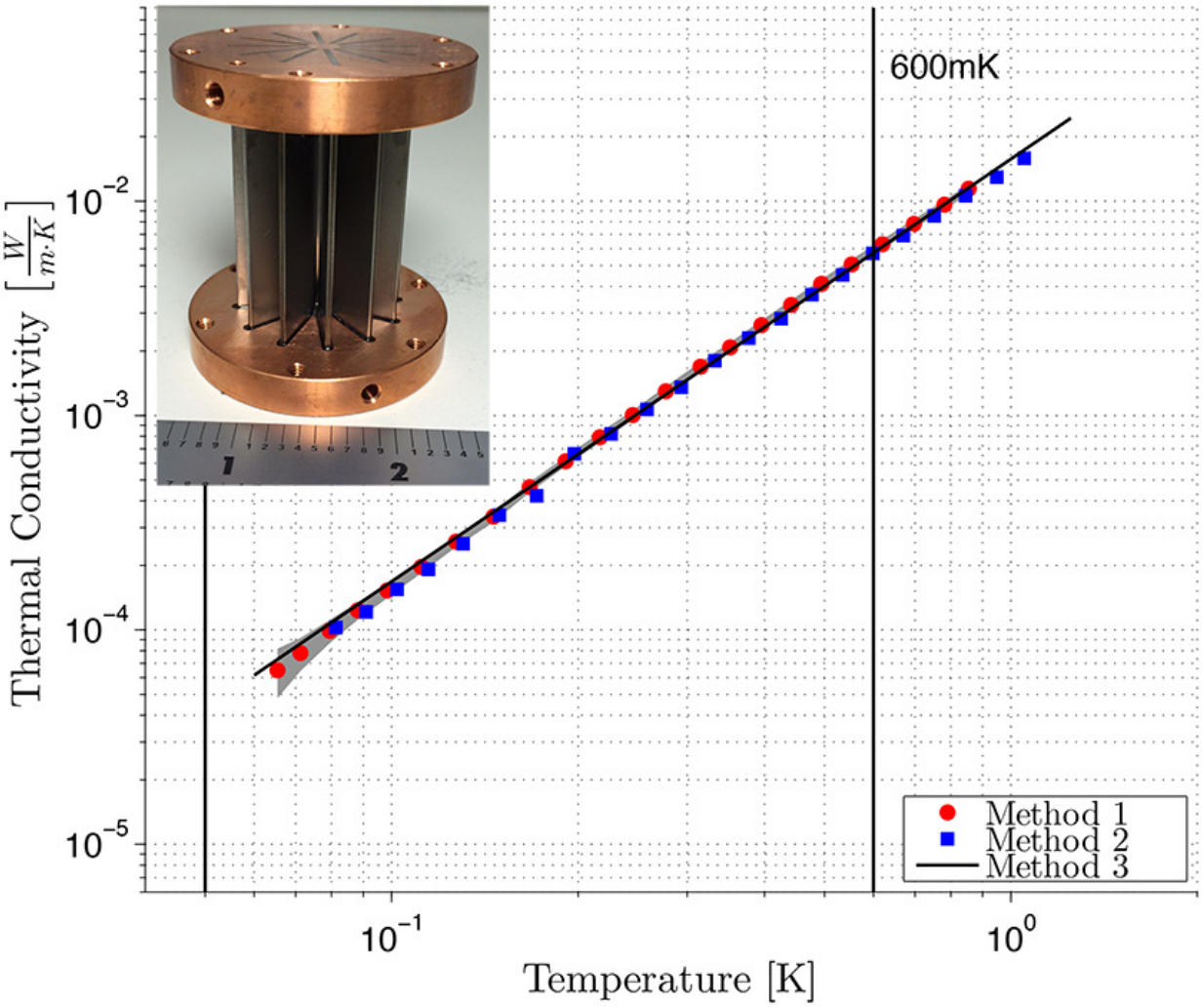


Figure C.10: Ti-15V-3Cr-3Sn-3Al plate thermal conductivity

was last anneal at a thickness of 0.001 inch, i.e. 20% cold reduction. In this condition it was measured to have a yield strength 151.5 kpsi at 2.9% elongation, and an ultimate tensile strength of 154.2 kpsi. Thermal conductivity results presented in Figure C.11.

C.3.2.1.3 Rod The sample was manufactured by ReTi Metal Company in China and it was supplied in full annealed, condition. The rod obtained was approximately ∅2 inch. It was EDM cut to a smaller diameter rod for the measurement and had a radial slit cut in it.

We believe that either a poor thermal connection between the fridge and the sample or insufficient cooling power of the fridge is the reason for the systematically lower than data points in Method 2 when compared to the other two methods. Either of these problems will result in the temperature of the cold end of the sample raising appreciable as we apply heat.

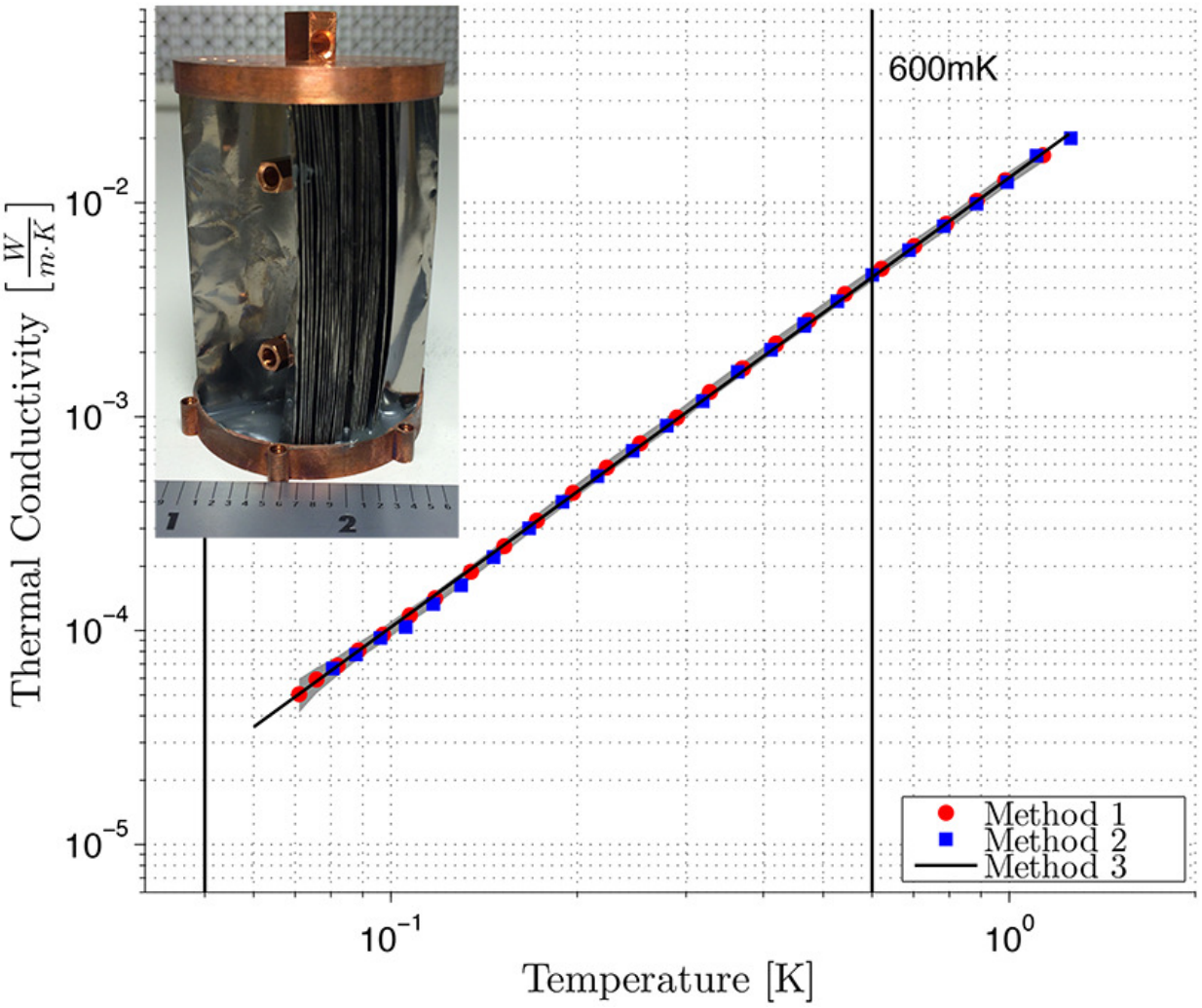


Figure C.11: Ti-15V-3Cr-3Sn-3Al foil thermal conductivity.

Method two assumes that the temperature of the cold end of the sample does not change as different amounts of heat are applied. If the cold end temperature rose as a result of increasing heat, then the thermal conductivity calculated would come out to be lower than the true value. Method 2 failed for this measurement in the same way it failed for SCP-5000 method. Ti 15-3-3-3 rod thermal conductivity results presented in Figure C.12

C.3.2.2 Ti 21S Alloy

The composition of Ti 21S is nominally Ti-15Mo-3Al-2.5Nb-0.25Si. Ti 21S is another strip producible metastable β-titanium alloy with excellent cold formability (e.g. machining and bending), and age hardenability. Molybdenum, instead of vanadium is chosen as the β stabilizer to give the alloy improved oxidation resistance. Alloy 21S was specifically designed for

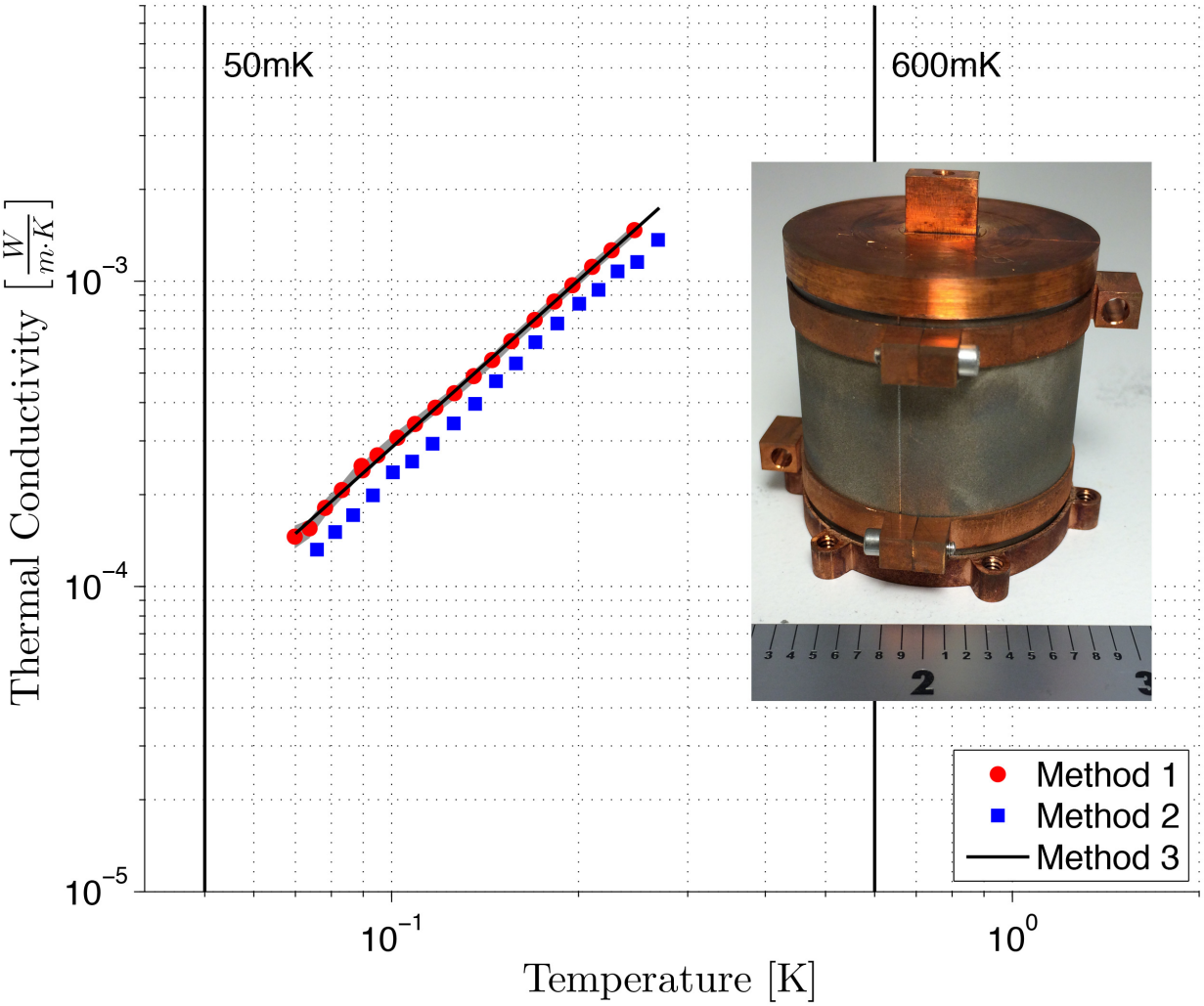


Figure C.12: Ti-15V-3Cr-3Sn-3Al rod thermal conductivity.

improved oxidation resistance, elevated temperature strength, creep resistance, and thermal stability [61, 131]. It can attain an ultimate tensile strength of 210 kpsi (1470 MPa) with better than 2% elongation and is suitable for use at temperatures up to 593 °C. Not surprisingly, its primary application is in the plug-and-nozzle assembly of jet engines where where it is exposed to hot exhaust gas.

C.3.2.2.1 Plate The sample was manufactured by TIMET and it was in solution treated and pickled condition at the time of the thermal conductivity measurement. The plate thickness was 0.09 inch. Thermal conductivity results presented in Figure C.13.

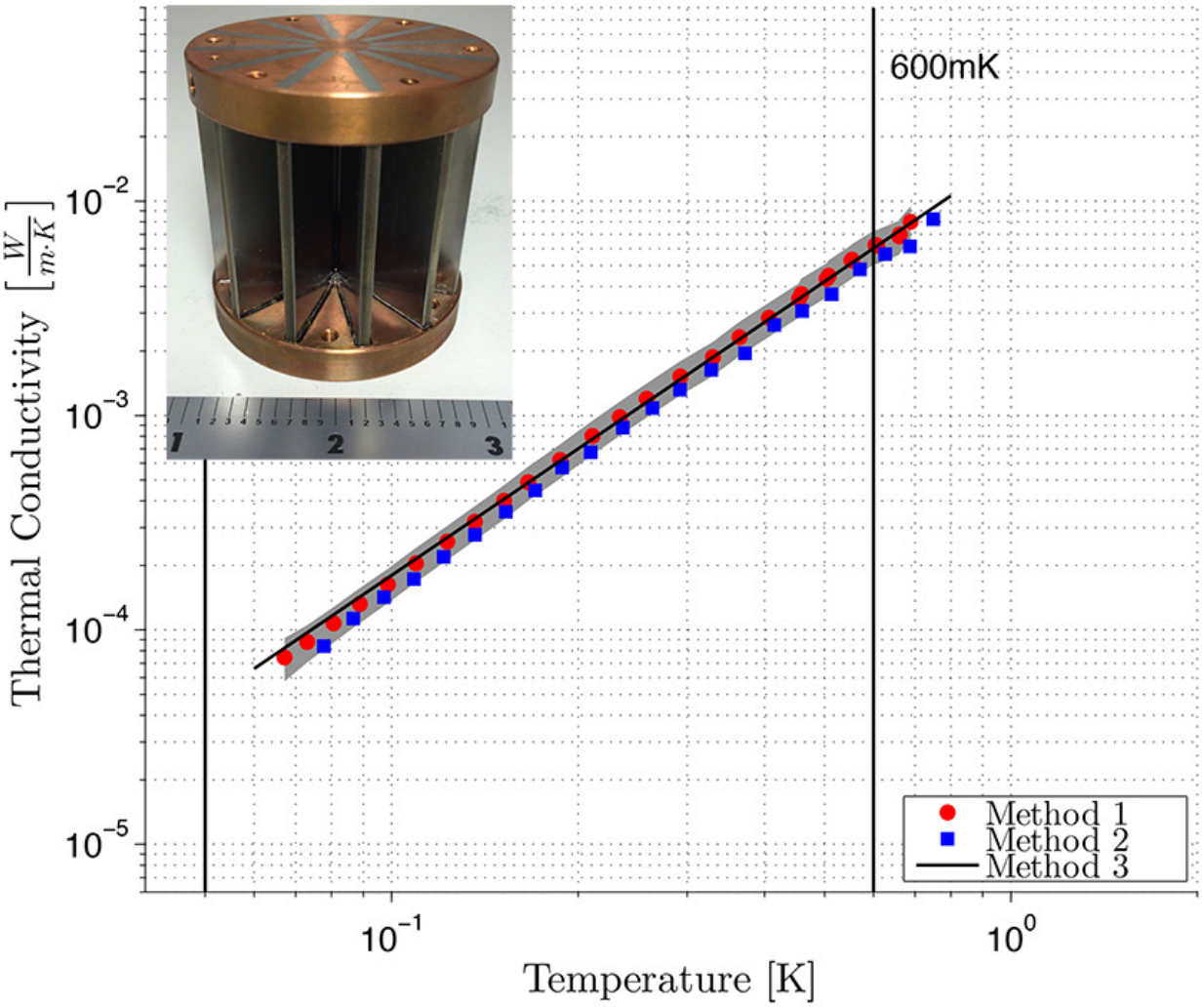


Figure C.13: Ti 21S plate thermal conductivity

C.3.2.3 Nb-47Ti Alloy

Niobium-titanium alloy is useful for its high upper and lower critical fields and relatively high superconducting transition temperature. The material can be readily be rolled or drawn in to fine wire due to its high ductility. Choice of the alloying percentage, mechanical work, and application of heat treatment are used to tune the critical fields, transition temperatures and mechanical properties. It is thought that mechanical work and heat treatment create crystal defects and precipitates, like α-phase titanium, which provide flux pinning sites that stabilize the transport current against vortex drift and thereby enhance the critical fields [45]. Typical heat treatment for the purpose of precipitation occurs in the range of 300–500 °C for 1–400 h. At higher temperatures precipitates are redissolve into the solid solution and defects disappear; the material is annealed.

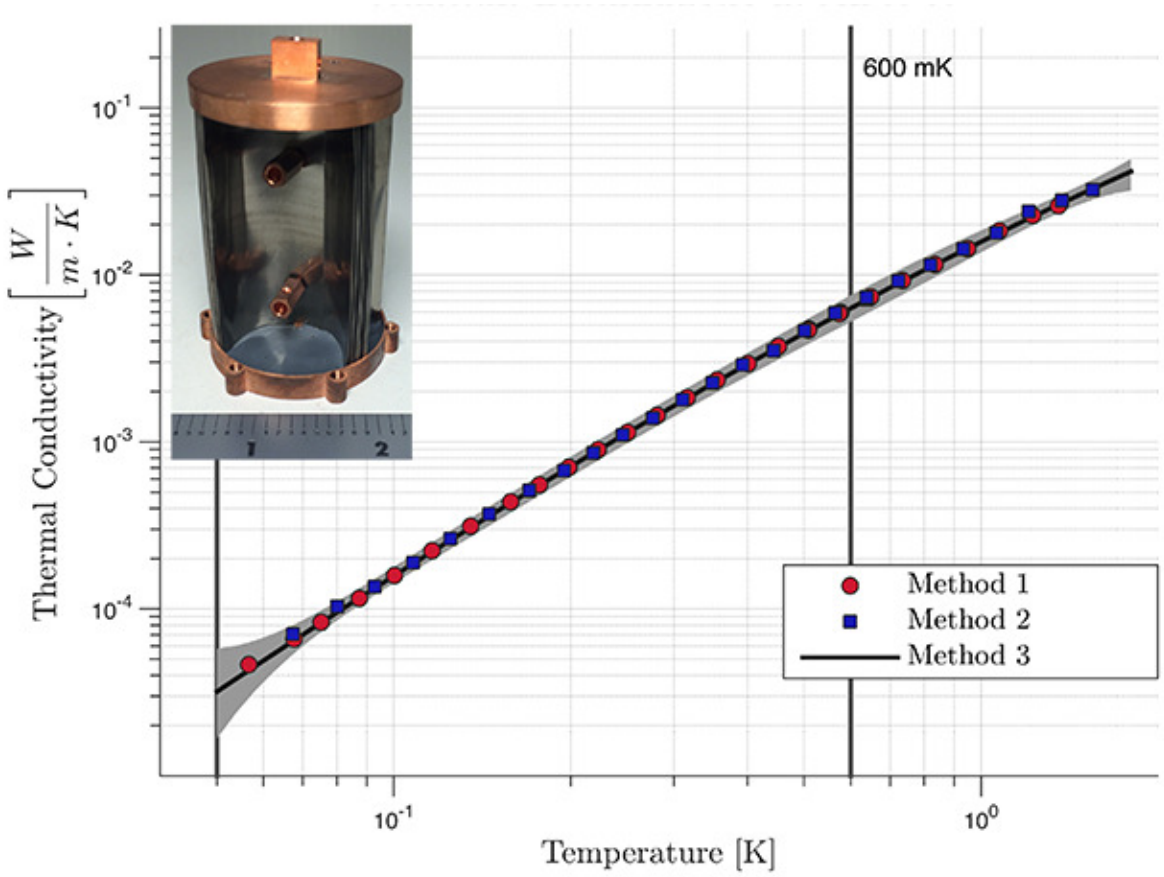


Figure C.14: Nb-47Ti foil thermal conductivity.

C.3.2.3.1 Foil The thermal conductivity data, Figure C.14, was measured from Nb-47Ti foil, approximately 0.0025 inch in thickness, manufactured by ATI Wah Chang Corporation. The foil was last annealed at a thickness of 0.01 inch at 800 °C for 30 min. Hence, the measurement specimen was at 76% cold roll. Based on its alloy composition, the foil should have a superconducting transition temperature of approximately 8.2 K and a density of $6.02\,\mathrm{g\,cm^{-3}}$.

C.3.2.4 Nitinol Alloy

Nitinol stands for nickel titanium, Navel Ordinance Laboratory where the shape memory properties of the alloy were discovered in 1962. Below a certain phase transition range the material is an weak Martensite phase and exhibits shape memory. Above the phase transformation range the material is in a stronger Austenite phase and exhibits superelastic characteristics. When materials in the shape memory Martensite phase are formed, they retain that shape until the material is heated to the Austenite phase where the shape reverts to the shape at its last anneal. Attempts to form the material in the superelastic Austenite phase are unsuccessful as the material immediately reverts to its shape at last anneal.

There are several temperatures associated with the Martensite-Austenite phase transformation which occurs over an temperature interval. Roughly, there is a start, finish and middle phase transformation temperature for the interval. The transformation interval is typically 40–70 °C wide. Furthermore, there is hysteresis between the Austenite to Martensite transformation that occurs upon cooling, and the Martensite to Austenite transformation that occurs upon warming. The middle temperature for each interval can vary from 20–50 °C depending on the alloy and the heat and mechanical treatment it has received. The hysteresis can be decreased by doping the alloy composition. The transformation upon cooling occurs lower than the transition upon warming.

Nitinol alloys are approximately 50% - 51% atomic (55% - 56% weight) nickel, with the balance being titanium, and may be doped with other metals like chromium and niobium to tune transformation temperatures. Because the transition temperatures are very sensitive to the alloy composition and other conditioning, the transformation temperatures in the material's final thermomechanical condition are called out. For example, the transformation temperatures of the ingot material are different from those of the final worked and heat treated stock.

C.3.2.4.1 Plate The thermal conductivity data presented here are from a flat annealed nitinol plate sample, 55.7Ni-43.89Ti in composition by weight. The material is certified to have an active Austenite finish temperature, A_f, of 6.8 °C (the transformation finish temperature for the warming direction), and an ingot Austenite mid-transformation temperature, A_p, of −8 °C (the transformation point temperature for the warming direction). It has an ultimate tensile strength of 198 kpsi. Based on the above, we can assume that the nitinol is in the Martensite phase during the thermal conductivity measurement and in the Austenite phase at room temperature. Generally, nitinol alloys are superelastic at temperatures up to about 50 °C above A_f. So the material studied is superelastic at room temperature. One can imagine cryogenic applications for this material that take advantage of its shape memory properties at low temperature, starting either from the shape memory or superelastic state at room temperature. Thermal conductivity results presented in Figure C.15

Another series of alloys consisting of 68–80% copper and 32–20% zinc and aluminum are reported to be cheaper to produce and, machine and fabricate than Nitinol [129]. This series, and Nitinol are most widely used in industry.

C.3.3 Graphites

C.3.3.1 Mersen 2020 Graphite, ⊥ to grain

This is an anisotropic nuclear grade graphite with a porosity of 9%. In Figure C.16 we present the thermal conductivity perpendicular to the grain structure. The grains are about 15 µm in size. We find that the thermal conductivity is about the same as POCO AXM-5Q graphite and comparable to nuclear grade graphites [95, 195]. It is possible to have have this (and other types of) graphite purified. Purification involves placing the graphite in an

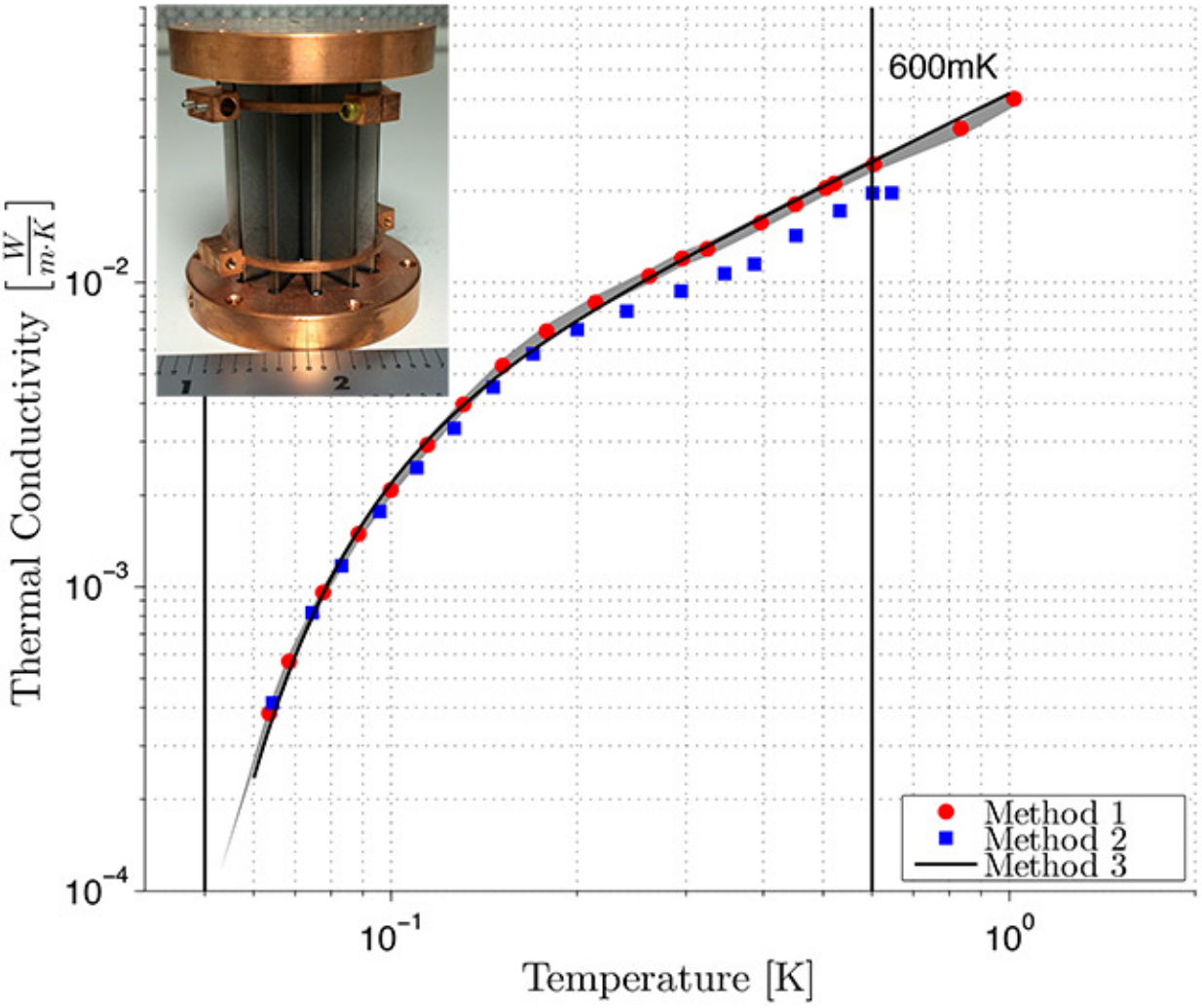


Figure C.15: Thermal conductivity of Nitinol alloy. Specimen in plate form and superelastic at room temperature.

atmosphere of chlorine gas pressurized above 15 psi and heated to approximately 2000 °C. The chlorine permeates the graphite and forms volatiles with impurities, allowing them to be pumped away. This process works even with bulk samples, e.g. impurities in our graphite were reduced from 1000 ppm to <1.4 ppm for 4 inch cube samples by this process.

C.3.3.2 Mersen 2020 Graphite, ∥ to grain

In Figure C.17, we present the thermal conductivity parallel to the grain structure. This sample and the sample measured in Figure C.16 come from the same billet and were cut and aligned so that heat would flow parallel and perpendicular to the grains, respectively.

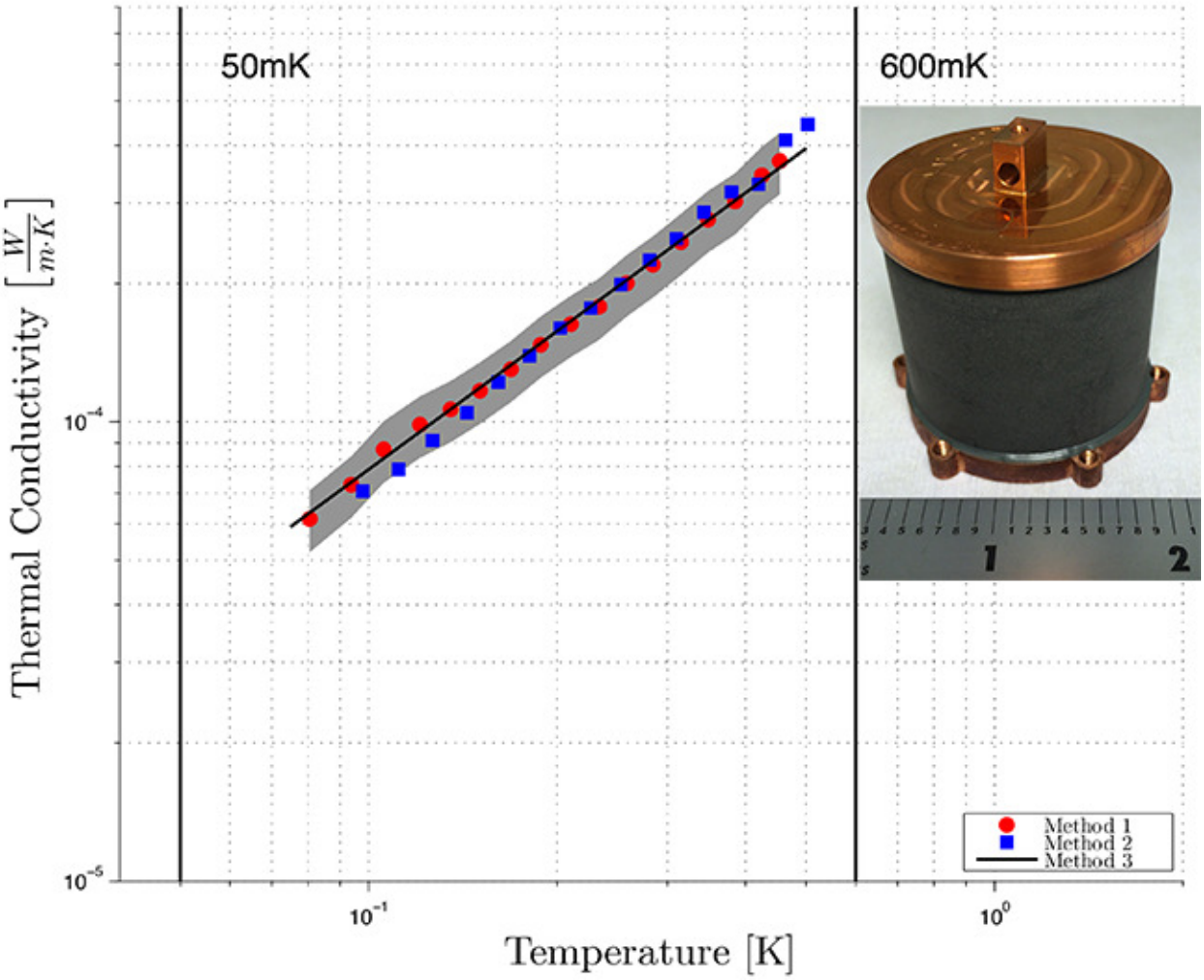


Figure C.16: Mersen 2020 Graphite thermal conductivity. Heat is directed perpendicular to grain.

C.3.4 Graphlite CFRP

Most of the carbon fiber in the world comes from two companies, Toho Tenax and Toray. The manufacturing process uses a specialized grade of acrylic fiber, called PAN (PolyAcryloNitrile), as the precursor material to make the carbon fiber. This is a variety of the acrylic one encounters in garments and processing using traditional technologies acrylic textile fiber manufacturing. Another type of carbon fiber is made from petroleum pitch or coal pitch in stead of PAN. Either process involves a carbonization step where the fibers are exposed to high heat (somewhere around 1800 °C), and this is followed by a graphization process at even higher temperature (somewhere around 3000 °C) for certain fiber grades. Bundles ranging from 1000 to 30 000 carbon fibers called "tow" are sold on spools for use in CFPR products.

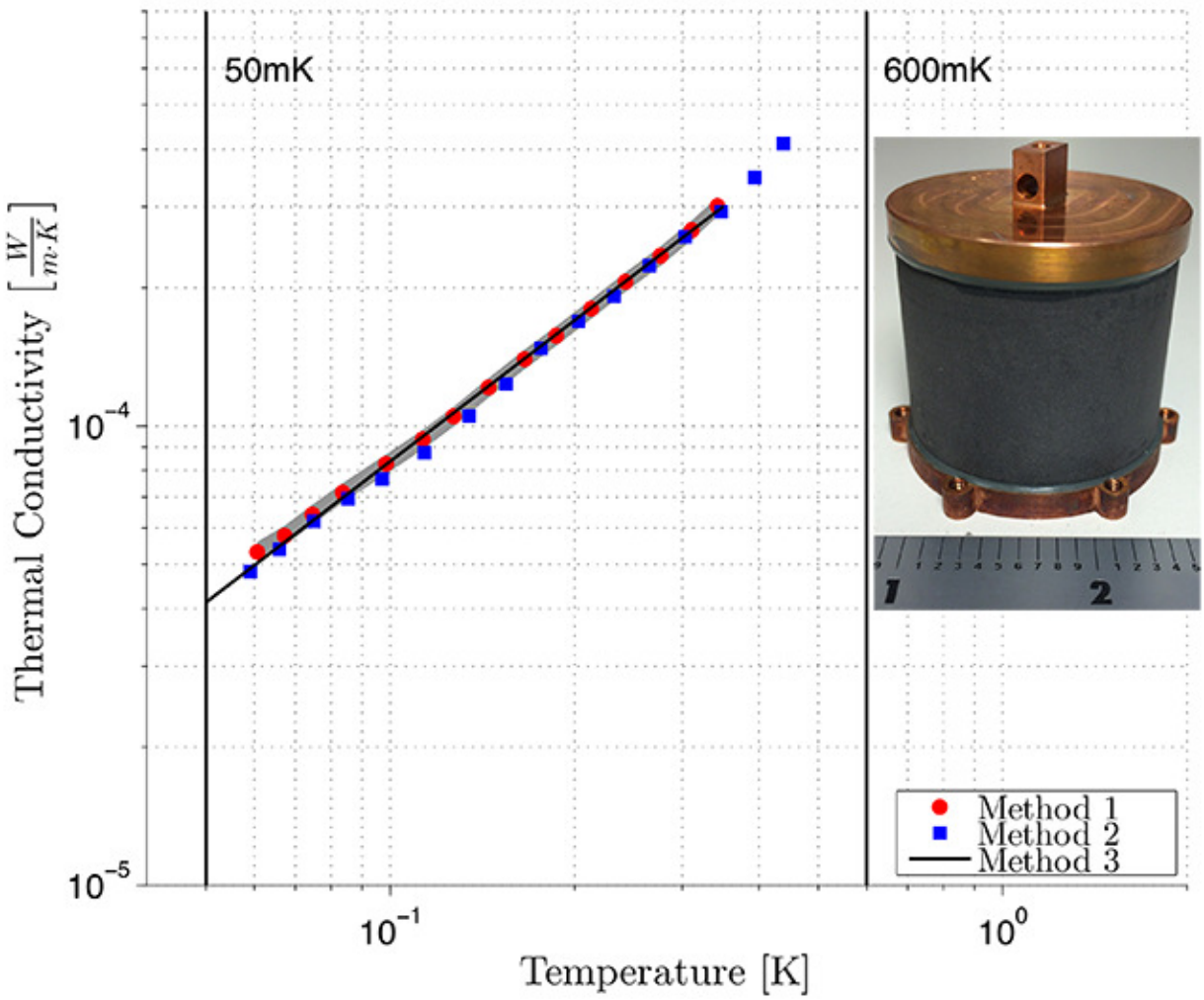


Figure C.17: Mersen 2020 Graphite thermal conductivity. Heat is directed parallel to grain.

Different grades of carbon fiber are available having tensile elastic modulus up to 1000 GPa and tensile strength 1–7 GPa. The mechanical properties of the carbon fiber can be choose to achieve mechanical properties desired for the CFRP products in which they are used.

Graphlite is a very low cost, pultruded carbon-fiber composite made by Avia Sport Composites. Short carbon fibers are suspended in bisphenol-based epoxy and oriented approximately parallel to the pultrusion direction. Thermal conductivity was measured for a 0.156 inch diameter rod of "standard" modulus material, parallel to the axis of the rod which is also the pultrusion axis. The material has 67% fiber fill volume. The thermal conductivity measured here, Figure C.18, is comparable to that measured in [158] for a similar pultruded carbon fiber reinforced polymer.

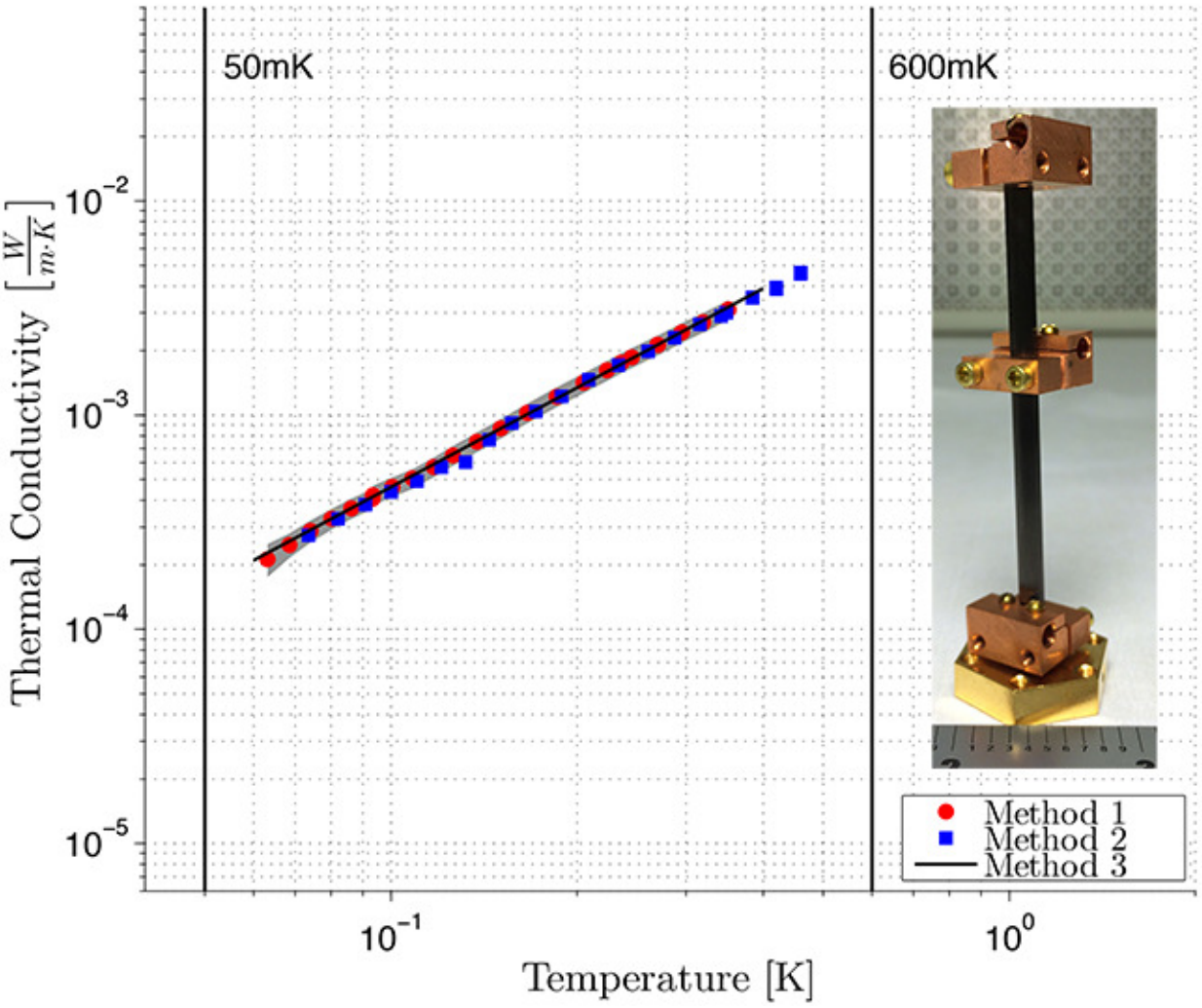


Figure C.18: Graphlite CFRP thermal conductivity.

C.4 Fit Parameters

Material	Shape[a]	Model & parameter fit values				Range [K]
		$^{e}\log_{10}\left(\kappa(T)\ \left[\frac{W}{m\cdot K}\right]\right) = \sum_{i=0}^{3} a_i \cdot [\log_{10}(T)]^i$				
		a_0	a_1	a_2	a_3	
Nb-47Ti	F	−1.801 784	1.727 441	−0.307 130	−0.033 778	0.056–1.60
Nikaflex	P	−2.19	1.01	−0.348		0.06–0.8
Pyralux	F	−1.907 570	1.261 380	0.115 360	0.350 719	0.0635–1.65
Cirlex	F	−2.326 051	0.544 251	−0.435 886	0.075 411	0.0518–1.41
		$\kappa(T)\ \left[\frac{W}{m\cdot K}\right] = a \cdot T^b$				
		a	b			
Graphite 2020 $\parallel$[b]	R	$8.77 \cdot 10^{-4}$	1.02			0.05–0.35
Graphite 2020 $\perp$[c]	R	$7.88 \cdot 10^{-4}$	1.00			0.075–0.5
Graphlite CFRP	R	$1.60 \cdot 10^{-2}$	1.54			0.06–0.4
Vespel SCP5000	R	$1.380 \cdot 10^{-3}$	1.113			0.08–0.6
Vespel SCP5050	R	$1.11 \cdot 10^{-3}$	1.98			0.09–0.45
Vespel SCP5050[d]	R	$1.16 \cdot 10^{-3}$	1.98			0.14–5.2
Vespel SP22	R	$2.48 \cdot 10^{-3}$	2.24			0.12–0.3
Ti 15333	F	$1.3112 \cdot 10^{-2}$	2.101			0.06–1.25
Ti 15333	P	$1.570 \cdot 10^{-2}$	1.97			0.06–1.1
Ti 15333	R	$1.884 \cdot 10^{-2}$	1.82			0.07–0.250
Ti 21S	P	$1.639 \cdot 10^{-2}$	1.96			0.06–0.8
		$\kappa(T)\ \left[\frac{W}{m\cdot K}\right] = \alpha \cdot T \cdot e^{\beta T^{\gamma}}$				
		α	β	γ		
Ni-Ti	P	$4.179 \cdot 10^{-2}$	−0.0013	−2.5336		0.05–1.0

[a] Abbreviations are:"P" - plate; "F" - foil, film or sheet; "R" - rod or round.
[b] Thermal conductivity for heat flowing parallel to grain structure.
[c] Thermal conductivity for heat flowing perpendicular to grain structure.
[d] Data set for second run of Vespel SCP-5050. This run uses narrower thermometer mount contact interval, shorter sample length, and different thermometers. We obtain good agreement with other SCP-5050 run suggesting a robust measurement technique.
[e] This equation is a logarithmic polynomial in both variables. We found this model to be effective since changes in thermal conductivity are often on log scales. It also allows us to confidently extrapolate past the range of validity without having to worry too much about the polynomial quickly going to positive or negative infinity.

Table C.1: Best fit parameters values for thermal conductivity data measured in our 75 µW dilution cryostat. Values were determined using method 3 in § C.2. All data points used in the fit are within a 60% confidence interval.

Appendix D

Part Drawings

D.1 Thermal resistance test device

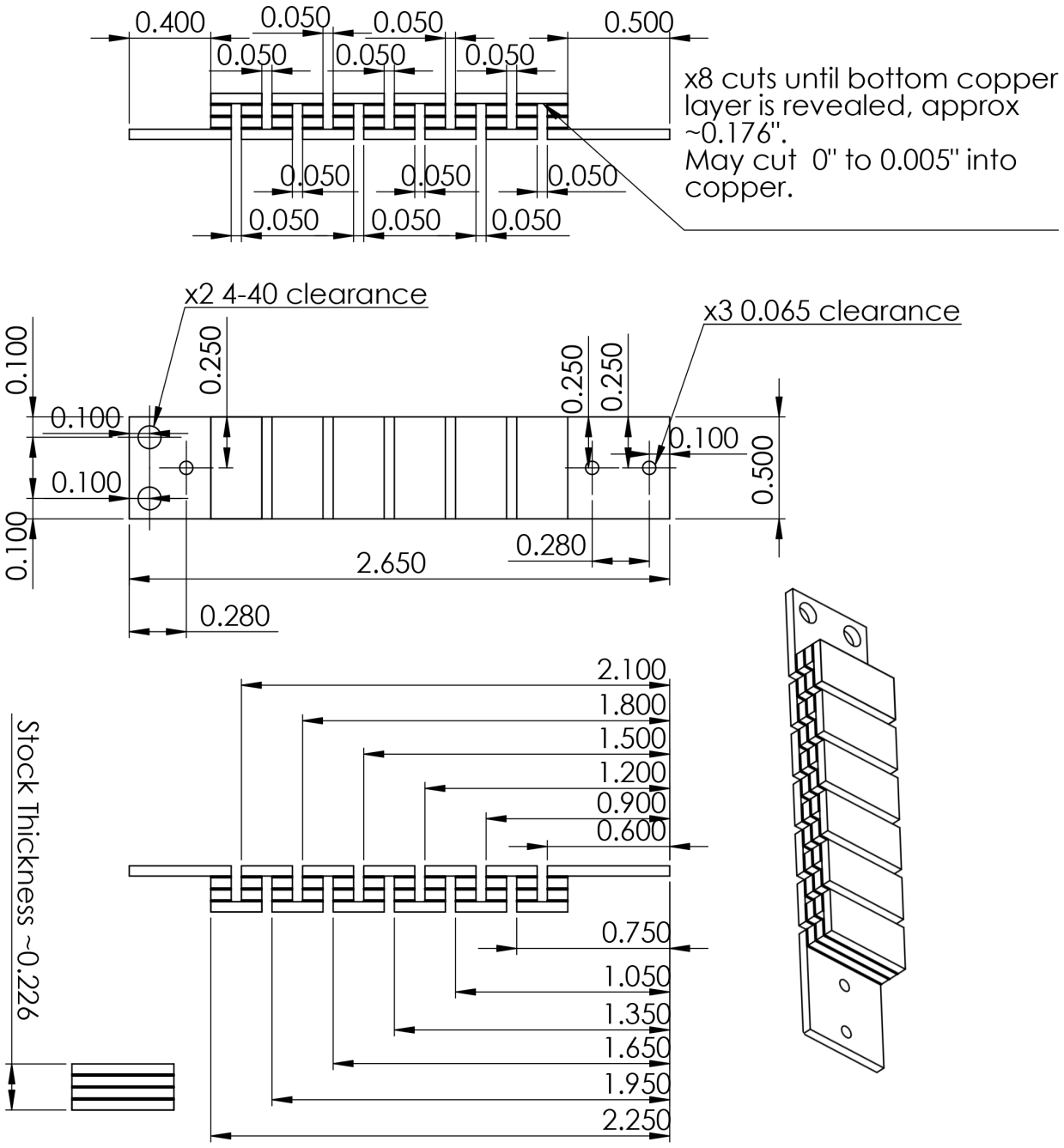


Figure D.1: Thermal resistance sample fabrication drawing. Dimensions are in inches.

D.2 Transition pad

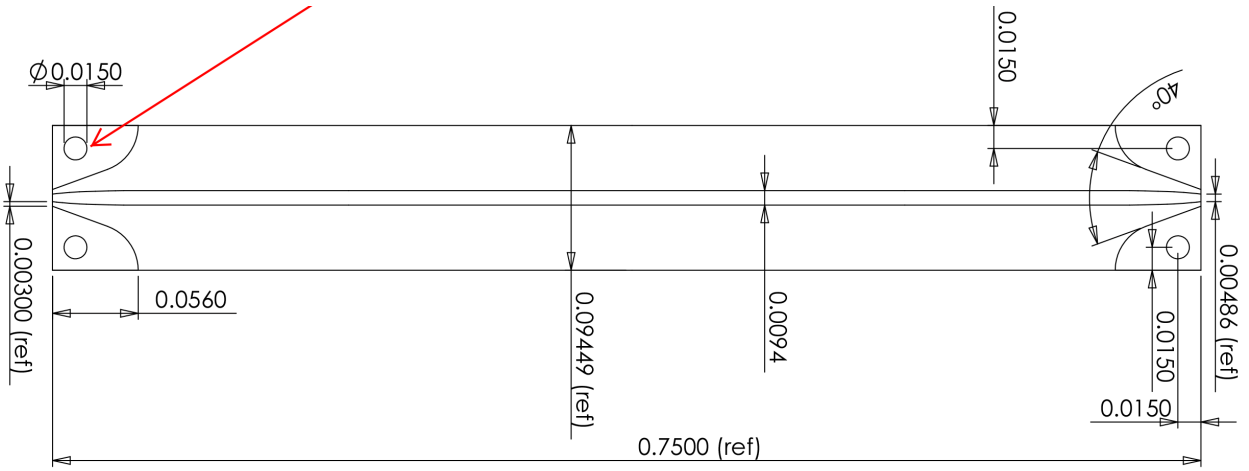


Figure D.2: Microstrip to coplanar waveguide transition pad with selected dimensions, in inches. Material is Rogers duroid 6010LM, 0.010" thick, 1/2 oz. copper backing. Top and bottom metal plated with 40 µinch nickel, then 100 µinch min gold per MIL-G-45204 C, Type III - 99.9%, Grade A - Knoop hardness 90 Max, Class 2. Line tolerance is ±0.001 inch. Red arrow points to plated through hole, or which there are four. The pads are cut somewhere in the microstrip section and the end is glued or soldered in to place.

D.3 KIDs test box

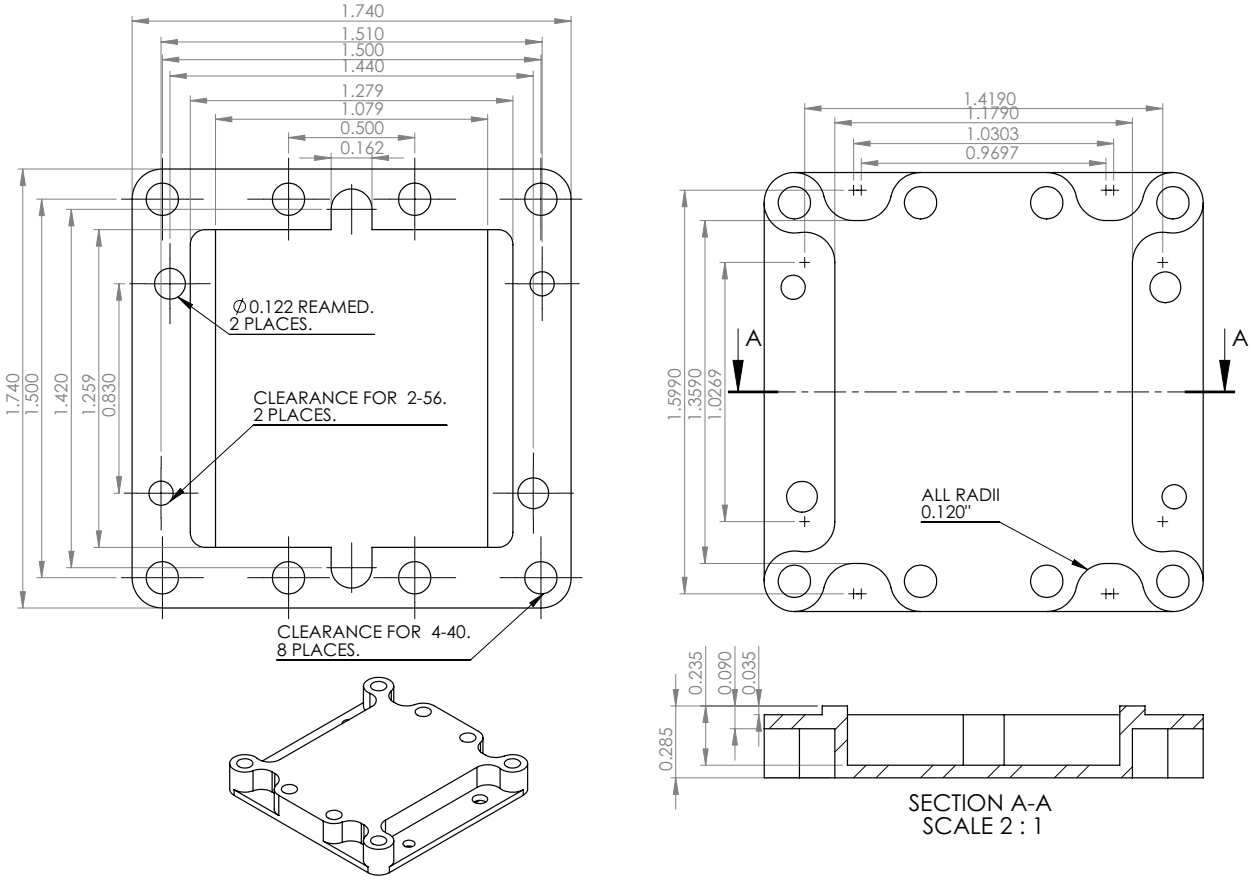


Figure D.3: KIDs test box top fabrication drawing. Dimensions are in inches.

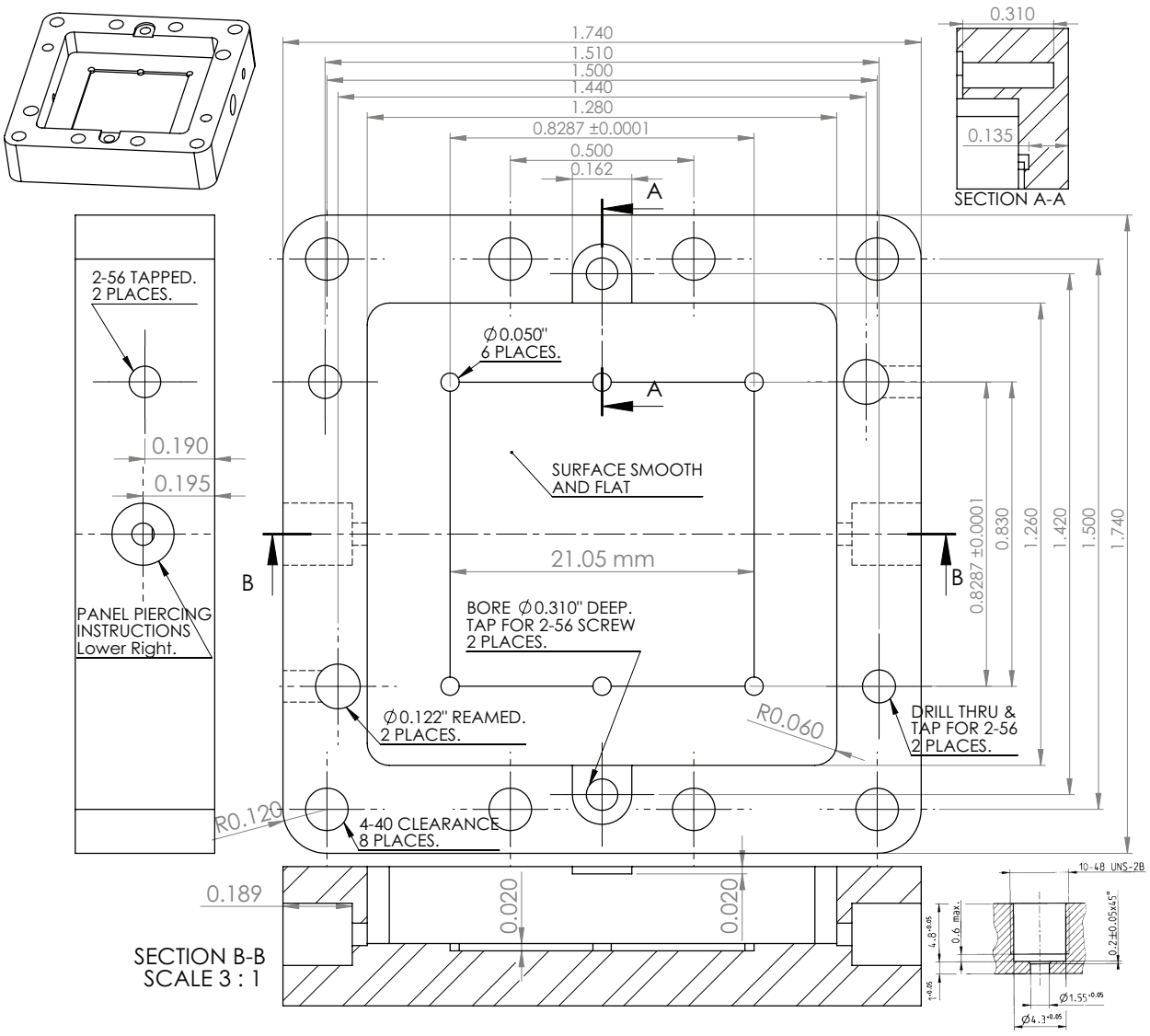


Figure D.4: KIDs test box bottom fabrication drawing. Dimensions are in inches except for the panel peircing instructions in the lower right, which are in millimeters. These instructions are taken from Rosenberger drawing MB_227A and are for their bulkhead SMP plug limited detent 19S105-500L5 connector.

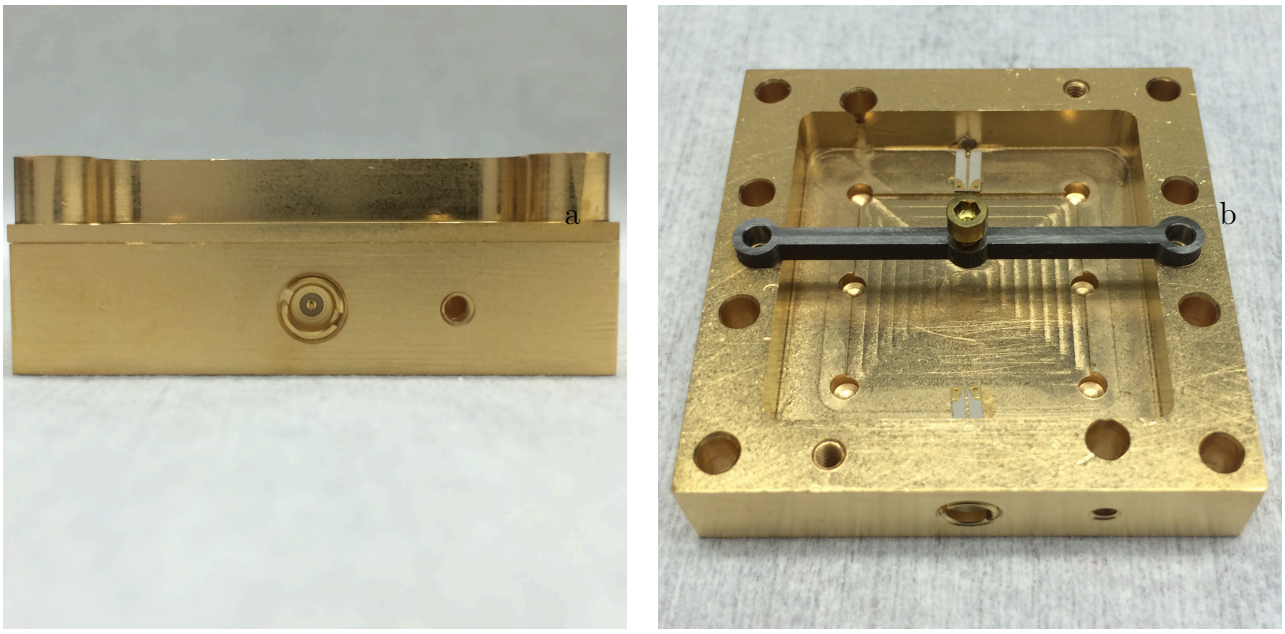


Figure D.5: View if a fabricated KIDs test box, made of copper plated with gold, no nickel diffusion barrier plate. (a) – One sees the SMP blind mate connector. (b) – The titanium cross bar for the press and the transition pads are in place.

D.4 Tower standoffs

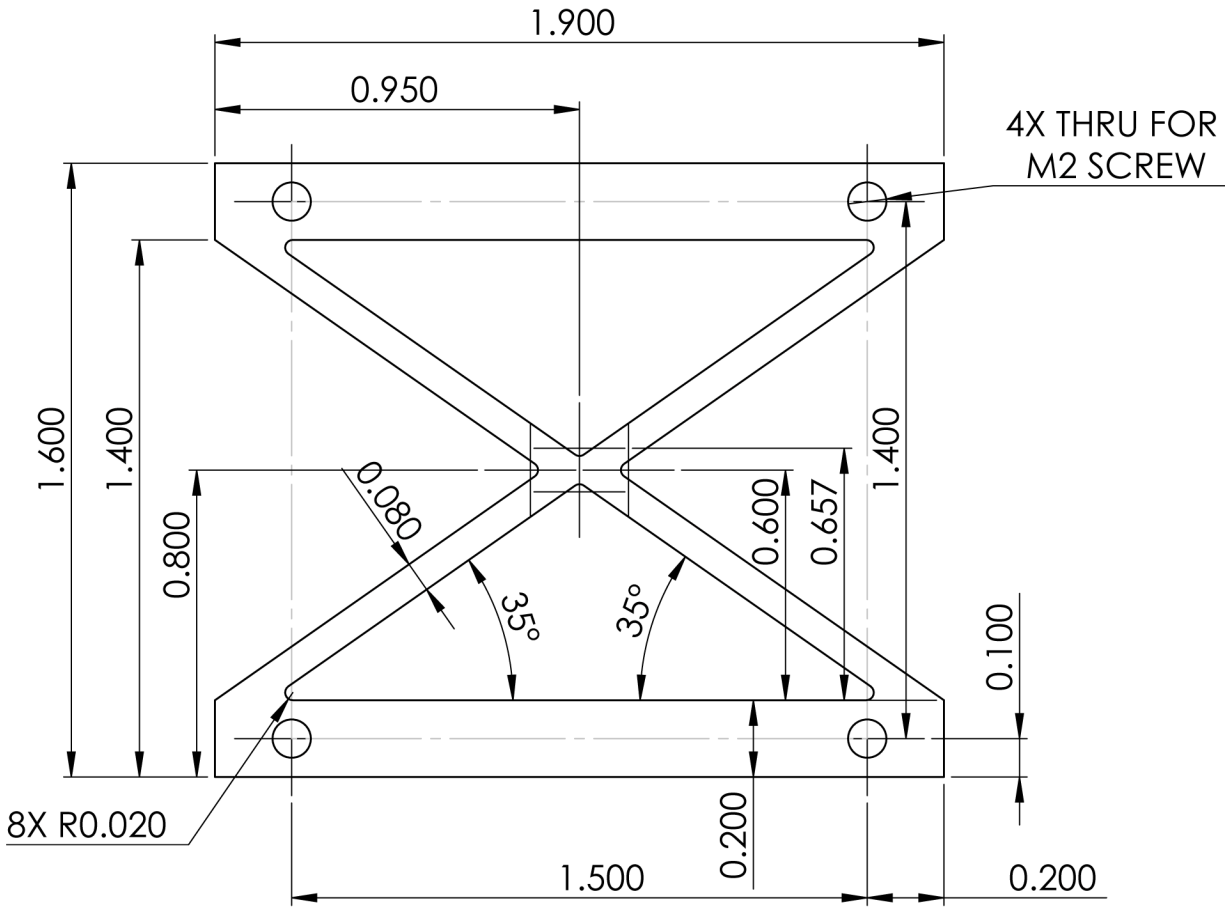


Figure D.6: Ti 15-3-3-3 X-frame fabrication drawing.Dimensions are in inches.

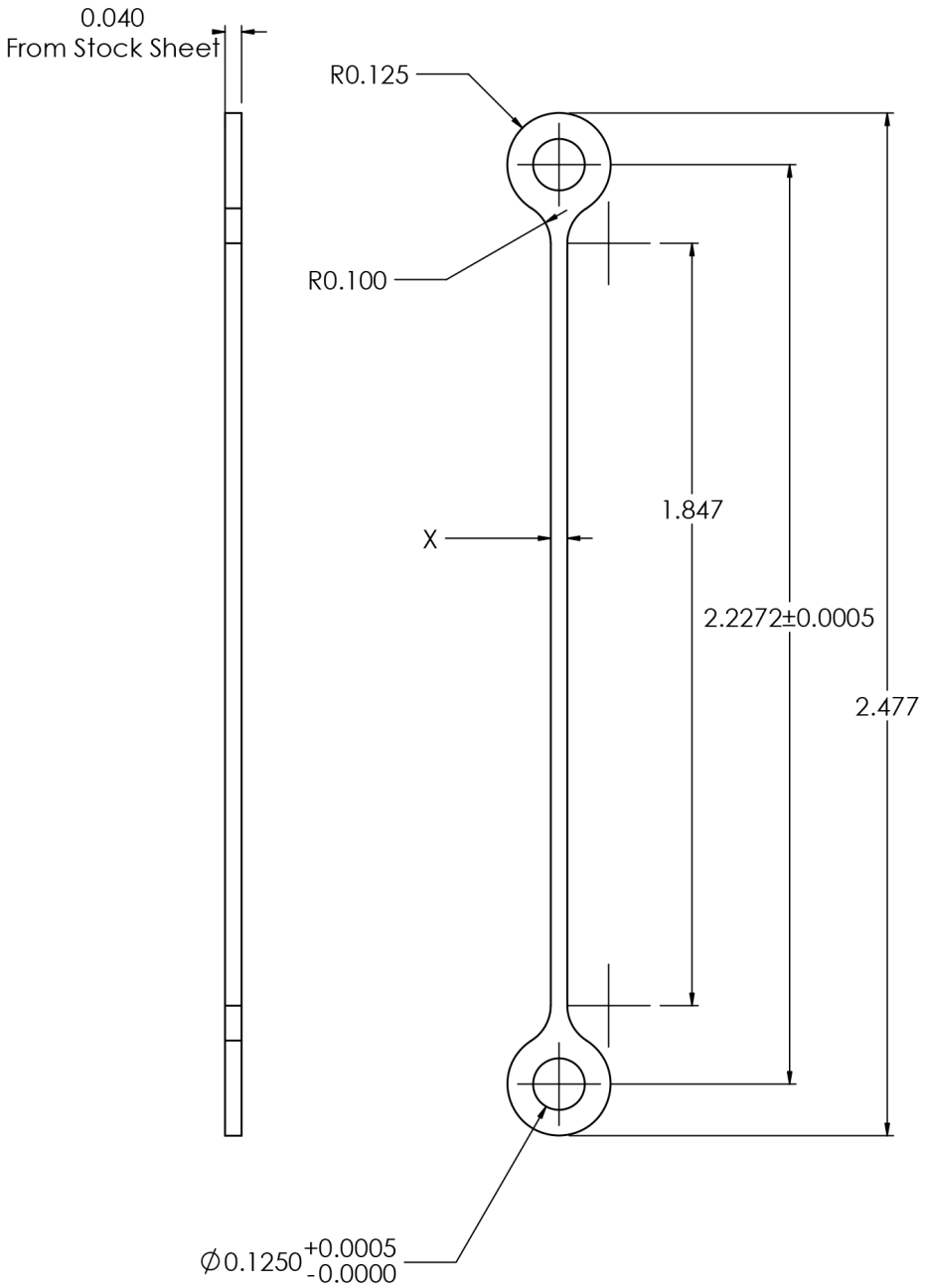


Figure D.7: Ti 15-3-3-3 hexipod member fabrication drawing. Dimensions are in inches. The dimension X is either 0.06 inch or 0.04 inch

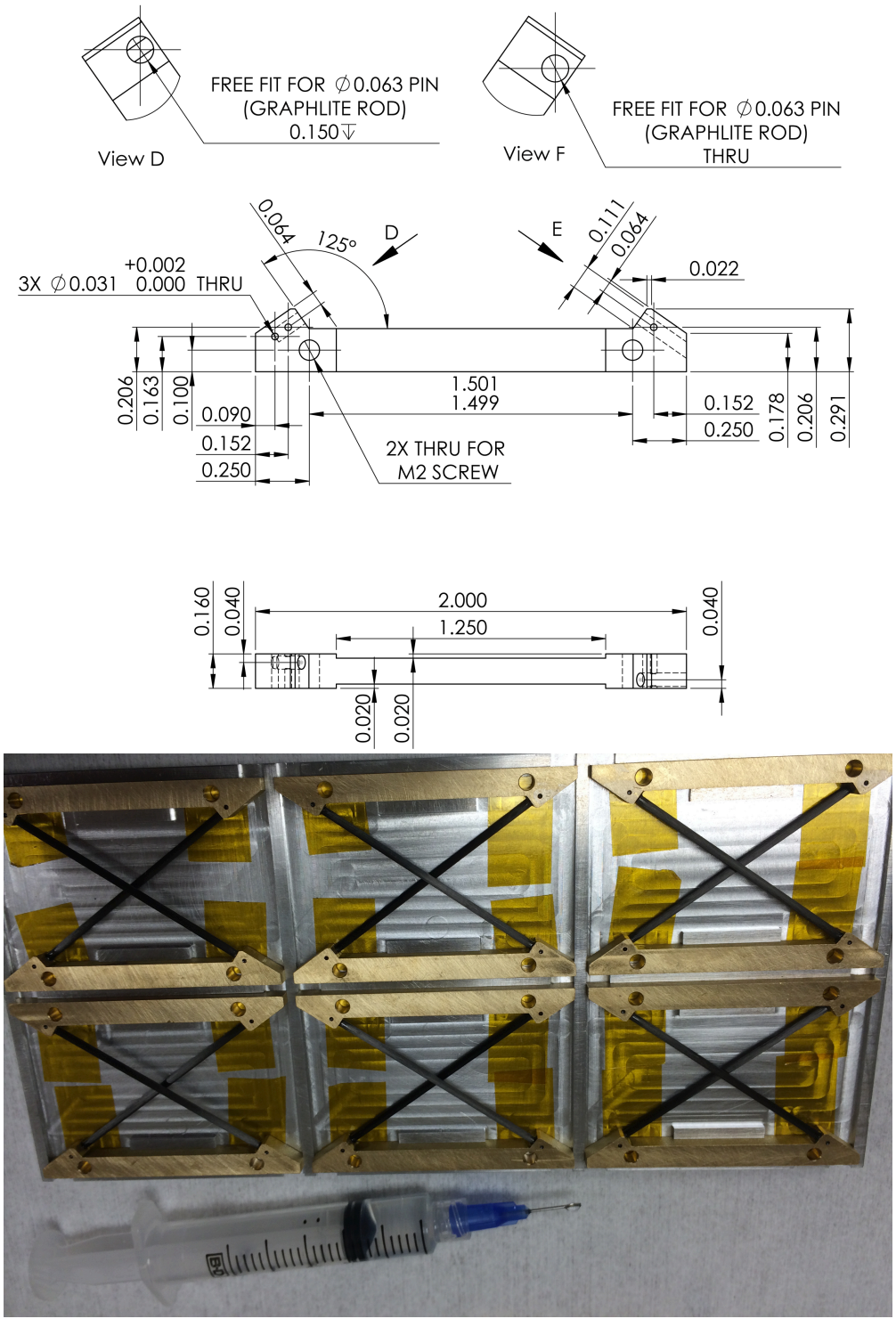


Figure D.8: Graphlite rod X-frame fabrication drawing and gluing fixture. Dimensions are in inches. The rods are cut to 2.221 inch long by ∅0.02 inch (nominal stock diameter). Stycast 1266 epoxy is applied into holes using a syringe. X-frame base is made of copper (in the SNOLAB experiment) or brass.

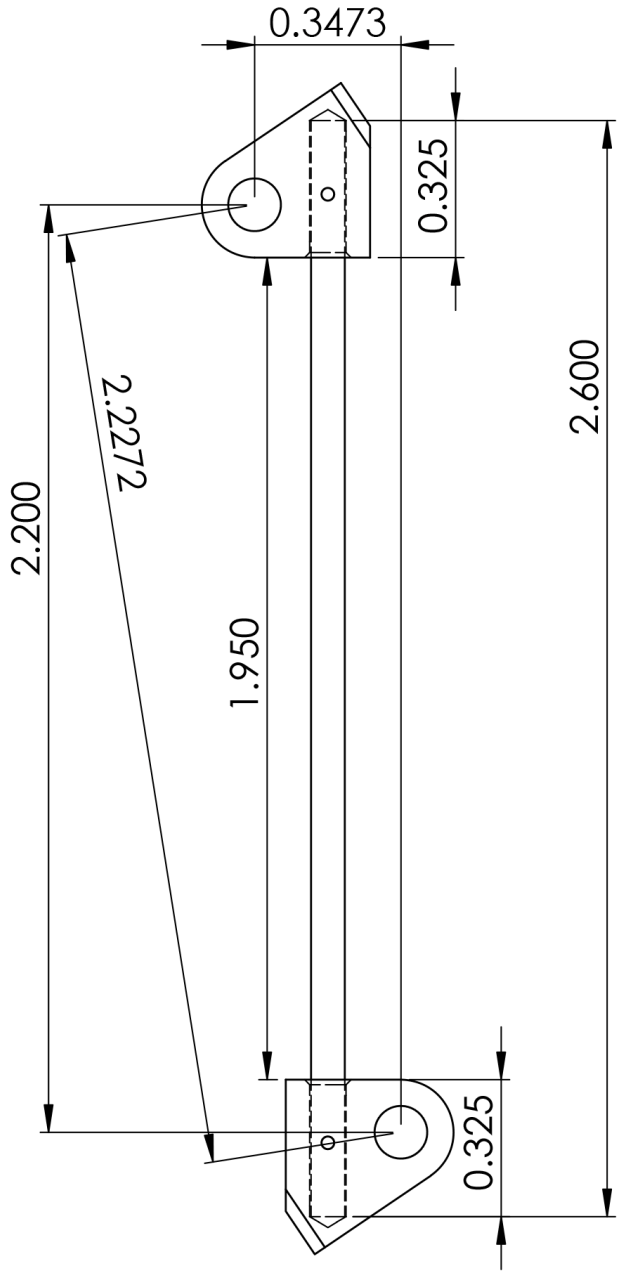


Figure D.9: Graphlite hexipod member fabrication drawing. Dimensions are in inches. Notice that the rod is not aligned with a line connecting the attachment hole centers. This leads to twisting and is a bad design. End caps made of brass. Graphlite rod epoxied into caps using gluing fixture and Stycast 1266.

D.5 Coaxial vacuum passthrough

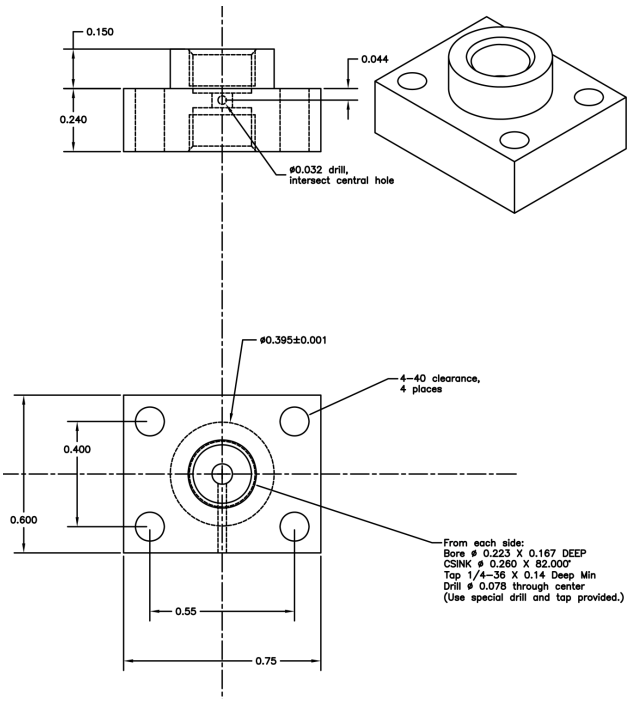


Figure D.10: Coaxial vacuum passthrough fabrication drawing. Dimensions are in inches. Design is from Dr. Peter Day at the NASA Jet Propulsion Laboratory. Material is brass.

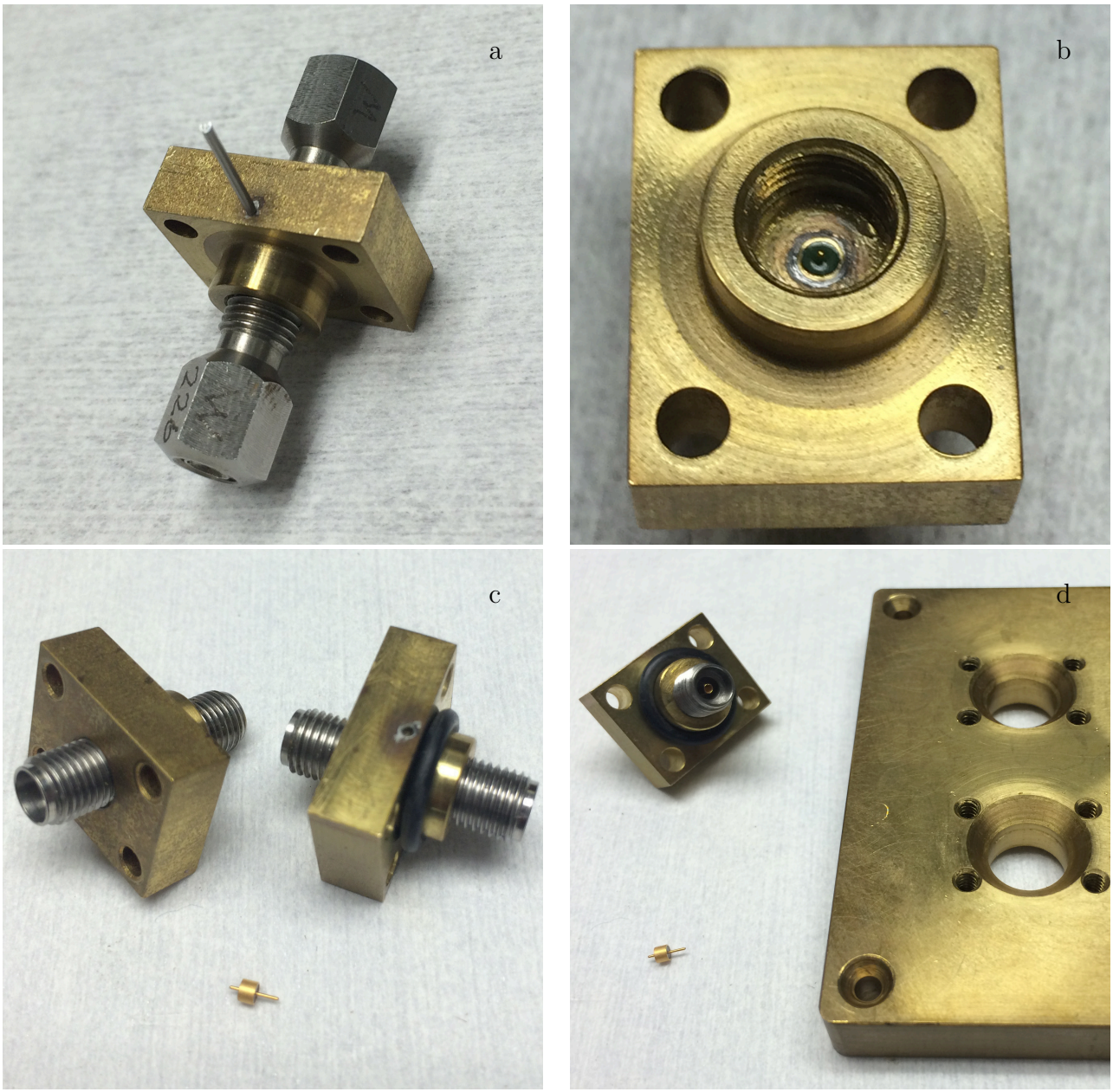


Figure D.11: Coaxial vacuum passthrough in preparation for use. (a) – positioning fixtures for the bead are screwed into place. Solder is loaded in to hole that intersects bead. The assembly is then placed on a hotplate and heated until solder melts, then quickly removed from heat. (b) – the bead is now soldered into place. (c) – SMA "spark plug" connectors are torqued to 16 inchlb. The o-ring fits over the nipple of the passthrough. A glass bead is displayed, and one can see the gold plating of its cylindrical surface, as well the the center pin. (b) – a mating flange is displayed with the passthrough. In this case, the seal is formed with a triangular gland. A standard axial gland is also a choice. These same passthroughs can also be used at cryogenic temperatures. In this case, an indium seal is used and no mating gland is needed.